Springer Series on Chemical Sensors and Biosensors 10
Series Editor: Gerald Urban

Wolfgang Fritzsche
Jürgen Popp *Editors*

Optical Nano- and Microsystems for Bioanalytics

Springer

10
Springer Series on Chemical Sensors and Biosensors

Methods and Applications

Series Editor: G. Urban

For further volumes:
http://www.springer.com/series/5346

Springer Series on Chemical Sensors and Biosensors

Series Editor: G. Urban

Recently Published and Forthcoming Volumes

Optical Nano- and Microsystems for Bioanalytics
Volume Editors: W. Fritzsche, J. Popp
Vol. 10, 2012

Mathematical Modeling of Biosensors
An Introduction for Chemists and Mathematicians
Volume Authors: R. Baronas, F. Ivanauskas, J. Kulys
Vol. 9, 2010

Optical Guided-wave Chemical and Biosensors II
Volume Editors: M. Zourob, A. Lakhtakia
Vol. 8, 2010

Optical Guided-wave Chemical and Biosensors I
Volume Editors: M. Zourob, A. Lakhtakia
Vol. 7, 2010

Hydrogel Sensors and Actuators
Volume Editors: Gerlach G., Arndt K. -F.
Vol. 6, 2009

Piezoelectric Sensors
Volume Editors: Steinem C., Janshoff A.
Vol. 5, 2006

Surface Plasmon Resonance Based Sensors
Volume Editor: Homola J.
Vol. 4, 2006

Frontiers in Chemical Sensors
Novel Principles and Techniques
Volume Editors: Orellana G., Moreno-Bondi M. C.
Vol. 3, 2005

Ultrathin Electrochemical Chemo- and Biosensors
Technology and Performance
Volume Editor: Mirsky V. M.
Vol. 2, 2004

Optical Sensors
Industrial, Environmental and Diagnostic Applications
Volume Editors: Narayanaswamy R., Wolfbeis O. S.
Vol. 1, 2003

Optical Nano- and Microsystems for Bioanalytics

Volume Editors:
Wolfgang Fritzsche
Jürgen Popp

With contributions by

A. Aloisi · P.C. Ashok · H. Becker · G.G. Bentini · B.P. Cahill · J. Cao · M. Chiarini · S. David · K. Dholakia · W. Fritzsche · A. Funfak · C. Gärtner · E. Gheorghiu · M. Gheorghiu · T. Henkel · M. Hoffmann · S. Julich · M. Kielpinski · R.K. Kribich · D. Kürsten · L. Leroy · T. Livache · E. Maillart · D. Malsch · A. März · J. Metze · J. Michael Köhler · P. Mike Günther · R. Möller · A. Olaru · C. Polonschii · J. Popp · P.D. Puiu · M. Riedel · R. Rinaldi · P. Rösch · S. Schneider · S. Sinzinger · M. Urban · S. Wagner · S. Werres

Springer

Editors
Professor Dr. Wolfgang Fritzsche
Institute of Photonic Technology
(IPHT)
Nanobiophotonics Department
Albert Einstein Straße 9
07745 Jena, Germany

Professor Dr. Jürgen Popp
Institute of Physical Chemistry and
Abbe Center of Photonics
Friedrich-Schiller University Jena
Helmholtzweg 4
07743 Jena, Germany
and
Institute of Photonic Technology (IPHT)
Albert Einstein Straße 9
07745 Jena, Germany

ISSN 1612-7617
ISBN 978-3-642-25497-0 e-ISBN 978-3-642-25498-7
DOI 10.1007/978-3-642-25498-7
Springer Heidelberg Dordrecht London New York

Library of Congress Control Number: 2012931152

Printed on acid-free paper

Springer is part of Springer Science+Business Media (www.springer.com)

Series Editor

Prof. Dr. Gerald Urban

IMTEK - Laboratory for Sensors
Institute for Microsystems Engineering
Albert-Ludwigs-University
Georges-Köhler-Allee 103
79110 Freiburg
Germany
urban@imtek.de

Aims and Scope

Chemical sensors and biosensors are becoming more and more indispensable tools in life science, medicine, chemistry and biotechnology. The series covers exciting sensor-related aspects of chemistry, biochemistry, thin film and interface techniques, physics, including opto-electronics, measurement sciences and signal processing. The single volumes of the series focus on selected topics and will be edited by selected volume editors. The *Springer Series on Chemical Sensors and Biosensors* aims to publish state-of-the-art articles that can serve as invaluable tools for both practitioners and researchers active in this highly interdisciplinary field. The carefully edited collection of papers in each volume will give continuous inspiration for new research and will point to existing new trends and brand new applications.

Preface

The detection and identification of biomolecules represents an ever growing part of analytics that influences our lives in various fields, e.g., the diagnosis of genetic or acute diseases, and forensic identification or the monitoring of food safety regarding infections or genetically modified contributions.

Although these and more applications have been enabled by the progress in both molecular biology and detection technology in the past, there is no standard use yet directly at the various points of interest (on-site). Instead, rarely these analytical techniques are applied on a routine base, and when applied they are conducted in specialized laboratories. In order to fully explore their potential socioeconomic impact, they would have to be applied routinely and preferably at (or near) on-site. Then the information provided would not be delayed and could be used immediately for a swift response.

There are practical obstacles hindering such on-site methods. The technology used would have to be robust and self-contained, so that users with minimal training could also use them as well as understand the results. On the other hand, contrary to the high-end, high-throughput analytics in specialized laboratories, the equipment costs would have to be significantly decreased. These two points represent probably the main factors still limiting a wider application. Moreover, miniaturization that decreases the required sample volume (which assists in increasing sensitivity) and thereby the costs for reagents represents another point to consider, as well as a sufficient specificity, which is usually determined by the utilized biomolecular assay.

In order to address these requirements of robustness and cost-effectiveness in the context of miniaturization, sensitivity, and specificity, a certain set of bioanalytical technologies has been proposed based on optical detection in microsystems. This book will introduce this field by surveying promising approaches, presenting the state of the art, and discussing future developments.

Micro- and nanotechnologies are driven by the needs of microelectronics, such as the need for ever smaller functional elements (e.g., transistor) in the context of higher integration at the IC level. This technological development is nowadays also used to miniaturize equipment in other fields such as sensorics, and it is widely

applied for miniaturization of optical elements. A variety of integrated light sources, spectrometer, etc., have been developed and can be adapted into miniaturized and integrated analytical devices. Typical examples—which are also the subject of chapters in this book—represent functional elements for guiding as well as characterizing light. Optical waveguides are a key part of optical systems and enable the miniaturization of such systems. On the other hand, the realization of miniaturized optical approaches for the characterization of light such as interferometers or spectrometers allows the design of compact optical systems with optical waveguides for an on-chip transfer of light as well as the analysis of light using different integrated interferometric approaches.

Optical detection can rely on various properties of light which are used as measurement signal, such as intensity (photometry), the description of light as composed of a set of fundamental primary colors (such as RGB) in colorimetry, the use of molecules exhibiting fluorescence, or the extended spectral decomposition as done in spectroscopic methods. From the point of robustness and costs, this list starts from a rather simple technology and ends rather sophisticated. This is also the justification for colorimetry, which yields less quantitative results as spectroscopy, but is doing this with a simpler technique resulting in a robust and cost-efficient technique. The application and its requirements then decide the choice, because the question is not about the best system possible, but about the sufficient one. On the other hand, more complicate techniques such as fluorescence and spectroscopy allow for a new quality in sensitivity and differentiation, respectively, which could open possibilities for applications not covered by the simpler techniques.

Another important aspect of the described approaches represents the parallelization of analytical assays. Due to miniaturization, the parallel incubation and readout of a number of sensor fields is possible and thereby enables answering not just one but a number of analytical questions in one experiment. This ability represents also a motivation for the use of microtechnologies in the context of bioanalytics, because just one assay could (when a certain sensitivity is sufficient) be also realized using the well-known lateral flow assays (test stripes) as established for pregnancy and similar tests. This parallelization at the miniaturized scale requires also new developments in positioning technology, such as spotting or the described electrochemical approach using microelectrodes for localized deposition of the various complementary binding partners.

In order to increase the sensitivity, labels have been introduced. For optical detection, such labels can be dyes with increased absorption or fluorescent abilities. On the other hand, label-free techniques would be preferred when achieving sufficient sensitivity, because they tend to be more robust from the assay process as well as cost efficient when certain incubation and washing steps can be avoided. Typically label-free techniques detect the binding of target molecules by the mass difference, by electrochemical means, or using optical approaches. Although there are established methods for the detection of mass differences such as quartz crystal microbalance, and even integrated developments in this direction based on microstructured cantilever arrays, the detection is connected with movable parts and not easy to integrate higher. Optical detection techniques are often aiming at the

changed refractive index at the sensor surface, which will change when target molecules bind to the complementary capture molecules located there. An established sensoric principle in this field is the use of surface plasmon resonance where conduction band electrons at metal–dielectric interfaces are excited by the electromagnetic field of light. The resulting resonances depend on the refractive index of the dielectric at the interface and are changed upon binding of analyte molecules there. Already in the 1980s converted into a biosensing technology, such surface plasmon resonance (SPR) sensing approaches are widely used in life science for detection and investigation of molecular binding, which is a key process in biological processes. The limitation of the original SPR sensing approach to just one assay is overcome by the imaging SPR approach (SPRi) as described and discussed in a chapter of this book. This approach allows for the monitoring of several assays in parallel and is another example of the general trend to parallelization in bioanalytics.

Raman spectroscopy is another label-free approach. In contrast to SPR detecting only mass changes, Raman represents a powerful method for identification of the respective compound by their fingerprint. This high specificity allows also multicomponent detection. The inherent limitation of low intensities is usually addressed by the use of surface enhancement at metal nanostructures resulting in surface enhanced Raman spectroscopy (SERS) as discussed thoroughly in this book.

Another point of interest in this context refers to the choice of materials. Materials which allow for a rapid and cost-effective replication of microsystem reactors are needed when a mass application is envisioned. Usually plastic materials fulfill these requirements, as discussed in the respective chapter, and allow for the required number of copies. But as several contributions to this book show, already in the demonstrator setups, one can often find materials like PDMS which are not only easily machined but also highly compatible with the biomolecule solution of interest.

Finally, the integration of the several components such as microfluidics, actuators, and optical detection devices is a key issue for the field. Supported by technical developments in the field of miniaturization and optics, approaches have been established allowing for the combination of optical approaches with microfluidics and microsystems. Numerous examples for successful integration of such optical functional elements into microsystems have been demonstrated, with representative examples thoroughly discussed in this book.

This book shows that proofs of principle for a wide field of promising directions for optical bioanalytics in microsystems have been demonstrated. It also presents the fast development in the field, which ensures that over the next years we will witness these techniques finding increasing applications in real-world applications.

Jena, Germany

Wolfgang Fritzsche
Jürgen Popp

Contents

Part I
Photometry, Color Sensors, and Fluorescence Labels

Color Sensors and Their Applications

Poenar Daniel Puiu

Abstract This chapter intends to provide an introduction to and a very brief summary of the principal categories of color sensors and of their applications, both relatively little known to the general public.

First, an introduction describes the background of the topic(s) and the overall context. The main differences between two major but complementary techniques, colorimetry and spectrometry, will be presented here, as well as a quick summary of the scientific, technical, and industrial applications of color sensing. The second section will summarize the basic operational principles and architectures of color sensors realized in silicon. Although stand-alone detectors will also be described and discussed, the main focus will be on solid-state microsensors which can ideally be monolithically integrated together with signal processing circuits onto the same chip as "smart sensors" or intelligent microsystems. First, sensors realized only in monocrystalline silicon are summarized, followed then by those fabricated in other materials, with amorphous silicon and its alloys as the key players in this latter category.

Finally, the chapter ends with the sections devoted to Conclusions and References.

This chapter presents only a few of the most relevant aspects related to color sensors and examples of their practical applications. It is, in fact, an extensively abbreviated version of a much more detailed and exhaustive review dedicated to both color sensing and microspectrometry, and which is presently in preparation for future submission to Springer Verlag.

Keywords Smart sensors • Color filter array (CFA) • Two-junction color sensors • Triple-junction color sensors • Thin film color sensors

P.D. Puiu (✉)
School of Electrical and Electronic Engineering, Nanyang Technological University, 50 Nanyang Avenue, Singapore, Republic of Singapore 639798,
e-mail: epdpuiu@ntu.edu.sg

W. Fritzsche and J. Popp (eds.), *Optical Nano- and Microsystems for Bioanalytics*,
Springer Series on Chemical Sensors and Biosensors (2012) 10: 3–46
DOI 10.1007/978-3-642-25498-7_1,

Contents

1 Introduction—The Color Sensor: Necessity or Just a Curiosity?

Color is one of the most important characteristics of light, although we may not always be aware of this fact and of its importance, taking it for granted.

However, even though color plays a unique role of great importance in our daily life and—as we shall soon see—in quite a few industrial and scientific applications, the number of sensors dedicated to color sensing is surprisingly small and—more importantly—the existence or operation principles of such sensors are very little known to the general public. When "microelectronics" is mentioned, most of the people think of mobile phones, computer microprocessors, or other familiar applications such as DVD players, GPS, or game consoles. In general, the media typically focuses its attention on the latest developments in these areas which are very familiar to everybody, such as telecommunications, computers, and new consumer electronic gadgets.

However, another extremely important area deals with sensors and actuators. Sensors can be briefly defined as devices or systems which detect relevant signals from the environment and convert them into an electric signal or data that are further processed into electronic circuits. Without sensors, most of our technological equipment, from complicated machinery to gadgets that we use daily, would be unable to operate. Sensors pick up the signals containing precious information necessary to either correctly operate equipments or control processes by providing vital data for their feedback. Presently, the trend is to no longer realize discrete sensors which can then be combined with various integrated circuits on a printed circuit board in order to perform a certain desired function. Instead, the technological advances in the area of microelectronic fabrication made it possible to integrate a complete microsystem on a single chip both the sensor and its intelligent signal conditioning circuits as well as digital processing blocks which manipulate the

obtained data. This high degree of integration is possible due to the progresses in two areas. The first key factor is the miniaturization of integrated circuits which has been going on aggressively in the last decades and which has now reached Ultra-Large Scale Integration (ULSI) levels in which the feature size of the transistors is at submicron scale. For instance, Intel's Atom processors presently integrate features as small as 45 nm using a high-k metal gate technology, and this will soon be replaced by a 32-nm silicon process technology [1]. Such advanced fabrication technology allows the realization of extremely complex circuits like microprocessors and Digital Signal Processors (DSPs).

The second factor is the development of Micro-Electro-Mechanical Systems (MEMS) or Micro-Opto-Electro-Mechanical Systems (MOEMS) that can be fabricated in silicon (or other materials) using modified microelectronic processing derived from IC fabrication in order to achieve various structures with different functionalities other than purely electronic ones. This enabled the realization of new and complex structures that can be used as sensors or actuators of various types.

The co-integration of both the sensor(s) and its/their signal processing circuits is demanded by practical considerations such as the reduction of the useful signal magnitude for smaller scale sensors, and the needs to minimize parasitic components and to perform amplification as well as other signal conditioning operations such as scale linearization, filtration, and elimination or minimization of offset and drift. Additional functions can be easily added subsequently using digital circuits of great complexity, and in certain cases, these can process data not only from a single sensor but also from an array of sensors, as is the case in, for example, the "electronic nose," or can control both sensors and actuators embedded in the same microsystem.

Actuators can be defined—in the most general meaning—as devices performing a function complementary to that of sensors; namely, they convert a type of signal (most often electric ones) into another type which is re-introduced back into the environment, either for its feedback control, or by carrying an information/meaning that can be perceived only by the human used. For instance, the computer monitor can be considered as one such actuator since it converts an electrical signal coming from the computer into an optical signal provided into the environment to the human user.

The term "signal" may refer to six different types of measurands: physical/mechanical (e.g., force, acceleration, or displacement), thermal, magnetic, (bio) chemical, radiative, and electric [2].

Yet, despite their importance and ubiquity, sensors and actuators are much less known to the general public, given that, on the one hand, they are usually "hidden" from view, and, on the other hand, the measurement and control field—to which sensors and actuators belong—are not as often and widely popularized as, e.g., consumer electronics.

This introduction may now explain the seeming obscurity of color sensors: they represent just a diminutive group in the family of optical sensors, which is just a small part in the larger category of sensors, which, on its turn, represents only

a niche domain in the measurement and control field, in itself a smaller and less known area than, e.g., consumer electronics or microelectronics.

The same situation is also reflected even in the area of scientific papers. A very quick review of the papers published in reputed scientific journals dedicated to the general topic of sensors (e.g., IEEE Sensors; IEEE Journal of MEMS; Sensors and Actuators; Journal of Micro/Nanolithography, MEMS, and MOEMS; or Sensors & Transducers, to name just the more prominent ones) would quickly confirm to the curious reader that the amount of papers dedicated to color sensors represents only a relatively small percentage of the total number of papers published in those journals. Indeed, many—if not the great majority—of the optical sensors detect only the intensity of light, while other science and technology applications have required the detection of other parameters, such as polarization or phase (whose manipulation, or capture and storage are necessary in certain applications, of which holography is the best known to the public).

There is also confusion or a lack of clear understanding among most people regarding the definition of what exactly colorimetry is and how it differs from spectroscopy—its older, more widely spread, and much better known relative. Without going too much into details which are beyond the limited scope and space of this chapter, we can clarify this by providing quick definitions and highlighting the fundamental principles underlying these two measurement techniques. This is necessary because the difference between these two major but complementary approaches, the spectrometric and the colorimetric approach, is a very significant and fundamental one.

Thus, the colorimetric method relies on the decomposition, analysis, and description of incoming light by means of a set of fundamental primary colors, such as red (R), green (G), and blue (B). In contrast, spectrometry decomposes the incident light into a large multitude of extremely narrow passbands by using a dispersion element, such as a prism or a grating. This spectral decomposition is carried out within a certain wavelength range of the incident light, and this fact highlights another major difference between colorimetry and spectrometry: colorimetry always processes only *visible* light, whereas spectrometric analysis is not limited to the visible range alone and can also be carried out in many other spectral ranges of interest, e.g., ultraviolet (UV) or infrared (IR). Moreover, each of these ranges is typically divided in subdomains, each of which can also constitute the subject of detailed spectrometric investigations. For instance, the IR domain is considered to comprise three such narrower domains: near infrared (NIR; $\lambda \cong 0.7$ μm–3 μm), medium infrared (MIR; $\lambda \cong 3$ μm–8 μm), and far infrared (FIR; $\lambda \cong 10$ μm–100 μm). The ultraviolet (UV) range is "partitioned" in narrower domains as well. The application of spectrometry in such a large number of ranges, domains, and sub-domains, as well as its older age and great importance for a great deal of scientific and technical applications, can all explain the much wider usage of spectrometry and the fact that it is better known even among non-specialists.

Because it splits the operational wavelength range in a large number of very narrow channels and provides a "point-by-point" approximation of the entire spectral information of interest of the analyzed light, spectrometry can be

considered to be much more accurate in comparison with colorimetry, which would offer only a more limited, and rather "averaged," evaluation. However, the spectrometric approach has its own major drawbacks.

First, it requires a much more complicated setup which is considerably more difficult to miniaturize, particularly in a monolithic solid-state solution and/or when high performance is desired, although such microspectrometric solutions can be realized and have indeed been reported. Unfortunately, due to the very limited space of this chapter, we cannot review here the interesting solutions found for the implementation of such microspectrometers. However, it is worth mentioning that many of them do indeed require complicated fabrication and that the requirement to use (monocrystalline) silicon for their fabrication (in order to enable easy integration with signal processing circuits) is not always easily satisfied (in fact, it is very rarely satisfied), particularly for the visible range. This is due to two main reasons. On the one hand, a microspectrometer is not just a simple single device, but it is truly a microsystem of increased complexity and which must include many additional (micro)optical elements (e.g., lenses and gratings) besides photosensors and signal processing circuits in order to perform its function. On the other hand, the usage of silicon is much more convenient for the realization of devices that would operate instead in the IR range.

Second, the very fact that spectrometry offers a dramatically increased amount of information from a large number of output channels makes much more challenging the simultaneous processing of all these data. This further increases the complexity of a spectrometric smart microsystem since it requires the addition of many signal conditioning circuits for all the channels, as well as a complicated digital circuit(s) for subsequent data processing.

Third, one cannot find a single standardized solution for all spectrometric systems. Instead, custom solutions have to be found, depending on each type of operational wavelength domain or sub-domain, and the desired performance requirements for the intended specific task. Even for the visible range, a multitude of solutions and implementations can be found, and the variety is also multiplied by the fact that the number of channels is not fixed and may vary from one application to another.

In contrast, colorimetry is a solution which is not only simpler to implement but is also easier to standardize, making it much cheaper. More importantly, the standard RGB output is directly compatible with the human vision response and thus is immediately applicable for imaging applications. All these factors made colorimetry to become a very valuable analytical tool in its own right. If, for the moment, our attention focuses not on the color sensors but on the real-life applications of color detection and quantification, it will quickly become evident that colorimetry is actually quite a well-established technique with many important applications in a large range of fields or industries. The main areas of such applications can be loosely divided into the following categories: Chemistry, life sciences, food & beverages industry, cosmetics, wood & paper processing as well as the printing and textile industries, and electronics & optoelectronics. Given the fact that the importance of colorimetry for practical applications is relatively little

known to the general public, the following subsections will provide several examples of real-life applications of color sensor and colorimetry in some of these fields. The description of color sensors and their operation principles will be subsequently presented in a separate section after this short review.

1.1 Chemistry

Chemistry, and by extension, biochemistry and the Life Sciences, as will be presented in the next sub-section, heavily rely on color detection for many practical purposes. Indeed, chemistry and medicine were most probably the very first fields in which colorimetry has been extensively applied even from their early stages of development. The Beer–Lambert law and the direct connection between the concentration of a substance and its color in a solution are the underlying principles on which are based the technical applications in organic and inorganic chemistry as well as biochemistry.

One of the first—and probably one of the best known—applications of colorimetry was for the measurement of pH, and its subsequent extension to the measurement of pK and even to complex tasks such as the analysis of multicomponent mixtures and precision measurements for various routine industrial chemical processes, had already been achieved before World War II [3–8].

Presently, colorimetry still plays an important role in chemistry, but it is applied in practice using new and different methods, which will be briefly presented here. Thus, one technique relies on the usage of sol–gel films that can be used for measuring pH as well as the concentration of metal ions. These sensors proved to be inexpensive, accurate, unaffected by temperature up to 40°C, fast, and reusable.

Another is the usage of polymers, which have become an attractive alternative due to their availability, low cost, and ease of usage. One such sensor employed a polyester–cellulose acetate double layer onto which a pH indicator dye was covalently immobilized and which could be employed in an optoelectronic setup to determine the pH value in the range 6–10 [9]. Another example is that of an autonomous sensor, i.e., which could be deployed and used repeatedly in varied conditions with minimal or no human input. This was achieved by moving the sensor in either a measurement zone or in regenerative ones (one acidic and one basic). The movement was obtained using a compact trilayer membrane comprising polypyrrole (PPy) outer films as actuating elements and a central polyvinylindene fluoride (PVDF) membrane as the central backing material. The pH sensor itself consisted of a polyethylene film coated with bromocresol green dye [10].

Much more recent trends in this area are the application of "smart textiles," or of nanotechnology. An example of the former was obtained by the immobilization of a dye—to which various concentrations of dimethylamine (DMA) have been added—in a viscose textile matrix. Both color changes and fluorescence quenching resulted as a function of the pH, while reactions with ammonia and methylamine were also observed and they were more efficient than those with the dye solution

alone. This realization has thus proven that "smart textiles" may become in a near future a very convenient, low-cost alternative of high sensibility and reproducibility that is also highly suitable for mass production for easy, fast, and accurate analysis for medical or environmental applications [11].

An example of the latter is the family of chemical sensors which employ color change induced by the swelling of a detecting matrix or another type of modification brought onto a material with a periodic structure. A key advantage offered by such sensing materials that are structurally colored is that they eliminate the need for dyes or tags, hence they do not suffer from any photobleaching effects, while at the same time also simplifying the sample pre-processing. Two types of such chemical sensors can be briefly mentioned here.

An example of the first type is a hologram-based humidity sensor which used the holographic pattern recorded in an acrylamide-based photopolymer as a diffraction grating. Since the material swells or shrinks when exposed to various relative humidity values, the fringe spacing is modified, resulting in a change in the observed color [12]. A related realization employed molecules attached to the gratings surface so that the reflected wavelength (color) shifted correspondingly when target molecules linked to the grating surface's receptors due to the change in the optical path of light coupled into the grating. This technique was experimentally demonstrated to detect the binding of biotin to avidin, of a five amino acid peptide, and the cleavage of a portion of the bound molecule, respectively [13].

An example of the second type of chemical sensors employs a three-dimensional (3D) colloidal crystal realized by embedding mono-disperse polystyrene nanoparticles in PDMS. Because PDMS swells in nonpolar organic solvents, when the resultant colloidal composite was subjected to such substances, its lattice constant and thus the wavelength of the Bragg diffracted light increased, resulting in a colorimetric detection of such volatile organic compounds (VOCs) [14]. Another interesting example of a chemical sensor that also made creative usage of nanotechnology is that of colloidal crystal films formed from composite core/shell nanospheres for selective sensing of multiple vapors at very low concentrations The nanospheres consisted of a core made of a material preferentially responsive to one class of chemicals (e.g., polystyrene), which was then coated with a shell made of a second material which was preferentially responsive to another class of chemicals (sol–gel). The chemical compositions of the core and the shell could be varied depending on the analytes of interest, thus enabling the designer to tune the sensor response. A colloidal crystal array was then self-assembled into a 3D ordered film. Sorption of polar or nonpolar vapors induced a change in the optical lattice parameters of the colloidal crystal array as a function of analyte concentration, determining on its turn a variation in the Bragg diffraction wavelength, i.e., of the film's reflected color [15].

Similarly, a photonic crystal with an inverse polymer-gel opal could be swelled or shrunk by electrochemical oxidation/reduction, resulting in modification of the wavelength of the light diffracted by it in a large range, from UV through the visible to NIR [16]. Another analogous structure comprised 1D multilayer stacks (also known as Bragg stacks) of mesoporous TiO_2 and SiO_2. The color exhibited by

this mesoporous Bragg stack (MBS) is dictated by its high reflectivity at a certain wavelength of light λ_B which is caused by the periodic variation in the effective refractive index (RI). The overall response of this MBS was observed to depend not only on the RI of an analyte but also on other physical properties, such as hydrophilicity. Various such MBS structures were successfully used to detect a large range of volatile compounds, such as alcohols, and exhibited superior sensitivity in comparison with a conventional Bragg reflector with just a single porous layer as the chemical sensing element. The MBS provided different responses even when it was exposed to two substances with very similar RIs [17].

Finally, dyes and chromophores form a vast section of considerable importance in chemistry and biochemistry and with a great many applications. For brevity, only two examples of reported applications in this area will be mentioned here.

In the first one, a copolymer bearing a covalently attached solvatochromic dye (the so-called Reichardt's dye) was used as an optical sensor to detect interactions with β-cyclodextrin [18]. The second one employed chromoionophores (i.e., molecules changing their color on complexation with the compound that is to be measured) in order to detect a metal ion in solution (e.g., Ca^{2+}) [19].

Fluorescence is another area of major relevance within the same section related to dyes and chromophores. Since it was one of the first bio/chemical investigational methods developed more than a century ago, fluorescence has been gradually perfected to a high level of performance and finesse and is presently one of the most convenient detection techniques widely used in numerous variants, including multi-dye (i.e., multi-color) applications and single-photon detection.

A great wealth of work has been carried out and an overwhelming number of papers dealing with the application of fluorescence, particularly in life sciences, have been generated. From this tremendous volume of information, we shall highlight here just a few, related to lesser known applications in Chemistry. For instance, fluorescence was employed for optical pH sensing with aminofluorescein as indicator [20], for detecting Li ions using two-color fluorescence [21], or for monitoring of commercial gasolines by quantifying the intensity of the Stokes-shifted fluorescence from some of the heavier polycyclic aromatic hydrocarbons C_xH_y, $(x,y) \geq (14,10)$, that are present in gasolines as minor constituents [22]. A fluorescence smart detector for capillary analysis was realized and employed for concentration and molecular discrimination from the average wavelength of fluorescence spectrum. The microsystem comprised a buried double *pn* junction color sensor integrated onto the same chip with CMOS signal processing circuits and has been tested using FITC and Rhodamine B in different concentrations with a capillary having an illuminated volume of about 5 nl. The best results have been obtained with FITC, which was detected in concentrations as low as 10^{-10} M [23].

Other applications focused on the challenging task of detecting numerous analytes that are neither intrinsically fluorescent nor can be rendered fluorescent by means of labeling, e.g., pH, O_2, CO_2, ammonia, and glucose. In such cases, a preferred solution is the usage of a "paint" that can be applied (by painting or spraying, or by direct manufacturing as a thin film) on a suitable substrate and

which would modify its optical properties when exposed to the (bio)chemical analyte of interest if/when placed in the system to be studied [24].

More applications dedicated exclusively to life sciences are detailed in the next sub-section.

1.2 Life Sciences

In medicine, the alteration in color of a tissue is typically a clear indication of inflammation or of any other deviation from the normal healthy standard outlook, e.g., edema, burns, or necrosis. Moreover, color interpretation has recently become a key ingredient necessary in interpreting the images captured inside the human body using endoscopic probes. Presently, this endoscopic exploration is no longer limited only to analyzing simple reflected light, but also uses fluorescent light, or light scattered or re-emitted due to some physical process (e.g., two-photon excitation, second harmonic generation, or other nonlinear processes) [25]. However, in this case, the color reading and interpretation are not done by a specialized detector, but by examination and analysis of the image captured by the imaging camera chip of the endoscopic probe. This analysis is increasingly relying on specialized image-processing software which implement various algorithms on the captured digital image in order to extract from it valuable markers that could indicate the onset of a certain disease, or determine its stage of advancement.

Nevertheless, purely colorimetric investigation methods have been applied for a long time in medicine and played quite an important role in various applications. Blood oxygenation and urine analysis are just two of the best known applications of colorimetry in medicine. Blood has a particularly well-established history in this respect, with a distinctive place devoted to hemoglobin measurements that are carried out almost exclusively using such colorimetric methods. Very early work had measured the absorption spectrum of anhydrohemoglobin (Hb), and determined the transition points of the system $Hb \rightleftarrows Hb \bullet H_2O$ as well as the thermodynamic constants for the combination of one molecule of water with the iron atom contained within the Hb molecule [26]. Subsequent studies deduced the oxygen equilibrium in a wide range of concentrations for both deoxygenated and oxygenated hemoglobin using colorimetric methods. This enabled to calculate the oxygen equilibrium constants and the association–dissociation constants for deoxyhemoglobin and oxyhemoglobin. Later, both *transmission* and *reflectance* methods were established (alone or in combination) to determine the blood oxygen content in a quick and reliable manner, and both of them relied on the differences between the absorption coefficients of oxy- and deoxyhemoglobin [27]. Other essential blood-related parameters which were measured colorimetrically are the glucose content [28] and the detection of saccharides [29].

The need to carry out faster bio/chemical analyses in a shorter time, at a lower cost, and using samples of significantly reduced volume demanded the realization of miniaturized microsystems which were implemented using dedicated microfluidic

platforms. An ingenious realization of this type employed rapid prototyping of a CD fluidic platform in PDMS, being successfully used in enzymatic assays [30]. A much more recent development used super audio compact disks (SACDs) and computer optical disk drives for multi-wavelength chemical measurements, and it exploited the availability of optical laser pick up heads that produce the wavelengths of 405, 650, and 780 nm (normally used for reading Blu-ray disks, DVDs and CDs, respectively) for determining the chlorine concentration in water [31].

Other efforts focused on the integration of a color sensor within a monolithic chip that also included microfluidics as well as signal processing circuits. An initial simple version consisted of a photodiode formed on a glass substrate and covered by a recrystallized polysilicon thin film which, due to its extremely high absorbance at very short wavelengths, could detect fluoresced light (450 nm) in the presence of the UV excitation light (340 nm). The device was aimed at monitoring enzymatic reactions that convert nicotinamide adenine dinucleotide (NAD) to its fluorescent product NADH (nicotinamide adenine dinucleotide-reduced form) in any of the subnanoliter cuvettes within a large array [32]. This initial realization was further perfected into a fully monolithic microsystem using SU8 microfluidics on top of a Si substrate that integrated the filtered photodiode array together with the readout electronics [33].

Another example of a miniaturized realization is a DNA microarray employing CMOS Buried Double *pn* Junction (BDJ) detectors and a fiber-optic bundle-based illumination and fluorescence collection system [34].

In the area of medical diagnosis, the identification of different types of bacteria after staining with one (or more) suitable indicator(s) is a very well-known and established practice. However, the standard staining procedures are complicated and time consuming, and the development of new, simpler (or more accurate) solutions could be more convenient and attractive. Thus, a zinc-based chromogenic complex was reported to bind preferentially to adenosine triphosphate (ATP) in aqueous solution at physiological pH, causing a visual change in color. This complex was used as a staining agent for different biological cells which could be viewed subsequently with normal light microscopy. Very importantly, this non-lipophilic zinc-based reagent could even be used for distinguishing both Gram-positive and Gram-negative bacteria (prokaryotes) while at the same time being nontoxic to living microbes (both eukaryotes and prokaryotes). The viability of the stained microbes even after staining was confirmed by their subsequent growth in their respective media, in stark contrast with many other dyes available commercially [35].

A similar and very relevant application in the same area is the fluorescent-based detection of the human immunodeficiency virus (HIV). A fluorescence resonance energy transfer (FRET)-based technique was developed to detect changes in fluorescence caused by viral protein receptor binding [36].

Just as for chemistry and many other fields, nanotechnology-based applications become increasingly common in medicine as well. Thus, a colorimetric method employing fluorescent or immunogold assays was developed using a protein

microarray with the ability of serodiagnosis of IgM antibodies, directed against pathogens such as *Toxoplasma gondii*, rubella virus, cytomegalovirus, and herpes simplex virus [37]. Another example is a simple and rapid colorimetric bioassay for the detection of cholera based on a specifically synthesized lactose derivative that has been self-assembled onto gold nanoparticles 16 nm in diameter [38].

Similar realizations were reported for DNA and protein detection, respectively, and were all based on the usage of Au nanoparticles and of their nanocluster-enhanced absorption [39]. The basic operation principle was a strong color shift (from intense red to deep purple) induced by the aggregation of the nanoparticles in the presence of the antigen to be detected. A rather different approach was employed for DNA detection using the variation in opacity of self-assembled nanometallic particles before and after DNA strands pairing which was monitored with a CMOS image sensor [40].

Other important examples of nanotechnology application in medicine can also be cited. One of them is the usage of aptamer-conjugated nanoparticles for sensitive detection of cancer cells. Just as in the previous case, the aggregation of gold nanoparticles in clusters of different sizes induced by their adhesion to cancerous cells results in chromatic changes [41]. In another realization, unmodified silver nanoparticles were used to implement a sensitive, selective, simple, and label-free colorimetric assay to detect enzymatic reactions of ATP dephosphorylation by alkaline phosphatase (CIAP) and of peptide phosphorylation by protein kinase (PKA). In the absence of the enzymes, unreacted ATP protected the silver nanoparticles from salt-induced aggregation, whereas in the presence of the enzymes, the reaction product of ATP (i.e., adenosine for CIAP and ADP for PKA) did not, resulting in a color change of the initial yellow colloidal silver solution with a strong absorption peak at ~400 nm [42].

Although the applications for medicine and biochemistry are by far the most numerous, plant and animal biology are also part of life sciences, and applications like chromatography, electrophoresis, tissue health estimation, fluorescence reading, etc., heavily depend on colorimetric measurements, either in transmission or in reflection. For instance, colorimetric analysis of spectral reflectance was used for a selective herbicide spraying system that could distinguish between crops and weeds [43].

Additionally, oceanography and pedology also include colorimetry in their metrological arsenal. The former uses color measurement and analysis from absorption and scattering of phytoplankton from which chlorophyll concentration, and consequently the phytoplankton population and its general health and biomass, can be deduced. Such measurements enable a more accurate assessment of the state of the observed ocean area and prevent any undesired large-scale event like algae bloom, or monitor a large variety of other important parameters, such as overall photosynthetic potential and amount of yellow substance and suspended matter. Similar judgments related to photosynthesis and biomass could also be done by monitoring the land vegetation's spectrum [44, 45]. A realization employing a 4-channel color sensor was used for a similar purpose, namely, for measuring phytoplankton pigments. The results revealed a strong dependence between the

concentrations of chlorophyll *a* and carotenoid pigments in the phytoplankton cells [46].

Finally, a color sensor was successfully employed in pedology to assess the content of six nutrients in farmland soil [47].

1.3 Food and Beverages Industry

In the food & beverages industry, color is a very important measurand which can be used either for quality estimation, or for automatic selection of products in different categories. Reflectivity measurements can be easily employed for solid foods, whereas for liquid samples, it is much more appropriate to measure the sample in transmission. The previously mentioned dependence of blood color on the concentration of deoxygenated and oxygenated hemoglobin can also be applied to estimate quantitatively the freshness of fresh meat. Thus, by analyzing the reflectance spectrum of beef meat and its variation in time during storage, it was deduced that the typical spectrum changes in time due to exposure to oxygen, which causes the oxymyoglobin to be oxidized into methemyoglobin, resulting in a quality degradation-induced color change that can be automatically sensed so that packaged meat that exceeded its shelf-life could be promptly removed and replaced with fresh one. Similar color-based quality analysis has also been successfully performed on other foods (for diagnosis of storage conservation or for estimation of their alimentary properties), e.g., milk, orange or strawberry juice, or peach nectar [48].

Another example is the reported realization of an accurate real-time color classification microsystem that integrated the photosensors (in this case, not an array of dedicated color sensors but simple CMOS photosensors), together with pre-processing circuitry and a subsequent neural network processor, onto a single IC. The usage of neural networks offers distinct advantages, such as extreme ease of usage by the user of the final product, flexibility by self-adaptation to new circumstances, and reduced cost and extreme suitability of monolithic integration with standard CMOS fabrication processes. This one-chip smart sensing microsystem had low cost, was robust, was mass-producible using standard commercial CMOS processes, and exhibited a significantly higher performance. The chip was successfully applied practically in freshness tests for several fruits (apples, tangerines, and lemons) [49].

Colorimetry has also been a useful tool in wine characterization for quite some time. An earlier method had been developed by Folin and Ciocâlteu [50] and perfected later by Lowry et al. [51] to determine the total phenolic content of the red wines [52]. The phenolic content is important because phenolic compounds are responsible for the characteristic color, flavor, and aroma in wines and also act as antioxidants, with alleged beneficial effects on human health (reduced incidence of coronary heart disease and certain forms of cancer). More recent research modified the initial spectrophotometric method and improved its performance. Thus, the more modern realization could be used to analyze totally opaque (i.e., highly optically absorbing) samples that otherwise would be difficult to analyze

classically, and did not require any dilution (as was necessary with the previous Folin– Ciocâlteu method). Moreover, the method was equally well suitable for other types of samples, such as pastes, suspensions, and semifluids [52].

Color sensing has been employed not only for fresh produce but also to characterize the cooking of foods. This is important in order to avoid under- or overcooking, and also to ensure objectivity of assessment since human evaluation is highly subjective, may also depend on other variables, and does not guarantee accurate reproducibility. One reported realization for this purpose comprised an optical fiber sensor in conjunction with a small portable Ocean Optics spectrometer in order to monitor the color of the food while it was being cooked by examining the light reflected from both the sample's surface and core [53].

Finally, a system was reported for colorimetric nondestructive online inspection of white foods (e.g., flour, but obviously the method could be equally well applied for milk, cheese, etc.). For the specific purpose of characterizing four flour samples, the selection of just two different wavelengths was proposed: one out of the {440 nm, 480 nm} set, and another out of the {520 nm, 540 nm, 600 nm} set, respectively. Based on this operational principle, a fiber-optic-based system was built and successfully tested in industrial conditions [54].

1.4 Scientific, Technical, and Industrial Applications of Color Sensing

Many modern manufacturing processes require the detection of different colors and hues of visible light, i.e., wavelengths in the range 400–700 nm. Color detection can be used to sort objects, verify position of objects, recognize color sequence, control color in dying and coating applications, and detect changes in color of liquid during titration. Hence, color sensors are becoming an integral part in many industries, e.g., cosmetics, textile, food, publishing, optoelectronics, and image processing, including digital cameras. This sub-section will present some of the most important applications of color sensing in industry. It will be seen, however, that the sensors that can be used in various applications are not necessarily only solid state or monolithic.

For instance, in the textile industry, it is useful to measure color in order to access quantitatively the color variations in printed textile material during the online manufacturing process. Moreover, color monitoring should not be limited only to checking small areas but also large ones. In this latter case, however, employing a colorimeter may no longer be a viable option for real-time monitoring and other solutions had to be found. Such a solution used machine vision and image processing for large-area continuous textile process monitoring [55].

One of the first usages of color sensing was to determine the color of light emitted by various illumination sources by using colorimeters [56–59]. However, one can extend the meaning of "light source" to include other, less obvious,

physical phenomena that either emit light, or which can be characterized using colorimetric and optical methods. A first category of such phenomena is the characterization of plasmas [60], including the online monitoring of thin semiconductor films—initially deposited on a substrate—during their processing with an RF plasma [61].

The second category is related to the characterization of a combustion source either directly (by monitoring the flame color, when this is applicable) or indirectly (by monitoring the properties of the smoke's particulates). Color sensors can, therefore, play important roles in flame monitoring, either for fire prevention or for characterization of the combustion by-products. An illustrative example of this latter category is a system that monitored smoke in order to characterize combustion material and which was capable to identify uniquely a combustion material by variations in lightness and saturation over a range of hue values [62]. This system employed "chromatic modulation" (sampling white/polychromatic light after it was affected by the sample via three separate optical detectors with different but partly overlapping spectral responses). The same principle was also employed to monitor particles of sizes between 2 and 10 μm in a system employed for air pollution monitoring [63]. A relatively similar approach was employed for *in situ* monitoring of chromatic changes in particulate mass fraction and variations in the mean particle size of diesel exhaust particulates. The extracted mass fraction of these particulates in the exhaust gas is an indicator of fuel consumption, while variation in mean particle size is a primary indication of incomplete combustion [64]. Two similar systems were demonstrated practically for liquids. One system successfully discriminated between single-phase liquids (fuel and water) and distinguished between single-phase aviation fuel types and a range of mixtures of water in fuel [65], whereas the other was used for online monitoring of oil in industrial vacuum pumps detecting the quality of these oils as well as the presence of any air leaks [66]. Another system was also reported for liquid fuel quality monitoring, but based on a distinct fiber-optic-based architecture and operation. One version employed neural networks, solution which proved to be more advantageous as it could easily relearn to adapt to various tasks and examined samples, and was also faster and significantly cheaper [67].

A different approach for particulate characterization was based on a three-wavelength scattering technique. A first example of this technique was also employed for smoke characterization in order to determine the average particle size and mass concentration of smoke from transmission data using Mie theory [68]. The second example is an optical fiber-based system that was used to characterize monodisperse particulates in liquid suspensions in terms of their size, refractive index, and density per unit volume. The system was used to characterize both absorbing and non-absorbing particulates, with specific focus on the investigation of suspensions of solid particles in liquids, and excellent agreement between theory and experimental results was obtained [69].

Another example of color sensing application in industry is white balance testing. This is an instrument that adjusts the purity of the white emitted by color TVs, monitors, and PC displays. It employed simple photodiodes in conjunction

with colored filters, and the entire system was controlled by a 16-bit single-chip microcomputer that automatically controlled the emitted luminance level [70].

The wood-processing and paper industries as well as any printing-related application also need colorimetric measurements. One first example is the application of color sensing to assess the effects of thermal treatment of birch with respect to color and mechanical strength. However, it was concluded that color is not a useful parameter for prediction of mechanical strength, and the color homogeneity of the treated boards was not good [71].

A second and much more successful example is the real-time measurement of lignin content in moving paper sheets which enabled high-speed automated sorting of papers according to lignin content in a mixed-waste stream for efficient recycling. However, it was not the actual paper color *per se* that was monitored, but rather the fluoresced one. It was found that the magnitude of the fluorescence peak at 650 nm was directly proportional to the lignin content of the paper, while the dependency on paper weight was nonlinear, saturating at higher paper basis weights. The effect of other important variables was also investigated [72].

A third and different reported application in the same industry investigated the optical surface quality of two different commercial laser print papers before and after printing of R, G, and B color inks. It was observed that the R, G, and B color print inks had influence on the reflectance, transmittance, and optical anisotropy of the print paper [73].

The colorimetric characterization of printers using more than three colorants is another very important practical problem in the printing industry, since typically there is no unique combination of colorants that would exactly reproduce a particular color, not only in standard CMYK printers but also in high fidelity ones which employ RGB colorants in addition to the CMYK ones. Two methods were developed and implemented using software in order to solve this problem by determining the best combinations of colorant amounts which can provide the most suitable match: the variable reduction method and the division method. The variable reduction method used connecting functions to reduce the number of variables controlling the colorant amounts. It was a simple method but did not always utilize the entire color gamut. The division method employed sub-gamuts composed of appropriate sets of three or four colorants that were combined to form the desired final hue. This latter method enabled access to the entire color gamut, but had the drawback that its boundaries tended to cause pseudo-contours due to abrupt changes in one or more colorants [74].

2 Monolithic Color Sensors

As mentioned above, in the *colorimetric approach*, the visible light range (400–700 nm) is analyzed based on its tri-stimulus decomposition based on the usage of “primary” colors, typically red (R), green (G), and blue (B). Although one can envisage many different types of realizations that could perform such a colorimetric analysis, for brevity we shall focus our attention only on monolithic

sensors fabricated in semiconductors. This type of sensors may be implemented in silicon (Si) using either monocrystalline substrates, or polycrystalline, or—more often—amorphous thin films. The next sub-section will briefly introduce the fundamental concepts on which such Si-based color sensors are based. The following sub-sections will then succinctly review some of the most relevant examples of Si-based color sensors of each type, i.e., realized either in monocrystalline substrates or in amorphous thin films.

2.1 Basics of Solid-State Color Sensing

As is well known, a photon with energy greater than the bandgap energy of silicon, $h\nu > E_g$, can excite an electron from the valence band to the conduction band. This causes the generation of an electron–hole (e–h) pair, i.e., free carriers which, under right circumstances, can be separated and give rise to a current in an external circuit. After transferring energy to the electron, the photon disappears and is "absorbed." Conversely, photons with less sufficient energy will not be absorbed and are, therefore, transmitted. This explains why short wavelengths (i.e., with photon energy above the threshold energy equal to that of the material's band gap) will be absorbed, but larger ones will be transmitted. Since silicon has a bandgap energy of 1.12 eV, it can absorb light with wavelengths equal to or below 1,100 nm [75].

However, the absorption process for photons with energy around the bandgap value is strongest only in direct bandgap semiconductors. When a semiconductor does not have a direct bandgap, which is also the case of silicon, the absorption of a photon does not take place unless a phonon (or lattice vibration) also participates in the process. The absorption coefficient of photons in crystalline Si, an indirect semiconductor, is lower than that of a direct material and rises only slowly at energy levels near the bandgap (1.12 eV). Once the photon energy is sufficient to cross the direct gap region (3.4 eV), the absorption coefficient increases rapidly since direct transitions are possible [76].

The absorption of photons in silicon is of particular interest for understanding how one can fabricate color sensors in this material. More specifically, the optical properties of any materials are dictated by the so-called characteristic (optical) admittance of a medium, $\boldsymbol{N} = \boldsymbol{n}\text{–}\mathbf{i}\,\boldsymbol{k}$, which is typically referred to as the "complex refractive index." Its two components are $\boldsymbol{n}$, the refractive index, and $\boldsymbol{k}$, the extinction coefficient. We are particularly interested in the latter coefficient, which is directly related to losses, i.e., the attenuation of light propagating through the respective material. Most importantly, the value of the coefficient $\boldsymbol{k}$ decreases significantly (quasi-exponentially) with the wavelength [77]. The direct consequence of this fact is that the violet-blue hues (short wavelengths) of the visible range will be extremely quickly and efficiently absorbed in an extremely thin layer situated at the top-most of the silicon substrate. As light advances deeper in silicon, the longer wavelengths (green and yellow) begin to be absorbed, though not as well

as the shorter ones, so that these colors are absorbed only mildly at a greater depth (1–3 μm from the surface). Finally, k has the smallest values for the longest wavelengths so that the red hues are only slightly absorbed in Si and at great depths (>5 μm). This means that the orange-red colors can be detected only in a very wide detecting region located deep inside the Si structure within which this radiation can be absorbed and optoelectrically converted into an electrical signal. If a normal Si substrate is used (650 μm thick for a wafer with a 6-inch diameter; even thicker for larger diameters of 8 or 12 in.), then the visible light will be totally absorbed and no transmitted component will appear.

Hence, the silicon's dependence of k on λ is the most fundamental principle on which are based all the color sensors to be subsequently presented in the next subsections. However, this dependence will also prevent practical Si-based solutions to exhibit spectral responses very similar to ideal ones, i.e., which would equally split the visible range in three domains (R, G, and B) and characterized by peaks at 450, 550, and 650 nm, each with FWHM of 100 nm. Additional mathematical transformations would need to be applied to the photogenerated currents collected at the sensor's output terminals in order to address this issue.

2.2 Color Sensing Using Standard Solutions

A pragmatic way to conceive a color sensor (especially for practical real-life imaging applications) is to fabricate it as an array of cells comprising three identical independent photosensors, each of them detecting only one primary color. Therefore, the easiest implementation of such color sensors used colored filters obtained by depositing different polymer dyes on top of neighboring photosensors [78, 79]. In the simplest case, a *pn* junction, i.e., a photodiode, can be used as a photodetector. Figure 1 shows the classical configurations used in typical photodetectors. Various other detectors may also be used depending on the desired application and the available technology used for the fabrication of the sensors and of the adjacent signal processing circuits. The same conceptual solution shown in Fig. 1b is applied, e.g., in photo cameras and camcorders that use either Charge-Coupled Devices (CCDs) or CMOS detectors.

Knowing the transmittance characteristics of the polymer dyes and the photocurrent output of each of the three photodiode elements, it is possible to calculate the unique position of the color of the incident light. However, this *classical approach* of realizing a color sensor has two important *disadvantages*:

1. *It employs polymer dyes as color filters*. This can lead to inherent variations in the color selectivity of the filters (mainly due to aging), and/or incompatibility with other technological steps, especially when smart sensors are desired to be realized.
2. *A complete color sensing cell must employ more than one single photosensing element, such as a photodiode*. A minimal number of at least three photodiodes are necessary for a complete pixel in order to provide the full RGB output, with each photodiode covered by a different filter.

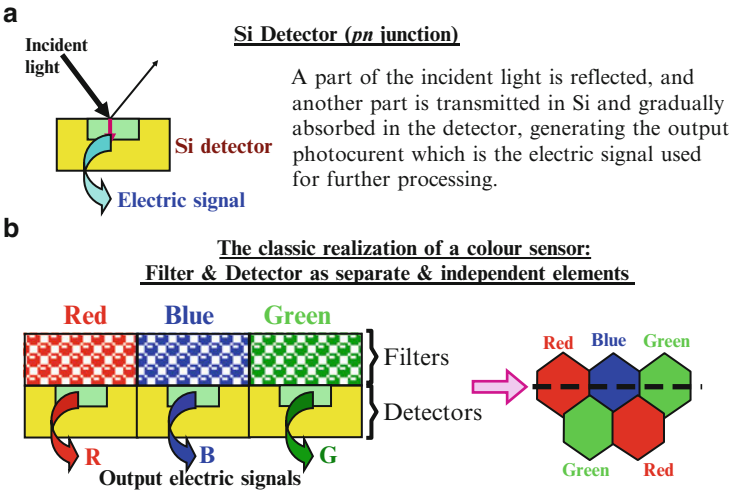

Fig. 1 Classical implementation of optical sensors: (**a**) A simple photodiode; (**b**) the principle used for typical color detection in standard imagers, e.g., video cameras. The detector represented here is a photodiode, but any optical sensor such as a CCD element or a MOS sensor can also be employed, depending on the exact architecture used to fabricate the chip

The 2D arrangement of the photodiodes and of their corresponding overlying colored (polymer) filters forms a *color filter array* (CFA) and is essential for the correct reconstruction of the original illuminated color. Numerous types of CFAs have been developed for different applications, but the most popular one is the *Bayer pattern* developed by Kodak in the 1970s, based on work in spatial multiplexing. Using a checkerboard pattern with alternating rows of filters, the Bayer pattern has twice as many green pixels as red or blue. This is justified by the greater acuity of the human eye toward detail contained in the green part of the spectrum. Hence, the green channel has more weight in generating the luminance (or brightness) data for the image [80–82]. However, special RGB-type CFAs with various alterations in the pattern and employing a different sample reconstruction algorithm had to be designed in order to better capture the properties of the human visual system [83]. Moreover, at least in this specific case of a Bayer pattern with a double number of G filters, a total of four photodiodes would be required to form a complete pixel. In any case, the increased number of photodiodes necessary to provide all RGB signals leads to a large area occupied by one entire pixel, and thus to a larger cost of the final chip, since the latter is directly proportional to the silicon "real-estate" surface. Another important drawback of the CFAs is that severe *color aliasing* can appear, due to the fact that the pixel array is a two-dimensional sampled data system. In practice, this aliasing appears as *Moiré effects* and *color artifacts* [80–82]. Technologically, this means that one can also obtain undesired Moiré effects if errors appear in the alignment/positioning of one (or more) filter(s) with respect to the underlying photodetector. Therefore, special care must be taken

in the design, as well as in the fabrication, of these structures in order to prevent such misalignments taking place.

2.3 The Simplest Color Sensing Approach: The Single Junction

The above-mentioned drawbacks of the classical CFA-based color sensing solutions required the finding of novel alternative solutions which would exhibit improved performance, without their disadvantages. This sub-section and the following ones will briefly explain how a monolithic Si-based color sensor can be realized using *pn* junctions instead of the more conventional solutions, e.g., CCDs. The essential underlying idea is to attempt to stack more junctions vertically one on top of each other. This approach should thus provide a much more compact pixel element due to two reasons: first, more detectors would be integrated in the same physical space of a single pixel, and second, the functions of filtration and detection are now merged together in a single structure. The latter feature appears because silicon's light absorption capabilities which carry out light filtering (due to the spectral dispersion of the absorption coefficient k) are now intrinsic part of the sensor together with the photo-detecting junctions.

This sub-section will present the case when the simplest detector—a single *pn* junction—is used for a color sensor, while the following sub-sections will introduce the more efficient color sensors with two or three vertically stacked junctions.

In the simplest case, just one light-detecting region, namely, a single *pn* junction, is employed. If the *p*-type top layer has a high doping level, the space-charge region will extend almost entirely into the underlying *n*-type region. Since photo-generation must take place only in the depleted region of a junction in order to separate effectively the photogenerated electron–hole pair in order to lead to electric output signals, it logically follows that one can perform color sensing with such a single junction only if the width of the junction's depleted region is modulated. This can be realized practically by fabricating the junction such that the optical absorption peaks around a wavelength in the middle of the desired spectral range. Its spectral response can be electronically tuned by varying the reverse voltage applied across the photodiode, enabling an electrical output that is thus the cumulative or successive contribution of different wavelengths. This principle can be applied in two versions: static or dynamic (at different moments in time). The information regarding the various incident wavelengths can then be extracted using subsequent signal processing.

The static version reported in the literature employed two neighboring junctions of identical depths, both of which were illuminated simultaneously by the incident light. However, different reverse biases were applied: one photodiode was kept at a constant reverse bias (hence it was denominated as reference photodiode), while the bias of other one was varied so as to find the appropriate reverse voltage value required for detecting a fixed ratio of the two photocurrents. In practice, the reference photodiode may have a much smaller exposed area than that of

the sensing one, in order to maximize the overall optoelectronic efficiency of the sensor. The imbalance in photocurrents between the two junctions caused by the unequal sensitive areas (assuming an initial identical reverse bias voltage applied on both of them) can be compensated by decreasing the bias unto the sensing photodiode (or alternatively, increasing that unto the reference photodiode), until current balance (at the desired ratio) is achieved. Practically, however, the two junctions should be identical in size in order to present identical electrical characteristics, the most important being the dark current. The difference in sensing areas (or, rather the equivalent resultant difference in photocurrents) can then be implemented either by covering a part of the reference photodiode's exposed area with an opaque material (e.g., metal), or (more conveniently) by simple subsequent signal conditioning of its photocurrent.

Therefore, the basic operation of this color sensor using two separate single junctions can be summarized as follows. The reverse voltage across the reference photodiode was held constant, while that applied unto the sensing photodiode was first adjusted using a feedback loop until the photocurrents were in balance. After obtaining stationary conditions, the variation in the reverse voltage across the sensing photodiode (as dictated by the feedback) could be monitored continuously. An almost linear relation between the reverse voltage ratio and the "average color" of the incident light was then obtained. Further elements were added in the subsequent version to boost the performance of the sensor [84–87].

A first modification of the static concept employed just a single junction as sensing photodiode, and the bandpass central wavelength of it spectral response was electronically tunable by varying the applied reverse voltage, while readout circuits integrated in the same chip enabled easy decoding of the incident light by providing an output proportional to its "average" color [88–90].

Starting from the latter type of realization, we can easily propose a fully dynamic approach in which the reverse bias of the photodiode would be scanned periodically using a sawtooth voltage. The colorimetric information could then be extracted using complex subsequent signal processing of the photocurrents detected at different moments in time. The concept is illustrated in Fig. 2.

However, one can also easily realize that the single-junction-based color sensors are characterized by some severe drawbacks:

1. The static approach (i.e., with a depleted region of constant width in time) can provide an output dependent on the "average" color, not a truly RGB output. Moreover, the presence of an additional reference junction next to the color sensing one defeats the purpose of minimizing the area occupied by a single pixel necessary to provide the desired colorimetric output.
2. When the depleted region's width is varied in the proposed dynamic approach, since a single absorption curve is used (although dynamically modified by the periodically varying reverse bias modulation), one cannot achieve a very good selectivity between very different wavelengths.

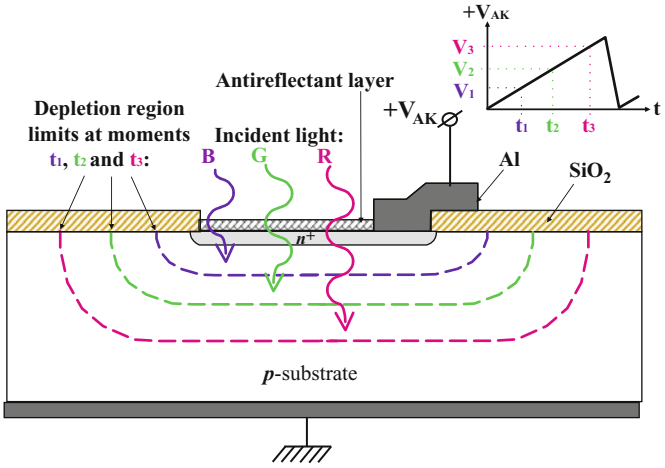

Fig. 2 Color detection by reverse-bias scanning of a n^+p photodiode fabricated in monocrystalline silicon. Different reverse-biasing voltages result in width variations of the depletion region which will thus collect the carriers photogenerated at different depths by incident light of different wavelengths

3. The magnitude of the collected photocurrent will vary correspondingly with the applied reverse bias; hence a feedback loop has to be incorporated with other signal processing circuits to first balance the current with respect to a fixed and known reference before performing an actual color measurement, as was done for the static version.
4. In the proposed fully dynamic approach, the extraction of the color signals from the photodiode's outputs would require extensive signal processing in complex circuitry. Moreover, since it is based on time scanning, it will be limited by the speed of variation for the reverse bias voltage. This limitation is not related to the capability of following very fast changes in the color signal (since usually such changes are typically slow), but rather to the subsequent processing of the photocollected signals required in order to provide the necessary RGB outputs in real time. While this may not be a concern for a stand-alone sensor, it is a very critical issue in an array realization consisting of millions of pixels, in which each pixel must be accessed only for a very limited time. Therefore, this method is not indicated for imaging in large arrays as the complexity of the signal processing and the timing requirements for decoding each pixel's output in real time could be tremendous.

In conclusion, it is necessary to find new solutions capable of providing more compact realizations, e.g., by vertically stacking two or more photo-detecting junctions, as is shown in the following sub-sections.

2.4 Color Sensor Structures with Two Vertically Stacked Photo-Detecting Junctions

In this case, the photodetectors, i.e., the *pn* junctions, are placed not horizontally but integrated in a ***vertical*** structure. This vertical placement implies that *all* the color sensing elements are now incorporated in one single pixel. Consequently, the extraneous area used in the CFA approach for three (or more) separate horizontally placed sensors (at least one sub-pixel for each primary color) is no longer needed since each pixel can now provide all the three necessary RGB outputs. Therefore, in principle, either the resolution of the imaging array can be increased (minimally) three times (for a given constant chip area in which new multi-junction pixels are used instead of the redundant polymer-covered photodetectors that can now be eliminated), or the area of the chip (and hence the cost of the chip) can be theoretically decreased three times if the resolution, i.e., the number of pixels, is desired to be maintained constant. Furthermore, all the previous disadvantages related to Moiré artifacts and polymer aging are now completely eliminated, while at the same time the optoelectrical conversion efficiency increases since the light falling on one and the same pixel is now used to generate all the three signals, not just a single one of them.

The basic operational principle remains the same, only that now it is implemented differently: since photons of different energies (i.e., colors) are gradually absorbed at different depths, they can be sensed by inducing photocurrent generation in various junctions placed at different depths within the monocrystalline silicon substrate. The depleted width of one or more of these junctions can be fixed or—if necessary—could be controlled electrically via the applied reverse bias, i.e., the static and dynamic approaches are again possible, although—just as in the previous single-junction case—the dynamic realization would be an extremely challenging one.

It can thus be concluded that the three-junction approach—which will be reviewed in the next section—can provide most conveniently an RGB output (or which can be most easily converted into an RGB output), but it is more complex and more challenging technologically. For this reason, simpler two-junction realizations have been sought, implemented, and successfully demonstrated in practical applications by many researchers. This section presents just a few examples of two-junction color sensors.

One of the earliest reported two-junction color sensors was used to monitor the color of a combustion flame in house gas heaters and provide an alarm in case the flame extinguishes, thus minimizing the risk of carbon monoxide poisoning. It is comprised of two *pn* junctions monolithically integrated in a *pnp* vertical structure with peak responsivities at around 600 nm and 1 μm, respectively. The short-circuit current ratio of the two photodiodes on a log scale varied monotonically with the wavelength in the range 600–1,000 nm. Furthermore, using the ratio of the two currents allowed to cancel out the influences of adverse effects such as temperature

and contamination of the optical window of the sensor and provided information about the "average color" of the incident light [91].

This simple structure was slightly modified in a subsequent improved realization. Although it still exhibited two junctions, they were not all realized by diffusion; the bottom junction was formed between an *n*-type epitaxial layer and a *p*-type substrate, and only the *p*-type top region was realized by diffusion in the *n*-epi layer. More importantly, the two junctions were reverse biased such that their space-charge regions almost completely depleted the entire epi layer. This enabled electric tunability, i.e., user-controlled spectral response shaping of the sensor's spectral responses, by changing the applied reverse biases. Such a realization was demonstrated by R.F. Wolffenbuttel and allowed electronic tuning of the spectral response to match various desired spectral curve shapes, but the sensor obviously could ultimately provide only two output color signals [92]. Subsequent versions were further developed in order to achieve a fully dynamic sensor, using a method very similar to the previously mentioned principle of reverse-bias scanning by employing a translinear logarithmic amplifier fabricated using a bipolar process in the first improved version [93] and a dual slope A/D converter in the second one [94]. In the latter case, switching between several reverse-bias values of the top and bottom junctions combined with the integration of very complex signal and data processing circuits enabled the realization of a smart integrated microsystem which was tested against Munsell and CIE colorimetric standards and demonstrated good overall performance [94].

However, probably the largest contribution in the area of two-junction color sensors and associated smart sensing systems is that of the group led by Mohammed ben Chouikha (Université Paris Pierre et Marie Curie, Paris).

The earliest and simplest realization of M. Ben Chouikha was a fully diffused two-junction structure with peak responsivities at ~450 nm and 700 nm, and which therefore was much better suited for measurements in the visible range than the realizations previously mentioned above in [91, 92]. The logarithm of the two junctions' photocurrents ratio (which is independent of the light intensity) was again employed for color estimation, and since the sensor was fully CMOS compatible, it was therefore integrated together with signal processing circuits in a simple microsystem [95]. A more detailed presentation of the theoretical aspects of such a CMOS-compatible, two-junction, color sensing structure, called by the authors a "Buried Double Junction" (BDJ), was presented in a much more recent paper. The calculations were then supported by C-V and I-V (dark and illuminated) measurements [96]. Subsequent papers from the same research group provided some considerations for the design of such CMOS- or BiCMOS-compatible BDJ sensors and the deduction of the photocurrents and their spectral variation, the pixel structure, pixel testing, and the interface electronics, as well as giving a few illustrative examples of demonstrated successful implementations [97–99]. Further work in establishing a solid design environment was done to develop an optoelectronic design library based on the BDJ sensor within the Cadence Virtuoso Custom Design Platform (using parameter extraction based on measurements of actual devices fabricated with a commercially available 0.35-μm CMOS process),

and also to provide accurate behavioral description models in Verilog-A implemented in the Spectre simulator [100].

The BDJ was then employed as a pixel sensor in arrays of imaging chips. In one example, a linear array of 64 BDJ cells was designed and fabricated in a l.2-μm CMOS process. As each BDJ detector provided information on both the wavelength and the intensity of a monochromatic component, the linear array was used to build a self-calibrated micro-spectrophotometer [97, 101]. A synchronous detection scheme for a BDJ-based sensor further developed the integrated signal processing circuits to an even more complex level. The CMOS circuit associated with the BDJ sensor contained in this case two channels, and each channel consisted of a transimpedance amplifier, a fully differential amplifier, a multiplier, and a low-pass filter, thus performing low-noise pre-amplification and synchronous demodulation. This approach enabled to increase both the SNR and the detection sensitivity of the entire sensing microsystem significantly [102]. However, one can easily realize that such a level of circuit complexity adjacent to the color sensor is applicable only for a stand-alone BDJ device, and cannot be used as a "smart active" pixel structure when large arrays of many (i.e., on the order of 10^5 or much more) BDJ-based pixels have to be implemented.

In conclusion, the two-junction color sensor provides a reasonable compromise between performance and integrability with standard CMOS fabrication, while at the same requiring only relatively simple read-out circuits to be added next to each pixel when arrays of such sensors are necessary. The combination of these two key features explains its popularity in many applications, including a few demanding ones, such as imaging and spectrometry. Nevertheless, the color information provided by them is not an RGB (or similar) set of outputs, and the accuracy of their performance is inherently limited. Due to these reasons, more complex structures have been employed to achieve complete RGB color sensing, as will be detailed in the next sub-section.

2.5 Three- and Multi-Junction Color Sensors

As was already mentioned in the previous section as well as in Sect. 2.1, vertically stacking three junctions should provide an RGB output as well as increased compactness. Figure 3 represents schematically such a triple-junction color sensor. The "active" region represents the area directly exposed to the incident light. Although not shown in Fig. 3, the rest of the chip is usually covered with an additional metal shield deposited on top of protective dielectric layers that cover the metallization contacts. The shield will allow light penetration only in the "active" region and protect against parasitic illumination of other areas (e.g., where the signal processing circuits are located). Furthermore, for clarity, in Fig. 3 the extension of the depleted regions has been represented only within the "active" region.

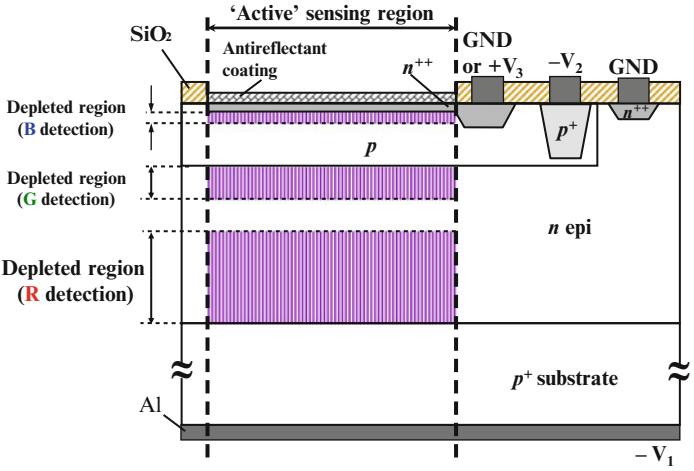

Fig. 3 Simplified schematic cross-sectional image of a triple- junction color sensor fabricated in monocrystalline silicon, showing qualitatively the width and location of the regions sensing different colors of the visible range

One of the first triple-junction color sensors was reported in 1993. It was apparently intended to be an elementary pixel in an imaging camera and was realized entirely using a standard CMOS/CCD process that probably had ~3 μm design rules. The authors used a so-called color-rendering index R_a to quantify the color reproduction performance of this device. A value of 69.5 was obtained, which was considered as "unexpectedly high" and compared well with that of ~80 for CCD color cameras with good color reproduction quality. However, the paper did not mention anything about the actual usage of this pixel in an imaging array and the resulting overall performance of such a camera [103].

A very interesting implementation is that done by Bartek and Wolffenbuttel, which most probably is the first one implemented in monocrystalline silicon using an advanced fabrication processing method called selective epitaxial growth (SEG). The resulting relative spectral responses of this sensor peaked at ~410 nm, ~510 nm, and 700 nm, and they were achieved when the depletion region of the top diode extended between 50 and 200 nm below the top surface, the middle depletion region extended from 200 to 800 nm, and the lower depletion region extended from 1,500 to 5,000 nm in the bulk of the Si (the substrate-epi junction was not used) [104].

Soon after Bartek's SEG device, a thyristor-type *pnpn* structure was analyzed and reported by Moharjerzadeh et al. as capable of simultaneous detection of the three primary colors. However, in contrast with the SEG-based device, the paper dealt only with simulation results. Thus, the doping profiles and reverse bias conditions of the junctions were tailored by using TCAD process and device simulators (TSUPREM-IV and PISCES-2B), respectively [105].

M. Ben Chouikha et al. [106, 107] have also proposed a *npnp* triple-junction structure for color detection that could be implemented with bipolar or BiCMOS technology. The peaks of the three spectral response curves were situated at ~480, 530, and 770 nm, respectively. Unfortunately, the spectral responses of this device are not as suitable (for color discrimination) as those of the previous SEG-based device. Nevertheless, the peak responsivities values for the B, G, and R output response curves were about half, comparable to, and twice as large than those provided by a CCD with identical corresponding color filters with 40% peak transmission, respectively [107].

Both M. Ben Chouikha's and Bartek's devices proved that the triple-junction structure can be effectively used for color sensing. This function can be achieved even when the output spectral curves may not be optimal. The correct color interpretation will just need to take into account mathematically their individual responses and perform the necessary transformations—using on-chip signal processing circuits—that would deliver the desired correct output. Therefore, even if a fabricated triple-junction device exhibits far-from-ideal response curves, one can still obtain the desired RGB output signals after performing mathematical transformations of the collected photocurrents, as demonstrated by Ben Chouikha. This property, coupled with the capability of providing the complete RGB outputs, could make triple-junction color sensors very attractive for practical smart microsystems, in which the integration of the signal processing circuits next to the sensor could provide the computing power necessary to perform the desired matrical transformations. A confirmation in this direction was provided by the work of Thomson & Westland, who described a method for characterizing the colorimetric and photometric properties of any three-channel color imaging device. They demonstrated that it was possible to fit the effective spectral sensitivity profiles with a low-dimensional parametric model that can be repeated at a variety of illumination levels. The end result was an illuminant-independent characterization of the imager's performance [108], which is an important feature given the fact that the color sensors would normally not provide color output signals independent of the illumination level, as is mentioned below.

A triple-junction sensor was patented by R.B. Merril of Foveon Inc., Santa Clara, CA (USA) [109]. However, this device was the starting point of a more complex multi-junction device but which still provided just RGB outputs. Such a significantly more complicated structure and with a much more difficult fabrication was sought in order to improve drastically the performance of the triple-junction-based color sensor and eliminate its perceived drawbacks [110]:

1. The three color sensing regions are not fully independent and interact with one another, thus demanding complex mathematical manipulations to extract the necessary RGB components from the sensor's outputs. Furthermore, the direct connection of the three photodiodes with alternating polarity also required complicated biasing, read-out, and signal processing circuitry.
2. The junction depths and (probably) the photon collection widths of the depleted regions for the initially patented triple-junction structure provided non-optimal selectivity.

3. Foveon's first triple-junction sensor was operated by reverse-biasing the middle junction. This was inconvenient for the subsequent signal processing circuitry, requiring special bias values and/or special circuits incorporating PMOS transistors and thus increasing the complexity and especially the overall area of the corresponding read-out circuits.
4. The triple-junction sensor was fabricated with a technology that required an annular isolation ring to be added within each pixel. This increased the pixel area and, therefore, reduced the overall fill factor and optical efficiency, while at the same time increasing the total chip area, and thus the final cost.

The basic idea of Foveon's final multi-junction solution is—at least in principle — quite simple: insulate each and every color-detection region from one another. To achieve this, the photogeneration of carriers was initially considered to take place in lightly doped *n*-type regions separated from one another by *p*-type regions. At the same time, a different biasing approach was employed, in which the necessary reverse bias was applied onto the *n*-type regions, while the *p*-type regions were all connected to the substrate potential (GND), serving as references. The resulting six-layer structure patented by Foveon with its alternating polarity diodes can now provide RGB output signals that are all identical in polarity, thus greatly simplifying the read-out circuitry of the pixel [110]. However, the price to pay for the superior performance of Foveon's 6-layer color sensor and its optimal RGB outputs is a special and very complex fabrication process necessary to realize the color sensors.

Finally, a last type of color sensor worth mentioning is the so-called transverse field detector (TFD) which, although does not comprise vertically stacked junctions, is an intriguing alternative solution for color sensors. The TFD is a very ingenious solution which, although makes use of very superficial single junctions, does not employ them just as simple photodiodes. Instead, they form surface contacts which, when suitably biased, generate various electric field configurations between different such contacts that drive the carriers photogenerated at different depths to the corresponding surface contacts. The photogenerated carriers are collected by means of superposing a depletion electric field perpendicular to the device surface, with transversal field components, parallel to the device surface, that are generated by suitably biased surface electrodes. Consequently, the carriers photogenerated by various colors at different depths in a depleted region under the semiconductor surface would now be collected at different surface electrodes due to the orientation of the composite electric field that would compel the carriers to move along the resultant field lines in each region controlled by corresponding surface contacts [111]. One can easily notice that this is a very elegant solution to the very thorny and insolvable problem/necessity of using triple- or multi-junction devices, which would result in increasingly complex structures if one were to follow the approach based on vertically stacked junctions in order to detect 3, or more, colors. We have already seen that only for 3 junctions Foveon already has employed a complex architecture that required a correspondingly mature technology. In this case, however, the concept can, in principle, be easily extended beyond just the trichromatic RGB-like type of sensing and provide more outputs.

Indeed, the authors of the TFD have already suggested the possibility of its usage to obtain a 4-color response [112], which is a reasonable and feasible implementation. However, further increasing the number of discerned colors would become gradually more difficult in terms of both device complexity (larger number of surface contacts of reduced size) and increased surface potentials that would have to be controlled with much higher accuracy in order to control the spectral selectivity of each color contact.

The TFD sensor has also been used to implement small size imaging arrays. Thus, a 32-pixel array implementation of the TFD was reported. It was fabricated with a standard 90-nm CMOS process, using a 4-μm-thick, low-doped, *p*-type epi layer as the substrate; exhibited measured quantum efficiency for each type of n/n^+ contact; and exhibited peak wavelengths of 500, 560, and 620 nm, respectively, with FWHMs of approximately 300 nm [111].

2.6 Thin Film Color Sensors

This last sub-section will briefly detail some of the color sensors realized using thin films instead of vertically stacked junctions in a monocrystalline substrate. Typical silicon-based materials that are easily available in any semiconductor manufacturing environment and which can be used for this purpose are polysilicon, microcrystalline, or amorphous silicon (a-Si:H). This approach that would combine junctions/structures realized in both the thin film(s) and substrate could offer several advantages. First, the structure of the device to be fabricated in the substrate is simpler, as only two junctions (for G & R capturing) or a single junction (only for R capturing) can now be used, or even none, i.e., all the colors are detected exclusively in one or more thin films. Such an alternative may, therefore, also provide a very compact vertical integration in which the color sensors are implemented in one (or more) thin film(s) deposited on top of CMOS circuits. Furthermore, this type of solution is potentially easier to fabricate using a standard CMOS process than the previously mentioned triple- or multi-junction sensors.

The preferred material in which thin film color sensors are most often realized is a-Si:H. Without going too much in details regarding the basic features of a-Si:H, it must be highlighted that using a typical *pn* junction for photovoltaic optoelectric conversion/detection of light in a-Si:H, although possible, would provide a much lower efficiency than a similar junction realized in monocrystalline silicon. For this reason, a-Si:H-based photodetectors typically employ instead a *pin* structure (or more, vertically stacked within the same device), in which photoconductivity is the key principle of operation for optoelectric conversion/detection. The letter *i* symbolizes a so-called intrinsic region, i.e., which has an extremely low doping level (typically unintentionally added/present in the semiconductor, due to the inherent presence of contaminants). The *p* and *n* layers should provide the internal field to the *i* layer, in order to enable efficient separation and collection of the photogenerated carriers.

The main applications of a-Si:H thin film structures, besides photovoltaic solar cells, are contact image sensors for facsimile machines, thin film transistors (most often as active-matrix control elements in color displays, e.g., LCDs), position sensitive detectors (PSDs), and various large-area image sensors, and charged particle or X-ray image sensors for medical imaging or high-energy physics [113–115]. Color sensors have a smaller niche market, and very few seem to have been commercialized, although numerous a-Si:H devices have been reported in the literature until now. However, in contrast with the color sensors realized in monocrystalline silicon, the family of thin film color sensors has a very rich diversity. Thus, most of the thin film color sensors are usually based on multi-*pin* structures in extremely numerous variations. Furthermore, one or more sections of the color sensing structure may comprise other materials than a-Si:H, typically two or three alloys of a-Si:H with other elements (most often either C or Ge). The end result is an extremely large number of reported devices with an astounding variety of structures. Due to the limited available space, only very few examples of such thin film color sensors will be presented in this sub-section.

Thus, from the operation principles previously presented above, it results that the simplest sensor that can discriminate two colors should employ a *pinip* structure. One of the first such realizations was a photosensing array of 180 × 180 a-Si:H *pinip* pixels with a 500-μm pitch reported in 1993. This was fabricated on a steel substrate but was employed, however, for overall 2D imaging, not for color sensing [116]. Improved performance of a 1D color sensing array (600 dpi, 7,320 pixels × 3 colors) or a denser 2D imaging array with smaller pixels (200 dpi, 600 × 400 pixels) *actively* addressed by thin-film transistors (TFTs) and with complete filter-based tri-color sensing was reported 3 years later. However, in this case, only a simple *pin* diode with the size of 42.3 μm × 32.3 μm was used as the photosensor in each pixel [117].

Among the first reports that document the usage of a-Si:H in imaging arrays is that of a-Si:H photoconductors in 120 × 120 and 128 × 128 arrays, respectively [118, 119]. The former, smaller, array was connected to an artificial neural network with 14,400 synaptic connections of variable strength which was used to perform simple pattern recognition successfully. The combination of such a photoconductive array with a spatial light modulator then enabled a flexible analog processing module [118]. A much more intricate design was that of a two-million-pixel CCD image sensor with an overlaid a-Si:H photoconversion layer [120]. It is noteworthy to highlight that in this case, the a-Si:H layer was not patterned so that no independent regions were isolated or defined for each pixel, since the lateral diffusion of charges photogenerated in the layer was reported to be negligible because of the intrinsic very high resistivity of the a-Si:H layer. Once electron–hole pairs were photogenerated, the holes were swept into the underlying ITO film under the influence of the electric field applied across the a-Si:H layer, while the electrons were forwarded into storage diodes that were arranged in a staggered configuration in order to design a wide and uniform vertical CCD channel in the substrate. Unlike the classical CCD, however, in this case the a-Si:H layer was the active photosensor, and the CCD integrated in the substrate was used only as a register

to transfer and manipulate the generated signals in order to provide the necessary frames and the complete image. The spectral sensitivity extended approximately between 400 and 720 nm after which the spectral sensitivity decreased abruptly. The quantum yield of the a-Si:H layer had the highest values between 0.6 and 0.8 in the 450–680 nm wavelength range, with the peak located at around 680 nm, corresponding to the bandgap of the a-Si:H. This imaging array achieved a high sensitivity of 210 nA/l×, high resolution of 1,000 TV lines, and a wide dynamic range of 72 dB [120]. Nevertheless, despite its innovative usage of a-Si:H in a functional imaging array, the pixels in this realization were clearly not performing any color sensing.

True two-color imaging sensors employing a *pinip* structure realized only in a-Si:H were demonstrated in a 512 × 512 array for document imaging. The sensor exhibited peak responses at 520 and 650 nm, with "reasonably good" color separation but with excellent response linearity as a function of the incident light intensity, while the resolution of the images captured with this array exceeded 300 dpi [121, 122].

One of the earliest reported a-Si:H-based color sensors is a four-color discriminating photodiode. The diode was operated in drift mode with increasing reverse bias so that the photocurrent increased as the depletion widened. The device, realized on either stainless steel or glass, was a Schottky barrier cell with a Min^{+} structure, where M was a top electrode metal, in this case a 10-nm Au film. The primary wavelengths considered for the decomposition of the incident light were $\lambda_1 = 470$ nm (blue), $\lambda_2 = 530$ nm (green), $\lambda_3 = 590$ nm (yellow), and $\lambda_4 = 650$ nm (red), for which bias voltages of −0.25 V, 0 V, 1 V, and 4 V were used, respectively. Very good color discrimination capability was obtained, with accuracy of the measured photocurrent and average accuracy of the overall color composition of 0.5% and about 10%, respectively [123].

Although a-Si:H has been a popular choice for a large range of simple photoconductive arrays and even imaging arrays, very few true color sensors have been realized in this material. Moreover, their operation required subsequent biasing at three or more different voltages, which makes them less suitable for complex and high-precision color sensing arrays. In contrast, an extremely large number of various types of color sensors were realized using various alloys of amorphous silicon. An additional "weapon" used to improve the efficiency of multi-*pin* color sensing structures is the modulation of the bandgap of different layers by intentional and controlled introduction of various other chemical elements, resulting in a-Si:H alloys with modified electrical and optical properties. The most common additives for such purposes are Ge and C, resulting in the corresponding a-SiGe:H and a-SiC:H materials. The average bandgap values for a-SiGe:H, a-Si:H, and a-SiC:H are around 1.5 eV, 1.75 eV, and 2 eV, respectively [115]. Consequently, a triple-*pin* structure in which each *i* layer is realized with a different material (a-SiC:H at the "bottom," a-Si:H in the middle, and a-SiGe:H at the "top") would enable increased optical efficiency since each different material would—in principle—absorb a different wavelength range within the visible spectrum.

A first example is that of *pinpin* structures realized using a-SiC:H, except for the *i* layers adjacent to the outer/last *n* region which were always a-Si:H. The spectral responses for all types of structures exhibited a peak at ~500 nm, but had different behaviors as a function of the applied voltage and illumination bias, with the first type providing the largest responsivity and a marked dependence on the applied reverse bias. Color recognition could be achieved by varying the reverse bias to appropriate values in order to suppress the R, G, or B signal. Combining the signals thus extracted could provide a color image, although this was not practically demonstrated in an actual imaging application [124].

A unique heterojunction device combining both amorphous layers and monocrystalline silicon has also been proposed. It comprised a *pn* junction 0.3-μm deep realized in the monocrystalline substrate, on which amorphous layers were deposited: at the bottom, an *n*-type a-Si:H layer 0.83-μm thick in contact with the substrate's *n* region, followed by an *i* a-Si:H layer 0.5-μm thick and a *p*-type a-SiC:H layer ($E_G = 2$ eV) 140 Å thick, on top of which Al metallization was patterned in a grid with finger widths and spacings of 50 μm. The device exhibited a very clearly differentiated spectral response as a function of the applied bias: for -2 V, the response peaked at ~500 nm with a full width at half maximum (FWHM) of about 160 nm and covering the entire visible range (from 300 to 750 nm), whereas for 2 V the response was significantly red-shifted (peak at ~820 nm), covering the range 600–1,200 nm and was also much broader (FWHM of ~300 nm) [125].

Another large category of thin film color sensors include more complex structures in which two intrinsic regions are present within the device structure, and which are not adjacent to one another but separated by at least one doped region. Devices of this type include *nipin* (or *pinip*) structures, as well as *pinpin* (or *nipnip*) ones, all of which could thus easily be employed as two-color sensors.

One of the first devices of this kind was a TCO/*nipin*/metal (Al)/Si substrate structure, with top a-SiC:H *nip* layers ($E_G = 1.9$ eV) and bottom *in* a-Si:H layers ($E_G = 1.74$ eV). The entire structure was deposited on an insulator covering an ASIC IC in order to demonstrate the full compatibility of this technology. However, in order to optimize the RGB separation and detection, the structure of the device was modified to *niipiin*, with bottom *ni* and top *in* a-Si:H layers, while two additional intrinsic a-SiC:H layers were added on both sides of the a-SiC:H *p* region. The thicknesses of the layers in the TCO/*niipiin* structure were 90, 12, 50, 46, 20, 246, 200, and 25 nm, respectively. Both the measured and simulated results showed that the device was blue sensitive for 0 V or positive applied bias voltage, with the peak at ~490 nm. With increasing the positive voltage bias, the peak shifted toward shorter wavelengths while increasing in amplitude, and hence broadening. Long wavelength sensitivity resulted under negative bias, with the spectral responses peak situated at ~630 nm [126]. Other optimization studies of a very similar *nipin* structure with layer thicknesses of 12, 150, 12, 380, and 25 nm were carried out by the same authors, only that in this case just the *ni* layers were made of a-SiC:H ($E_G = 1.94$ eV) and the other layers were a-Si:H ($E_G = 1.72$ eV). It was noticed that the introduction of two defect layers on both sides/interfaces of the central

p layer improved the green separation for small positive bias drastically. The device was sensitive in B, G, and R regions for applied bias voltages of >1 V, 0.5 V, and negative values, respectively [127]. Indeed, an analogous *nipin* structure exhibited a spectral response whose peaks were situated at 485, 550, and 620 nm for applied bias voltages of 1 V, –0.6 V, and −1.5 V, respectively (no information was given about the layer thicknesses), thus enabling effective RGB separation. However, the G peak had a much reduced magnitude (~120 mA/W compared to ~200 mA/W for the B peak) and exhibited a secondary peak that broadened it. For the applied reverse bias of −1.5 V, this secondary peak became the main component of the R curve which reached the largest magnitude (300 mA/W); the previous main component of the G peak also increased its magnitude but remained a secondary element, while a tertiary peak also developed around 700 nm. Not only that the spectral response curves had a complicated variation, but studies of the transient behavior of such a structure highlighted a strong illumination dependence of the transient response time after bias and light switching. This would hamper the usage of such a two-terminal *nipin* structure as pixel color sensing element in a imaging array as more complicated circuitry, and signal processing would be required to generate a standard RGB video signal, including a deconvolution [128].

Nevertheless, the initial *nipin* sensor mentioned above [126] was successfully employed as pixel detector in a 32 × 32 array with dedicated pixel electronics (a simple op amp under each pixel) embedded in the monocrystalline substrate and fabricated using a 0.7-μm CMOS process. Although no details were provided regarding the colorimetric performance of this array, it was reported that the color definition voltage in each column was changed every 13.3 ms to enable sequential capturing/scanning of the R, G, and B components of the image, resulting in an overall frame time of 40 ms [126].

Louro et al. realized a double vertically stacked *pinip*/*pinip* device in which the bottom *pinip* structure was the color sensor (with layer thicknesses of 20, 400, 20, 100, and 20 nm, respectively) and the top one was a switching device. All doped layers were a-SiC:H, whereas the intrinsic ones were a-Si:H. A dark current density below 10 nA/cm^2 was measured for the pixels of a 42 × 42 array operated at a line scan frequency of 1 kHz. The authors concluded that "good color separation between blue–green and red" was observed for applied bias values of ±2 V [129].

For improved performance that enables separation of more than two colors, more complex structures, i.e., with more than 2 intrinsic regions, have to be employed. Thus, very good results have also been obtained from a simple two-terminal sensor with a *piiin* structure, in which each of the intrinsic layers was realized with a different material, namely, a-SiC:H/a-Si:H/a-Si-Ge:H, with band gaps of 1.95/1.7/1.6 eV, respectively (the thicknesses of the layers were not indicated) [130]. Its spectral response had a clear dependence on the applied bias: at 0 V, the device exhibited the lowest responsivity with a main peak at 460 nm, while a secondary peak at 530 nm was also observed. For an applied bias of –2 V, this secondary peak became the main peak outrunning the former peak, whereas for an applied bias of –5 V, a third new peak at 640 nm appeared and became

predominant. As a drawback, the spectral response was dependent on the illumination level: the B responsivity increased while the R one decreased with increasing illumination intensity for the three operating voltages. Nevertheless, for a given illumination level, the necessary color signals could be obtained by algebraic manipulations from the raw outputs corresponding for the three applied reverse biases. Indeed, the photocurrents resulted for the three voltages were first integrated and then a linear 3×3 matrix transformation was applied in order to generate corrected RGB output signals. Although the resultant normalized spectral responses after this transformation were satisfactory and of significantly increased color purity compared to the initial raw outputs, they still were not optimal. The authors suggested that further improvement could be accomplished by using supplementary nonlinear transformations.

Most importantly, the sensor was employed in a 512×104 imaging array with a pixel size of 33×35 μm^2 and fabricated using a 0.8-μm CMOS process. Each pixel comprised 16 transistors as well as an integration capacitor and 3 analog memory cells for storage of the RGB signals. The authors demonstrated successfully that this imaging array's color rendering performance was at least comparable to that of conventional arrays using mosaic color filters [130]. However, the comparison was carried out using still images and no information was provided regarding the row and column scanning frequencies of the array, or at least the number of frames per second that could be provided by this imaging array. It is, therefore, probable that the necessary sequential biasing through the 3 voltages and the entire subsequent signal processing for each pixel may have necessitated a significant period of time until the entire image was finalized, resulting in a very low imaging speed that rendered the array suitable only for still images or with very slow variations.

A similar sensor with a *piiin* structure was proposed and tested by Zimmer, Knipp, and Stiebig [126, 131, 132]. Particularly the latter two authors, many times together with M. Böhm, have carried out a large volume of work in this field and have an impressive number of papers related to a-Si:H-based devices, imagers, and color sensors which, due to the very limited space, will not be reviewed here.

Imaging arrays based on *nipiin* two-color sensors were also realized and tested. In a first version, the sensor had the *nip* layers made of a-SiC:H with $E_G = 2$ eV, the first *i* layer after the *p* region and the last *n* region were also a-SiC:H but with $E_G = 1.9$ eV, and the last *i* region was a-SiGe:H with $E_G = 1.55$ eV and had a gradual composition change with linearly varying E_G at both ends [133–136]. This sensor may have constituted the starting point for subsequent improvements, and such a modified version was probably employed in successful imaging arrays of 512×512 pixels with a pixel pitch of 100×100 μm [137–139]. In these arrays, amorphous silicon TFTs were first fabricated on a glass substrate to realize the pixel addressing circuitry. After a thick (3–10 μm) oxynitride layer was used for planarization and Cr contact via formation, the color sensor and a top transparent electrode were deposited. Interestingly, only the back contact and the *n* layer of the sensor were patterned, while all the remaining sensor layers and the top electrode array were unpatterned. Besides the addressing circuitry, each pixel also contained

a contact pad occupying 67% of the pixel area. The internal *ipi* layers of the sensor were a-SiC:H with E_G values of 2.2, 1.9, and 1.9 eV, respectively, while the first/top *n* layer and the last/bottom *in* layers were a-Si:H with $E_G = 1.74$ eV. The layer thicknesses of the employed *nipiin* structure were 15, 85, 30, 145, 365, and 30 nm, respectively. This modified structure enabled an improved spectral responsivity variation as a function of the applied bias, which could also be varied in a larger range of values than in the initial a-SiC:H + a-SiGe:H-based version. Images were taken with a resolution of 185 × 280 pixels, at the bias voltages of 1.5 V, −0.6 V, and −3.5 V, respectively. A full color image was then formed by merging these separately obtained chromatic images [137–139].

All the devices that have just been reviewed earlier in this sub-section were all simple two-terminal devices. Because of this minimal type of configuration, the different colorimetric outputs had to be obtained typically by modifying the applied bias, and in this respect, they were almost identical to the voltage-scanning approach for the single-junction color sensor realized in monocrystalline silicon. Therefore, such structures—even when successfully tested—would be plagued by the same disadvantages, namely, it is not feasible to integrate them in large arrays as they are incapable of providing fast outputs containing data from rapidly changing images, as was proven by a *piiin* device with a-SiC:H/a-Si:H/a-Si-Ge:H intrinsic layers [140], or by other realizations just reviewed above. Moreover, the trichromatic discrimination with such two-terminal devices is not straightforward due to inherent nonlinearities which hamper the correct separation of the G primary which can be detected only in a limited region of bias values. This results in just a satisfactory color separation, and such structures are thus not suitable for large arrays for imaging and high-speed video capturing. Clearly, a more complex multi-*pin* structure—that is the equivalent of the multi-junction sensors in monocrystalline silicon—should be employed in order to provide immediate, simultaneous, and complete RGB outputs without the need to perform voltage scanning. Although such a solution would require more complex pixel and read-out signal processing electronics for such a three-terminal trichromatic color sensor, it would enable a much easier and more convenient deconvolution of RGB signals from the detected outputs than the two-terminal approach. However, this performance improvement is obtained at the cost of an increased complexity not only of the sensing pixel/device but also of the overall fabrication process together with newly arising problems, such as realizing good electric contacts with all the doped layers and handling a highly nonuniform surface relief on which deposition and patterning of metal layers for this purpose can be realized.

Such three-terminal trichromatic color sensors were realized using structures with two or more nonadjacent intrinsic regions and separately contactable doped regions. One of the first amorphous thin film-based color sensors of this type was a glass/TCO/*p*'*i*'*n*'/TCO/*p*'*inip*'/metal device. Here, *i*' and *i* stand for a-SiC:H and a-Si:H intrinsic layers with $E_G = 1.91$ eV and 1.78 eV, respectively. As expected, the top *p*'*i*'*n*' part detected B light, while the *p*'*in* and *nip* elements of the second section detected G and R light, respectively. Although in principle a *pinip* or *nipin* structure should perform equally well in the second section of the device,

preliminary simulations have indicated that the former *pinip* type of structure outperformed the *nipin* one. The top *p'i'n'* part exhibited a spectral response curve with a peak at ~410 nm when biased with −2 V, while the *p'inip'* section showed peaks at 530 and 635 nm when biased with −2 V and +2 V, respectively. The FWHMs of all peaks were all below 150 nm and were, therefore, considered to be "narrow" [141, 142]. Further work highlighted that instead of the previous structure, it was more advantageous to employ a sequence of the type glass/TCO1/*p'i'ni'p'*/TCO2/*p'in*/metal (Al) [142, 143]. Subsequent more substantial optimization was carried out for the entire device, and yielded thicknesses of 10, 30, 60, 200, 10, 10, 370, and 20 nm, respectively, for all semiconductor layers in this latter structure. Its spectral responses featured main peaks situated at 440, 560, and 650 nm with FWHMs of 155, 130, and 90 nm, respectively [144].

A similar sequence, but in which the initial *p'i'ni'p'* section was split in two separate sections, respectively, resulted in a four-terminal device with a glass/TCO1/*p'i'n*/TCO2/*ni'p'*/TCO3/*p'in*/metal (Al) structure which was demonstrated as a trichromatic color sensor. The top, middle, and bottom sections exhibited spectral response curves with maxima at 450, 565, and 640 nm, with FWHM values of 185, 125, and 120 nm, respectively [133, 145]. Furthermore, this three-color sensing device can be easily transformed into a six-color detector by replacing the *pin*-type section between the TCO contact layers with *pinip* sequences, as was demonstrated by the same authors [146, 147]. Multiple polynomial regression could then be used to reconstruct the desired tristimulus (or complete spectrum) values from the sensor output signals. In this case, the specific spectral sensitivities of the sensor are not required. However, a sensor characterization independent of a specific stimulus data set may be necessary. This would allow reconstructing the spectrum of the stimulus from the sensor response, but the sensor responses now need to be known. Even so, solving this problem may still be mathematically impossible in closed form, hence the so-called smoothing (or Wiener) inverse was employed instead. Both the three- and the six-channel versions of this type of color sensors were compared with a Sharp commercial scanner and also a moiré-free CMOS monocrystalline color sensor. The results showed that the three-channel sensor performed slightly better than the CMOS one, but clearly worse than the scanner. However, the performance of the six-channel color sensor was clearly superior to both commercial references. It provided very accurate tristimulus values, particularly when using the smoothing inverse, which—despite the introduction of average errors worse than the simple polynomial reconstruction—proved to be a more robust and generally applicable method [146–148].

3 Conclusions

Although relatively little known to the general public, the field of color sensors is by now quite a mature area, in which it is difficult to expect breakthrough developments such as the discovery and/or application of a totally novel color

sensing principle. By saying that we implicitly assumed that the color sensor would satisfy at least two underlying conditions: that it is realized in a semiconductor (preferably silicon) in which the previously described principle of solid-state color sensing (see again Sect. 2.1) would be applied, and—most importantly—that its fabrication would be compatible with standard CMOS processing in order to ensure integrability with signal processing circuitry as well as an easy fabrication of the final products at low cost and in a mass production. Of course, one can argue that there may still be other possible color sensing principles which were not detailed here, e.g., the application of a birefringent material in combination with polarizers, or the usage of electrically controlled LCD filters, etc. However, this requires an additional optical setup that will not only make the final system quite complex, but could even contradict the requirement of an on-chip solution and its compatibility with standard microelectronic processing.

At the same time, however, it is clear that there is still much room for improvement in the area of color sensing smart systems. As for any other product, one has to carefully design and optimize a certain device for its intended application, and then find the best fabrication process that can implement it practically. Irrespective of the material used for sensing (monocrystalline silicon or a-Si-based thin films), the resulting spectral responses will always be quite different from the initial idealized ones. In order to address this issue, as well as to achieve the final RGB (or XYZ or CIELAB, as required by the specific application/user) outputs, significant subsequent signal processing—typically based on matriceal transformations—has to be carried out. Therefore, the addition of signal processing circuits becomes a necessity, not only at the pixel stage to ensure a good quality signal, but also in subsequent stages, together with other blocks as well, e.g., for performing signal deconvolution and/or to enable correct scanning of the imaging matrix, fixed noise cancellation, modulation (e.g., sigma-delta) of the initial outputs, etc. It thus becomes clear that a more extended design team is necessary in dealing with such a complex task that extends far beyond the initial sensor design target.

Nevertheless, one may not exclude the possibility that other novel solutions for colorimetry could probably appear in a relatively near future, e.g., using nanotechnology or NanoElectroMechanical Systems (NEMS). Ultimately, only time will tell what the future keeps in store for us in this respect.

References

1. http://www.intel.com/technology/atom/index.htm?iid=tech_as+micro_atom and http://www.intel.com/products/processor/atom/index.htm
2. Middelhoek S, Audet SA (1989) Silicon sensors. Academic, London
3. Holmes JG (1935) Rapid mathematical methods for trichromatic colorimetry. Phys Soc 47(3):400–409
4. Hiskey CF (1949) Principles of precision colorimetry. Anal Chem 21(12):1440–1446
5. Hiskey CF, Young IG (1951) Principles of precision colorimetry – absorption law deviations in measurements of relative transmittance. Anal Chem 23(9):1196–1201

6. Hiskey CF, Rabinowitz J, Young IG (1950) Principles of precision colorimetry – measuring maximum precision attainable with commercial instruments. Anal Chem 22(12):1464–1470
7. Reilley CN, Crawford CM (1955) Principles of precision colorimetry – a general approach to photoelectric spectrophotometry. Anal Chem 27(5):716–725
8. Hiskey CF, Firestone D (1952) Precision colorimetry – general method of improving precision in multicomponent spectrophotometry and some practical consequences thereof. Anal Chem 24(2):342–347
9. Holobar A, Weigl BH, Trettnak W, Beneš R, Lehmann H, Rodriguez NV, Wollschlager A, O'Leary P, Raspor P, Wolfbeis OS (1993) Experimental results on an optical pH measurement system for bioreactors. Sens Actuators B 11B:425–430
10. Smyth C, Lau KT, Shepherd RL, Diamond D, Wu Y, Spinks GM, Wallace GG (2008) Self-maintained colorimetric acid/base sensor using polypyrrole actuator. Sens Actuators B 129:518–524
11. Staneva D, Betcheva R, Chovelon J-M (2007) Optical sensor for aliphatic amines based on the simultaneous colorimetric and fluorescence responses of smart textile. J Appl Polym Sci 106:1950–1956
12. Naydenova I, Jallapuram R, Toal V, Martin S (2008) A visual indication of environmental humidity using a color changing hologram recorded in a self-developing photopolymer. Appl Phys Lett 92:031109
13. Lin B, Qiu J, Gerstenmeier J, Li P, Pien H, Pepper J, Cunningham B (2002) A label-free optical technique for detecting small molecule interactions. Biosens Bioelectron 17:827–834
14. Endo T, Yanagida Y, Hatsuzawa T (2007) Colorimetric detection of volatile organic compounds using a colloidal crystal-based chemical sensor for environmental applications. Sens Actuators B 125B:589–595
15. Potyrailo RA, Ding Z, Butts MD, Genovese SE, Deng T (2008) Selective chemical sensing using structurally colored core-shell colloidal crystal films. IEEE Sens J 8(6):815–822
16. Choi SY, Mamak M, von Freymann G, Chopra N, Ozin GA (2006) Mesoporous Bragg stack color tunable sensors. Nano Lett 6(11):2456–2461
17. Puzzo DP, Arsenault AC, Manners I, Ozin GA (2009) Electroactive inverse opal: a single material for all colors. Angew Chem Int Ed Engl 48:943–947
18. Koopmans C, Ritter H (2007) Color change of n-isopropylacrylamide copolymer bearing reichardts dye as optical sensor for lower critical solution temperature and for host-guest interaction with β-cyclodextrin. J Am Chem Soc 129:3502–3503
19. Van Gent J, Lambeck PV, Kreuwel HJM, Gerritsma GJ, Sudhelter EJR, Reinhoudt DN, Popma ThJA (1989) Chromoionophores in optical ion sensors. Sens Actuators 17:297–305
20. Fritzsche M, Barreiro CG, Hitzmann B, Scheper T (2007) Optical pH sensing using spectral analysis. Sens Actuators B 128B:133–137
21. Obare SO, Murphy CJ (2001) A two-color fluorescent lithium ion sensor. Inorg Chem 40:6080–6082
22. Ozanyan KB, Yeo TL, Hindle FP, Poolton NRJ, McCann H, Tan KL (2004) Fiber-based UV laser-diode fluorescence sensor for commercial gasolines. IEEE Sens J 4(5):681–687
23. Galvan J-M, Lu G-N, Pittet P, Blum L, Leca-Bouvier B (2004) CMOS optical detector system for capillary fluorescence measurements. In: Chatard J-P, Dennis PNJ (eds) Proceedings of SPIE: proceedings of the detectors and associated signal processing international conference, Feb 2004, vol 5251, pp 154–161
24. Wolfbeis OS (2008) Sensor Paints. Adv Mater 20(19):3759–3763
25. Prasad PN (2003) Introduction to biophotonics. Wiley-Interscience, Hoboken, NJ
26. Haurowitz F (1951) Hemoglobin, anhydrohemoglobin and oxyhemoglobin. J Biol Chem 193(1):443–452
27. Dohi Y, Sugita Y, Yoneyama Y (1973) The self-association and oxygen equilibrium of hemoglobin from the lamprey, entosphenus japonicus. J Biol Chem 248:2354–2363
28. Grumann M, Steigert J, Riegger L, Moser I, Enderle B, Riebeseel K, Urban G, Zengerle R, Ducrée J (2006) Sensitivity enhancement for colorimetric glucose assays on whole blood by on-chip beam-guidance. Biomed Microdevices 8:209–214

29. Ward CJ, Patel P, James TD (2002) Molecular color sensors for monosaccharides. Org Lett 4(4):477–479
30. Madou MJ (2002) Fundamentals of microfabrication, 2nd edn. CRC, Boca Raton, FL, pp 69–70, ref.161 of Chapter 1
31. Potyrailo RA, Morris WG, Wroczynski R, Hassib L, Miller P, Dworken B, Leach AM, Boyette S, Xiao C (2009) Multi-wavelength operation of optical disk drives for chemical and biological analysis. Sens Actuators B 136B:203–208
32. Iordanov VP, Lubking GW, Ishihara R, Wolffenbuttel RF, Sarro PM, Vellekoop MJ (2002) Silicon thin-film UV filter for NADH fluorescence analysis. Sens Actuators A 97A-98A:161–166
33. Iordanov VP, Bastemeijer J, Ishihara R, Sarro PM, Bossche A, Vellekoop MJ (2004) Filter-protected photodiodes for high-throughput enzymatic analysis. IEEE Sens J 4(5):584–588
34. Pittet P, Hannati L, Lu GN (2004) Using fiber optic probe and CMOS BDJ detector for microarray spot scanning. In: Mazuray L, Rogers PJ, Wartmann R (eds) Proceedings of SPIE: proceedings of the "Optical design and engineering" international conference, vol 5249, pp 508–515
35. Ghosh A, Shrivastav A, Jose DA, Mishra SK, Chandrakanth CK, Mishra S, Das A (2008) Colorimetric sensor for triphosphates and their application as a viable staining agent for prokaryotes and eukaryotes. Anal Chem 80(14):5312–5319
36. Grant SA, Xu J (2002) Investigation of an optical dual receptor method to detect HIV. IEEE Sens J 2(5):409–415
37. Jiang L, Yu Z, Du W, Tang Z, Jiang T, Zhang C, Lu Z (2008) Development of a fluorescent and colorimetric detection methods-based protein microarray for serodiagnosis of TORCH infections. Biosens Bioelectron 24:376–382
38. Schofield CL, Field RA, Russell DA (2007) Glyconanoparticles for the colorimetric detection of cholera toxin. Anal Chem 79:1356–1361
39. Golden JP, Rowe-Taitt CA, Feldstein MJ, Ligler FS (1999) Array biosensor: recent developments. In: Lakowicz JR, Soper SA, Thompson RB (eds) Proceedings of SPIE: proceedings of the "advances in fluorescence sensing technology IV" international conference, May 1999, San Jose, CA, USA, 25 January 1999, vol. 3602, pp 132–138
40. Wang Y, Xu C, Li J, He J, Chan M (2007) A CMOS image sensor utilizing opacity of nanometallic particles for DNA detection. IEEE Trans Electron Dev 54(6):1549–1554
41. Medley CD, Smith JE, Tang Z, Wu Y, Bamrungsap S, Tan W (2008) Gold nanoparticle-based colorimetric assay for the direct detection of cancerous cells. Anal Chem 80:1067–1072
42. Wei H, Chen C, Han B, Wang E (2008) Enzyme colorimetric assay using unmodified silver nanoparticles. Anal Chem 80(18):7051–7055
43. Paap A, Askraba S, Alameh K, Rowe J (2008) Photonic-based spectral reflectance sensor for ground-based plant detection and weed discrimination. Opt Express 16(2):1051–1055
44. Smith SD, Bowers DG, Mitchelson-Jacob EG (1997) Optical determination of phytoplankton floristic composition. In: Ackleson SG, Frouin RJ (eds) Proceedings of SPIE: proceedings of the "Ocean Optics XIII" international conference, Halifax, Nova Scotia, Canada, 22 Oct 1996, vol 2963, pp 532–537
45. Rast M, Bezy J-L (1990) ESA's medium resolution imaging spectrometer: mission, system, and applications. In: Vane G (ed) Proceedings of SPIE: proceedings of the international conference on imaging spectroscopy of the terrestrial environment, Sept 1990, vol 1298, pp 114–126
46. Brown S, Tett PB, Wilton R (1997) Four-channel color sensor to measure chlorophyll and carotenoid concentration. In: Ackleson SG, Frouin RJ (Eds) Proceedings of SPIE: proceedings of the "Ocean Optics XIII" international conference, Halifax, Nova Scotia, Canada, 22 Oct. 1996, (Feb. 1997), vol 2963, pp 603–608
47. Yokota M, Okada T, Yamaguchi I (2007) An optical sensor for analysis of soil nutrients by using LED light sources. Meas Sci Technol 18:2197–2201
48. Kress-Rogers E (ed) (2001) Instrumentation and sensors for the food industry. CRC, Boca Raton, FL

49. Fiesler E, Campbell SR, Kempen L, Duong TA (1998) Color sensor and neural processor on one chip, Invited Paper. In: Proceedings of SPIE: proceedings of the international conference on applications and science of neural networks. Fuzzy systems, and evolutionary computation, San Diego, CA, USA, July 1998, vol 3455, pp 214–221.
50. Folin O, Ciocalteu V (1927) On tyrosine and tryptophane determination in proteins. J Biol Chem 73(2):627–650
51. Lowry OH, Rosenrough NJ, Farr AL, Randall RJ (1951) Protein measurement with folin reagent. J Biol Chem 193(1):265–275
52. Doka O, Bicanic D (2002) Determination of total polyphenolic content in red wines by means of the combined he-ne laser optothermal window and Folin-Ciocâlteu colorimetry assay. Anal Chem 74:2157–2161
53. Sheridan C, O'Farrell M, Lewis E, Lyons WB, Flanagan C, Jackman N (2006) Monitoring food quality using an optical fibre based sensor system—a comparison of Kohonen and back-propagation neural network classification techniques. Meas Sci Technol 17:229–234
54. Marszalec E, Kopola H, Myllylä R (1993) Non-destructive testing of the quality of naturally white food products. Sens Actuators B 11B:503–509
55. Hunt MA, Goddard JS Jr, Hylton KW, Karnowski TP, Richards RK, Simpson ML, Tobin KW Jr, Treece DA (1999) Imaging tristimulus colorimeter for the evaluation of color in printed textiles. In: Tobin KW Jr, Chang NS (eds) Proceedings of SPIE: "Machine vision applications in industrial inspection VII" conference, San Jose, CA, USA, 25 Jan 1999, vol 3652, pp 118–128
56. Kok CJ, Boshoff MC (1971) New spectrophotometer and tristimulus mask colorimeter. Appl Opt 10(12):2617–2620
57. Wharmby DO (1975) Improvements in the use of filter colorimeters. J Phys E Sci Instrum 8:41–44
58. Campos J, Pons A, Corrons A (1987) Description of a precision colorimeter. J Phys E Sci Instrum 20:882–884
59. Sametoglu F (2007) Relation between the illuminance responsivity of a photometer and the spectral power distribution of a source. Opt Eng 46(9):093607
60. Yokomizu Y, Spencer JW, Jones GR (1998) Position location of a filamentary arc using a tristimulus chromatic technique. J Phys D Appl Phys 31:3373–3382
61. Jones GR, Russell P, Khandaker I (1994) Chromatic interferometry for an intelligent plasma processing system. Meas Sci Technol 5:639–647
62. Aspey RA, Brazier KJ, Spencer JW (2005) Multiwavelength sensing of smoke using a polychromatic LED: mie extinction characterization using HLS Analysis. IEEE Sens J 5(5):1050–1056
63. Reichelt TE, Aceves-Fernandez MA, Kolupula YR, Pate A, Spencer JW, Jones GR (2006) Chromatic modulation monitoring of airborne particulates. Meas Sci Technol 17:675–683
64. Aspey RA, Brazier KJ (2003) In situ optical sensing of diesel exhaust particulates using a polychromatic LED source. Meas Sci Technol 14:751–758
65. Barroqueiro S, Jones GR (2004) Chromatic single point sensor for aircraft fuel systems. Meas Sci Technol 15:814–820
66. Khandaker II, Glavas E, Jones GR (1993) A fibre-optic oil condition monitor based on chromatic modulation. Meas Sci Technol 4:608–613
67. Sierakowski M, Domanski AW, Lesiak P (2006) Application of neural network for fiber-optic color sensor. In: Culshaw B, Mignani AG, Bartelt H, Jaroszewicz LR (eds) Proceedings of SPIE: Proceedings of the international conference on optical sensing II, 3 April 2006, Strasbourg, France, vol 6189, pp 61892C
68. Cashdollar KL, Lee CK, Singer JM (1979) Three-wavelength light transmission technique to measure smoke particle size and concentration. Appl Opt 18(11):1763–1769
69. Brenci M, Guzzi D, Mencaglia A, Mignani AG, Pieraccini M (1995) Quasi-monodisperse particulate characterization with optical fibers and a three-wavelength scattering technique. Sens Actuators B 29B:115–118

70. Chen J, Zhu X (1996) White balance tester with color sensor for industrial applications. In: Mu G, Jin G, Sincerbox GT (eds) Proceedings of SPIE: proceedings of the international conference on holography and optical information processing (ICHOIP '96), Nanjing, P.R. of China, 26 Aug 1996, vol 2866, pp 443–445
71. Johansson D, Morn T (2006) The potential of colour measurement for strength prediction of thermally treated wood. Holz als Roh- und Werkstoff 64:104–110
72. Ramasubramanian MK, Venditti RA, Ammineni C, Mallapragada V (2005) Optical sensor for noncontact measurement of lignin content in high-speed moving paper surfaces. IEEE Sens J 5(5):1132–1139
73. Palviainen J, Sorjonen M, Silvennoinen R, Peiponen K-E (2002) Optical sensing of colour print on paper by a diffractive optical element. Meas Sci Technol 13:N31–N37
74. Hung P-C (1999) Colorimetric characterization beyond three colorants. In: Eschbach R, Marcu GG (eds) Proceedings of SPIE: proceedings of the international IS&T/SPIE conference on color imaging: device-independent color, color hardcopy, and graphic arts V, San Jose, CA, USA, 25 Jan 2000, vol 3963, pp 196–207
75. Wolfe CN, Holonyak N Jr, Stillman GE (1989) Physical properties of semiconductors. Prentice Hall, Englewood Cliffs, NJ
76. Singh J (1995) Semiconductor optoelectronics – physics and technology. McGraw-Hill International Edition, Electrical Engineering Series, McGraw-Hill, New York
77. (1988) Properties of silicon, EMIS Datareviews No.4, INSPEC. The Institution of Electrical Engineers, London
78. Dillon PLP, Barrault AT, Horak JR, Garcia E, Martin TW, Light WA (1978) Fabrication and performance of color filter arrays for solid-state imagers. IEEE Trans Electron Dev ED-25(2):97–101
79. Dillon PLP, Barrault AT, Horak JR, Garcia E, Martin TW, Light WA (1978) Fabrication and performance of color filter arrays for solid-state imagers. IEEE J Solid-State Circ SC-13(1):23–27
80. Dillon PLP, Lewis DM, Kaspar FG (1978) Color imaging system using a single CCD area array. IEEE Trans Electron Dev ED-25(2):102–107
81. Dillon PLP, Lewis DM, Kaspar FG (1978) Color imaging system using a single CCD area array. IEEE J Solid-State Circ SC-13(1):28–33
82. Grotta SW (2001) Anatomy of a digital camera: image sensors. Available at http://www.extremetech.com/article/0,3396,apn%253D2%2526s%253D1009%2526a%253D2036%2526ap%253D1,00.asp
83. Parmar M, Reeves SJ (2004) Color filter array design based on a human visual model. In: Bouman CA, Miller EL (eds) Proceedings of SPIE: proceedings of the international conference on computational imaging II, San Jose, CA, USA, 19 Jan 2004, vol 5299, pp 73–82
84. Wolffenbutel RF, Regtien PPL (1986) A novel approach to solid-state colour sensing. Sens Actuators 9:199–211
85. Wolffenbutel RF (1987) A simple integrated color indicator. IEEE J Solid-State Circ SC-22 (3):350–356
86. Wolffenbuttel RF, Blaauw EJ, Wolffenbuttel MR, de Graaf G (1991) Tri-colorimetric detector in silicon with one photodiode. In: Proceedings of the IEEE 49th annual device research conference, 17–19 June 1991, p IIB8
87. Wolffenbuttel RF (1987) Photodiodes in silicon with an intrinsic colour filtering capability. In: Proceedings of the 4th international conference on solid-state sensors and actuators – Transducer '87, Tokyo, Japan, pp 219-222; also see the Method and circuit for determining the wavelength of light. US Patent 4,749,851, 7 June 1988, awarded to the same author
88. Wolffenbuttel RF (1989) Operation of the silicon colour filtering element. Sens Actuators 16:13–23
89. Wolffenbuttel RF (1987) Color filters integrated with the detector in silicon. IEEE Electron Dev Lett EDL-8(1):13–15

90. Wolffenbuttel RF (1988) Integrated all-silicon color filtering element integrated with an enhanced wavelength tunability. IEEE Electron Dev Lett 9(7):337–339
91. Kako N, Tanaka N, Suzuki C (1983) Combustion detection with a semiconductor color sensor. Sens Actuators 4:655–660
92. Wolffenbuttel RF (1989) Flexible spectral-response shaping of silicon photodiodes. Sens Actuators 17:249–253
93. Wolffenbuttel RF, de Graaf G, Engen E (1995) Bipolar circuits for readout of an integrated silicon color sensor. In: Proceedings of the IEEE international symposium on circuits and systems 1995 – ISCAS '95, 28 Apr–3 May 1995, vol 1, pp 299–302
94. Wolffenbuttel RF, de Graaf G (1990) Performance of an integrated silicon colour sensor with a digital output in terms of response to colours in the colour triangle. Sens Actuators A A21-A23:574–580
95. Lu GN, Ben Chouikha M, Sou G, Sedjil M (1996) Colour detection using a buried double p-n junction structure implemented in the CMOS process. Electron Lett 32(6):594–596
96. Feruglio S, Hanna VF, Alquié G, Vasilescu G (2005) Modelling of the CMOS buried double-junction photodetector. Microw Opt Technol Lett 45(6):507–514
97. Lu GN, Sou G, Ben Chouikha M, Sedjil M (1999) Design and implementation of integrated BDJ detector in a standard CMOS technology. In: Courtois B, Crary SB, Ehrfeld W, Fujita H et al (eds) Proceedings of SPIE: proceedings of the international conference on design, test, and microfabrication of MEMS and MOEMS 1999, vol 3680, pp 358–366
98. Lu GN, Ben Chouikha M, Sedjil M, Sou G, Alquié G, Rigo S (1997) Buried double p-n junction structure using a CMOS process for wavelength detection. In: Motamedi ME, Herzig HP (eds) Proceedings of SPIE: proceedings of the international conference on microelectronic structures and MEMS for optical processing III, Sept 1997, vol 3226, pp 204–213
99. Alexandre A, Sou G, Ben Chouikha M, Sedjil M, Lu GN, Alquie G (2000) Modeling and design of multiple buried junctions detectors for color systems development. In: Courtois B, Crary SB, Gabriel KJ, Karam JM et al (eds) proceedings of SPIE: Proceedings of the international conference on design, test, integration, and packaging of MEMS/MOEMS, Apr 2000, vol. 4019, pp 288–298
100. Haned F, Ben Chouikha M, Desormeaux AB, Alqué G (2005) Optoelectronic library for color sensor design. In: Blouke MM (ed) Proceedings of SPIE: proceedings of the international conference on sensors and camera systems for scientific and industrial applications VI, San Jose, CA, USA, 18 Jan 2005, vol 5677, p 16
101. Ben Chouikha M, Lu GN, Sedjil M, Sou G (1998) CMOS linear array of BDJ color detectors. In: Bernard TM (ed) Proceedings of SPIE: proceedings of the international conference on advanced focal plane arrays and electronic cameras II, Sept 1998, vol 3410, pp 46–53
102. Lu GN, Sou G, Aubert A, Carrillo G, El Mourabit A (2002) On-chip synchronous detection for CMOS BDJ optical detector. In: Courtois B, Karam JM, Markus KW et al. Proceedings of SPIE: proceedings of the international conference on design, test, integration, and packaging of MEMS/MOEMS'02, Apr 2002, vol 4755, pp 208–217.
103. Seitz P, Leipold D, Kramer J, Raynor JM (1993) Smart optical and image sensors fabricated with industrial CMOS/CCD semiconductor processes. In: Blouke MM (ed) Proceedings of SPIE: proceedings of the international conference on charge-coupled devices and solid state optical sensors III, San Jose, CA, USA, 2 Feb 1993, vol 1900, pp 21–30
104. Bartek M, Gennissen PTJ, Sarro P, French PJ, Wolffenbuttel RF (1994) An integrated silicon colour sensor using selective epitaxial growth. Sens Actuators A 41A-42A:123–128
105. Ben Chouikha M, Lu GN, Sedjil M, Sou G (1996) Color-sensitive photodetectors in standard CMOS and BiCMOS technologies. In: Bernard TM (ed) Proceedings of SPIE: proceedings of the international conference on advanced focal plane arrays and electronic cameras, 7 Oct 1996, Berlin, Germany, vol 2950, pp 108–120
106. Ben Chouikha M, Lu GN, Sedjil M, Sou G (1998) Colour detection using buried triple pn junction structure implemented in BiCMOS process. Electron Lett 34(1):120–122

107. Sedjil M, Lu GN, Ben Chouikha M, Alexandre A (1999) Modeling of BDJ and BTJ structures for color detection. In: Courtois B, Crary SB, Ehrfeld W, Fujita H, Karam JM, Markus KW (eds) Proceedings of SPIE: proceedings of the international conference on design, test, and microfabrication of MEMS and MOEMS 1999, vol 3680, pp 388–397
108. Thomson M, Westland S (2001) Colour-imager characterization by parametric fitting of sensor responses. Color Res Appl 26(6):442–449
109. Merill RB (1999) Color separation in an active pixel cell imaging array using a triple-well structure. US Patent 5,965,875, 12 Oct 1999.
110. Merill RB (2003) Vertical color filter detector group and array. US Patent 6,632,701, 14 Oct 2003
111. Longoni A, Zaraga F, Langfelder G, Bombelli L (2008) The transverse field detector (TFD): a novel color-sensitive CMOS device. IEEE Electron Dev Lett 29(12):1306–1308
112. Langfelder G, Longoni A, Zaraga F (2009) The transverse field detector: a CMOS active pixel sensor capable of "on-line" tuning of the spectral response. In: Proceedings of the IEEE sensors conference 2009, paper 5990
113. Street RA (ed) (2000) Technology and applications of amorphous silicon. Springer, Berlin
114. Street RA (2005) Hydrogenated amorphous silicon, Solid state science series. Cambridge University Press, Cambridge
115. Luft W, Tsuo YS (1993) Hydrogenated amorphous silicon alloy deposition processes. Marcel Dekker, New York
116. de Cesare G, Di Rosa P, La Monica S, Salotti R, Schirone L, Saggio G, Verona E (1993) Two dimensional image sensors based on amorphous silicon alloy p-i-n diodes. J Non Cryst Solids 164–166:789–792
117. Tomiyama S, Ozawa T, Ito H, Nakamura T (1996) Amorphous silicon thin film transistors and application to image sensors. J Non Cryst Solids 198–200:1087–1092
118. Rietman EA, Frye RC, Wong CC, Kornfeld CD (1989) Amorphous silicon photoconductive arrays for artificial neural networks. Appl Opt 28(15):3474–3478
119. Stearns RG, Weisfield RL (1992) Two-dimensional amorphous-silicon photoconductor array for optical imaging. Appl Opt 31(32):6874–6881
120. Manabe S, Mastunaga Y, Furukawa A, Yano K et al (1991) A 2-million-pixel CCD image sensor overlaid with an amorphous silicon photoconversion layer. IEEE Trans Electron Dev 38(8):1765–1771
121. Lemmi F, Mulato M, Ho J, Lau R, Lu JP, Street RA, Palma F (2001) Active matrix of amorphous silicon multijunction color sensors for document imaging. Appl Phys Lett 78(10):1334–1336
122. Mulato M, Lemmi F, Ho J, Lau R, Lu JP, Street RA (2001) Two-color amorphous silicon image sensor. J Appl Phys 90(3):1589–1599
123. Yang D, Ambo KS, Holm-Kennedy JW (1988) Four-color discriminating sensor using amorphous silicon drift-type photodiode. Sens Actuators 14:69–77
124. Vieira M, Louro P, Fantoni A, Fernandes M, de Carvalho CN, Lavareda G (2005) Tuning the spectral distribution of p–i–n a-SiC:H devices for colour detection. Sens Actuators A 123A–124A:326–330
125. de Cesare G, Galluzzi F, Irrera F, Lauta D, Ferrazza F, Tucci M (1996) Variable spectral response photodetector based on crystalline/amorphous silicon heterostructure. J Non Cryst Solids 198–200:1189–1192
126. Zhu Q, Stiebig H, Rieve P, Giehl J, Sommer M, Böhm M (1994) New type of thin film color image sensor. In: Becker M, Daniel RW, Loffeld O (eds) Proceedings of SPIE: proceedings of the International conference on sensors and control for automation, Frankfurt, Federal Republic of Germany, 19 June 1994, vol 2247, pp 301–310.
127. Stiebig H, Böhm M (1993) Optimization criteria for a-Si:H nipin color sensors. J Non Cryst Solids 164–166:785–788
128. Stiebig H, Ulrichs C, Kulessa T, Fsch J, Finger F, Wagner H (1996) Transient photocurrent response of a-Si:H based three-color nipin detector. J Non Cryst Solids 198–200:1185–1188
129. Louro P, Vygranenko Y, Martins J, Fernandes M, Vieira M (2007) Colour sensitive devices based on double p-i-n-i-p stacked photodiodes. Thin Solid Films 515:7526–7529

130. Rieve P, Sommer M, Wagner M, Seibel K, Böhm M (2000) a-Si:H color imagers and colorimetry. J Non Cryst Solids 266–269:1168–1172
131. Zimmer J, Knipp D, Stiebig H, Wagner H (1999) Amorphous silicon-based unipolar detector for color recognition. IEEE Trans Electron Dev 46(5):884–891
132. Zimmer J, Knipp D, Stiebig H, Wagner H (2000) Thin film detector for color recognition: an experimental and numerical study. J Non Cryst Solids 266–269:1173–1177
133. Knipp D, Stiebig H, Wagner H (2001) Thin film color sensors in multichannel technology. In: Blouke MM, Canosa J, Sampat N (eds) Proceedings of SPIE: proceedings of the international conference on sensors and camera systems for scientific, industrial, and digital photography applications II, San Jose, CA, USA, 23 Jan 2001, vol 4306, pp 156–167
134. Knipp D, Stiebig H, Fölsch J, Finger F, Wagner H (1998) Amorphous silicon based nipiin structure for color detection. J Appl Phys 83(3):1463–1468
135. Stannowski B, Stiebig H, Knipp D, Wagner H (1999) Transient photocurrent response of three-color detectors based on amorphous silicon. J Appl Phys 85(7):3904–3911
136. Stiebig H, Knipp D, Zimmer J, Wagner H (1998) Transient behavior of optimized nipiin three-color detectors. IEEE Trans Electron Dev 45(7):1438–1444
137. Knipp D, Street RA, Stiebig H, Krause M, Lu J-P, Ready S, Ho J (2006) Vertically integrated thin film color sensor arrays for imaging applications. Opt Express 14(8):3106–3113
138. Knipp D, Street RA, Stiebig H, Krause M, Lu J-P, Ready S, Ho J (2006) Vertically integrated amorphous silicon color sensor arrays. IEEE Trans Electron Dev 53(7):1551–1558
139. Knipp D, Street RA, Stiebig H, Krause M, Lu J-P, Ready S, Ho J (2006) Color aliasing free thin-film sensor array. Sens Actuators A 128A:333–338
140. Neidlinger T, Bruggemann R, Brummack H, Schubert MB (1998) Colour separation in a-Si: H based p-i-i-n sensors: temperature and intensity dependence. J Non Cryst Solids 227–230:1335–1339
141. Topič M, Smole F, Furlan J (1996) Bias-controlled three-color a-Si:H detectors. In: Proceedings of the 8th mediterranean electrotechnical conference 1996 – MELECON '96, 13–16 May 1996, vol 3, pp 1287–1290. Digital Object Identifier 10.1109/MELECON.1996.551181
142. Topič M, Smole F, Furlan J, Kusian W (1996) Stacked a-SiC:H/a-Si:H heterostructures for bias-controlled three-colour detectors. J Non Cryst Solids 198–200:1180–1184
143. Topič M, Smole F, Furlan J, Kusian W (1998) Stacked a-Si:H-based three-colour detectors. J Non Cryst Solids 227–230:1326–1329
144. Topič M, Stiebig H, Knipp D, Smole F (1999) Optimization of a-Si:H-based three-terminal three-color detectors. IEEE Trans Electron Dev 46(9):1839–1845
145. Knipp D, Stiebig H, Folsch J, Wagner H (1998) Four terminal color detector for digital signal processing. J Non Cryst Solids 227–230:1321–1325
146. Herzog PG, Knipp D, Stiebig H, König F (1998) Characterization of novel three- and six-channel color moiré-free sensors. In: Beretta GB, Eschbach R (eds) Proceedings of SPIE: proceedings of the international conference on color imaging: device-independent color, color hardcopy, and graphic arts IV, San Jose, CA, USA, 26 Jan 1999, vol 3648, pp 48–59
147. Herzog PG, Knipp D, König F, Stiebig H (1999) Performance of amorphous-silicon-based multiple-channel color sensors. In: Eschbach R, Marcu GG (eds) Proceedings of SPIE: proceedings of the international conference on color imaging: device-independent color, color hardcopy, and graphic arts V, San Jose, CA, USA, 25 Jan 2000, vol 3963, pp 60–69.
148. Herzog PG, Knipp D, Stiebig H, König F (1999) Colorimetric characterization of novel multiple-channel sensors for imaging and metrology. J Electron Imaging 8(4):342–353

Addressing of Concentration Spaces for Bioscreenings by Micro Segmented Flow with Microphotometric and Microfluorimetric Detection

J. Michael Köhler, Anette Funfak, Jialan Cao, Dana Kürsten, Steffen Schneider, and P. Mike Günther

Abstract Microfluid segments allow the efficient realization and application of well-separated test volumes for high-resolved and multidimensional investigations. With typical volumes in the nanoliter and lower microliter range, screening runs with several hundred up to several thousand single volumes can be realized with a total consumption of less than 1 mL test solution. The fluid segments act as confinements for the determination of the dose-related cell response on different effectors which can be applied in a precision better than 1% in concentration. One, two, or higher dimensional concentration spaces are addressed by PC-controlled low-pulsation syringe pumps. Micro flow-through photometric measurements allow the characterization of the quality of segment sequences and the determination of up to four optical channels with typical measurement frequencies between 500 and 5,000 Hz. The generation and characterization of microfluid segment sequences for screening purposes, the realization of different concentration spaces for the determination of effects of single substances and combinatorial effects, and the cultivation of different organisms are reported. The investigations have shown the applicability of micro segmented flow for fast microtoxicological screenings with prokaryotic and eukaryotic microorganisms like *E. Coli*, *Chlorella vulgaris,* and *Saccharomyces cerevisiae* and for multicellular systems like embryos of *Danio rerio*.

Keywords Microfluidics • Micro photometry • Micro fluorometry • Micro segmented flow • Droplets • Screening • Cell cultivation • Toxicology

J.M. Köhler (✉) • A. Funfak • J. Cao • D. Kürsten • S. Schneider • P.M. Günther
Institute of Micro- und Nanotechnologies, Technical University Ilmenau, PF 10 05 65, 98684 Ilmenau, Germany
e-mail: michael.koehler@tu-ilmenau.de

W. Fritzsche and J. Popp (eds.), *Optical Nano- and Microsystems for Bioanalytics*, Springer Series on Chemical Sensors and Biosensors (2012) 10: 47–82
DOI 10.1007/978-3-642-25498-7_2,

Contents

1 Introduction

The large application of optical methods in the characterization of liquids in microfluidic systems is due to the enormous progress in the development of optical devices and methods during the last 3 decades. They combine the application of efficient light sources with strict definition of spatial light distribution, wavelength selection, time control or pulsation, and highly sensitive optical detection. In particular, the development of compound semiconductor devices led to a high number of powerful devices like LEDs, laser diodes, and light detectors. A huge number of chemical and bioassays were adapted to this development in order to exploit the technical advantages of optical systems. Hence, a lot of assays and screening protocols are based on highly sensitive fluorometric read-outs. The inclusion of suited optical labels such as functionalized dyes and quantum dots allowed the realization of highly sensitive and selective analytical procedures and the development of fast-working screening systems [1–3].

Starting in the late 1970s, microfluidics was developed in parallel to the vigorous development of microoptical devices and its development was intensified in the beginning of the 1990s [4]. But, the high expectations on the exploitability of fluidic microsystems for information transfer from chemical and biological systems into digital electronic systems were only fulfilled partially. Despite some special efforts like for example the introduction of DNA chips, the progress in the design,

development, and practical introduction of analytical microsystems and so-called Micro Total Analysis Systems (μ-TAS) were slower than expected. The reason therefore was the complexity of problems in the system development reaching from design itself and microfabrication over back-processing, assembling and handling to chemical and biological compatibility, stability of surfaces, and robustness in use.

The determination of a dose-related response of cells or multicellular organisms on chemical substances is a fundamental issue for the protection of environment, for application of agrochemicals, for food production and food quality control, for industrial safety, for toxicology, for medical treatments, and for pharmaceutical developments [5, 6]. The effect of a substance on an organism depends not only on the species and the specific genotype, but also on the individual environment of this organism, the preconditioning effects or predamaging, and the individual "life-history." Therefore, toxicological tests are carried out frequently with larger ensembles of individuums in order to obtain an averaging and to filter individual effects. Strongly standardized conditions should ensure reproducible results by application of selected test systems [7, 8]. Such an approach improves the comparability of test results, but suppresses the plurality of influence factors for dose-related responses. Thereby, the information about the distribution of individual behavior gets lost.

A particular serious problem is the effect of a second or third effector substance which can compensate or enforce the effect of the first substance [9–11]. Under real environmental conditions and also in many technical applications or in medicine, human beings or other organisms are not only exposed to one substance; they are confronted with complex mixtures of effectors and changing compositions. Hence, new screening approaches are demanded for the evaluation of the effect of one substance under different conditions and under the presence of other effectors. This new approach should offer a set of options for overcoming the limitations of the recent standard tests including:

- Large sets of single test volumes in order to get statistical information instead of an averaging
- Application of small numbers of test organisms, single individuals or cells instead of large ensembles of test organisms
- Step-wise variation of two or more parameters in one screening experiment
- Precise control of concentrations of test substances
- Realization of long-time tests (up to weeks) for slowly growing organisms
- Avoiding of open surfaces and undesired solvent evaporation
- Automated and time-resolved measurement of biological response
- Minimal test volumes and minimal amounts of consumed organisms and chemicals

These challenges demand a microfluidic strategy. Normally, micro or nanotiterplates are applied for high-throughput screenings. Concentration spaces are addressed in these systems by micropipetting and micro dispensers. High-resolved dose–response functions demand a very precise and reproducible pipetting. This can be realized to a certain extent by microtechnical pipetting and

dispensing devices if test volumes in the range of some tens of microliters are used and the transferred volumes for dosing are in the upper nanoliter range. In principle, dosing is possible down to the picoliter range; but with decreasing transfer volumes, the applicability is reduced strongly by increasing sensitivity of the dispensing devices from changes in the composition of transferred liquids, surface, and environmental effects. The main problems are the increasing difficulties due to the open liquid surfaces and the changing wetting conditions.

All these difficulties are avoided by the application of droplet-based microfluidics or the so-called micro segmented-flow technique [12–15]. This technique uses the spontaneous but very reproducible formation of small droplets during the injection of one liquid into a microchannel or microtube with a streaming second liquid which is immiscible with the first one. The size of the regular formed segments can be controlled by the tube diameter and is moderately affected by the flow rates, the viscosities of liquids, the nozzle geometry, and the wetting conditions [16–22]. The typical segment size is in the range between picoliters and some microliters. Microfluid segments can be manipulated in different ways: switched, split, and fused [23–28]. Most applications are found in the upper nanoliter range. The technique was originally developed for the flow-injection analysis, but attracts increasing attention from fundamentals in microfluidics as well as for application in chemical synthesis [29, 30], formation of nanoparticles [31–36], medical diagnostics [37], and drug development. These applications use the controlled wetting and evaporation conditions, the plug-like segment transport connected with a very narrow residence time distribution in micro continuous-flow processes, a convenient dosing of small amounts of reactants, a fast mixing of reactants supported by the flow-induced segment-internal convection, and the easy handling of segments inside microtubes and microchannels. Finally, the large fluidic dispersion which disturbs the application of microfluidic systems in homogeneous phase processes can be completely suppressed by the application of a droplet-based flow.

The segmented flow technique is particularly suited for biological screenings. In this case, the aqueous test solutions are embedded in a carrier liquid of an alkane or a perfluorinated hydrocarbon. High contact angles between the cultivation liquid and the hydrophobic wall as well as the formation of a thin film of carrier liquid during the segment motion decouple the aqueous phase from the wall and help to protect the wall for adsorption of substances, adhesion of cells, and fouling by biomacromolecules and cells. A biological or chemical cross-talk between fluid segments is nearly completely excluded.

These advantages allow an improvement of screenings and open a lot of interesting and new possibilities for investigating the behavior of cells and organisms [38–43]. Beside statistical information, the cocultivation of cells is studied under well-defined conditions. The microfluidic compartments can be understood as examples of microenvironments with a strictly reduced but precisely defined set of parameters. Hence, low amounts of substances added to the segment or released from a cell are stored in the pico- or nanoliter droplets, and their effect on other cells can be studied at a comparatively higher concentration because a lowering of

concentration of a released substance by diffusive dilution is suppressed by the restricted test volume.

After the successful demonstration to cultivate cells in microfluid segments, the principle was applied for the separation and individual cultivation of highly diverse mixtures of microorganisms [44]. It is used for DNA diagnostics [45–48], for cryoconservation, and for food characterization [49]. The applicability of sequences of microfluid segments in toxicology was shown for procaryotic [50, 51] and eucaryotic microorganisms as well as for multicellular systems such as embryos [52]. Recently, it also was shown that combinatorial effects with large segment series can be investigated [53, 54]. In the following, the dosing into microfluid segments, the addressing of two- and three-dimensional concentration spaces and the methods of concentration control will be reported. Some examples of applications in micro toxicology will be given and some prospects for future developments will be discussed.

2 Micro Flow-Through Characterization of Microfluid Segment Sequences

2.1 Microtube Flow-Through Spectrometry

The principle of miniaturized spectrometry is well known from light microscopic investigations. In most cases, collected light from a non-moving object or a microscopic image area is guided to a monochromator and an optical detector. The illumination, optical imaging, and light collection are supported frequently by the application of optical carriers (slides or micro cuvettes) with plan-parallel walls.

Spectrometry and spectrophotometry on microfluid segments have to reconsider the fact that the fluid segments are moving. Thus, the integration time of the measurements has to be low, typically in the sub-second range. Otherwise, the flow rates have to be kept below about 10 μL/min. In addition, the optical imaging is affected in many cases by non-planar interfaces. The microfluid segments possess preferably a rotational symmetry and half-spheric pole regions. The shape of segments is controlled by the interaction between shear forces and interface forces. The refractive indices of tube wall material, of the carrier liquid, and of the process liquid are different so that refraction takes place at all interfaces.

Despite these difficulties, it is possible to get spectra from moving fluid segments with volumes in the sub-microliter and in the nanoliter range. Therefore, we applied a fiber-based experimental arrangement. The illumination light was guided through an aperture in a cube-like detector unit which fits the outer diameter of the micro tube. A second aperture and fiber collect the light at the opposite position of the input element (transmission configuration). This light is guided by the second glass fiber to a compact spectrometer (Fig. 1). The arrangement was successfully applied for spectrophotometric characterization of microfluid segments in a micro continuous-flow synthesis of azo dyes [30].

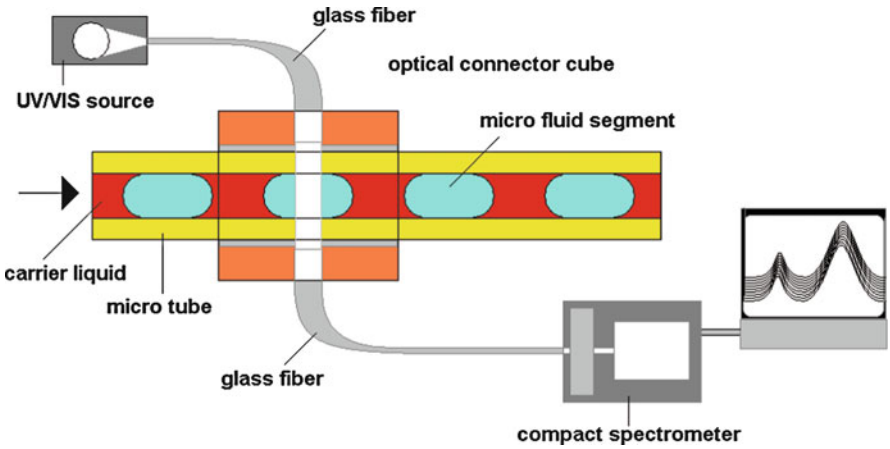

Fig. 1 Experimental arrangement of the fiber-based micro flow-through spectrometry

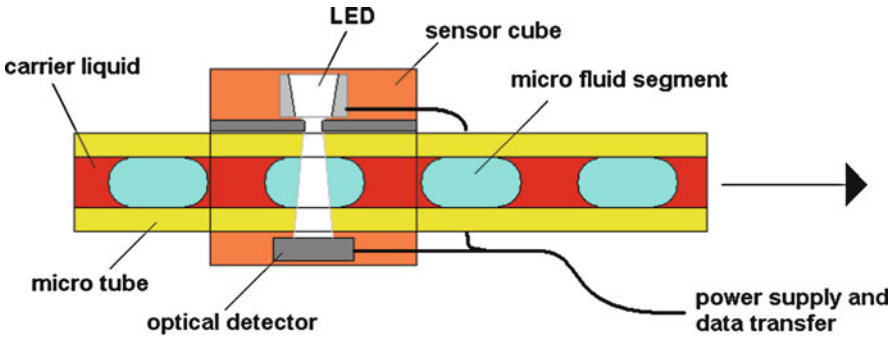

Fig. 2 Compact microphotometer arrangement for fast optical characterization for microfluid segment sequences

2.2 Microtube Flow-Through Photometry

The monitoring and control of faster moving fluid segments demand for a measurement method with short measurement time. Exposure times in the lower millisecond range (< 25 ms) are required for photometric characterization of nanoliter fluid segments moving with volume flow rates of 0.6 mL/min and above and a segment length of about 1 mm.

These requirements can be met by micro flow-through photometers. These micro devices consist of a light-emitting diode for light supply in the desired spectral range, an input aperture, and a photodiode for detection. All components are mounted in a compact housing with a central borehole for the uptake of the microtube. A mono channel device has a volume of about 1 cm^3 (Fig. 2). For simultaneous measurement in different spectral ranges, two or three LED/

photodiode pairs are integrated in one housing. The high-output power of these LEDs and the high sensitivity and temporal resolution of the photo detectors allow measurement frequencies up to 10 kHz. Figure 3 shows examples for the optical monitoring of microfluid segment sequences with single volumes in the sub-µL range. Each spot represents a single optical measurement. The data prove the precision of fast photometric measurements as well as the high reproducibility in the formation and transport of fluid segments. The passage of one single fluid segment through the optical channel of a microphotometer during a time period of about 350 ms is shown in Fig. 3b.

The microphotometric flow-through measurement inside tubes can also be applied for further reduced liquid volumes: Dyed aqueous solutions can also be detected with high resolution in case of tubes with an internal diameter of 75 µm, where single-fluid segments with volumes of only 1 nL are formed (Fig. 4).

The micro flow-through photometry is not only applied for the determination of concentrations of substances inside the fluid segments, but can also be used for the evaluation of the quality of a complete sequence of fluid segments. The precise automated determination of the entrance and the exit time of a segment supplies data for segment size- and segment distance-related times. These values can be

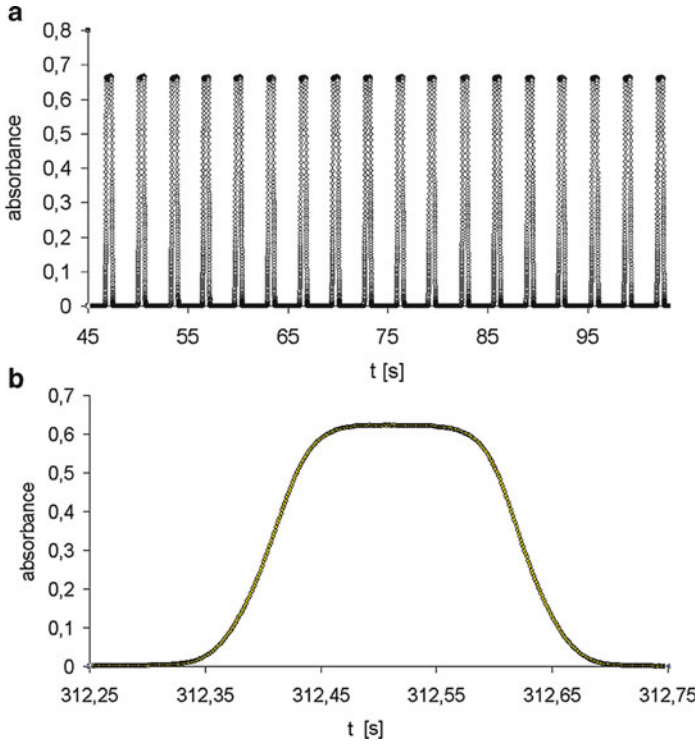

Fig. 3 (**a**) Example of a microphotometric monitoring of a microfluid segment sequence (internal tube diameter: 0.5 mm), (**b**) Highly resolved microphotometric profile of a microfluid segment passing the optical channel (measurement frequency: 1 kHz)

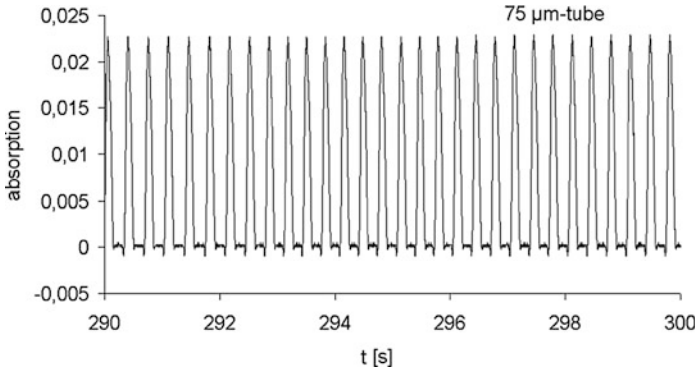

Fig. 4 Microphotometric characterization of a sequence of microfluid segments with single volumes in the lower nL-range (internal tube diameter: 75 µm)

plotted in a two-dimensional diagram in order to visualize deviations in these both parameters inside the segment sequence. Low scattering of both parameters indicates a high quality in formation and transport of the fluid segments (Fig. 5a); a larger distribution indicates less-controlled conditions during the segment generation (Fig. 5b). This technique is particularly suited for the characterization of segment sequences integrating different populations of segments. The stacking of two segment sequences with different segment size and content but synchronization of segments results in a strong periodic segment pattern which is well reflected by the microphotometric data (Fig. 6a). The size/distance diagram also proves the both included sub-populations of liquid segments clearly (Fig. 6b), but it shows differences in the homogeneity of sizes and distances: the segment sizes are in a comparatively small interval whereas the segment distances are distributed over a larger range. Micro flow-through photometry is applied also for the monitoring of sequence labeling (Fig. 7) and for the quality of segment operations such as segment fusion and splitting (Fig. 8).

2.3 Microtube Flow-Through Fluorometry

The arrangement for micro flow-through fluorometry in microfluid segments inside tubes is configured like the micro spectrophotometric system. But in contrast to this system, an orthogonal arrangement of fiber connectors at the tube surface was chosen in order to suppress the background of excitation light in the emission channel. A cross section of the arrangement is shown in Fig. 9. One glass fiber connects the light source with the input filter and the input aperture. The monochromatic excitation light is illuminating the central part of the internal lumen of the microtube. The fluorescence light generated in this volume is collected and guided through the outlet aperture and the emission filter into a second glass fiber which connects the tube with a photomultiplier.

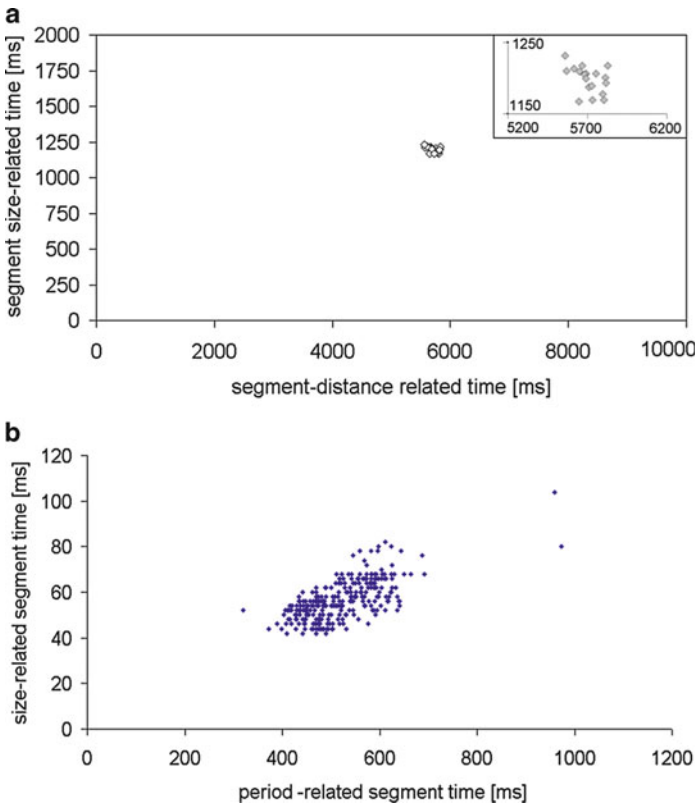

Fig. 5 Microphotometric online characterization of the quality of microfluid segment sequences by size/distance plots: (**a**) size/distance plot of a homogeneous sequence, (**b**) sequence with a larger distribution of segment sizes and distances

3 Realization of Complete Two- and Three-Dimensional Concentration Spaces

3.1 Microphotometric Quality Control of Microfluid Segment Sequences

The generation of segment series of high quality is an essential precondition for the realization of highly resolved concentration series and the addressing of multidimensional concentration spaces. In particular, the size of the segments and the distance between them must be constant in order to achieve well-defined compositions. The injection of a certain volume of an effector solution into preformed segments of larger size leads to a reduced effector concentration inside the segment, for example. The importance of the segment distance for the accuracy of concentration addressing can be explained by the fact that the effector solution is

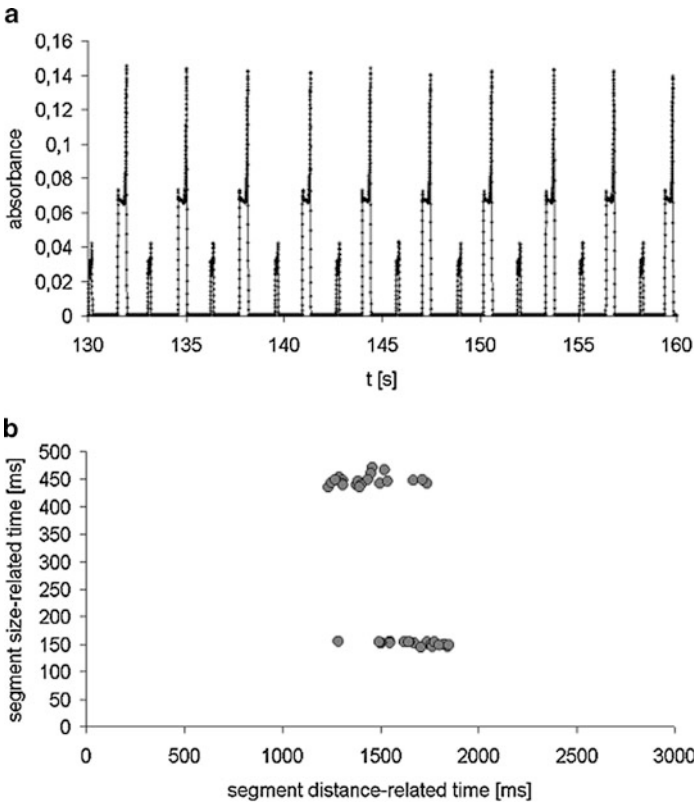

Fig. 6 Online characterization of a fluid sequence with alternating single segments: (**a**) microphotometric data, (**b**) size/distance plot

continuously pushed forward on a microfluidic injector. Therefore, the volume of effector solution increases with increasing time during a single dosing process in the segmented flow technique. So, short segment distances result in lowered concentrations and high segment distances in enhanced concentrations.

Micro flow-through photometry gives an easy opportunity to control the quality of segment sequences. The optical measurements are used for detection of the first interface (carrier liquid/process liquid) and the second interface (segment liquid/carrier liquid) during the passage of the fluid segment on a detector position. The microphotometers own a precision of about 0.1–0.5 % if measurement frequencies of 5 or 1 kHz are applied and the residence time of a single segment in the optical channel of the photometer is about 0.2 s.

The application of a special software (LabVIEW) allows the automated calculation of the duration of segment passage and of the time between two segments. Both these times are determined for each segment and can be plotted in a size/distance diagram for a complete segment sequence as shown in Fig. 5.

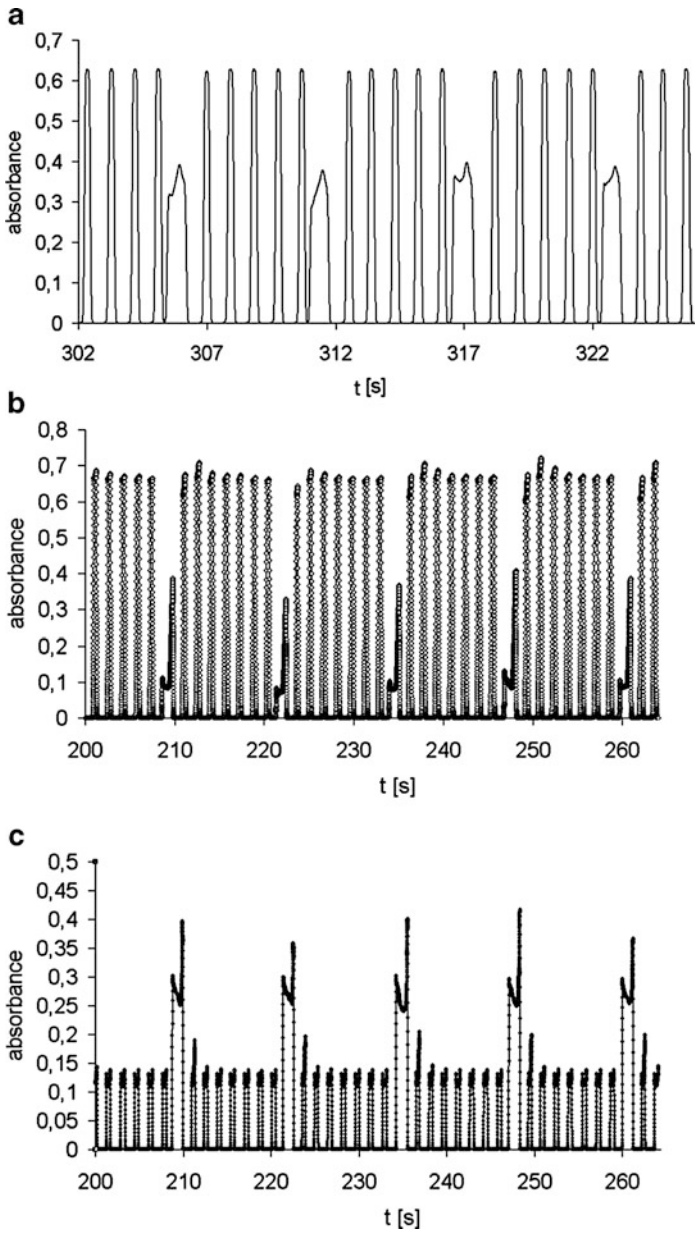

Fig. 7 Flow-through photometric monitoring of mixed segment sequences: (**a**) smaller segments of higher absorbance subdivided in groups of five segments by larger segments of lower absorbance, (**b**, **c**) characterization of a binary segment sequence in two different optical channels (470 nm, 505 nm); larger segments contain a mixture of Orange G and Methylene Blue, small segments contain Methylene Blue only

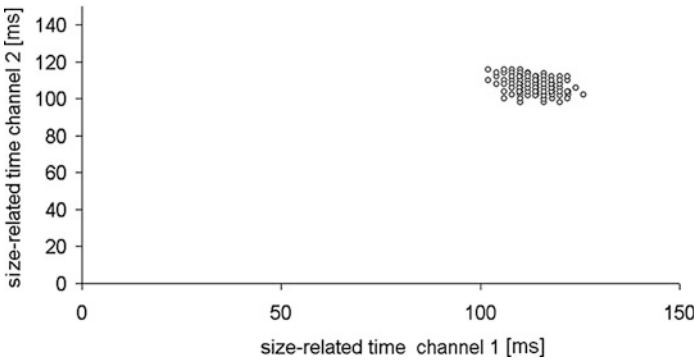

Fig. 8 Size/size plot for two sequences generated by a regular segment splitting (the close cloud of points indicates regular and symmetric splitting of original segments)

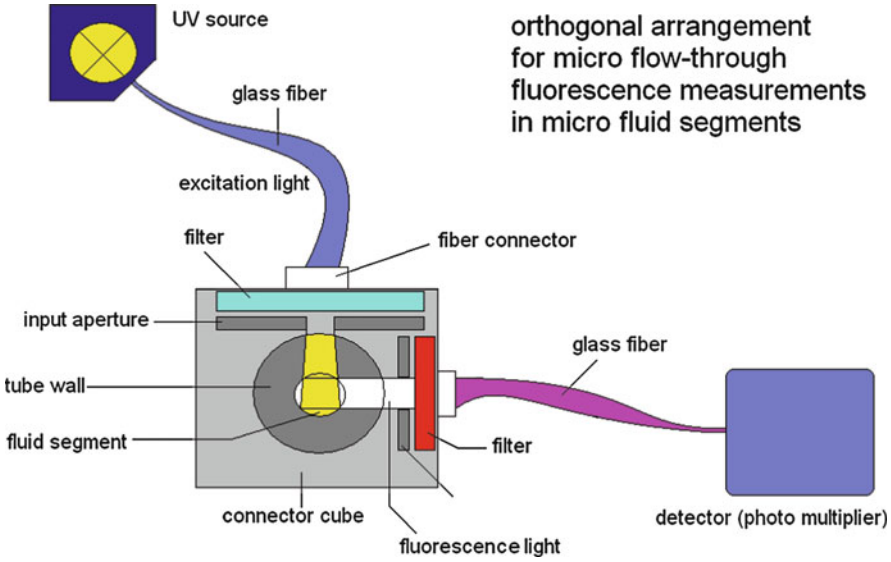

Fig. 9 Fiber-based arrangement for micro flow-through fluorometric characterization of microfluid segments inside tubes (internal diameter of the tube: 0.5 mm)

3.2 Stepwise Variation of Concentration

The technique of micro segmented flow is particular suited for the realization of stepwise varied concentrations in a sequence of well-separated microfluidic compartments. The easy realization of segment sequences with continuously varied segment composition results from the spontaneous formation of fluidic compartments of equal size during the segmentation and the possibility of computer-controlled shift of flow rates which can be used for changing concentrations in

segments by shifting two or more flow rate ratios. The superposition of a continuous shift of flow rate ratios and periodic droplet release leads to a discretization of the chemical composition inside the segments.

The reproducibility of segment formation and the applicability of the strategy of shifting flow rates for concentration tuning are well reflected by micro flow-through spectrophotometric measurements in a segment sequence containing two different dyes in changing concentrations. The small but systematic change in spectra from segment to segment is caused by the shifting ratio of the both applied dyes. The example demonstrates that the strategy can be easily applied for the realization of highly resolved concentration series. The dosing accuracy is estimated from optical measurements: the scattering in optical absorbance is better than 1%. A precision in the order of magnitude of 10^{-13} mol (0.1 pmol) results in case of a maximum concentration in the order of magnitude of 10^{-4} mol/L and a typical segment volume in the order of magnitude of 100 nL (10^{-7} L).

In contrast to dispensing procedures in the micro or nanotiter plate technique, the segmented flow technique avoids open surfaces. Thus, it is not necessary to generate small free droplets and transport them through the gas phase. The evaporation of solvent can be excluded completely.

3.3 Two-Dimensional Concentration Spaces

The complete combination of all pairs of concentrations of two substances in a certain concentration range and with a certain concentration resolution is called a "two-dimensional concentration space". The complete covering of two-dimensional concentration spaces is required, for example, for the evaluation of combinatorial effects of drugs or components in a polluted environment. Toxicological investigations in a two-dimensional concentration space are particularly important if non-linear effects as synergy or compensation take place.

A typical experimental arrangement for a two-dimensional microfluidic screening for dose/response functions includes five PC-controlled syringe pumps, a fluid manifold for mixing and segment generation, micro-optical control units and tube coils for the storage of segment sequences and incubation (Fig. 10). A liquid alkane (for example tetradecane) or an alkane mixture (mineral oil) of low vapor pressure or a liquid perfluorinated alkane (perfluoroctane for example) is used as carrier liquid. The carrier liquid is actuated with constant flow rate. The total flow rate of all other liquids is also kept constant. So, constant hydrodynamic conditions are realized of the whole experiment. This results into constant conditions for the formation of each microfluidic segment. The ratio of the carrier flow rate and the total flow rate of aqueous solutions defines the distance of segments. The initial cell suspension is also actuated with constant flow rate in order to ensure that each fluid segment starts with the same cell content. The flow rates of both the effector solutions are varied in order to realize a certain concentration program. An example

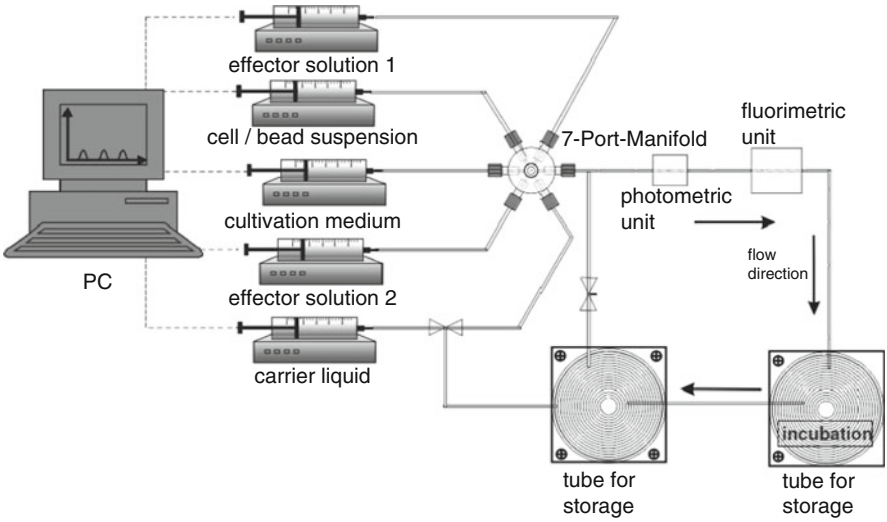

Fig. 10 Experimental setup for generation of larger fluid segment sequences for screening of complete concentration spaces, for incubation of segments in tube coils and combined flow-through photometric and fluorometric characterization

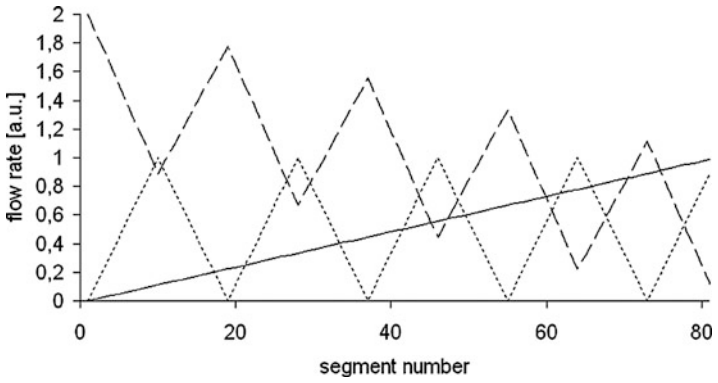

Fig. 11 Flow rate program for complete addressing of a two-dimensional concentration space (effector 1 and effector 2) and solvent

of a flow rate program for regular scanning of concentrations in a two-dimensional concentration space is given in Fig. 11.

The quality of segment formation—homogeneity of segment sizes and distances—was checked by a fast-working microphotometric unit. The same measurement devices can be applied for the determination of the increase of cell density by increasing optical density (scattering of light). In addition, changes in the composition of the segment liquid can also be detected by suited micro flow-

through photometers, for example, for measuring an increase in the intensity of auto-fluorescence of cells or for read-out of the fluorescence of sensor particles.

In most cases, the optical channels for detection of segment components are not completely separated. But, the application of two dyes for a two-dimensional concentration addressing illustrates the realization of a complete concentration scanning in two directions. Figure 12 shows the primary microphotometric data of an experiment for the generation of a segment sequence with about 1,700 segments. Sensor 1 is sensitive for the absorption of the dye with the fast-changed concentration. Sensor 2 is sensitive for the absorption of the dye with the slowly varied concentration (Fig. 12a). The absorbance/absorbance plot (Fig. 12b) indicates the complete covering of a two-dimensional absorption area which corresponds to the two-dimensional concentration space.

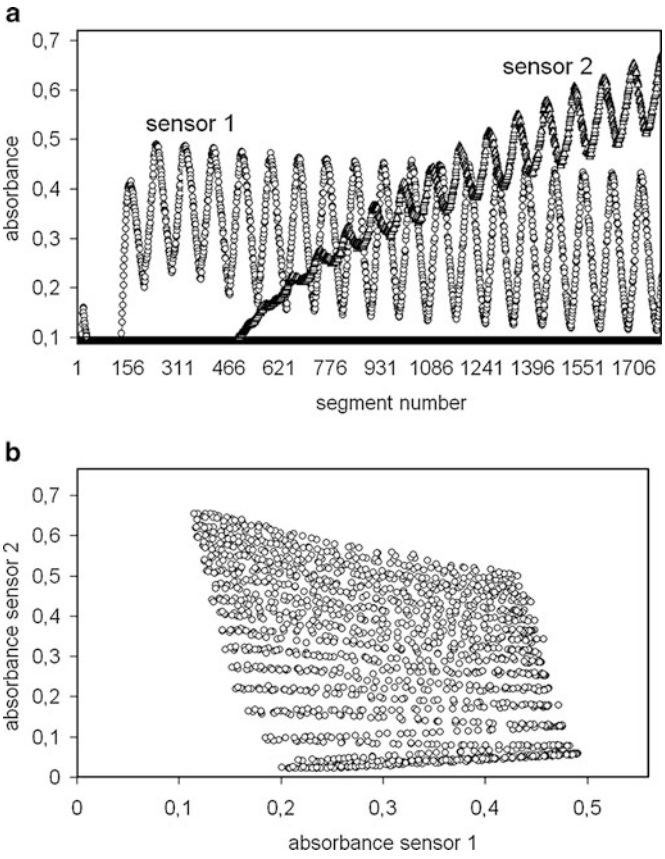

Fig. 12 Original microphotometric data for a microfluid sequence (1861 segments) with a two-dimensional concentration addressing (slowly varied dye: Acridine orange 2 mM, fast varied dye: Azure II: 1 mM), (**a**) Absorbance in two photometric channels (sensor 1: 610 nm, sensor 2: 470 nm; each spot represents the absorbance signal of one fluid segment), (**b**) absorbance/absorbance plot illustrating the complete coverage of a two-dimensional concentration space

3.4 Three-Dimensional-Addressing and Higher Dimensional Concentration Spaces

The high number of segments in a single sequence allows also the generation of three-dimensional concentration screenings. A 10% variation of each concentration (11^3) requires 1,331 segments; a 6% variation of each concentration (17^3) needs a sequence of about 5,000 segments at least. A scheme of the flow rate actuation for three concentration channels and the complementary actuated buffer solution is given in Fig. 13.

A liquid exchange in the internal volume of the fluid manifold causes a certain weakening of the concentration steps in these experiments. In addition, a certain contribution of fluctuations in the hydrodynamic conditions influences the accuracy of the obtained concentrations. Therefore, it is advantageous to represent each addressed combination of the three concentrations by more than one segment. Hence, a block-wise organization of concentration scanning is recommendable in case of a three-dimensional screening.

Figure 14a shows the concentration program of a blockwise-organized three-dimensional screening with a 20% variation of the three concentrations. The whole sequence contains about 2,300 segments. $6^3 = 216$ concentration points are addressed in this experiment. Hence, each concentration point is represented by about 11 single segments. The microphotometric characterization of the generated sequence shows that the expected concentration screening was realized (Fig. 14b). There is also a certain noise in the single concentration values. But, the deviations are smaller than the 205 steps in the variation by the flow rate program. The complete scanning over the three-dimensional concentration space is well illustrated by the pseudo-3D representation of the measured concentrations (Fig. 15). In the upper diagrams, the exact expected 216 concentration points are illustrated. Each of the three diagrams is related to one optical measurement channel. The spot size reflects the absorbance in this channel. The three figures beneath represent the

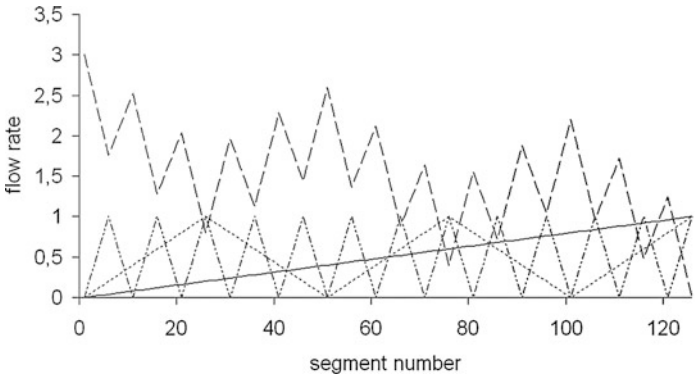

Fig. 13 Example of a flow rate program for complete addressing of a three-dimensional concentration space (effector 1, effector 2 and effector 3) with 125 segments

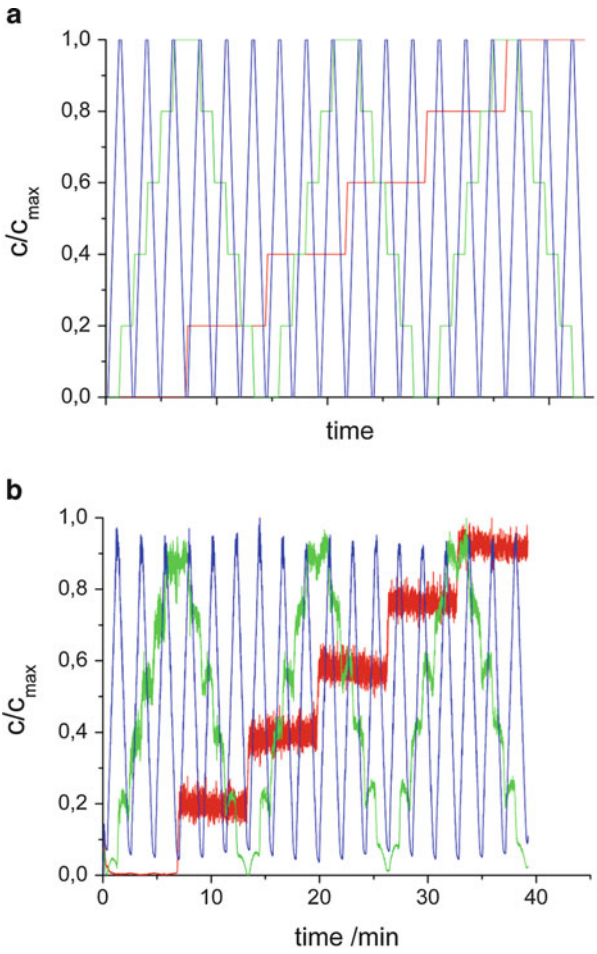

Fig. 14 Experimental realization of three-dimensional concentration space: (**a**) flow rate program with blockwise organization of segments (six concentration levels), (**b**) verification of realized concentrations by photometric determination of concentrations of three dyes (Congo *Red*, *Orange* G, Methylene *Blue*)

experimentally obtained concentrations. Despite a certain noise, the result clearly indicates the complete coverage of the three concentration dimensions.

The dimensionality of a screened concentration space and the resolution of the concentrations have to be regarded as two complementary aspects in the combinatorial screenings. The screening in the lower dimensional spaces leads to results with a high value in the precise quantitative data. Very high concentration resolutions can be achieved in one- or two-dimensional microfluidic screenings. The screening of higher dimensional spaces gets more the character of a semi-quantitative or qualitative screening. The role of accuracy of concentrations becomes less important than the presence or absence of a substance and the number and type of present substances. The characteristic differences between a three-dimensional and a 10-dimensional screening are illustrated by a simple calculation for a segment sequence with about 1,000 addressed concentration points

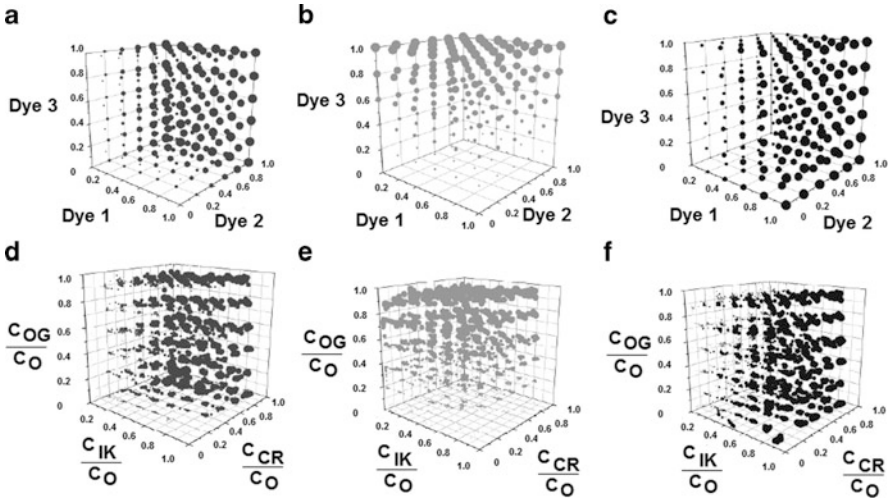

Fig. 15 Three-dimensional representation of concentration program (upper three diagrams) and realized concentrations (determined by micro flow-through photometry; lower three diagrams), the spot sizes characterize the expected (*upper row*) and the obtained concentration (*lower row*) of the three dyes (**a**, **d**: Congo *Red*; **b**, **e**: *Orange* G; **f**, **c**: Methylene *Blue*)

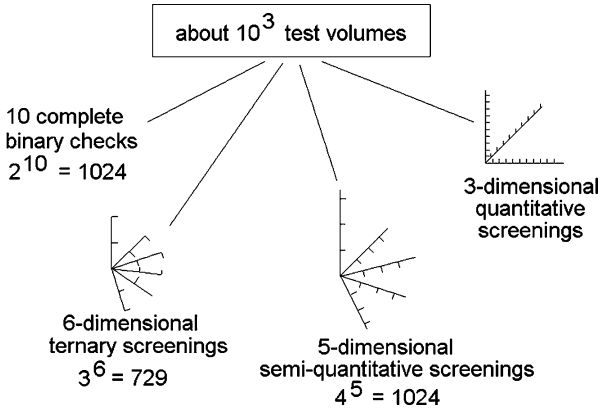

Fig. 16 Dimensionality and concentration resolution: possibility to use a segment sequence with about 10^3 different concentration sets

(scheme in Fig. 16). In this case, a three-dimensional screening can still be regarded as a real quantitative analysis. The four-, the five- and the six-dimensional addressing have the character of a semi-quantitative screening. The concentration axes are subdivided in a few concentration classes only. In case of a 10-dimensional investigation, the screening is reduced to a qualitative check because the concentration of a single substance is not further quantified, but the absence or presence of a substance is distinguished only. At higher dimensional screenings, it is not necessary to define the concentrations very precisely. So, a certain noise in the substance mixing during the formation of segments is well tolerated.

The validity of the above-mentioned concept was checked by the realization of a five-dimensional combinatorial screening in one microfluidic run. Therefore, five substances were applied in three concentration categories: (1) absence, (2) 50% of maximal concentration, and (3) maximal concentration. This program resulted in $3^5 = 243$ concentration points in the five-dimensional space. A sequence of 5,400 segments was generated, so that each concentration point was presented by about 22 segments. The result of microfluidic addressing was checked by application of five dyes and evaluation in five microphotometric channels. Despite a certain noise level, all five axes are well represented in the obtained measurement data (Fig. 17). This result proves that the technique of micro segmented flow is suited for semi-quantitative screenings in higher dimensional concentration spaces, too.

4 Determination of Highly-Resolved Dose/Response Functions

4.1 Experimental Arrangement and Procedures

The stepwise variation of concentrations in large sequences of microfluid segments is very attractive for the determination of highly resolved dose/response functions in toxicology and for the investigation of combinatorial effects. Each segment contains a test volume in the range between some tens up to a few hundred nanoliters. So, detailed data can be gained by application of a very small total of test liquids.

The experiments reported here have been carried out by microtube arrangements. The mixing of cells and effector solutions as well as the segment formation has been realized by tubes and fluid devices of perfluorinated plastic material. The experimental setups are identical or analogous arranged as shown in Fig. 10. After segment formation, the whole sequence of segments was stored in a tube coil and incubated for a certain time. The whole segment sequence was moved through microphotometers and/or microfluorimeters in order to determine cell growth and physiological activity after the complete incubation time or in certain time intervals.

The change in the photometric or in the fluorometric signals was used for the effect of a certain concentration or combination on the cellular activity inside a fluid segment.

4.2 Determination of Dose/Response Functions of the Effect of Single Substances on E. coli

The segmented-flow technique was applied for the determination of the effect of different substance classes on the growth of *E. coli* inside fluid segments. The

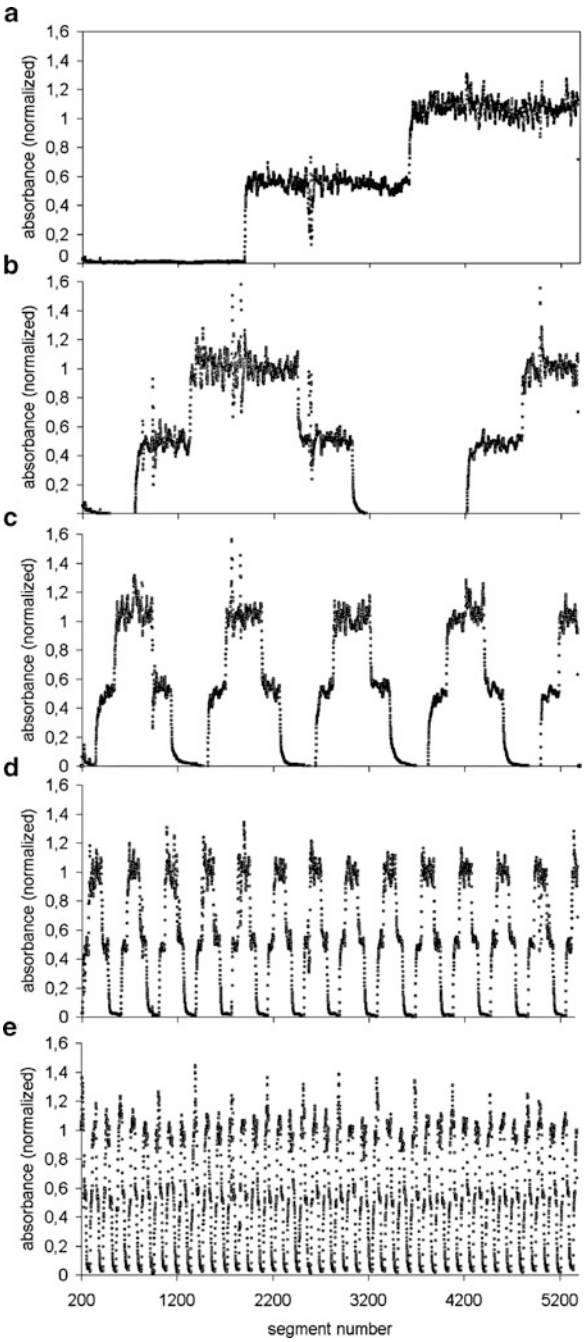

Fig. 17 Experimental realization of five-dimensional concentration space (five dyes); each dye was applied in three different concentrations; (**a**–**e**): normalized concentration-related absorbances for the five optical channels corresponding to the five applied dyes

growth was characterized by microphotometry or by the growth-induced increase of autofluorescence. Highly resolved dose/response functions were obtained.

Copper ions are an example of a typical inorganic effector on the growth of bacteria. We studied the response of *E. coli* on the addition of $CuCl_2$. We found that the growth of *E. coli* inside the fluid segments is not effected at concentrations below about 5 µmol/L. But, a strong inhibition was observed at a content of $CuCl_2$ above 6 µmol/L.

Dinitrophenol (DNP) is known to act as an inhibiter due to its uncoupling function in the dissimilation. The growth of *E. coli* was checked in the concentration range up to 150 µmol/L. The bacterial growth was only slightly reduced up to a concentration of about 65 µmol/L (Fig. 18). The EC50 value in the microfluid segments was about 74 µmol/L. No growth took place at concentrations above 0.1 mmol/L. The cultivation in microfluid segments was also used in order to investigate the growth kinetics as a function of the effector concentration. Therefore, the cell density and the autofluorescence have been determined after 24 h, 27 h, and 31 h incubation (Fig. 19). It was found that the critical value for the toxicity was shifted considerably from lower than 25 µmol/L (24 h) to more than 60 µmol/L (31 h).

The microfluid segment technique was also used for checking the toxic effects of plasmonic nanoparticles. This is of particular interest due to the application of plasmonic nanoparticles as optical labels for biomolecules and cells. The well-known toxicity of silver nanoparticles was also found in microfluid segments (Fig. 20). A lower EC50 value of 90 fmol/L was found for non-spherical nanoparticles, and a higher value (23 pmol/L) was found in case of spherical particles. Obviously, the spherical nanoparticles are much more toxic than the non-spherical. It is unknown if this fact is due to a higher corrosion sensitivity and ion release of the non-spherical particles by differences in the endocytosis behavior. The high number of segments in one single experiment gives the possibility to getting also some statistical information on the response of cell growth in different ranges of the effector concentrations. An increasing cell growth in some segments and larger differences between single segments were observed in screening experiments with *E. coli* on Au/Ag core/shell nanoparticles (Fig. 21). It seems

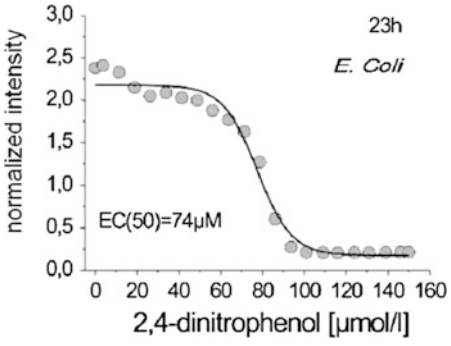

Fig. 18 Dose/response function for the growth of *E. coli* in the presence of 2,4-dinitrophenol in microfluid segments, characterized by a microfluorometric measurement using the autofluorescence of bacteria

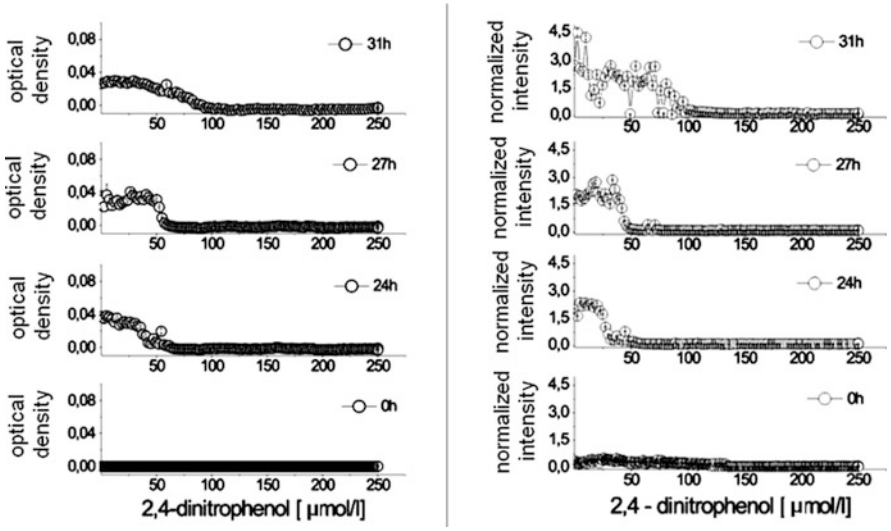

Fig. 19 Comparison of microphotometric signal (optical density) and fluorescence signal (bacterial autofluorescence) for the determination of dose/response functions for the growth of *E. coli* in the presence of 2,4-dinitrophenol in microfluid segments after increasing incubation time

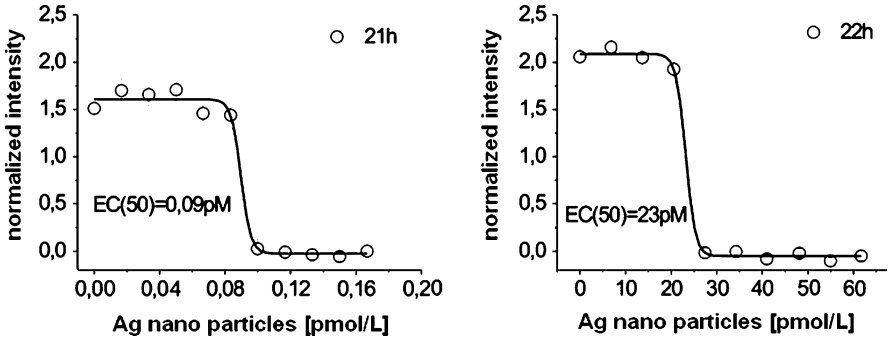

Fig. 20 Dose/response function for the growth of *E. coli* in the presence of silver nanoparticles in microfluid segments, characterized by microphotometric signal (optical density) and fluorescence signal (bacterial autofluorescence)

that in some cases a sublethal dose causes a stimulation of cellular growth or aggregation resulting in an unexpected high increase of light scattering.

4.3 Chlorella vulgaris

The growth of *chlorella* should result in an increase of the optical density of fluid segments as well as to a significant increase of fluorescence due to the strong

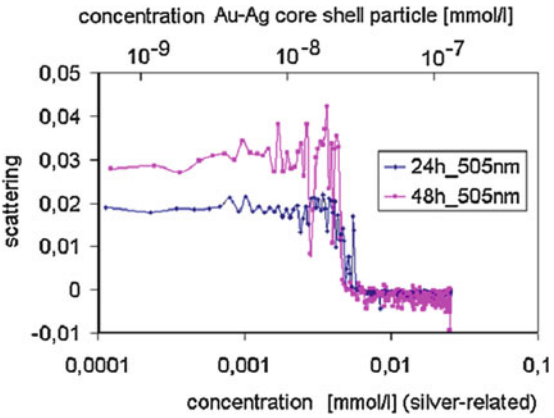

Fig. 21 Highly resolved dose/response function for the growth of *E. coli* in the presence of silver nanoparticles in microfluid segments, characterized by microphotometric signal (optical density)

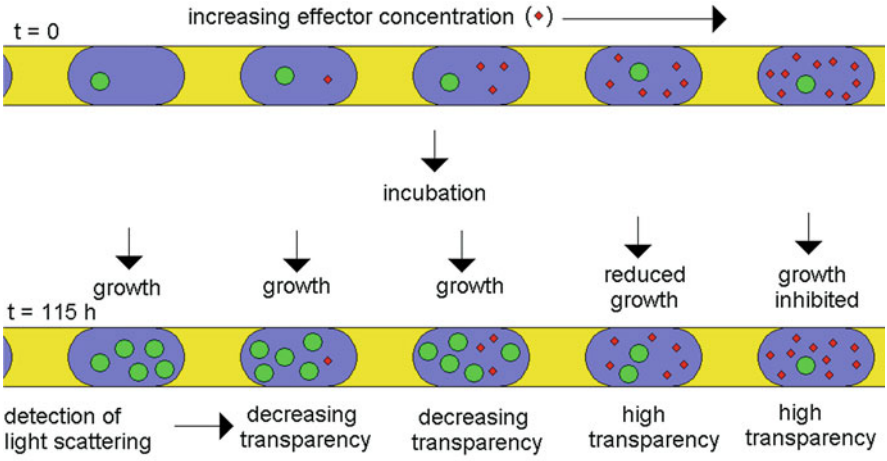

Fig. 22 Principle of determination of dose/response functions in microfluid segments. Examples for optical characterization of the quality of segment sequences by size/distance plots

autofluorescence of this alga. Both parameters should remain low in case of toxic effects (Fig. 22).

It is known that *chlorella* is sensitive to heavy metals, in particular copper ions. But, these ions were frequently released from technical processes and materials into the environment and cause an inhibition of alga development. So, the measurement of the effect of $CuCl_2$ on *chlorella* is a representative example for an environmental-relevant investigation under conditions of the microfluid segment technique.

Chlorella was cultivated in microfluid segments in PTFE tubes. A halogen light source (50 W) was applied for illumination. The cultivation proceeded over 5 days, but the growth was checked already after 67 h. The EC50 values have been estimated in the range between 10 and 15 µg/L $CuCl_2$ (Fig. 23). The values

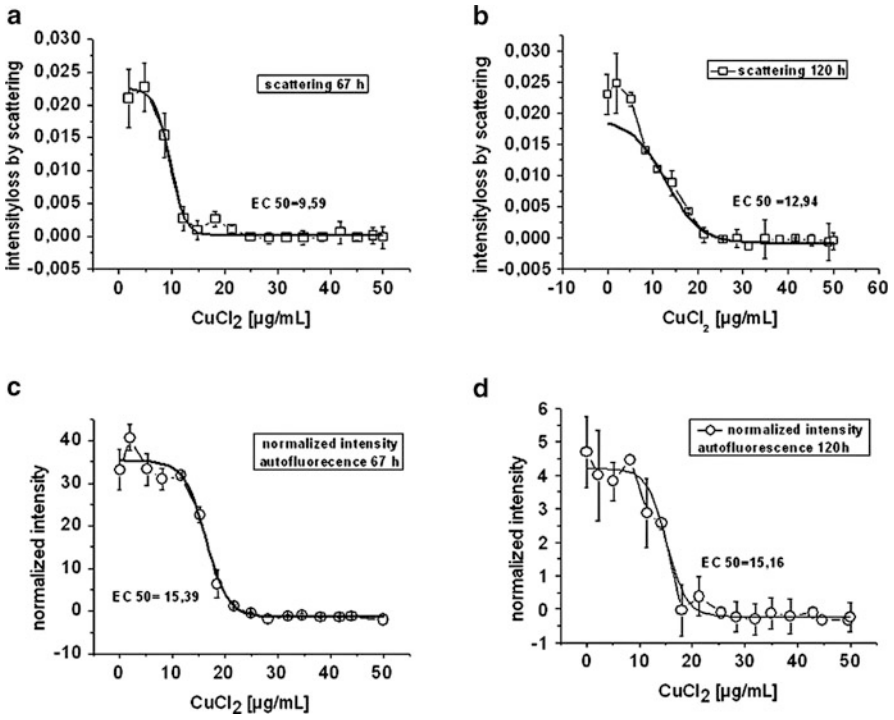

Fig. 23 Determination of dose/response functions of the growth of *chlorella* in the presence of $CuCl_2$. (**a**) microphotometric signal after 67 h, (**b**) microphotometric signal after 120 h, (**c**) autofluorescence signal after 67 h, (**d**) autofluorescence signal after 120 h

determined with light scattering (Fig. 23a, b) are a little smaller than the obtained EC50 values measured by the use of the autofluorescence (Fig. 23c, d).

5 Two-Dimensional Microtoxicological Screenings

5.1 Toxicological Studies on the Zebra Fish Development

Besides microorganisms, multicellular systems can also be brought into microfluid segments. Hence, the embryonic development of even a vertebrate can be observed under microfluidic conditions. We have studied the cultivation of larvae of zebra fishes (*Danio rerio*) inside microfluid segments. These segments have to be larger with respect to the diameter of the egg and the required space of the young fish. Therefore, microfluidic segments of 8 µL were applied.

The gas permeability of PTFE tube is obviously high enough for a sufficient gas exchange. That is why an obviously normal development of larvae was observed in

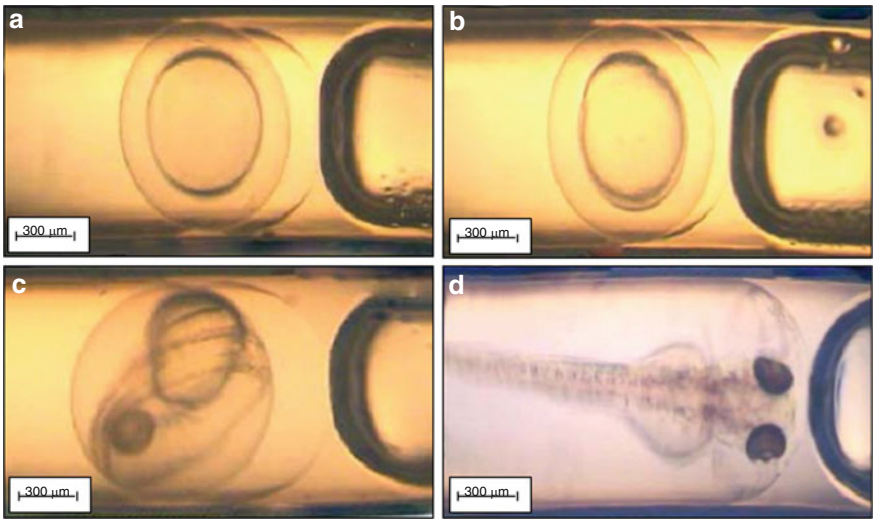

Fig. 24 Egg and different states of developing embryos of zebra fishes [52] in microfluid segments (enlarged volume: about 8 µL)

most cases (Fig. 24). The animals can be cultivated inside the fluid segments up to 5 days. After release in water, they showed a regular development and behavior. In a few cases only, some dysfunctions have been observed, for example, related to an incomplete tail detachment.

The microfluidic cultivation of zebra fish embryos gives the possibility to study the early development of complex organisms under microfluidic conditions and in dependence of added effectors. So, the combination effect of a surfactant (sodium dodecylsulphate, SDS) and heavy metal ions (copper(II)chloride) has been investigated. It was found that SDS in concentrations above 10 µg/mL is significantly toxic. It lowered the chances of survival and is also affecting differentiation processes as gastrulation, the development of eyes, and the tail detachment (Fig. 25). A lower concentration of copper ions (4.1 µmol/L) has no negative effect. A higher concentration (33 µmol/L) shows a lethal effect on most embryos after 1 day.

5.2 *High-Resolved Two-Dimensional Microtoxicological Screenings with* E. Coli

Combinatorial screenings are mainly realized by the variation of one component in the presence of a further compound with a fixed concentration. This conventional method gives only an incomplete view of the dose/response relations for two substances on an organism. The screening in a complete two-dimensional

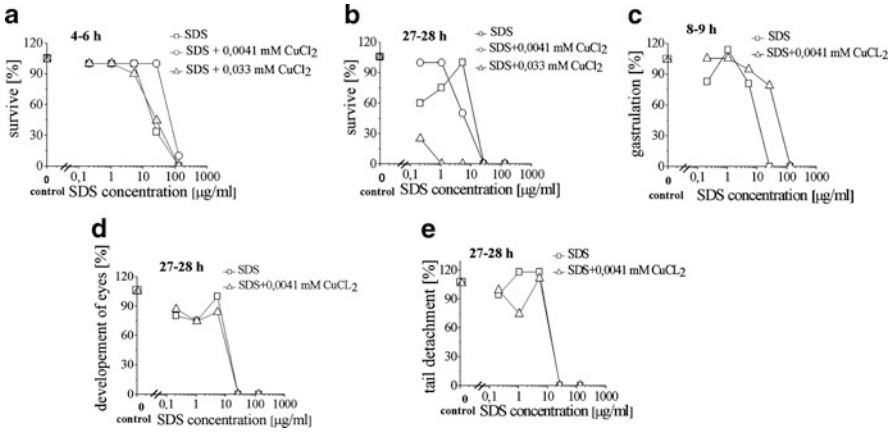

Fig. 25 Determination of the effect of a surfactant (sodium dodecylsulphate, SDS) and copper ions on the development of zebra fish embryos inside microfluid segments [52]

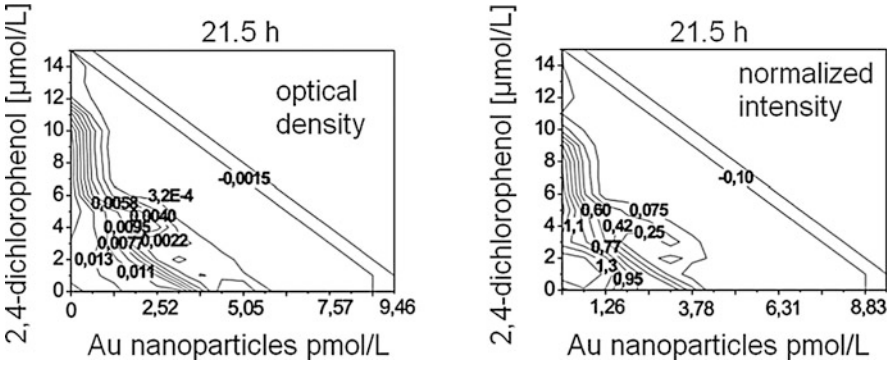

Fig. 26 Investigation of toxic combination effects of 2,4-dichlorophenol and gold nanoparticles on *E. coli* in microfluid segments: (**a**) bolographic map obtained by microphotometric data, (**b**) bolographic map obtained by microfluorometric data

concentration space allows the characterization of non-linear effects in the interaction of toxic substances. Hence, it becomes possible to determine dose/response maps ("bolographic charts") with hundreds or thousands of concentration points for combination effects in a single experimental run.

The result of such a two-dimensional microtoxicological screening is well reflected by an isobolographic plot. Such plots are obtained directly from the optical data measured during the passage of each single microfluid segment through the microphotometer or the microfluorimeter. An example of the results of a two-dimensional screening with a microfluid segment sequence is shown in Fig. 26. *E. coli* was incubated with different concentrations of gold nanoparticles and 2,4-dichlorophenole (DCP). The change in the optical density (photometrically

determined, light scattering) as well as the autofluorescence clearly indicates the interference of both toxic substances. The lines in the graphs represent levels of equal cellular growth or equal fluorescence (isoboles). A small concentration of Au nanoparticles led to a significant lowering of the critical concentration of DCP. This means that the bacteria become more sensitive against DCP in the presence of the metal particles. The effect is a little stronger than additive. The interaction of both toxic substances is not symmetrical: The effect of small concentrations of Au nanoparticles on the DCP toxicity is stronger than the effect of small DCP concentrations on the toxicity of the gold nanoparticles.

An opposing picture was obtained in the investigation of the effect of two antibiotics—chloramphenicol and ampicillin—on *E. coli* (Fig. 27a). The transition between non-toxicity and lethal effect is much less sharp than in the case of DNP and Ag nanoparticles. In addition, there is a certain interaction of both substances. But, the effect is weaker than additive. The convex shape of the isobolographic lines indicate that the both antibiotics do not show synergetic enforcement of their activity. In contrast, concave isobolographic lines indicate a synergistic effect of two substances. This is obviously the case in the presence of both DNP and dichlorophenol (Fig. 27b). Low DNP concentrations cause a strong reduction of the lethal value of DCP.

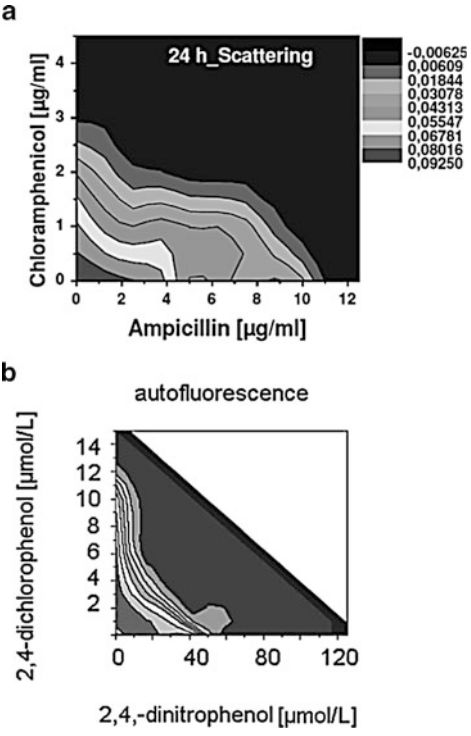

Fig. 27 Two-dimensional presentation of combination effects: (**a**) microphotometric data of the combination effect of two antibiotics (chloramphenicol and ampicillin) on the cultivation of *E. coli* in microfluid segments, (**b**) two-dimensional presentation of microfluorometric data of the combination effect of two phenolic uncouplers (2,4-dinitrophenol, 2,4-dichlorophenol) on the cultivation of *E. coli* in microfluid segments

6 Outlook

6.1 *Multi Effector Studies*

The application of micro segmented flow and the optical read-out by fast-working micro flow-through photometers and fluorimeters will help to accelerate the development of automated screening systems for multiparameter studies. The optical detection methods are well developed such that a faster read-out (integration time in the range of about 1 ms) can be applied in automated analytical microsystem on areas of some hundreds of μm^2. Hence, the volumes for biological screening can be scaled down to the picoliter range.

The recent state of screenings with submicroliter fluid segments or segment volumes in the upper nanoliter range means a reduction of volume by the factor of 1,000 in comparison with a conventional test tube (Fig. 28). Thus an initial volume of 0.2 mL can be used for 1,000 single experiments. This matches the order of magnitude of segment numbers per run (10^3–10^4) in the recent screenings as shown above. The reduction of the volume to the 200-pL-level would mean a further volume reduction by a factor of 1,000, leading to segment population of one million which can be generated from a volume of 200 µL.

It seems that the miniaturization of volumes and the reduction of the diameters of optical channels are not the limiting factors for the further development. So, it will become possible to extend the precise quantitative toxicology from single and two-parameter screenings to higher dimensional parameter spaces. The calculated accuracy in a screening run with 10^6 separated fluid compartments would allow a resolution of concentration of about 3% in the case of a four-dimensional screening, or still a resolution of about 10% in the case of a six-dimensional investigation.

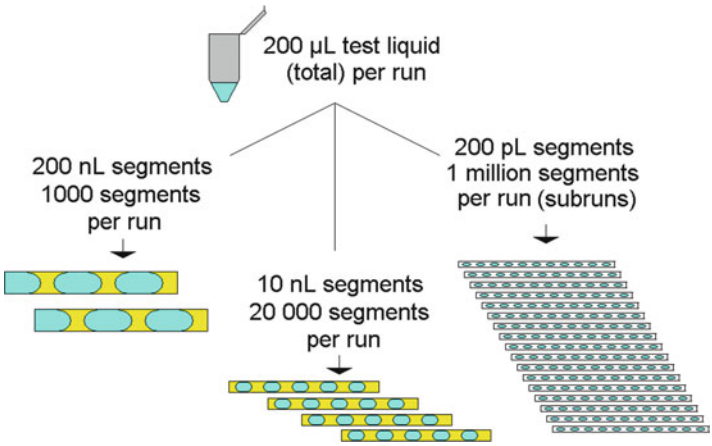

Fig. 28 Subdivision of a sub-mL volume in microfluid segments: upper nL-range, mid-nL-range, sub-nL-range

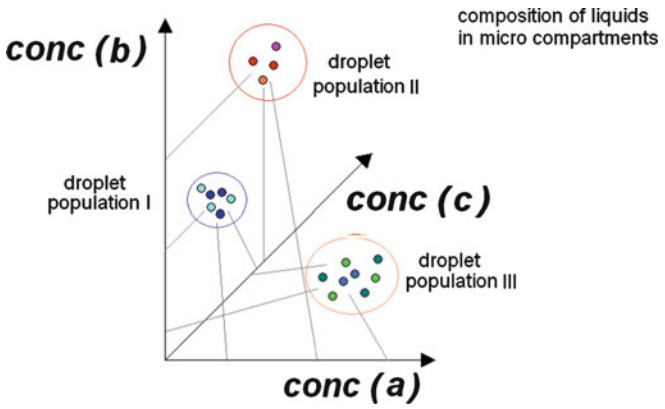

Fig. 29 Non-homogeneous screening in a multi-dimensional concentration space: addressing of groups of microfluid segments or droplet populations (schematically)

Probably, it will be still more important to find intelligent strategies for the planning of screening runs and a problem-adapted addressing of concentration spaces in order to optimize the extraction of biological information from the dose/response measurements. This would concern, for example, a non-homogeneous distribution of concentration points in the multidimensional concentration space and the definition of special segment or droplet populations (scheme in Fig. 29). Therefore, also devices and software for segment generation and manipulation on demand are required. The vision is an arbitrary distributed set of points in a multidimensional concentration space which can be designed by rules originating from specific diagnostic or research tasks.

6.2 Multi Endpoint Detection

One parameter is used as end-point in the most part of recent studies on dose/response relations. The application of new optical devices and in particular the connection of specific chemical, bimolecular, or cellular signal transduction with a specific optical channel give the opportunity to use several different endpoints in an automated screening procedure within one single run. So, not only information about the dead or alive status, cell density, or the general physiological activity is obtained, but much more detailed information about the biological response on a drug or a combination of drugs and toxic substances can be derived.

The precondition is the possibility of a primary signal transduction from the chemical or biological object in an optically readable signal. Some of such methods are already available; for example, the detection of changes in pH values and of oxygen release or consumption. Other parameters would be very interesting like the change in substrate concentrations, the consumption or release of transmitter

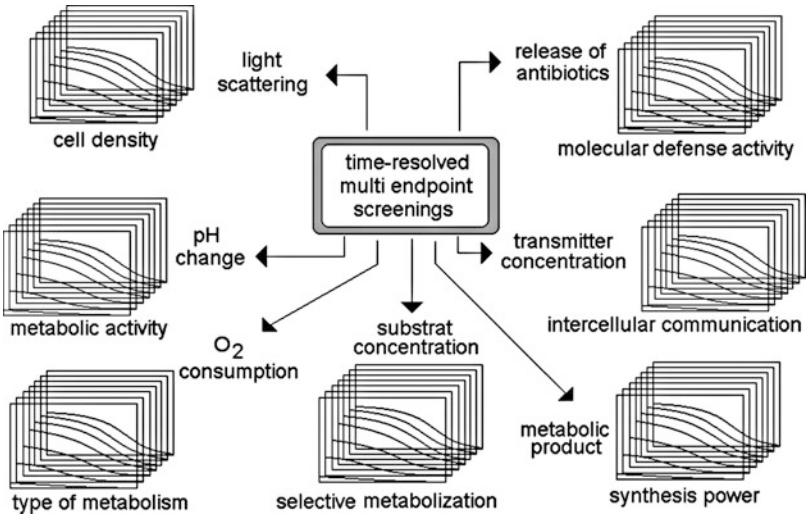

Fig. 30 Possible parameters for time-resolved characterization in a miniaturized and highly parallelized multi-endpoint strategy for the determination of responses in multi-effector screenings

substances for intercellular communication, and the release of antibiotics or other metabolites of interest (scheme in Fig. 30).

A fast non-contact read-out is desired for an efficient multi-endpoint detection in larger microfluid segment sequences. This challenge can be met by the application of optical active sensor particles for the primary signal transduction (Fig. 31). Such indicator particles can be handled like substances if they are well solvated and dispersed inside the solution. They change an optical feature, for example, their fluorescence wavelength or the fluorescence quantum yield in dependence on the presence of a certain analyte. In principle, the general chemo-optical transduction principle can be paired with a specific molecular recognition in order to get a read-out strategy with an individual addressing of analytical problems, but a universal physical principal for the signal transduction chain. The sensing particles should be either nanometer-sized or consist of a sensitive thin shell deposited on an inert core in order to achieve short response times. Sensor nanoparticles could be bundled together in a hydrogel micro particle for getting better manipulation and higher local signals.

The incorporation of sensor particles inside microfluid compartments can be regarded as an introduction of micro messengers that monitor the state and ongoing processes inside the fluidic micro compartments and report about them to an outside information processing system. This principle can also be applied to receive information of nested fluidic compartments or even living cells (Fig. 32). Smaller sensor nanoparticles of different sensing properties could be assembled inside a larger nano or submicron particle. Such cell-internal messengers could be introduced by endocytosis.

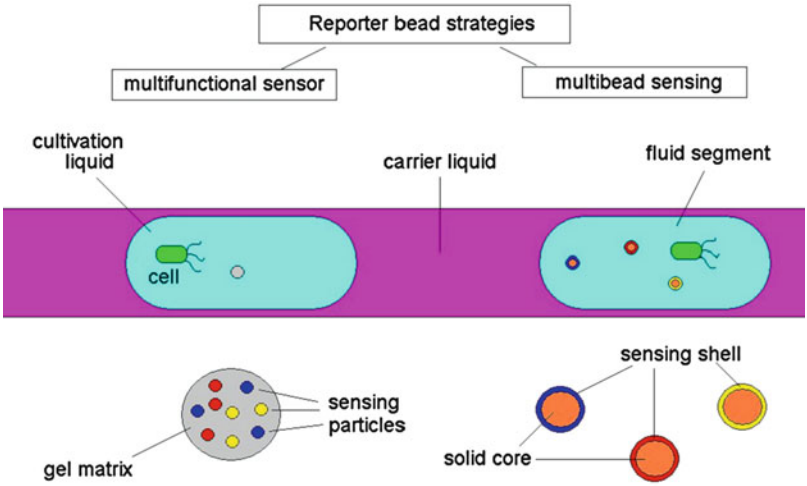

Fig. 31 Application of micro sensor beads for transduction of molecular signals into optical signals inside microfluid segments

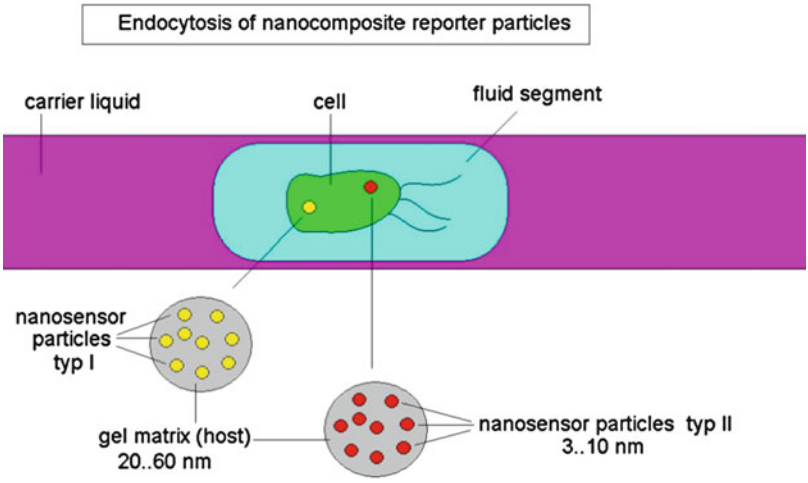

Fig. 32 Application of sensor beads for monitoring of intracellular data after endocytosis

A set of several optical channels which can work in parallel is required for the read-out of the sensor information from the liquid micro compartments. The use of different time response behaviors of sensor particles (for example fluorescence or phosphorescence life time) could be used for satisfying these multichannel requirements beside the signal transfer in different spectral channels.

6.3 *Investigation of Cellular Interactions and Screening of Microenvironments*

The microfluidic compartments represent an ideal experimental environment for the investigation of the behavior of single cells and other small biological objects under precisely defined local conditions. The small amounts of substances exchanged between the cell and the surrounding compartment liquid correspond to measurable concentration changes due to the small volumes. Hence, microfluid segments could be used as a nearly perfect place for studying physiological effects and activities of biological micro objects.

Microfluid segments can be applied for the generation of monoclonal cell cultures of well-defined size and growth history. Further, they can also be used for the introduction of small numbers of cells of different species or different

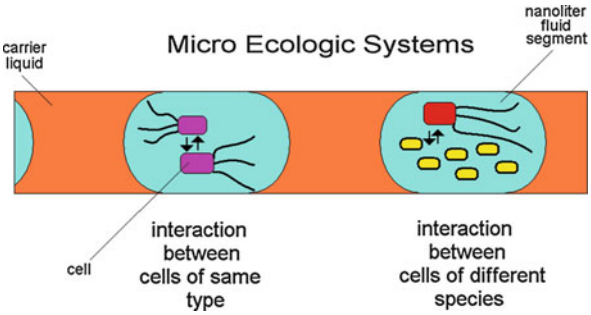

Fig. 33 Micro ecological screenings: implementation of large sets of minimal environments and investigation of cell/cell interactions for multidimensional sets of environmental parameters

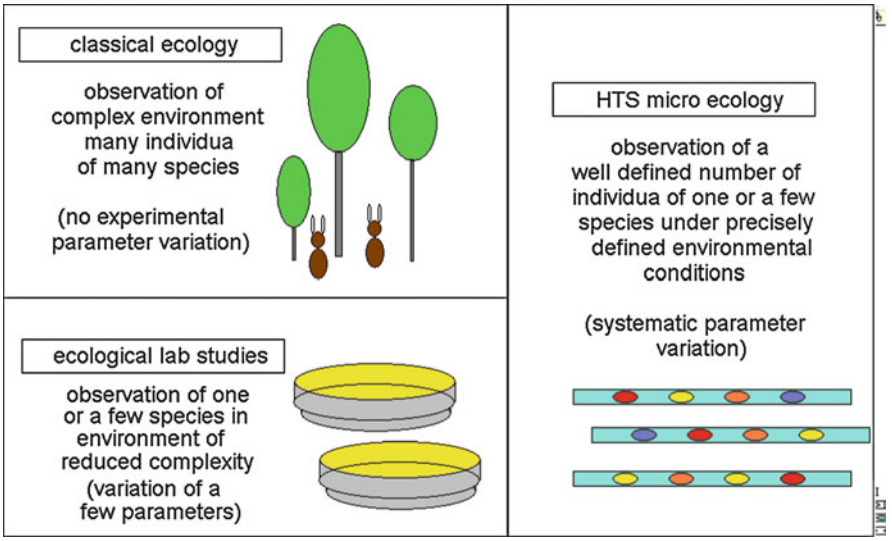

Fig. 34 Vision of microecological high-throughput screenings

differentiation states. Microfluidic compartments are also a very promising experimental platform for studying cellular interactions on the level of single cells or small groups of cells (Fig. 33). Hence, they allow microecological screenings under strongly reduced environmental conditions. Microfluid segments can be considered as a minimal ecological system in case of these investigations. Such studies would be an interesting complement to the conventional ecological methods (Fig. 34). The application of larger sequences of fluid segments for microecological investigations would lead to an ecological research under high-throughput conditions for the environments. A lot of different, but well-defined environments were studied with a few individuals instead of a large number of species in a single and very complex environment.

Acknowledgment The research on micro segmented flow, on multidimensional concentration spaces, and segment switching was supported by the BMBF (VDI/VDE-IT, Kz. 16SV3701 and 16SV5065). The investigations on microreaction technology and microtoxicology have been financed by the German Environmental Foundation (DBU).

References

1. Csaki A, Kaplanek P, Möller R, Fritzsche W (2003) The optical detection of individual DNA-conjugated gold nanoparticles labels after metal enhancement. Nanotechnology 14:1262–1268, DOI:dx.doi.org
2. Stehr J, Hrelescu C, Sperling RA et al (2008) Gold nano-stoves for microsecond DNA melting analysis. Nano Lett 8:619–623
3. Li Y, Schluesener HJ, Xu S (2010) Gold nanoparticle-based biosensors. Gold Bull 43:29–41
4. Hardt S, Schönfeld F (eds) (2007) Microfluidic technologies for miniaturized analysis systems. Springer, New York
5. Fent K (1998) Ökotoxikologie. Thieme, Stuttgart
6. Alloway BJ, Ayres DC (1996) Schadstoffe in der Umwelt. Spektrum, Berlin
7. Zakrzewski SF (1997) Principles of environmental toxicology. ACS, Washington, DC
8. Wang RGM (1994) Water contamination and health. Marcel Dekker, New York
9. Grimme LH, Faust M, Boedecker W, Altenburger R (1996) Hum Ecol Risk Assess 2:426–433
10. Berenbaum MC (1985) Environ Res 38:310–318
11. Berenbaum MC (1989) Pharmacol Rev 41:93–141
12. Therberge AB, Courtois F, Schaerli Y et al (2010) Microdroplets in microfluidics: an evolving platform for discoveries in chemistry and biology. Angew Chem Int Ed Engl 49:5846–5868
13. Köhler JM, Henkel T, Grodrian A, Kirner T, Roth M, Martin K, Metze J (2004) Digital reaction technology by micro segmented flow – components, concepts and applications. Chem Engn J 101:201–216, DOI:dx.doi.org
14. Song H, Chen DL, Ismagilov RF (2006) Reactions in droplets in microfluidic channels. Angew Chem Int Ed Engl 45:7336–7356
15. Malsch D, Gleichmann N, Kielpinski M et al (2009) Dynamics of droplet formation at T-shaped nozzles with elastic feed lines. Microfluid Nanofluid 10:479–507
16. Köhler JM, Kirner T (2005) Nanoliter segment formation in micro fluid devices for chemical and biological micro serial flow processes in dependence on flow rate and viscosity. Sens Actuators A 119:19–27

17. Vanapalli SA, Banpurkar AG, Vanden Ende D, Duits MHG, Mugele F (2009) Hydrodynamic resistance of single confined moving droplets in rectangular microchannels. Lab Chip 9:982–990
18. Baroud CN, Willaime H (2004) Multiphase flows in microfluidics. CR Phys 5:547–555
19. Baroud CN, Gallaire F, Dangla R (2010) Critical review: dynamics of microfluidic droplets. Lab Chip 10:2032–2045
20. Adzima BJ, Velankar SS (2006) Pressure drops for droplet flows in microfluidic channels. J Micromech Microeng 16:1504–1510
21. Gross GA, Thyagarajan V, Kielpinski M, Henkel T, Köhler JM (2008) Viscosity-dependent enhancement of fluid resistance in water/glycerol micro fluid segments. Microfluid Nanofluidics 5:281–287
22. Malsch D, Gleichmann N, Kielpinski M, Mayer G, Henkel T (2008) Proc. ICNM 2008, No 62328
23. Mazutis L, Baret JCh, Griffith AD (2009) A fast and efficient microfluidic system for highly selective one-to-one droplet fusion. Lab Chip 9:2665–2672
24. Wang W, Yang Ch, Li ChM (2009) On-demand microfluidic droplet trapping and fusion for on-chip static droplet ass ays. Lab Chip 9:1504–1506
25. Hsieh YS, Crouch SR (1995) Air-segmented flow injection: a hybrid technique for automated, low dispersion determinations. Anal Chim Acta 303:231–239
26. Nisisako T, Okushima S, Torii T (2005) Controlled formulation of monodisperse double emulsions in a multiple-phase microfluidic system. Soft Matter 1:23–27
27. Chae S-K, Lee ChL, Lee SH, Kim T-S, Kang JY (2009) Oil droplet generation in PDMS microchannel using an amphiphilic continuous phase. Lab Chip 9:1957–1961
28. Zhu J, Hayward RC (2008) Hierarchically structured microparticles formed by interfacial instabilities of emulsion droplets containing amphiphilic block copolymers. Angew Chem Int Ed Engl 47:2113–2116
29. Ismagilov RF (2003) Integrierte mikrofluidsysteme. Angew Chem Int Ed Engl 115:4262–4264
30. Günther PM, Möller F, Henkel T, Köhler JM, Gross GA (2005) Formation of monomieric and novolak azo dayes in nanofluid segments by use of a double injector chip reactor. Chem Eng Technol 28:520–527
31. Donnet M, Jongen N, Lemaitre J, Bowen P (2000) New morphology of calcium oxalate trihydrate precipitated in a segmented flow tubular reactor. J Mater Sci 19:749–750
32. Jongen N, Donnet M, Bowen P et al (2003) Development of a continuous segmented flow tubular reactor and the scale-out concept – in search of perfect powders. Chem Eng Technol 26:303–305
33. Yen BKH, Stott NE, Jensen KF, Bawendi MG (2003) A continuous-flow microcapillary reactor for the preparation of a size series of CdSe nanocrystals. Adv Mater 15:1858–1862
34. Shestopalov I, Tice JD, Ismagilov RF (2004) Multi-step chemical reactions performed on millisecond time scale in a microfluidic droplet-based system. Lab Chip 4:316–321
35. Chan EM, Alivisatos PA, Mathies RA (2005) High-temperature microfluidic synthesis of cdse nanocrystals in nanoliter droplets. J Am Chem Soc 127:13854–13861
36. Li S, Günther PM, Köhler JM (2009) Micro segmented-flow technique for continuous synthesis of different kinds of ZnO nanoparticles in aqueous and DMSO solution. J Chem Eng Jpn 42:338–345
37. Bu W-B, Sung M, Gu S-Q, Zhu Y, Fang Q (2010) Automated microfluidic screening assay platform based on DropLab. Anal Chem 82:9941–9947
38. Köhler JM, Henkel T (2005) Chip devices for miniaturized biotechnology. Appl Microbiol Biotechnol 69:113–125
39. Boedicker JQ, Li L, Kline TR, Ismagilov RF (2008) Detecting bacteria and determining their susceptibility to antibiotics by stochastic confinement in nanoliter droplets using plug-based microfluidics. Lab Chip 8:1265–1272
40. Clausell-Tornos J, Lieber D, Baret J-Ch et al (2008) Droplet-based microfluidic platforms for the encapsulation and screening of mammalian cells and multicellular organisms. Chem Biol 15:427–437

41. Hufnagel H, Huebner A, Gülch C, Güse K, Abel Ch, Hollfelder F (2009) An integrated cell culture lab on a chip: modular microdevices for cultivation of mammalian cells and delivery into microfluidic microdroplets. Lab Chip 9:1576–1582
42. Chronis N (2010) Worm chips: microtools for *C. elegans* biology. Lab Chip 10:432–437
43. Crane MM, Chung K, Stirman J, Lu H (2010) Microfluidics-enabled phenotyping, imaging and screening of multicellular organism. Lab Chip 10:1509–1517
44. Martin K, Henkel T, Baier V et al (2003) Generation of large numbers of separated microbial populations by cultivation in segmented-flow microdevices. Lab Chip 3:202–207
45. Kopp MU, DeMello AJ, Manz A (1998) Chemical amplification: continuous-flow PCR on a chip. Science 280:1046–1948
46. Auroux P-A, Koc Y, DeMello A, Manz A, Day PJR (2004) Lab Chip 4:534–546
47. Hartung R, Brösing A, Sczcepankiewisz G et al (2009) Application of an asymmetric helical tube reactor for fast identification of gene transcripts of pathogenic viruses by micro flow-through PCR. Biomed Microdevices 11:685–692
48. Williams R, Peisajovich SG, Miller OJ, Magdassi S, Tawfik DS, Griffith AD (2006) Amplification of complex gene libraries by emulsion PCR. Nat Methods 3:545–550
49. Schemberg J, Grodrian A, Römer R, Cahill BP, Gastrock G, Lemke K (2010) Application of segmented flow for quality control of food using microfluidic tools. Physica Status Solidi 207:904–912
50. Funfak A, Hartung R, Cao J, Martin K, Wiesmüller K-H, Wolfbeis OS, Köhler JM (2009) Highly resolved dose–response functionsfor drug-modulated bacteria cultivation obtained by fluorometric and photometric flow-through sensing in microsegmented flow. Sens Actuators B 142:66–72
51. Funfak A, Cao J, Wolfbeis OS, Martin K, Köhler JM (2009) Monitoring cell cultivation in microfluid segments by optical pH sensing with a micro flow-through fluorometer using dye-doped polymer particles. Microchim Acta 164:279–286
52. Funfak A, Brösing A, Brand M, Köhler JM (2007) Micro fluid segment technique for screening and development studies on Danio rerio embryos. Lab Chip 7:1132–1138
53. Günther PM, Funfak A, Cao J, Schneider S, Möller F, Köhler JM (2010) Realization of two- and three-dimensional concentration spaces by micro segmented flow for microtoxicological screenings. Proc μ-TAS 14:1565–1567
54. Funfak A, Cao J, Knauer A, Martin K, Köhler JM (2011) Synergistic effects of metal nanoparticles and a phenolic uncoupler using microdroplet-based two-dimensional approach. J Environ Monit 13:410–415

Nanotechnology for Diagnostic and Sensing: Soft and Advanced Imaging/Sensing Approaches to Analyze Biomolecules

Alessandra Aloisi and Ross Rinaldi

Abstract Different nanotechnological strategies have been designed to implement the production of innovative diagnostic and optical sensing devices for genomic and proteomic applications. In this chapter, we will give an overview on the novel nanobiotechnological approaches recently developed, combining top-down nanostructuring and bottom-up molecular self-assembly to soft lithography, with molecular biology tools, aimed at the production of high-performance plastic chips for diagnostics and nanostructured materials to be applied in advanced sensing and imaging. Highly sensitive fluorescence imaging/sensing schemes, enabling the enhancement of sensors sensitivity and detection limits, such as Metal Enhanced Fluorescence- and Photonic Crystals-based approaches, will be discussed as novel tools for the detection of biological targets (e.g., DNA, proteins, and fibrils).

Keywords Biosensing • Fluorescence • Nanotechnology

Contents

A. Aloisi
National Nanotechology Laboratory, Istituto di Nanoscienze - CNR - Lecce, Via per Arnesano, 73100 Lecce, Italy

R. Rinaldi (✉)
National Nanotechology Laboratory, Istituto di Nanoscienze - CNR - Lecce, Via per Arnesano, 73100 Lecce, Italy

Dipartimento di Ingegneria dell'Innovazione, Università del Salento, Via per Monteroni, 73100 Lecce, Italy
e-mail: ross.rinaldi@unisalento.it

W. Fritzsche and J. Popp (eds.), *Optical Nano- and Microsystems for Bioanalytics*, Springer Series on Chemical Sensors and Biosensors (2012) 10: 83–100
DOI 10.1007/978-3-642-25498-7_3,

1 Introduction

In the last 2 decades, various modes of optical detection and measurement, including absorption, reflection, fluorescence, chemiluminescence, and phosphorescence [1–5], have been exploited in the biosensoristic field. Despite considerable advances, extensive work has still to be done in order to develop and optimize a general optical detection sensing platform in terms of signal high sensitivity, linear dynamic range, and robustness to relevant biomatrices such as serum, urine, saliva, or cell lysates. In recent times, various organic molecules possessing unique assets kept the attention of investigators to achieve the recognition of different targets [6, 7]. Molecular probe design represents a key element in biosensing systems; moreover, the conjugation of functional molecules (nucleic acid based as aptamer, DNAzyme, or modified peptides and proteins) with nanomaterials has resulted in great improvement in the field of molecular recognition. With their unique physical and chemical properties, nanomaterials facilitate the sensing process and amplify the signal of recognition events. As functional surfaces, they provide an ideal platform for biomolecules immobilization achievable by physical adsorption, including electrostatic and hydrophobic binding, covalent bonding, and specific interactions such as biotin–avidin, antibody–antigen interaction, and DNA hybridization [8]. Generally bio-interaction methods lead to high functionality within the biosensor fabrication process [9] and combination of self-assembly and nanolithography can be considered as an effective nanofabrication methodology for device realization.

This chapter mainly intends to provide an overview of the different molecular and nanotechnological interaction-mediated biosensor fabrication route that leads to sensing systems with controlled structures on both nanofunctionalized surfaces and functional nanomaterials. Herein soft and advanced technical approaches suitable for biosensor architecture are discussed, in particular referring to a combination of top-down and molecular self-assembly to soft lithography, as well as novel, highly sensitive fluorescence imaging/sensing schemes, such as those exploited in Metal Enhanced Fluorescence (MEF)- and Photonic Crystals (PCs)-based analytical system.

2 Nanoscale Fabrication of Biomolecular Layer: Soft and Advanced Approach

Micro- and nanofabrication have provided several possibilities for chemical, biological, and physical processes at molecular scale, as well as for the design of synthetic devices capable of interacting with biological systems at this level. Since 1990s, micro- and nanofabrication have represented the main contribution for the

development of sensors [10], microreactors [11], combinatorial arrays [12], micro-analytical systems [13, 14], and micro-optical systems [15, 16].

Particularly, analysis of complex biological samples and the requisite to test multiple analytes simultaneously has led to the development of multiplex analytical strategies which are essentially based on array technologies. The main technique exploited in this field is photolithography, and as an emerging procedure, Xia et al. more than 10 years ago developed an alternative, non-photolithographic process of microfabrication referred to as soft lithography [17–19].

Soft lithography, similar to photolithography, is a method also used to transfer a pattern onto a surface. Xia et al. [20], describing different softlitography approaches, focused on microcontact printing (μCP) [21], replica molding (REM) [22], microtransfer molding (μTM) [23], micromolding in capillaries (MIMIC) [24], solvent-assisted micromolding (SAMIM) [25], and phase-shift photolithography [26], as also cast molding [27], embossing [28], and injection molding [29, 30].

Aiming to depict a map of different routes for biosensor architectures, it is useful to basically divide them into top-down or bottom-up approaches. Many of such applications have been described in a recent review [31] and shown in Table 1; essentially, the top-down approach for nanoscale patterning besides traditional soft lithography methods includes electron-beam lithography, nanoshaving, nanografting, dip-pen nanolithography, colloid lithography, block copolymer micelle lithography, and extreme UV-interference lithography too [32, 33]. On the other hand, the bottom-up approach for nanofabrication of biosensors involves self-assembly of biomolecules

Table 1 Nanoscale patterning methods using biomolecules

Technique	Advantages	Limitations	Highest resolution
Electron beam lithography (EBL)	Maskless, stampless, high-resolution, arbitrary patterning with different shapes and sizes	Slow (serial process), complicated, expensive (requiring equipment, clean room, and vacuum condition), small area patterning	~30 nm
Nanocontact printing (NCP)	Simple (direct patterning), parallel, cheap, fast process, large area patterning	Preparing nanoscale stamp with high-feature density, mechanical stability of stamp, diffusion of SAM inks	~70 nm
Nanoimprint lithography (NIL)	Large area patterning with a high-throughput and low-cost, parallel	Stress and wear of mold, use of polymer, slow (molding, demolding, and etching process)	~75 nm
Nanografting/ nanoshaving	High-resolution, ambient, quick change of fabricated patterns	Small area patterning	~10 nm
Dip-pen annolithography (DPN)	High-resolution, ambient, variety of inks usable, parallelization possible	Slow (serial process), small area patterning	~30 nm

Table 1 adapted with permission from [31]

onto nanomaterials by interaction and recognition of the complementary molecule as well as physicochemical synthesis of nanomaterials such as nanoparticles, nanorods, nanotubes, and nanowires [34, 35].

Basically, self-assembly is referred to the property of self-organizing of organic molecules occurring spontaneously at solid–fluid interfaces, with reference to a paper by Netzer and Sagiv [36]. The physicochemical phenomenon of molecular auto-assembly is based on thermodynamically favored interactions of molecules such as peptides, proteins, and DNA, and other organic or inorganic molecules [37]; several advantages are provided, including the ability to fabricate three-dimensional structures and the potential for molecular control of the material [33]. Engineered surfaces for protein immobilization include two different types of immobilization: (1) physical adsorption onto surfaces through weak contact of proteins and (2) formation of covalent bonds between protein and surface; the last is typically preferred due to the molecular orientation, density, and activity control [38]. Considerably, by using the nanopatterning techniques, biomolecules can be positioned within desired nanoregions with well-defined feature size and shape retaining their native 3D structures and, hence, biological functionalities [33]. Biomolecules' high-resolution nanopatterning has been achieved by applying various kinds of lithographic techniques to self-assembled monolayers (SAM) containing Layer by Layer (LBL) assembly [37]. Essentially, it consists on the consecutive deposition of multiple thin polyion films from solution, with intermediate washes, exploiting the electrostatic attraction between oppositely charged molecules as well as covalent bonding and specific interaction as a driving force for assembly [39, 40]. Allowing a variety of materials to be incorporated within the film structures, LBL is widely accepted as a versatile and powerful bottom-up nanofabrication technique [40] that provides great control over the film structure, thickness, and function and permits the use of numerous materials, including macro-biomolecule such as both proteins [41] and DNA [42]. A key role in soft nanofabrication approach for bioanalytical devices is represented by scaffold material too; actually, this kind of top-down approach can be easily performed on several nanomaterials such as nanotubes, nanorods, nanowires, and nanoparticles [43] as well as polymeric ones, providing fascinating integration between bio/organic and inorganic structures. Mainly, certain plastic organic polymers such as poly (methylmethacrylate) (PMMA) and poly(dimethylsiloxane) (PDMS) have been exploited for the fabrication of various devices, including microchannels and valves [44], and as substrates for DNA/protein arrays [45, 46]. Specifically, PDMS has been used widely in the biomedical and pharmaceutical application fields because of its biocompatibility and good thermal, mechanical, and optical properties. In this respect, what is valuable to note is that such materials can be processed by various techniques, such as soft lithography, hot embossing, laser ablation, micromilling, and in situ polymerization, while maintaining, in some cases, the typical properties of resist materials (i.e., photoresist or electronic resist for micro- and nanofabrication).

These features provide the additional possibility to create tailored integrated bioanalytical platforms, and in this respect, some examples of advanced strategies will be reported, herein, as demonstration of applications in device fabrication.

A few years ago, Tan and colleagues [47], exploiting Parylene-C, a biocompatible inert polymer, showed a high-throughput plain method to generate multicomponent biomolecular arrays with sub-100 nm nanoscale feature width, namely "Print-and-Peel." Briefly, they first aligned an inkjet printer to a parylene template containing nanoscale openings. After printing, they peeled off parylene to reveal uniformly patterned nanoscale features, despite the imperfect morphologies of the original inkjet spots. Moreover, they attempted to expand the multiplexing capability of the applied technique to combinatorial nanoarrays by performing a second print-run superimposed over the first pattern. In Fig. 1, the schematic process of PNP is represented. Antibody arrays created using this method could be used effectively for immunoassays, molecular diagnostics, and screening.

Optimization of suitable and reproducible surface (bio)chemistry approaches for the high-density immobilization of biomolecules probe onto various substrates is a key point to improve the detection sensitivity and selectivity of the biochip toward specific bioanalytes. A reliable strategy that combines self-assembly and lithographic techniques has been recently applied by Sabella et al. [48], leading to very precise micro- or nanopositioning of biomolecules for the realization of micro- and nanoarrays of functional DNA and antibodies. In Fig. 2, a schematic process of this advanced approach is showed. In addition, combining polymer flexibility and photophysical properties of nanostructures such as colloidal nanocrystals (NCs), novel outcomes in the form of solid-state optical detection platforms have been achieved. Sabella et al. [49], in a recent paper, presented an integrated plastic biochip that exploits a "smart" polymeric layer with both optical and biorecognition properties that allows optical monitoring of biomolecular interactions, DNA hybridization, and quantitative offline analyses of real-time polymerase chain reaction (RT-PCR). The microdevice, represented in Fig. 3,

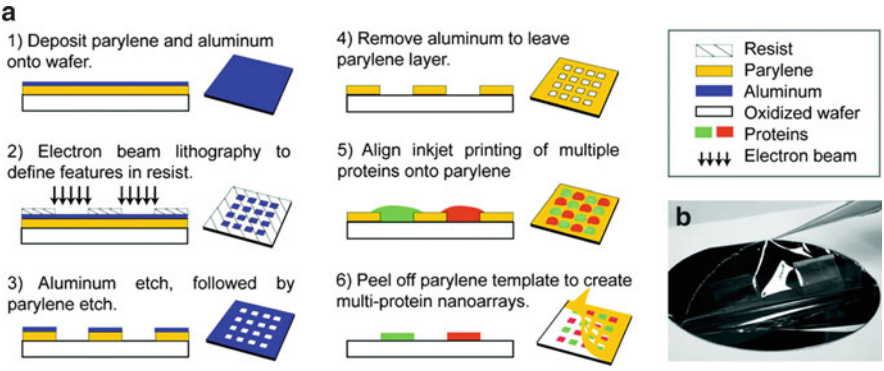

Fig. 1 Fabrication process of the parylene template and the PNP process to generate the protein nanoarrays. (**b**) Peeling off the parylene template from a wafer substrate. For simplicity of illustration, the parylene peeling is shown in dry conditions, but the protein nanopatterning and parylene peeling were performed in aqueous environments that did not require drying. Reproduced with permission from [47]

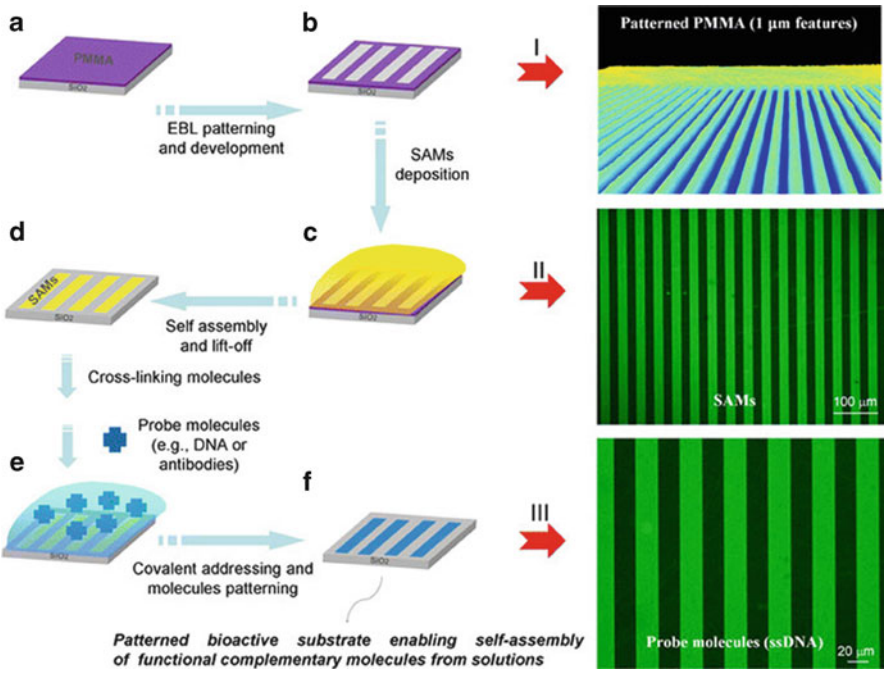

Fig. 2 Biomolecular patterning based on E-beam lithography and multistep self-assembly. *Left*: (**a**) A resist layer (PMMA) was deposited onto silicon dioxide by spin coating; (**b**) EBL patterning and development; (**c**) selective SAM deposition by self-assembly in the exposed regions of the substrate; (**d**) lift-off; (**e**, **f**) spatially confined self-assembling of cross-linking molecules and probe biomolecules. *Right*: real images of the steps (**b**), (**c**), and (**f**), respectively. (I) Holographic microscopy 3D image of 1 µm wide PMMA stripes after EBL patterning and development; (II) confocal microscopy image of Fluorescein isothiocyanate (FITC)-labeled 3-aminopropyl-triethoxysilane (APTES) stripes (features: 20 µm); and (III) confocal microscopy image of Cy3-labeled ssDNA stripes (features: 20 µm). Reproduced with permission from [48]

consists of a layer with both optical and sensing properties, and is made of NCs uniformly dispersed in a polymeric a poly(methylmethacrylate) (PMMA) matrix.

The thin NCs/PMMA layer acts as the bottom of a PDMS microchamber. The upper surface of the hybrid polymeric blend is chemically modified to covalently immobilize, by a multistep solid-state chemistry, biomolecules, such as specific sequences of amino-modified single-strand DNA probes (ssDNA) or antibodies, receptors, and aptamers selective toward the analytes, such as target DNA sequences (or antigens, ligands, etc.) present in the biological sample.

The obtained hybrid material is suitable for multiplexing analysis by controlling the probe species immobilization outline and the consequent spatial confinement of the resulting FRET signals in the patterned areas; in this respect, two methods can be performed: (1) directly patterning in a controlled manner the

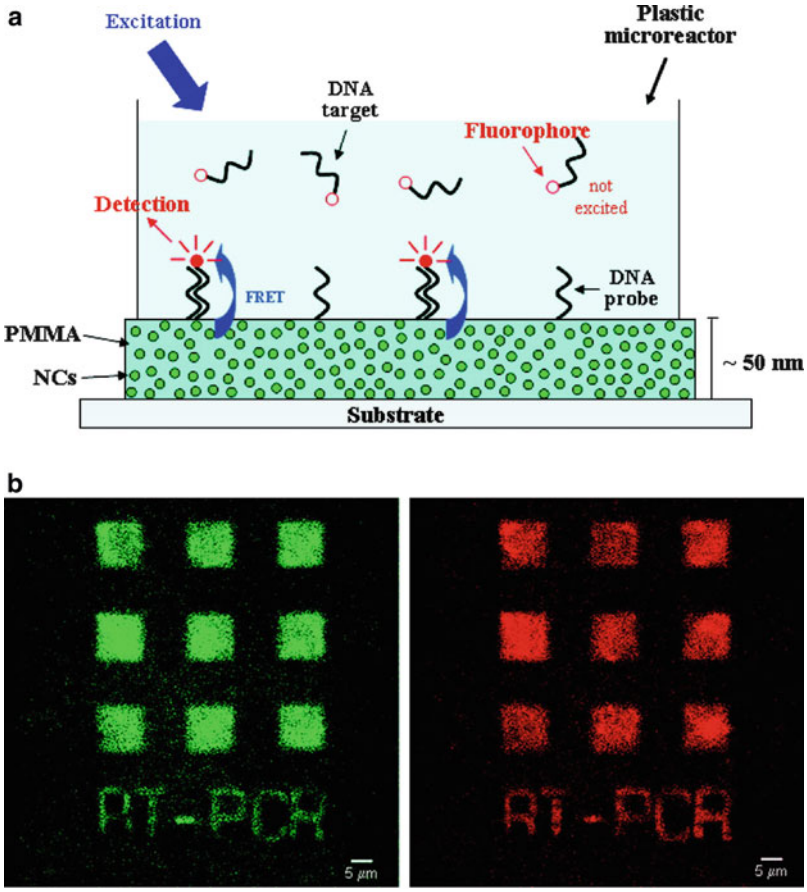

Fig. 3 (**a**) Optical scheme for the real-time monitoring of biomolecular interactions. The detection principle is based on resonance energy transfer processes (FRET) from a thin film of CdSe/ZnS core/shell NCs, dispersed in a PMMA matrix, to the fluorophores conjugated to the target biomolecules (for instance, a specific DNA sequence). Adapted with permission from [49]. (**b**) High-resolution patterning of NCs/PMMA blend for multiplexing applications: simultaneous imaging of E-beam patterned 500 nm emitting CdSe/ZnS core/shell NCs (*left*) and of solid-state DNA hybridization events by FRET (*right*), according to the optical detection scheme reported in (**a**)

active polymeric blend, thus localizing the detection process (since PMMA is an electronic resist and the hybrid NCs/PPMA film can be patterned by electron beam lithography (EBL) [49] without significant perturbation of the NCs spectral features [50]), or (2) as above reported, by biomolecular patterning based on EBL [48]. Similar advanced fluorescence schemes will be discussed in more detail in the next section.

3 Nanostructured Materials for Advanced Sensing/Imaging

Optical sensing has become one of the dominant sensing technologies in medical diagnostics. In various detection platforms such as ELISAs or protein microarrays [51, 52], the readout is based on a fluorescent or colorimetric signal. Intrinsic matrix autofluorescence or optical absorption of relevant biological samples or reagents represents for such sensing approach a crucial limiting factor as well as the quantum yield and photostability of the fluorophores. Within the last decade, functional nanomaterials have been exploited to highly enhance the assay sensitivity, specifically improving the detection ability of biosensing devices; nanostructured materials offer wide combinations of various compositions and shapes with unique and controllable size- and structure-dependent properties [53].

3.1 Metal-Enhanced Fluorescence

Recently, the great developments in the MEF technology have been exploited to favorably modify the spectral properties and to play down photophysical limitations of the dye molecules [54]. In fact, the ability to control the surface structure, in particular of noble metals, gives rise to the possibility to engineer the spectral properties of the molecules/fluorophores positioned in its vicinity, thanks to plasmonic coupling. In the early 1990s, Johnson and Aroca [55] reported a model on the distance dependence of the transfer of electronic energy from a donor plane of molecules to an acceptor plane. Changing experimental parameters (such as material, shape, and dimensions of the metallic nanostructures, as well as the average fluorophore—nanostructure distance) [54, 56], the efficiency of the coupling, and therefore the spectral properties of the dye, can be properly modified. Really, metal surfaces can amplify or decrease the radiative decay rates of fluorophores and increase the extent of resonance energy transfer [56–60].

In the last few years, several interesting MEF approaches have been demonstrated [56, 60–64]. The interactions between the dipole moments of the dye molecule and the surface plasmon field of the metal can increase the incident light field and may result in a local MEF [56, 65–68] as an important increase of fluorophore emission intensity, significantly enhancing the signal detectability [69]. A comprehensible example of the theoretical model was presented in the first report on “the release of self-quenching of fluorophores near-to metallic surfaces” [70]. The authors, underlining the need of brightness of labeled antibodies for maximal sensitivity and observability over sample autofluorescence in bioassays, and since the obvious approach to increasing the molecule brightness by increasing the extent of labeling is not useful due to self-quenching (homo RET), examined fluorescein-labeled human serum albumine (HSA) when bound to quartz and to silver island films (SIFs). As imaged in Fig. 4, Lakowicz and colleagues showed that

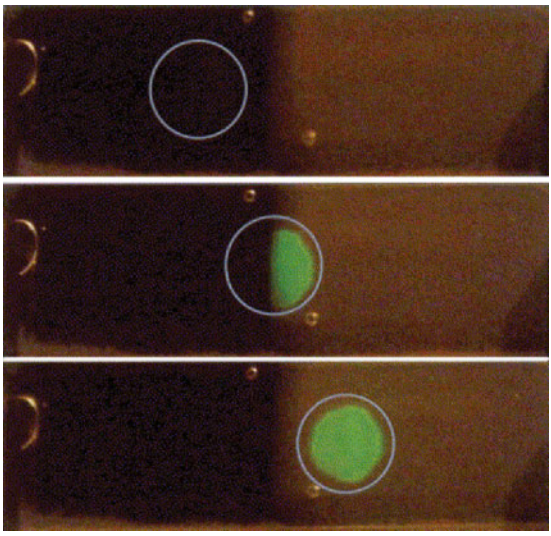

Fig. 4 Fluorescence enhancement from silver islands. Image of fluorescein-labeled human serum albumin (molar ratio of fluorescein/human serum albumin = 7) on quartz and on SiFs as observed with 430-nm excitation and a 480-nm long-pass filter. The excitation was progressively moved from the quartz side to the silver side. Adapted with permission from [70]

binding of fluorescein-labeled HSA to SIFs eliminated much of the self-quenching.

This outcome has a variety of applications in biodiagnostics imaging and sensing [54]. Specially, MEF has been employed to increase the sensitivity in the detection of DNA, RNA, and proteins in microarray systems [58, 71, 72].

Several routes have been followed; among these, an interesting approach was showed by Zhang and Geddes in 2010 that emphasized the high thermal stability (before and after autoclaving) of different density rhodium (Rh) nanoparticulate glass substrates fabricated by electron-beam physical vapor deposition in order to study the fluorescence scheme of fluorophores in close proximity. The authors did not observe a shorter fluorescence lifetime, suggesting only an enhanced electric field component as the mechanism for fluorescence enhancement; moreover, they concluded that Rh substrates may be of particular value for higher temperature MEF experiments or indeed may be used as an autoclavable substrate [73].

To address the two major shortcomings of fluorescence-based bioassays: sensitivity and rapidity, a new platform technology called microwave-accelerated metal-enhanced fluorescence (MAMEF) was recently introduced [74, 75]. In effect, the MAMEF method combines low power microwave heating, kinetically accelerating assays to completion within a few seconds with metal-enhanced fluorescence (MEF) [54]. As a specific application, Kadir Aslan [76] in 2010 has given the proof-of-principle demonstration of rapid whole blood bioassays based on microwave-accelerated metal-enhanced fluorescence (MAMEF) method by silver nanoparticle-deposited surfaces.

On the other hand, concerning topographical control of signal enhancement, highly reproducible EBL fabrication of ordered arrays of gold nanostructures coupled to NCs dispersed in a polymer blend was used by Pompa et al. [77] to

demonstrate that this approach can be exploited to obtain a spatially controlled amplification of the fluorescence signal in two different nanomaterials, namely colloidal Quantum Dots (QDs) and Quantum Rods (QRs). The authors highlighted the ability to modulate the spectral properties of semiconductor nanocrystals as useful strategies in various optical-based technologies, such as highly sensitive optical sensors and photonic devices operating at nanoscale and/or requiring very low densities of fluorescent emitters. Actually, microfabrication developments have enabled high-density chip-scale integration of optical elements, such as light sources and photodetectors [78, 79].

3.2 Photonic Crystals

Photonic crystal structures have their origin in an observed phenomenon called "Wood's anomaly." The so-called anomalies were effects detected in the spectrum of light reflected by optical diffraction gratings as rapid variations in the intensity of particular diffracted orders in certain narrow frequency bands [80].

It is now known that analogous bandgaps offered between the valence and the conduction energy bands of a semiconductor can subsist when electromagnetic (EM) waves propagate in a macroscopic periodic dielectric structure. EM waves with frequencies inside such a gap cannot propagate in any direction inside this lattice-like crystal that, since late 1980s, has been referred to as photonic crystals (PCs) or photonic band-gap (PBG) materials [81, 82]. Recently, PCs have been under intensive investigation as a novel label-free optical biosensing platform [83, 84]. By introducing "defects" into the PCs structure, the electric field can be strongly confined and enhanced in the vicinity of the sensing surface where target analytes are adsorbed. Thus the corresponding optical spectrum shows narrow transmission peaks or reflection dips in the photonic bandgap, which enables highly sensitive biomolecular detection. On the high-energy side, Luo et al. [85] concluded that for particles traveling through an all-air path inside a photonic crystal, a Cerenkov radiation (CR), with a spiky radiation wavefront, is possible, allowing complete absence of the impurity scattering and random ionization losses intrinsic in a dense medium. Indeed this possibility improves the performance of detectors, as they put forward in 2003; furthermore, the CR frequency that is set by the photonic crystal is selectively scalable beyond optical wavelengths, opening up the possibility of flexible radiation sources for frequencies that are otherwise difficult to access. Investigations on one-dimensional patterned dielectric slab PC have showed good sensitivity values, simplified light coupling schemes, and compatibility with plastic substrates [86, 87]. Moreover, many recent efforts have focused on the study of two-dimensional planar PC structures, where light is associated with in-plane guided modes from the narrow face of a slab, as reviewed by Mortensen and colleagues [88].

PCs, incorporated into standard 96-, 384-, or 1,536-well microplates, as sensor elements, have been used to detect antibody–antigen, small molecule, protein, and

whole cell–protein interactions on the biosensor surface, cheaply fabricated on sheets of plastic film, without the use of fluorescent labels [89].

Practically, PCs' surface may be coated with a thin layer of biorecognition molecules that bind specifically to an analyte (e.g., antibodies with affinity to a specific antigen, or streptavidin with an affinity to biotin). When excited at a guided resonance frequency, the PCs will have significant electric field energy surrounding the biorecognition layer [90]. In other words, when illuminated with white light, appropriately structured PCs are able to reflect a single wavelength, whose value is dependent on the local concentration of adsorbed biomolecules or cells [91].

Proper selection of photonic crystal slab design structure permits biosensing of a wide variety of analytes, including proteins, antigens, and cells. In this regard, ultracompact monitoring of reaction kinetics and protein concentration has been reported by Zlatanovic and colleagues [92]. In a PC microcavity, the field enhancement depends on confinement of light within a very small volume, enabling an ultra-small attoliter detection volume, many orders of magnitude smaller than in Surface Plasmon Resonance (SPR) and microtoroid sensors, thus allowing the reduction of sample required for sensing. Moreover, Martiradonna et al., in 2010 [93], proposed a strategy based on an efficient spectral modeling and enhancement of marker fluorescence through the insertion of PC nanocavities (PC–NCs) (Fig. 5) in the readout area of biochips to univocally associate a characteristic emission wavelength with a specific bioprobe immobilized on a nanocavity (as represented in Fig. 6), thereby guaranteeing multiplexed detection and faster analysis time in addition to higher sensitivity.

Toccafondo and colleagues [94] presented an experimental demonstration of single-strand DNA (ssDNA) sensing exploiting a photonic-crystal-waveguide-based optical sensor, and, in particular, they showed the possibility to observe DNA hybridization events using planar PCs structures, with a detection limit as low as 19.8 nM for the detection of the complementary DNA strand. In a similar way, Pisanello et al. [95] exploited nanofabricated arrays of 2D-PC cavities onto a thin oxide (silicon nitride (Si_3N_4)) membrane for highly selective enhancement of fluorescent molecules emission. Cyanine (Cy3)-labeled target DNA molecules

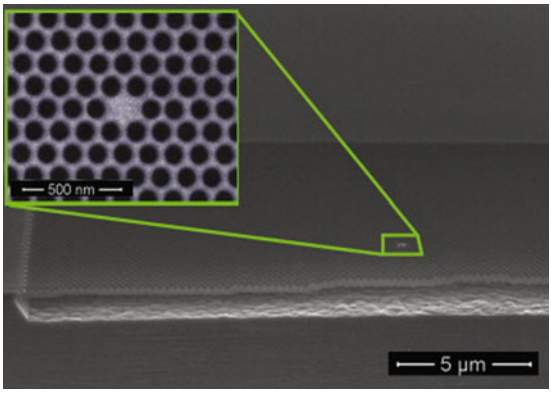

Fig. 5 Nanocavities in PC slab (explanation of the structure application will be given later in this section) Scanning electron microscopy (SEM) cross-section micrograph of an array of PC cavities fabricated on Si_3N_4. *Inset*: detail of the defect zone. Reproduced with permission from [94, 95]

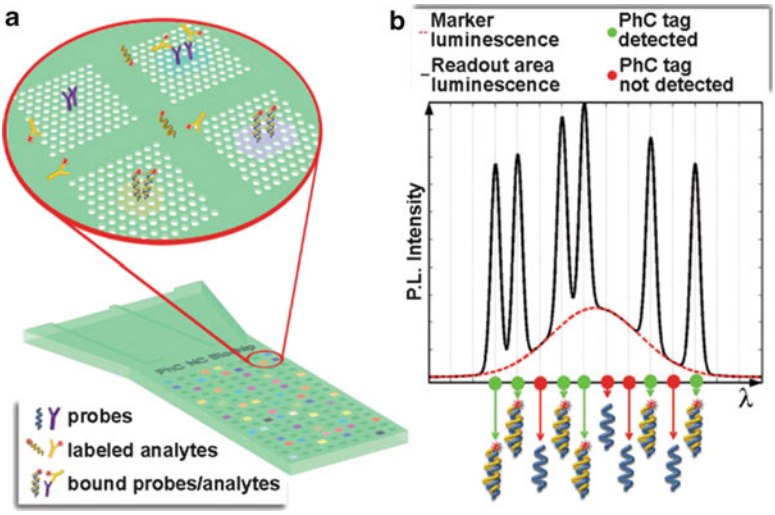

Fig. 6 Scheme of the proposed strategy for photonic crystal nanocavities (PhC–NCs) biochip. (**a**) Array of nanocavities patterned on the readout area. *Inset*: detail showing examples of NCs. The cavities are functionalized with different probes molecules, which specifically interact with complementary target analytes labeled with fluorescent markers. The signal is collected from this area and spectrally resolved in order to identify the different spectral tags univocally associated to each NC and thus to each bioprobe. (**b**) Example of a possible luminescence detected from the whole readout area (*black line*) as compared to the unmodified broad marker luminescence (*red dotted line*). The occurrence of each peak in the spectrum identifies the corresponding analyte in the performed assay. Reproduced with permission from [93]

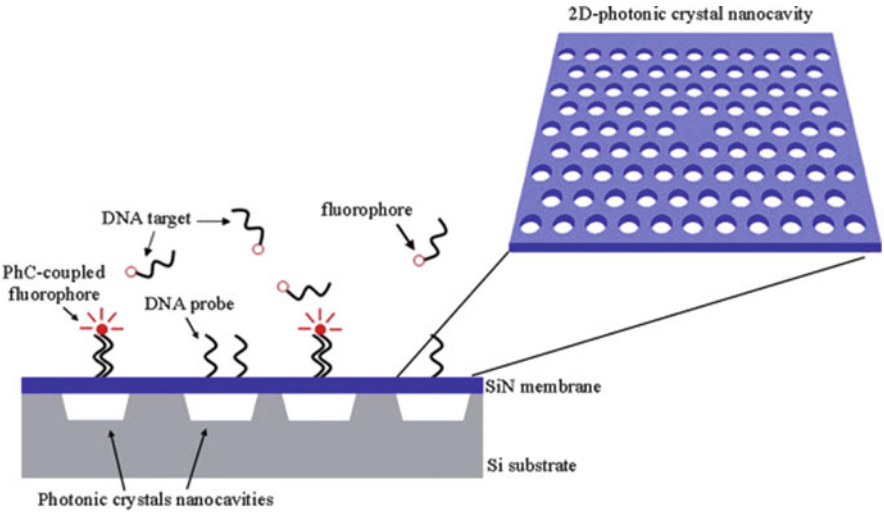

Fig. 7 Scheme of a DNA-chip integrated with array of PhC nanocavities. The cavities are functionalized with different DNA probes, which specifically interact with complementary target analytes labeled with fluorescent markers. *Inset*: detail showing an example of nanocavities. Adapted with permission from [95]

were immobilized on the 2D-PC, allowing the intensification of the emission of the organic dye due to resonating modes of the cavities, with high spectral resolution. By means of fine-tuning of the fabricated planar resonators, it was possible to assign a spectral fingerprint to targets bound to different resonators in the arrays, so that the presence of different DNA molecules in an investigated assay was assessed through spectral analysis of the emission coming from the whole array in a single shot. A clear sketch of the detection scheme in showed in Fig. 7.

4 Conclusion and Perspective

In this chapter, we have tried to illustrate the progress of nanotechnological strategies, which have been recently developed to implement the production of innovative diagnostic and optical sensing devices for genomic and proteomic applications. As many research works have shown, the recent trends in these nanobiotechnological platforms exploit the combination of top-down nanostructuring and bottom-up molecular self-assembly to soft lithography and molecular biology tools. The new generation of produced systems for diagnostics and nanostructured materials demonstrates that high information content, high sensitivity, and selectivity can be joined with ultra-high-throughput in advanced sensing and imaging. The current status of mature technologies for the fabrication of MEF and PCs-based platforms for sensing, combined with FRET and BRET methods, is expected to evolve in a rapid fashion on many different aspects to produce systems more and more miniaturized, sensitive, and with high performances, to be applied in the fields of molecular recognition and drug discovery, and be involved in several strategies for the molecule-based identification and diagnostics in cellular systems which comprise genotyping, phenotyping, DNA sequencing, and proteomics. The need is to perform different methodologies to apply for rapid sensitive detection system in multiplexed channels and for sensitive detection of single nucleotide polymorphism (SNP), genetic variation, and protein markers for cancer and other diseases, with the aim to contribute quickly and positively to the improvement of current early-diagnostic methods.

References

1. Cooper MA (2002) Optical biosensors in drug discovery. Nat Rev Drug Discov 1(7):515–528
2. Fan XD, White IM, Shopoua SI et al (2008) Sensitive optical biosensors for unlabeled targets: a review. Anal Chim Acta 620(1–2):8–26
3. Ligler FS (2009) Perspective on optical biosensors and integrated sensor systems. Anal Chem 81(2):519–526
4. Martin-Palma RJ, Manso M, Torres-Costa V (2009) Optical biosensors based on semiconductor nanostructures. Sensors 9(7):5149–5172
5. Collings AF, Caruso F (1997) Biosensors: recent advances. Rep Prog Phys 60(11):1397–1445
6. Gellman SH (1997) Introduction: molecular recognition. Chem Rev 97(5):1231–1232

7. deSilva AP, Gunaratne HQN, Gunnlaugsson T, Huxley AJM, McCoy CP, Rademacher JT, Rice TE (1997) Signaling recognition events with fluorescent sensors and switches. Chem Rev 97(5):1515–1566
8. Jung Y, Jeong JY, Chung BH (2008) Recent advances in immobilization methods of antibodies on solid supports. Analyst 133(6):697–701
9. Rauf S, Zhou D, Abell C et al (2006) Building three-dimensional nanostructures with active enzymes by surface templated layer-by-layer assembly. Chem Commun (Camb) 16:1721–1723
10. Barrett CR (1993) Silicon valley, what next. Mrs Bull 18(7):3–10
11. Clark RA, Hietpas PB, Ewing AG (1997) Electrochemical analysis in picoliter microvials. Anal Chem 69(2):259–263
12. Xiang XD, Sun XD, Briceno G et al (1995) A combinatorial approach to materials discovery. Science 268(5218):1738–1740
13. Manz A (1996) What can chips technology offer for next century's chemistry and life sciences? Chimia 50(4):140–143
14. Kovacs GTA, Petersen K, Albin M (1996) Silicon micromachining – sensors to systems. Anal Chem 68(13):A407–A412
15. Wu MC, Lin LY, Lee SS et al (1996) Integrated devices make an optical bench on a chip. Laser Focus World 32(2):64–68
16. Nussbaum P, Volke R, Herzig HP et al (1997) Design, fabrication and testing of microlens arrays for sensors and microsystems. Pure Appl Opt 6(6):617–636
17. Xia YN, Tien J, Qin D et al (1996) Non-photolithographic methods for fabrication of elastomeric stamps for use in microcontact printing. Langmuir 12(16):4033–4038
18. Xia YN, Rogers JA, Paul KE et al (1999) Unconventional methods for fabricating and patterning nanostructures. Chem Rev 99(7):1823–1848
19. Xia YN, Whitesides GM (1998) Soft lithography. Angew Chem Int Ed Engl 37(5):551–575
20. Xia YN, Whitesides GM (1998) Soft lithography. Annu Rev Mater Sci 28:153–184
21. Kumar A, Whitesides GM (1993) Features of gold having micrometer to centimeter dimensions can be formed through a combination of stamping with an elastomeric stamp and an alkanethiol ink followed by chemical etching. Appl Phys Lett 63(14):2002–2004
22. Xia YN, Kim E, Zhao XM et al (1996) Complex optical surfaces formed by replica molding against elastomeric masters. Science 273(5273):347–349
23. Zhao XM, Xia YN, Whitesides GM (1996) Fabrication of three-dimensional micro-structures: microtransfer molding. Adv Mater 8(10):837–840
24. Kim E, Xia YN, Whitesides GM (1995) Polymer microstructures formed by molding in capillaries. Nature 376(6541):581–584
25. Kim E, Xia YN, Zhao XM et al (1997) Solvent-assisted microcontact molding: a convenient method for fabricating three-dimensional structures on surfaces of polymers. Adv Mater 9(8):651–654
26. Rogers SS, van der Walle C, Waigh TA (2008) Microrheology of bacterial biofilms in vitro: *Staphylococcus aureus* and *Pseudomonas aeruginosa*. Langmuir 24(23):13549–13555
27. Terris BD, Mamin HJ, Best ME et al (1996) Nanoscale replication for scanning probe data storage. Appl Phys Lett 69(27):4262–4264
28. Chou SY, Krauss PR, Renstrom PJ (1995) Imprint of sub-25 Nm vias and trenches in polymers. Appl Phys Lett 67(21):3114–3116
29. Masuda H, Fukuda K (1995) Ordered metal nanohole arrays made by a 2-step replication of honeycomb structures of anodic alumina. Science 268(5216):1466–1468
30. Hoyer P (1996) Semiconductor nanotube formation by a two-step template process. Adv Mater 8(10):857–859
31. Kim DC, Kang DJ (2008) Molecular recognition and specific interactions for biosensing applications. Sensors 8(10):6605–6641
32. Blattler T, Huwiler C, Ochsner M et al (2006) Nanopatterns with biological functions. J Nanosci Nanotechnol 6(8):2237–2264

33. Mendes PM, Yeung CL, Preece JA (2007) Bio-nanopatterning of surfaces. Nanoscale Res Lett 2(8):373–384
34. Whitesides GM (2001) The once and future nanomachine – biology outmatches futurists' most elaborate fantasies for molecular robots. Sci Am 285(3):78–83
35. Yu B, Meyyappan M (2006) Nanotechnology: role in emerging nanoelectronics. Solid State Electron 50(4):536–544
36. Netzer L, Sagiv J (1983) A new approach to construction of artificial monolayer assemblies. J Am Chem Soc 105(3):674–676
37. Miyake T, Tanii T, Kato K et al (2007) Selectivity improvement in protein nanopatterning with a hydroxy-terminated self-assembled monolayer template. Nanotechnology 18(30):e6
38. Ferretti S, Paynter S, Russell DA et al (2000) Self-assembled monolayers: a versatile tool for the formulation of bio-surfaces. TrAC-Trends Anal Chem 19(9):530–540
39. Decher G (1997) Fuzzy nanoassemblies: toward layered polymeric multicomposites. Science 277(5330):1232–1237
40. Ariga K, Hill JP, Ji Q (2007) Layer-by-layer assembly as a versatile bottom-up nanofabrication technique for exploratory research and realistic application. Phys Chem Chem Phys 9(19):2319–2340
41. Lvov YM, Lu ZQ, Schenkman JB et al (1998) Direct electrochemistry of myoglobin and cytochrome p450(cam) in alternate layer-by-layer films with DNA and other polyions. J Am Chem Soc 120(17):4073–4080
42. Taton TA, Mucic RC, Mirkin CA et al (2000) The DNA-mediated formation of supramolecular mono- and multilayered nanoparticle structures. J Am Chem Soc 122(26):6305–6306
43. Wohlstadter JN, Wilbur JL, Sigal GB et al (2003) Carbon nanotube-based biosensor. Adv Mater 15(14):1184–1187
44. Shaikh KA, Ryu KS, Goluch ED et al (2005) A modular microfluidic architecture for integrated biochemical analysis. Proc Natl Acad Sci USA 102(28):9745–9750
45. Fixe F, Dufva M, Telleman P et al (2004) Functionalization of poly(methyl methacrylate) (PMMA) as a substrate for DNA microarrays. Nucleic Acids Res 32(1):e9
46. Wingren C, Borrebaeck CAK (2007) Progress in miniaturization of protein arrays – a step closer to high-density nanoarrays. Drug Discov Today 12(19–20):813–819
47. Tan CP, Cipriany BR, Lin DM et al (2010) Nanoscale resolution, multicomponent biomolecular arrays generated by aligned printing with parylene peel-off. Nano Lett 10(2):719–725
48. Sabella S, Brunetti V, Vecchio G et al (2009) Micro/nanoscale parallel patterning of functional biomolecules, organic fluorophores and colloidal nanocrystals. Nanoscale Res Lett 4(10):1222–1229
49. Sabella S, Vecchio G, Cingolani R et al (2008) Real-time PCR in a plastic chip based on solid state FRET. Langmuir 24(23):13266–13269
50. Martiradonna L, Stomeo T, De Giorgi M, Cingolani R, De Vittorio M (2006) Nanopatterning of colloidal nanocrystals emitters dispersed in a PMMA matrix by e-beam lithography. Microelectron Eng 83(4–9):1478–1481
51. Mitchell P (2002) A perspective on protein microarrays. Nat Biotechnol 20(3):225–229
52. Chan SM, Ermann J, Su L, Fathman CG et al (2004) Protein microarrays for multiplex analysis of signal transduction pathways. Nat Med 10(12):1390–1396
53. Rosi NL, Mirkin CA (2005) Nanostructures in biodiagnostics. Chem Rev 105:1547–1562
54. Aslan K, Gryczynski I, Malicka J, Matveeva E, Lakowicz JR, Geddes CD (2005) Metal-enhanced fluorescence: an emerging tool in biotechnology. Curr Opin Biotechnol 16(4):55–62
55. Johnson E, Aroca R (1991) Energy-transfer between langmuir-blodgett monolayers of organic-dyes. Can J Chem Revue Canadienne De Chimie 69(11):1728–1731
56. Lakowicz JR (2001) Radiative decay engineering: biophysical and biomedical applications. Anal Biochem 298(1):1–24
57. Lakowicz JR, Shen B, Gryczynski Z et al (2001) Intrinsic fluorescence from DNA can be enhanced by metallic particles. Biochem Biophys Res Commun 286(5):875–879

58. Lakowicz JR, Shen Y, D'Auria S et al (2002) Radiative decay engineering. 2. Effects of Silver Island films on fluorescence intensity, lifetimes, and resonance energy transfer. Anal Biochem 301(2):261–277
59. Gryczynski I, Malicka J, Shen YB et al (2002) Multiphoton excitation of fluorescence near metallic particles: enhanced and localized excitation. J Phys Chem B 106(9):2191–2195
60. Neal TD, Okamoto K, Scherer A (2005) Surface plasmon enhanced emission from dye doped polymer layers. Opt Express 13(14):5522–5527
61. Tovmachenko OG, Graf C, van den Heuvel DJ et al (2006) Fluorescence enhancement by metal-core/silica-shell nanoparticles. Adv Mater 18(1):91–95
62. Aslan K, Lakowicz JR, Geddes CD (2005) Rapid deposition of triangular silver nanoplates on planar surfaces: application to metal-enhanced fluorescence. J Phys Chem B 109(13):6247–6251
63. Nakamura T, Hayashi S (2005) Enhancement of dye fluorescence by gold nanoparticles: analysis of particle size dependence. Jpn J Appl Phys 44(9A):6833–6837, Part 1-Regular Papers Brief Communications & Review Papers
64. Shimizu KT, Woo WK, Fisher BR et al (2002) Surface-enhanced emission from single semiconductor nanocrystals. Phys Rev Lett 89(11):e4
65. Fort E, Gresillon S (2008) Surface enhanced fluorescence. J Phys D Appl Phys 41(1):e31
66. Aslan K, Lakowicz JR, Szmacinski H et al (2004) Metal-enhanced fluorescence solution-based sensing platform. J Fluoresc 14(6):677–679
67. Aslan K, Badugu R, Lakowicz JR et al (2005) Metal-enhanced fluorescence from plastic substrates. J Fluoresc 15(2):99–104
68. Aslan K, Holley P, Geddes CD (2006) Metal-enhanced fluorescence from silver nanoparticle-deposited polycarbonate substrates. J Mater Chem 16(27):2846–2852
69. Geddes CD, Gryczynski I, Malicka J et al (2003) Metal-enhanced fluorescence: potential applications in HTS. Comb Chem High Throughput Screen 6(2):109–117
70. Lakowicz JR, Malicka J, D'Auria S et al (2003) Release of the self-quenching of fluorescence near silver metallic surfaces. Anal Biochem 320(1):13–20
71. Aslan K, Malyn SN, Geddes CD (2006) Multicolor microwave-triggered metal-enhanced chemiluminescence. J Am Chem Soc 128(41):13372–13373
72. Sabanayagam CR, Lakowicz JR (2007) Increasing the sensitivity of DNA microarrays by metal-enhanced fluorescence using surface-bound silver nanoparticles. Nucleic Acids Res 35(2):e13
73. Zhang YX, Geddes CD (2010) Metal-enhanced fluorescence from thermally stable rhodium nanodeposits. J Mater Chem 20(39):8600–8606
74. Aslan K, Geddes CD (2005) Microwave-accelerated metal-enhanced fluorescence: platform technology for ultrafast and ultrabright assays. Anal Chem 77(24):8057–8067
75. Aslan K, Geddes CD (2006) Microwave-accelerated metal-enhanced fluorescence (MAMEF): application to ultra fast and sensitive clinical assays. J Fluoresc 16(1):3–8
76. Aslan K (2010) Rapid whole blood bioassays using microwave-accelerated metal-enhanced fluorescence. Nano Biomed Eng 2(1):1–9
77. Pompa PP, Martiradonna L, Della Torre A, Carbone L, del Mercato LL, Manna L, De Vittorio M, Calabi F, Cingolani R, Rinaldi R (2007) Fluorescence enhancement in colloidal semiconductor nanocrystals by metallic nanopatterns. Sens Actuators B Chem 126(1):187–192
78. Kang C, Weiss SM (2008) Photonic crystal with multiple-hole defect for sensor applications. Opt Express 16(22):18188–18193
79. Wojciechowski JR, Shriver-Lake LC, Yamaguchi MY et al (2009) Organic photodiodes for biosensor miniaturization. Anal Chem 81(9):3455–3461
80. Wood RW (1902) On a remarkable case of uneven distribution of light in a diffraction grating spectrum. Proc Phys Soc London 18:269–275
81. Yablonovitch E (1987) Inhibited spontaneous emission in solid-state physics and electronics. Phys Rev Lett 58(20):2059–2062
82. John S (1987) Strong localization of photons in certain disordered dielectric superlattices. Phys Rev Lett 58(23):2486–2489

83. Cunningham BT, Laing L (2006) Microplate-based, label-free detection of biomolecular interactions: applications in proteomics. Expert Rev Proteomics 3(3):271–281
84. Mandal S, Erickson D (2008) Nanoscale optofluidic sensor arrays. Opt Express 16(3):1623–1631
85. Luo C, Ibanescu M, Johnson SG et al (2003) Cerenkov radiation in photonic crystals. Science 299(5605):368–371
86. Schudel BR, Choi CJ, Cunningham BT et al (2009) Microfluidic chip for combinatorial mixing and screening of assays. Lab Chip 9(12):1676–1680
87. Block ID, Ganesh N, Lu M et al (2008) Sensitivity model for predicting photonic crystal biosensor performance. IEEE Sens J 8(3–4):274–280
88. Mortensen NA, Xiao SS, Pedersen J (2008) Liquid-infiltrated photonic crystals: enhanced light-matter interactions for lab-on-a-chip applications. Microfluid Nanofluidics 4(1–2):117–127
89. Cunningham BT, Li P, Schulz S et al (2004) Label-free assays on the BIND system. J Biomol Screen 9(6):481–490
90. El Beheiry M, Liu V, Fan SH, Levi O (2010) Sensitivity enhancement in photonic crystal slab biosensors. Opt Express 18(22):22702–22714
91. Shamah SM, Cunningham BT (2011) Label-free cell-based assays using photonic crystal optical biosensors. Analyst 136(6):1090–1102
92. Zlatanovic S, Mirkarimi LW, Sigalas MM et al (2009) Photonic crystal microcavity sensor for ultracompact monitoring of reaction kinetics and protein concentration. Sens Actuators B Chem 141(1):13–19
93. Martiradonna L, Pisanello F, Stomeo T et al (2010) Spectral tagging by integrated photonic crystal resonators for highly sensitive and parallel detection in biochips. Appl Phys Lett 96(11):e6
94. Toccafondo V, Garcia-Ruperez J, Banuls MJ, Griol A, Castello JG, Peransi-Llopis S, Maquieira A (2010) Single-strand DNA detection using a planar photonic-crystal-waveguide-based sensor. Opt Lett 35(5–8):3673–3675
95. Pisanello F, Martiradonna L, Pompa PP, Stomeo T, Qualtieri A, Vecchio G, Sabella S, De Vittorio M (2010) Parallel and high sensitive photonic crystal cavity assisted read-out for DNA-chips. Microelectron Eng 87(21):747–749

Part II
Optical Waveguides

Integrated Optical Microsystems for Interferometric Analytics

Gian Giuseppe Bentini and Marco Chiarini

–Lux: etsi per immundos transeat non inquinatur–
Augustinus Aurelius Hipponensis, Operae, Vol. III, 5. (A.D. 416)

Abstract Integrated optical (IO) microsystems for interferometric analysis can be used in sensing applications playing quite different roles; in particular they can operate by detecting the transmission changes induced by some chemical or biological adsorbate coming in contact with the optical chip in a region close to an integrated waveguide and interacting with the evanescent field coupled to the waveguide. Alternatively, IO microsystems can act as transducers of the variations of the properties of an optical signal, namely the intensity, originated by the presence of chemical or biological compounds along the optical path between a light source and the IO microsystem. In the last case, we are dealing with IO microsystems suitable to perform Absorption or Emission Fourier Spectroscopy.

In both cases, interferometry is the most convenient tool that can be used to perform high resolution measurements of the variation of the optical signal and convert it into a set of data that can give rise to very precise quantitative information.

To favour a concise and coherent presentation, most of this chapter will be devoted to the description of the basic principles of both these analytical techniques including a synthetic overview on the data-handling problems.

At first, the basics of Fourier Spectroscopy will be given, considering in particular the peculiarity introduced by the use of IO microsystems. In fact, it must be taken into

G.G. Bentini (✉)
Institute for Microelectronics and Microsystems IMM-CNR and Laboratory for Micro and Submicro enabling Technologies of Emilia-Romagna Region, MIST E-R Scrl, Via Gobetti 101, 40129 Bologna, Italy
e-mail: bentini@bo.imm.cnr.it

M. Chiarini
Compagnia Generale Spazio SpA, CGS and Laboratory for Micro and Submicro enabling Technologies of Emilia-Romagna Region, MIST E-R Scrl, Via Gobetti 101, 40129 Bologna, Italy

W. Fritzsche and J. Popp (eds.), *Optical Nano- and Microsystems for Bioanalytics*,
Springer Series on Chemical Sensors and Biosensors (2012) 10: 103–154
DOI 10.1007/978-3-642-25498-7_4,

account that, besides the usual physical factors (optical path, spectral window, etc.) affecting the absorption spectroscopy technique in the detection of chemical compounds, in the case of IO microdevices, the performances of this technique strongly depend on both the spectrometer design and the fabrication process.

In particular, the integrated microinterferometer can allow the capability of performing the analyses in situ, possibly without sample manipulation and remaining almost free from the poisoning problems frequently present in other kinds of detectors for chemical compounds. This feature explains the reason why the IO microsystems for interferometric analytics are under strong consideration in many different scientific areas such as Astrophysics, Environment, Biosciences, Space Science and Exploration without mentioning the peculiar interest in the Safety and Security field.

Under the combined driving force of the space research and of the biological and environmental demand, there has been a particular interest in the development of integrated interferometric microdevices, allowing to perform the Fourier Transform Spectroscopy with very interesting performances. In fact, due to their very small sizes and very small power consumption, battery-operated portable instruments can nowadays be fabricated.

Successively, a synthetic discussion of the integrated microdevice fabrication procedures with an analysis of the performances limitation connected to the micro-manufacturing processes will be presented.

Finally, it will be given a concise description of a new generation of optical microsystems addressed to different scientific areas, including Bioanalytics, which has appeared on scientific literature, even if their presence on the market has been very limited so far.

Keywords Chemical sensors • Evanescent-field sensors • Integrated optical sensors • Mach–Zehnder interferometers • MEOS sensing devices

Contents

1 Introduction

Most of the numerous techniques developed for fabrication of Optical sensor systems frequently require large, bulky optical setups [1, 2]. The reduction of system size by monolithic integration of all optical components is therefore attractive for the realisation of compact and robust sensing microsystems [3–5]. In fact, one of the main problems nowadays affecting the design and fabrication of a complete Integrated Optics microsensor systems concerns the need of the hybrid integration of a miniaturized monolithic sensor chip with a number of mechanical, optical and electronic peripheral components, which are necessary to provide the appropriate input to the Integrated Optics sensor chip and to convert the opto-chemical effect into a convenient output signal.

This applies in particular to Integrated Optics refractometric sensors in which a measurand, typically in liquid or vapour state, must enter in contact with the optical sensing-pad region. These devices are suited for measuring and monitoring a great variety of important (Bio)-chemical processes that affect the evanescent field built in an optical waveguide structure, giving rise to a change of refractive index profile in the vicinity of the waveguide surface, within the evanescent field region. The resulting change of the waveguide configuration can be measured by a variety of optical methods based on the conversion of the value of the physical parameter to be measured into a corresponding value of the effective refractive index, n_{eff}, of the guided modes.

Besides the performances of the sensing system that are frequently fixed by the basic opto-chemical sensor effect, the main problem that must be faced when designing an integrated microsystem is to try to find the best compromise among different requirements, such as, for example:

- The size of the whole system must be of the same order of the monolithic Integrated Optics sensing-pad
- The need to design a true on-chip system integrating the maximum number of functions, i.e. microfluidics for measurand supply and optics for opto-chemical transduction
- A simple and low complexity design
- A rugged packaging
- The integration with electronic circuitry, etc.

There are several refractometric sensor types, differentiating as a function of the choice of the components needed to provide the appropriate input to the Integrated Optic sensor chip and to convert the opto-chemical effect (i.e., the changes in the n_{eff} values) into a convenient output signal. Actually, the change of the waveguide configuration resulting from the n_{eff} variations can be measured by a variety of optical methods [6, 7].

Among the different methods, certainly interferometry is one of the most appropriate techniques to be associated with Integrated Optic sensor design and fabrication. This is particularly true when high resolution is a major importance

requirement and when a relatively simple monolithic chip, possibly including more than one function, is required to be integrated in the whole miniaturized system.

In fact, in an interferometric set-up, the change in the propagation parameters of the light passing through the waveguide is detected allowing a very precise and sensitive evaluation of the phase shift induced by the n_{eff} variation.

In Integrated Optics applied to interferometric devices, the Mach–Zehnder (MZ) set-up is often the most adequate configuration and certainly the most frequently used due to both the relatively simple geometry and the possibility of a monolithic fabrication of the device.

Moreover, for sensing problems, the MZ configuration is particularly interesting because it combines the possibility of high resolution and high-sensitivity performances with the presence of an easily accessible reference arm allowing the compensation of perturbing effects such as mechanical vibrations, temperature variations and other common environmental effects.

Besides the domain of Refractometric Sensors, there is another very important domain in which Integrated Optics applied to interferometric devices can play a fundamental role with respect to sensing applications. In particular, integrated microinterferometers can be of fundamental importance in Absorption and Emission Spectroscopy, which are a well-known and powerful tool for sensing chemical compounds diluted in liquid or gaseous media.

In this case, the sensing principle is not based on the variation of an optical parameter, n_{eff}, induced by the presence of an analyte to be detected, but it is based on the measurement of the attenuation (Absorption Spectroscopy) or the enhancement (Emission Spectroscopy) in well-defined wavelength bands of the light generated from an external source and transmitted through the measurand material.

Among the spectrometer performances, the sensitivity of this technique depends on the length of the optical path of the source radiation, on the spectral window used for analysis and, more generally, on the optimisation of the compromise between the resolution and the Signal-to-Noise Ratio (SNR) required.

Examples of MZ microinterferometers monolithically fabricated by using Micro Electro Optical Systems (MEOS) technologies have been reported in the literature [8–10], demonstrating very good performances in absorption spectroscopic analyses for environmental and agro-food application.

For this kind of applications, the MZ geometry has been used to build an integrated Scanning Fourier Transform Microinterferometer. In this case, the device is monolithically fabricated using an electro-optic material ($LiNbO_3$) and the refractive index variation is generated by the application of a suitable electric field to the optical waveguides and not by the presence of an analyte in direct contact with the interferometer-integrated optical structures. The system works as a scanning interferometer because the intensity of the light transmitted through the microspectrometer is monitored as a function of the variation of Δn_{eff} generated by the variation of the applied (driving) electric field.

The physical principle of this methodology is based on the observation that the average intensity of the light transmitted through the interferometer, $I(\delta)$, as a

function of the optical path variation (δ) represents the Fourier Transform of the spectral distribution of the input radiation. So, by performing the Fast Fourier Transform of the output signal it is possible to measure the spectral absorption (or emission) bands induced by the measurand material.

To complete the above-reported synthetic description of the working principles of both refractometric and spectroscopic detection techniques reported in this introductory part, we only add some information on the size, performance and other general characteristics of the MEOS microinterferometer. The microdevice can be obtained by fabricating integrated optical waveguides on $LiNbO_3$ crystals, and it is electrically driven without moving parts. The microinterferometer typically weighs a few grams, has a power consumption of a few mW and, in principle, can operate in the LN transmittance range (0.36–4.5 μm) if a suitable micro-photodetector is used.

The "Optical Nano- and Microsystems" designed to be used as device sensors for Bioanalytics and other scientific areas is a typical multidisciplinary subject that involves contemporaneous arguments that are the typical domain of Physics, Chemistry, Micro-Engineering, Biology, Medicine and even other disciplines. For this reason, in the following sections we will make a synthetic but correct description of the main different multidisciplinary aspects to hopefully allow a more easy comprehension of the different problems involved in the design of Optical Microsystem sensing devices.

In particular, a detailed discussion on the physics involved in the detection mechanisms will be reported in Sect. 2, a description of the MEOS fabrication process will be reported in Sect. 3, whereas Sect. 4 will report a discussion of the parameters affecting the microdevice performances and, finally, in Sect. 5 some examples of optical microsensors belonging to a new generation of devices will be presented.

2 Basic Principles of Interferometric Sensing

Before speaking of interferometric optical sensors, let us recall some basic elements about light propagation and about the effects produced in the light radiation (in this case intended as a probe) by the properties of the medium in which it propagates.

Light, and in general electromagnetic radiation, can represent a very effective probe tool in the study of many physical and compositional properties of an object. The effectiveness of electromagnetic radiation in interacting with materials resides in its intrinsic nature of propagating wave: this feature allows to reveal the properties of the medium in which it propagates, through the measurements of the modifications experienced by the radiation travelling in it.

2.1 Light and the Wave Nature of Electromagnetic Radiation. Superposition Principle

To understand the fundamental principles of the interferometric sensing, we must consider the properties of electromagnetic radiation as a travelling wave, interacting with the propagation medium.

An electromagnetic wave is a perturbation of the electromagnetic field ($\boldsymbol{E}$, $\boldsymbol{H}$), propagating in space at a speed c and periodically time dependent, i.e.

$$\boldsymbol{E} = \boldsymbol{E}(r,t) \text{ and } \boldsymbol{H} = \boldsymbol{H}(r,t) \tag{1}$$

Starting from the Maxwell's Equations [11, 12], it is possible to show that electromagnetic waves satisfy, under very general conditions, the D'Alembert's wave equation [13] and that the description of one of the e.m. field components, namely, $\boldsymbol{E}$, is sufficient to describe the phenomena because the other component, e.g. $\boldsymbol{H}$, is automatically defined.

For an electromagnetic wave propagating in vacuum the following relationship holds:

$$\nabla^2 \boldsymbol{E}(r,t) = \varepsilon_0 \mu_0 \frac{\partial^2 \boldsymbol{E}(r,t)}{\partial t^2} \tag{2}$$

where ε_0 is the vacuum electric rigidity, μ_0 is the vacuum magnetic permittivity, and $c = (\varepsilon_0\, \mu_0)^{-½}$ is the speed of the wave, namely the speed of light in vacuum.

Among all possible solutions, the harmonically oscillating ones are of particular interest for our discussion. A convenient way to represent such solutions is[1]

$$\begin{aligned} \boldsymbol{E}(r,t) = \boldsymbol{E}_0\ \mathbf{exp}(-\mathbf{i}(k \cdot r - \omega \cdot t + \varphi)) = \boldsymbol{E}_0\,(\cos(k \cdot r - \omega \cdot t + \varphi) \\ - \mathbf{i} \sin\,(k \cdot r - \omega \cdot t + \varphi))/\mathbf{2} \end{aligned} \tag{3}$$

where $\boldsymbol{k} = \hat{\boldsymbol{e}}\, 2\pi/\lambda$, called the propagation constant, is a vector directed along the propagating direction $\hat{\boldsymbol{e}}$, which defines the wave space periodicity, whereas $\omega = 2\pi\, v$ is the oscillating frequency of the wave, defining the wave periodicity in time ($v = 1/T$, as T is the oscillation period), φ is the phase angle, indicating the shift of maximum oscillation at time $t = 0$ and $\boldsymbol{r} = 0$, whereas $\boldsymbol{E_0}$ is a constant vector, directed perpendicularly to the propagation direction $\hat{\boldsymbol{e}}$ and defining the oscillation amplitude. In addition, the following relationship holds:

$$k = \left|\vec{k}\right| = \frac{\omega}{c} \tag{4}$$

[1] Equation (3) is a convenient mathematical representation, strongly simplifying the computations: in practice only the real part is considered for actual measurements.

For a wave travelling in a transparent medium characterised by an homogeneous refractive index n, the propagation constant becomes $\boldsymbol{k}' = n \cdot \boldsymbol{k}$.

A solution in the form described by (3) is normally addressed as a *monochromatic wave* and constitutes only an idealized representation of actual radiation sources. Nevertheless, in many common experimental cases, where narrow band laser sources are applied, the monochromatic notation can offer a good model to describe the observed phenomena (Fig. 1).

The linearity of the wave equation (2) has as an immediate consequence that, given a set of different solutions, a linear combination of such solutions is a solution itself. This means that different propagating waves compose in each point of the space and at each time by simply summing up their contribution, following the so-called superposition principle [14] (Fig. 2).This principle can be expressed as in the following:if $\boldsymbol{E}_l(\boldsymbol{r},t) = \boldsymbol{E}_{0l} \exp(-\mathrm{i}(\boldsymbol{k}_l \boldsymbol{r} - \omega_l t + \varphi_l))$ $(l = 0, 1, 2, \ldots)$ represents a set of solutions of (2), then

$$\boldsymbol{E}(r,t) = \Sigma_l \mathrm{c}_l \mathbf{E}_\mathbf{l}(r,t) = \Sigma_l \mathrm{c}_l \boldsymbol{E}_{0l} \exp(-\mathrm{i}(k_l \cdot r - \omega_l \cdot t + \varphi_l)) \tag{5}$$

is also a solution of (2).

The $\boldsymbol{E}_l(r,t)$ terms represent the monochromatic components of the electromagnetic wave: if the ω_l frequency terms are not all equal then the electromagnetic wave is said to be polychromatic. The ensemble of the c_l and ω_l parameters defines the spectrum of the polychromatic wave.

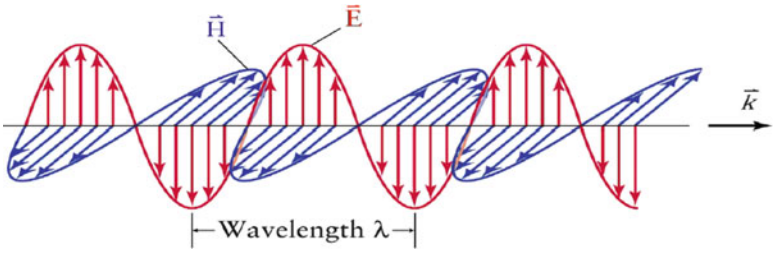

Fig. 1 Pictorial representation of an electromagnetic wave: $\boldsymbol{E}$ and $\boldsymbol{H}$ fields are represented by *arrows* of different colours

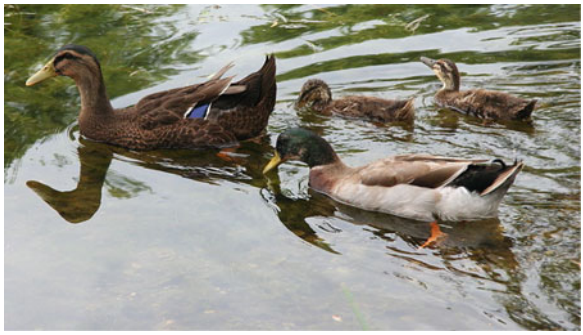

Fig. 2 Example of the application in nature of the superposition principle. From the interferometric pattern, we can have information (number, size, speed, etc.), on the swimming ducks

Equation (5) allows to formally describe interference phenomena: interference is in this view the result of the superposition (addition) of two or more waves which produces a new wave pattern.

Starting from Maxwell's equations [15, 16], it can be shown that the intensity of the electromagnetic radiation, i.e., the associated energy density, is proportional to the temporal average of the square modulus of the field

$$I(r) \sim |\boldsymbol{E}(r,t)|^2 \mathrm{d}t \tag{6}$$

Hence, interference usually refers to the interaction of waves that are correlated or coherent, i.e. with correlated phases φ_l and with frequencies nearly identical or very tightly spaced: in fact, the interference pattern generated by two incoherent waves oscillates locally at the mean wave frequency (typically 10^{14}–10^{15} Hz for visible light) and it is therefore uniform in time average, as detected at normal experimental measurement time scale.

As a consequence, we can say that *Interferometry is a technique allowing to quantify the properties of two or more waves on the basis of patterns emerging from their superposition*.

From (5) it is clear that a variation of one of the components producing the interference pattern immediately reflects in a variation of the pattern itself. An analysis of (5) effectively shows that many parameters can affect the variation of the interference pattern: e.g., a variation of the superposition coefficients c_l can reveal absorption/emission phenomena, whereas a phase change can be exploited to detect a variation in the properties of a surface through which the radiation travelled. As a general remark, the knowledge of the phenomena affecting the above-mentioned parameters allows to apply interferometry as a very sensible measurement tool.

As an example, showing the potential of interferometry, we can observe a bubble soap which may be addressed as the simplest interferometric optical sensor. In fact with this "elementary device", we can have very detailed information on the thickness profile of the bubble soap "skin", by analyzing the interferometric colours distribution (see Fig. 3), once a suitable calibration curve is defined. In fact, the

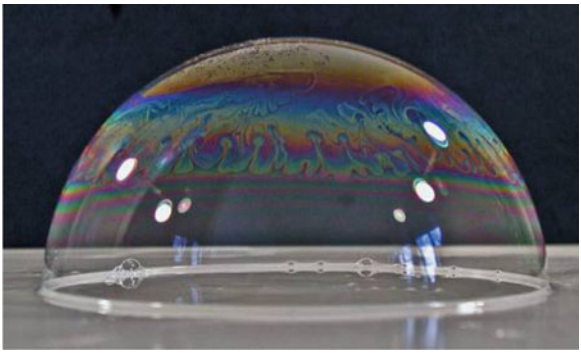

Fig. 3 Example of interference phenomena produced by a thin soap pellicle: different patterns reveal non-homogeneity in the pellicle layer and can be exploited in principle to obtain information on the bubble soap structure

interference between the incident wave and the wave reflected by the rear surface of the soap film gives rise to the colour pattern in which each colour depends on the optical thickness of the bubble skin.

2.2 *Fourier Transform Spectroscopy (FTS)*

As already anticipated in Sect. 1, a fundamental technique in bio-chemical analysis is represented by Spectroscopy. The fundamental task of Spectroscopy is to characterize the spectrum of a light source in order to analyse the phenomena producing it.

The most intuitive way to obtain a spectrum is to process light through a *dispersing* element (a diffraction grating, a refractive prism, etc.), i.e. an element that spatially spreads the light components at different angles and then allows their direct measurement by applying a suitable photodetector at the corresponding angle.

Fourier Transform Spectroscopy (FTS) allows to get the same information in a less intuitive way. This technique consists in measuring the total beam intensity containing many different wavelengths of light at the same time. The same beam is then modified to contain a changed combination of wavelengths, giving a second data point. This operation is repeated many times in order to produce a set of data points which is called an *interferogramme*.

The instrument used for FTS is an Interferometer, i.e., an apparatus allowing to recombine two initially split radiation beams, and to register their interference pattern once a variation of the optical path of one of the beams has been produced. Many interferometer models and geometries have been developed since the beginning of interferometric techniques. Due to its wide application to integrated optics and photonics, we will focus our attention to the MZ type. In a traditional MZ interferometer, Fig. 4a, the incoming light to be analysed is split in two beams constituting the interferometric arms: the length of the arms is defined by the position of two mirrors which redirect the beams travelling along separate arms towards a second beam splitter which allows the split beams to recombine and gives rise to interference. If the position of one of the optical elements (e.g., mirror) is continuously moved, the instrument is addressed as a "scanning interferometer" and the movement of the element gives rise to an optical path difference between the two arms that generates

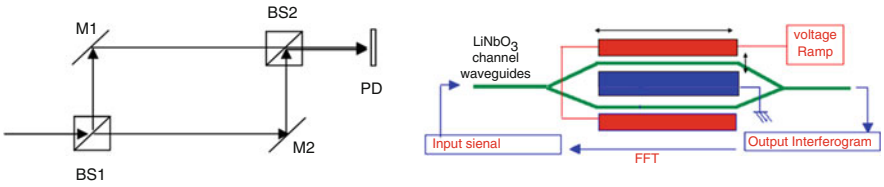

Fig. 4 Mach–Zehnder interferometer geometry: (**a**) traditional apparatus, (**b**) integrated optical version. *M1, M2* mirrors, *BS1 BS2* beam splitters, *PD* photo-detector

an intensity modulation which can be detected by a proper photodetector, as a function of the optical path difference (interferogramme).

Figure 4b reports the schematics of an integrated structure which is usually addressed as the integrated optical version of the MZ interferometer. In the integrated optical version, the combination of Mirror and Beam-Splitter is realized by Y-branches, which provide to split the incoming beams into two separated arms, constituted by integrated optical waveguides, and to recombine them at the output channel waveguide. In this view, particularly considering the second Beam Splitter, there is a slight conceptual difference between the traditional and the integrated version of the MZ interferometer. Nevertheless, in both cases, the ideal transfer function of the MZ interferometric apparatus is given by the following expression:

$$I_{\text{out}}(\delta) = \int_{-\infty}^{\infty} S(k) \cdot \cos(2\pi \cdot k \cdot \delta) \cdot \mathrm{d}k + \text{const}, \tag{7}$$

where $k = 1/\lambda$ (λ is the light wavelength) is the wave number, $S(k)$ is the spectral distribution of the impinging radiation and δ is the optical path difference experienced by the luminous radiation beams when travelling along the two different interferometer arms. In the case of the traditional scanning configuration (Fig. 4a), the optical path difference δ is varied by mechanically moving the interferometer mirrors, whereas in the integrated optical version, a variation of the optical path difference is obtained by varying the propagation properties of the travelling waves. Equation (7) states that the *transfer function* of the instrument is in practice the real part of the Fourier Transform of the spectral distribution of the impinging radiation.

To describe in deeper detail the Interferometer functioning principle, let us first consider a perfectly monochromatic light source with wavelength λ. The beams' recombination will produce constructive or destructive interference at the detector depending on the δ value.

When $\delta = m\,\lambda$ (with m integer), the two beams are in phase and constructive interference is produced and the intensity at the detector reaches the maximum value whereas, when $\delta = (m{+}1)\,\lambda/2$ (with m integer), the two beams are out of phase and a destructive interference is produced and the intensity at the detector is null. By scanning the movable mirrors over some distance, the δ value passes through many $m\,\lambda$ values and consequently the intensity $I(\delta)$, recorded on the detector, shows a sinusoidal form, depending on the reached δ value (see Fig. 5):

$$I(\delta) = \frac{I_0}{2} \cdot \left(1 + \cos\left(\frac{2\pi\delta}{\lambda}\right)\right) \tag{8}$$

When the light source is characterized by a wide-band spectrum, the conceptual behaviour is not so much different. For example, consider the spectrum shown in

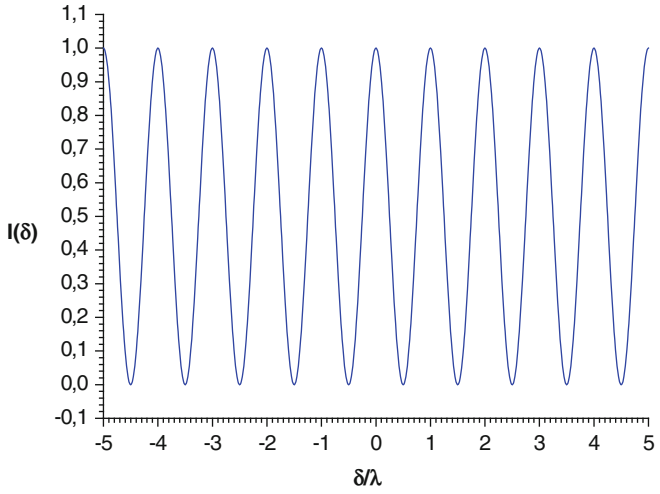

Fig. 5 Monochromatic light interferogramme

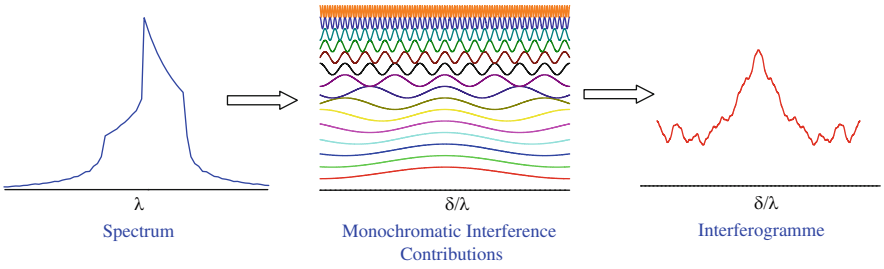

Fig. 6 Polychromatic light interferogramme

Fig. 6: each spectral component of the light source can be thought of as producing an interferogramme with its characteristic wavelength λ_i and the amplitude weighted by the relative spectral intensity.

Usually, one is interested in the spectrum of the light producing the interferogramme. The Fourier transform has the useful property of having an inverse, which allows calculating back the spectrum $S(k)$ from the interferogramme $I(\delta)$ (Fig. 7). The inverse cosine Fourier transform is very simply expressed by:

$$S(k) = \int_{-\infty}^{\infty} I_{\text{out}}(\delta) \cdot \cos(2\pi \cdot k \cdot \delta) \cdot \mathrm{d}\delta + \text{const.} \tag{9}$$

In conclusion, the essential idea is that there is a one-to-one correspondence between the spectrum and the interferogramme, a particular spectrum is related to a unique interferogramme as well as a particular interferogramme is always associated

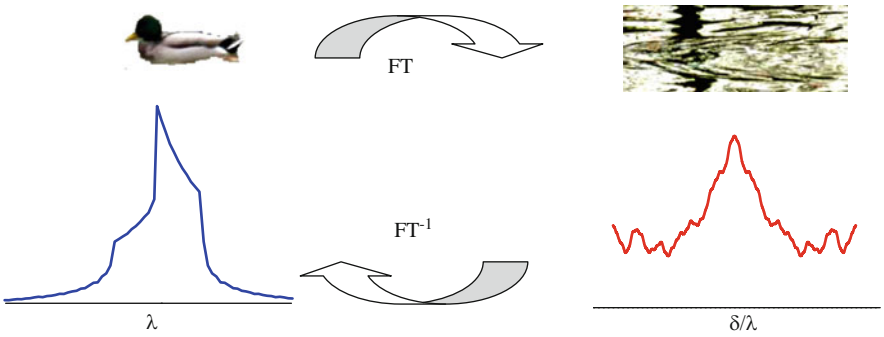

Fig. 7 Principle of FTS: i.e. the duck generates perturbations, and by an inverse Fourier transformation of the interfering waves, it is possible to have information on the duck state. In this case, the water plays the role of FT spectrometer as the one used to get information on the light spectral composition

to a unique spectrum. The mathematical relationship between the spectrum and the interferogramme is the Fourier Transform.

2.3 Interferometric Sensing and Micro-Optical Electrical Systems

The interest in integrated optical devices is remarkably growing, particularly with the purpose of implementing integrated optical sensors. In fact, as remarked in Sect. 1, sensors based on integrated optical principles present all advantages inherent to an integrated optical device, i.e., reduced sizes and consumptions, compactness, versatility, etc., generally without loss of performances. Such sensors are often part of more complex systems, comprising the sensing elements, the front-end optoelectronics interfaces, the driving/control, the readout electronics, etc. and are addressed as MEOS, as already reported. One of the fundamental elements constituting integrated optical circuits is the integrated optical waveguide, which is analogous for photons of conducting wires for electrons. In practice, an integrated optical waveguide is constituted by a well-defined volume of the substrate material within which light is strictly confined without propagating in the substrate surroundings. The physical parameter which produces the electromagnetic wave confinement is the refractive index of the waveguide: for our purposes, we will consider only traditional waveguides where the refractive index of the waveguide material is greater than the refractive index of the surrounding substrate. In the following section, a description of the principles governing the propagation of light in waveguides structures is reported to highlight how these principles can be exploited for refractometric or interferometric sensing purposes.

2.3.1 Propagation of Light in Optical Waveguides

By applying the techniques developed in integrated optics, a whole system of optical elements can be fabricated on a substrate having the size of a microscope deck glass. Figure 8 shows the equivalence between integrated and some traditional optical components, i.e. lenses, mirrors, beam splitters or even full optical spectrum analyzers. In some cases, it is sufficient to confine the light beam only in one dimension and slab optical guides can be applied, whereas other elements such as directional couplers, optical modulators or active elements such as laser diode cavities and mode filters need optical waveguides that confine light in two dimensions.

To confine the component waves inside an optical waveguide, *total internal reflection* at the waveguide boundaries must occur. For this purpose, the more standard way to obtain total internal reflection is to create a volume in the optical material where the refractive index is raised by a defined amount.

Let us first examine the simplest form of waveguide, namely the Slab Optical Waveguide. The device consists of three material planes and can be classified into two main types: symmetric and asymmetric waveguides. The refractive indices of the top and bottom layers of a symmetric waveguide are identical, as indicated in Fig. 9, whereas those of an asymmetric structure are different. In a symmetric waveguide, the core material is completely embedded inside the substrate material which constitutes the cladding material, whereas an asymmetric waveguide consists of a layer as the guiding core layer, with air or some other covering material as upper-cladding layer, and the substrate as lower-cladding layer. In integrated optics, both types are used, depending on the application and on the available micro-fabrication technique.

As it will be shown, the parameters determining the propagation features of a light wave travelling in an integrated waveguide are basic elements for the design

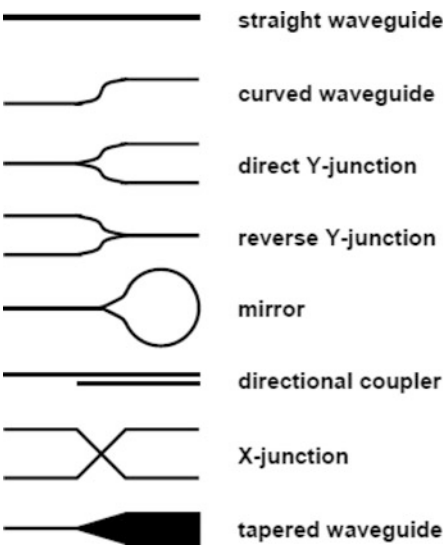

Fig. 8 Examples of integrated optical elements based on integrated optical waveguides [17]

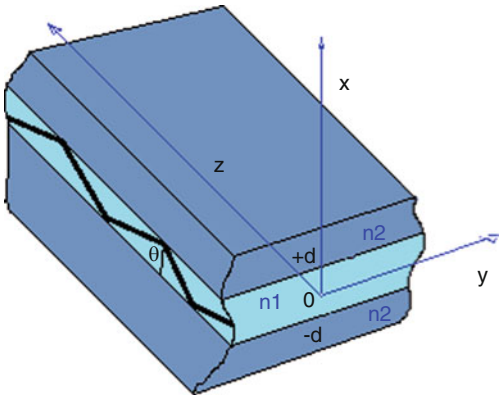

Fig. 9 Geometry of a slab symmetric optical waveguide

and fabrication of an integrated microsensor. To illustrate this, in the following a treatment of the simplest case, namely the symmetric slab waveguide, is reported.

Following the geometries represented in Fig. 9, let a monochromatic wave propagate in the z direction. If the propagation constant in the z direction is β, then the electric $\boldsymbol{E}(\boldsymbol{r},t)$ and magnetic $\boldsymbol{H}(\boldsymbol{r},t)$ components of the wave can be expressed respectively as [17]

$$\begin{aligned} \boldsymbol{E}(r,\mathrm{t}) &= \boldsymbol{E}_0(x,y)\exp(-\mathrm{i}\ (\beta\cdot z-\omega\cdot \mathrm{t}))\ \text{ and }\ \boldsymbol{H}(r,t) \\ &= \boldsymbol{H}_0(x,y)\exp\left(-\mathrm{i}\ (\beta\cdot z-\omega\cdot t)\right) \end{aligned} \tag{10}$$

After substitution in the wave equation and assuming that $\partial/\partial y = 0$ and $H_z = 0$, conditions that define a particular set of solutions defined as the TM modes,[2] the following equations are obtained:

[2] The first assumption means that the propagating wave field distribution does not vary in the y direction. This assumption implies that the field extends indefinitely in the y direction, which is in practice only an ideal condition but that can be assumed as reasonable constraint when the lateral dimensions of the slab waveguide are largely greater than the wavelength of the propagating radiation: further an infinite dimension does not guarantee in principle this first assumption as the infinity of the y dimension of the layer is only a necessary condition for $\partial/\partial y = 0$, but not a sufficient condition. For instance, a plane wave can experience variations even in an infinitely large medium in the direction of propagation: the manner the light is launched determines for example this condition. The second assumption leads to a natural way of cataloguing the solutions, but it is not the only way to do it. The solutions are then separated into two wave families: one type has only transverse but no longitudinal magnetic field, that is, $\boldsymbol{H}_z = 0$, whereas the other one has only transverse but no longitudinal electric field, that is, $\boldsymbol{E}_z = 0$. The former are called *transverse magnetic* or TM modes whereas the latter are defined as *transverse electric* or TE modes. In general, a propagating wave has both $\boldsymbol{H}_z$ and $\boldsymbol{E}_z$ components and the field is composed of both TM and TE modes in general: on the other hand the application of particular micro-fabrication techniques can produce waveguides supporting either only TM or TE modes.

$$\nabla^2\vec{\boldsymbol{H}} + n_{1,2}^2 \cdot k^2 \cdot \vec{H} = 0 \text{ and } \frac{\partial^2 \boldsymbol{H}_y}{\partial x^2} + \left(n_{1,2}^2 \cdot k^2 - \beta^2\right) \cdot \boldsymbol{H}_y = 0 \tag{11}$$

which are applicable for both core and cladding layers by using for $n_{1,2}$ the corresponding n_1 or n_2 values.

Two families of solutions can be found for the differential equation [17], i.e. trigonometric solutions such as $\cos(Kx)$ or $\sin(Kx)$ when a positive value of $n_{1,2}^2 \cdot k^2 - \beta^2$ is verified, and exponential solutions such as $\exp(-\gamma x)$ or $\exp(+\gamma x)$ for negative values of $n_{1,2}^2 \cdot k^2 - \beta^2$, where K and γ are constants emerging from boundary conditions (see below). In practice, all possible solutions of (11) define a set of "propagating modes". In particular, for TM modes (defined by the condition $H_z = 0$), the general set of solutions can be represented as:

$$\boldsymbol{H_y} = \begin{cases} A(\cos Kd)e^{-\gamma(x-d)} & \text{in the upper cladding} \\ A\ \cos\ Kx & \text{in the core} \\ A(\cos Kd)e^{\gamma(x+d)} & \text{in the lower cladding} \end{cases} \tag{12}$$

for even TM modes and

$$\boldsymbol{H_y} = \begin{cases} B(\sin Kd)e^{-\gamma(x-d)} & \text{in the upper cladding} \\ B\ \sin\ Kx & \text{in the core} \\ -B(\sin Kd)e^{\gamma(x+d)} & \text{in the lower cladding} \end{cases} \tag{13}$$

for odd TM modes, where A and B are integration constants.

A similar set of solutions can be obtained for TE modes, when $\partial/\partial x = 0$ and $\boldsymbol{E}_z = 0$ conditions are assumed. Setting up continuity conditions on the boundaries between cladding and core layers, *which is one of the most important waveguide regions for many sensing applications*, further conditions emerge, namely
for even TM modes

$$n^2\, Kd\, \tan\, Kd = \gamma d, \tag{14}$$

and for odd TM modes

$$-\, n^2\, Kd\, \cot\, Kd = \gamma d, \tag{15}$$

which are called the "characteristic equations" of the TM waveguide modes and allow to establish solutions for the K and γ parameters. In particular, for the existence of the propagating modes, the following relationship must hold:

$$(Kd)^2 + (\gamma d)^2 = V^2, \tag{16}$$

where

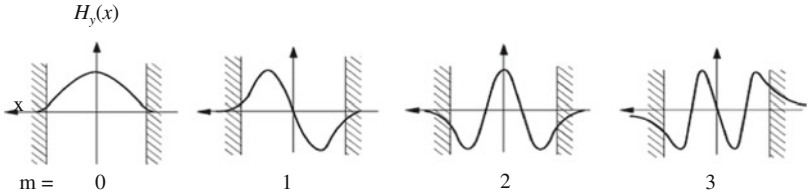

Fig. 10 Distribution of the H_y field in the slab optical guide for the first four TM modes

$$V = kd\sqrt{n_1^2 - n_2^2}. \tag{17}$$

An important aspect resulting from this simple analysis is that the way a light beam propagates in a waveguide is *quantised* in a discrete set of well-defined modes. In Fig. 10, the qualitative $\boldsymbol{H}_y$ field component distribution for the first four TM modes of the propagating wave is reported.

Since the quantity V consists of only physical constants, i.e. the waveguide thickness, the core and cladding refraction indices, as well as the wavelength, V is commonly referred to as the *normalized thickness of the guide*. The normalized thickness V is a very important parameter specifying the characteristics of the guide. In particular, the number of modes supported by the waveguides increases for every $\pi/2$ increase in V; hence the highest mode number N is the largest integer that still satisfies

$$\frac{2\pi}{\lambda} d\sqrt{n_1^2 - n_2^2} > N\frac{\pi}{2}. \tag{18}$$

On the other hand, with a decrease of the V value, the number of modes that the guide can support progressively decreases one by one. When the value of V is smaller than $\pi/2$, then only one mode exists and no other modes can be excited. In case that the modes set is constituted by only one mode, then the waveguide is defined as *single-mode* operating. The mode that is capable of being the only excited mode is called the *dominant mode*. The single mode behaviour of a waveguide is often a key element in the design of integrated optical waveguides, particularly when interferometric apparatuses are designed, because the excitation of higher order modes would produce complex interferometric patterns. This unwanted effect would remarkably increase the difficulties in pattern interpretation, or even give rise to a loss of information due to local compensation originating from different interference patterns of the various modes.

The second important aspect, resulting from the characteristic equations, is that the constituting parameters of the waveguide determine the form of the supported mode field distribution. In fact, a variation of any of such parameters affects the form of the field and the propagation characteristics of the excited mode that, on the other hand, can be used as a diagnostic tool to have indications about the changes occurred at the waveguide characteristics. In this view the waveguide can become a

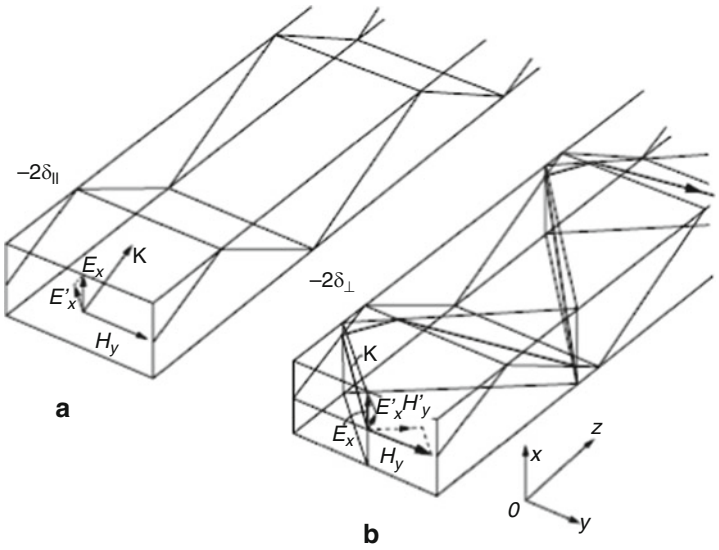

Fig. 11 Possible ray paths of a light wave propagating in a channel waveguide: (**a**) Zigzag only in the *x* direction. (**b**) Zigzag in both *x* and *y* directions (from [17])

sensing probe for objects coming in contact with its constituting layers and in particular with the cladding. Figure 10 shows that associated with the field distributed inside the core of the waveguide are exponentially decaying e. m. field tails present outside the waveguide core, spreading in the contouring cladding layers.

These tails, commonly addressed as the "evanescent field", are particularly interesting for sensing applications because they are extremely sensible to the changing of the cladding characteristics, and strongly affect the propagation loss of the radiation travelling along the waveguide.

A more complex case is represented by *channel waveguides* (see Fig. 11) which allow to confine the propagating radiation in both *x* and *y* directions, constituting actual photon ducts in the substrate material.

The analysis of channel waveguides is by far more complex than that above exposed for simple slab symmetric waveguides, and though we will not go into detail here. We only notice that the basic principles of discrete mode excitation as a function of the fabrication characteristics apply again, offering an even more complex set of parameters to be exploited for interferometric sensing purposes.

2.3.2 Interferometric Sensing Through Narrow Band Radiation

As described in the previous paragraph, the simplest case to treat in the analysis of an interferometric pattern is represented by interference of monochromatic radiation.

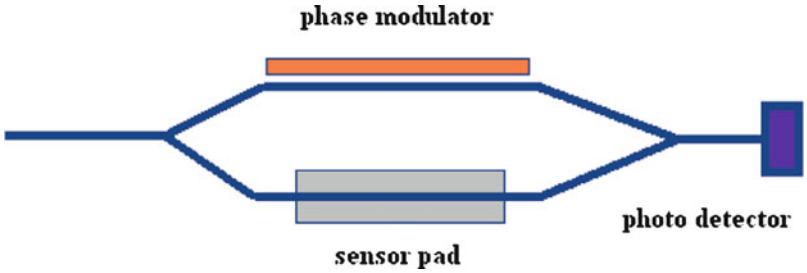

Fig. 12 Schematics of an integrated optical refractometer, based on an MZ geometry

Even if the perfectly monochromatic radiation is only an ideal approximation of actual radiation sources, the development of laser-based light sources has offered the possibility to access very narrowband characteristics, allowing very high degrees of both temporal and spatial coherence. These features can be exploited in integrated optical interferometric apparatuses in order to fabricate refractometers characterised by high sensitivity.

A basic schematic of a refractometric apparatus, based on the integrated MZ geometry, is reported in Fig. 12.

The working principle of the refractometer is as follows: the evanescent tail of the waveguide mode in the waveguide sensor pad extends into the analyte medium outside the chip. A refractive index change of the analyte leads to an effective index change in the waveguide and thus to a phase shift at the end of the measurement arm of the interferometer. The phase shift can be determined from the interference pattern seen at the interferometer output.

The phase shift is related to the analyte refractive index change Δn_c as

$$\Delta\Phi = 2\pi \frac{L}{\lambda} S_{\eta c} \Delta \eta c \tag{19}$$

with L being the sensor pad length, λ *the* laser emission wavelength and S_{nc}, $= \partial N/\partial n_c$ is the calculated sensitivity, which is set by the dielectric film structure of the sensor pad, and defines the variation of the effective refractive index of the waveguide as a function of the analyte refractive index change. The calculation is normally based on an effective index model for the dielectric waveguide sensor pad. From (19) it is clear that the sensitivity of the refractometer strongly relies on the S_{nc}, parameter, whose value is conditioned by all the waveguide fabrication parameters, as mentioned in the previous paragraph.

2.3.3 Interferometric Sensing Through Broadband Radiation

An alternative way of interferometric sensing can be obtained through MEOS devices operating as microspectrometers for the analysis of a broadband radiation source. An

example of the integrated microinterferometer can be obtained by fabricating integrated optical channel waveguides on single crystal electro-optical substrates, with the characteristic MZ geometry as already represented in Fig. 4b. In this case, the scanning operation is accomplished without moving parts, by exploiting the electro-optical properties of the material. A voltage ramp is applied to both the microinterferometers arms (push-pull geometry), in order to produce a corresponding proportional variation of the material refractive index and thus generating an output interferometric scansion of the light injected in the optical waveguide circuit. A single detector synchronously collects an output intensity interferogramme, which contains the information on the spectral distribution of the incoming radiation. In Sect 2.2, we have shown that the application of suitable computational Fourier Transform Techniques to the output interferogramme allows the reconstruction of the spectral distribution of the input radiation. Such a device can therefore perform a Fourier Transform Spectroscopic analysis of the incoming radiation, revealing, from the measured spectral characteristics, the qualitative and quantitative analysis of the chemical molecules present along the path of the incoming radiation.

An important feature of microinterferometers based on electro-optical materials is represented by the spectral resolution. By applying a voltage ramp to the interferometer arms, a consequent linear variation of the optical refractive index is produced due to the Pockel's effect. This variation induces an optical path difference between the light beams travelling different interferometer arms, due to the change of the relative phase velocity of the propagating beams. In this case, the optical path difference can be expressed as follows:

$$\Delta p = L\Delta n, \tag{20}$$

where L is the arm length, supposed to be the same for both arms (balanced interferometer), and Δn is given by the following expression:

$$\Delta n = r \cdot n^{\mathbf{3}} \cdot \boldsymbol{E}/\mathbf{2}, \tag{21}$$

where r is the linear electro-optic coefficient along the axis to which the field is applied, n is the material refractive index and $\boldsymbol{E}$ is the electric field applied to the driving electrodes.

The application of a linear voltage ramp ($\boldsymbol{E} = V/d$, where d is the gap between the opposite electrodes and V is the applied voltage) varies the output intensity, which must be synchronously collected. In practice, a sensor is synchronised with the applied voltage ramp and collects, at each voltage step, the corresponding modulated output intensity. This way an interferogramme can be obtained that can be then handled by e.g. Fast Fourier Transform (FFT) techniques to reconstruct the input spectrum. The instrument resolution can be estimated by means of the following identity:

$$\Delta\lambda = \mathbf{0.5}\lambda^{\mathbf{2}}/\Delta p. \tag{22}$$

From (22) it is evident that the spectral resolution is dependent on the analysed spectral window. It must be remarked that such interferometer has a working spectral window that is given in principle by material transmittance, thus allowing, from a theoretical point of view, the operation of a miniaturised interferometer over this whole spectral range, *if suitable front-end optics are available*. Generally, to obtain high resolution measurements, the whole transmittance spectral window is divided in smaller spectral intervals and, due to the miniaturization allowed by monolithic integration, the spectrometer is fabricated by integrating an array of microinterferometers in the front optics. Each microinterferometer is optimised on relatively small spectral windows that are part of the total spectral range to be analysed, i.e., the waveguides dimension and the refractive index profiles are designed to allow single-mode operation over each partial spectral interval. In practice, the integrated optic structures must be optimised in terms of refractive index tailoring and geometries on the relatively small spectral intervals. Further, the instrument's front-end optics' characteristics, and in particular the output photodetectors, impose the fabrication of dedicated interferometric channels.

Following the above reported concepts, the choice of the base material is fundamental because it affects the design parameters needed to achieve the required spectral resolution.

In Table 1, the main characteristics of commercially available materials are reported. From that table, it is possible to highlight that:

- Some very interesting materials showing very high electro-optical coefficients (SBN family) are available, but, unfortunately, they present some unwanted features, such as very low Curie transition temperatures, reduced maximum available sizes, etc.
- $LiTaO_3$ (Lithium Tantalate) could represent a base material, but shows a relatively low Curie transition temperature, which can make it critical in microdevice production processes.
- KTP can be used to extend the spectral window towards the UV region.

In practice, at the actual state of the art, $LiNbO_3$ appears to be the most suited material, which is available for the production of MEOS microinterferometers, also considering the dimensions of the nowadays available substrates, allowing to obtain the maximum achievable microinterferometer length L.

Table 1 Commercially available most common electro-optical materials

Material	Highest electro-optic coefficient (pm/V)	Transition Curie temperature (°C)	Transmittance range (nm)	Max available size
$LiNbO_3$	32	1160	350–5,000	5″ wafers
$LiTaO_3$	30.4	607	350–5,000	5″ wafers
SBN60	235	75	350–6,000	2×1 cm^2
SBN75	1,340	56	350–6,000	2×1 cm^2
KNSBN	400	150–250	350–5,000	2×1 cm^2
KTP	36	936	200–2,500(5,000)[a]	3×2 cm^2

[a]*Notes*. Transmittance range depends on the provider

3 Integrated Interferometric Microsensor Fabrication Process

Recalling what is already anticipated in the previous sections, theMZ geometry, due to the possibility of a relatively simple monolithic design, is probably the most adequate configuration when Integrated Optics is applied to interferometric devices' fabrication [7, 8, 18]. In fact, the MZ configuration is particularly interesting for sensing problems because it combines the possibility of high-resolution and high-sensitivity performances with a remarkable insensitivity towards perturbing effects, such as mechanical vibrations, and other common environmental effects.

Many optical sensors based on MZ configuration have been reported in the literature [4, 5, 8, 19, 20] for (Bio)-chemical analyses. In this device, when a monochromatic light is transmitted through the MZ interferometer, the detection principle is based on the phase shift between the electromagnetic waves transmitted in the two arms, generated by the ad-layer of the analyte on the sensing arm.

In fact, the analyte absorption/adsorption/binding processes gives rise to a change in the refractive index of the areas where the (bio)-chemical or molecular interactions are taking place, without affecting the reference arm. In Fig. 13 is reported a sketch of a device of this kind as described in [19].

Due to the interference process, the phase shift gives rise to an intensity variation of the light transmitted through the second Y-junction of the interferometer. When designing a monolithic device of this kind, it must be considered that the phase shift depends on the change in the optical path $\delta = \Delta(n_{\text{eff}} L)$, i.e., on the product of the effective refractive index (n_{eff}) and the length (L) of the sensing area. So, to have a very low detection limit, it is necessary to have relatively long interferometric arms.

In general, it can be said that the MZ interferometer allows to perform high sensitivity analyses; nevertheless it must be pointed out that the very low detection limit of this microdevice, obtained when working with monochromatic light, is counterbalanced by the inability to distinguish it among different specimens. For this reason in the literature [19] it has been suggested to realize hybrid detection

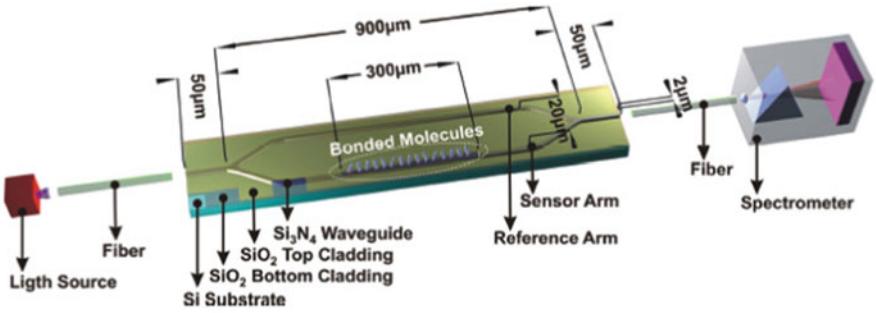

Fig. 13 Schematics of an interferometric (Bio)-chemical sensor allowing selective multi-analyte detection

systems, typically oriented to bio-chemical applications, having the capability of both very high sensitivity and selective multi-analyte detection.

This performance can be obtained integrating an MZ interferometer with a spectrum analyzer and using a multi-wavelength "white" light source to distinguish the spectral "signature" of the different species (see Fig. 13).

The possibility to join selectivity and sensitivity can also be obtained in a particularly wide area of applications if the monolithic MZ device is fabricated with an electro-optic material. In general, Lithium Niobate ($LiNbO_3$) is used due to its commercial availability in the form of good quality optically polished single crystal wafers.

In this case, the MZ interferometer is used as a Fourier Transform (FT) Spectroscope, allowing the spectral analysis of liquid or gaseous analytes. In Sect. 2, a theoretical description of the working principle of an FT optical sensor has been reported, whereas in paragraph 4 of this section, we will describe in some detail the design problems of this kind of optical sensor.

As already mentioned, the key element of any Integrated Optical device is the Integrated Optical Waveguide. The basic technological steps for the fabrication of integrated planar or channel waveguides are based on the physical principle that in order to obtain the light confinement it is necessary that the refractive index of the guiding region is higher than the refractive index of the surrounding regions [20]. For this reason, it is necessary to perform technological processes that can change the optical properties of the base material in well-defined regions, following the design of the particular integrated device that is under study. In principle, to obtain Integrated Optics devices, including microsensors, the same planar technology processes, already successfully applied on silicon substrates to obtain microelectronic devices, can be used.

The main problem to be faced becomes a material science problem because there is the need to adapt and make compatible all the technological steps of the fabrication flowchart with the optical material used as a substrate. Most often, this is not a simple job because many optical materials (in particular the non-linear optical materials) are often unstable and chemically reactive compounds. Furthermore, many non-linear optical materials have a Ferroelectric, Pyroelectric and/or Piezoelectric nature, which gives rise to problems of difficult solution when even simple technological processes, such as the annealing stages normally used for silicon, are applied to this new kind of materials. Waveguides can be produced by several techniques, depending on the optical material used as a substrate or on the type of integrated device geometric constraints. In general, to fabricate an integrated waveguide, it is possible to choose one of the following different ways:

1. *Increase the material refractive index in the guiding region (dopant diffusion, ion exchange,* etc.*)*
2. *Decrease the material refractive index around the guiding region (chemical etch, ion implantation, thin film deposition,* etc.*)*

In the case of $LiNbO_3$, the following three categories of processes are the most frequently used:

- *Diffusion-based processes enhancing the refractive index in the waveguide region. In this case, the most frequently used are Proton Exchange and Titanium diffusion but also High fluency UV irradiation has been reported* [21–23].
- *Ion bean processes tailoring the refractive index profile towards relatively low values in the region surrounding the waveguide. In this case, high-energy Ion Implantation is probably the simplest solution* [24, 25].
- *Etch-ridge processes giving rise to a waveguide that is not embedded inside the base material but is built above the substrate surface. In this case some different fabrication techniques based on surface-engineering processes can be adopted and will be briefly described later* [26–31].

Let us rapidly examine the different above-mentioned processes, considering, in the following examples, $LiNbO_3$ as material substrate.

1. Proton exchange

In Fig. 14a, b, are schematically reported the integrated waveguide fabrication steps for Proton exchange (a) and diffusion from a Ti film (b) through a patterned mask.

In both cases presented in Fig. 14, the dopant introduction produces the increase of the refractive index in the region of the substrate material ($LiNbO_3$ in this example) interested by the dopant diffusion. The diffusion-based techniques are conceptually very simple, but in practice they suffer several limitations:

- *The mask geometry is not maintained due to the lateral diffusion below the mask edge (see Fig. 14).*
- *If narrow single-mode waveguides working in the short wavelength part of the visible spectrum are required, due to the lateral diffusion below the mask edge, it is necessary to perform a very complicate submicron lithographic patterning of the mask.*
- *The refractive index profile cannot be tailored as it is fixed by the diffusion laws.*
- *The dopant introduction can severely degrade the electro-optic properties of the base material. The effect can be reduced only if suitable multi-step annealing cycles are performed after the dopant introduction* [22].

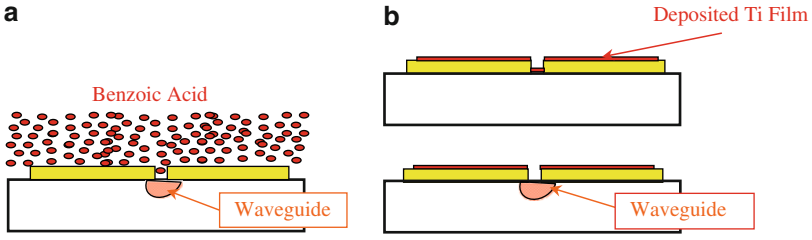

Fig. 14 (**a**) Proton exchange by diffusion in the waveguide region, through a photolithographically patterned mask, from a dopant environment. Typically molten Benzoic Acid in the case of $LiNbO_3$ substrate. (**b**) The same as in (**a**) but in this case the dopant diffusion takes place from high temperature annealing of a pre-deposited Titanium film coating as a dopant source

2. Ion-implanted waveguide

Many of the previously indicated limitations can be overcome if a different, even if less common, technique is used. In fact, these problems have already been encountered in Microelectronic devices' fabrication with Si substrates, where the Ion Implantation technique has been adopted with excellent results. The same technique has been applied to the fabrication of Integrated Optics devices giving rise to High quality waveguides with micron size geometries and very low transmission loss. The only difference is that in Integrated Optics applications, high-density substrate materials are often used (e.g., $LiNbO_3$ has approximately twice the density of Si); hence, High-Energy accelerators in the MeV range must be used to allow a sufficient depth penetration of the implanted ions. Besides the advantage of the very precise geometrical definition, this technique is remarkably insensitive to the chemical properties of the base material so it is not necessary to redefine the process flowchart if different optical materials are used as substrates, as it happens in the case of wet chemical/diffusion processes. As a consequence, it is relatively easy to change the base material because it is usually sufficient to make a simple adjustment of some process parameters in the simulation programs, without major changes in the fabrication process [50].

Let us synthetically describe the physical principles of High-Energy Ion Implantation technology. The ion beam, at MeV energy, is uniformly scanned on the target substrate to be processed, previously covered with a photolithographically patterned metal film mask.

The energetic ions penetrate in the region below the surface, and gradually lose energy until they get a complete stopping at a well-defined depth. It must be pointed out that the energy loss mechanism changes as a function of the ion velocity. In the first part of the trajectory, i.e., in the near surface region where the velocity is high, the electronic energy loss process dominates, whereas, in the end of range region where the velocity is low, nuclear energy loss mechanism dominates.

The effect of ion implantation on the optical properties of the implanted material is dependent on the energy loss mechanism involved and is summarized in Table 2, valid for $LiNbO_3$ substrate and for ions having electronic energy loss lower than the threshold value [32]

Table 2 Defects produced by Ion Implantation and their effect on optical properties of $LiNbO_3$

Target material $LiNbO_3$	Energy loss mechanisms	
	Electronic	Nuclear
Defect typology	Few distributed point defects, Colour Centres	Crystal amorphisation due to collision cascades
Annealing conditions	Full defects annealing at low temperature (T~300°C)	Defects remain even after annealing
Ordinary Refractive Index (n_o)	Almost unchanged if $dE/dX < 220$ eV/Å	Remarkable reduction towards the amorphous value of n
Extraordinary Refractive Index (n_e)	Small enhancement of n_e even after annealing	Remarkable reduction towards the amorphous value of n

$$(\mathrm{d}\boldsymbol{E}/\mathrm{d}X) \leq 220 \text{ eV/Å}. \tag{23}$$

Figure 15 schematically reports the basic process steps of a waveguide formation by Ion Implantation on an optical substrate previously masked with a metal film patterned with a photolithographic process. In this case, the waveguide formation can be performed with a single-step process. In practice, in $LiNbO_3$ base material, all the ions lighter than Nitrogen do not exceed the energy loss threshold value, reported in (23), over an interval of energies that allows a penetration depth of several microns. If the base material is changed, the threshold value can change but the general considerations made for the $LiNbO_3$ example remain valid.

In practice, by adjusting the energy of the bombarding ions and the thickness of the metal masking film, it is possible to create low index regions in the desired position. In fact, below the metal film acting as mask, the ion penetration is smaller as part of the energy is lost crossing the masking film due to which the end-of-range defects are placed close to the surface, whereas in correspondence of the patterned window the ions can penetrate at higher depth.

In the shadowed areas shown in Fig. 15b, the refractive index is lowered by the presence of end-of-range defects, whereas, in the area below the mask window, geometrically surrounded by the shadowed areas in Fig. 15b, the refractive index remains unchanged, if an annealing stage is performed after the Ion Implantation step. In this way, an integrated waveguide embedded in the base material is formed; in fact light is confined in the region limited by the surrounding low index regions.

The waveguide performances in terms of mode transmission as a function of the wavelength and of attenuation are defined by both the geometrical definition and the refractive index profile of the low-index regions. Figure 16 displays a near-field image of the cross section of a waveguide obtained by Ion Implantation of 3.9 MeV Carbon ions in $LiNbO_3$ substrate.

3. Ridge waveguide

In this case, the waveguide is fabricated above the substrate surface, the process is somehow more complicated and a few techniques are possible. If it is preferred to

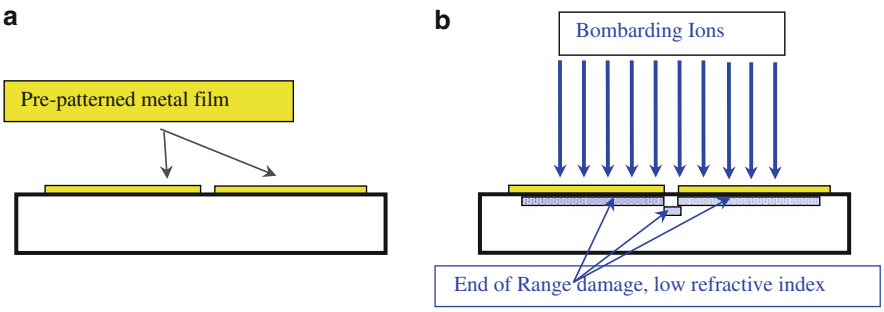

Fig. 15 Schematic drawing of the waveguide formation by ion implantation processing. (**a**) Pre-masked substrate before implantation, (**b**) single-step formation of low refractive index regions, surrounding the undamaged area to form the integrated waveguide

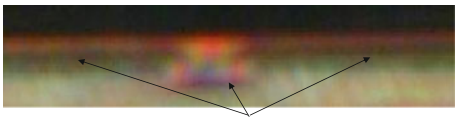

Fig. 16 Cross-section image of an ion-implanted waveguide confining a white light beam. The *dark* regions indicated by the *arrows* show the low-index region where the light transmission is not allowed. The waveguide dimensions are about 3 × 3 μm^2

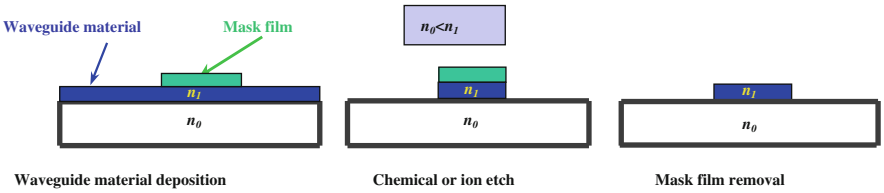

Fig. 17 Schematics of the process steps for the fabrication of an integrated ridge waveguide by deposition of a heterogeneous optical material film on the surface of the base material

have a ridge waveguide fabricated with a material different from the substrate (heterogeneous waveguide) it is convenient to deposit and pattern a thin film of the desired waveguide material. In this case, the ridge waveguide can be fabricated by depositing a thin film of an optical material on a substrate and then process it by a standard mask/etch procedure like the one sketched in Fig. 17. In the case schematically described in Fig. 17, a heterogeneous ridge waveguide is fabricated.

If both the substrate and waveguide are made with optical materials, to avoid important propagation losses towards the substrate, it is important that the substrate refractive index, n_o, is lower than the waveguide refractive index, n_1. Heterogeneous ridge waveguides' fabrication is frequently used when integrated optical devices made with organic materials are designed.

On the contrary, if a ridge waveguide with the same material properties of the substrate is desired as, for instance, in the case in which the exploitation of electro-optic properties is needed, Ion Implantation once more becomes an interesting alternative. In this second case, it is particularly convenient to exploit the effect produced by the severe lattice damage on the etch rate of the base optical material. In the case of $LiNbO_3$, the etch rate in the damaged region can increase to a factor of 1,000 or even more. The damage in the regions to be etched can be easily produced by Implantation of ions having sufficient high mass to have an Energy Loss much higher than the threshold value of 220 eV/Å, already seen in (23). In practice, ions with mass ranging from Oxygen ($A = 16$) to Cu ($A = 63.6$) have been successfully used [28–31, 44, 45].

In Fig. 18, a schematic illustration of the main process steps used to obtain a ridge waveguide is displayed. Note that the first implantation step is performed with light ions having $dE/dx < 220$ eV/Å (typically Carbon ions), to create a buried damaged layer without affecting the near surface regions. The low refractive index buried layer ensures the light confinement in the surface region.

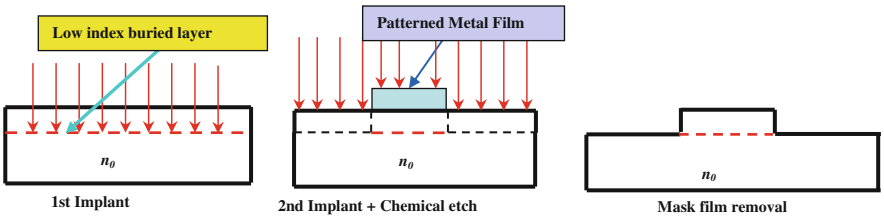

Fig. 18 Schematics of the process steps for the fabrication of an integrated ridge waveguide on the surface of the base optical material

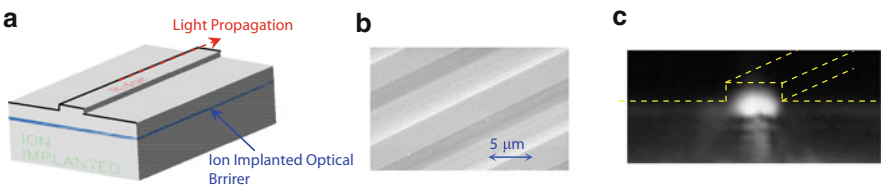

Fig. 19 (**a**) Schematics of an implanted ridge waveguide, (**b**) Magnified SEM image of a ridge waveguide fabricated by Ion Implantation on LiNbO3 and (**c**) near-field image of a transmission test of the waveguide

The second implantation is then performed after the deposition of a metal film that is successively patterned by a standard photolithographic process. The masking metal layer must be sufficiently thick to obtain a complete stop of the heavy ions before they can reach the $LiNbO_3$ substrate. The subsequent chemical etch in diluted HF solution proceeds with a speed that is more than 1,000 times faster in the damaged region than in the non-implanted one, allowing an excellent and high-contrast reproduction of the mask pattern. In this way, ridge waveguides can be obtained having very low transmission loss because the lateral confinement is ensured by the large jump of the refractive index between the base material (n_0~2.2 in $LiNbO_3$) and the external air ($n = 1$). The confinement towards the substrate is ensured by the "mirror" effect generated by the low index region produced by the first implantation stage.

Whichever fabrication process is chosen for the ridge waveguide, it can be said that, in general, the more complicated fabrication process is usually compensated by the good propagation loss values that are much lower than in the case of embedded waveguides. Moreover, particularly in the cases in which the exploitation of the electro-optic properties of the waveguide material is required, the ridge configuration allows a better coupling between the applied electric field in the most effective electro-optic axis and the e.m. field of the wave propagating in the waveguide region. Nevertheless, it must be noticed that, in the case of fabrication of integrated optic microdevices having higher complexity than a simple channel waveguide, the computer simulation of the structure can become rather complicated and time-consuming. In Fig. 19a, a schematic drawing of an implanted ridge wave guide is reported, whereas in Fig. 19b, c, are respectively displayed the SEM picture

of a ridge waveguide fabricated by Ion Implantation on $LiNbO_3$ substrate and the near-field image of the transmitted light. Finally, we can add that the ridge waveguides fabricated with this process on $LiNbO_3$ substrate have demonstrated a transmission loss of the order of $0.1 \div 0.2$ db/cm.

4. Processes for the fabrication of an integrated interferometric sensor device

As an example of technological process fabrication of an integrated interferometric sensor, let us synthetically examine the main steps of the fabrication flowchart of a monolithic

MZ microinterferometer on $LiNbO_3$ substrate. The fabrication flowchart is schematically reported in Fig. 20.

With a single technological run, have been fabricated simultaneously on a single $LiNbO_3$ wafer, many (25 chips) high resolution monolithic interferometers having the length of the order of the wafer diameter ($4''$) and the waveguides forming the interferometer with a width of the order of $2.5 \div 4.0$ μm [10, 25]. Figure 21 displays a picture of a single interferometric sensor under test together with a microscope image of the Y-junction that is the most critical point to be designed and fabricated. Even if the geometry is rather simple, it is necessary to consider since the design phase, that a useful interference phenomenon takes place only if the integrated waveguides forming the interferometer arms are designed to be single mode in the wavelength spectral window of interest. This needs both the capability

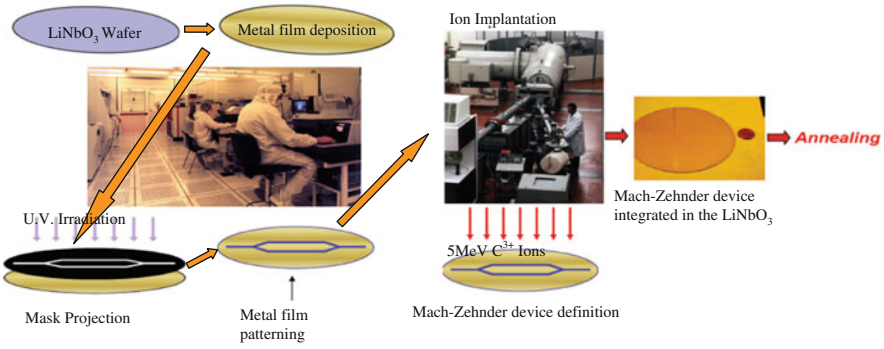

Fig. 20 Schematic flowchart of the fabrication process of an integrated Mach–Zehnder interferometric optical sensor using Ion implantation to tailor the waveguide's refractive index

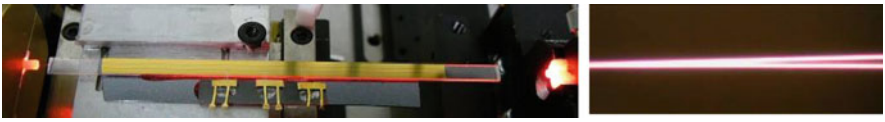

Fig. 21 Example of a complete Mach–Zehnder microinterferometer under test and a detail of one of the two Y-branches for fifty–fifty splitting/combining the radiation between the interferometric arms, which is one of the most critical points in the fabrication step

of low loss micron-size waveguide fabrication and the availability of rather complex computer simulation tools to evaluate the propagation and losses behaviour of the electromagnetic field inside the whole integrated device.

For geometrical or other design considerations, we will refer to Fig. 4 in Sect. 1.

As already described in Sect. 2, the detection principle of an MZ interferometer for Fourier Transform Spectroscopy is based on the possibility to produce a controlled phase shift between the electromagnetic waves transmitted in the two arms of the interferometer (see Fig. 4b). The desired phase shift can be obtained by using an electro-optic substrate material ($LiNbO_3$ in our case) and applying a suitable electric field to one of the waveguides forming the arms of the interferometer. By using this procedure it is possible to change continuously the refractive index of the waveguide in a controlled way. Finally, by detecting the intensity of the light transmitted through the interferometer as a function of the applied voltage, it is obtained the interferogramme that is the Fourier transform of the light spectrum to be analysed. In practice, it is frequently convenient to choose an X-cut $LiNbO_3$ substrate wafer, the waveguides are Y oriented and a voltage ramp is applied to the Z crystallographic direction to exploit the maximum electro-optic effect in the waveguide volume.

Finally, an important technological aspect in the fabrication of a monolithic optical sensor is the Front- and End-Optic system. This is needed to provide the appropriate input to the Integrated Optics sensor chip and to convert the output optical signal, containing the chemical information, into an electrical signal, suitable for successive elaboration.

These problems become of primary importance if it is desired to avoid that Front-Optics and End Optics systems become much larger than the monolithic optical sensor chip. In fact, many literature works make use of grating couplers or other optical systems [33, 34], but these are very complex systems and the total sensor size is several orders of magnitude larger than the chip size because they generally need the use of external measuring variables, such as the angle of incidence or the out-coming angle to extract the value of the parameter to be measured. These peripheral equipments need space and a careful adjustment of the focused optics for light coupling to the waveguide.

Moreover, these systems always need a big alignment effort of the external focusing optics by means of precision mechanical parts, particularly when end-face coupling or prism-coupling configurations are used. To avoid these problems, it is necessary to integrate in a hybrid microsystem both the light injection and extraction stages together with the monolithic optical sensor. The best option, derived from the Fibre Optics Communication technology, is the “Pig-Tailing” process that allows the full integration of both the front and end optics with the sensor. Alternatively the fabrication of optical micro-benches by using mechanical micromachining (MEMS) techniques can be used to couple the numerical aperture of the optical fibre with the numerical aperture of the integrated device waveguide.

To illustrate this type of light injection device, in Fig. 22a is reported a magnified picture of a end-optics system using two ball lenses supported on a micro-optical bench fabricated by micromachining of an Si substrate, whereas in Fig. 22b is shown a picture of a front optics system based on the Pig-Tailing coupling of an optical fibre with an MZ monolithic interferometer.

Fig. 22 (**a**) Picture of a micromachined Silicon micro-optical bench with ball lenses for optical coupling of an optical fibre with an integrate waveguide (end optics). (**b**) Magnified picture of a Pig-Tailing coupling of a Mach–Zehnder monolithic interferometer with an optical fibre (Front optics connection)

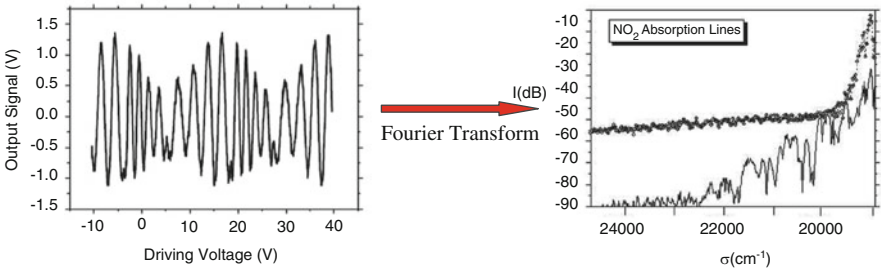

Fig. 23 Example of the output signal of an MZ interferometer used as gas sensor. Figure (**a**) shows the output interferogramme, whereas figure (**b**) shows the gas analyte (NO_2) absorption spectrum as obtained with a Fourier Transform process

In Sect. 2, the expected intensity variation as a function of the applied driving voltage has been discussed and will not be repeated here; as an example, we report in Fig. 23 the interferogramme and the relative FFT in the case of NO_2 detection in the atmosphere.

The experimental data of Fig. 23 refer to a test performed to evaluate the MZ performance in measuring atmospheric pollution. The test was performed with a calibrated 2-cm long cell filled with NO_2 and inserted between the radiation source and the front optics of the interferometer. The absorption spectrum of NO_2 was obtained by comparing the spectrum of the light source before and after the insertion of the calibrated cell, thus performing a differential optical absorption spectroscopy (DOAS).

Figure 23a reports the interferogramme when the cell is inserted, whereas Fig. 23b reports the spectra of the light source with and without the NO_2 absorption cell. It must be pointed out that the insertion of the gas cell produced a reduction of 30 db in correspondence of the absorption bands of NO_2. This figure allows to evaluate a sensitivity of about 10 ppb for NO_2 detection, if an optical path of about 200 m is used in free atmosphere or by means of a multipass White cell.

In Fig. 24, is shown the result of a Fourier Transform spectroscopic analysis in a liquid solution using a monolithic MZ microsensor. Both analyses are of agro-food interest; in the case of liquid samples, it has been used as a probe like the one sketched in Fig. 24a. Figure 24b, c shows the absorption spectra obtained by 330 ppm of an organic dye (patent blue E131) diluted in isopropyl alcohol, and a

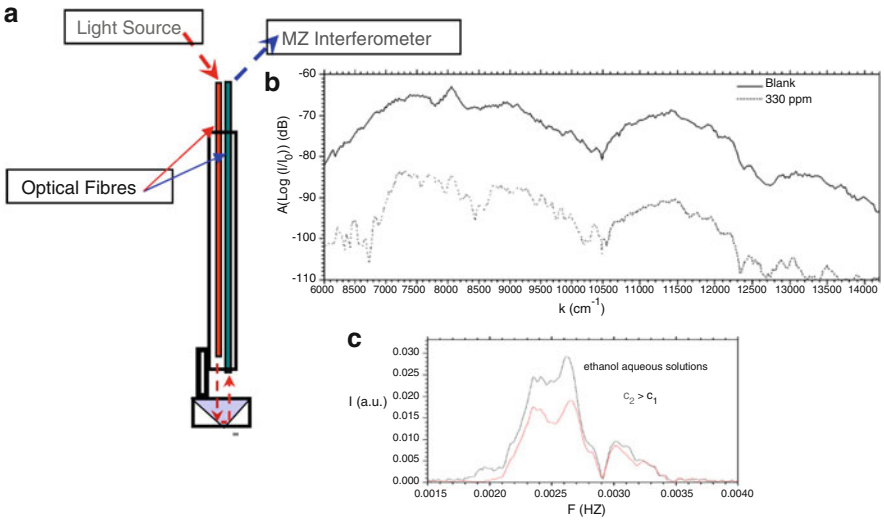

Fig. 24 Schematic drawing of the probe for liquid samples used with the monolithic Mach–Zehnder microsensor (**a**), and absorption spectra of 330 ppm of Patent Blue dye dissolved in isopropyl alcohol (**b**) and different ethanol concentrations in aqueous solutions (**c**)

measurement of the ethanol concentration in two different aqueous solutions, actually two different qualities of wine, respectively.

4 Parameters Affecting the IO Microdevice Performances

As already mentioned in the previous paragraphs, integrated optic devices operating as MZ microinterferometers can be successfully applied for both in situ and remote sensing of chemical species, offering all the advantages which are characteristic of Micro-Optical Electrical Systems (MOES) devices. Nevertheless, some important considerations must be outlined, arising particularly from the fact that contrary to macroscopic conventional devices, in MOES interferometers, the radiation that is analyzed to obtain the desired information, does not propagate in vacuum but in a material medium. This aspect is of particular importance when these microdevices are operated as miniaturised spectrometers with broadband radiation. In fact in this configuration , some main complications can affect the features of the generated interferometric signals, which must be considered in detail during the device design process and often require the adoption of nontrivial procedures in the obtained interferogramme analysis.

In particular, the following aspects are strictly related to the material nature of the propagating medium:

(a) Dispersion induced by the material itself, due to the dependence of the refractive index on the wavelength of the propagating wave.

(b) Effects induced by the waveguide structure, which geometries impose further dispersion conditions as a function of the radiation wavelength, setting different effective refractive indexes n_{eff}, as well as different mode distributions.

Furthermore, these effects give rise to a wavelength dependence also for the intrinsic power loss. Non-ideal behaviours can arise, also considering the case of devices operating with narrow band radiation, particularly related to non-linear characteristics (photo-refractivity, non-linear components of the dielectric constant, etc.) of the substrate material. The non-ideal behaviour of the base material can appear at some wavelengths or by eventually applying driving voltages, as well as due to the presence of surface strains induced by the fabrication process, etc.

Further, contributions due to the material characteristics which show a dependence on temperature (e.g. refractive indexes) can become important depending on the application field and on the selected substrate material. A representative example is constituted by the already mentioned integrated MZ microinterferometer, fabricated on $LiNbO_3$ single crystal substrates, and will be analysed in more detail. In this case, several problems must be faced as a function of the spectral window and of the performances required by a monolithic interferometric device as that represented in Fig. 4b: such issues can be connected as well to the technological processes involved in the microdevice fabrication that must convert the Opto-chemical effect into a convenient output signal (usually electrical) as well as to the data-handling techniques that are chosen to convert the electrical output in an information having Physical (or Chemical) meaning. In particular, the issues encountered in the design, fabrication, and application of an integrated MZ microinterferometer are principally related to micro-fabrication and to data analysis. A detailed description of the most important aspects related to these topics is reported in the followings.

4.1 Critical Micro-Fabrication Aspects

Critical issues related to micro-fabrication procedures can arise in the production process of an integrated microinterferometer based on $LiNbO_3$ when enhanced performances of the miniaturised spectrometer are requested. These aspects have an important impact on the microdevice design, which must be developed considering all the limitations imposed by both the technological processes and the physical characteristics of the material. In particular, in the design and fabrication of a rugged microdevice, at least the following critical aspects must be taken into account:

1. *If the spectral window to be analysed is the near UV or visible short wavelength region (380 ÷ 450) nm, the need of single-mode transmission involves that the interferometer waveguides must have lateral and vertical dimensions of the order of few microns (typically 1.0 ÷ 2.0 μm).*

This aspect ratio is very difficult to be obtained, with fine geometries, by diffusion processes due to the lateral diffusion below the mask edge. In this case, if a suitable technology is not available, in the short-wavelength part of the spectrum the waveguides allow a partial multimode transmission degrading the SNR value and consequently the sensitivity of the measurement. In this case, High-Energy Implantation becomes almost the only viable option to obtain high sensitivity and high resolution devices. On the other hand, High-Energy Implantation has the capability to exactly reproduce all the features of the implantation masks (contrarily to in-diffusion which tends to smoothen the geometric contours); hence a very high definition of the implantation masking layers has to be reached at a sub-micrometric level on the processed substrate. This is particularly stringent when defining y-branches bifurcation region (taper), and for the precise patterning of the mask edges. In fact, any irregularity introduced by photolithography is consequently replicated in the integrated optical waveguides characteristics, leading often to important degradations of the waveguide performances, due to the roughness of the waveguide walls.

As partially anticipated in Sect. 3, the photolithographic aspect is in general an important element to be considered when High Energy Ion Implantation is adopted, even if the microdevices are designed for the operation in lower frequency spectral regions (e.g. VIS–NIR). In fact, though less stringent aspect ratios are needed, roughness features produced at the edge of the implant layers will be replicated on the waveguide walls, with detrimental effects on the propagation losses: on the other hand, the ion stopping layers must be constituted by high-density materials or alternatively must present thickness values of several microns (typically ~10 μm, depending on the implanted ion). High-density masking materials are mostly represented by noble metals (Au, Pt, etc.), which tend to form micrometric grains when deposited on the substrate. The low compatibility of $LiNbO_3$ with dry etching processes often imposes the application of wet etching techniques, that is strongly affected by the grain structure of the metal film so giving rise to an irregular mask edge.

Alternative techniques are represented by galvanic growth of noble metal layers, which require the application of strongly unsafe reagents and dedicated growing bath structures. On the other hand, the definition of thick low-density material layers, e.g., photo-resist, can result difficult when high aspect ratio structures are to be obtained.

2. *If high spectral resolution is required, then relatively long optical path differences must be reached.*

The length of the interferometric arms must be in this view as long as possible, i.e., in the range of several cm. In practice the dimensions of the commercially available substrates impose a first physical constraint. At present, up to 5″ diameter wafers are produced, nevertheless due to the very recent introduction of such substrates, a little is known concerning their optical and physical homogeneity. A further limit to the arm length of the microinterferometers can arise from the increase of the aspect ratio at the photolithographic level: the increase in size often

results in a non-homogeneity in the clean room processing parameters (e.g. radial homogeneity of the thickness of the masking layers, issues related to the layers' adhesion and stresses introduced by processing layers when large substrate areas are covered) which can also result in remarkable deviations of the photolithographically produced structures from the designed ones.

The requirement of long interferometric arms involves, for any spectral window, the fabrication of the integrated waveguides forming the MZ interferometric structure having both single mode and very low specific loss characteristics to obtain a good value of the SNR ratio. This figure of merit will orient the sensor design and, correspondingly the technology flowchart, towards the choice of ridge waveguides fabrication. Alternatively, the applied driving voltage must be high, in the order of 100 V, with the risk that the electric field can generate non-linear behaviours or, at limit, approach the surface breakdown value of the $LiNbO_3$; consequently, the surface of the device must result particularly free from any fabrication residuals. The post-processing treatment of LN surfaces is particularly difficult, as thermal or plasma-based surfaces cleaning processes must be avoided due to the susceptibility of this pyro-electric material to break discharges. This often imposes the deposition of processing sacrificial layers. Moreover, post-processing high electrical rigidity protecting layers (e.g., SiO_2) are needed to avoid surface contamination during fabrication and current leakage during the application of the driving voltage ramps, rendering the fabrication process further complex.

3. *The integrated waveguides forming the MZ interferometric structure must be both single mode and low loss.*

Some of the main issues related to this aspect have already been examined in the previous parts; nevertheless, some important considerations must be outlined. As already described in Sect. 2, the single-mode characteristic of integrated optical waveguides can be obtained only by properly configuring the fabrication parameters (namely, the refractive index profile of the waveguiding structure and its geometrical dimensions) as a function of the operation wavelength. Hence, the design process must start with a precise knowledge of the refractive index profiles which can be generated by means of the available waveguide fabrication technologies. This aspect is well defined when in-diffusion processes are adopted, whereas it is still a matter of debate when less conventional technologies such as High Energy Ion Implantation or UV laser processing are applied. Once the index profile is known or is considered as acceptably acquired, a detailed simulation process must define an unavoidable trade-off between the optimal dimensions allowing rigorous broadband single-mode operation (which tends to reduce the waveguide dimensions) and waveguide optical transmission (which tends to enlarge the waveguides cross section, leading towards unwanted multimode operation). Automated simulations concerning this aspect can become particularly demanding in terms of computer time and resources, when non-continuously varying index profiles are required (such as in the case of High Energy Ion Implantation) and even worse when 3D simulations must be performed in order

to design more complex structures such as y-branches. In those cases, simplified simulation models must be adopted with the eventual introduction of heuristic parameters which are obtained through the experimental evidence, when possible. On the other hand, the integrated optical structures must be at the end interfaced with input/output coupling optical systems, often constituted by optical fibres. In this view, the design of the mode profiles and particularly of the final mode distribution must match as much as possible the corresponding modes distributions and numerical apertures of the different input/output optical systems (optical fibres), allowing to maximise the energy transfer between the various integrated optical elements and maximally reduce the so-called "insertion losses". This aspect can become particularly tricky when operating in the near UV–VIS short-wavelength spectral region, where the dimensions of the optical fibres cores, due to the great difference in the refractive index values (1.5 in Silica vs. 2.5 in LN), are often significantly larger than those produced in LN integrated waveguides structures.

All these aspects are further complicated by the need to operate on a broadband spectral window. Generally, the best compromise to apply consists in dividing a spectral segment in sub-portions over which the design results are less tricky. In this view, the integrated optical and miniaturised nature of MEOS devices results as a key element.

4. *The electrodes structure must ensure the best coupling between the applied electric field and the waveguides forming the arms of the MZ interferometer.*

As what concerns these problems, it is necessary to consider that it is of crucial importance to have a very good coupling between the applied driving electric field and the maximum electro-optic tensor component, r_{33}, in the waveguide volume. Observing the force lines of the applied electric field, as schematically reported in Fig. 25, it appears that ridge geometry allows a better coupling than in the planar case. In this case in fact, almost all the field lines are coupled with the waveguide volume. This means that it is necessary to apply a lower driving voltage to obtain the desired phase shift between the waves propagating in the interferometer arms, allowing the possibility to improve the spectral resolution.

5. *The two Y-branches of the MZ geometry are probably the most critical points because they must ensure both a fifty–fifty splitting of the light intensity and a low-loss transmission of the light (see Fig. 26).*

Y-Branch waveguides are one of the key elements in integrated optics. In order to make the Y-branches compact, it is necessary to develop low-loss structures with a possibly wide branching angle, which is of great importance. Many types of

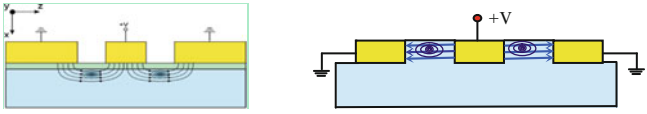

Fig. 25 Coupling of the force lines of the applied electric field in planar and ridge geometry

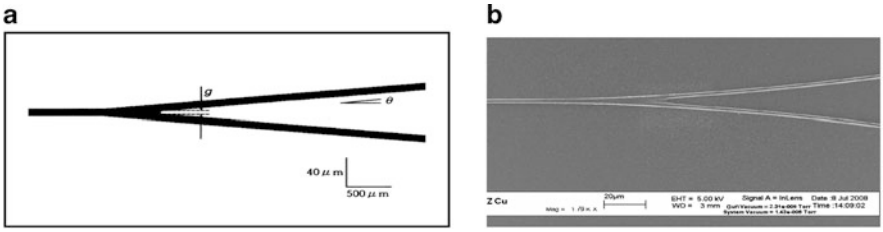

Fig. 26 (**a**) Schematics of a Y-Branch drawing, (**b**) Y-Branch with ridge waveguides

Y-branches inhibiting radiation losses have been proposed so far [35–38, 46]. A well-designed Y-branch should provide low losses, with small wavelength-dependence and low polarisation-dependence. The design of Y-branch has been widely studied because, Y-shaped splitters, made with planar technology, play important roles as optical signal dividers/combiners in functional Fibre Optics Communication devices.

In general, a higher refractive-index difference Δn between the waveguide core and cladding is used to achieve more compact and highly integrated devices because a high Δn value, like in ridge waveguides, gives rise to a strongly guiding waveguide that enables to reduce the waveguide-bending radius. However, the excess loss of Y-branches with a higher Δn waveguides increases for the following reason.

The main loss factor in a Y-branch is produced by the mode mismatch at the interface between the tapered waveguide region and the two output waveguides. The loss is mostly originated by the gap g (see Fig. 26 a, b), produced by the limitations of the photolithographic and etching processes. When Δn increases, the waveguide width decreases whereas the gap becomes correspondingly more important because it remains unchanged as it depends only on the quality of the photolithographic process. Thus, the mode mismatch between the fundamental mode at the end of the tapered region and the fundamental local normal mode at two output waveguides becomes relatively more important as Δn increases. Many solutions based on an optimization of the Y-branch geometry and the refractive index profile have been studied [37, 38]; nevertheless, the design and fabrication of high-quality Y-Branches involve an important computer simulation work. We will not go into detail because a deeper discussion of this topic exceeds the aims of this chapter.

4.2 Interferogramme Acquisition and Analysis

Once the interferometric device has been fabricated and interfaced with all necessary equipments (front-end optics, front-end electronics, packaging, etc.), one can in principle start collecting data, i.e. the instrument can be applied to acquire interferogrammes (Fig. 27).

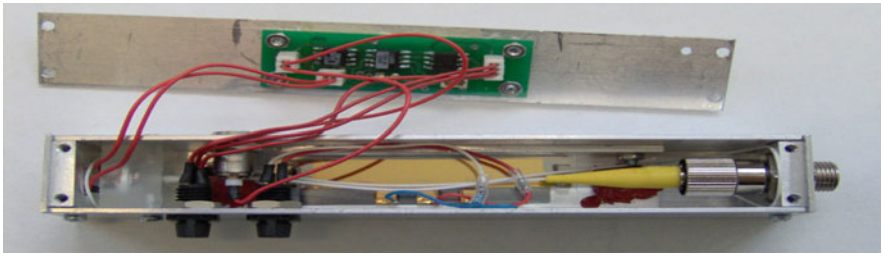

Fig. 27 Integrated MZ microinterferometer equipped with front-end optics, readout electronics and packaging, ready to use (the overall package length is 12 cm)

As described in Sect. 2, the output interferogramme is basically the real part of the Fourier transform of the input radiation spectrum; hence, in principle, a simple operation of inverse Fourier Transform should produce the spectral analysis of the radiation source. In practice the as-described situation is only an ideal one, as the form of the output interferogramme is due not only to the input radiation spectrum, but also to a series of contributions, arising from different effects, which must be taken into account during the original spectrum reconstruction process. Referring to (9) Sect. 2, a more general form addressing an actually operating microinterferometer can be expressed as:

$$I_{\text{out}}(\Delta p) = \int_{-\infty}^{\infty} S(k) \cdot \cos(2\pi \cdot k \cdot \Delta p(k)) \cdot \mathrm{d}k, \tag{24}$$

where $k = 1/\lambda$ is the wave-number of the impinging radiation, and

$$S(k) = I_{\text{in}}(k) \cdot F(k) \tag{25}$$

represents the convolution between the actual spectral distribution $I_{\text{in}}(k)$ of the analysed radiation and the so-called instrumental window $F(k)$ introduced by the different optical components constituting the instrument, namely:

1. *Front optics*. this element contributes in determining an optical coupling which is in general a function of the radiation wavelength, due to the different constituent materials, and to the various interfaces that the impinging light must cross to reach the input channel of the integrated microinterferometers; in particular the optical fibre "pig-tail" can introduce a remarkably dependent coupling function between the input optical fibre and the input channel waveguide.
2. *Integrated optics*. as already mentioned, integrated optical components are characterised by a wavelength dependence of the propagation properties of the excited modes.
3. *End optics*. the system allowing to collect the output interferometric signal and to direct it to the sensing elements of the associated photo-detector, jointly to the spectral sensitivity characteristics of the photo-detector itself, produces a further contribution to the overall transfer function.

In practice, by transforming the output interferogramme, the *S(k)* function is obtained rather than the simple input spectrum $I_{\text{in}}(k)$. The possibility to extract the effective $I_{\text{in}}(k)$from the transformed interferogramme cannot in principle be done on the basis of simple theoretical considerations: in practice, the instrument must be calibrated by means of a known input reference spectrum $I_{\text{in}}{}^{\text{REF}}(k)$which must allow to operate the deconvolution between the effective $I_{\text{in}}{}^{\text{REF}}(k)$and the $F(k)$function, accounting for all instrumental contributions.

It must be noticed that at this level the analytical treatment of the output interferogramme is in principle the same of that applied for classical interferometers: once the instrumental window is defined, then the transformed interferogramme can be corrected in order to "release" the actual spectral distribution.

At this point, the proper reconstruction of the *k*-scale (wave-number) is a very important aspect in the treatment of the collected interferometric data. As already explained, the output interferogramme is obtained by registering the output intensity as a function of the reached optical path difference, i.e. of the voltage applied to the driving electrodes.

Hence from the set of data $\{V, I_{\text{out}}(V)\}$, or in practice $\{t, I_{\text{out}}(V(t))\}$ where t is the sampling time, one has to recover the spectrum of the impinging radiation $\{k, I_{\text{in}}(k)\}$.

The application of the Fourier Inverse Transform to the dataset $\{t, I_{\text{out}}(V(t))\}$ produces a new dataset $\{f, F(f))\}$, where f is a frequency (inverse of time) and is a function of the spectral wave-number k, i.e. of the wavelength:

$$f = f(k) = f(\mathbf{2}\pi/\lambda) \tag{26}$$

Hence, by determining the $f(k)$, one obtains a direct calibration of the reconstructed spectrum in the k space (i.e., as a function of wavelength).

The $f(k)$ function can be in principle obtained theoretically by knowing the constituting parameters of the integrated MZ interferometer and in particular the following relationship holds[3]:

$$f(k) = \frac{2\pi \cdot r \cdot n^3 L \cdot e_0}{\lambda \cdot D} = \frac{2\pi \cdot r n^3 L \cdot e_0}{D} \cdot k = \alpha \cdot k, \tag{27}$$

where r is the electro-optic coefficient of the substrate material, n is its refractive index, L is the interferometer arm length, D is the gap between the driving electrodes and e_0 is the applied linear voltage ramp rate, namely

$$V(t) = e_{\mathbf{0}}\, t. \tag{28}$$

[3] Equation (27) can be obtained from (7) and (21), by considering the effect of the interferometer transfer function on a monochromatic component with wave-number k and remembering that the Fourier Transform of sinusoidal function $\sin(k\ t)$ is $\frac{\pi}{i} \cdot (\delta(\omega - k) - \delta(\omega + k))$ with δ(x) the Dirac's delta distribution [Douglas Cohen (2007) Performance analysis of standard Fourier-transform spectrometers. Chap. 2.1, pp 144–159]

Equation (27) is of particular interest stating a *linear relationship* between the temporal frequency of the interferogramme transform, f, and the spectral frequency of the input radiation, k.

With respect to classical interferometric apparatuses a further complication in the reconstruction of the input spectrum from the output interferogramme arises from the term $\Delta p(k)$ of (24). This term states that the generated optical path difference producing the interferometric pattern is a function of the wavelength, due to the dispersive properties of the constituting material ($n = n(k)$). This term, nested in the cosine function of the integral transform, produces a *non-linearity* in the transfer function of the instrument, which has major effects:

(a) A redistribution of the relative intensities of the features characterising the original input spectrum
(b) A distortion of the scale in the k space of the reconstructed spectrum

An immediate consequence on (27) is that the linearity of the $f(k)$ relationship is lost due to the dependence on k of the α factor too:

$$f(k) = k\,\alpha(k). \tag{29}$$

This effect can be mitigated by selecting operating spectral intervals upon which the variation of the refractive index of the material is limited, a condition more easily verified in the IR spectral segment, but difficult to reach in the near UV—short-wavelength VIS spectral interval. Nevertheless, for accurate data calibration, particularly when high-resolution spectra are needed, as in the case of highly diluted species analysis (e.g., gaseous species in atmosphere), the $f(k)$ function, or alternatively a model of it, e.g. a polynomial model, must be precisely determined at experimental level. This task can be onerous and implies the application of a sufficient number of calibrated sources, allowing to establish $f(k)$ with the required precision.

Another parameter to be considered is the linearity of the applied voltage ramp, in particular the e_0 constant of (28). This instrumental feature is basically related to the electronics generating the driving voltage ramp and must be well analysed during the instrument calibration process. The introduction of distortions in the driving voltage ramp has immediate consequences on the interferogramme sampling, introducing further non-linear contributions in the $f(k)$ function which must be maximally avoided. This cannot be a simple task when high voltage spans are applied to reach high spectral resolution performances.

In practice, further non-ideal behaviours can appear during the operation of the microdevice, due to non-linearity features present in the readout electronics, in the end optics, etc., giving rise to a distortion of the output interferogramme. This distortion can be in general described as an effect introduced by a phase shift varying non-linearly with the reached optical path difference.

A great deal of attention must then be devoted to configure the instrument in order that phase-shift non-linear behaviours are maintained as small as possible. In that case, in fact, the application of suitable phase-recovery procedures, which can

be directly implemented at software level, allows a correction of the raw data and the recovery of the contained information.

The treatment of the data is in fact a crucial point in the output interferogramme reconstruction; in fact, simple Fast Fourier Transform (FFT) procedures applied at raw interferogramme can in fact produce unwanted effects on the reconstructed spectra. In this view, proper linearization, apodization and symmetrisation procedures must often be implemented in order to recover the linear shift of the interferogramme phase with the optical path difference variation.

An exhaustive description of the art of FTS data treatment is far beyond the scope of this book, as is referred to specific literature; nevertheless, in order to highlight the importance of a correct interferogramme transform approach, in the following figures is reported an impressive example illustrating how raw data post processing can impact on the extraction of the information contained in the interferogramme.

Figure 28a reports a raw interferogramme obtained in the SWIR spectral window by means of an integrated MZ microinterferometer applied in on-field measurements of the atmospheric spectrum. It is possible to observe how many of the above-described non-linear behaviours affect the form of the collected data.

A direct application of FFT procedures, obtained by means of standard commercial software package, generates a reconstructed spectrum (red line) which apparently shows a relatively low resolution and compares with a 2.6-nm resolution reference atmospheric spectrum (black line in Fig. 28b, c).

A suitable software treatment of the interferogramme allows for its correction, strongly reducing the non-linear features present in the original raw data (all the operations performed via software), as shown in Fig. 28c. Figure 28d clearly shows the impressive gain obtained by software post-processing, allowing to recover the information contained in the original data and masked by non-linear features. The reconstructed spectrum (red line) compares in this case with a 1-nm resolution reference spectrum (blue line) evidencing the characteristic signatures of the gaseous species present at that moment in the atmosphere and absorbing in the selected spectral window.

5 Examples of New Generation Optical Microsensors

In this section, a concise description of a relatively new generation of monolithic optical microsensors, addressed to different scientific areas, will be given. We will fix the attention to two different types of devices that have already appeared on scientific literature even if their presence on the market as monolithic integrated sensors is almost not existent so far.

In particular, we will synthetically describe first the Integrated Optics version of a "Programmable Micro-Diffraction Grating" (PMDG) that can have interesting applications in advanced spectroscopy, even if this device was originally studied for beam steering in image projection techniques. Successively, at point b), we will describe the "Tuneable Photonic Cavity" that can have very interesting application

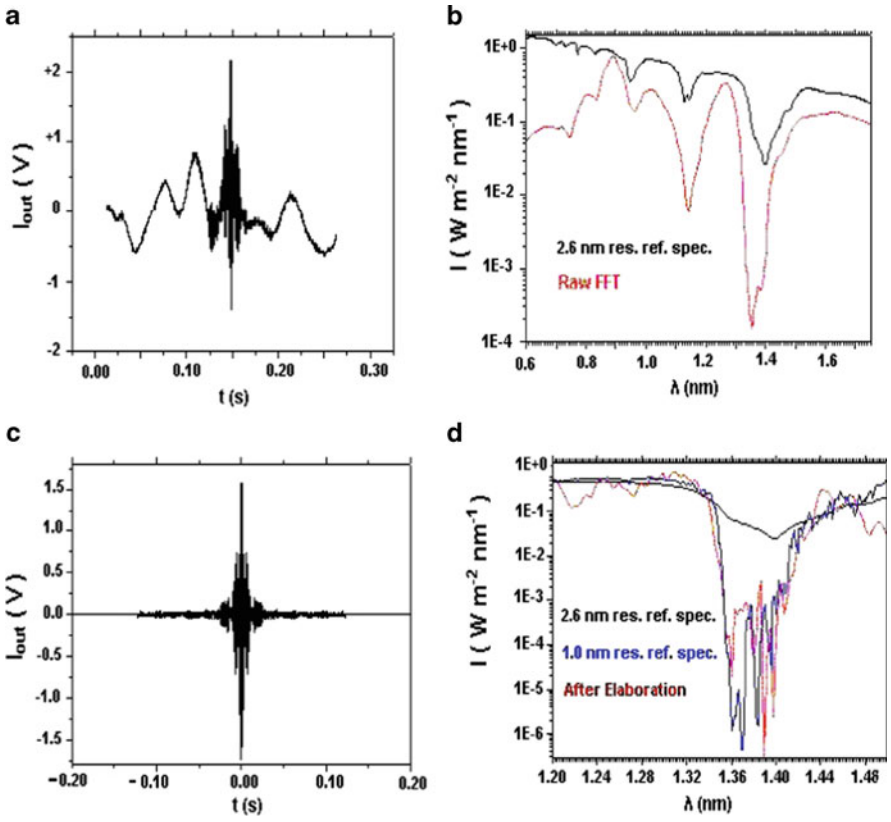

Fig. 28 Example of interferogramme treatment for atmospheric spectra reconstruction: (**a**) Raw interferogramme showing a distortion of the baseline. (**b**) Direct FFT of the distorted interferogramme, *red line*, compared with a low-resolution (2.6 nm) reference atmospheric spectrum (*black line*). (**c**) The interferogramme data after linearization, apodization and symmetrisation. (**d**) Reconstructed spectrum from treated interferogramme data (*red line*), also compared with higher resolution (1 nm), reference spectrum, (*blue line*)

in high selectivity chemical sensing, even if in the recent years this structure has been widely studied as functional elements in Optic Fibres communications systems.

(a) *Programmable micro-diffracting grating for correlation spectroscopy*

In general, a Diffracting Grating (DG) is constituted by a patterned surface relief or by pattern variations of the refractive index of a specific substrate. In Fig. 29a is shown an historical example (Michelson) of diffractive grating. In this case, the grating is formed by a package of glass platelets of different height where the upper part is characterised by a stair-like region having point-to-point different thickness (see Fig. 29a).

If a planar wave front is transmitted through the stair-like structure, each step transmits a wave front with a well-defined phase. The different wave fronts,

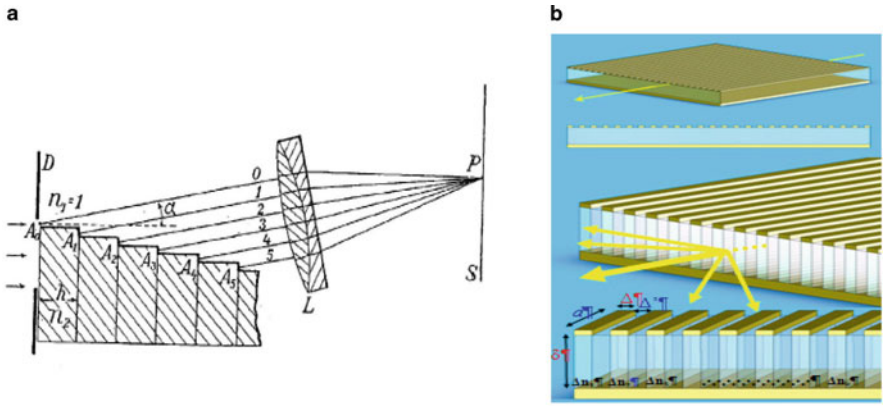

Fig. 29 Historical diffractive grating (Michelson),producing a wave front with phase shift depending on the position (**a**) and schematics of Programmable integrated Micro-Diffractive Grating (**b**)

crossing different thicknesses, have different phases and interfere with each other, giving rise to a diffraction pattern visible on the screen *S*. The phase shift generated by each step can be decided during the grating fabrication by choosing the suitable step thickness (static diffractive grating). In the integrated optical structure of Fig. 29b, the same phase shift can be obtained even if the material has uniform thickness, but the optical material has different refractive index values in stripes of selected areas. Figure 29b reports an example of the monolithic structure of Electro-Optical material (e.g., $LiNbO_3$) in which stripe electrodes induce different values of the refractive index through a suitable electric field applied to the material creating an active micro-diffractive grating. In fact, in this case, the different phase shifts among the wave fronts crossing the different stripes can be changed as a function of the needs, by changing the electric field distribution.

This configuration, contrary to the case of a static grating, allows the full control of the spectral content of the diffracted light. In particular, a miniaturised, fast integrated Programmable Micro-Diffraction Grating (PMDG) based on electro-optical substrates without moving parts and emulating diffractive optical elements can be designed by using the electro-optic effect to locally modify the refractive index through the application of a driving electric field [39, 40, 47].

This allows to fabricate an Integrated Optics device in which the diffractive properties can be programmed as a function of the application required. The key point for the design of a fully integrated PMDG, based on electro-optically driven substrates, is the determination of a suitable driving voltage pattern, able to introduce the required phase changes on the incident electromagnetic field. In this way, the electromagnetic radiation will generate, by diffraction, the desired (reference) output spectra for an assigned direction in the far-field region.

The creation of a controlled optical wave-front modulation is a powerful concept, with numerous applications in Optical Sensing, and in particular, the use of

PMDG for correlation spectroscopy seems to appear as one of the most interesting applications of Integrated Optics microdevices for its impact on many fields ranging from analysis of hazardous materials to safety and security applications. Let us examine in some detail the possibilities of a PMDG in correlation spectroscopy sensing problems.

It can be useful to recall that correlation spectroscopy is an attractive technique for sensing and analysis applications because it combines high selectivity and good sensitivity.

In conventional correlation spectroscopy, the procedure involves the comparison of the absorption spectrum of a known gas at a given concentration in a reference cell, with the spectrum of the same gas, contained at unknown concentrations in a measurement cell.

Gas materials are characterized by narrow transmission lines, so the cross-correlation between the absorption spectra of different compounds can usually be neglected and a significant correlation will be observed only when both the sample and the reference cells contain the same compound, giving rise to excellent selectivity measurements.

Correlation spectroscopy also achieves good sensitivity for materials with narrow absorption bands, since the transmission autocorrelation functions of these materials are sharp, and small modulations of the transmission of the reference cell can impose a large modulation on a beam.

In a typical correlation spectrometer, broadband light first passes through the gas sample to be analysed to know if it contains a certain compound (target to be detected). Then the light passes through a reference cell containing the compound to be detected (Fig. 30). If the absorption spectrum of the gas of the measurement cell matches the spectrum of the reference cell, then an absorption in the output signal will be detected. The actual concentration of the gas can be determined by measuring the optical contrast between the two signals (also referred to as the "*intensity modulation index*").

In practice, the measurement is performed modulating the amplitude of the transmission spectrum of the reference cell, by modulating the target gas pressure or by other suitable means. Consequently, the output of the detector is recorded,

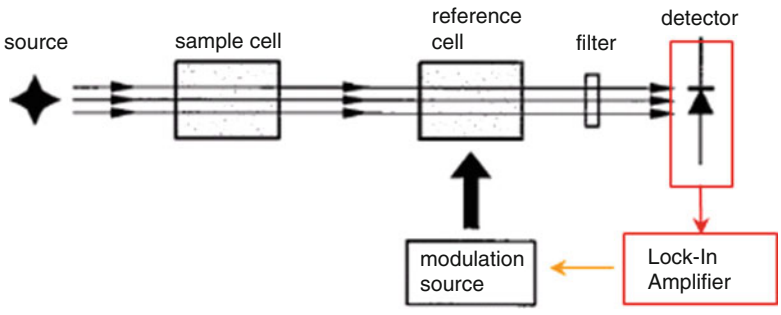

Fig. 30 Schematics of a traditional correlation spectrometer

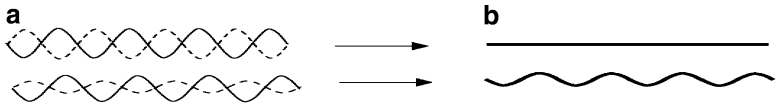

Fig. 31 (**a**) Zero-intensity modulation (absence of gas in the sample cell); (**b**) intensity modulation indicating the presence of the target gas in the sample cell

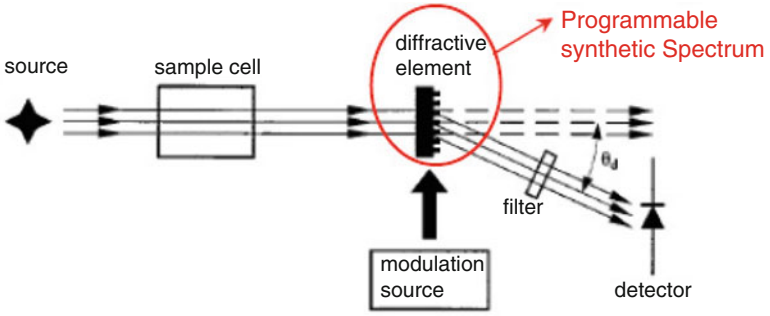

Fig. 32 Schematics of a correlation spectrometer, where the reference cell is substituted by a properly designed diffractive optical element

with a lock-in set-up, at the modulation frequency. If there is no reference gas present in the measurement cell, there will be no absorption and there will be no intensity modulation (Fig. 31a). However, when the desired gas is present in the measurement cell, there will be an output absorption spectrum having the intensity modulated as the reference gas cell modulation (Fig. 31b). The lock-in set-up allows a quantitative measurement of intensity modulation index

Unfortunately, even if correlation spectroscopy is an attractive tool for chemical sensing, the need for reference cells containing target compounds has the consequence that correlation spectrometers tend to be large and it becomes almost impossible to detect a large number (up to ~10^3) of compounds. A great improvement in the realization of correlation spectrometers consists in replacing the reference cell with a specifically designed diffractive element (grating) (Fig. 32), with the capability to generate synthetic spectra to be used as reference spectrum [41, 48].

In the configuration shown in Fig. 32, the total power measured at a diffraction angle θ_d is determined by the cross-correlation between the transmission of the sample cell and the diffraction efficiency of the grating at the angle θ_d. If the diffraction efficiency of the grating as a function of wavelength closely corresponds to the absorption spectrum of the compound of interest, then the effect of the diffractive element is analogous to that arising from a reference cell containing a physical (gas) sample. In particular, using as diffractive element a PMDG, a number of improvements can be obtained:

- As a consequence of its programmable feature, it is possible to choose the characteristics of the reference spectrum that are free of interferences.

- The programmable transfer function can be modulated directly by using the same control mechanism that is used to set the reference spectrum. Programmability allows to "change" quickly the target species, simply by software changing the driving voltage pattern, and consequently the diffraction characteristics of the grating. This allows to generate synthetic spectra to be used as "reference spectrum" for the correlation process. This feature allows the detection and sensing of highly toxic or labile species without the problem arising by need to have a reference cell physically containing a certain amount of such a material, which is one of the problems in a conventional correlation spectrometer.
- Finally, in contrast with a gas reference cell, which transmits most of the incident light and absorbs only a fraction at the wavelengths of interest, the PMDG can be set to transmit the light only at the wavelengths where the gaseous species to be detected shows useful absorption lines. This possibility allows to greatly reduce the total amount of light impinging on the detector thus reducing the detector shot noise. This selective operating principle creates remarkable advantages in performing the spectral correlation because all non-useful wavelengths can in principle be removed.

In summary, besides the enormous reduction in size and power consumptions, the PMDG can have the compactness and versatility typical of I.O. microdevices. Moreover, due to its programmable optical transfer function, it can fully replace the reference cell. This feature not only simplifies the construction and the operation of a correlation spectrometer, but it also creates powerful new tools to enhance the versatility and performances of this instrument, which can be fabricated in a very compact and robust form, as in the case of Remote sensing or in Space Application.

(b) *Resonant cavity*

Photonic crystals are artificial functional materials in which the refractive index varies regularly on the length scale of optical wavelengths and are characterized by photonic band gaps [42, 43, 49]. Photonic crystals can be obtained, for example, by generating integrated structures characterised by a periodic variation of the refractive index on an homogeneous optical substrate (e.g. in the core of an optical fibre, on top of an integrated optical waveguide, etc.) and allow to change the transmission properties of the material itself which can be functionalised to generate new optical features.

Of particular interest are Bragg Gratings' structures which allow to introduce forbidden transmission gaps in the functionalised materials where they are fabricated, thus deeply changing the optical characteristics of the starting medium.

In Fig. 33a is reported a schematic drawing of a photonic structure generated on an integrated waveguide. The presence of the periodically varying refractive index profile of the waveguide surface allows to introduce forbidden transmission band gaps in which the photonic structure acts as a high efficiency mirror. Figure 33b reports the Reflectivity spectrum as calculated for a Bragg grating structure fabricated on a $LiNbO_3$ waveguide. In this case, the photonic structure has a periodic variation of the refractive index of 1 μm pitch, i.e. it alternates 500 nm

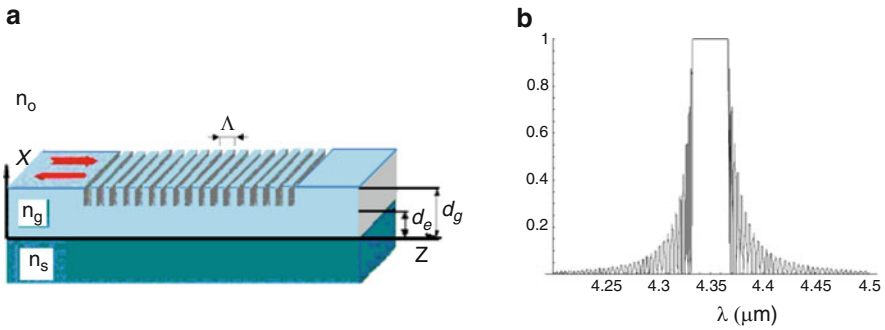

Fig. 33 (**a**) Schematics of a Bragg's Grating generated on a waveguide. (**b**) Reflectivity spectrum calculated for a Bragg grating structure formed on $LiNbO_3$ with a 1-μm pitch periodic variation of the refractive index alternating 500 nm $LiNbO_3$ with 500 nm air

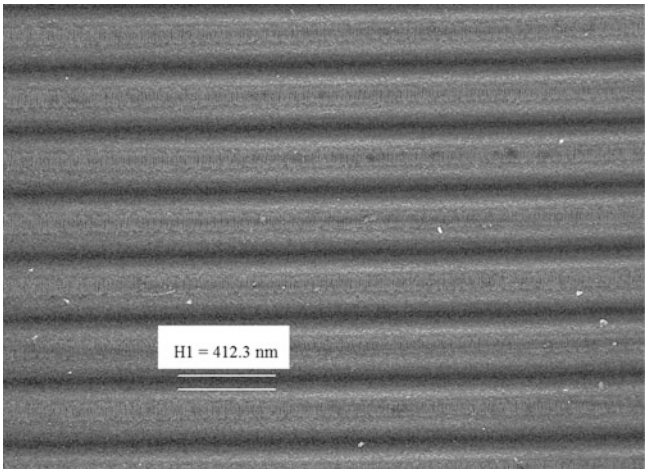

Fig. 34 Example of Integrated optical Bragg Grating generated on a channel $LiNbO_3$ waveguide. The SEM micrograph shows a detail of a grating structure

$LiNbO_3$ with 500 nm air. From Fig. 33b it appears that the transmittance spectrum of this photonic crystal has a box-like shape peaked around 4.35 μm of wavelength. This structure has been designed and fabricated for a very selective detection of CO_2 gas.

Figure 34 shows an SEM detailed image of an example of Bragg's grating on $LiNbO_3$. The photonic structure has a 1432-nm pitch.

The optical transmittance of a photonic structure like the one reported in Fig. 37, shows, in particular, the transmittance variation of the periodic structure as a function of the applied ramp voltage.

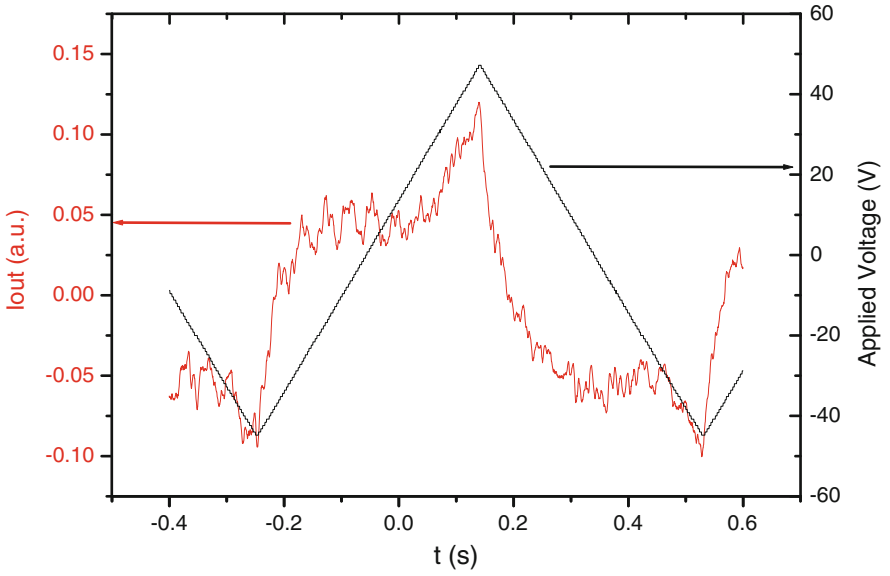

Fig. 35 Optical transmission signal of a Bragg Grating (*red line*), generated on a $LiNbO_3$ channel waveguide varying through the application of a driving voltage (*black line*)

All the above-reported concepts can be applied for the construction of compact sensing tools for the optical analysis of trace analyte quantities, which remains an important goal in the development of integrated systems. Miniaturization of appropriate light sources and detectors can enable very compact and versatile "laboratory-on-a-chip" devices, in which different analytical functions can be monolithically combined.

A first example of simple but versatile resonant cavity photonic microsensor can be obtained by patterning either the surface or the body of a waveguide structure with two separate gratings, thus giving rise to a couple of Bragg Mirrors that generate (the formation of) a micro-cavity resonant for some optical frequency bands, in between them. The sketch of the device is reported in Fig. 36.

The basic principles of a photonic micro-cavity like the one represented in Fig. 36 are the following. The optical frequency bands for which the cavity is resonant are defined by the gratings' characteristics. If the device is fabricated on $LiNbO_3$ base material, it is convenient that the crystal orientation is chosen as x-cut; the propagation of light along the y crystallographic direction and the metallic electrodes are placed both along the mirror structures and the cavity region, as sketched in Fig. 36.

This way it is possible to apply along the crystal *c*-axis a suitable electric field, where the electro-optic coefficient, a_{33}, is maximum. The application of the electric field produces a change of the optical refractive index through the Pockel's effect, thus allowing to tune both the mirror reflectivity and the optical cavity length.

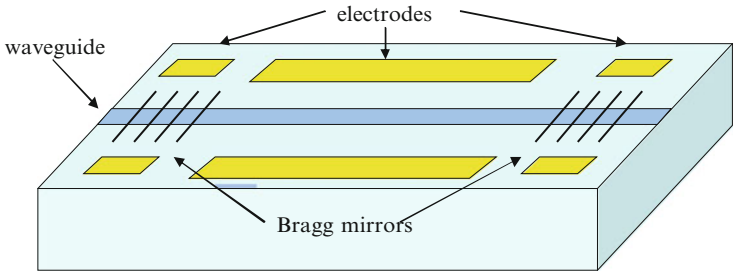

Fig. 36 Schematic representation of a resonant cavity photonic microsensor

If proper optical parameters are designed, the photonic micro-cavity can be tuned and put in resonance with the particular frequencies' characteristic of the chemical species which have to be detected, by adjusting the electric fields applied to the cavity and/or to the Bragg mirrors. Thus, if the cavity surface is put in contact with an analyte, a certain amount of molecules adheres and interacts with the cavity surface. When the resonance frequency of the cavity coincides with the proper molecule frequencies, then a certain amount of energy is absorbed giving rise to a loss in the device output signal.

More generally, if a suitable voltage ramp is applied to the cavity walls, then loss peaks will appear in correspondence to the cavity optical lengths which match the resonating optical frequencies of the molecules interacting with its surface.

The range of frequencies is defined on the basis of the cavity geometry, the mirrors band gaps, and the applied voltage ramp span. These characters make the device particularly selective, because of the narrow width of the characteristic molecular absorption bands, together with the possibility to finely tune its optical parameters through the application of suitable electric fields

An example of a prototype photonic microsensor based on a tuneable resonant cavity like the one described above and fabricated by surface engineering of $LiNbO_3$ is shown in Fig. 37. The good quality pattern of the base material, necessary to obtain the photonic mirrors at the sides of the cavity, has a periodic pitch of ~1 μm.

In the complete device, both cavity and mirrors are tuneable; the transmissivity of the cavity depends on the applied voltage. This effect can be exploited for the very sensible detection of chemical species absorbing in the spectral range where band-gap transmission of integrated micro-cavity occurs.

In this device, the interaction of analytes with the surface of the photonic cavity can generate, at some specific electric field values, a variation (typically absorption peaks) of the transmission properties which are in general very sensible and can be exploited to generate high-performance sensors. Due to the physical characteristics of resonance phenomena, resonant cavity sensor devices can be specifically designed to operate in a particular spectral window by properly dimensioning their geometrical features.

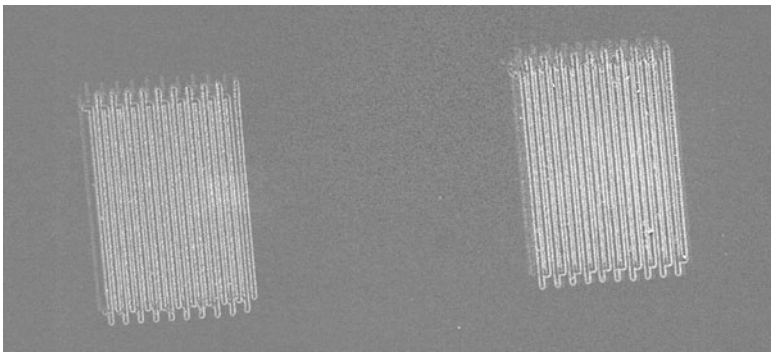

Fig. 37 SEM image of a resonant cavity photonic sensor, before electrodes deposition

References

1. Stamm C, Lukosz W (1993) Integrated optical difference interferometer as refractometer and chemical sensor. Sens Actuat B 11:177–181
2. Lechuga LM, Lenferink ATM, Kooyman RPH, Greve J (1995) Feasibility of evanescent wave interferometer immunosensors for pesticide detection: chemical aspects. Sens Actuat B 24–25:762–765
3. Lukosz W (1995) Integrated optical chemical and direct biochemical sensors. Sens Actuat B 29:37–50
4. Kunz RE (1997) Miniature integrated optical modules for chemical and biochemical sensing. Sens Actuat B 38:13–28
5. Kunz RE (1992) Totally integrated optical measuring sensors. Proc SPIE 1587:98–113
6. Dessy RE (1989) Waveguides as chemical sensors. Anal Chem 61:1079
7. Maisenholder B, Zappe HP, Moser M, Riel P, Kunz RE, Edlinger J (1997) Monolithically integrated optical interferometer for refractometry. Electron Lett 33:986
8. Heideman RG, Kooyman RPH, Greve J (1993) Performance of a highly sensitive optical waveguide Mach–Zehnder interferometer immunosensor. Sens Actuat B 10:209–217
9. Bentini GG, Bianconi M, Cerruti A, Chiarini M, Dinicolantonio W, Guzzi R, Nubile A, Pennestrì G (2006) A new miniaturized optical system for chemical species spectroscopic detection based on a scanning integrated Mach–Zehnder microinterferometer on $LiNbO_3$. Orig Life Evol Biosph 36:597
10. Bentini GG, Bianconi M, Cerruti A, Chiarini M, Pennestrì G, Sada C, Argiolas N, Bazzan M, Mazzoldi P (2007) Integrated Mach–Zehnder microinterferometer on $LiNbO_3$. Optics Lasers Eng 45:368
11. Born M, Wolf E (1999) Principles of optics. Seventh, (expanded) Edition, Chap. 1. Cambridge University Press, Cambridge, pp 1–3
12. Loudon R (1983) The quantum theory of light, Chap. IV, 2nd edn. Oxford University Press, Oxford, pp 120–126
13. Born M, Wolf E, Principles of Optics", Seventh (expanded) Edition, Chap 1.2, pp 11–25
14. Born M, Wolf E, ibid., Chap. I, pp 24–25
15. Loudon R, ibid., Chap. 1.2, pp 5–7
16. Fabien Malbet et al (1999) Integrated optics for astronomical interferometry I. Concept and astronomical applications. Astron Astrophys Suppl Ser 138:1–10
17. Iizuka K (2002) Elements of photonics, Volume II, fiber and integrated optics, vol 2. Wiley, NY

18. Kempen LU, Kunz RE (1997) Replicated Mach–Zehnder interferometers with focusing grating couplers fur sensing applications. Sens Actuat B 38–39:295–299
19. Kitsara M, Raptis I, Misiakos K, Makarona E (2008) Broad-band Mach–Zehnder Interferometry as a detection principle for label-free biochemical sensing. IEEE (2008) Sensor Conf., p. 934
20. Wilson J, Hawkes J (1998) Optoelectronics, 3rd edn. Prentice Hall, NJ
21. Wong KK, Nutt ACG, Clark DF, Winfield J, Laybourn PJR, De La Rue RM (1986) Characterization of proton-exchange slab optical waveguide in X-cut $LiNbO_3$. IEE Proc 133(Pt J No. 2):113
22. Korishko Yu N, Fedorov VA (1996) Structural and optical characterization of annealed proton exchanged $LiNbO_3$ optical waveguide. Optical Mater 5:175–185
23. Kunevaa M, Toncheva S, Pashtrapanskaa M, Nedkov I (2000) Proton exchange in Y-cut $LiNbO_3$. Mater Sci Semicond Process 3:581–583
24. Bentini GG, Bianconi M, Chiarini M, Correra L, Sada C, Mazzoldi P, Argiolas N, Bazzan M (2002) Effect of low dose high energy O^{3+} implantation on refractive index and linear electro-optic properties in X-cut LiNbO3: Planar optical waveguide formation and characterization. J Appl Phys 92:6477
25. Sugliani S, Bianconi M, Bentini GG, Chiarini M, De Nicola P, Montanari GB, Menin A, Malacarne A, Potì L (1910) Refractive index tailoring in congruent lithium niobate by ion implantation. Nucl Instr Meth Phy Res B 268:2911
26. Yi-Kuei Wu, Wang W-S (2008) J Lightwave Technol 26:286
27. Anwar N, Obayya SSA (2002) The effect of fabrication parameters on a ridge Mach–Zehnder interferomatric (MZI) modulator. J Lightwave Technol 20(5):854
28. Hu H, Ricken R, Sohler W, Wehrspohn RB (2007) Lithium niobate ridge waveguides fabricated by wet etching. IEEE Photonics Technol Lett 19(6):417
29. Bianconi M, Bergamini F, Bentini GG, Cerutti A, Chiarini M, De Nicola P, Pennestrì G (2008) Modification of the etching properties of x-cut Lithium Niobate by ion implantation. Nucl Instr Meth Phys Res B 266:1238
30. Lei Wang, Ke-Ming Wang, Xue-Lin Wang, Feng Chen, Yi Jiang, Chuan-Lei Jia, Yang Jiao, Fei Lu, Ding-Yu Shen, Hong-Ji Ma, Rui Nie (2007) Selective etching in $LiNbO_3$ combined MeV O and Si ion implantation with wet etch technique. Surf Coat Technol 201:5081
31. Becker RA (1983) Comparison of guided wave interferometric modulators fabricated via Ti in diffusion and proton exchange. Appl Phys Lett 43:131
32. Bentini GG, Bianconi M, Correra L, Chiarini M, Mazzoldi P, Sada C, Argiolas N, Bazzan M, Guzzi R (2004) Damage effects produced in the near-surface region of x-cut $LiNbO_3$ by low dose, high energy implantation of nitrogen, oxygen, and fluorine ions. J Appl Phys 96:242
33. Tiefenthaler K, Lukosz W (1989) Sensitivity of grating couplers as integrated-optical chemical sensors. J Opt Soc Am B 6:209–220
34. Lukosz W, Clerc D, Nellen PhM (1991) Input and output grating couplers as integrated optical biosensors. Sens Actuat A 25–27:181–184
35. Minoru Saito, Hideki ONO, Takahashi H (1999) Design of low-loss Y-branch optical waveguides. Jpn J Appl Phys 38:115–116
36. Tetsuro Yabu, Masahiro Geshiro, Shinnosuke Sawa (2001) New design method for low-loss Y-branch waveguides. J Lightwave Technol 19:1376
37. Sakamaki Y, Saida T, Tamura M, Hashimoto T, Takahashi H (2007) Low-loss Y-branch waveguides designed by wavefront matching method and their application to a compact 1×32 splitter. Electron Lett 43:217–219
38. Hashimoto T et al (2005) Optical circuit design based on a wavefront matching method. Opt Lett 30:2620–2622
39. Thomas JA, Fainman Y (1995) Programmable diffractive optical element using a multichannel lanthanum-modified lead zirconate titanate phase modulator. Opt Lett 20:1510
40. Song QW, Wang X-M, Bussjager R (1996) High-efficiency electro-optic grating switch with improved performance. Appl Opt 35:7031

41. Sinclair MB et al (1997) Synthetic spectra: a tool for correlation spectroscopy. Appl Opt 36 (15):3342–3348
42. Yablonovitch E (1993) Photonic band-gap crystals. J Phys Condens Matter 5:2443
43. Joannopoulos JD, Meade RD, Winn JN (1995) Photonic crystals: molding the flow of light. Princeton University Press, Princeton, NJ
44. Canut B, Ramos SMM, Brenier R, Thevenin P, Loubet JL, Toulemonde M (1996) Surface modifications of LiNbO3 single crystals induced by swift heavy ions. Nucl Instrum Meth Phys Res B 107:194–198
45. Bergamini F, Bianconi M, Cristiani S (2007) Wet and vapor etching of tracks produced in SiO_2 by Ti ion irradiation. Nucl Instrum Meth Phys Res B 257:593–596
46. Hanaizumi O, Miyagi M, Kawakami S (1985) Wide Y-junctions with low losses in three-dimensional dielectric optical waveguides. IEEE J Quantum Electron 21:168–173
47. GG Bentini, et al. (2007) Monolithic fully integrated programmable micro diffraction gratings based on electro-optical materials. Proc of SPIE 6593
48. Sinclair B et al (2004) A MEMS based correlation radiometer. Proc SPIE 5346:37–47
49. Chigrin DN, Lavrinenko AV, Yarotsky DA, Gaponenko SV (1999) Observation of total omni directional reflection from a one-dimensional dielectric lattice. Appl Phys A 68:25
50. Ziegler JF, Ziegler MD and Biersack JP (2011) The Stopping and Range of Ions in Matter SRIM code, http://www.srim.org

Refractometric Photonic Chips for Biosensing

Raphael K. Kribich

Abstract Light is the historical medium for analysis in biology. Micro/nanotechnologies renewed the optical components fabrication processes following the example of electronics integration. A full optical system, as an interferometer or a spectrometer, for instance, can be integrated on a single chip and light can be confined at the nanometer scale allowing for interaction with a single biological entity (cell, enzyme, antigen, etc.). Thus, robust, portable, and sensitive systems can be developed by optical integration. Main ways to confine and propagate the electromagnetic wave will be introduced for the non-specialist: optical and plasmonic waveguides and photonic crystals will be discussed. Fabrication technologies for optical integration will be presented depending on the nature of the materials to be considered as semiconductors, glasses, metals, or polymer. Further is explained the sensing principle based on the detection of refractive index change. Finally, a review of the actual trends for the realization of biosensors is presented, discussed, and compared in terms of refractive index change resolution to come out with design strategies to enhance the sensors resolution for small volume detection and earlier diagnostic.

Keywords Biosensors • Integrated optics • Optical sensors • Photonic crystal • Plasmon • Waveguide

Contents

R.K. Kribich (✉)
IES, the Electronics Institute (UMR UM2/CNRS 5214), Université Montpellier 2, Place E. Bataillon, CC84, 34095 Montpellier, France
e-mail: raphael.kribich@ies.univ-montp2.fr

W. Fritzsche and J. Popp (eds.), *Optical Nano- and Microsystems for Bioanalytics*, Springer Series on Chemical Sensors and Biosensors (2012) 10: 155–180
DOI 10.1007/978-3-642-25498-7_5,

1 Introduction

Thanks to the development of micro- and nanotechnologies, scales at which basic mechanism of biology occur can be studied. Optics is historically a scientific domain used in biology for the observation of living mechanism. From this it is clear that a deep understanding of biochemistry needs micro/nano-optics techniques. Managing and observing matter or light/matter interaction at this scale is not an easy task, and perturbation brought by mechanical vibrations or temperature, for instance, strongly impacts the noise level of the analysis. Classical optical setup used in free space optics suffers more from misalignment and high spatial frequency spreading over the distance; they cannot reach the nanometer scale resolution. Guided optics was developed strongly 50 years ago with the apparition of semiconductor-based laser sources and low-loss optical fibers for fast and long distance telecommunication. Informatics development brought by computing density has increased, microelectronics integration pushed toward more and more data exchange and thus a need for more efficient telecommunication networks. Optical technologies have been developed following the path of electronics, and the race toward integration is now at the nanometer scale using fabrication techniques inherited partly from electronics and using the same planar integration model. Integrated optics deals with the integration of passive or active optical functions on planar substrates for fabrication of photonic chips. These chips can integrate an optical system using waveguiding, diffraction, and near-field or plasmon resonance phenomena among others. Such integrated systems using biofunctionalized surface are converted in bio-optical chips and can be used as a high resolution, reliable, easy-to-use, and cheap platform for biodiagnostics.

In this chapter, we will explain the basic mechanisms used in integrated optics as guided propagation modes, photonic crystals diffraction, and plasmon resonance for the reader who is not familiar with those fields. In a second step, we will briefly introduce some of the most common materials and associated fabrication process for the realization of photonic chips. Then, we will discuss a detection principle based on the refractometric approach for the sensing of biological agent based on

the modification of the optical structure in terms of optogeometrical properties. Finally, before concluding this chapter, we will present, through bibliographic work, some of the numerous optical architectures that have been proposed and developed during the last 25 years. We will focus on their resolution performance which depends of course on the optoelectronics detection scheme signal-to-noise ratio but also on the optical sensitivity.

2 Photonic Structures

In this part, we will explain three ways to exploit electromagnetic properties of light that are widely used in integrated photonics for bioapplications: the guidance of an optical beam in a high index transparent medium as in optical fiber applications, the diffraction of light by a periodical dielectric structure, and the coupling of light to a propagating surface plasmon.

2.1 Optical Waveguides

Guided wave optics is based on the total internal reflection phenomenon. It occurs when a light ray is refracted from a high index medium to a lower index one. When the incident angle is large enough (larger than a critical angle), no physical solution can be found using the Snell–Descartes' law for the transmitted ray to propagate in the low index medium. This means that the incident ray is totally reflected. Let us consider a waveguide in 2D. A waveguide is composed of a transparent high refractive index-guiding medium oriented along the propagation direction known as the core and surrounded by a low index buffer medium. When light is injected in the guiding medium, the rays for which angles are larger than the critical angle experience successive total internal reflections at the guiding/buffer media interface. Light propagates in the core, the center of a standard optical fiber, for instance.

Considering the wave optics model, a plane wave is associated to the ray. The twice-reflected plane wave is superimposed on the initial wave to form an interference pattern. For angles at which the interference is constructive, a standing wave is obtained in the transverse dimension (perpendicular to the propagation direction) and a propagating wave in the propagation direction z. This constructive interference condition, known as the self-consistency condition, is fulfilled for a discrete set of angles, leading to different transverse (y direction) interference patterns associated with different propagating (z direction) waves and thus different propagation speeds.

These propagating interference patterns are known as guided propagation modes and are solutions of the Helmoltz propagation equation derived from the Maxwell's equations with specific boundaries conditions depending on the waveguiding transverse structure. Other types of solutions as radiated or leaky modes do not

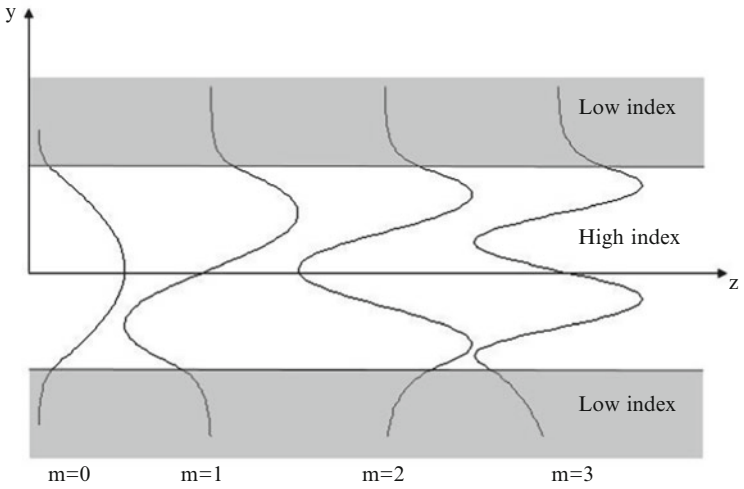

Fig. 1 Fourth lowest order propagation modes' transverse amplitude distribution

propagate along the propagation axis. Propagating patterns can occur for two types of transverse light polarizations (orientation of electric and magnetic fields) which are the transverse electric (TE) when the electric field is perpendicular to the waveguide plane (yz) and transverse magnetic (TM) when the magnetic field is perpendicular to the waveguide plane.

Figure 1 illustrates the transverse field amplitude profile (amplitude versus y) of different propagation modes. Each mode number m is related to one of the permitted ray angle. The part of the intensity out of the waveguide core (due to Fresnel phase shift at the reflecting interface) decays exponentially (evanescent behavior) in the y direction. Higher is m, higher is the penetration depth of the mode intensity in the buffer region. A virtual material, in which light would propagate straightly with the same velocity in the z direction as the zigzag path, would have a refractive index known as the effective index. This index is an eigenvalue linked with the eigenmode intensity distribution and depends upon wavelength, waveguide shape, and dimensions as well as on the refractive indices of the materials in which light propagates. Effective index is the main value that is monitored through interrogation optical functions which convert the optical length toward optoelectronics detection.

2.2 Diffractive Structures

Diffraction is the basic theory for the study of propagation of light [1]. Under certain assumption (Fresnel and Fraunhofer approximation, for instance), using Fourier optics and space harmonic analysis, the incident wave can be decomposed

as a sum of plane waves propagating at different angles which, in the incident plane, corresponds to different harmonic frequencies. As stated by the Huygens principle, an incident wave can also be decomposed in an infinite sum of elementary point sources that generate secondary spherical waves. Transfer function of free space can be calculated and shows that propagation can be regarded as a Fourier transform [2].

When matter is on the propagation path, it modulates the optical wave through its optical and geometrical parameters as dimensions and refractive indices. The amplitude and phase distribution of the wave are then modified and thus its propagated intensity profile. Transfer function of optical elements can be used to predict their impact on the light propagation.

A 1D periodic optical structure is defined through its periodic permittivity (or dielectric) function. Coupled mode theory, transfer/scattering matrix method, or rigorous solving of the Helmoltz equation using periodic boundaries allows to compute the solutions [2]. The incident wave is modulated by the 1D periodic structure, which gives rise to diffracted waves. Transmission is computed depending on wavelength and angles, and total reflection (or transmission) spectral bands may be obtained. Such 1D structure, known as diffraction gratings, can be used for coupling between free space wave and a guided wave, between guided/free space waves, or to confine light, they are used in optical components as reflectors, mode converters, polarization or wavelength filters, input/output couplers, and in numerous high sensitivity optical fiber sensors [3].

2D and 3D periodic structures, known as photonic crystals, can be analyzed by generalizing the 1D approach. The Helmoltz equation is solved using mathematical tools initially developed in solid-state physics for solving the Schrödinger equation to obtain the electronic potentials in a periodic atom lattice. Bloch modes are found for which the optical intensity distribution is periodical in accordance with the crystal design. A photonic energy band diagram can be plotted which depends on the permittivity function. This diagram may exhibit forbidden photonic energy band gap (analog to forbidden electronic energy band gap in semiconductors) known as photonic band gap (PBG) and that can be engineered depending upon the photonic crystal's design. Photons in the forbidden band gap cannot propagate through the structure along the direction of the studied wavevector (partial PBG) or for all wavevectors' directions (full PBG only for 3D crystals). Depending on their position relatively to the PBG, Bloch modes exhibit intensity peaks in, out, or at the edge of the crystal elementary pattern [2].

2D and 3D crystalline structures can include defects in their periodicity. Photonic crystals properties among others are spontaneous emission control, anomalous refraction, superprism effect, low-loss and sharp bending waveguiding, PBG optical fiber [4]. As for waveguiding structure, diffraction gratings and photonic crystal properties are altered by a change of the refractive index of materials/structures due to adsorption or presence of analyte molecules in or close to the lattice. The dispersion curves are modified, resonant frequencies are shifted, amplitude peaks vary, and photonic band gaps close or open.

2.3 Plasmonic Coupling

Plasmonics, as photonics manages photons, deals with generation, transport, manipulation, coupling, and detection of plasma waves (electrons density oscillation) and their associated quasiparticle the plasmon. X photons and electrons can transfer their energy to plasmons by bombarding a metal, for instance.

2D or 1D plasma waves can be excited as well, by bombarding with an electromagnetic wave at optical frequencies a metal in contact with a dielectric. Surface plasmonic propagating modes can be computed [5] in a way analog to optical guided modes in a dielectric structure. The difference lies in the fact that the conductive properties of metals and thus the presence of free charges must be taken into account when deriving Maxwell's equation. This gives rise to the Helmoltz wave equation including the relation between the dielectric function and the conductivity of the metal. When solving the wave equation, solution can be found only for electromagnetic waves at metal/dielectric interfaces and for which the magnetic field is totally in the interface plane (transverse magnetic polarization).

Dispersion relation can be derived neglecting damping due to absorption in the metal. Wave vector tends to be infinite at a certain frequency (lower than the bulk plasma frequency); the wave acquires electrostatic character and is associated with a surface plasmon (SP). This surface wave's amplitude decays exponentially away from the interface in the metal as well as in the dielectric. When considering real metals, damping must be taken into account through imaginary part of the metal dielectric function. Wave vector values for the surface plasmon become complex and the plasma wave is attenuated over a propagation distance typically between 10 and 100 μm in the visible range regime. A trade-off has to be found regarding this propagation length and the field confinement at the interface as the better the confinement the lower the propagation length.

When considering a metal layer sandwiched between two dielectrics, air and glass for instance, a surface plasmon exists at both interfaces, and for a thin metallic layer, the two plasmons are coupled. Coupling generates two plasmonic modes that exhibit even or odd symmetry, depending on how each nonperturbed plasmon couples to the other and lower penetration depth in the metal. When the sandwiching layers exhibit similar refractive indices, these modes can propagate on much longer distance than single interface plasmon and are called long-range surface plasmon [6]. These latest can propagate along metal stripes used as a plasmonic waveguide [7]. Bending and splitting branches are the basis for plasmonic circuit's conception like the Mach–Zehnder interferometer for instance [8].

When the metal-dielectric interface forms a cavity or is a closed surface, resonance happens. In the case of nanoparticles, specific solutions give rise to dipole (or multipole) oscillations called localized plasmon resonance. When two nanoparticles are sufficiently close to one another, the plasmons interact and coupling occurs. Linear chains and lattice arrays of metallic nanospheres have been studied [9] and can be used in sensing layers.

Biofunctionalization of a metallic layer deposited on glass slide permits to fabricate surface plasmon resonance-based biosensors as commercialized by the Swedish company Biacore since the early 1990s. When the analyte molecules bind to the ligands present on the metal surface, the adlayer presence shifts and/or attenuates the plasmon resonance. The plasmon is excited using an out-of-plane laser signal. The angular reflection spectrum is monitored during the binding processes. This configuration is not integrated, but some solutions exist for planar integration and will be presented in the section devoted to interrogation techniques.

3 Fabrication Technologies

This part is devoted to the different materials used for photonic/plasmonic chips as glasses, polymer, semiconductors, or metals, and the associated fabrication processes used for their deposition in thin films and to pattern them to realize the desired architectures.

3.1 Materials and Optical Waveguides' Fabrication

Materials generally used for waveguides' fabrication are those inherited from classical optics as glasses and polymers, as well as crystalline semiconductors associated with microelectronics fabrication processes. Semiconductor technologies are mainly based on Silicon and III–V materials as InP and GaAs. III–V materials are commonly used for high-speed photodetectors and sources. Waveguides are integrated with these active components [10, 11] using epitaxial growth, photolithography, and dry or wet etching, to optimize the performances of the system. They are compact, due to high refractive index, and exhibit low propagation losses in the infrared range and strong nonlinear behavior. Silicon technology is slower for electronics applications but benefits standard microelectronics technology as Silicon On Insulator for instance [12]. Those materials exhibit strong absorption in the visible range and are thus not suitable for direct wavelength interaction with biological labeled molecules, since commonly available fluorescent markers work in the visible range, but they can be used for refractometric sensors when their surface can be biofunctionalized. Promising solutions are porous silicon and silicon on insulator technologies. Silicon exhibits good adhesion after thermal oxidation and aminosilanization of its surface for cell, enzyme, or DNA binding [13, 14].

Glass is the most obvious material for optical applications. Bulky glasses must be modified so as to induce waveguiding properties. Waveguides are created by locally inducing a refractive index increase. Germanium-doped glasses, used in optical fiber cores, are photosensitive to UV exposure. The irradiation modifies defects present in the matrix and leads to index increase, but this effect is poor if not

enhanced under high hydrogen pressure, and high power lasers are needed to trigger the reactions [15, 16]. Other ways to induce waveguides are ion exchange [17] and implantation techniques. Due to exchange between ions present in the glass and heavier ions, the index is increased. Diffusion techniques are quite mature: lasers, amplifiers, couplers among others have been realized and commercialized [18]. Due to the diffusion process, good lateral resolution may be difficult to obtain and complex circuits' designs suffer from this limitation. A compromise can be found by using electronics nano/microtechnologies and glass material through thermal oxidation of a Silicon substrate to create a buffer SiO_2 layer and further deposition of higher index glass using chemical vapor deposition or sol–gel process. The waveguides are then patterned using classical photolithography steps and reactive ion etching. Index changes are smaller than with semiconductors, waveguides are thus bigger, but propagation losses stay small in the visible and near-infrared ranges and complex functions can be realized.

Polymer materials own versatile properties that can be tuned thanks to their chemical synthesis process. Their mechanical and optical properties make them easy to pattern. Indeed, lots of polymers exhibit strong photosensitivity property (ultraviolet epoxy glue, microelectronics resins) and can be soft enough, at an early fabrication stage for imprinting techniques. Direct laser photolithography [19] permits to avoid lateral resolution errors due to cascaded exposures through several masking steps, which is crucial since polymer, like glass, exhibits low index change, thus large waveguide dimensions, and thick layers (several microns) to write through. Another point is their organic nature that makes them compatible with biomolecules. Biofunctionalization during synthesis or after deposition processes is possible as the fabrication temperature process is moderate, which reduces biodamage risks. Deposition techniques are simple; dip-coating and spin-coating process at ambient conditions can be used. All this make polymers compatible with low cost at small/medium-scale production, and thus throwable sensing probes or on demand sensors can be realized. Propagation losses are usually higher than in glass. The main drawback of polymers is their poor robustness which makes them fragile; aggressive conditions may damage them and their lifetime is shorter. There are solutions that combine mechanical robustness and optical transparency of glasses with chemical versatility and ease of fabrication of the polymer using organic–inorganic materials synthesized through the sol–gel process [20].

3.2 Periodical Patterning

Micro/nanostructuration of layer usually uses different techniques for fabricating periodical structure as self-assembly [21, 22], interference, or periodic pattern imprinting. In-plane diffraction gratings (1D photonic crystals) in semiconductors materials can be realized by submicrometer photolithography associated with focused ion beam- [23] or electron beam- [24] etching techniques. Photoinscription techniques are based on the interference pattern created at the crossing of the

writing laser beams. Holographic techniques use diffractive optical elements as phase masks to produce the periodical pattern [25]. The laser beam is diffracted by the phase mask and the interference is created at the cross of the two first-order diffracted beams close to the mask output face. Free space optics offers versatility in writing wavelength when phase mask's technique brings alignment robustness.

Embossing [26, 27] or nanoimprint [28] techniques work well in polymers for several hundreds of nanometers period grating imprinting, are cheap, and reproducible. A master mold is fabricated, usually by dry etching of a glass, which is used to fabricate polymer replicas. Replica molds are used to stamp the polymer in which one desires to imprint the grating. The modulation shape's versatility is mainly limited by the molding process.

Fabrication of vertical (modulation axis perpendicular to integration plane) gratings is widely realized by multilayer techniques for free space dichroïc mirrors or filter. The multilayer structure is made using evaporation [29], sputtering [30], or dip/spin-coating techniques [31] of different layers of alternating high and low refractive indices. Distributed Bragg grating reflectors used in semiconductors lasers are realized using successive epitaxial growths [32].

2D and 3D photonic crystals use as well some kind of embossing technique as nanoimprint lithography applied to soft materials [33, 34]. 2D crystals can be realized using nanosphere lithography; the self-assembly of nanoparticles acts as a mask for further deposition and/or etching techniques [35, 36] to directly realize the crystal or a nanoimprint lithography mask; combined techniques as LIGA mixing X-ray, masking, and imprinting [37] originated from micro-electro-mechanical-systems fabrication can be applied to glass, polymer, or metal materials. For creating patterns that are not homogeneously periodical (defects inclusion for instance), one can use electron beam lithography [38] or inductively plasma etching [39] for creating periodic holes/rods structure, thus exhibiting high index contrast necessary for PBG opening; other techniques such as two-photon absorption-based lithography [40, 41], self-assembly [42], or X-ray fabrication [43] permit 3D fabrication as well.

3.3 Plasmonics Technologies

As plasmons only propagate at metal/dielectric interface, these two types of material are used for plasmonic waveguides' fabrication. Metals are usually noble ones as gold or silver which exhibit strong plasmon coupling. Common methods for metal deposition such as chemical vapor deposition, sputtering methods [44, 45], electrochemical deposition [46, 47], or spattering [48] permit deposition of up to several hundred nanometers thick layer with nanometer accuracy. Metallic layers are deposited either on a glass substrate [49] or on polymer coatings [50, 51]. Micro/Nanopatterning of the metallic layer is performed using lithography techniques used in microelectronics as photolithography [50], nano-imprinting [52], and electron beam lithography [53], mainly electron beam deposition [46]

and focused ion beam etching [45], are also used to fabricate 3D objects or nano-aperture dedicated for out-of-plane photonic integration. These methods are compatible with optical waveguide fabrication techniques and materials. Monolithic integration of planar or 3D optical waveguides with plasmonic waveguides permits to realize in plane architectures including the excitation, interrogation, and detection circuits. Such fully integrated photonic/plasmonic biosensor will be presented in the last part of this chapter. Plasmon can be localized at the surface of metallic nanoparticles that can couple when they are close to one another and give rise to propagating plasmon. Various oxidoreduction reactions can be used for the synthesis of nanosphere colloids [54, 55]. Nanorods can be grown over the spheres using two-step seed-mediated CTAB-assisted protocol [56, 57]. Modifying these protocols one can synthesize various shape nanoparticles as stars [58], bipyramids [59], etc. Nanoshells use a silica core on which metal is deposited [60]. Such particles can tune the plasmon resonance over the 600–1,500 nm range by changing the shell structure parameters as the core/shell thicknesses ratio [61]. 1D, 2D, or 3D arrays of nanoparticles can be fabricated by different techniques [62] based on solvent evaporation, electrostatic attraction, DNA-driven assembly, etc.

4 Detection Principle

Surface-enhanced Raman scattering, infrared spectroscopy, and fluorescence quenching/shifts are widely used techniques in the area of biophotonics [63]. While spectroscopy techniques bring information relative to the composition of biomolecules, fluorescence is used to study reactions between them as in affinity and immunosensors. The use of refractometric techniques combined with biofunctionalized surface [64] and micro/nanofluidic circuits are compatible with integration techniques. Lab-on-a-chip design offers multiparametric detection and measurement. The selectivity of such sensors depends strongly on the immobilized ligands, antigens, or DNA probes that are used to functionalize the sensors surface, but attention must be paid to sensitivity to undesirable fluctuations due to temperature, for instance. High sensitivity leads to high resolution sensors for early diagnostics without the need for biological amplification. In this part, we will focus on the detection principle based on modal effective index changes and its sensitivity depending on the confining properties as an adlayer thickness or the surrounding refractive index for waveguiding structures.

In the case of optical waveguides, the sensor effect is based on the measurement of propagation modes' effective index changes due to the presence and/or binding of the analyte which modifies/perturbs the waveguiding structure. Biodetection uses surface chemistry often at the core/cladding interface of the waveguide. Probing can be realized using either the evanescent part or the central part of the mode field. Specific biosensors, as affinity and immunosensors, commonly integrate a functionalized material area on which the biomolecules to be detected bind.

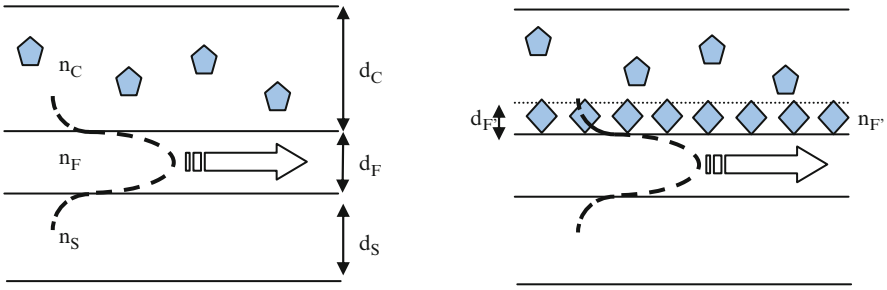

Fig. 2 Modal sensing in 3- and 4-layer structures (pentagons are non-binding molecules; diamonds are adsorbed molecules)

Adsorption/desorption strength and kinetic studies are done by measuring amplitudes and response times of the signal generated by the optical chip. Sensitivity and resolution of the sensors are key parameters to be enhanced so as to permit early diagnostics for more efficient treatment.

Basically, a 1D waveguide transverse structure for biosensing is made of three (substrate, waveguide, and cover) or four (addition of an adlayer) layers with n and d the refractive indices and thicknesses of the layers named S, F, F′, and C standing for substrate, waveguide core film, adlayer film, and cover layer, respectively (see Fig. 2). Sensitivity of a refractometric sensor can be defined as the probing mode effective index changes δN (measured using interrogation techniques) versus waveguide parameters changes as the adlayer thickness or the surrounding refractive index. Using modes' equations, one can derive the sensitivity for a three- or four-layer structure [65]. The sensitivity to the cover layer refractive index in a three-layer system is governed by $\delta N/\delta n_C = (n_C/N) \times (P_C/P) \times \left[2(N/n_C)^2 - 1\right]^{\rho}$ with $\rho = 0$ for TE modes and $\rho = 1$ for TM modes, P the total power carried by the guided mode, and P_C the fraction of total power flowing in the cover.

Sensitivity to refractive index change presents two cases according to whether the cover refractive index is higher or lower than the substrate's one. When cover exhibits low index, the light is best confined at the cover/waveguide core interface and consequently the evanescent field penetration is larger in the substrate. An optimal sensitivity is found for a waveguide layer slightly thicker than the cutoff thickness for which the effective index tends to equal the substrate refractive index value. When the layer is thinner the mode expands infinitely in the substrate region and sensitivity sharply drops down to zero; when the layer gets thicker, the light is more confined in the waveguide core and the evanescent field expands less in the cover so that sensitivity progressively falls down to zero. When the refractive index of the cover layer is higher than the substrate's one, the field penetrates much more in the cover than in the substrate and the interaction with the analyte is stronger. This is all the more true as waveguide thickness gets thinner and evanescent field penetration larger until sensitivity rises up to one at the cutoff thickness. When a layer is adsorbed on the surface of the waveguide, at the core/cover interface,

its thickness adds to the core thickness. If the adsorbed layer exhibits a refractive index higher than the core's one then thickness is even more increased, and inversely in the opposite case. The sensitivity to the adsorbed layer thickness is given by [65] $\delta N/\delta d_{F'} = \left(n_F^2 - N^2\right)/(N \times d_{eff}) \times \left(n_{F'}^2 - n_C^2\right)/\left(n_F^2 - n_C^2\right) \times \left\{\left[(N/n_C)^2 + (N/n_{F'})^2 - 1\right]/\left[\left((N/n_C)^2 + (N/n_F)^2\right) - 1\right]\right\}^{\rho}$ with d_{eff} the effective waveguide thickness defined as the sum of the waveguide film thickness d_F and the penetration depths in the cover and the substrate.

The behavior of the thickness sensitivity versus waveguide thickness is identical as previously mentioned in the low index cover case. Highest sensitivities are obtained for a small waveguide thickness and a high index contrast between the waveguide and the substrate. Such sensitivities permit to measure H_2O monolayer even when only partially adsorbed [65]. Increased sensitivity is found for structures including porous materials due to volume adsorption [66]. So as to optimize the sensitivity to an adlayer thickness without increasing the noise due to undesirable fluctuations caused by temperature for instance, one has to design a reference part in the sensor and/or to reduce the sensitivity part due to refractive indices' changes.

In a way analog to the optical case, evanescent wave sensing can be performed using the field from a surface plasmon propagating at the interface of a metallic layer and a dielectric containing the analyte. W. Lukosz, from the Swiss Federal Institute of Technology, computed plasmonic waveguides sensitivity using perturbation theory and compared it with the optical waveguide sensitivities. Both electromagnetic waves exhibit similar behavior. Plasma waves decay exponentially in the metal and the dielectric. Plasma decay length in the dielectric is larger than for optical waves. As for optical sensors, the field is in interaction with an adlayer and/or a changing index cover layer. Refractometric and adlayer thickness sensitivities are [67] $\delta N/\delta n_C = (N/n_C)^3$ and by $\delta N/\delta d_{F'} = (\Delta z_C)^{-1} \times (\delta N/\delta n_C) \times n_C^3 \times \left(n_C^{-2} - n_{F'}^{-2}\right)$ for gold and silver metals and with Δz_C the penetration depth in the cover.

Lukosz compares the sensitivity of optical and plasmonic waveguides to an adlayer presence which refractive index depends on its protein concentration. The change in refractive index is given for optical TE, TM, and SP waves depending on indices, evanescent fields' penetration depths, and adsorbed surface coverage in weight per unit surface. For affinity and immunosensors using chemoresponsive coatings, the adlayer is thin as compared with the penetration depth. The adlayer thickness sensitivity approximates the overall sensitivity of the sensor. Discussion on resonance peak and free space interrogation techniques permits to compute minimal effective index and surface coverage detection. The authors' assumptions lead to highest predicted sensitivities for optical sensors of an order of magnitude. Change in absorbance, scattering, spatial inhomogeneities, chemical stabilities among others must be taken into account to get closer to real experimental conditions. Nevertheless, due to much longer propagation length for optical sensors, these latest should be more sensitive. Moreover, both TE and TM waves can be supported by an optical waveguide to measure index and thickness of the adlayer with a single mode.

Truncated periodical structures as 1D vertical photonic crystals in dielectric materials are composed of a multilayer stack and can support a surface wave [68, 69]. The surface wave associated to a Bloch mode strongly confined in the stack termination region is greatly sensitive to the structure termination [70] and can be used like an SP-based sensor; both structures can excite the surface wave using the prism-coupling method [71, 72]. This PBG surface wave has been used for thin films' characterization [73]. Application to biosensors has been realized in [72, 74]. Lower damping, use of both TE and TM polarization, and versatility brought by engineering of the crystal are advantages of the dielectric periodical design. Multilayer index contrast, the number and thicknesses of layers, and mode position in the band gap influence the field distribution, the resonant peak position, and its width.

5 Photonic Interrogation Circuits

Optical interrogation techniques will now be discussed; their role is to transduce and enhance the waveguide changes into outcoupled light properties. A number of the optical functions implemented are inherited from the telecommunication domain [75].

5.1 Interferometers

Interferometers are widely used to transform a change in the optical path to a change in light intensity through the interference of two or more beams. The phase difference brought by a change in the trajectory of the optical beam or in the effective index of the propagation mode is detected when mixing the two beams and observing their interference pattern or intensity. As in free space, the guided wave has to be divided to maintain coherence between the two beams. Either the wavefront or the intensity of the incoming beam can be divided. In this section we will focus on amplitude division interferometry. Wavefront division will be studied in more detail through diffraction approach used in phased arrayed waveguides' structures.

Common two-wave integrated interferometers are based on directional couplers and/or Mach–Zehnder architecture. Directional couplers are composed of two, generally single-mode, waveguides parallel to each other and separated by a weak coupling distance. Indeed, when this distance is small enough, the optical modes of the single waveguides overlap and thus energy exchange can occur. Perturbation theory permits to compute the energy exchange between what are modes in the isolated waveguides and to take into account more complex perturbation as the presence of a grating [76]. A simple way to understand this optical tunneling effect for which photons cross the cladding between the waveguides core is to remember that optical ray reflection in a waveguide occurs in the cladding. If one computes the propagation mode transverse profile and effective indices of the

resulting double core structure, results will give two (when isolated waveguides are single mode) modes with even and odd symmetry with different effective indices. For a zero, respectively π, phase change between modes, the modal interference gives rise to optical energy in the incoupling waveguide, respectively the other guide. The sensitivity of this resulting interference pattern on the effective indices' change depends on symmetric and antisymmetric effective indices' proximity as the beat length, for which energy is transferred from one waveguide to another, is inversely proportional to these indices' difference. Closer are the waveguides, lower is the cladding/core refractive indices' difference, higher is the wavelength, or in other words stronger the isolated modes overlap, shorter is the beat length and higher is the sensitivity for a fixed length. Such devices made using ion exchange in glass for the measurement of different concentrated sucrose solutions were fabricated and tested [77] and a resolution of 5×10^{-5} RIU could be achieved. More complex design using multichannel coupling arms have been studied for sensitivity enhancement [78]. This kind of circuits is highly sensitive on fabrication errors as a slight change in the waveguides' coupling distance, shape, size, or refractive index impacts strongly on the outcoupled intensity. A nonsymmetric perturbation puts the coupler out of the synchronization regime and total energy coupling cannot occur anymore, which reduces sensitivity. Fiber-based couplers are used in biophotonics system design for signal extraction and monitoring, laser surgery, spectroscopy, etc. Numerous integrated two-wave interferometers are based on a Mach–Zehnder architecture.

As in free space, this interferometer is composed of a beam splitter, here a power splitter, to divide the signal power by two. Each divided signal experiences specific optical path propagation in each interferometer arm and recombines with the other through a combiner. The power splitter is usually a Y junction, less sensitive to wavelength than directional couplers-based splitters, and dedicated to 1×2 power coupling. The combiner is as well a Y junction used as 2×1 coupler. It is based on modal excitation of the tapered waveguide used to connect two waveguides into one. This variable width waveguide is bimodal at its wider parts and single mode at the end. Depending on phase match of each propagation mode, input power is more or less coupled onto the fundamental and first-order modes. Interferometer output intensity is related to tapered waveguide fundamental mode excitation. The junction part of the Y coupler is critical since fabrication quality and design impact strongly on the adiabatic behavior of the taper and on the insertion losses due to imperfect mode matching at the single-mode waveguide connection. One arm of the interferometer experiences phase shift due to analyte presence and interference is modified. Coupled waveguides can be used as a recombiner to increase the stability in terms of reference and operation point [79]. Specific vertical confining structure [80] has been proven efficient to improve regular resolution [81] to a 2×10^{-5} RIU value obtained in a silicon technology sensor.

An alternative to Mach–Zehnder and directional coupler interferometers, which uses two modes of interference, is the multimode interferometer. Multimode interference (MMI) couplers have first been studied by Ulrich and Tamiya who explored the self-imaging and multiple-imaging phenomena of multimode

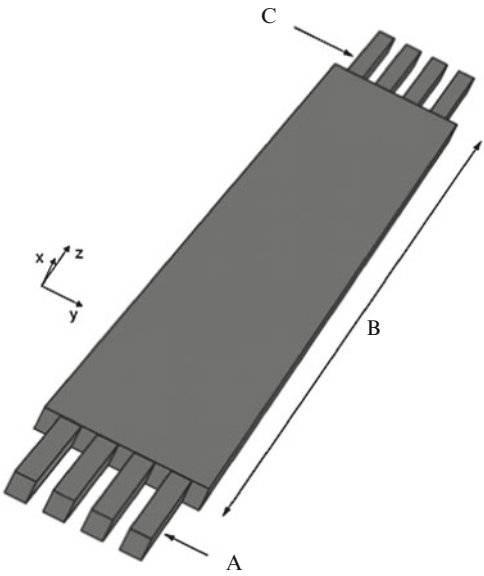

Fig. 3 Topology of a multimode interferometer

waveguides [82]. When light is incident from an input waveguide to a multimode waveguide (see Fig. 3, A are input waveguides, B the length of the multimode region, and C the output waveguides), its transverse intensity profile can be regarded as a composition of guided and radiated modes of the structure. Depending on the incoupled power distribution, radiation mode can be neglected. When light propagates in the multimode waveguide (generally wider than the input single mode), it spreads and bounces on waveguide edges in such a way that it recovers itself and interference takes place. Modal analysis helps to describe specific interference patterns according to propagation length. When all the modes have experienced a several 2π phase shift, their interference reconstructs the image of the input transverse profile; this is called the self-imaging property. The distances at which the self-images occur are multiples of the beat length defined for the two lowest order modes, which depend on their effective indices. At intermediate distances, one can prove [83] that multiple images are created along the transverse direction due to periodization properties. This circuit can be used to realize compact, high-order, homogeneous power splitters. Due to interference nature, this design is highly sensitive to wavelength and fabrication errors, but the shape of this interferometer is simple and easy to pattern. Multimode interference sensitivity has been compared with two modes interference sensitivity for the same interaction length and it was found increased sensitivity for an increasing number of modes. When modes are too numerous, a correct phase matching between them becomes more difficult and the image quality (hence the sensitivity) is lowered [84] for a reasonable device length. Resolution down to 2×10^{-6} RIU has been estimated for a relative humidity sensor based on organic–inorganic sol–gel technology.

5.2 Resonators

Other multiwave interferometers are based on resonator architecture for which the wave propagated several times in the same waveguiding region. The well-known Fabry–Perot cavity when integrated consists in a single-mode waveguide with partially reflective mirrors at the input and output position. The major power of the wave bounces back and forth at each mirror and creates an interference pattern which is constructive when the distance between the mirrors is a multiple of the half effective wavelength. There exists a free range between two wavelength peaks in the transmitted spectrum. The width of the resonant peak depends on the number of interfering waves and thus on the reflectance of each mirrors as well as losses and imperfections of the cavity. When the modal effective index is altered, the effective wavelength changes and the transmission peak is shifted. The interrogation system can measure intensity or wavelength peak position [85].

Another kind of resonator is based on ring architecture which does not need high reflectivity facets. Micro-ring resonators are versatile wavelength-selective elements that can be used to synthesize a wide class of filter functions [86, 87]. Many theoretical designs have been proposed to optimize the filter response and other properties using various coupled resonator arrays [88, 89], while compact resonators have been demonstrated in a number of semiconductor materials [90–92] and glass waveguides [93]. A ring-shaped waveguide is located between two parallel waveguides used as input, transmitted and reflected output ports (see Fig. 4). The light is coupled to the ring thanks to the optical tunneling effect and propagates several (depending on the coupling ratio and on the losses) times around the ring creating interferences. Non-resonant wavelengths cannot be coupled to the ring and are directly transmitted to the output port corresponding to the reflection port of a Fabry–Perot cavity. Resonant wavelength is coupled to the ring and outcoupled to the second output port. The peaks' width is larger when losses are stronger. External losses are due to the coupling between the waveguide ports and the ring and cannot be too small as they are necessary to couple the light to the ring.

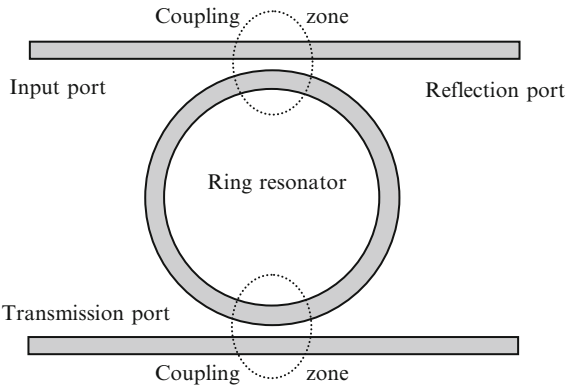

Fig. 4 Topology of a ring resonator

Internal losses of the ring are mainly due to absorption and to bending losses due to coupling of the bent guided mode to the radiation modes. Internal losses must be superior to the external losses to avoid the signal to vanish in the cavity and not being coupled out. Thus strongly confining structures with a high index contrast are needed to limit bending losses; this as well permits small curvature radius ring for high free spectral range values. Glucose sensors have been realized which exhibit a 10^{-3} RIU resolution [94]. Fully integrated platform combining optical and microfluidic circuits using multiplexing schemes lead to higher sensitivity with a 7×10^{-6} RIU resolution [95] for methanol and ethanol detection. Using optofluidic configuration [96] measurand modifies directly the waveguide core index, and a resolution down to 2.8×10^{-7} could be obtained with a noise detection limit of 3.8×10^{-8} RIU.

5.3 Gratings

In the early 1990s, the design of a grating-based spectrometer has been implemented [97–99] into a planar lightwave circuit. The spectrometer is integrated in a vertically single-mode layer and is composed (see Fig. 5a) of single-mode input/output waveguides (Fig. 5a, zones A and E, respectively) connected to laterally strong multimode regions (Fig. 5a, zones B and D, zoom on Fig. 5b) that act as free space propagation zones. The extremities of these regions are curved so as to adapt to the circular wavefront of the propagating light and realize collimating/focusing functions (Fig. 5b shows the angular opening B for a device length A). The light injected from the single-mode input is captured by waveguides regularly spaced along the curved termination; the wavefront is divided and each divided signal is in phase with the other ones. This kind of coupler is called a star coupler due to its shape when numerous waveguides are connected at the input and the output of the free propagation region. The two symmetrical star couplers are connected through waveguides of different lengths which bring dispersive properties and are called the phased arrayed waveguides (PHASAR, zone C) or an arrayed waveguide grating (AWG). Indeed, phase brought by each guide depends on its optical length. When the phase difference, constant for each pair of adjacent waveguides, increases, the reconstructed wavefront at the input of the second star coupler is tilted due to shifted zero phase location. This results in a lateral spatial shift of the focused spot at the output of the second star coupler. This kind of device exhibits free spectral (or effective index change or length difference) range due to periodic behavior. When the wavefront is captured at the input of the phasar, its profile is sampled, and each sample is transposed into the fundamental mode of the phasar guides, the result at the focus line is a periodization of the input mode of the device modulated by the approximately Gaussian profile of the phasar waveguide's fundamental mode. All these parameters have to be taken into account when designing such a device. Phasar devices are usually used as wavelength (de)multiplexers for wavelength division multiplexing in optical

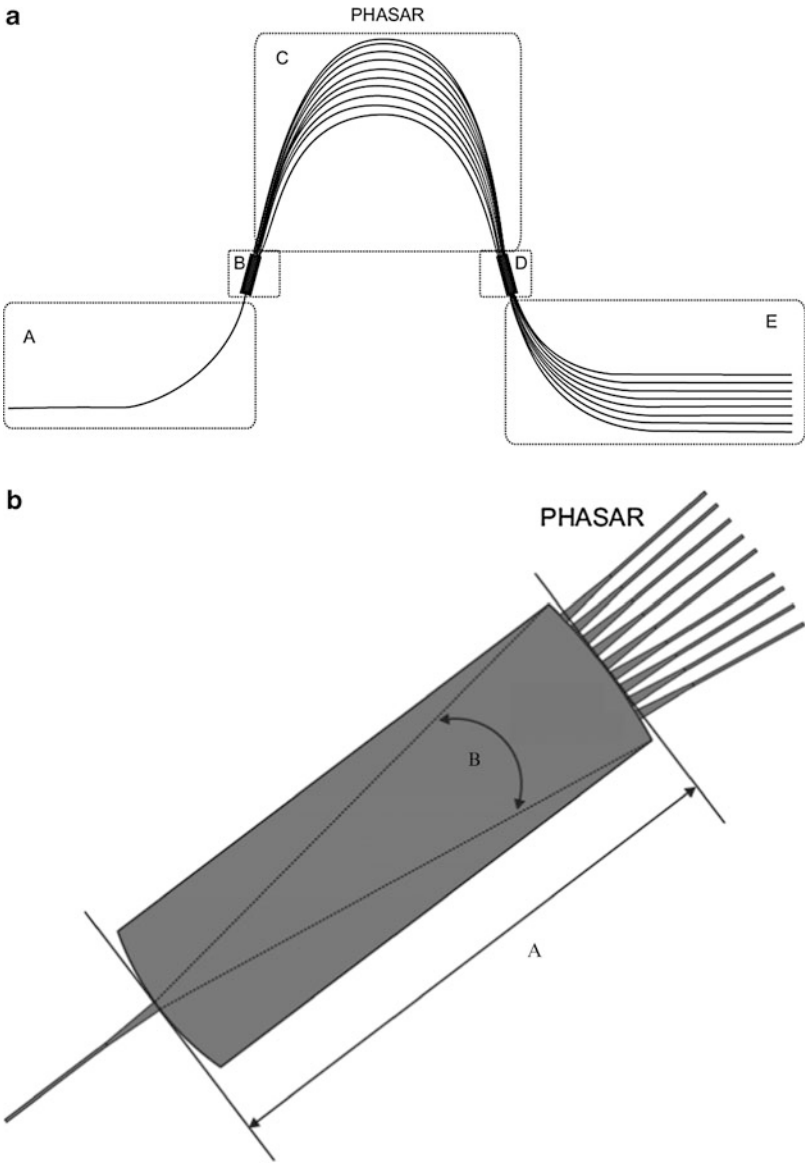

Fig. 5 (**a**) General topology of an integrated spectrometer. (**b**) Zoom on the Star coupler topology

telecommunication networks and exhibit approximately channel separation down to 100 pm and wavelength working range up to 100 nm when used with outcoupling waveguides; specific integrated optics and a line of photodetectors can be used to adapt these performances. It can be used as a spectrometer for signal analysis.

Specific Raman or infrared spectroscopy as well as fluorescence peaks can be monitored. Infrared and visible excitations can be guided to the sample to enhance integration of the system. As up to few micrometers Raman shift can be observed, integration technologies using chalcogenide glasses, specific polymers, or semiconductors may be used for transparency in the middle infrared range interrogation and detection components. When using the circuit at a single wavelength operation mode, the length difference in the phasar can experience an effective index change. The focal spot shift Δs along the output curvature can be related to the phasar waveguide's effective index change ΔN using the approximate relation $\Delta s/\Delta N \approx R/(n.d)$ where R is the curvature radius of the star coupler, n is the refractive index of the waveguide core, and d is the distance between two adjacent waveguides in the phasar. For micrometer resolution in focal shift measure, one can detect theoretically index change down to 10^{-9} RIU assuming a 0.01 dB resolution detection scheme and a single-mode low index difference ($\Delta n = 0.01$) technology. One difficulty may lie in the effective index change homogeneity across the measuring phasar. Indeed, the arrayed waveguides are a few micrometers wide and spaced of several hundreds of micrometers and index inhomogenity in this region would strongly impact the output response of the sensor. Multimode interferometers can be used as well in a phasar architecture. Indeed, an MMI-based power splitter results in multiple images and the phases of these images depend on their lateral position [100]. As the multiple images occur several times along the propagation axis, one can change their phase so as to jump virtually from one propagation distance to another. Moreover, the phase transverse distribution depends on the input image lateral position; changing the phase one can modify the interference pattern so as to self-image the input signal to a different lateral position. Using this approach, one can design an MMI-phasar device for which each output waveguide mode is excited depending on wavelength [101] for multiplexing or depending on effective index [102] for switching or sensing application.

Diffraction-based components are very dispersive due to their periodic design matched for a specific wavelength. Diffraction gratings are commonly used for sensor applications as reflectors in optical fiber [103, 104]. Their use for chemical or biological sensing has been reported in optical fibers [105] and planar configuration [106–108] where the grating is illuminated from an out-of-plane beam at the Bragg angle and reflected diffracted beams are measured versus their outcoupling angle. Semi-integrated solutions consist in using the gratings as in/out couplers with a waveguiding structure [109]. The incoupling configuration needs a rotary stage to scan the different input angles to interrogate the effective index change and thus mechanical problems affect the sensors' performances as response time and accuracy. The sensitivity to the refractive index change of a layer covering the grating is measured through the effective index of the guided mode traveling in the grating. The following equation links the modal effective index and the coupling angle: $N = n_{\text{air}} \times \sin(\alpha) + k \times \lambda/\Lambda$ where N is the effective index, α is the coupling angle, n_{air} is the index of the surrounding medium, k is the diffracted order, λ is the vacuum wavelength, and Λ is the grating period. For small angles, the relative transverse displacement Δu related to an effective index ΔN change when the outgoing beam is focused by a f focal length lens is $\Delta u = f \times \Delta N$. For a 300-mm

focal length and a minimum displacement of 1 μm measurable by a position sensitive detector, a resolution of $\Delta N_{\min} = 3.3 \times 10^{-6}$ RIU in effective index change is expected [109]. Surface gratings or Bragg gratings in waveguides can be used to fully integrate the sensor. Surface grating vector has to be parallel to the surface to permit coupling between vertically guided modes propagating in different horizontal directions. The configuration is then the same as previously, with an in-plane optics and a position detector on the chip surface or edge. The main limitation is due to chip dimension and optical losses that limit the focal length of the focusing optics. Bragg gratings in fiber or waveguides are widely used in telecommunication for filtering and multiplexing purposes. Their wavelength transmission spectrum is tuned depending on grating period and index values. Thus, peak wavelength or output intensity can be monitored using integrated or pigtailed devices as photodetectors and spectrometers.

5.4 Photonic Crystals

The most common configuration for 2D photonic crystal interrogation is to measure the transmission or reflection of a laser beam at normal incidence on the photonic crystal plane. The transmitted/reflected spectrum exhibits a peak at the Bragg wavelength. The peak intensity [33] and/or wavelength [110] are modified when biomolecules bind on the crystal surface and a 2D image showing the shift intensities gives the location and amount of bound molecules. Using low index porous materials [111, 112] or nanorod structuration [113] can enhance the sensitivity of these biosensors by increasing the exchange surface. This 2D-imaging interrogation technique prevents the overall system from being integrated in a plane. For in-plane interrogation, one need to launch the light in the structure using end-face coupling; the light is then vertically confined using a classical slab waveguide structure. 2D photonic crystals including defects [114, 115] form linear, bent, or split waveguides for horizontal confinement and light guidance to the sensing region, as well as cavities or rings [116], to enhance the sensitivity. The cavities in photonic crystals provide strong light confinement and can be designed to localize the electric field in the low refractive index region [114], which makes the sensors extremely sensitive to a small refractive index change produced by biomolecule immobilization on the pore walls. By introducing a point defect into a PC, defect states can be pulled down from the air band or up from the substrate band. The corresponding optical spectrum shows narrow transmission peaks inside the bandgap, whose precise position is determined by the refractive index of the pores. The presence of molecules inside the pores can be detected by monitoring a small spectral shift, especially if high-Q microcavities, which have been reported both theoretically [117] and experimentally [118]. In [14], the authors present a silicon on insulator-fabricated microcavity with a resonant wavelength at 1.58 μm in an hexagonal lattice. The internal surface of holes is functionalized using thermal oxidation followed by aminosilanization. Glutaraldehyde and bovine serum

albumin bindings redshift the resonance of 1–2 nm in wavelength. Authors assume that the minimum adlayer weight measurable is of 2.5 fg for a minimum measurable wavelength shift of 0.1 nm. In another work [38], using a similar configuration, the authors report the detection of less than 4.5 fg of biotinylated-bovine serum albumin. Hexagonal cavity coupling via linear defect waveguide has also been used for the same serum detection [119]; detection limit of 4 fg is compatible with the other experiments and the architecture is compatible with fluid flow cell on chip coupling. The crystal size used for microcavity design is comprised between 10 and 20 μm. By using the following relation [67]: $\Delta N = (\Delta z_C)^{-1} \times \delta N/\delta n_C \times \mathrm{d}n/\mathrm{d}c \times h \times \Delta\Gamma$, with c the protein concentration, h a factor evaluated at 2, and $\Delta\Gamma$ the surface coverage in g/cm, estimated RIU resolution can be calculated under certain assumptions [67] around 10^{-6} value, which is in good accordance with [120].

5.5 Surface Plasmons

Due to its poor propagation length and its large evanescent field penetration in the dielectric, the surface plasmon-based biosensors may be less sensitive than optical biosensors for adlayer detection. Yet, this solution [121, 122] is commercialized since the early 1990s to fabricate immunosensors thanks to antibodies' functionalization and its fabrication simplicity. As opposed with photonic crystals that need nanopatterning techniques, simple thin film deposition techniques on glass slide and further functionalization are sufficient to realize the plasmonic sensor. Classical interrogation techniques are based on prism-coupling techniques [71] to couple the out-of-plane incident laser light to the plasmon. Absorption angle or wavelength monitoring is used to measure affinity strength, kinetics, and concentration [123] with resolution down to 10^{-7} and 10^{-8} RIU [124, 125]; free space Fabry–Perot interferometry combined with prism coupling permits to lower the resolution [126]; and the use of a shot noise limited detection scheme permits to reach resolution down to 10^{-9} RIU [127]. So as to integrate the biosensor, coupling through other techniques is necessary. Gratings, for instance, can couple waves thanks to their modulation property expressed as the grating vector. Matching between optical wave and surface plasmon can then be realized and plasmon frequency can be tuned by using active materials [128]. The same kind of coupling can be realized using a photonic crystal to tune the guided wave propagation constant to the surface plasmon one [129]. On the other way around, finite thickness metal-insulator-metal structures [130], due to thinness of the dielectric (less than 100 nm), couple each central insulator side plasmons together so as to match their overall propagation constant with that of the guided wave. Modifying thicknesses and materials, one can as well engineer the plasmon location; moreover, as this solution uses propagation constant matching instead of mode overlap to couple the waves, the modal shape is not disturbed and modal mismatch losses are reduced. Resolutions of 1.53×10^{-5} RIU and 0.016 nm in thickness for refractometric and affinity sensing modes were obtained [130]. Many works have been reported [131] on nanoparticle

use for localized surface plasmon resonance detection. They are used in imaging for enhancing fluorescence or Raman scattering [132] and permit to reach single-molecule detection. So as to integrate the interrogation, optical or plasmonic waveguides have to be aligned with the nanoparticle emission. Coupling of a single nanoparticle to another can occur when fabricating metallic periodic structures [35] and may be a way to take advantage of localized surface plasmon sensitivity and of surface propagating plasmon functionality. Metallic layers can be deposited on optical fiber or waveguides to fabricate hybrid sensors. In the case of optical fiber [133–136], metal can be deposited on the polished end face to measure the diffracted light [137], on the cone microprism-like tip end of the fiber for back-reflected light detection, or on the core surface after cladding removal to reach a resolution of several 10^{-6} RIU [138]. The main drawback of optical fibers is that they are not directly compatible with planar integration making fiber-plasmon technology difficult to couple with microfluidic systems and other optical components but is well suited to solve issues related to sensing region difficult to reach. Planar waveguides-SP configuration benefits from planar technology facilities and many sensing elements and microfluidic channels can be integrated on the same chip allowing for lab-on-a-chip systems. Multimode [139] and ridge [140] waveguides allow for double TM or TE-TM plasmon excitation for film thickness and refractive index measurements. Referencing [141] and multiplexing [142] techniques used in optical sensors can be applied to SP sensors. Depending on the vertical and horizontal structuring, plasmon propagation length can be increased and coupled to grating structure for sensitivity enhancement purposes; 1.3×10^{-6} RIU resolutions have been obtained [143]. Planar integration allows as well hybridization with microelectronics components as detectors [144] close to the plasmonic structure to reduce the noise and obtain better resolution: 1.2×10^{-4} RIU have been obtained. Planar optics-SP systems are commercialized by the American company Sensata and integrate light source, metal/dielectric interface, and detectors. 5.2×10^{-4} RIU resolutions have been demonstrated [145] for a cheap integrated system. Sensors using index-dependent plasmon damping and glass technology [146] and sensors based on plasmon interferometry using Mach–Zehnder [144, 147] or coupled plasmons of a thin metal layer in silicon on insulator technology [148] permit to reach 10^{-6} RIU resolutions under the assumption of a 0.01 dB intensity change resolution optoelectronics detection scheme. Other work has been realized including nanoparticle doped layers where the different localized plasmons interact with propagating SP. To avoid the nanoparticle from influencing the binding process [149] gold particles were encapsulated in a hydrogel matrix whose swelling, when binding occurs, modifies gold particles distance and shift the SP resonant frequency.

6 Conclusion

After a brief presentation of the photon and plasmon manipulation mechanisms, we have presented fabrication technologies and the detection principle based on refractometric sensing. Through analysis of the working principle of different photonics

architectures and their results in terms of resolution for sensors realized with different technologies, we could detect some interesting solutions for high resolution-integrated biosensors.

Plasmonic techniques are the most mature ones; gold is widely used, easy to deposit, and well-established immobilization techniques are available. As we could see in the section devoted to interrogation techniques, they lead to the best resolution when in a free space configuration. Nonetheless, when integrated in a planar configuration, most of the techniques do not reach yet the beyond 10^{-6} RIU level.

Some of the metals, silicon, SiO_2, and polymers' biofunctionalization processes are known and associated fabrication techniques are compatible. Multimode interferometers, resonant structure based on rings, 1D and 2D photonic crystals, and plasmon waveguides and circuits seem to be the most promising solutions. Dielectric technologies are compatible with metal deposition and widely mastered in electronics and photonics integration; mixing optics and plasmonics structure could be a solution to take advantage of each technique. A fully integrated system on a chip using matured plasmonic biosensors coupled with long-distance propagation and functionalities (division, multiplexing, referencing, multiwave interferometry, etc.) of optics would permit to develop a high resolution lab-on-a-chip for bioapplications.

Extensive work has been realized on nanoparticle for imaging applications. The coupling between nanoparticles, realization of periodical metallic nanostructures, and 2D photonic crystals including defects are other solutions for the detection of low concentration analyte in a small volume and can be parts of the platform. Micro/nanofluidic circuits would help to bring such small volumes to the desired particle/hole/elementary pattern to transpose the perturbation in a periodical system and provide the resonance resolution to a localized detection.

Design strategy based on the coupling of the different effects will permit to increase sensitivity. Hybrid fabrication process based on different materials will allow the implementation of such designs. Low-cost for small/medium scale production or on-demand biosensors can be realized as well through chemical processes. Finally, the ease of use of integrated technologies will allow a non-specialist user to obtain the desired data. Integration should lead to a better spreading of these efficient tools for improving the overall health research and diagnostic system.

References

1. Stamnes JJ (1986) Waves in focal regions. Adam Hilger, Bristol and Boston
2. Saleh BEA, Teich MC (2007) Fundamentals of photonics, 2nd edn. Wiley, New York
3. Hill KO, Meltz G (1997) J Light Technol 15(8):1263–1276
4. Joannopoulos JD et al (2008) Photonic crystals: molding the flow of light, 2nd edn. Princeton University Press, Princeton, NJ
5. Maier SA (2007) Plasmonics: fundamentals and applications. Springer, Heidelberg
6. Sarid D (1981) Phys Rev Lett 47:1927–1930

7. Weeber J-C et al (2005) Appl Phys Lett 87:221101
8. Charbonneau R et al (2008) Sensor Actuat B 134:455–461
9. Ghoshal A, Kik PG (2008) J Appl Phys 103:113111
10. Van Roijen R, Verbeek GH (1995) Philips J Res 49:279–292
11. Vandertoi JJGM et al (2010) Prog Quant Electron 34:135–172
12. Masini G et al (2008) Germanium photodetectors enable scalable silicon photonics Proc. SPIE: Optoelectronics & communications DOI: 10.1117/2.1200806.1141
13. Palestino G et al (2008) Sensors and Actuators B 135(1):27–34
14. Lee M, Fauchet PM (2007) Opt Express 15:4530–4535
15. Lemaire PJ et al (1993) Electron Lett 29(13):1191–1193
16. Svalgaard M (1997) Electron Lett 33(20):1694–1695
17. Almeda RM, Marques AC (2008) Mat Sci Eng B 149:118–122
18. http://www.teemphotonics.com Website still available on 20th December, 2011
19. Kribich RK et al (2007) Photonic circuits writing with UV pulsed laser, Physica Status Solidii C 4(1)
20. Brinker C Scherer G (1989) Sol-gel science: the physics and chemistry of sol-gel processing, Elsevier Science (USA), Academic Press
21. Xie J et al (2006) J Cryst Growth 292(2):227–229
22. Zhang J et al (2009) Curr Opin Colloid Interface Sci 14(2):103–114
23. Cakmak B et al (2010) Microelectron Eng 87(11):2343–2347
24. Sun KW et al (2005) Opt Quant Electron 37:425–432
25. Tahir BA, Ali J, Rahman RA (2006) J Optoelectron Adv Mat 8(4):1604–1609
26. Lukos W (1995) Sensor Actuat B 29:37
27. Voros J (2002) Biomaterials 23:3699–3710
28. Plachetka U et al (2008) Microelectron Eng 85:886–889
29. Behrndt KH, Doughty DW (1966) J Vac Sci Technol 3(5):264–272
30. Deparis O et al (2009) Plasma Process Polym 6:S746–S750
31. Kakisawa H et al (2010) Mat Sci Eng B 173(1–3):94–98
32. Mizutani M et al (2006) Phys Status Solidi C 3(3):659–662
33. Endo T et al (2010) Sensor Actuat B 148:269–276
34. Block ID et al (2006) Sensor Actuat B 120:187–193
35. Zheng YB, Huang TJ (2008) Surface plasmons of metal nanostructure arrays: from engineering to active plasmonic, original report, 1535-5535/532.00
36. Jeong GH (2010) Fabrication of low-cost mold and nanoimprint lithography using polystyrene nanosphere. Microelectron Eng Arch 87(1):1978–1983
37. Maleka CK, Saileb V (2004) Applications of LIGA technology to precision manufacturing of high-aspect-ratio micro-components and -systems: a review. Microelectron J 35:131–143
38. Zlatanovic S et al (2009) Sensor Actuat B 141:13–19
39. Skivesen N et al (2007) Opt Express 15:3169–3176
40. Tormen M et al (2004) Microelectron Eng 73–74:535–541
41. Zhou M et al (2008) J Mater Proc Technol 200:158–162
42. Kim HJ et al (2007) Sensor Actuat B 124:147–152
43. Romanato F et al (2003) Microelectron Eng 67–68:479–486
44. Thirstrup C et al (2004) Sensor Actuat B 100:298–308
45. Kim DW et al (2008) Mat Sci Eng B 149:242
46. Das G et al (2008) Microelectron Eng 85(5–6):1282–1285
47. Sakai N et al (2009) J Electroanal Chem 628(1–2):7–15
48. Matsushita T et al (2008) Sensor Actuat B 129:881–888
49. Hong S-H et al (2010) Microelectron Eng 87:1315–1318
50. Daviau R et al (2010) Microelectron Eng 87:1914–192
51. Pedersen RH et al (2007) Microelectron Eng 84:895–898
52. Buzzi S et al (2008) Metal direct nanoimprinting for photonics. Microelectron Eng 85:419–24
53. Hohenau A et al (2006) J Microelectron Eng Arch 83(4–9):1464–1467

54. Boisselier E, Astruc D (2009) Chem Rev 38:1759–1782
55. Daniel MC, Astruc D (2004) Chem Rev 104:293–346
56. Jana N et al (2001) J Phys Chem B 105:4065–4067
57. Nikoobakht B, El-Sayed MA (2003) Chem Mater 15:1957–1962
58. Nehl CL et al (2006) Nano Lett 6:683–688
59. Liu M, Guyot-Sionnest P (2005) J Phys Chem B 109:22192–22200
60. Brinson BE et al (2008) Langmuir 24:14166–14171
61. Oldenburg S et al (1998) Chem Phys Lett 288:243–247
62. Glomm WR (2005) J Disp Sci Technol 26:389–414
63. Popp J, Strehle M (2006) Biophotnics – visions for better health care. Wiley, Berlin
64. Kumar CSSR (2005) Biofunctionalization of nanomaterials. Wiley, Weinheim
65. Tiefenthaler K, Lukosz W (1989) J Opt Soc Am B 6(2):209–220
66. Tiefenthaler K, Lukosz W (1985) Thin Solid Films 126:205–211
67. Lukosz W (1991) Biosens Bioelectron 6:215–225
68. Meade RD et al (1991) Phys Rev B 44(19):10961–10964
69. Vandenbem C (2008) Opt Lett 33:2260–2262
70. Robertson WM (1999) J Light Technol 17:2013–2017
71. Kaneko F et al (2002) Mat Sci Eng B 22:409–412
72. Konopsky VN, Alieva EV (2007) Anal Chem 79:4729–4735
73. Villa F et al (2002) Opt Lett 27:646–648
74. Shinn M, Robertson WM (2005) Sensor Actuat B 105:360–364
75. Keiser G, Kao F-J (2008) Prog Biomed Opt Imaging 9(38):69911E1–69911E8
76. Nishihara H, Haruna M, Suhara T (1985) Optical integrated circuits. McGrawHill, New York
77. Luff BJ et al (1996) J Opt Lett 21(8):618–620
78. McCosker RJ, Town G (2010) Sensor Actuat B 150:417–424
79. Luff BJ (1998) J Light Technol 16(4):583
80. Prietoa F et al (2003) Sensor Actuat B 92:151–158
81. Shipper EF et al (1997) Sensor Actuat B 40:147–153
82. Ulrich R, Kamiya T (1978) J Opt Soc Am 68(5):583–592
83. Soldano LB, Pennings EM (1995) J Light Technol 13(4):615–627
84. Mazingue T et al (2007) Opt Commun 278:312–316
85. Palestino G et al (2008) Functionalization of nanostructured porous silicon microcavities for glucose oxidase detection. Sensors & Actuators B 135:27–34
86. Little BE et al (1997) J Lightwave Technol 15:998–1005
87. Chin MK, Ho ST (1998) J Lightwave Technol 15:1433–1446
88. Little BE et al (2000) IEEE Photonics Technol Lett 12:320–322
89. Griffel G (2000) IEEE Photonics Technol Lett 12:810–812
90. Little BE et al (1998) IEEE Photonics Technol Lett 10:549–551
91. Chin MK et al (1999) IEEE Photonics Technol Lett 11:1620–1622
92. Suzuki S, Oda K, Hibino Y (1995) IEEE J Lightwave Technol 13(8):1766–1771
93. Kominato T et al (1992) IEEE J Lightwave Technol 10(12):1781–1788
94. Chen Y et al (2009) Front Optoelectron China 2(3):304–307
95. Carlborg CF et al (2010) Lab Chip 10:281–290
96. Li H, Fan X (2010) Appl Phys Lett 97:011105
97. Smit MK (1988) Electron Lett 24(7):385–386
98. Takahashi H et al (1990) Electron Lett 26(2):87–88
99. Dragone C (1991) IEEE Photonics Technol Lett 3(9):812
100. Bachman M, Besse PA, Melchior H (1994) Appl Optics 33(18):3905–3911
101. Porque J et al (2000) Opt Commun 183:45–49
102. Kribich RK et al (2004) Thermo-optic switches using sol-gel processed hybrid materials, Integrated Optics and Photonic Integrated Circuits. Edited by Righini, Giancarlo C.; Honkanen, Seppo. Proceedings of the SPIE, Volume 5451, pp. 518–528
103. Hill KO et al (1978) Appl Phys Lett 32:647

104. Liu Y (2001) Advanced fiber gratings and their application. Ph.D. Thesis, Aston University
105. Canning J (2008) Laser Photonics Rev 2(4):275–289, Wiley, USA
106. Clerc D, Lukosz W (1993) Sensor Actuat B 11:461–465
107. Brandenburg A, Gombert A (1993) Sensor Actuat B 17:35–40
108. Desfours C et al (2009) Hybrid materials, France
109. Lukosz W et al (1990) Sensors and Actuators B: Chemical Volume 1, Issues 1-6, January 1990, Pages 585–588
110. Chan LL et al (2007) Sensor Actuat B 120:392–398
111. Block ID, Chan LL, Cunningham RT (2006) Sensor Actuat B 120:187–193
112. Block ID, Chan LL, Cunningham RT (2007) Microelectron Eng 84:603–608
113. Zhang W et al (2008) Sensor Actuat B 131:279–284
114. Busch K et al (2007) Phys Rep 444:101–202
115. Nair RV, Vijaya R (2010) Prog Quant Electron 34:89–134
116. Hsiao F-L, Lee C (2009) Procedia Chemistry 1:417–420
117. Srinivasan K, Painter O (2002) Opt Express 10:670–684
118. Akahane Y et al (2003) Nature 425:944–947
119. Dorfner D et al (2009) Biosens Bioelectron 24:3688–3692
120. Cunningham BT et al (2002) Sensor Actuat B 85:219
121. Homola J (2006) Surface plasmon resonance based sensors, vol 4, Springer series on chemical sensors and biosensors. Springer, Berlin
122. Liedberg B, Nylander C, Lundstrm I (1983) Sensor Actuat B 4:299–304
123. http://www.biacore.com Website still available on 20th December, 2011
124. Kabashin AV, Patskovsky S, Grigorenko AN (2009) Opt Express 17(23):21191–21204
125. VanWiggeren GD et al (2007) Sensor Actuat B Chem 127(2):341–349
126. Ho HP et al (2007) Opt Commun 275:491–496
127. Wang X et al (2011) Opt Express 19(1):107–117
128. Massenot S et al (2007) Opt Commun 275:318–323
129. Skorobogaity M, Kabashin AV (2006) Appl Phys Lett 89:143518
130. Liu Y, Kim J (2010) Sensor Actuat B 148:23–28
131. Sepulveda B et al (2009) Nano Today 4:244–251
132. Schneider T et al ISSN 1864-6972, LIFIS online 06/09/10
133. DeMaria L, Martinelli M, Vegetti G (1993) Sensor Actuat B 12(3):221–223
134. Fontana E (2002) IEEE Trans Microw Theory Tech 50(1):82–87
135. Brambilla G (2010) Opt Fiber Technol 16:331–342
136. Huang K-T, Lin T-J, Hsu M-H (2010) Biosens Bioelectron 26:11–15
137. Kurihara K et al (2004) Anal Chim Acta 523(2):165–170
138. Piliarik M, Vaisocherova H, Homola J (2007) Sensor Actuat B Chem 121(1):187–193
139. Stocker P et al (2004) Sensor Actuat A Phys 116(2):224–231
140. Wang TJ et al (2004) IEEE Photonics Technol Lett 16(7):1715–1717
141. Harris RD et al (1999) Biosens Bioelectron 14(4):377–386
142. Lin CW et al (2004) The second Asian and Pacific rim symposium on biophotonics, APBP 2004. pp 223–224
143. Lin CW et al (2006) Sensor Actuat B Chem 113(1):169–176
144. Nikitin PI et al (1999) Sensor Actuat B Chem 54(1–2):43–50
145. Suzuki A et al (2005) Sensor Actuat B Chem 106(1):383–387
146. Homola J (1997) Sensor Actuat B 41:207–211
147. Sepulveda B et al (2006) J Opt A Pure Appl Opt 8(7):S561–S566
148. Debackere P et al (2006) Opt Express 14(16):7063–7072
149. Matsui J et al (2005) Anal Chem 77(13):4282–4285

Part III
Surface Plasmon Resonance

Surface Plasmon Resonance Bioanalytical Platform to Appraise the Interaction Between Antimicrobial Peptides and Lipid Membranes

Mihaela Gheorghiu, Sorin David, Andreea Olaru, Cristina Polonschii, and Eugen Gheorghiu

Abstract Surface Plasmon Resonance (SPR) sensors gain a wide applicability as a direct, label-free, and real-time approach to analyze biomolecular reactions occurring in the vicinity of a functionalized sensor surface. Lipid-modified sensor chips provide an accessible platform for SPR exploration of membrane—peptide interactions. While pore formation and subsequent membrane destabilization is a common feature for the interaction process between a large number of compounds such as peptides, toxins, and viruses with lipid membranes, this process has been just recently related to sensing applications.

Using POPC and melittin as model systems we show that SPR quantitative appraisal of the interaction between an antimicrobial peptide and lipid-modified sensors is capable to provide both novel sensing avenues and detailed mechanistic insights into effects of pore-forming compounds.

This new and exciting biosensing avenue is based on assessment of the nonmonotonous, concentration-dependent effect of pore formation and enables quantitative evaluation of the whole process, including full dissolution of the lipid.

Insight will be provided on a novel kinetic model that relates, via the Transfer Matrix, surface plasmon resonance (SPR) data with actual concentrations of interacting partners. In agreement with literature data, association and dissociation rates, concentration thresholds, evolution within each interacting layer of lipid and peptide concentrations, as well as of peptide to lipid ratios are derived. Although based on Biacore 3000 data, the general principles and guidelines may be applicable to other SPR assays. This biosensing approach is suitable to an entire set of pore-forming compounds including antimicrobial peptides and toxins and different lipid matrices. Recent developments in terms of surface

M. Gheorghiu (✉) • S. David • A. Olaru • C. Polonschii • E. Gheorghiu
International Centre of Biodynamics, 1 B Intrarea Portocalelor, 060101 Bucharest, Romania
e-mail: mgheorghiu@biodyn.ro http://www.biodyn.ro

W. Fritzsche and J. Popp (eds.), *Optical Nano- and Microsystems for Bioanalytics*,
Springer Series on Chemical Sensors and Biosensors (2012) 10: 183–210
DOI 10.1007/978-3-642-25498-7_6,

functionalization and electro-optical integration toward a portable analytical platform are discussed.

The proposed approach combined with appropriate design of the experimental protocol adds a new depth to the classic SPR investigation of peptide–lipid interaction offering a quantitative platform for detection, improved understanding of the manifold facets of the interaction, and for supporting the controlled design of novel antimicrobial compounds.

Keywords Bio(mimetic) sensing platform • EIS • Kinetic analysis • SPR

Contents

Abbreviations

DOPC	1, 2-Dioleoyl-*sn*-glycero-3-phosphocholine
DOPG	1, 2-Dioleoyl-*sn*-glycero-3-[phospho-*rac*- (1-glycerol)]
HBM	Hybrid bilayer membrane
HEPES	4-(2-Hydroxyethyl)-1-piperazineethanesulfonic acid
P/L	Peptide to lipid ratio
POPC	1-Palmitoyl-2-oleoyl-*sn*-glycero-3-phosphocholine
SPR	Surface plasmon resonance

1 Introduction

Pore formation and subsequent membrane destabilization is a common feature for the interaction process between a large number of compounds, such as peptides, toxins and viruses, with lipid membranes [1–3].

Assessment of the complete profile of interaction between pore-forming compounds and (cellular and artificial) membranes has potential impact in disease diagnosis, toxicology, and pharmaceutical research [4–6] and represents an important, yet under-investigated issue in biosensing.

Using the advantages offered by surface plasmon resonance (SPR) technique, i.e., label-free, real-time monitoring of analyte–ligand interaction, we propose

a novel biosensing approach based on dynamic, quantitative assessment of the concentration-dependent nonmonotonous processes associated with lipid- or cell-modified SPR platform—target analyte (i.e., pore-forming compound) interaction [7, 8]. The particular cases of melittin, a natural pore-forming peptide, and Triton X 100 detergent are considered. The comprehensive SPR measurements on melittin binding to an artificial lipid membrane (POPC) using lipid-modified L1 sensor chip (Biacore) and on cellular platforms, via a combined SPR and impedance approach, are used as a dynamic framework to highlight how to (a) retrieve quantitative information on membrane processes, (b) advance a biosensing tool, and (c) cope with matrix instability.

2 Why Antimicrobial Peptides?

Antimicrobial peptides offer an attractive solution to the problem of increasing resistance of bacteria to conventional antibiotics. The formation of transmembrane pores in the target cell is suggested as a compelling mechanism for direct interaction with membranes and subsequent lysis of the pathogen cell membrane.

Despite the already documented efficient antimicrobial activity against a wide range of pathogens and viruses [9], the potential cytotoxic activity against mammalian cells [10] limits the direct use of these peptides as therapeutics.

There are continuous efforts to modify the native antimicrobial peptides or to design new peptides to achieve better specificity against microbial infections while limiting host organism cytotoxicity.

Elucidation of the complete interaction mechanism represents a key step in peptide design and in detection of new pore-forming compounds. It requires quantitative appraisal of these compounds and access to lipid platforms for quantitative assessment of the interaction kinetics.

3 SPR Lipid Membranes

Recent advances in the preparation of stable membrane-like surfaces and the commercialization of sensor chips has enabled widespread use of SPR in protein–membrane interactions. The prerequisite was the development of surfaces that mimic natural membranes. There are two main approaches for preparation of membrane-mimetic surfaces: the hybrid bilayer membrane (HBM) and immobilized membrane bilayers (tethered). Both systems provide a well-defined model membrane in which both upper and lower layers are fluid and with an additional aqueous layer between the chip and the membrane essential for the functional incorporation of transmembrane proteins—while retaining good electrical resistance, excellent stability, and fluidity in order to sufficiently represent a pseudo-natural environment. HBM are formed on a hydrophobic surface that is generated by the deposition of an alkanethiol self-assembled monolayer (SAM) on the gold surface.

Biological molecules can be easily attached to carboxymethylated chips via amino, thiol, aldehyde, or carboxyl groups. Such covalent attachment of ligands to a dextran-layered sensor chip is probably the most common in Biacore applications. Alternatively, membrane bilayers can be tethered on the gold chip by the use of thiolipids (a thiol group, linked via a hydrophilic linker to the lipid headgroup) and thio-peptides (have a flexible linker comprising a short peptide that possesses at one end a thiol group and on the other end a lipid) [11].

One of the most popular surfaces for SPR lipid platforms is Biacore's L1 sensor chip that allows capture of liposomes or even subcellular preparations. Similar to other Biacore sensor chips, it has a dextran layer attached to the surface of the gold, while specificity is given by proprietary lipophilic groups adorning the dextrane. Here, intact liposomes are stably retained after the injection [12] or spontaneously rupture forming a bilayer [13, 14]. The dispute around actual conformation is explained by the intricate role of surface charge density and electrostatic interaction (variable with experimental conditions) in formation of supported phospholipid bilayers on molecular surfaces [15].

The type of lipids used and the dimension of the liposomes influence the SPR profile upon lipid immobilization: a maximal SPR response has been reported in the range of 11,000–12,000 RU, yet if mixtures of zwitterionic and charged lipids are used, such as 1, 2-dioleoyl-*sn*-glycero-3-phosphocholine (DOPC) and 1, 2-dioleoyl-*sn*-glycero-3-[phospho-*rac*- (1-glycerol)] (DOPG), lower amounts 7,000–8,000 RU are retained [16].

A typical protocol to form lipid membranes involves: sensor surface pretreatment to activate the binding sites, formation of the lipid membrane via liposome attachment and spreading, and chip regeneration (e.g., injections of suitable detergents).

Lipid vesicles are prepared by dissolving the lipid (e.g., POPC) in chloroform followed by drying under vacuum in a rotary-evaporator for several (three) hours. The lipid film is hydrated with (HEPES) buffer, subjected to (five) sonication cycles, 30 min/cycle and the suspension is extruded 22–25 times (using the Mini-extruder—Avanti Lipids, Alabaster, USA) through 1 μm pore membrane (polycarbonate). Stock solution (1.5 mM) aliquots are stored at +4°C prior to use.

Two–three brief washes with 100 mM NaOH are then used at a higher flow rate to remove loosely bound vesicles. An injection of bovine serum albumin is used finally to cover all nonspecific binding sites and to check for the quality of the lipid coverage.

This procedure yields homogeneous surfaces that are stable and can be directly used for binding studies.

4 Melittin–Lipid Interaction

Melittin, a 26-amino acid component of bee venom [17], is often employed as a pore-forming model compound in interaction studies with natural and artificial membranes [18–20]. Various methods are used for investigation: infrared spectroscopy

[21], fluorescence [22], transmission electron microscopy [10], X-ray diffraction [23], circular dichroism [24], and SPR [25, 26], while the distinct steps of the model of interaction, have been experimentally validated using different lipid membrane matrices: liposomes, supported lipid bilayers, micelles, phospholipid multilayers [19, 27].

Accordingly, the interaction is a complex, multiphase process, applicable to most pore-forming compounds, that exhibits concentration dependency with distinct thresholds [3, 25, 28, 29], through which melittin induces membrane disruption and lysis upon spontaneous binding to biological and model membranes [18], followed by reorientation [21], accumulation, insertion, and pore formation [3]. This interaction depends on the lipid composition and charge, on the hydration level and on the peptide concentration, orientation on membrane surface, and protonation state [30, 31].

5 Monitoring the Whole Process of Interaction Between Melittin and a Lipid Matrix

Assessment of peptide–lipid interactions by SPR assays has been reported before recommending the technique as a powerful tool for investigating real-time interactions between membrane-disrupting compounds and lipid matrices. It gave information on initial membrane attachment of pore-forming proteins [32–34] and membrane-interacting peptides [25, 26].The use of SPR and various lipid systems enabled differentiation between different steps in mechanism of action of membrane-active peptides [34–36]. Previous SPR studies on model membranes have used small (<0.37 μM) or extremely large (90 μM) peptide concentrations and 6–16 min injection times, emphasizing either attachment and insertion of the peptide [26, 28, 29] or membrane solubilization [2, 37–40], i.e., lipid disintegration as a function of peptide concentration.

These SPR analyses related the SPR sensorgrams (i.e., time variation of the reflectance dip position, or SPR angle) to the quantity of interest, assuming one effective layer (characterized by an effective thickness d_{eff}, and dielectric constant ε_{eff}) on top of the SPR chip. Simplified kinetic models [26, 28, 29], two-state or parallel reaction models, have been proposed based on equilibrium values of the overall SPR signal, without any reference to the dynamics of interacting partners.

In contrast, a longer (1 h) injection of melittin (1.6–3.6 μM), combined with a detailed kinetic model and a realistic fitting procedure [7, 8], relates the evolution of interacting compounds to the "evolving" layers on the chip and is able to provide the dynamic assessment of the whole process of melittin—lipid matrix interaction, including: melittin attachment, insertion, and membrane solubilization at various peptide-to-lipid ratios (P/L).

To this end, a mathematical model comprising a system of kinetic equations to describe the evolution of lipid and peptide concentrations within distinct layers on the chip as well as a procedure, based on Transfer Matrix Analysis, to relate the kinetics to the SPR has been designed. This approach is applicable to other SPR

techniques (waveguide spectroscopy [41, 42] and interferometry [20, 43]) and not only to the Biacore assay [44].

A representative SPR experiment concerning peptide–lipid interaction is presented in Fig. 1a and highlights the distinct steps involved in the assay: (a) Sensor chip pretreatment; (b) Formation of lipid matrix as a model cell membrane for investigation of the pore-forming peptide binding; (c) Removal of the loosely bound vesicles structures; (d) Peptide–lipid interaction; and (e) Sensor regeneration. Figure 1b reveals the multiphase process involved in peptide-to-lipid interaction: attachment, attachment and insertion, and lipid dissociation.

6 SPR Bioanalytical Platform

The effective thickness d_i and dielectric constant ε_i of each layer in the system shape the reflectivity spectrum, influence the SPR angle and are important parameters in the construction of a transfer matrix (see Fig. 2). The Transfer Matrix [45] involves repeated application of the Fresnel equation [46], and relates, in conjunction with a kinetic model, the SPR angle shift to the surface concentration of compounds in the multilayer system associated with the experimental platform.

The transfer matrix combines the entire set of field components and involved layers and can therefore be used to calculate the reflectivity of the complete system provided that thickness and refractive index of all layers, the wavelength, and the angle of incidence θ are given.

To derive the time evolution of the dielectric permittivity, for each layer comprising a mixture of different dielectric media, the following equivalence has been used [47]: $\varepsilon_{\text{ech}}(t) = \sum_i \Phi_i(t) \times \varepsilon_i$ where $\Phi_i(t)$ is the actual volume fraction of the compound indexed i that obeys the $\sum_i \Phi_i(t) = 1$ rule. According to Fig. 3, four distinct layers are considered: the layer above the lipid where the peptide attaches, the actual lipid layer where melittin inserts and eventually forms aqueous pores, the layer on top of L1 matrix where, upon lipid dissociation, the peptide can attach, and last, the bulk, characterized by a mixture of running buffer and peptide of various concentrations.

The equivalent dielectric permittivities for each layer have been considered within the transfer matrix to compute the variation of the position of the reflectance minimum (the SPR angle) and relate it with the SPR data. This algorithm and the proposed model have been used to fit the experimental data, to derive the concentration thresholds and kinetic parameters for each constitutive phase (association, insertion, and lipid membrane destabilization) and provide time evolutions of actual P/L ratios within each layer.

The hallmarks of this fitting routine are:

1. Numerical integration of the set of four coupled differential equations for the concentrations of each component in the multilayer system.

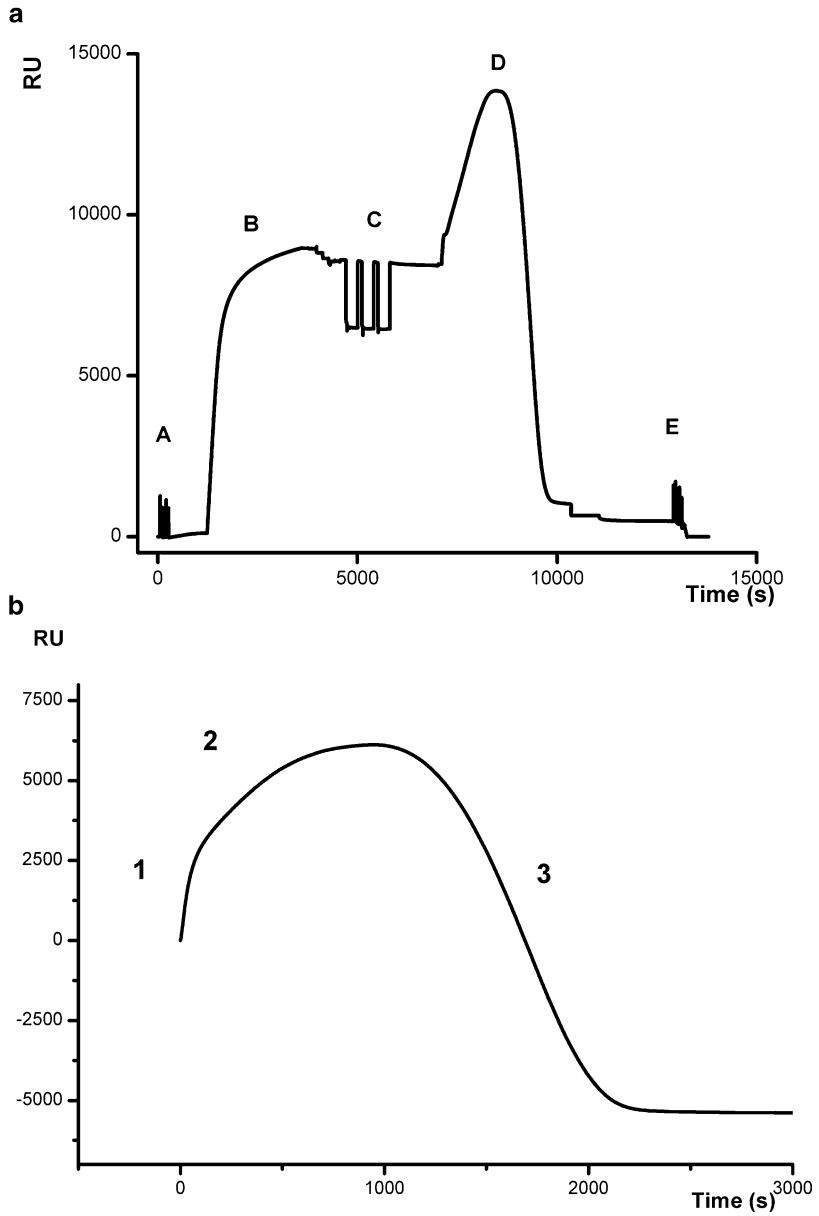

Fig. 1 (**a**) Steps of the SPR assay (A) Sensor chip pretreatment; (B) Formation of lipid matrix as a model cell membrane for investigation of the pore-forming peptide binding; (C) Removal of the loosely bound vesicles structures (D) Peptide–lipid interaction and (E) Sensor regeneration. (**b**) Representative sensorgram detailing step (D), Peptide–lipid interaction normalized to the moment of peptide injection (1) attachment, (2) attachment and insertion, (3) lipid dissociation

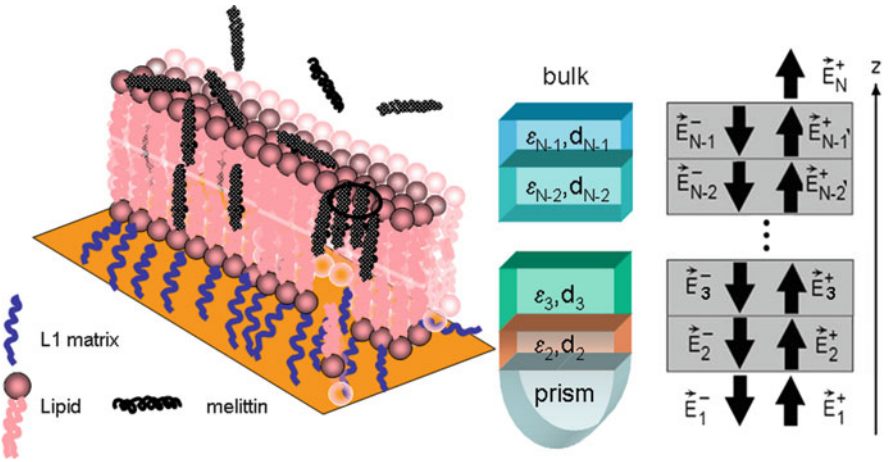

Fig. 2 The multilayer structure of the lipid platform, each component, characterized by thickness d_i and complex dielectric constant ε_i. The set of layers is considered stacked between a hemispherical prism (Biacore 3000 set-up) with dielectric constant ε_p and the semi-infinite medium (running buffer) with dielectric constant ε_h. The corresponding Transfer Matrix is constructed by considering the field distribution, reflection, and transmission within each component of the multilayer system

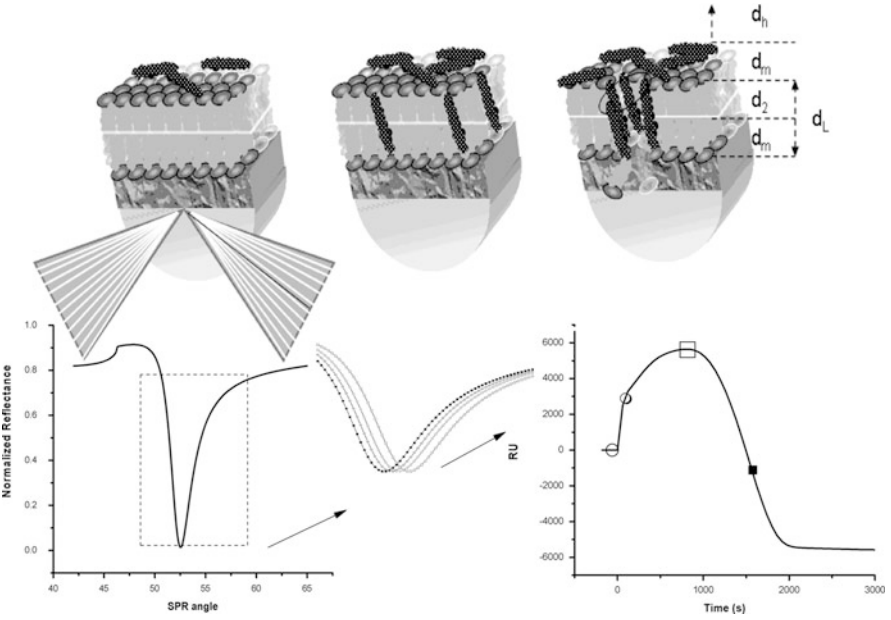

Fig. 3 Schematic representation of peptide–lipid interaction steps, the equivalent layers of the lipid platform and the corresponding SPR data (SPR angle and sensorgram)

2. Computation of the effective permittivity of the distinct layers. Relate volume concentrations to corresponding volume fractions in the distinct layers.
3. Derivation of the SPR angle based on the application of the transfer matrix on the multilayer system. As the SPR sensorgram is expressed in relative units, 8.2 Relative Units for every millidegree SPR angle shift equivalence relation has been used for Biacore 3000 data [48].

The detailed numerical analysis of SPR measurements for the kinetic characterization of the complete interaction process between melittin and lipid membranes is made under two assumptions, based on experimental findings: (1) a homogeneous planar lipid coating uniformly covers the L1 surface and (2) the interaction of the peptide with the lipid matrix is not dependent on the multi-bilayer structure of the lipid coating.

The first assumption is consistent with current knowledge (theoretical [49] and experimental [13, 15] evidences) on rupture of adsorbed (zwitterionic) lipid vesicles to form supported phospholipid bilayers when strong interaction with the substrate surface, appropriate surface charge density, appropriate buffer, and a prior large-size liposome accumulation to the surface conditions are met. Based on the second assumption, different thicknesses of the lipid matrix (not individual layers) are considered to account for different SPR signals upon lipid immobilization.

7 The Kinetic Model

The dynamics of the nonmonotonous process of interaction, as revealed by the SPR signal, is highly dependent on the balance between the kinetics of melittin association and insertion, which in turn are modulated by the surface and bulk concentrations of melittin. With increasing peptide binding, upon reaching a threshold, melittin begins to insert into the membrane and undergoes reorientation [50].

Designed in compliance with the present mechanistic knowledge, the set of kinetic equations are related to distinct steps of interaction (e.g., attachment and insertion) and provide time evolution of both lipid and melittin concentrations as function of several threshold concentrations (m_0, m_i, and m_L) and constants: K_{a1} for association, K_{a2} for melittin insertion, K_{d0} for melittin dissociation, and K_{dl0} for lipid membrane destabilization:

– Association

$$m'[t] = K_{a1}N_m(N_l[t] - m[t]) \times H[N_l[t] - m[t]] - K_{d0} \times N_l[t]/N_{l0} \times m[t] \times H\left[N_l[t]\right] - k_{ai} \times m'_{ins}[t], \quad (1)$$

where K_{a1} is the association constant, N_m is the bulk concentration of melittin, $N_l[t]$ is the number of available "binding sites" associated with the immobilized lipid,

m'_{ins} stands for kinetics of melittin insertion in the lipid matrix, and K_{d0} affects the dissociation induced by flow conditions.

– Insertion

$$m'_{\text{ins}}[t] = K_{\text{a2}}\left(m[t] - m_0\frac{N_1[t]}{N_{\text{l0}}}\right) \times \left(m_{\text{i}}\frac{N_1[t]}{N_{\text{l0}}} - m_{\text{ins}}[t]\right) \times H\left[m[t] - m_0\frac{N_1[t]}{N_{\text{l0}}}\right] \times H\left[m_i\frac{N_1[t]}{N_{\text{l0}}} - m_{\text{ins}}[t]\right], \tag{2}$$

where K_{a2} is the insertion constant, $m[t]$ is the concentration of associated melittin, m_0 is threshold for melittin reorientation and insertion into the membrane, and m_{i} is the threshold concentration that limits the progression of insertion.

– Lipid destabilization and dissociation

$$N'_1[t] = -K_{\text{dl0}}\frac{N_1[t]}{N_{\text{l0}}}\left(m[t] - m_{\text{L}}\frac{N_1[t]}{N_{l0}}\right) \times H[N_1[t]] \times H\left[m[t] - m_{\text{L}}\frac{N_1[t]}{N_{\text{l0}}}\right] \tag{3}$$

where m_{L} is the threshold concentration of associated melittin that triggers lipid destabilization, K_{dl0} is the lipid dissociation constant

– Direct melittin binding to the uncovered L1 chip, as melittin is injected as well during lipid dissociation stage,

$$m_{\text{L1}}{}'[t] = K_{\text{a3}}N_{\text{m}}(RR - N_1[t]/N_{\text{l0}}) \times (N_{\text{CO}} - m_{\text{L1}}[t]) \times H[RR - N_1[t]/N_{\text{l0}}] \times H \times [N_{\text{CO}} - m_{\text{L1}}[t]] \tag{4}$$

where K_{a3} is the related association constant, RR is the percentage of uncovered sensor and N_{C0} is the concentration of L1 binding sites for melittin.

Due to the structure of the kinetic equations (comprising terms accounting for thresholds—represented by step functions H[x]), and the inherent complexity of the SPR response of the evolving layers involved in peptide–membrane interaction, no analytical solution exists.

The set of coupled differential equations [8] provides the dynamics for each of the components within the multilayer system which are related via the transfer matrix to the SPR angle corresponding to the actual SPR data (Fig. 3). As such, the model allows a high degree of flexibility with no a priori consideration of a molecular model of interaction. It enables compact evaluation of rather diverse SPR data (e.g., different peptide concentrations on similar lipid coverage—Fig. 4a, and extreme P/L ratios—Fig. 4b), independent of the sensor characteristics. These representative data at different P/L ratios show significant variability in the measured values, dependent on the peptide concentration and lipid immobilization level. Peptide concentration influences the slopes of the upward and downward regions (attachment and insertion and lipid destabilization

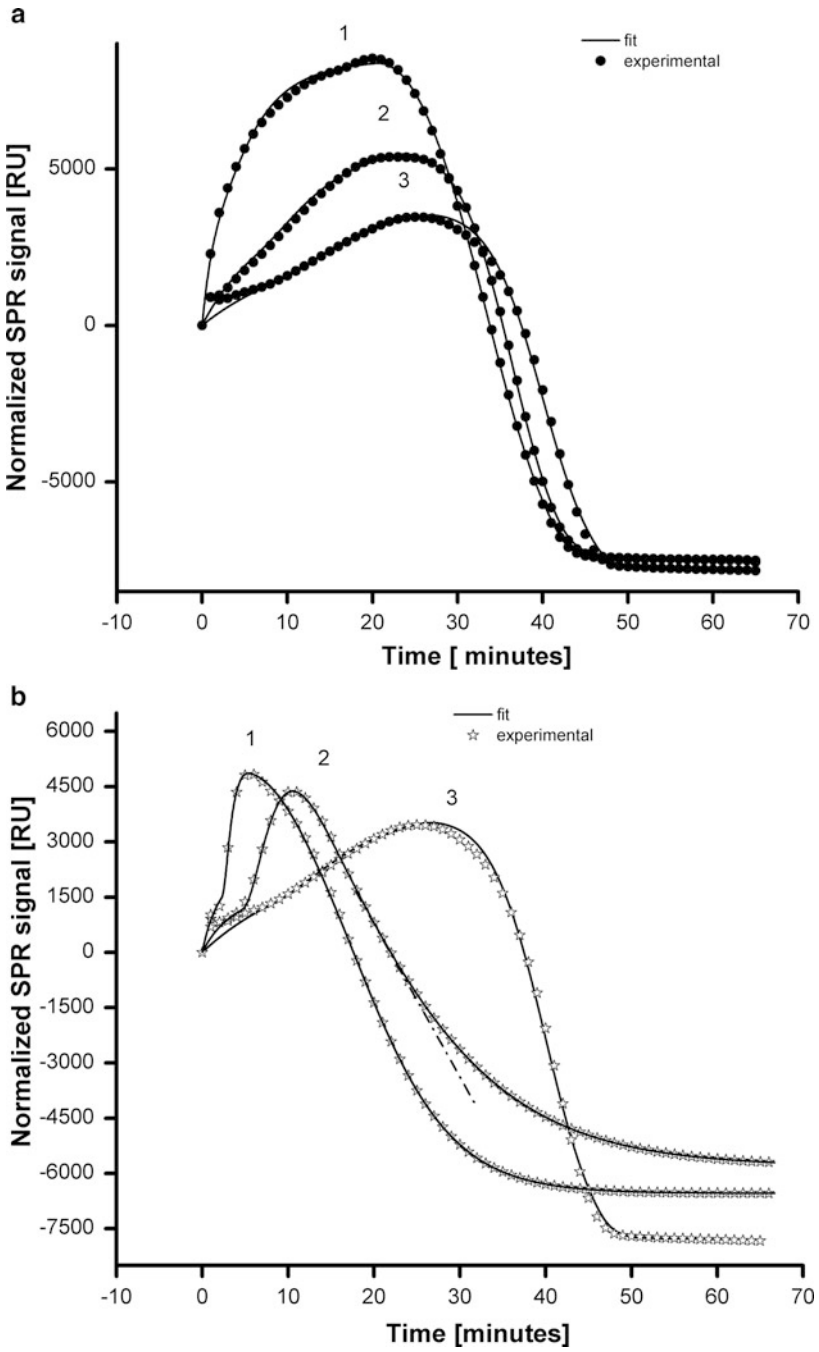

Fig. 4 (**a**) Characteristic SPR sensorgrams (experimental and fitted curves) corresponding to different melittin concentrations (1) 2.55 μM, (2) 2.43 μM, and (3) 2.35 μM, injected to similar

respectively): the higher the peptide concentration, the steepest the slope and the earlier the occurrence of the peak, while the lipid amount in conjunction with peptide concentration, modulates the level of the peak (the higher the peptide concentration and the lipid level, the higher the summit level).

8 Relevance

The proposed sensing platform has far-reaching implications:

1. Provides the pattern of evolution of the complex, nonmonotonous process of peptide–lipid interaction and a direct way to quantify the concentration of peptide.
   Fitting the experimental data (Fig. 4), the model provides kinetic parameters and time evolutions of concentrations of melittin, attached and inserted (Fig. 5), and related volume fractions of the lipid (Fig. 6), comparable with data reported in the literature.
   Despite model limitations (e.g., advancement of insertion process assessed only as the progress of the areas where full insertion of melittin has occurred, a homogenous structure of the lipid membrane), we consider that the evolution of the effective peptide attached or inserted provided by our approach is consistent with the actual overall molar values. As such, the evolution of the actual P/L ratios can be as well derived [8].
2. Enables novel biosensing avenues:
   In "classical" biosensing platforms, there is a monotonous time evolution of measured parameter(s) as a function of the target analyte, thus allowing for equilibrium analysis or use of arbitrary chosen time points to examine an interaction or for quantification.
   Since the interaction between a pore-forming compound and a lipid membrane is related to a nonmonotonous effect determined by the target analyte, a novel sensing procedure to quantify the concentration of melittin is proposed [7].
   The pattern of evolution of the complex, nonmonotonous process of peptide–lipid interaction provides a direct way to quantify the concentration of melittin. Specifically, the concentration of the test compound can be inferred from T_{max}, the time point when the nonmonotonous evolution of SPR signal due to peptide–lipid interaction reaches its summit. The timing of this characteristic value is related to the ability of the pore-forming compound to insert into and destabilize the lipid matrix. It occurs during pore formation and destabilization of lipid membrane

Fig. 4 (continued) lipid coverage ~8,550 RU lipid. (**b**) Characteristic SPR sensorgrams (experimental and fitted curves) corresponding to extreme P/L: low lipid versus high melittin concentration (1) 6,500 RU lipid—3.62 μM melittin and (2) 5,800 RU—2.81 μM melittin, high lipid versus low melittin concentration (3) 8,600 RU lipid—2.35 μM melittin

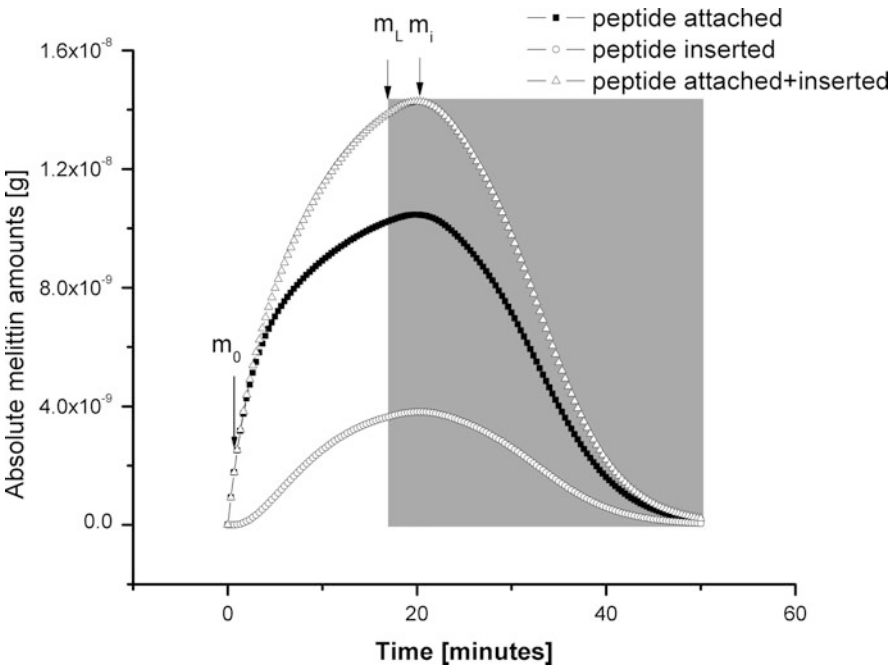

Fig. 5 Characteristic evolutions of derived absolute amounts of peptide attached and inserted on POPC lipid matrix (8,800 RU) upon ~1 h injections of melittin (2.6 μM). Also indicated are the time points when they are attained: the threshold concentrations for initiation of insertion, m_0, of lipid dissociation, m_L, and limiting peptide insertion, m_i. Lipid dissociation that affects both peptide insertion and attachment is indicated as the *gray zone*

phase due to dynamic removal of lipids (and associated peptide) from the sensor surface once a destabilization threshold of peptide is reached.

The timing of this characteristic value is related to the ability of the pore-forming compound to insert into and destabilize the lipid matrix. It occurs during pore formation and destabilization of lipid membrane phase due to dynamic removal of lipids (and associated peptide) from the sensor surface once the destabilization threshold of peptide is reached. Such a calibration curve (Fig. 7a), based on $T_{max,}$ does not require any theoretical assumption or modeling, yet for large T_{max} (corresponding to small peptide concentrations) $1/T_{max}$ is asymptotically progressing toward 0, rising experimental difficulties in determining T_{max}.

As revealed by the occurrence of T_{max}, there are two aspects that lead to a nonlinear behavior:

- Lipid dissociation occurs upon melittin accumulating and reaching sequentially two threshold concentrations: one corresponds to the beginning of insertion, and the other one to initiation of lipid destabilization.
- The larger the peptide concentration, the larger the SPR signal related to the direct peptide–lipid binding. This process is significant in the first few, up to 5 min (for the highest melittin concentration considered 3.5 μM), masking the

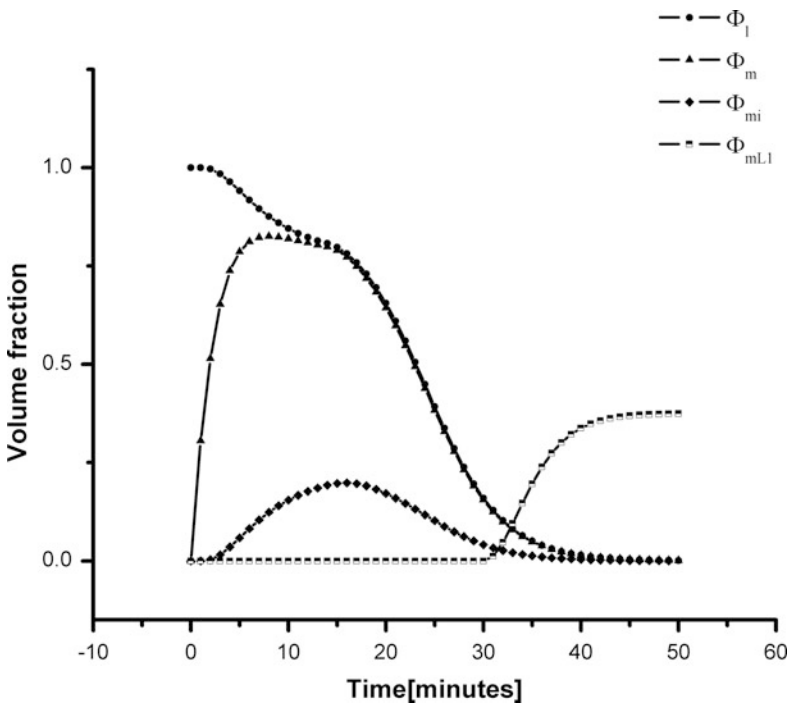

Fig. 6 Derived volume fractions of lipid, within the lipid matrix, and of melittin a) associated with the lipid Φ_m, inserted in the lipid matrix Φ_{mi} or associated directly with the L1 matrix Φ_{mL1} upon lipid destabilization and removal

decrease in the SPR signal due to lipid dissociation and correspondingly delaying the occurrence of T_{max}.

Additionally, as revealed in Fig. 7b, the proposed set of differential equations can be also used to assess T_{ins} (the moment when the peptide insertion is initiated), which proves useful in deriving the concentration of the pore-forming compound and hence supports the "biosensing process". The linearity domain is nevertheless limited since, for large peptide concentrations, the lipid dissociation and possible bulk effects can shadow the SPR signal connected to melittin attachment and insertion.

We envisage that this approach is able to support accurate detection and that the related analysis platform, could be further extended to membranes with different lipid compositions and other pore-forming compounds, as well.

3. Provides checking tools for sensing platform optimization: L1 regeneration conditions are not fully optimized [51, 52]; hence lipid coating reproducibility in time can change dramatically. Therefore, assessment of melittin attachment directly to the chip [as described by (4)] in relation to different regeneration conditions could support improvement of the experimental protocol toward sensing applications.

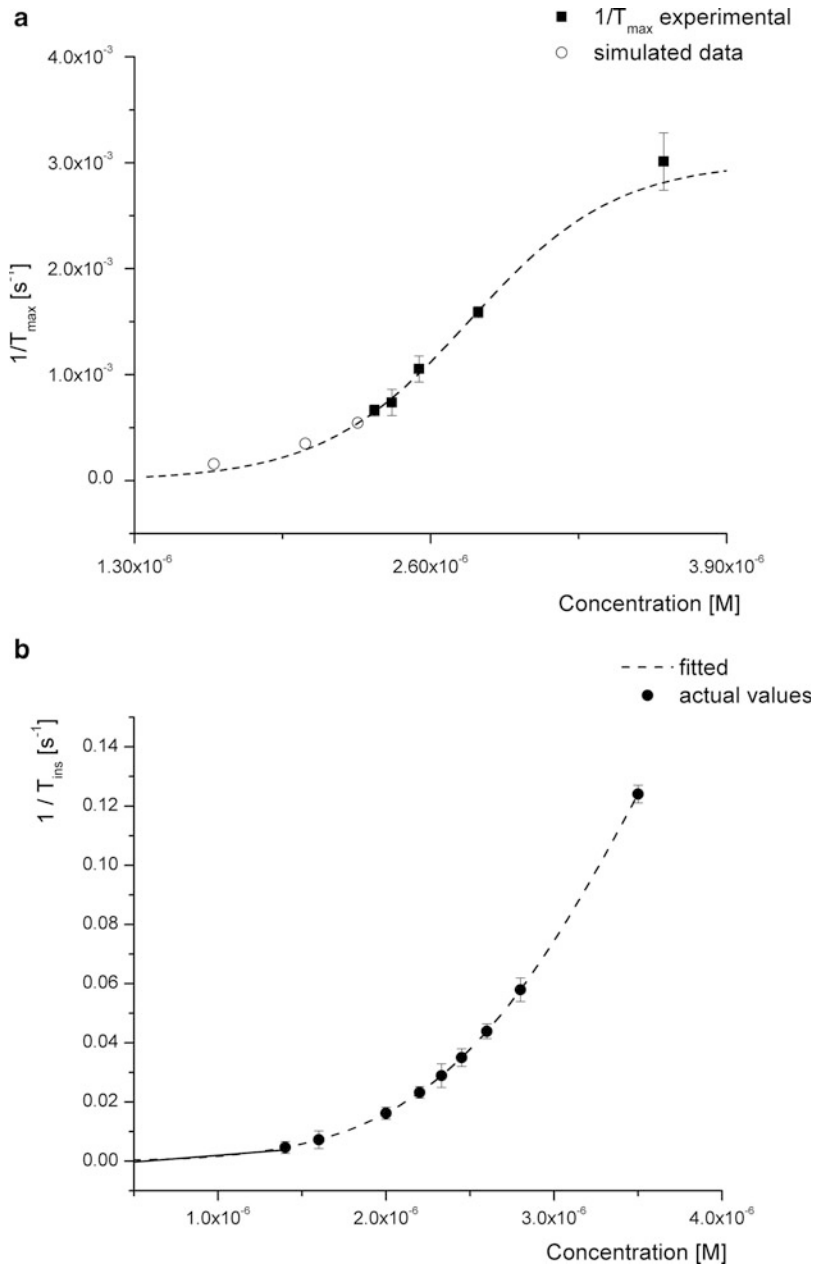

Fig. 7 (**a**) Calibration curve based on T_{max}, the time point when the nonmonotonous evolution of SPR signal due to peptide–lipid interaction reaches its summit, within the experimental data *square* and simulated *open circle* based on the model and corresponding to low peptide concentrations. (**b**) Calibration curve based on the moment when the peptide insertion is initiated (m_0 threshold according to the kinetic model)

Moreover, the same transfer matrix approach can be used in characterizing the L1 matrix and subsequently the lipid membrane attached on the surface.

4. Supports insight on interaction mechanisms depending both on various antimicrobial peptides and lipid composition of lipid membrane. We consider the L1 chip as a scaffold to analyze the process of interaction between a pore-forming compound and a lipid matrix. The composition of the lipid membrane developed on top of the L1 chip depends only on the composition of the vesicles in solution upon lipid matrix formation. Moreover, the target of antimicrobial peptides is believed to be the lipid membrane regions of bacterial and fungal biomembranes, regardless of their final cellular targets, with lipid composition (including cholesterol) playing a determinant role [53].
   As many factors (including temperature, lipid composition, pH, or presence of a synergistic partner peptide) determine how membrane-active peptides interact with the lipid bilayer, different modes of membrane interaction have been suggested: (a) binding to the bilayer or water interface; (b) "carpet"-like interaction; (c) detergent-like action; (d) disintegration of the bilayer producing bicelle-like discs; (e) transient or long-lived "barrel-stave"; (f) "toroidal" or "wormhole" pores; (g) insertion into a transmembrane alignment; (h) formation of a "slit"; (i) diffusion across the membrane; (j) modulation of the membrane curvature, induction of non-bilayer lipid phases and/or translocation via an inverted micelle [54].

Among these, most commonly considered are pore formation via a "barrel – stave" mechanism or by membrane solubilization (detergent-like) "carpet" mechanism. Both mechanisms depend on the peptide charge and the mode of self association in the target membrane [3, 55]. Nevertheless, the latter gains more and more support from experimental and molecular dynamics simulation data [56–58] as the general model of interaction of antimicrobial peptides with lipid membranes.

Though the SPR approach does not provide details on the molecular interaction mechanism, it is worth noting that our results show that lipid dissociation is largely dependent on randomly associated/inserted melittin, with no defined pore structure. This makes our results consistent with "carpet-like"/"toroidal pore" models. A further confirmation is provided by SPR analysis of specific action of a detergent (Triton X 100) on POPC lipid membranes revealing similar, nonmonotonous patterns of evolution (Fig. 8).

The proposed approach for lipid matrix formation is applicable for various lipid matrices with slight modification of the immobilization protocol. Tests have already been made for simple anionic (POPG) and mixtures of anionic and zwitterionic lipids (POPG:POPC) with 2.6 μM melittin concentration (Fig. 9).

As such, the proposed approach is a suitable experimental platform for accessible evaluation of the interaction of peptides/pore-forming compounds, capable to support detailed mechanistic research in conjunction with complementary techniques. Having in view the similar interaction patterns reported [2] for virus mimetic attack, we stress on a wider applicability of our approach for quantitative

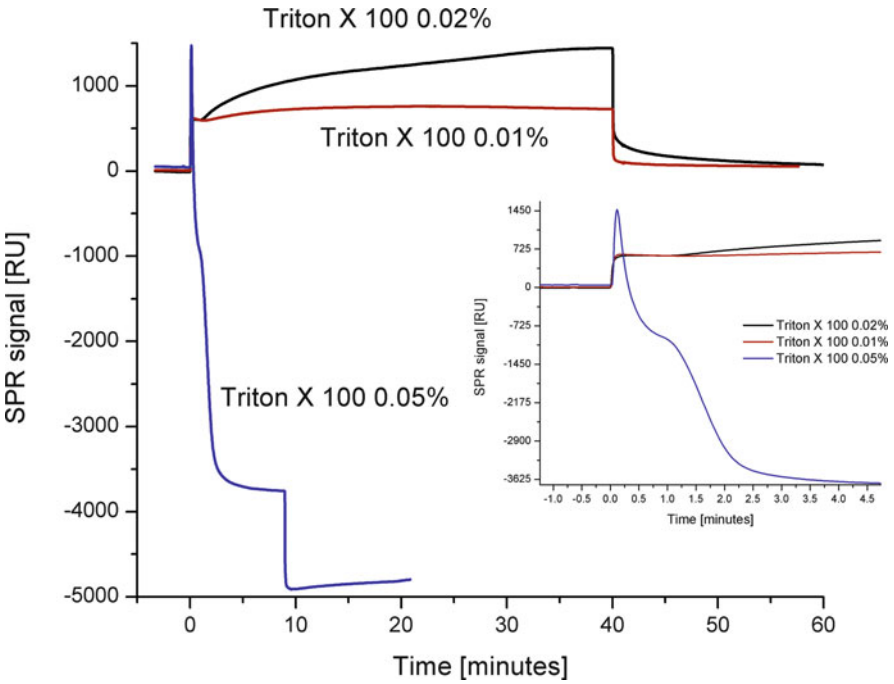

Fig. 8 Lipid detergent interaction for three concentrations of Triton X 100 a nonionic detergent. *Inset*, focus on the first 4 min after injection revealing nonmonotonous dynamics concentration dependent

assessment of the effect of other pore-forming compounds on different lipid membranes, thus on a broader biophysical significance. Nevertheless, the assessment of other systems should involve amendments of both kinetic model and Transfer Matrix approach in agreement with data concerning layer structure, molecular arrangements, etc.

9 Whole Cell Approach

While further enrichment with proteins (proteoliposomes [59]) and cholesterol (mixed liposomes [10, 60]) is possible for these synthetic membranes, the complexity and dynamics of natural cell membranes recommends the use of cellular extracts or directly the target cells.

There are inherent limitations of SPR assessment of biological cells related to: (a) the depth of the sensitivity domain (reaching down to several hundreds of nanometers) versus the actual dimensions of the cells (microns), (b) the large cell dimensions versus the fluidics of commercial instrumentation (e.g., 20 μm for

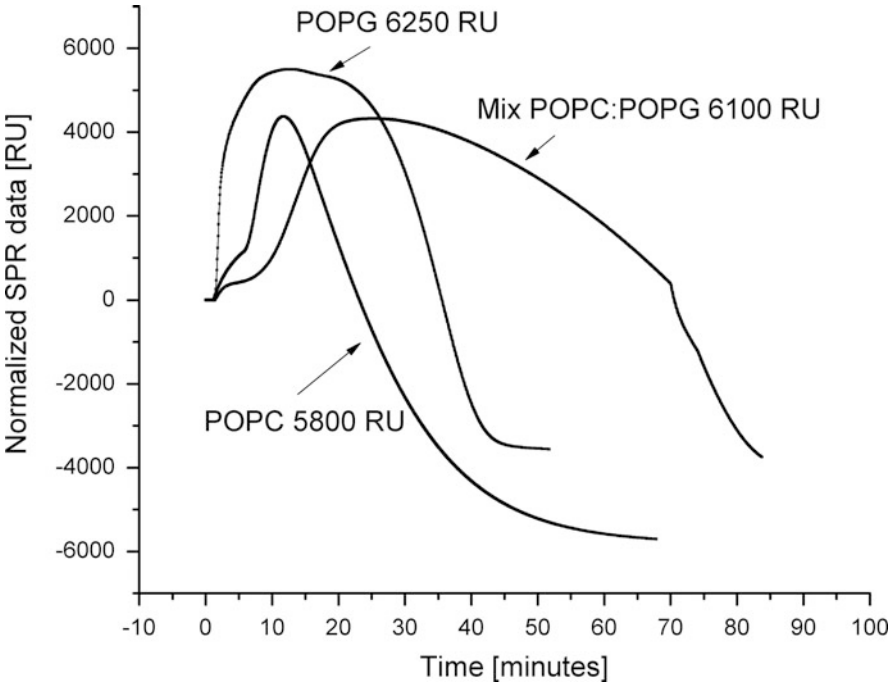

Fig. 9 Interaction of melittin with lipid matrices of different compositions: zwitterionic (POPC), anionic (POPG), and mixture (3 POPC:1 POPG); 2.6 μM melittin concentration

Biacore) rendering a high probability of flow cell clogging, (c) the surface and volume inhomogeneity related to highly variable biological cells randomly attached to the surface.

The SPR analysis using commercial instrumentation such as Biacore 3000 and the proposed kinetic model presented so far is based on the fact that all changes in adsorbed mass within the SPR sensitivity domain are revealed by the corresponding SPR value. While decomposition (seen as lipid dissociation, with subsequent removal from the surface due to continuous injection of lipid-free running buffer with peptide) is encompassed by the model, there are inherent limitations of the Biacore SPR approach (basically an "effective refractive index" method) to reveal localized, discrete processes such as the eventual deformation of a cell.

Hence, in relation to the necessary cellular assays, we propose a combined SPR and impedance approach to test for the direct effect of model pore-forming compounds on mammalian cells. This approach could bring significant advantages versus (pre)clinical trials (prone to high costs and rising ethical issues) for optimization and evaluation of the efficiency in modifying the native antimicrobial peptides or designing new peptides to achieve better specificity against microbial infections while limiting/eliminating their cytotoxic activity.

To this end, a combined SPR and impedance system based on the SPREETA TSPR2K23 SPR sensor (Texas Instruments, TX, USA) has been developed within

the International Centre of Biodynamics, Bucharest, Romania. The combination of SPR with impedance investigations is straightforward as the thin gold films used for the generation of surface plasmon waves can be simultaneously used as sensing electrodes.

Impedance evaluation has matured into a powerful technique for monitoring cellular systems. It is based on measuring the response (current and its phase) as a function of frequency of an electrochemical system to an applied weak, noninvasive oscillating potential (up to 50 mV) in the frequency range 1 Hz–10 MHz.

As proven by the commercially available ECIS type devices [61], attachment and spreading of cells on the electrode surface change the impedance in such a way that morphological information of the attached cells can be directly inferred enabling noninvasive, continuous assessment of cell attachment, spreading, and proliferation. The inherent sensitivity and ability to eliminate stray effects are dependent on the electrode geometries, measurement set-up, integration of controlled flow through capabilities, and complementary analytic methods (e.g., optical). The technique (a) can provide valuable real-time cellular activities of viable cells, (b) it is a label-free method, (c) it is more sensitive in monitoring early cell responses compared with traditional image analysis, and (d) it reveals quantitative information about the cell responses in a dose-dependent manner. Nevertheless, the appropriateness/uniqueness of the circuit model influences the quality of the parameters derived from experimental data. Both microscopic [62–64] and circuit models [65, 66] are available and can be integrated for real-time data analysis and the combination with SPR could provide some internal control conditions (Fig. 10).

The circuit elements required for accurate modeling of the impedance experimental data are presented in Fig. 11 and are related to: interfaces at the two electrodes—constant phase elements (CPE), allowing suitable parameterization of chip nonhomogeneities; R1 and R3—representing the metal layer's resistance and C3 and C4 the equivalent capacitance of the cell layer covering each electrode; R2 and C2 are the resistance and capacitance of the solution over the electrodes [66].

From the difference between the impedance of the chip with cells and the impedance of the chip without cells (in the same experimental conditions), we obtain the information on cell impedance as:

$$Z^*_{\text{cells}} = Z^*_{\text{withcells}} - Z^*_{\text{withoutcells}}. \tag{5}$$

The corresponding resistance and capacitance of cell layer is derived for each frequency and time points.

The system developed combines the label-free monitoring capabilities of both techniques for affinity detection and cell-based biosensing helping to overcome some of the limitations both techniques have when used alone.

The system schematically presented in Fig. 12 enables optical and electric addressing of interfacial processes related to a wide choice of functional surfaces and flow conditions. Polymer thin films or matching liquids (this is the convenient approach used in the following) enable optical interfacing with chips with variable configurations.

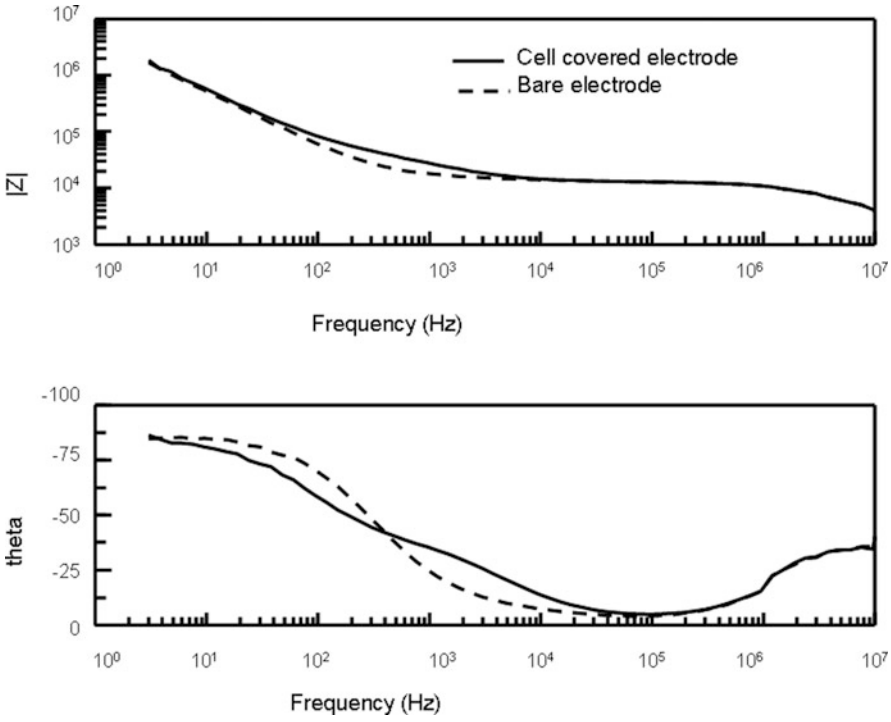

Fig. 10 Impedance spectra (magnitude and phase) of the electrodes with (*black line*) or without cell (*dashed*)

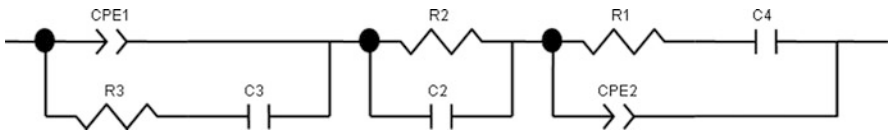

Fig. 11 Equivalent circuit—cell-coated electrodes

Polydimethylsiloxane (PDMS) flow cells are mounted on the Spreeta sensor and the liquid sample is delivered over the sensor surface by the automated fluidic system comprising syringe pumps and valves actuated by computer.

The flow rate range is 40–1,000 µl/min with increments of 1 µl/min. Sample injection is achieved using electrically actuated injection valves, one for each flow circuit. The sample loops of the injection valves are loaded with the desired sample through a selection valve and injected in the system simultaneously or independently. Sample loading, injections, and washing protocol are preprogrammed and the user has only to select the measurement flow channel, the sample volume, and flow rate of the buffer or sample. Data acquisition and processing is realized with an interface controlled by a LabView software. The signal received

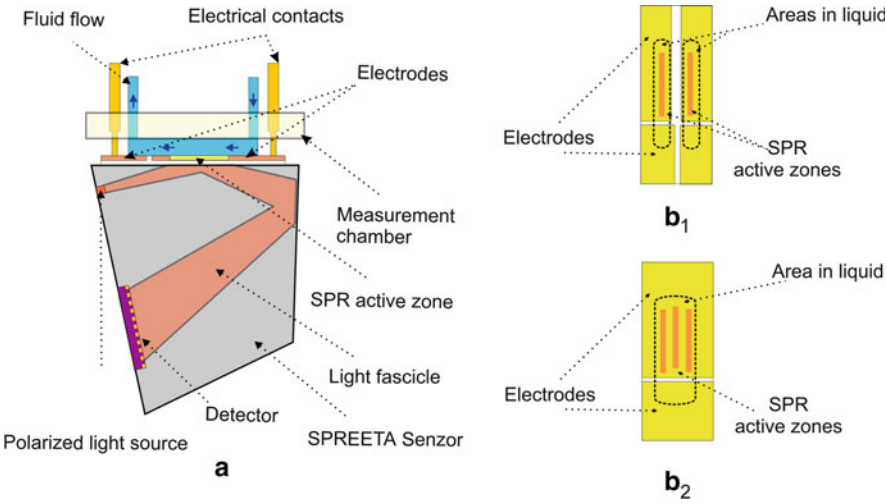

Fig. 12 Combined SPR and impedance set-up (**a**) with dual (**b1**) and living cells (**b2**) flow cells

from the SPR sensor is processed through various software routines to subtract background and reference data in order to obtain the SPR curve. The SPR minimum is calculated online by analysis of the SPR curve. This data is converted then to refractive index units, or response units using a calibration protocol. The software also allows saving the SPR data (as refractive index units or response units) as well as the SPR curve for each point for further analysis.

The impedance recording, LabView interface, parallels the SPR ones and can be performed by either commercial instrumentation (e.g., Solartron 1260 or Agilent 4294 A) or custom designed, multichannel one developed within ICB. Plane-parallel electrodes (one larger and one smaller) are custom designed in connection with the specific flow channels and SPR-sensing domains.

For dual channel evaluations (differential affinity sensing), the flow channels are 8 mm long by 0.8 mm wide with a height of 150 μm. Each flow channel is connected to an independent flow circuit controlled by a syringe pump, allowing simultaneous as well as independent analyses.

Alternatively, for whole cell analyses, a single flow cell has been designed that covers all three SPR-active regions (of the SPREETA chip).

By culturing biological cells on the conductive surface, both techniques can directly sense detailed information about cellular activities occurring on the substrate's surface allowing label-free and noninvasive study of cellular properties.

Madin–Darby Canine Kidney (MDCK) cells are frequently utilized as a model cell system surface attachment dependent. Cells attach to the surface and grow in monolayers linked together by specialized tight junctions. In culture, epithelial cells tend to experience strong contact inhibition of migration and form monolayers similar to the epithelial sheets that occur in vivo. While rather flat when cultivated in normal conditions, they round up and detach from the surface when dying.

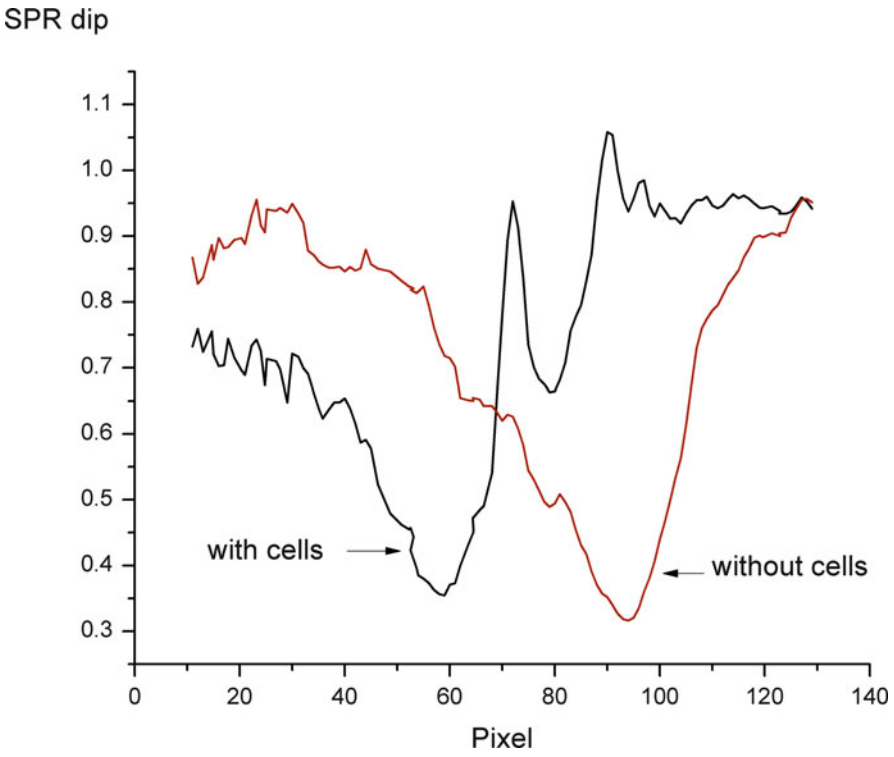

Fig. 13 SPR dip with and without MDCK cells grown on the surface

MDCK cells were grown, in controlled conditions (Dulbecco's Eagle's Medium—DMEM, Sigma supplemented with 10% Fetal Bovine Serum, 5% penicillin–streptomycin, at 37°C, 5%CO_2), to confluence on dual impedance and SPR chip, mounted in the dual measurement chamber and exposed to pore-forming compound injections.

As expected, when using the same buffer, cell presence on the sensing chip, is related to a noisier SPR curve and a shifted SPR angle as compared to cell-free chip (Fig. 13).

When cells are subjected to injections of pore-forming compounds (for generality, Triton X 100 was chosen as model analyte), the whole SPR dip structure, not only the position of the main resonance, changes, possibly indicating cell structural and morphological changes in addition to expected mass differences (when cells fully detach or the compound is adsorbed on the cellular layer).

Adequate fitting routines implemented *online* enable the derivation of the SPR angle (pixel position where reflectance minimum occurs) even on cellular platforms (with a "noisier" SPR dip).

The whole evolution, as seen in Fig. 14, during one long injection reveals highly nonmonotonous processes to be attributed to direct interaction with the cell

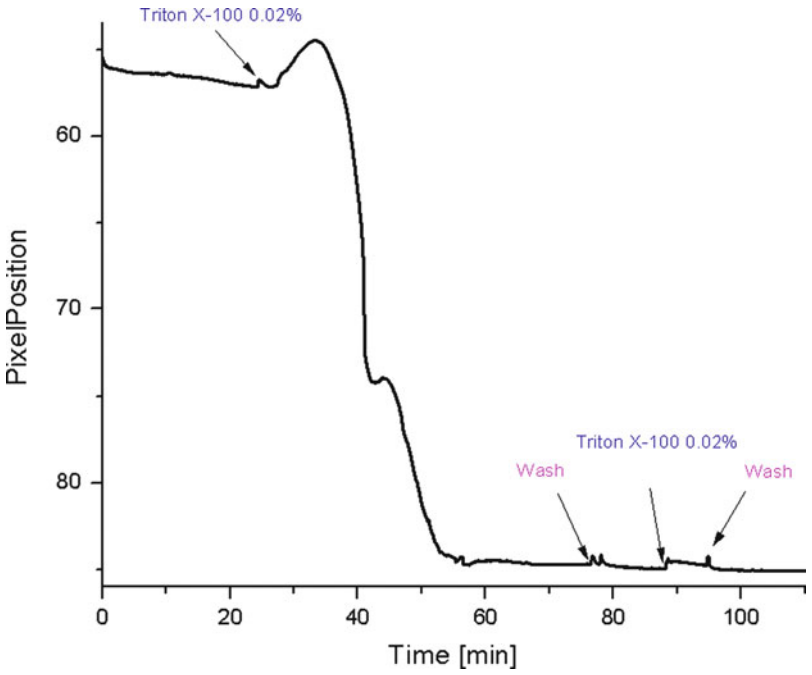

Fig. 14 Interaction between MDCK cell monolayer and a pore-forming compound as revealed by custom-made SPR set-up with integrated microfluidics

membrane, insertion, and subsequent destabilization of cell monolayer. The lack of response to a second injection proves that most of the cells were detached from the surface as confirmed by optical inspection (data not shown).

While the linear relationship between pixel position and the absolute refractive index is straightforward via calibration with standard solutions, since this calibration is rather elusive for cell platforms, in Fig. 14 the evolution of the interaction between cells and a pore-forming compound is represented via the pixel position corresponding to the derived minimum, via first derivative of the fitted SPR curve.

Quantitative ways to better characterize the richness of the SPR dip features and their particular evolutions in relation to distinct domains within the time evolution of the pixel position (this classical, "integrative" SPR information overshadows the complexity of SPR spectra in case of cells) are currently under development.

Major changes of the SPR dip were obtained in preliminary experiments on bacterial cells settling gravitationally on the surface (data not shown) proving that both bacterial and mammalian SPR platforms can be designed.

In conjunction, impedance data reveal—as seen in Fig. 15—an initial increase in Resistance and a simultaneous decrease in Capacitance values that can be related to cell swelling upon exposure to growth medium with Triton. This effect may be related to occurrence of the peak in SPR data (Fig. 14). Notably, prolonged

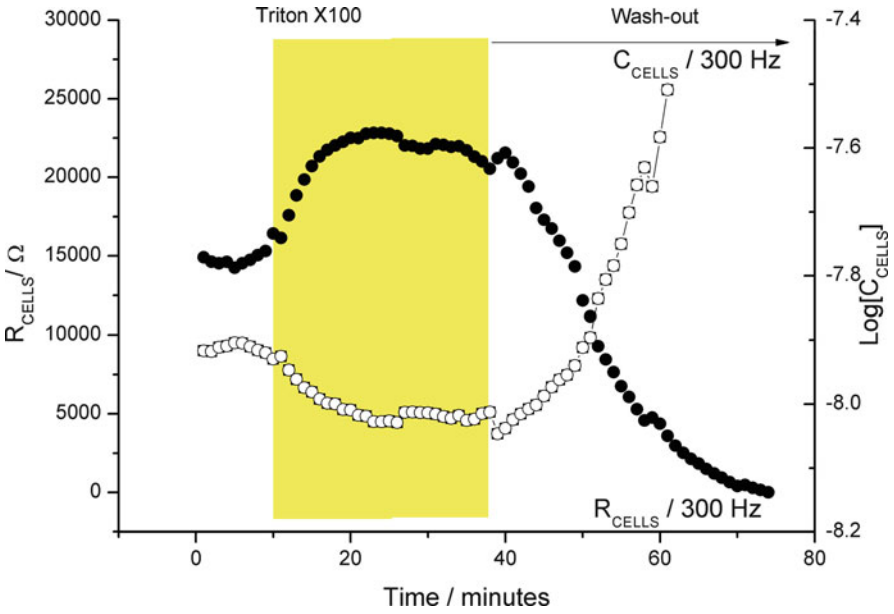

Fig. 15 Time evolution of the resistance/capacitance of the cell monolayer upon 0.02% Triton X 100 exposure

exposure to Triton X 100 destabilizes the monolayer until full detachment from the electrode layer occurs (washout region in Fig. 15).

These impedance data add to the plethora of recent reports [67–69] emphasizing the virtues of impedance spectroscopy (with or without electrochemical probes) to reveal morphological and electrical changes of cell monolayers and substantiate the effectiveness of a combined SPR-impedance cellular platform to evaluate the effect of pore-forming compounds in general and antimicrobial peptides in particular, and for detailed, real-time monitoring of the interaction process.

10 Conclusions

SPR monitoring of analyte–ligand interaction enables label-free, real-time assessment of the complex, multiphasic interaction mechanism between pore-forming compounds (including antimicrobial peptides), and model lipid matrices synthetic or cell based, paving the way for advancing SPR approaches in cell-based biosensing format.

Using specialized commercial chips (L1 Biacore) and POPC supported lipid membranes, as a first step, the entire *nonmonotonous* interaction process between melittin as a model antimicrobial peptide and zwitterionic membranes was revealed and assessed. The interaction process is quantitatively described by fitting

the experimental data with a mathematical model encompassing the distinct stages involved in peptide–lipid interaction: association, insertion of melittin into lipid matrix, pore formation, and destabilization of lipid membrane. This numerical analysis offers direct insight into representative, effective, kinetic parameters, and time evolutions of lipid and melittin concentrations during these distinct, yet interlinked phases of the entire process, and provides relevant parameters for biosensing. Consequently, the pattern of evolution of the complex, nonmonotonous process of peptide–lipid interaction and a direct way to quantify the concentration of peptide can be derived while gaining insight on interaction mechanisms depending both on various antimicrobial peptides and lipid composition of lipid membrane.

Two approaches for sensing antimicrobial peptides concentration via related effects on lipid matrix are advanced: (a) a "calibration curve" relating peptide concentration to the inverse of the characteristic peak time: $1/T_{max}$; the detection limit, e.g., in the μM range, for melittin, is imposed by the characteristic peptide: lipid thresholds dominating the complete interaction process and realistic injection times <3,600 s; (b) another one based on the threshold values and the corresponding time points of their occurrence provided by the quantitative analysis.

In an attempt to close the gap between experiments with synthetic membranes and the ones with living cells, a combined SPR-Electrical Impedance set-up is proposed. Complementary data on detergent—cell monolayer interaction as revealed by SPR and complex impedance emphasize the virtues of this combined approach for monitoring cell-pore-forming compound interaction including cell dissociation from the surface.

It is envisaged that this approach is able to support a comprehensive analysis platform, which could be further extended to a wider class of lipid matrices including mammalian and bacterial cells in relation to other pore-forming compounds, as well.

The proposed kinetic model combined with appropriate design of the experimental protocol adds a new depth to the classic SPR investigation of peptide–lipid interaction offering a quantitative platform for understanding the manifold facets of the interaction and for supporting the controlled design of new, improved antimicrobial peptides.

Acknowledgments Financial help from the Romanian National Authority for Scientific Research (program PNCDII, contract no. 81-028, 71-073, 41-013, 25 EU and 12-121) is acknowledged.

References

1. Anderluh G et al (2003) Pore formation by equinatoxin II, a eukaryotic protein toxin, occurs by induction of nonlamellar lipid structures. J Biol Chem 278(46):45216–45223
2. Chah S, Zare RN (2008) Surface plasmon resonance study of vesicle rupture by virus-mimetic attack. Phys Chem Chem Phys 10(22):3203–3208

3. Shai Y (1999) Mechanism of the binding, insertion and destabilization of phospholipid bilayer membranes by alpha-helical antimicrobial and cell non-selective membrane-lytic peptides. Biochim Biophys Acta 1462(1–2):55–70
4. Kass RS (2005) The channelopathies: novel insights into molecular and genetic mechanisms of human disease. J Clin Invest 115(8):1986–1989
5. Panchal RG et al (2002) Pore-forming proteins and their application in biotechnology. Curr Pharm Biotechnol 3(2):99–115
6. Zasloff M (2002) Antimicrobial peptides of multicellular organisms. Nature 415(6870): 389–395
7. Gheorghiu M et al (2009) Sensing based on assessment of non-monotonous effect determined by target analyte: case study on pore-forming compounds. Biosens Bioelectron 24(12): 3517–3523
8. Olaru A et al (2009) Assessment of the multiphase interaction between a membrane disrupting peptide and a lipid membrane. J Phys Chem B 113(43):14369–14380
9. Asthana N, Yadav SP, Ghosh JK (2004) Dissection of antibacterial and toxic activity of melittin: a leucine zipper motif plays a crucial role in determining its hemolytic activity but not antibacterial activity. J Biol Chem 279(53):55042–55050
10. Wessman P et al (2008) Melittin-lipid bilayer interactions and the role of cholesterol. Biophys J 95(9):4324–4336
11. Naumann R et al (1999) The peptide-tethered lipid membrane as a biomimetic system to incorporate cytochrome c oxidase in a functionally active form. Biosens Bioelectron 14(7): 651–662
12. Kim K et al (2004) Surface plasmon resonance studies of the direct interaction between a drug/intestinal brush border membrane. Pharm Res 21(7):1233–1239
13. Erb EM et al (2000) Characterization of the surfaces generated by liposome binding to the modified dextran matrix of a surface plasmon resonance sensor chip. Anal Biochem 280 (1):29–35
14. Saenko E et al (2001) Comparison of the properties of phospholipid surfaces formed on HPA and L1 biosensor chips for the binding of the coagulation factor VIII. J Chromatogr A 921(1): 49–56
15. Cha T, Guo A, Zhu XY (2006) Formation of supported phospholipid bilayers on molecular surfaces: role of surface charge density and electrostatic interaction. Biophys J 90(4): 1270–1274
16. Anderluh G et al (2005) Properties of nonfused liposomes immobilized on an L1 Biacore chip and their permeabilization by a eukaryotic pore-forming toxin. Anal Biochem 344(1):43–52
17. Habermann E, Jentsch J (1967) Sequence analysis of melittin from tryptic and peptic degradation products. Hoppe Seylers Z Physiol Chem 348(1):37–50
18. Dempsey CE (1990) The actions of melittin on membranes. Biochim Biophys Acta 1031(143–161)
19. Lundquist A et al (2008) Melittin-lipid interaction: a comparative study using liposomes, micelles and bilayer disks. Biochim Biophys Acta 1778(10):2210–2216
20. Popplewell JF et al (2007) Quantifying the effects of melittin on liposomes. Biochim Biophys Acta 1768(1):13–20
21. Frey S, Tamm LK (1991) Orientation of melittin in phospholipid bilayers. A polarized attenuated total reflection infrared study. Biophys J 60(4):922–930
22. Matsuzaki K, Yoneyama S, Miyajima K (1997) Pore formation and translocation of melittin. Biophys J 73(2):831–838
23. Lee MT et al (2008) Mechanism and kinetics of pore formation in membranes by water-soluble amphipathic peptides. Proc Natl Acad Sci USA 105(13):5087–5092
24. Zhu WL et al (2007) Cell selectivity of an antimicrobial peptide melittin diastereomer with D-amino acid in the leucine zipper sequence. J Biochem Mol Biol 40(6):1090–1094
25. Mozsolits H et al (2001) Analysis of antimicrobial peptide interactions with hybrid bilayer membrane systems using surface plasmon resonance. Biochim Biophys Acta 1512(1):64–76

26. Papo N, Shai Y (2003) Exploring peptide membrane interaction using surface plasmon resonance: differentiation between pore formation versus membrane disruption by lytic peptides. Biochemistry 42(2):458–466
27. Popplewell J et al (2005) Quantification of the effects of melittin on liposome structure. Biochem Soc Trans 33(Pt 5):931–933
28. Lee TH, Mozsolits H, Aguilar MI (2001) Measurement of the affinity of melittin for zwitterionic and anionic membranes using immobilized lipid biosensors. J Pept Res 58(6):464–476
29. Mozsolits H, Thomas WG, Aguilar MI (2003) Surface plasmon resonance spectroscopy in the study of membrane-mediated cell signalling. J Pept Sci 9(2):77–89
30. Berneche S, Nina M, Roux B (1998) Molecular dynamics simulation of melittin in a dimyristoylphosphatidylcholine bilayer membrane. Biophys J 75(4):1603–1618
31. Lin JH, Baumgaertner A (2000) Stability of a melittin pore in a lipid bilayer: a molecular dynamics study. Biophys J 78(4):1714–1724
32. Puu G (2001) An approach for analysis of protein toxins based on thin films of lipid mixtures in an optical biosensor. Anal Chem 73(1):72–79
33. Chenal A et al (2002) Membrane protein insertion regulated by bringing electrostatic and hydrophobic interactions into play. A case study with the translocation domain of diphtheria toxin. J Biol Chem 277(45):43425–43432
34. Hong Q et al (2002) Two-step membrane binding by Equinatoxin II, a pore-forming toxin from the sea anemone, involves an exposed aromatic cluster and a flexible helix. J Biol Chem 277(44):41916–41924
35. Thomas CJ, Surolia A (1999) Kinetics of the interaction of endotoxin with polymyxin B and its analogs: a surface plasmon resonance analysis. FEBS Lett 445(2–3):420–424
36. Thomas CJ, Surolia N, Surolia A (1999) Surface plasmon resonance studies resolve the enigmatic endotoxin neutralizing activity of polymyxin *B*. J Biol Chem 274 (42):29624–29627
37. Maulet Y, Brodbeck U, Fulpius B (1984) Selective solubilization by melittin of glycophorin A and acetylcholinesterase from human erythrocyte ghosts. Biochim Biophys Acta 778(3): 594–601
38. Pott T, Dufourc EJ (1995) Action of melittin on the DPPC-cholesterol liquid-ordered phase: a solid state 2H-and 31P-NMR study. Biophys J 68(3):965–977
39. Pott T, Paternostre M, Dufourc EJ (1998) A comparative study of the action of melittin on sphingomyelin and phosphatidylcholine bilayers. Eur Biophys J 27(3):237–245
40. Yu L et al (2009) Interaction of an artificial antimicrobial peptide with lipid membranes. Biochim Biophys Acta 1788(2):333–344
41. Mashaghi A et al (2008) Optical anisotropy of supported lipid structures probed by waveguide spectroscopy and its application to study of supported lipid bilayer formation kinetics. Anal Chem 80(10):3666–3676
42. Andra J et al (2008) Surface acoustic wave biosensor as a tool to study the interaction of antimicrobial peptides with phospholipid and lipopolysaccharide model membranes. Langmuir 24(16):9148–9153
43. Terry CJ et al (2006) Characterisation of membrane mimetics on a dual polarisation interferometer. Biosens Bioelectron 22(5):627–632
44. Abdiche YN, Myszka DG (2004) Probing the mechanism of drug/lipid membrane interactions using Biacore. Anal Biochem 328(2):233–243
45. Born M, Wolf E (1980) Principles of optics: electromagnetic theory of propagation, interference and diffraction of light, 6th edn. Pergamon, Oxford, p 808
46. Reitz JR, Milford FJ, Christy RW (1993) Foundations of electromagnetic theory, 4th edn. Addison-Wesley, Boston, MA, USA, p 630p
47. Peterlinz KA, Georgiadis R (1996) In situ kinetics of self-assembly by surface plasmon resonance spectroscopy. Langmuir 12(20):4731–4740
48. Schasfoort BMR, Tudos JA (eds) (2008) Handbook of surface plasmon resonance. RSC Publishing, Cambridge, UK

49. Morigaki K, Tawa K (2006) Vesicle fusion studied by surface plasmon resonance and surface plasmon fluorescence spectroscopy. Biophys J 91(4):1380–1387
50. Yang L et al (2000) Crystallization of antimicrobial pores in membranes: magainin and protegrin. Biophys J 79(4):2002–2009
51. Baird CL, Courtenay ES, Myszka DG (2002) Surface plasmon resonance characterization of drug/liposome interactions. Anal Biochem 310(1):93–99
52. Nakajima H et al (2001) Kinetic analysis of binding between Shiga toxin and receptor glycolipid Gb3Cer by surface plasmon resonance. J Biol Chem 276(46):42915–42922
53. Tamba Y, Yamazaki M (2009) Magainin 2-induced pore formation in the lipid membranes depends on its concentration in the membrane interface. J Phys Chem B 113(14):4846–4852
54. Grage SL, Afonin S, Ulrich AS (2010) Dynamic transitions of membrane-active peptides. Methods Mol Biol 618:183–207
55. Oren Z, Shai Y (1998) Mode of action of linear amphipathic alpha-helical antimicrobial peptides. Biopolymers 47(6):451–463
56. Chen X et al (2007) Real-time structural investigation of a lipid bilayer during its interaction with melittin using sum frequency generation vibrational spectroscopy. Biophys J 93(3): 866–875
57. Leontiadou H, Mark AE, Marrink SJ (2006) Antimicrobial peptides in action. J Am Chem Soc 128(37):12156–12161
58. Marrink SJ, de Vries AH, Tieleman DP (2009) Lipids on the move: simulations of membrane pores, domains, stalks and curves. Biochim Biophys Acta 1788(1):149–168
59. Ritov VB et al (1993) Alamethicin as a permeabilizing agent for measurements of Ca(2+)-dependent ATPase activity in proteoliposomes, sealed membrane vesicles, and whole cells. Biochim Biophys Acta 1148(2):257–262
60. Allende D, Simon SA, McIntosh TJ (2005) Melittin-induced bilayer leakage depends on lipid material properties: evidence for toroidal pores. Biophys J 88(3):1828–1837
61. Giaever I, Keese CR (1993) A morphological biosensor for mammalian cells. Nature 366(6455): 591–592
62. Sandu T, Vrinceanu D, Gheorghiu E (2010) Linear dielectric response of clustered living cells. Phys Rev E Stat Nonlin Soft Matter Phys 81(2 Pt 1):021913
63. Gheorghiu E, Balut C, Gheorghiu M (2002) Dielectric behaviour of gap junction connected cells: a microscopic approach. Phys Med Biol 47(2):341–348
64. Gheorghiu E (1999) On the limits of ellipsoidal models when analyzing dielectric behavior of living cells. Emphasis on red blood cells. Ann N Y Acad Sci 873:262–268
65. Gheorghiu M, Gersing E, Gheorghiu E (1999) Quantitative analysis of impedance spectra of organs during ischemia. Ann N Y Acad Sci 873:65–71
66. Ursu GA et al (2007) Sensing the cell-substrate interaction towards development of “smart” surfaces. IFMBE Proc 17(Part 4):86–89
67. Tun TN, Jenkins ATA (2010) An electrochemical impedance study of the effect of pathogenic bacterial toxins on tethered bilayer lipid membrane. Electrochem Commun 12(10):1411–1415
68. Wilkop T, Xu DK, Cheng Q (2008) Electrochemical characterization of pore formation by bacterial protein toxins on hybrid supported membranes. Langmuir 24(10):5615–5621
69. Yu NC et al (2006) Real-time monitoring of morphological changes in living cells by electronic cell sensor arrays: an approach to study G protein-coupled receptors. Anal Chem 78(1):35–43

Biological Applications of Surface Plasmon Resonance Imaging

L. Leroy, E. Maillart, and T. Livache

Abstract This chapter will deal with versatile biochips. The presented biochips are prepared by the microarray functionalization of gold surface from millimetric to micrometric scale via different electrochemical approaches. Interactions occurring on these functionalized surfaces are monitored using surface plasmon resonance imaging approaches. Different size of spots including hyphenated techniques will be used to study biological interactions from molecular (i.e., DNA, proteins (toxins), and sugars) to complex objects such as living cells. Applications of this approach will be illustrated by examples from different biological fields including DNA hybridization studies, antibody screening in patients' samples, study of oligosaccharides–proteins interactions, and lymphocytes characterization and sorting. For each topic, optimized chemistry and optical developments will be specified.

Keywords Biochips • Biological interactions • Polypyrrole • Surface plasmon resonance imaging (SPRi)

Contents

L. Leroy • T. Livache (✉)
CREAB group, UMR SPrAM CEA/CNRS/ UJF-Grenoble 1, INAC, 17 rue des martyrs, Grenoble 38054, France
e-mail: thierry.livache@cea.fr

E. Maillart
Genoptics SA, Horiba scientific, centre R&D, ZI de la vigne aux loups, 5 avenue Arago, Chilly-Mazarin 91380, France

W. Fritzsche and J. Popp (eds.), *Optical Nano- and Microsystems for Bioanalytics*, Springer Series on Chemical Sensors and Biosensors (2012) 10: 211–226
DOI 10.1007/978-3-642-25498-7_7,

1 Introduction

Before starting with our main subject, the use of surface plasmon resonance imaging (SPRi) as a tool for biological studies, a short overview of the plasmon history and principle is proposed.

1.1 Chronology of Plasmonic Effect

The first observation of the plasmonic effect was reported by Wood in 1902 [1]. He detected a strange light behavior on a specific diffraction grating; but even if he suspected some interesting physical behavior, he was not able to explain this effect. Lord Rayleigh started to explain the theory of this phenomenon in 1907 [2]. The surface plasmon consequences were also observed in experiments of electron interactions with thin metallic films. These interactions were described and explained by Pines and Bohm [3–5], and the theory was explained in terms of dielectric complex coefficients by Ritchie and Ritchie et al. [6–8]. Even though from those works the phenomenon of plasmon was well understood, it took few years before optical configurations without grating were proposed by Otto [9, 10] and by Kretschmann and Raether [11–13] in 1967–1968. Thanks to these simpler and more practical configurations, it opened important development of surface plasmon studies. These developments will progressively allow changing from the studies of the plasmon phenomenon itself to its use as a measurement tool. Nevertheless, it was necessary to wait for the 1980s to have the use of surface plasmon resonance (SPR) as a biological sensor reported in Liedberg et al.'s works [14, 15] dealing with antibody–antigen interactions detected by SPR. Nowadays about 20 companies propose devices of analyses based on the SPR effect [16].

1.2 Plasmonic Effect

In this introduction, only a very short presentation of SPR will be written. For a complete and rigorous description of the SPR theory, one could refer to the previous references [2, 6–8], the review realized by Pitarke et al. [17], or the chapter produced by Kooyman [18].

SPRs are collective oscillations of electrons that occur at the interface between a dielectric material and some metal layers (gold, silver, etc.). In this chapter, we will

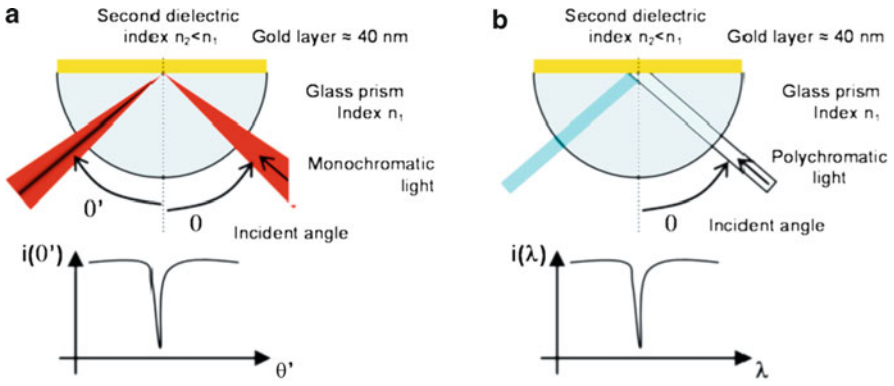

Fig. 1 Schematic representation of the two optical setup solutions in Kretschmann configuration and their corresponding response: (**a**) monochromatic excitation of the SPR at an adapted angle; (**b**) polychromatic excitation

limit this presentation of plasmon effect to our field of interest, i.e., optical excitation of the SPR in Kretschmann configuration. To produce the excitation of the plasmon waves by optical way, the only solution that fit with the dispersion relation is to use an evanescent wave [19]. To obtain this, Kretschmann proposed to place a thin layer of metal over a high optical index prism and provide the excitation by the prism at an incident angle over the total reflection condition in the appropriate transverse magnetic (TM) polarization (cf. Fig. 1). The two optical configurations which result from the Kretschmann configuration are represented in Fig. 1. In the first configuration (a), a monochromatic wavelength is used to provide the excitation. By monitoring the intensity of reflected light upon incidence angle, we can monitor the efficiency of the coupling process for a given angle (the more efficient the coupling, the less light is reflected). In the second configuration (b), a polychromatic light is used to illuminate the surface at a fixed angle. The reflected light is then spectrally analyzed. When the coupling process occurs, the corresponding wavelength is attenuated and it appears in the spectrum as a missing one.

The coupling efficiency between light and plasmon surface is the function of the following: the electromagnetic fields (wavelength, incidence angle, and polarization); the metal layer (thickness, dielectrically property); and the optical index of the dielectric media where the plasmon occurs (over the distance of the evanescent wave propagation, i.e., around 100 nm). Because the variation in coupling efficiency between light and plasmon is very sensitive to variations in the previous parameters (and specifically to the last one), the SPR phenomenon can be used as sensor base. For example (all other parameters fixed), the variation in index resulting of a monolayer adsorption of antibody over the metallic layer may induce detectable coupling efficiency variations. Experimentally, the absorption of molecules on the metallic layer induces an index change that produces the following: (1) in monochromatic mode, an angle shift for the effective coupling between light and SPR, and (2) in polychromatic mode, a modification of the wavelength that allows the coupling process. By following, respectively, the angle of the

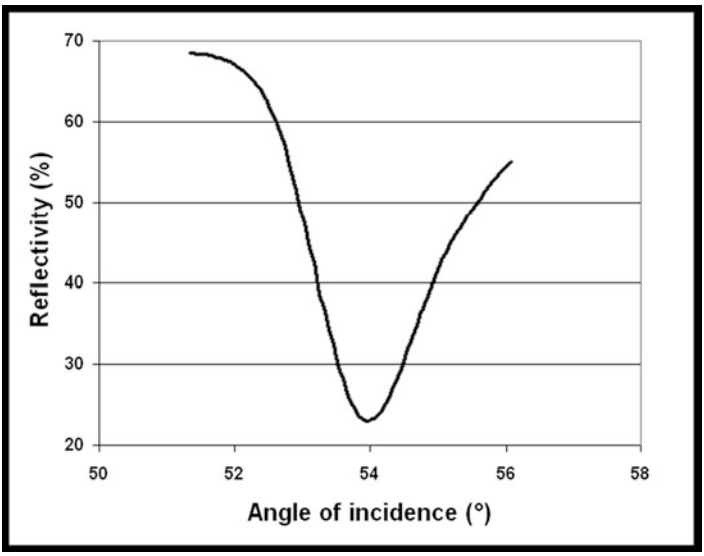

Fig. 2 Experimental SPR curve (reflectivity versus incident angle) obtained for a prism covered with 3 nm of chromium and 45 nm of gold, and in contact with phosphate-buffered saline (PBS) solution, illumination at 660 nm.

maximum attenuation of reflected light, or the missing spectral wavelength [20], we can determine the index changes. In the following part of this chapter, we will focus on the first one (monochromatic light). As an illustration, a typical plasmon curve (reflectivity variations vs. incident angle) obtained for a gold surface in phosphate-buffered saline (PBS) is reported in Fig. 2.

A simplification of the previous setup consists of the utilization of a well-selected angle of incidence, instead of the realization of a complete plasmon curve (i.e., reflectivity vs. incidence angle) (cf. Fig. 3). The variation in the optical index is then monitored by the variation in reflected light intensity. Upon index changes (adsorption at the interface), the SPR curve is shifted (to higher angle in case of increasing index). The consequences of this shift for a fixed angle of work are reflected light intensity amplification. This configuration at fixed angle allows the realization of spatially localized SPR measurements, the so-called SPRi configuration. This setup will be the subject described in the following paragraph.

1.3 Description of the Technical Approaches Used

1.3.1 SPR Imaging

The SPR setups previously presented are monosensor detectors. The reflectivity evolution can only characterize efficiently homogeneous surface behavior. By using a setup presented in Fig. 4, it becomes possible to obtain a spatially localized

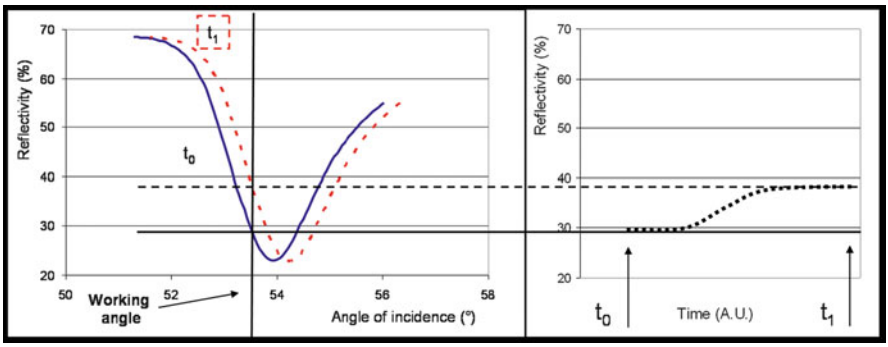

Fig. 3 SPR kinetics measurement: (**a**) typical curves percentage of reflectivity versus angle obtained before (*blue continuous line*) and after adsorption of molecules on the surface (*red dash line*), (**b**) corresponding variation in reflectivity versus time obtained for a fixed working angle

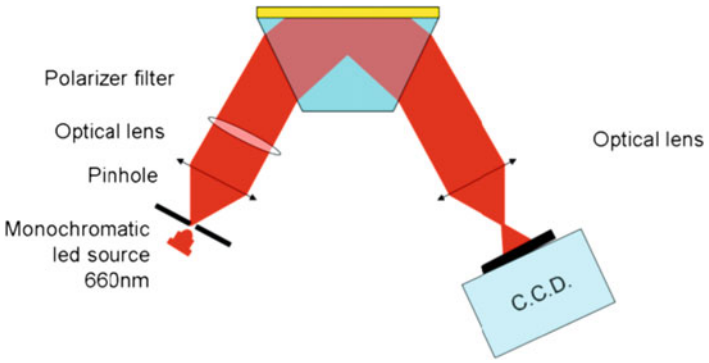

Fig. 4 Schematic representation of a SPRi minimum setup. *Left side* illumination, *right side* imagery. In order to reduce optical aberrations, lenses are often replaced by objectives composed of several lenses, and filters may be added to reduce perturbation of parasite wavelength

SPR information over the metallic layer. The metallic surface is homogeneously illuminated in the SPR conditions (monochromatic and TM light). The image of the metallic surface is formed on a CCD camera by the light that is not absorbed by the plasmon coupling and by the use of an appropriate objective. Each pixel of the camera acts as a monopoint SPR detector for the corresponding point of the object (the metallic layer): this allows following the local index variation over the whole surface and makes possible the realization of multiplexed detectors.

As a conclusion, SPRi is a technique adapted to quantify very small local variation in optical index at the metallic–dielectric interface. The technique is then well adapted to study localized molecular adsorption and can be used for multiplexed chips dedicated to biological interaction studies. However, the construction of these surfaces bearing addressed biological ligands remains difficult.

In this way, several strategies were developed ([21]). In the following chapters, the chemistry will be focused on the polypyrrole strategy.

1.3.2 Chemistry for SPR Imaging and Example of the Polypyrrole Approach

To immobilize molecules of interest over the metallic layer, a mix solution of pyrrole monomer and modified pyrrole (pyrrole link with the molecule of interest) is prepared. Electrochemical oxidation of this solution produces a polypyrrole film with a proportion of modified pyrrole (Fig. 5). The adherence of the film to the metallic layer ensures a stable link between the probe and the surface. This strategy and the appropriate chemistry were successfully developed and applied for numerous families of biomolecules: single-stranded DNA [22, 23], biotin [24], protein [25], peptide [26], lipids [27], and oligosaccharide [28].

Usually for an electrochemical polymerization process, the surface of a working electrode is dipped in the solution, that is to say, the entire surface will be covered by the polymer. In order to obtain different and independent areas functionalized by different electrochemical reactions on the same surface, a mobile miniaturized electrochemical cell is used. This microcell can move over the surface of the working electrode (Fig. 6a). This allows limiting the reactive area to the size of the electrochemical cell.

This process was described by Guedon et al. [29] and Livache et al. [30]. They used a micropipette tip as the moving electrochemical cell. The micropipette, including a platinum wire serving as a counter electrode, was filled with the pyrrole solution (20 mM) bearing pyrrole-ODN (1–100 μM) and $LiClO_4$ (0.1 M). This electrochemical system was connected to a potentiostat, and the micropipette tip was positioned and approached to the working electrode using step motor stage. Once the solution was in contact with the interface, a potential pulse difference (between the gold substrate and the platinum wire in the microcell) of 2 V is applied

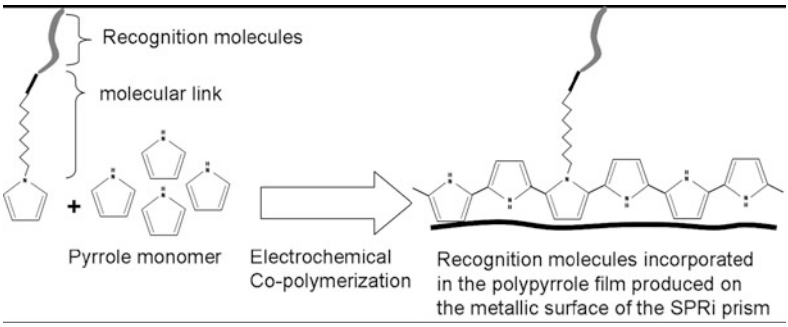

Fig. 5 Principle of functionalization of the surface with polypyrrole film. A solution of mixed unmodified pyrrole monomers and functionalized monomers is used to produce electrochemically a copolymerization of both pyrrole types. Statistically, some of the recognition molecules are bonded to the film and become accessible for recognition process

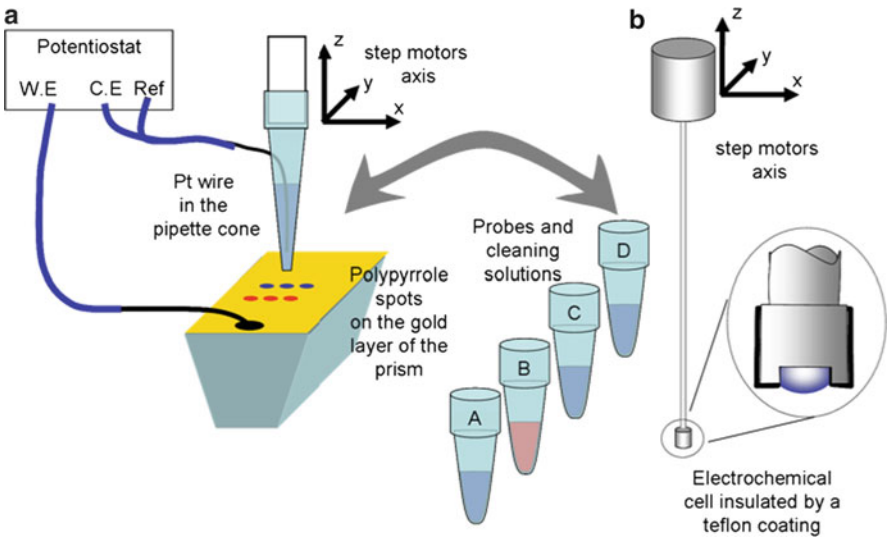

Fig. 6 Illustration of electro-spotting setup used to achieve the probe immobilization with matrices of polypyrrole spots. (**a**) Pipette cone-based electro-spotter and (**b**) electrochemical needle used to decrease spot diameters

for 250–500 ms. As a result, a disk polymer film is formed by electrosynthesis. In this experiment, the diameters of the deposited pyrrole-ODN spots were around 600 μm (size of the micropipette opening), but later experiment realized with dedicated smaller tip (Fig. 6b) [31] allowed the production of smaller spots (under 300 μm of diameter). In order to produce a multiparametric chip, the previous steps are repeated for each spots. A cleaning process is needed before changing the spotting solution. This suppresses cross-contamination of the different probes. By adjusting independently the polymerization duration and the relative ratio of modified/unmodified pyrrole, both the thickness of the spots (11-nm-thick polymer film for 500 ms) and the surface density of probes can be optimized. To reduce even more the diameter of the spot and therefore increase the complexity of the chip to over 250,000 spots per square centimeter, a cantilever (Fig. 7a)-based strategy was proposed by Leichle et al. [32]. This method was applied to pyrrole spotting by Descamps et al. [33]. To provide the electro-polymerization (Fig. 7b), cantilever positions are controlled by step motor. They are first filled with the pyrrole containing solution by dipping them in it. Tips are then placed over the gold layer and a 2 V difference of potential is applied between the gold surface (WE) and the gold canal of the silicon cantilever (CE). The array of spot is produced by a successive "touch and go." The electro-polymerization duration is controlled by the time of contact between the tip and the gold layer. The process gives spots of 5–10 μm diameter and 5 nm thick (for 100 ms contact duration). As conclusion, in all these techniques, the required quantities of biomolecules are furthermore very low. This together with the mild electrosynthesis conditions, the

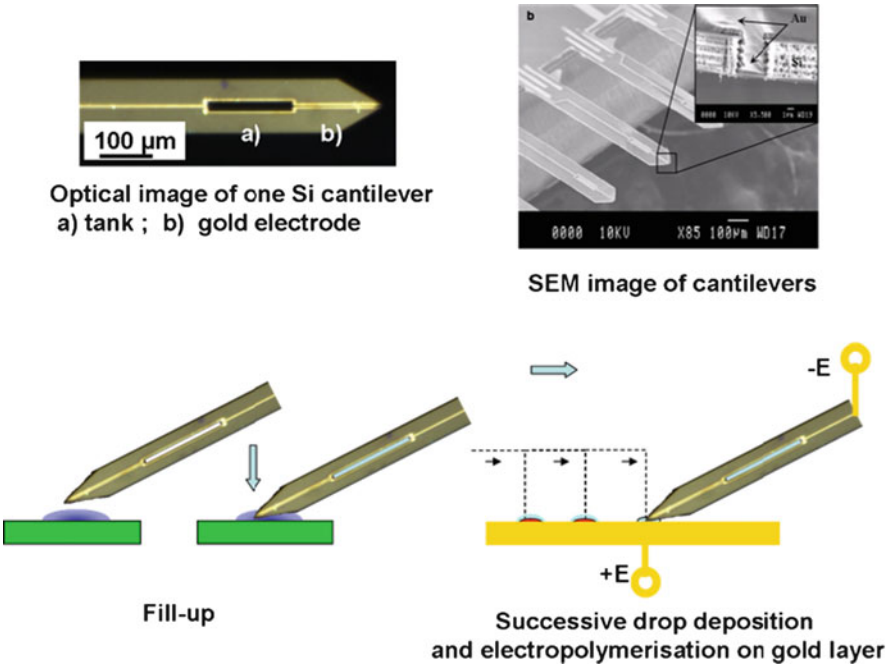

Fig. 7 Cantilever for miniaturized spots. *Upper left corner*: optical image of a single electro-spotting cantilever; *upper right corner*: scanning electron microscope images of a part of a 12-cantilever ship and magnification of a cantilever apex. *Down*: schematic drawing of electro-spotting protocol used with the cantilever technique. Filling of the tank by immersion of the tip apex in the probe solution. Successive electro-polymerization patterning controlled by contact duration

possible high density of parallelization, and the mechanical stability of the obtained films makes this immobilization process a versatile tool for substrate modification with a large range of biological probes including DNA and other biomolecules.

2 Biological Applications and Specific Developments

2.1 Molecular Interaction Studies

2.1.1 DNA Hybridization Using Temperature Controlled Chamber: Biophysics and Applications

Even if the large development of high-throughput DNA biochips based on fluorescence label techniques responds to the main part of the DNA analysis needs, some of the problems that may be encountered in DNA analysis are still difficult to solve by techniques in endpoint measurements (for example, thermodynamic behavior of

DNA hybridization on surfaces during temperature scan). Temperature-dependent studies are difficult to perform in SPRi. Upon changes in temperature, the optical index of water changes and induces a −0.3% reflectivity variation per °C. For comparison purposes, a variation of 3°C induces a reflectivity change of the same order of magnitude than those observed for a saturated monolayer hybridization of DNA (20 bases). Fiche et al. [34] developed a high precision temperature regulation setup for SPRi experiment. With this setup, Fiche et al. [35] and Fuchs et al. [36, 37] performed thermodynamic studies of DNA hybridization on biochip surfaces. This device allowed realizing very precise and stable temperature regulations and allowed very reproducible temperature scans (usually 2°C/min). This reproducibility is essential to measure thermodynamics parameters of the deshybridization process with SPRi. Two temperature scans rigorously identical were realized. The first one was carried out without injection of DNA targets, and was used as a reference. The second one was achieved after a step of hybridization. Variation induced by the temperature changes can be subtracted to the signal contribution by just performing the subtraction of the two reflectivity versus temperature scans. In Fig. 8, an example of this melting curve is reported. The reflectivity variations were renormalized (1 for full hybridization and 0 for complete deshybridization). The obtained reflectivity curve allowed them to determine which kind of sequence was present in the sample. The best DNA–DNA complex stability (observed at the highest temperature) occurred for the perfect complementary DNA sequence. A plateau in the melting curve results in a two-step melting behavior. Tested sample was prepared with heterozygous sample mismatching of only one nucleic base. This technique is then adapted for label-free point mutation detection and may be used to determine if samples are homogeneous (homozygote or heterozygote). DNA-

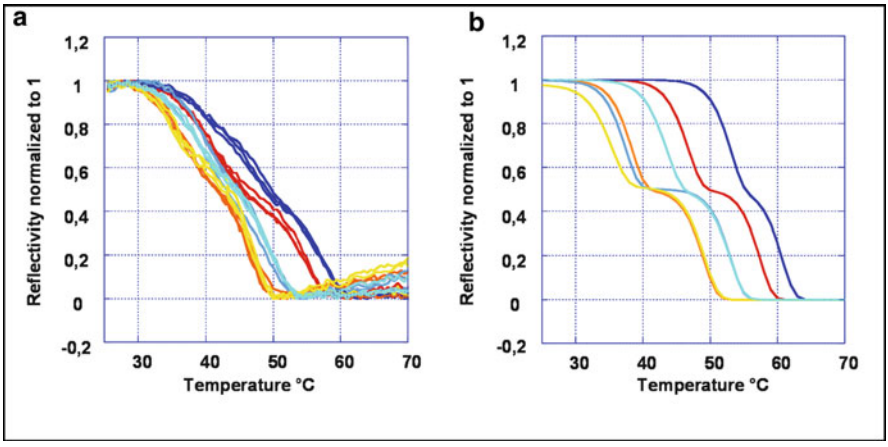

Fig. 8 (**a**) Experimental data and (**b**) simulation of normalized reflectivity variation upon temperature scan on a DNA SPRi biochip (after hybridization with an 250 nM heterozygous sample containing a 1:1 ratio of DNA sample mismatching of only one nucleic base). Plateau on curves are the results of faster deshybridization of the less stable DNA association

grafted surfaces can also be used for the scanning of DNA/protein interactions. A first example deals with the characterization of P53 protein binding with double-stranded DNA targets [38] and the second one with the possibility of DNA repair on chip [39].

2.1.2 Antibody Screening on Peptide Chips

Polypyrrole SPRi strategy was first developed in array format for DNA/RNA study. Unfortunately, the simple analysis of DNA or RNA is not directly adapted to study the interactions between proteins. As protein interactions triggered almost all cellular activities (receptor–ligand, enzyme–substrate binding, etc.), the studies of this kind of interactions have demonstrated their major importance to understand the cellular activity, for pharmacologic development and medical diagnostics [21]. SPRi/polypyrrole was successfully adapted and used to perform high-throughput study of protein–protein interactions [25] and peptide–antibody interactions [26]. In this last study, Cherif et al. analyzed peptide–antibody interactions on real patient sera. They used twelve peptide fragments, eleven of hepatitis C virus proteins and one from ovalbumin (as negative control). The fragments were maleimide modified and conjugated with SH-activated pyrrole [22]. The conjugated products were electro-co-polymerized with free pyrrole monomer on a SPRi prism gold layer. By successive injections of diluted patient sera, they proved the possibility to quantify the concentration of antibody directed against the different kinds of peptide present in each sample. By injection of competitive free peptide fragments, they also demonstrated the possibility to determine the difference in binding affinity for each antibody. As a conclusion, all these information improve the knowledge of patient-specific pool of antibodies and, therefore, in the future may allow to adapt the therapeutic strategy. The determination of affinity is possible with SPRi because it is a real-time technique and not an endpoint measurement contrary to the techniques based on indirect detection by use of labeled probes (e.g., fluorescence).

2.1.3 Oligosaccharide [28]

Following the wake of “genomics” and “proteomics,” “glycomics” becomes an emerging field that allows to study oligosaccharide structures and protein–oligosaccharide interactions. Nevertheless, the structure complexity and diversity of carbohydrates render these studies very difficult. Thus, tools for studying protein–carbohydrate interactions are necessary to gain an understanding of biological functions and the roles that these interactions play in disease states. The presentation of carbohydrates in an array format provides a means to monitor simultaneously multiple binding events between immobilized oligosaccharides and proteins in solution. In this last case, Mercey et al. [28] demonstrated the possibility to study with SPRi biochip the interactions between oligosaccharides and proteins

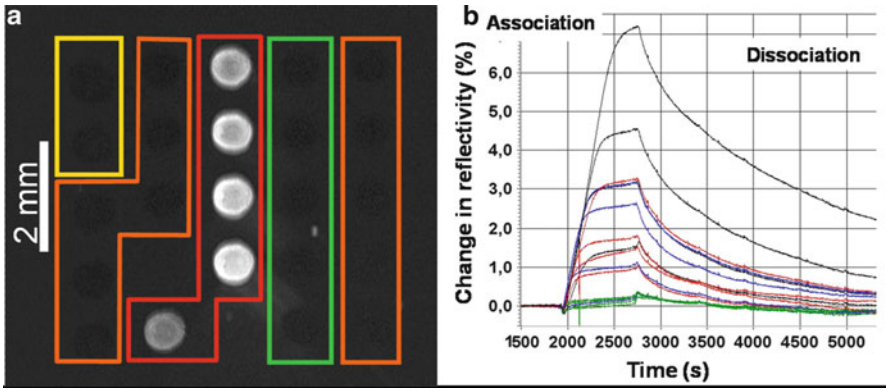

Fig. 9 Oligosaccharide biochip analyzed by SPRi. (**a**) Interaction of polypyrrole (*yellow*), HP6 (*orange*), CS (*red*), and DS (*green*) spots with 10 nM of IgM anti-CS monitored by differential SPRi image; (**b**) sensorgram for stromal-derived cell factor-1α (SDF-1α 12 nM) injection on the same chip

(this involved binding affinity comparison). The oligosaccharides used were from glycosaminoglycans (GAG) family: heparin (HP6), chondroitin sulfate (CS) A, and dematan sulfate (DS). The proteins studied for the experiment were interferons γ, IgM anti-CS antibody, and stromal-derived cell factor-1α (SDF-1α), a cytokine belonging to the chemokine family. As an illustration, Fig. 9a represents a SPRi differential image of the chip obtained for the injection of one of these proteins (10 nM IgM anti-CS). All the spots containing CS appeared bright as they were recognized by the antibody. The kinetics of reflectivity variation obtained for the cytokine (12 nM SDF-1α) injection on the same chip is reported in Fig. 9b. It shows that the recognition process is highly dynamic (high dissociation rate). This result is fully compatible with the biological properties of these compounds since these compounds play a major role in the collect and concentration of diluted chemokines present in the blood. In this part, we illustrated the use of SPRi combined with polypyrrole electro-spotting as an efficient and versatile tool for studying molecular interactions between the main biological molecules: DNA–DNA, DNA–protein, protein–protein, and polysaccharides–protein. The data obtained without labeling are precious to understand and quantify biological events. However, beyond the classical molecular approach, SPRi was also applied for the detection of complex objects and had encountered some significant results, some of which will be introduced in the next paragraph.

2.2 Complex Object Studies

2.2.1 Cell Characterization and Sorting

Biochips dedicated to cell analysis have generated important interest for the development of new tools for diagnostic or research purposes. Blood contains a

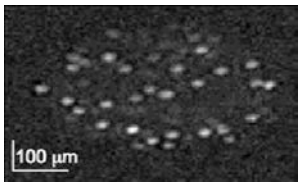

Fig. 10 SPR differential image of an anti-CD19 antibody spot 20 min after binding of lymphocyte B cells (injection of 300 µL of cells at 1.8×10^5 cells/mL). The clearer zones on this image represent individual cells bound onto anti-CD19

large number of different cell types. Part of them, leukocytes are large subject of investigation [40] because they are the main actors in the immunity response. A good understanding of their behavior may help diagnostic or drug design. In their works, Suraniti et al. [41] used functionalized SPRi prism as a tool for the detection of different kinds of blood cells. In order to mimic a population of leukocytes, two different murine cell lines were studied: one from B-type and another from T-type lymphocytes (lymphocytes are subtypes of leukocytes). To perform a specific identification of cell type, three different pyrrole-modified antibodies were electro-polymerized on the biochip. Monoclonal CD19 and CD3 antibodies were, respectively, directed against murine B lymphocytes and T lymphocytes. As a negative control, a human immunoglobulin G (IgG) nonspecific to any of the previous cell type was also used. By successive injections of the different cell types, the efficiency of this approach was demonstrated by observing specific binding between cells and corresponding antibody spots. For low concentration of cells, the individual cell binding events are clearly identified (Fig. 10). It opens new technical solutions for cell identification on miniaturized systems or surface adhesion kinetic studies.

2.2.2 Micrometric Spots for Individual Cell Arraying and Devoted Optical Instrumentation

The previous experiments clearly demonstrated the possibility to identify non-adherent cells type on polypyrrole spots functionalized with specific antibody. Even if this technique can be applied to detect individual biding event, it does not allow individual cell organization as far as the binding process is randomly distributed over specific spots. Cell–cell interactions are involved in a large number of relevant cellular mechanisms such as immune response, cell division, or stem cell differentiation. To study these interactions, a good localization of the immobilization of cells with regard to the others may be required. Using the microcantilever technique previously described [32, 33], Roupioz et al. [42] electro-polymerized pyrrole-modified antibody (anti-IAb and anti-CD90 antibodies), respectively, specific to B-type and T-type lymphocytes on gold-covered glass slide. Spot diameters are in the range of 7 µm, smaller than studied cells. After cell incubation and washing process, the authors

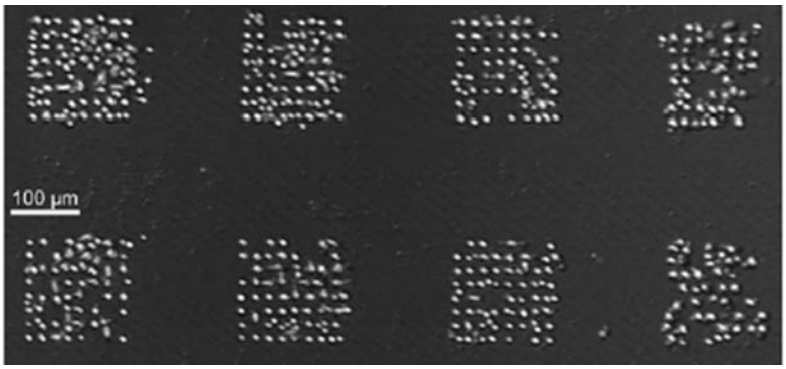

Fig. 11 Differential interference contrast (DIC) microscopy observation of blood cells immobilization in 8 × 8 matrix format

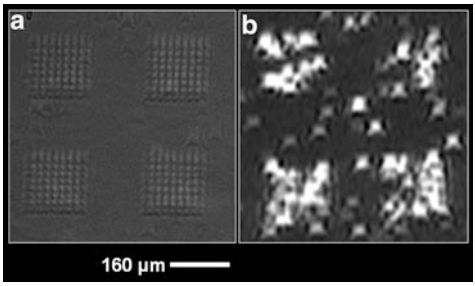

Fig. 12 SPR images of (**a**) antibody spots matrix and (**b**) cells matrix after binding of cells on an equivalent antibody pattern

obtained a specifically organized array of cells controlled by differential interference contrast (DIC) microscopy (Fig. 11). Selective capture of two cell types is demonstrated using intermingled array of the two antibodies. In our setup, the optical resolution of SPRi technique is not adapted for pitches of 20 µm, like used in these experiments, as can be observed in Fig. 12. This figure is the SPRi image of an 8 × 8 antibody spots array performed with a pitch of 20 µm on SPRi prism (a) and corresponding spots array with cell capture (b). As shown elsewhere [43], better resolution of cells can be achieved with SPRi in other configuration. Polypyrrole fixation strategy and SPRi will soon demonstrate their ability to realize and follow individual non-adherent cells' capture and 2D organization. Nevertheless, as the propagation length of the plasmon obtained with 638 nm wavelength excitation (necessary for appropriate sensitivity) will limit the resolution to few micrometers [44], we developed a coupled SPRi with classical optical microscopy.

2.2.3 Coupling SPR Imaging with Optical Microscopy

In the previous paragraph, we presented the SPRi efficiency for molecular label-free detection and cellular detection. But, as soon as microfluidics is involved, lots

of precautions must be taken, because diffusion processes and complex objects (cells or microparticles) having much bigger dimensions than the one of the evanescent field of the plasmon are not fully detected by SPRi. In order to overcome this difficulty and quantify its influence, we implemented one of our setups with a microscope on the top of the SPRi apparatus. It allowed us to compare the bulk events with the surface vicinity ones and to combine the high sensitivity to surface modification of the SPRi with the highest resolution of standard optical microscopy. For example, this coupled technique is used to distinguish cells captured on the surface from cells present in the solution.

3 Conclusion

In conclusion, SPRi is a technique that brings multiplexing to the conventional SPR sensors. SPRi is adapted to quantify very small local variations in optical index at metallic–dielectric interface and in turn, with an appropriate surface chemistry like electro-polymerization of pyrrole, can be adapted to detect various biological interactions. In this chapter, the versatility of applications has been illustrated through molecular interaction detection such as DNA, peptide, antibody, and oligosaccharide chips and also with an example dealing with complex object detection such as white blood cells. Strategies taking advantage of the multiplex, label-free, and real-time sensing characteristics of the SPRi have been developed to determine the affinities of the monitored interactions. These precious data quantifying biological events can be used in pharmacologic development and medical diagnostic. Moreover, recent applications in complex object studies like cells or developments like microspotting are pushing away the limits of SPRi by enlarging its fields of applications and increasing the multiplexing of the chip up to its intrinsic resolution. The continuous increase in peer-reviewed publications dealing with the use of SPRi for various applications together with the number of commercially available devices shows that SPRi is rapidly becoming an indispensable tool in biological studies.

References

1. Wood RW (1902) On a remarkable case of uneven distribution of light in a diffraction grating spectrum. Proc Phys Soc Lond 18:6
2. Rayleigh L (1907) On the dynamical theory of gratings. Proc R Soc Lond A 79:17
3. Bohm D, Pines D (1950) Screening of electronic interactions in a metal. Phys Rev 80(5):903
4. Bohm D, Pines D (1951) A collective description of electron interactions. I. Magnetic Interactions. Phys Rev 82(5):625
5. Pines D, Bohm D (1952) A collective description of electron interactions: II. Collective vs individual particle aspects of the interactions. Phys Rev 85(2):338
6. Ritchie RH (1957) Plasma losses by fast electrons in thin films. Phys Rev 1(5):874–881

7. Ritchie RH, Eldridge HB (1962) Optical emission from irradiated foils. Phys Rev 126(6):1935
8. Ritchie RH (1963) On surface plasma oscillations in metal foils. Progr Theor Phys 29 (4):607–609
9. Otto A (1968) Excitation of nonradiative surface plasma waves in silver by method of frustrated total reflection. Z Phys 216(4):398
10. Otto A (1968) Excitation of nonradiative surface plasma waves by light. Bull Am Phys Soc 13 (8):983
11. Kretschm E, Raether H (1967) Zur theorie der plasmaresonanzstrahlung an rauhen oberflachen. Z Naturforsch A Astrophys Phys Phys Chem A22(10):1623
12. Kretschm E, Raether H (1968) Radiative decay of non radiative surface plasmons excited by light. Z Naturforsch A Astrophys Phys Phys Chem A23(12):2135
13. Kretschm E, Raether H (1968) Plasma resonance emission in solids. Z Naturforsch A Astrophys Phys Phys Chem A23(4):615
14. Liedberg B, Nylander C, Lundstrom I (1983) Surface-plasmon resonance for gas-detection and biosensing. Sensors and Actuators 4(2):299–304
15. Liedberg B, Nylander C, Lundstrom I (1995) Biosensing with surface-plasmon resonance – how it all started. Biosens Bioelectron 10(8):R1–R9
16. Schasfoort RBM, McWhirter A (2008) SPR instrumentation. In: Schasfoort RBM, Tudos AJ (eds) Handbook of surface plasmon resonance. RSC Publishing Royal Society of Chemistry product, Cambridge, pp 35–79
17. Pitarke JM et al (2007) Theory of surface plasmons and surface-plasmon polaritons. Rep Progr Phys 70(1):1–87
18. Kooyman RPH (2008) Physics of surface plasmon resonance. In: Schasfoort RBM, Tudos AJ (eds) Handbook of surface plasmon resonance. RSCPublishing Royal Society of Chemistry product, Cambridge, pp 35–79
19. Sambles JR, Bradbery GW, Yang FZ (1991) Optical-excitation of surface-plasmons – an introduction. Contemp Phys 32(3):173–183
20. Frischeisen J et al (2008) Surface plasmon resonance sensor utilizing an integrated organic light emitting diode. Opt Express 16(22):18426–36
21. Scarano S et al (2010) Surface plasmon resonance imaging for affinity-based biosensors. Biosens Bioelectron 25(5):957–966
22. Livache T et al (1994) Preparation of a DNA matrix via an electrochemically directed copolymerization of pyrrole and oligonucleotides bearing a pyrrole group. Nucleic Acids Res 22(15):2915–2921
23. Livache T et al (1995) Biosensing effects in functionalized electroconducting conjugated polymer layers – addressable DNA matrix for the detection of gene-mutations. Synthetic Met 71(1–3):2143–2146
24. Da Silva S et al (2004) Biotinylated polypyrrole films: an easy electrochemical approach for the reagentless immobilization of bacteria on electrode surfaces. Bioelectrochemistry 63 (1–2):297–301
25. Grosjean L et al (2005) A polypyrrole protein microarray for antibody-antigen interaction studies using a label-free detection process. Anal Biochem 347(2):193–200
26. Cherif B et al (2006) Clinically related protein-peptide interactions monitored in real time on novel peptide chips by surface plasmon resonance imaging. Clin Chem 52(2):255–262
27. Suraniti E et al (2007) Construction of hybrid bilayer membrane (HBM) biochips and characterization of the cooperative binding between cytochrome-c and HBM. Langmuir 23 (12):6835–6842
28. Mercey E et al (2008) Polypyrrole oligosaccharide array and surface plasmon resonance imaging for the measurement of glycosaminoglycan binding interaction. Anal Chem 80 (9):3476–3482
29. Guedon P et al (2000) Characterization and optimization of a real-time, parallel, label-free, polypyrrole-based DNA sensor by surface plasmon resonance imaging. Anal Chem 72 (24):6003–6009

30. Livache T et al (2001) Polypyrrole electrospotting for the construction of oligonucleotide arrays compatible with a surface plasmon resonance hybridization detection. Synthetic Met 121(1–3):1443–1444
31. Szunerits S et al (2005) Comparison of different strategies on DNA chip fabrication and DNA-sensing: Optical and electrochemical approaches. Electroanalysis 17(22):2001–2017
32. Leichle T et al (2006) Copper electrodeposition localized in picoliter droplets using microcantilever arrays. Appl Phys Lett 88(25):4108
33. Descamps E et al (2007) Fabrication of oligonucleotide chips by using parallel cantilever-based electrochemical deposition in picoliter volumes. Adv Mater 19(14):1816
34. Fiche JB et al (2007) Temperature effects on DNA chip experiments from surface plasmon resonance imaging: Isotherms and melting curves. Biophys J 92(3):935–946
35. Fiche JB et al (2008) Point mutation detection by surface plasmon resonance imaging coupled with a temperature scan method in a model system. Anal Chem 80(4):1049–1057
36. Fuchs J et al (2010) Effects of formamide on the thermal stability of DNA duplexes on biochips. Anal Biochem 397(1):132–134
37. Fuchs J et al (2010) Salt concentration effects on equilibrium melting curves from dna microarrays. Biophys J 99(6):1886–1895
38. Maillart E et al (2004) Versatile analysis of multiple macromolecular interactions by SPR imaging: application to p53 and DNA interaction. Oncogene 23(32):5543–5550
39. Corne C et al (2008) SPR imaging for label-free multiplexed analyses of DNA N-glycosylase interactions with damaged DNA duplexes. Analyst 133(8):1036–1045
40. Toner M, Irimia D (2005) Blood-on-a-chip. Annu Rev Biomed Eng 7:77–103
41. Suraniti E et al (2007) Real-time detection of lymphocytes binding on an antibody chip using SPR imaging. Lab Chip 7(9):1206–1208
42. Roupioz Y et al (2009) Individual blood-cell capture and 2D organization on microarrays. Small 5(13):1493–1497
43. Peterson AW et al (2009) Surface plasmon resonance imaging of cells and surface-associated fibronectin. BMC Cell Biol 10:16
44. Huang B, Yu F, Zare RN (2007) Surface plasmon resonance imaging using a high numerical aperture microscope objective. Anal Chem 79(7):2979–2983

Part IV
Raman Spectroscopy

Lab-on-a-Chip Surface-Enhanced Raman Spectroscopy

A. März, P. Rösch, T. Henkel, D. Malsch, and J. Popp

Abstract In the area of bioanalytics reliable and sensitive detection methods for the analysis of a variety of molecules like, for example, drugs and DNA are required. As Raman spectroscopy is characterized by a high specificity, it is well suited for bioanalytical issues. However, a major drawback concerning this technique is the low sensitivity due to the weakness of the Raman effect. A possibility to achieve the sensitivity needed for bioanalytics is the use of surface-enhanced Raman spectroscopy (SERS). The addition of nanostructured metal surfaces leads to an enhancement of the Raman signal and a more sensitive detection method which is even able to detect single molecules.

Since the analysis of small samples and minimal sample volumes as well as the detection of low analyte concentrations are requested in bioanalytics, the combination of SERS and a lab-on-a-chip device seems to be a promising way to offer a sensitive detection method with reproducible measurement conditions and a highly defined detection area specified by a chip system.

The range of lab-on-a-chip devices applied for SERS detection varies from microarray platforms to microfluidic systems equipped with, for example, implemented SERS substrates fabricated by lithography or the possibility of in situ synthesis of colloidal substrates. Besides a multiplicity of designs and application areas, a variety of different materials and fabrication procedures for lab-on-a-chip

A. März • P. Rösch
Institute of Physical Chemistry and Abbe Center of Photonics, Friedrich Schiller University Jena, Helmholtzweg 4, 07743 Jena, Germany

T. Henkel • D. Malsch
Institute of Photonic Technology (IPHT), Albert-Einstein-Straße 9, 07745 Jena, Germany

J. Popp (✉)
Institute of Physical Chemistry and Abbe Center of Photonics, Friedrich Schiller University Jena, Helmholtzweg 4, 07743 Jena, Germany

Institute of Photonic Technology (IPHT), Albert-Einstein-Straße 9, 07745 Jena, Germany
e-mail: Juergen.popp@uni-jena.de

W. Fritzsche and J. Popp (eds.), *Optical Nano- and Microsystems for Bioanalytics*,
Springer Series on Chemical Sensors and Biosensors (2012) 10: 229–246
DOI 10.1007/978-3-642-25498-7_8,

systems are also established, for example, glass chips produced by wet etching or PDMS chips manufactured by pattern replication. Most of the devices are especially designed for a certain bioanalytical application. The combination of microarray platforms and SERS is, used for the detection of cancer, proteins, and microorganisms as well as for labelled and label-free detection of DNA and RNA. The applications of microfluidic systems vary from monitoring of proteins and drugs to the detection of cells. In addition to quantification using direct and indirect SERS measurements, multiplexing analysis in a microfluidic device is feasible.

The Lab-on-a-Chip Surface-Enhanced Raman Spectroscopy (LOC-SERS) as a reproducible and sensitive detection method enriches the field of bioanalytics.

Keywords Bioanalytic • Lab-on-a-chip (LOC) • Microarray • Microfluidic • SERS

Contents

1 Introduction

Lab-on-a-Chip Surface Enhanced Raman Spectroscopy (LOC-SERS) is becoming more and more important as a valuable and reliable detection method in the field of bioanalytics. The requirements needed for bioanalytical analysis like high sensitivity and specificity are provided by surface-enhanced Raman spectroscopy (SERS) whereas highly defined and reproducible measurement conditions are realized by the application of a lab-on-a-chip (LOC) device. This chapter gives an outline of the most common varieties and applications of LOC devices utilized in SERS. After a short summary of the basic principle of SERS, different types of LOC systems such as microfluidic devices, dielectrophoretic chips, microwell SERS chips, and microarrays as well as their applications are introduced.

2 Surface-Enhanced Raman Spectroscopy

Raman spectroscopy is based on the Raman effect, which is described as an inelastic light scattering between photons and molecules resulting in distinctive frequency-shifted scattered light. Even though Raman scattering is characterized by high specificity, a major drawback with respect to its application in bioanalytics is its low sensitivity as only one out of 10^6 photons is scattered inelastically. Considering the light-scattering effects, the incident laser radiation induces an electric dipole moment μ in the molecules, which can be described by

$$\mu = \alpha \cdot E_0 \tag{1}$$

with E_0 representing the electric field of the laser light and α the polarisability of the molecule. The intensity of a Raman signal is proportional to the square of the induced electric dipole moment. Therefore, an enhancement of the Raman intensity can be achieved according to (1) by an increase of the electric field as well as an increase of the polarisability α.

SERS takes advantage of the optical properties of nanostructured metal surfaces to achieve a Raman signal enhancement. Fleischmann et al. observed in 1974 an intense Raman signal of pyridine on a roughened silver electrode surface [1]. From that time, many researchers started to investigate this phenomenon to find an explanation for this Raman enhancement. Two mechanisms have been discussed to be responsible for the occurrence of an increased Raman signal intensity for molecules in close vicinity to a nanostructured metal surface. The first mechanism results from the long-range classical electromagnetic enhancement due to interaction of the incident laser light with the metal surface exciting surface plasmons leading to a local field enhancement. This electromagnetic enhancement mechanism shows a larger contribution to the overall enhancement of SERS as compared to the second mechanism, the so-called short-range chemical enhancement. The chemical enhancement mechanism is based on the interaction of a molecule with the metal surface causing the appearance of a new electronic charge transfer state due to chemisorption. This new electronic state acts as a resonant intermediate state and the enhancement can be explained according to electronic resonance Raman enhancement mechanism [2]. If both mechanisms appear simultaneously, the observed enhancement is composed multiplicative by both effects [3].

2.1 Electromagnetic Enhancement

The applied SERS active substrates vary in shape, size, and material. The largest enhancement factors have been achieved so far by applying gold, silver, and copper on a nanoscale of 10–100 nm. Concerning the shape of the substrate-roughened electrode surfaces, colloids, thin films, as well as lithographically produced

nanopatterns are feasible. Even though there is a large variation within size and shape of the used SERS substrate, a basic model can be applied for a general explanation of the electromagnetic enhancement mechanism: an isolated spherical particle much smaller than the incident laser wavelength is taken into account, so all processes taking place can be considered as quasi-static. The particle, characterized by a frequency-dependent dielectric function $\varepsilon_1(\omega)$, is surrounded by a medium or vacuum described by $\varepsilon_2(\omega)$. $\varepsilon_1(\omega)$ is supposed to be independent of the size of the particle and can be described by

$$\varepsilon_1(\omega) = n(\omega)^2, \tag{2}$$

$$n(\omega) = n'(\omega) + \mathrm{i}k(\omega), \tag{3}$$

where $n(\omega)$ represents the complex refractive index with $n'(\omega)$ (dispersion) as real and $k(\omega)$ (index of absorption) as imaginary part. The incident laser light with an electric field E_0 excites the surface plasmons within the metal nanoparticle inducing an electric field E_{out} outside the sphere according to the Lorenz–Mie theory [4]. The absolute square of E_{out} determines the intensity of the SERS signal and can be written as:

$$E_{\mathrm{out}}^2 = E_0^2 |g|^2 (1 + 3\cos^2\theta) \tag{4}$$

with θ being the angle along the polarisation direction and g given by:

$$g = \frac{\varepsilon_1(\omega) - \varepsilon_2(\omega)}{\varepsilon_1(\omega) + 2\varepsilon_2(\omega)}. \tag{5}$$

Equations (4) and (5) indicate that there are two factors which significantly influence the field intensity: first of all, a large field intensity is obtained when the angle θ is equal to 0° or 180°. Second, large g values lead to large field intensities. In order to maximize g, $\varepsilon_1(\omega)$ has to be approximately $-2\varepsilon_2(\omega)$. If the real part of $\varepsilon_1(\omega)$ is $-2\varepsilon_2(\omega)$, the imaginary part is small. This is the so-called plasmon resonance condition.

Considering now that the resulting electric field E_{out} induces an electric dipole moment within molecules in direct neighbourhood to the surface of the metal nanoparticle, the induced dipole radiates according to the Raman theory. This radiation, however, can now be enhanced too. The so-called second enhancement is much more complex and described in detail by Kerker et al [4]. To specify a rough overall enhancement, it is considered that the molecule is affected by the maximum enhancement and $|g| \gg 1$ with:

$$E_R = \frac{E_{\mathrm{out}}^2 {E'_{\mathrm{out}}}^2}{E_0^4}, \tag{6}$$

whereas $E'_{\text{out}}{}^2$ refers to the field appointed at the scattered frequency. For a more detailed description of the electromagnetic enhancement mechanism, the interested reader is referred to [4, 5].

2.2 Charge Transfer Enhancement

The charge transfer enhancement (CT) mechanism contributes much less to the overall enhancement of SERS than the electromagnetic mechanism. While the electromagnetic enhancement mechanism leads to typical enhancement factors of 10^6–10^8, the CT mechanism results in enhancement factors of 10–10^2 [2, 6, 7]. In order to explain the CT mechanism, the formation of a surface complex between the SERS active substrate M and the analyte molecule A (adsorbate) due to chemisorption is assumed:

$$\mathrm{M} + \mathrm{A} \rightarrow \mathrm{M} - \mathrm{A} \tag{7}$$

The formed metal–adsorbate complex M–A exhibits intermediate charge-transfer states similar to the ones known for inorganic complexes. If the energy of the incident laser light is in resonance with the energy of the newly formed charge-transfer transition according to

$$E_{\text{CT}} = E(S_1 - S_2) = h\nu, \tag{8}$$

an electronic resonance Raman excitation takes place. Since the resonance effect arises from the formation of the metal–adsorbate complex, the observed enhancement is comparable to the one observed for the well-known resonance Raman effect. The enhancement due to a resonance Raman effect is caused by an increase of the transition polarisability and, therefore, an increase of the Raman scattering [2, 3, 8]. For a more detailed description of the CT enhancement and resonance Raman effect, the interested reader is referred to [7].

2.3 Selection Rules

The selection rules for surface-enhanced Raman scattering are more relaxed compared to the ones for normal Raman scattering. It can be noticed that vibrational bands considered to be Raman inactive appear in a SERS spectrum. The selection rules for SERS take the interactions occurring between metal surface and analyte molecules into account. The CT enhancement mechanism originates from an adsorption of the molecule to the surface. The polarisability tensor α of a molecule adsorbed on a surface can be described as follows:

$$\alpha_{\text{eff}} = \frac{9}{(\varepsilon(\omega_0)+2)(\varepsilon(\omega_s)+2)} \begin{pmatrix} \alpha_{xx} & \alpha_{xy} & \varepsilon(\omega_s)\alpha_{xz} \\ \alpha_{yx} & \alpha_{yy} & \varepsilon(\omega_s)\alpha_{yz} \\ \varepsilon(\omega_0)\alpha_{zx} & \varepsilon(\omega_0)\alpha_{zy} & \varepsilon(\omega_0)\varepsilon(\omega_s)\alpha_{zz} \end{pmatrix} \quad (9)$$

with $\varepsilon(\omega_0)$ and $\varepsilon(\omega_s)$ representing the dielectric functions of the metal for incident laser frequency and the scattered frequency, respectively [9]. The tensor reveals that all vibrations parallel to the metal surface and, therefore, without contribution of α in z-direction are not enhanced. All vibrations with a contribution of α in z-direction are enhanced whereas vibrations oriented perpendicular to the surface experience the highest enhancement [10].

3 Lab-on-a-chip Devices

LOC devices applied in SERS vary in size, material, design, functionality, and application. Nevertheless, all LOC systems utilizing SERS have in common to achieve more reproducible SERS sample preparation and SERS measurement conditions. Before discussing the application of different LOC devices, the material and fabrication of these devices as well as the design and functions in particular of microfluidic devices concerning advantages, disadvantages, and innovations with respect to the implementation of such systems in SERS are introduced.

3.1 Materials and Fabrication

The two most common materials for LOC devices are polymers like polydimethylsiloxane (PDMS) and glass. They are either combined or applied as all-glass and all-polymer devices. Both materials offer advantages and disadvantages concerning the fabrication of LOC systems and their application in SERS.

Polymer devices (e.g., from polycarbonate (PC) or cyclo olefin copolymer(COC)) are suitable for mass production and can be used as disposables due to their low manufacturing costs. Another advantage of polymer devices is the fast availability of prototype devices made from PDMS. If the channel layout of a chip is designed, usually a moulding technique is utilized for the production of the device. Therefore a master of the chip design has to be created by, for example, photolithography, which is then used to mould the device in, for example, PDMS, and can be finally applied to produce a high quantity of the polymer-based chips with the same layout. A detailed description of the fabrication can be found in [11].

The polymer-based devices are usually used as disposable products as the material and fabrication is inexpensive and they are hard to regenerate after usage. However, a major drawback of polymer-based devices is the low chemical resistance of these devices. Some polymers exhibit moisture expansion by contact

with oil and are not resistant against organic solvents. Since most SERS experiments are carried out in an aqueous solution, this is not an issue to be concerned of. Another drawback is that polymers cause disturbing Raman signals when carrying out SERS measurement within purely polymer-based LOC devices [12]. In case the detection point is too close to the polymer material of the device or the excitation and scattered light has to pass through the polymer material, signals caused by the device material will appear in the spectrum. The combination of polymer-based devices with all-glass detection windows prevents this issue [13].

Glass as LOC material is more expensive and more difficult in terms of generating a large number of devices. One way to produce all-glass chips is the application of the wet-etching technique. Glass-wafers are coated with a microstructured nickel–chromium alloy mask, providing the channel layout of the LOC system. The structures are etched by using hydrofluoric acid. For the assembly of an all-glass microfluidic device, two mirror-inverted substrates with half channels are prepared and bonded (anodic) by using, for example, silicon as bond support layer [14]. All-glass devices provide a high chemical resistance and are reusable.

Most of the LOC devices applied for SERS are manufactured utilizing additional or individually modified productions steps to those mentioned above. Since the variety of LOC systems is quite high, just a brief overview concerning the used materials and assembly strategies is presented here.

3.2 Microfluidics and Their Functionalities

Microfluidic devices are often applied to work with solutions. For SERS to be implemented in microfluidic devices, special functionalities of microfluidic LOC systems are required to achieve reproducible sample preparation and measurement conditions and to allow the handling of small sample volumes. Lab-on-a-chip devices for SERS are designed to provide special functionalities for specific applications: for a SERS detection within solutions with colloids as SERS active substrate, an important issue is a reproducible mixing behaviour. To control the aggregation time and the mixing efficiency of colloid and analyte solution, the reagents are combined in situ. In general, the injection of the components into the fluidic device is realized by syringe pump systems, pressure-driven flow or capillary forces. An advantage of SERS measurements in a LOC fluidic device compared to cuvette measurements is a reproducible and high degree of mixing of the reagents by utilizing microstructures to initiate optimal mixing conditions. The group of Quang et al. introduced a pillar array PDMS microfluidic channel into their measurement arrangement (Fig. 1a) [15]. The pillar array fluidic channel is produced by a moulding technique. The pillars cause a stirring of the fluid rather than a turbulent flow. By doing so, a high mixing efficiency and a fast absorption of the analyte on the nanoparticles is achieved. Figure 1b represents another structured microfluidic channel applied by Lee et al. [16]. Here a zigzag-shaped PDMS microfluidic channel is created in order to obtain an efficient and fast mixing. The

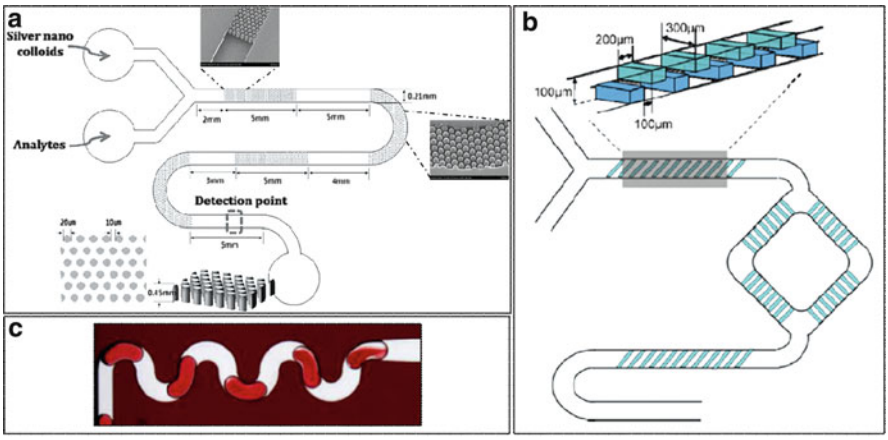

Fig. 1 Functionalities implemented in a microfluidic device to increase the mixing efficiency; (**a**) pillar array fluidic channel [15], (**b**) zigzag-shaped PDMS microfluidic channel [16], (**c**) all-glass chip with loops to provide mixing in droplets of the applied segmented flow. (Reprinted from Quang et al. Copyrights (2008) with permission from The Royal Society of Chemistry—Lab on a Chip, reprinted from Lee et al. Copyrights (2007) with permission from Elsevier—Analytica Chimica Acta)

zigzag shape is fabricated by stacking two PDMS layers. The layers with the upper and lower pattern of the zigzag channel are produced by a pattern replication method using a master and moulding it into the PDMS. Another possibility utilized to obtain a high mixing efficiency is the integration of loops into a microfluidic channel as shown in Fig. 1c. Both März et al. [18] who applied an all-glass chip as well as Wang et al. [17, 18] who employed a PDMS chip for their SERS measurements introduced mixing loops within their microfluidic devices. Both groups are working with the so-called segmented flow where the analyte and colloid solutions form droplets in an immiscible separation and transport fluid that usually is an oil. The application of a segmented flow prevents depositions in the microchannels and causes a high reproducibility of SERS measurements as "memory effects" are avoided [19]. The high degree of mixing initiated by the loops in combination with the application of a segmented flow can be proven by a visual experiment: two colourless components, iron chloride and ammonium thiocyanate, are injected into the LOC device. If these reagents coalesce a deep red complex, ferric thiocyanate, is formed. With a CCD camera, the mixing within the droplets is observed by investigating the build-up of the red complex in the droplets [17]. This simple visual experiment demonstrates the high mixing efficiency of integrated loops as functional element for mixing. Wilson et al. [20] implemented an in-situ colloidal synthesis within their microfluidic device, which requires an additional active mixing facility for the in situ colloidal synthesis. This operation is implemented by a stirring element. Besides the mentioned structures implemented in LOC devices, several others can be found in the literature all aimed at efficient mixing [13, 21].

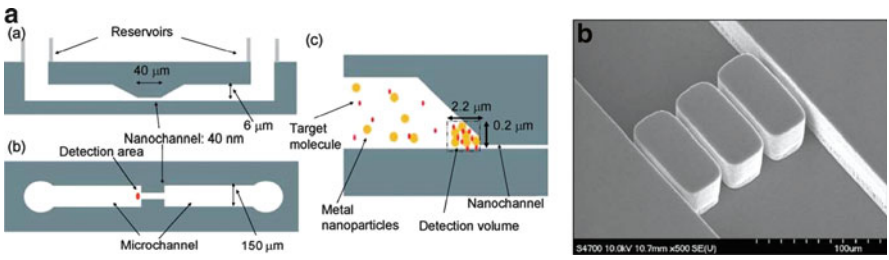

Fig. 2 Functionalities implemented into microfluidics for trapping of particles; (**a**) trapping of nanoparticles for the formation of a cluster and an increase of analyte concentration to create high detection sensitivity [23]; (**b**) PDMS posts in a microfluidic channel acting as membrane for trapping beads required for sample preparation steps like washing steps [24]. (Reprinted from Wang et al. Copyrights (2007) with permission from The Royal Society of Chemistry—Lab on Chip, reprinted from Monaghan et al. Copyrights (2007) with permission from American Chemical Society—Analytical Chemistry)

Besides introducing functional structures taking care of a high degree of mixing into a LOC fluidic device, there is the possibility of integrating some other functionalities: one function applied in LOC for SERS measurements is trapping of particles by membranes or reduction of channel diameters. Trapping of particles arises from different motivation, for example, some sample preparation steps require, trapping in advance to the SERS detection or the trapping is carried out in the area of the detection window to enhance the signal intensity. Wang et al. applied an optical device as shown in Fig. 2a where the micro-nanostructured fluidic channel allows the trapping of nanoparticles. A mixture of analyte and nanoparticle is added to one of the reservoirs (Fig. 2a) and drawn into the optical device by capillary forces. The nanoparticle size is larger than the diameter of the nanochannel; therefore they are trapped at the entrance resulting in the formation of a cluster. The capillary force still transports analyte through the cluster and an area of high analyte concentration is created achieving high detection sensitivity [22, 23]. Figure 2a presents in detail the parameters of the optical device used by Wang et al. like, for example, channel diameters, detection area, and detection volume. Monaghan et al. introduced a membrane into a microfluidic device for trapping microbeads needed for sample preparation (shown in Fig. 2b). The integrated membrane is fabricated by a moulding technique and consists of three 26 $\times$ 100 µm rectangular PDMS posts in a 110 µm-wide PDMS microchannel. The posts are spaced by 8 µm intervals and allow the passing of smaller particles. In this particular application, streptavidin-coated microspheres are trapped to provide the possibility of capturing biotinylated PCR products. The bead bed still enables washing steps and the flow of fluids containing the analyte molecules, which are supposed to be detected [24, 25]. Another approach for trapping nanoparticles and additionally controlling the aggregation is introduced by Tong et al. They apply a microfluidic device with implemented laser tweezers using an 830-nm laser for trapping metal nanoparticles and an excitation wavelength of 514 nm for the SERS detection. The trapping laser also induces inter-particle optical forces, which cause an agglomeration and are feasible for controlling the aggregation of nanoparticles [26].

Another functionality implemented by Huh et al. is the electrokinetic actuation of SERS nanoparticles at microwells, formed by three stacked layers: established of three stacked layers: the upper layer contains a gold electrode; the middle layer consists of a polyimide dielectric layer including microwells and an additional layer containing microchannels; the third layer includes again a gold electrode. This combination enables an active mixing to increase the binding efficiency of analyte and SERS substrate (nanoparticles) and rapid concentration of the product to be analysed in the detection area [27, 28].

The functionalities utilized with and within a microfluidic device are multifaceted. Besides the ones mentioned above, microfluidic devices implemented in SERS provide the transport of analytes to the detection area, the application of washing steps [29] or other more complex sample preparations like electrophoresis [30]. Other advantages offered by microfluidic LOC devices are the fast exchange of reagents within the detection window [31], online monitoring [32] of analyte concentration, multiplexing [33], stable and reproducible measurement conditions [19], as well as the possibility of high throughput. In terms of high throughput for sample preparation, Choi et al. designed a SERS-CD platform with the possibility of 12 different preparation steps on one LOC system [34].

3.3 Integrated Substrates in Microfluidic Devices

Beside the application of metallic nanoparticles as surface-enhanced Raman scattering active substrate in microfluidic devices, the direct integration of SERS substrates in the LOC devices for SERS measurements is more and more of interest. Several research groups are working on novel off-chip SERS substrates, which are also promising for on-chip applications [35–37]. However, there are already research groups that implement substrates into microfluidic channels. The group of Connatser et al. integrated nanostructures in microfluidic devices as shown in Fig. 3a. The periodic morphology is achieved by applying electron beam lithography on a polymer layer for the production of the structures. The dimension of the created patterns was 250 nm in height and 50–300 nm in diameter with a spacing of 50–200 nm. To achieve a Raman signal enhancement, a silver metal film with a thickness of 25 nm was evaporated on the completed pattern. Connatser et al. investigated the response factor of different types of patterns to compare the intensity of the enhanced Raman signals [38].

A new concept for the implementation of SERS active substrates in microfluidics was introduced by Vlasko-Vlasov et al. who integrated surface plasmon polariton (SPP) lenses in their device as shown in Fig. 3b. A silver layer with a thickness of 75 nm is applied to fabricate circular structures of eight nanoslits with a centre-to-centre distance of 460 nm and a width of each slit of approximately 110 nm in the flat metal surface by ion beam lithography. This structure provides high concentration of SPP energy in a subwavelength spot at the focal point as the surface plasmon polariton of the nanoslits excited with 633 nm, which corresponds to the SPP on the silver surface, interfere constructively. The combination of the SPP lens with a

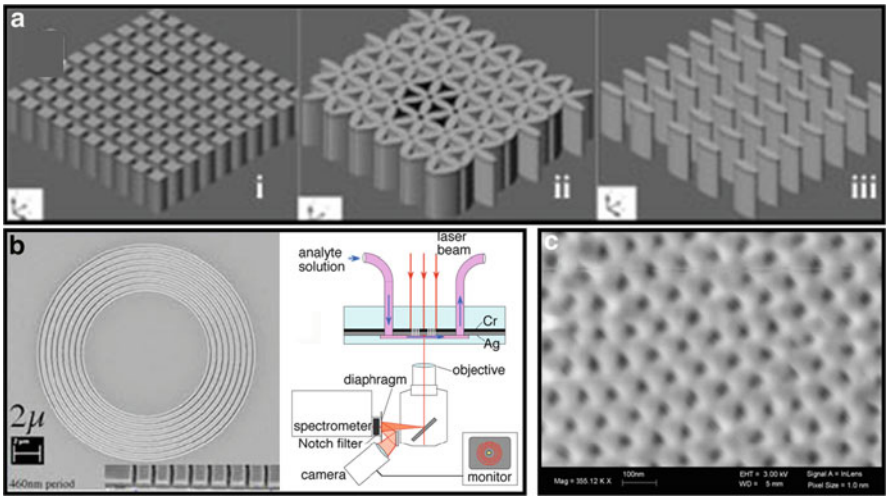

Fig. 3 Integrated structures used as SERS active substrate; (**a**) three patterns (pillars with a height of 250 nm capped with silver) of SERS active substrate integrated in a microfluidic device [38]; (**b**) surface plasmon polariton (SSP) lens—circles of nanoslits in a metal film applied for an enhancement of the electromagnetic field [39]; (**c**) nanoporous anodized aluminum oxide (AAO) on the top of a metallic aluminum substrate utilized as bio-compatible SERS substrate [40]. (Reprinted from Connatser et al. Copyrights (2008) with permission from Wiley-VCH Verlag GmbH & Co—Electrophoresis, reprinted from Vlasko-Vlasov et al. Copyrights (2010) with permission from American Institute of Physics—Applied Physics Letters, reprinted from Banerjee et al. Copyrights (2010) with permission from Elsevier—Chemical Physics Letters)

microfluidic device is also shown in Fig. 3b. Here, the analyte solution is pumped through a microfluidic channel passing the surface plasmon polariton lens. The excitation takes place from the top of the device and the scattered light is detected in transmission. Vlasko-Vlasov et al. demonstrate that the application of such a lens as SERS active substrate produces robust and stable spectra, which are comparable with spectra detected using colloidal solution for signal enhancement [39].

Another approach for integrated substrates in microfluidics is presented by Banerjee et al. who introduced a nanoporous anodic aluminum oxide (AAO) layer of hexagonally packed holes with a diameter of 20 nm and 50 nm in depth on the top of an aluminum substrate. The porous layer is shown in Fig. 3c. A microfluidic channel is placed on the substrate to provide the analyte solution and achieve a high throughput. The choice of AAO as substrate matrix is due to its high biocompatibility as this platform is applied in the area of bioanalytics for the monitoring of protein binding to a lipid bilayer [40].

There are several other research groups implementing SERS active substrates into microfluidic LOC devices. Huh et al. introduced ordered nanotube structures fabricated by metal evaporation through a shadow mask of AAO membrane [41]. Gordon et al. presents an array of nanoholes in a gold film applied as SERS substrate within a microfluidic device [42]. More detailed information and additional approaches concerning the implementation of nanostructures as SERS active substrate into a microfluidic device can be found in [42–46].

3.4 Microarrays

Considering LOC devices implemented in SERS, not just microfluidic systems but also microarrays have to be considered. Microarrays in SERS are applied as a chip-based assay with a spot-wise detection possibility for a specific issue. There are different approaches for this kind of LOC device; the microarray is either based on a chip with an integrated SERS active substrate or a functionalized platform is provided and labelled and label-free SERS active nanoparticles are introduced for the spectroscopic readout. Abell et al. presented a novel approach for a multiwell array SERS chip by introducing a PDMS array with integrated SERS active substrates of isolated microwells ensuring that no cross-contamination can occur. A high throughput and multiplexing can be achieved by the multiwall array [47]. Allain et al. also designed a microarray platform based on a silver-coated glass plate with microwells. They functionalized their SERS active substrate to bind labelled DNA for detection [48]. Another approach for a SERS array is presented by Wang et al. They applied a silver nanoparticle-coated Si nanowire array for the detection of pesticides [49].

Concerning the application of microarrays based on a functionalized platform, a lot of different approaches can be found in the literature: label-free microarray readout for microorganisms is introduced by Knauer et al. who present a chip device with a functionalized surface for a specific binding of microorganisms [50]. Label-free nanoparticles are added to achieve the signal enhancement for the detection [50]. Usually biomolecules are identified by using special SERS labels. Thereby a substrate is functionalized to bind the analyte molecule and nanoparticles equipped with specific antibodies and a Raman label used for the detection. The antibody sitting on the surface of the nanoparticle binds to the analyte molecule. The label is assigned to a specific antibody for the analyte molecule. The specific SERS spectrum of the label attached to the nanoparticle acting as SERS active substrate is used for the identification of the analyte molecule [51–55].

A novel approach regarding microarrays is presented by Islam et al. They demonstrate the great potential of an interdigitated array of electrodes for a LOC application [56, 57].

For more detailed and additional information on SERS mircoarrays, their fabrication, design, and application, the interested reader is referred to [58–61].

4 Application

The applications of LOC devices for surface-enhanced Raman scattering measurements in bioanalytics vary from investigations of cells, microorganisms, and DNA to quantitative and monitoring experiments of drugs and proteins. In the following section, some representative examples out of the broad variety of applications will be presented in more detail.

4.1 Quantitative and Monitoring Investigations

A major issue in SERS is the quantification and the monitoring of analyte molecules. Especially for monitoring experiments, the application of microfluidic devices is quite useful. A number of research groups utilized LOC-SERS measurements to perform quantitative analytics and monitoring experiments. The groups of Yea et al. and Lee et al. worked on sensitive trace analysis of cyanide water pollutant [62] and malachite green [16] applying PDMS microfluidic channels. Both groups [63] demonstrated the great potential of LOC-SERS for sensitive analyte quantification. Ackermann et al. presented investigations on online monitoring of concentration fluctuations of the drugs promethazine and mitoxantrone by applying a segmented flow in a microfluidic device [19, 32]. Subsequent studies by März et al. demonstrated that the additional implementation of an isotope-edited internal standard improves the monitoring of experiments by taking the influence of enhancement variations due to the applied colloid into account [17]. Abu-Hatab et al. applied a device with parallel microchannels for multiplex monitoring of influences of different pH values and different anions of the aggregation agent on the SERS spectra [33].

A different approach for quantitative studies on mercury (II) ions is presented by Wang et al. [18]. They demonstrate that quantification can be done indirectly: rhodamine B dye molecules in close vicinity to the surface of gold nanoparticles are replaced upon adding mercury (II) ions (Fig. 4) leading to decreasing SERS intensities of rhodamine B bands with an increase of the concentration of mercury (II) ions (see Fig. 4a). Figure 4b represents the change of the peak area of the rhodamine B band at 1,547 cm^{-1} for different mercury (II) ions concentration. Wang et al. applied segmented flow measurements in a PDMS microfluidic device for these investigations [18].

4.2 DNA and RNA Detection

The detection of DNA using LOC-based SERS is in the focus of several research groups. For example, Monaghan et al. developed a chip-based analysis for the detection of nucleic acid sequences of Chlamydia trachomatis [24]. Therefore, biotinylated PCR products are captured by polymer microspheres covered with streptavidine. The PCR products are subsequently hybridised against a labelled probe for detection. A sequence-specific DNA detection applying LOC-SERS is presented by Strelau et al. using a solid chip surface with immobilised capture DNAs, where target strands can be hybridised [29]. The target strands are labelled for SERS detection [29]. The detection of duplex dye-labelled DNA oligonucleotides applying SERS in a PDMS microfluidic chip was carried out by Park et al. [64]. Their method prevents the need of immobilisation steps and PCR amplification. A multiplexing of DNA and RNA has been carried out by Cao et al. by also applying

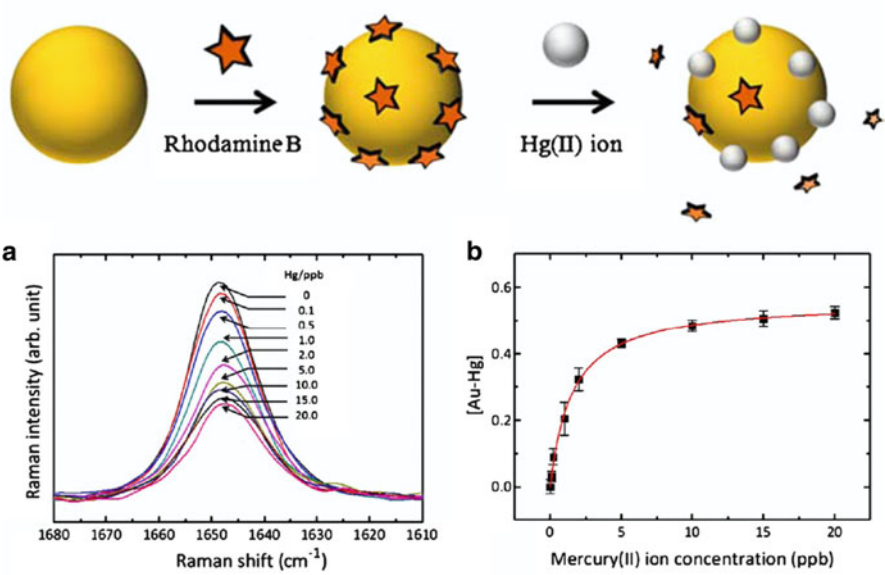

Fig. 4 Schematic mechanism of sensing of mercury (II) ion on gold nanoparticles based on the replacement of rhodamine B dye molecules; (**a**) change of SERS intensity of the band at 1,547 cm^{-1} referring to different concentrations of Hg (II) ion; (**b**) variation of the peak area with regard to the Hg (II) ion concentration for the band shown in Fig. 4a [18]. (Reprinted from Wang et al. Copyrights (2009) with permission from Springer—Analytical and Bioanalytical Chemistry)

a label-based method [51]. For more detailed information, the interested reader is referred to [65].

4.3 Investigations on Cells, Microorganisms, and Other Biomolecules

Furthermore, a lot of investigations are reported on cells, microorganisms, and other biomolecules utilizing SERS in a LOC system. The group of Zhang et al. successfully demonstrated the characterisation of a Chinese hamster ovary (CHO) cell in a microfluidic device by the means of SERS [66]. Figure 5a presents a picture of CHO cells in a microfluidic channel. By incubating the cells with gold nanoparticles, cellular SERS spectra can be recorded as shown in Fig. 5b (upper spectrum). Cells without gold nanoparticles do not exhibit any significant Raman information (lower spectrum). For a detailed cell characterization, a mapping experiment can be carried out with the applied setup.

A lot of other LOC-SERS studies to investigate microorganisms such as bacteria [50, 67, 68], peptides [25], proteins [22, 40, 69], pesticides [49], enzymes [28, 54,

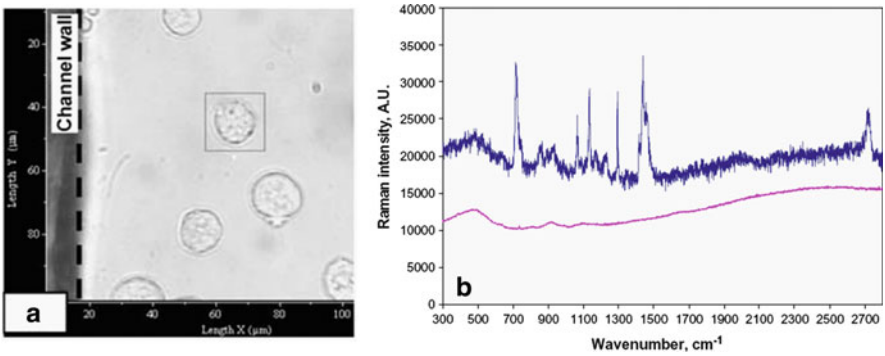

Fig. 5 Investigation of cells in a microfluidic device: (**a**) photograph of CHO cells in a microfluidic channel; (**b**) *upper graph*: SERS spectrum of CHO cells incubated with gold nanoparticles; lower spectrum: Raman spectrum of CHO cell without gold nanoparticles [66]. (Reprinted from Zhang et al. Copyrights (2008) with permission from Springer—Analytical and Bioanalytical Chemistry)

55, 70], and pathogens [52, 58] can be found. More detailed information concerning the application of LOC-SERS for molecular and cellular analysis can be found in the review article by Huh et al. [71].

5 Conclusion

SERS implemented in a LOC device is becoming more and more important in the area of bioanalytics. SERS as a detection method provides the sensitivity and specificity needed for the analysis of biomolecules, whereas the application of a LOC device allows the handling of small sample volumes, offers reproducible and highly definite measurement conditions, and exhibits a high analysis throughput.

The application of LOC systems allows the implementation of a variety of functionalities: for example, sample preparation like mixing, washing steps, separation, trapping, etc. can be integrated in microfluidic devices. Especially for small sample volumes the handling and the reproducibility of the sample preparation become much easier. Concerning the application of SERS, the integration of active substrates in flow-through devices is extremely promising to improve the LOC setups in terms of an even more reliable analysis. Microarrays utilized as LOC devices for SERS measurements provide the possibility of multiplexing as well as a high analysis throughput. The combination with fluidic channels seems to be even more effective as shown by several research groups [27–29].

Many research groups showed that the application of LOC-SERS exhibits a high potential for bioanalytics. Besides quantitative monitoring of drugs, sequence-specific analysis of DNA, investigations of microorganisms, as well as the

characterization of cells, many other biomolecules have been studied utilizing LOC-SERS demonstrating its versatility.

References

1. Fleischmann M, Hendra PJ, McQuillan AJ (1974) Chem Phys Lett 26:163–166
2. Campion A, Kambhampati PF (1998) Chem Soc Rev 27:241–250
3. Brandt SE, Cotton TM (1993) In: Rossiter BW, Baetzold RC (eds) Investigations of surfaces and interfaces – Part B, vol IXB, 2nd edn. Wiley, New York, pp 633–675
4. Kerker M, Wang D-S, Chew H (1980) Appl Opt 19:4159–4173
5. Schatz GC, Van Duyne RP (2002) In: Chalmers JM, Griffiths P (eds) Handbook of vibrational spectroscopy, vol 1. Wiley, Chichester, pp 759–774
6. Cotton TM (1988) In: Clark RJH, Hester RE (eds) Advances in spectroscopy, vol 16. Wiley, Chichester, pp 91–153
7. Robert B (2009) Photosynth Res 101:147–155
8. Arenas JF, López-Tocón I, Castro JL, Centeno SP, López-Ramírez MR, Otero JC (2005) J Raman Spectrosc 36:515–521
9. Otto A, Mrozek I, Grabhorn H, Akemann W (1992) J Phys-Condens Matter 4:1143–1212
10. Creighton JA (1985) Surf Sci 158:211–221
11. Beard NP, Edel JB, deMello AJ (2004) Electrophoresis 25:2363–2373
12. McAnally GD, Everall NJ, Chakmers JM, Smith WE (2003) Appl Spectrosc 57:44–50
13. Keir R, Igata E, Arundell M, Smith WE, Graham D, McHugh C, Cooper JM (2002) Anal Chem 74:1503–1508
14. Henkel T, Bermig T, Kielpinski M, Grodrian A, Metze J, Kohler JM (2004) Chem Eng J 101:439–445
15. Quang LX, Lim C, Seong GH, Choo J, Do KJ, Yoo SK (2008) Lab Chip 8:2214–2219
16. Lee S, Choi J, Chen L, Park B, Kyong JB, Seong GH, Choo J, Lee Y, Shin KH, Lee EK, Joo SW, Lee KH (2007) Anal Chim Acta 590:139–144
17. März A, Ackermann KR, Malsch D, Bocklitz T, Henkel T, Popp J (2009) J Biophoton 2:232–242
18. Wang G, Lim C, Chen L, Chon H, Choo J, Hong J, deMello AJ (2009) Anal Bioanal Chem 394:1827–1832
19. Strehle KR, Cialla D, Rosch P, Henkel T, Kohler M, Popp J (2007) Anal Chem 79:1542–1547
20. Wilson R, Bowden SA, Parnell J, Cooper JM (2010) Anal Chem 82:2119–2123
21. Chon H, Lim C, Ha SM, Ahn Y, Lee EK, Chang SI, Seong GH, Choo J (2010) Anal Chem 82:5290–5295
22. Wang M, Benford M, Jing N, Cote G, Kameoka J (2009) Microfluid Nanofluid 6:411–417
23. Wang M, Jing N, Chou IH, Cote GL, Kameoka J (2007) Lab Chip 7:630–632
24. Monaghan PB, McCarney KM, Ricketts A, Littleford RE, Docherty F, Smith WE, Graham D, Cooper JM (2007) Anal Chem 79:2844–2849
25. Chou IH, Benford M, Beier HT, Cote GL, Wang M, Jing N, Kameoka J, Good TA (2008) Nano Lett 8:1729–1735
26. Tong LM, Righini M, Gonzalez MU, Quidant R, Kall M (2009) Lab Chip 9:193–195
27. Huh YS, Chung AJ, Cordovez B, Erickson D (2009) Lab Chip 9:433–439
28. Huh YS, Lowe AJ, Strickland AD, Batt CA, Erickson D (2009) J Am Chem Soc 131:2208–2213
29. Strelau KK, Kretschmer R, Moller R, Fritzsche W, Popp J (2010) Anal Bioanal Chem 396:1381–1384
30. Becker M, Budich C, Deckert V, Janasek D (2009) Analyst 134:38–40
31. Lee S, Joo S, Park S, Kim S, Kim HC, Chung TD (2010) Electrophoresis 31:1623–1629

32. Ackermann KR, Henkel T, Popp J (2007) Chemphyschem 8:2665–2670
33. Abu-Hatab NA, John JF, Oran JM, Sepaniak MJ (2007) Appl Spectrosc 61:1116–1122
34. Choi D, Kang T, Cho H, Choi Y, Lee LP (2009) Lab Chip 9:239–243
35. Cialla D, Hubner U, Schneidewind H, Moller R, Popp J (2008) Chemphyschem 9:758–762
36. Lal S, Grady NK, Kundu J, Levin CS, Lassiter JB, Halas NJ (2008) Chem Soc Rev 37:898–911
37. Banholzer MJ, Millstone JE, Qin LD, Mirkin CA (2008) Chem Soc Rev 37:885–897
38. Connatser RM, Cochran M, Harrison RJ, Sepaniak MJ (2008) Electrophoresis 29:1441–1450
39. Vlasko-Vlasov V, Joshi-Imre A, Bahns JT, Chen L, Ocola L, Welp U (2010) Appl Phys Lett 96:203103
40. Banerjee A, Perez-Castillejos R, Hahn D, Smirnov AI, Grebel H (2010) Chem Phys Lett 489:121–126
41. Huh YS, Erickson D (2010) Biosens Bioelectron 25:1240–1243
42. Gordon R, Sinton D, Kavanagh KL, Brolo AG (2008) Acc Chem Res 41:1049–1057
43. Lee SK, Kim SH, Kang JH, Park SG, Jung WJ, Kim SH, Yi GR, Yang SM (2008) Microfluid Nanofluid 4:129–144
44. Lim C, Hong J, Chung BG, deMello AJ, Choo J (2010) Analyst 135:837–844
45. Myers FB, Lee LP (2008) Lab Chip 8:2015–2031
46. Liu GL, Lee LP (2005) Appl Phys Lett 87:074101
47. Abell JL, Driskell JD, Dluhy RA, Tripp RA, Zhao YP (2009) Biosens Bioelectron 24:3663–3670
48. Allain LR, Vo-Dinh T (2002) Anal Chim Acta 469:149–154
49. Wang XT, Shi WS, She GW, Mu LX, Lee ST (2010) Appl Phys Lett 96:053104
50. Knauer M, Ivleva NP, Liu XJ, Niessner R, Haisch C (2010) Anal Chem 82:2766–2772
51. Cao YWC, Jin RC, Mirkin CA (2002) Science 297:1536–1540
52. Driskell JD, Kwarta KM, Lipert RJ, Porter MD, Neill JD, Ridpath JF (2005) Anal Chem 77:6147–6154
53. Li T, Guo LP, Wang ZX (2008) Biosens Bioelectron 23:1125–1130
54. Li T, Liu DJ, Wang ZX (2009) Biosens Bioelectron 24:3335–3339
55. Yazgan NN, Boyaci IH, Temur E, Tamer U, Topcu A (2010) Talanta 82:631–639
56. Islam MM, Ueno K, Juodkazis S, Yokota Y, Misawa H (2010) Anal Sci 26:13–18
57. Islam MM, Ueno K, Misawa H (2010) Anal Sci 26:19–24
58. Grow AE, Wood LL, Claycomb JL, Thompson PA (2003) J Microbiol Methods 53:221–233
59. Song YJ, Elsayed-Ali HE (2010) Appl Surf Sci 256:5961–5967
60. Vo-Dinh T, Dhawan A, Norton SJ, Khoury CG, Wang HN, Misra V, Gerhold MD (2010) J Phys Chem C 114:7480–7488
61. Wang GQ, Wang YQ, Chen LX, Choo J (2010) Biosens Bioelectron 25:1859–1868
62. Yea K, Lee S, Kyong JB, Choo J, Lee EK, Joo SW, Lee S (2005) Analyst 130:1009–1011
63. Jung JH, Choo J, Kim DJ, Lee S (2006) Bull Korean Chem Soc 27:277–280
64. Park T, Lee S, Seong GH, Choo J, Lee EK, Kim YS, Ji WH, Hwang SY, Gweon DG, Lee S (2005) Lab Chip 5:437–442
65. Graham D, Faulds K (2008) Chem Soc Rev 37:1042–1051
66. Zhang XL, Yin HB, Cooper JM, Haswell SJ (2008) Anal Bioanal Chem 390:833–840
67. Wilson R, Monaghan P, Bowden SA, Parnell J, Cooper JM (2007) Anal Chem 79:7036–7041
68. Walter A, März A, Schumacher W, Rösch P, Popp J (2011) Lab Chip 11:1013–1021
69. Cao YC, Jin RC, Nam JM, Thaxton CS, Mirkin CA (2003) J Am Chem Soc 125:14676–14677
70. März A, Mönch B, Rösch P, Kiehntopf M, Henkel T, Popp J (2011) Anal Bioanal Chem 400:2755–2761
71. Huh YS, Chung AJ, Erickson D (2009) Microfluid Nanofluid 6:285–297

Microfluidic Raman Spectroscopy for Bio-chemical Sensing and Analysis

Praveen C. Ashok and Kishan Dholakia

Abstract The detection and analysis of bio-chemical analytes are important in the fields of personal healthcare, drug development, and environmental science, among others. The field of microfluidics aims to realize portable devices which can perform fast and sensitive bioanalyte detection with minimal sample preparation. Raman spectroscopy is a powerful tool for analyte detection owing to its high specificity and its ability for multi-component detection in an analyte. Combining microfluidics with Raman spectroscopy would help achieve miniaturized analytical devices that may provide rich information about a given analyte. However, the low cross-section of Raman process demands special geometries to achieve such a convergence. The majority of the previous embodiments were restricted to free-space geometry, limiting portability. However, in recent studies, fiber-based Raman detection system incorporated in microfluidics offers the opportunity to develop portable optofluidic bioanalyte detection devices. Here, we review various approaches used for using Raman spectroscopy in microfluidics for analyte detection, and various analytical approaches that could be used to enhance the detection sensitivity of Raman spectroscopy-based detection. This is followed by a detailed discussion about the fiber-based optofluidic Raman detection systems.

Keywords Analyte detection • Fiber Raman probe • Microfluidics • Raman spectroscopy • Soft lithography

P.C. Ashok (✉) • K. Dholakia
SUPA, School of Physics and Astronomy, University of St Andrews, North Haugh, St. Andrews, Fife, KY16 9SS Scotland, UK
e-mail: pca7@st-andrews.ac.uk

W. Fritzsche and J. Popp (eds.), *Optical Nano- and Microsystems for Bioanalytics*, Springer Series on Chemical Sensors and Biosensors (2012) 10: 247–268
DOI 10.1007/978-3-642-25498-7_9,

Contents

1 Introduction

The bio-chemical analysis communities are pushing toward the development of cheaper, miniaturized, and portable devices while simultaneously achieving lower detection limits, improved sensitivity, faster analysis, and high throughput with a reduced requirement upon sample volume [1]. This has resulted in the unprecedented advancement of the field that is variously addressed using terms such as "microfluidics and nanofluidics," "Lab on a Chip (LoC)," or "micro total analysis system (μTAS)" [2]. To achieve functionality, LoC technology requires integration of various tools for on-chip sample preparation, control, and sensing. To achieve sensing and detection within microfluidic devices, techniques such as chemical, thermal, or optical sensing are being widely used [1, 2].

Among these, optical detection techniques have played a crucial role in the development of LoC technology. Various optical imaging and spectroscopic techniques have been widely used for bio-chemical sensing and analysis as they have proven track records in achieving the lowest limits of detection while obtaining a high amount of information from the samples [3]. Among these, Raman spectroscopy is a potential optical detection technique which has found several applications within microfluidic platforms [1].

Over the past 3 decades, Raman spectroscopy has emerged as a powerful analytical tool for bio-chemical analysis. Raman spectroscopy is the result of inelastic scattering of photons from samples [4], yielding information about vibrational and rotational modes in a system. As it is a scattering process which does not involve any electronic process from the sample such as absorption or fluorescence, Raman spectroscopy can be performed irrespective of the electronic energy levels of the sample of interest. A vibronic energy level diagram for the Stokes Raman scattering process is shown in Fig. 1. Raman spectra are presented as a Raman shift with respect to the excitation wavelength, and this shift is expressed in wave numbers (units of cm^{-}). The particular advantage of using Raman scattering is

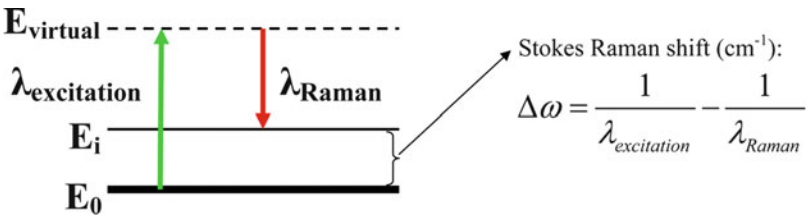

Fig. 1 Energy level diagram of Raman stokes scattering process. "$\lambda_{excitation}$" is the wavelength of the excitation photon, "λ_{Raman}" is the wavelength of Raman photon, "$\Delta\omega$" is the Stokes Raman shift, and "E" is the energy level of the atom or molecule. Raman shift is normally expressed in units of "cm^{-1}"

that it can be performed at a range of excitation wavelengths. Thus, the excitation pulse can be tuned to consider the absorption of the analyte and its surroundings, unlike infrared absorption spectroscopy which is incompatible with the water-rich environment of biological systems due to the strong absorption of water in the infrared region. In contrast to fluorescence spectroscopy, Raman spectra provide sharp, distinctive Raman peaks corresponding to the vibrational characteristics of the sample. Through deconvolution of the resulting spectra, it is possible to achieve simultaneous multi-component detection, effectively giving a "chemical fingerprint" of the composition of the sample of interest [1].

Even though this is a powerful spectroscopic technique, the cross- section of Raman scattering process is orders of magnitude lower than that of fluorescence. The availability of highly sensitive CCDs has given a boost for the field of Raman spectroscopy. One of the solutions to overcome the issue of low Raman cross-section is surface-enhanced Raman spectroscopy (SERS) [5]. However, for the implementation of SERS, one needs to either mix the samples with colloidal nanoparticles or rely on the adsorption of the sample on specialized SERS substrates. Consequently, even though SERS offers enhancement in orders of magnitude, the increased complexity and poor reproducibility of the process make it less favorable when compared to standard Raman spectroscopy.

Implementation of Raman spectroscopy as a viable analytical detection method in microfluidics is still in its infancy when compared to other spectroscopic techniques [6]. This chapter reviews the history of microfluidic Raman spectroscopy (MRS) and discusses some of the recent advancements in this field in terms of implementation. Such developments could lead to the development of microfluidic Raman analytical devices that are portable and alignment free, suitable for field applications.

2 History of Microfluidic Raman Spectroscopy

It has been over a decade since the birth of MRS. In the first reported work, microfluidics and Raman spectroscopy were combined. Since then, several groups demonstrated the power of Raman spectroscopy as a potential optical detection tool

to interrogate samples in microfluidic chips. Later years saw a wide variety of applications result from the marriage of these two powerful technologies. The reviews by Viskari and Landers (2006) [1] and Hunt and Wilkinson (2008) [3] discuss the implementation of Raman spectroscopy as a potential optical detection technique in microfluidics. MRS has seen variants of its implementation in terms of different microfluidic architectures and different Raman spectroscopic techniques such as normal Raman spectroscopy, confocal Raman spectroscopy, resonance Raman spectroscopy, and SERS [1]. Here, we review the evolution of MRS over last decade, mentioning the major works that helped the advancement of this technology. We present various relevant studies in the correct context and chronologically in order to illustrate the relevance of these works in the advancement of the field of MRS. A special emphasis is given to each study on the various microfluidic architectures and Raman detection schemes adopted for the implementation of this technology for bio-chemical analysis.

2.1 Initial Works

Since the late 1980s, there have been several papers where microcapillary-based electrophoretic systems were interrogated with Raman spectroscopy [7, 8]. A similar approach was used to analyze isotachophoretically concentrated ribonucleotides using Raman spectroscopy [9]. Capillaries, however, had limited surface area, reducing the sensitivity of detection, and the alignment requirement was higher for mounting a capillary on a conventional Raman microscope. These issues led to the implementation of a microchip-based version of the same separation technique, in which on-chip Raman spectroscopy of isotachophoretically separated herbicides—paraquat and diquat—was achieved [10]. In this work, a glass microfluidic chip was coupled to a free-space Raman microprobe; more efficient collection of Raman signal could be achieved with reduced background from the glass by carefully choosing the thickness of the coverslip under the microchip. This study envisages the opportunities for further enhancement of sensitivity by implementing SERS or resonant Raman spectroscopy.

In a later study, time-resolved resonance Raman spectroscopy (TR^3) was employed within a glass microfluidic chip in order to study chromophore structure [11, 12]. This study was achieved through miniaturization of the standard rapid-flow technique used to study photochemical kinetics and combining it with Raman spectroscopic detection. The standard rapid-flow technique was performed using a macro flow device, requiring high amounts of pigments at high flow rates. The implementation of a microfluidic version of the device reduced the required sample volume by shrinking the fluidic channel to match the confocal volume of the Raman detection system.

The pioneering work on the implementation of SERS in microfluidics was the detection of a derivative of trinitrotoluene (TNT) in a glass microfluidic chip using surface-enhanced resonance Raman spectroscopy (SERRS) [13]. In this device,

on-chip preparation of silver colloid was achieved which was further mixed with the sample to be detected followed by detection of SERRS. Microfluidic chip allowed reduction of the required reagent volume, and the sensitivity was improved by two orders of magnitude by using SERRS compared to macro flow cells. In addition, the long-term stability of the flow stream, offered by the microfluidic channel, allowed accumulation of signal for a longer duration.

2.2 Raman Spectroscopy to Probe Reactions

Microfluidics enables real-time study of chemical reactions through micro-reactors using reduced volume of reagents. This enables optimization of various parameters, which is essential for efficient large-scale production of chemicals commercially. Various detection methods—thermal, electrical, and optical—have been combined with micro-reactor-based microfluidic chips in order to probe the temporal and spatial evolution of a chemical reaction. The ability for Raman spectroscopy to perform simultaneous multi-component detection makes it a desirable method to monitor the progress of a reaction within a micro-reactor. There have been several architectures to integrate Raman detection in micro-reactors for temporal and spatial mapping of the chemical composition of the sample in micro-reactors. The formation of diazonium salts in anhydrous conditions and their subsequent chlorination in situ were studied using online, on-chip Raman spectroscopy by probing a glass-based microfluidic reactor using a Raman microscope [14]. Another reported study looked at spatially mapping the evolution of the reaction to form ethyl acetate from ethanol and acetic acid in a Pyrex glass-based microfluidic chip using a confocal Raman microscope [15]. It was observed in this work that SERS or resonance Raman spectroscopy should be employed to enhance the sensitivity and to reduce the acquisition time to achieve real-time monitoring of the reaction. The applicability of MRS on micro-reactors was further extended to studies of biologically relevant processes such as enzyme-catalyzed reactions for the synthesis of peptides from amino acids [16].

The first use of PDMS-based microfluidic chips in conjunction with Raman spectroscopic probing was to study the mixing of ethanol and isopropanol using confocal Raman microscopy [17]. Since PDMS is a polymer, it is highly Raman active and there are specific Raman lines due to PDMS in the fingerprint region. This work discusses the issues associated with the background signals from PDMS unless a confocal configuration is used for Raman detection. MRS for reaction optimization was further taken forward for studying various reaction dynamics with a variety of microfluidic architectures. This included designing specialized micromixers to enhance the efficiency of mixing dynamics [18, 19].

Apart from being used as a technique for studying chemical reactions, MRS was employed to study fluid dynamics. The diffusion of two miscible, non-reacting liquids was studied in a silicon glass-based microfluidic chip [20]. Confocal Raman spectroscopy was used to probe the interdiffusion of chloroform,

dimethylsulfoxide, acetonitrile, and dimethylformamide. The obtained data were used to estimate the diffusion coefficients of the liquids. Through their approach, the authors envisage exploiting the multi-component detection ability of Raman spectroscopy for probing the interdiffusion of more than two liquids, or situations where multiple chemical reactions occur simultaneously.

2.3 *Bio-chemical Detection Using SERS in Microfluidics*

As mentioned in Sect. 1, SERS-based detection is widely used to overcome the low cross-section of the Raman process and has additionally found a variety of implementations in MRS. The feasibility of combining microfluidic separation devices with SERS was demonstrated by integrating metal–polymer nanocomposite in a PDMS microfluidic chip and collecting SERS spectra using a confocal Raman microscope, as shown in Fig. 2a [21]. A mixture of riboflavin and resorufin was detected as a proof of principle to demonstrate the combination of a powerful separation technique (capillary electrophoresis) with structurally information-rich analytical technique (Raman spectroscopy).

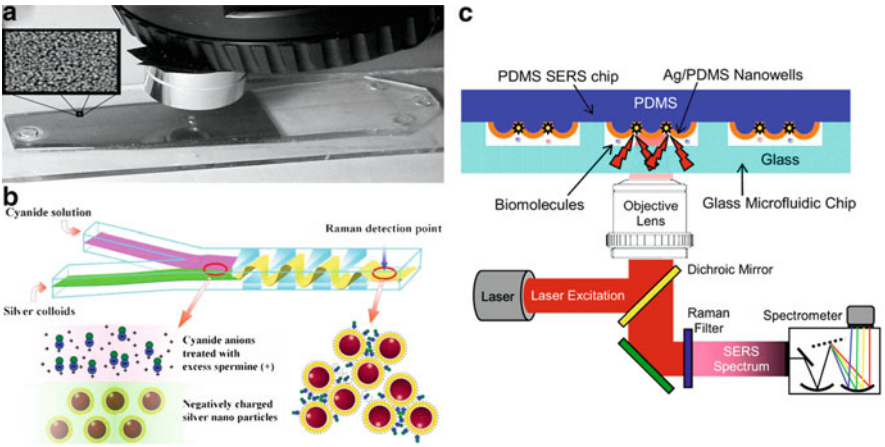

Fig. 2 (**a**) Depiction of integrated microfluidic SERS device under the 106 objective of the LabRam Raman spectrometer. Inset shows an SEM image of the silver-PDMS nanocomposite at approximately 90K magnification ([21], Copyright Wiley-VCH Verlag GmbH & Co. KGaA. Reproduced with permission). (**b**) Schematic illustration of alligator teeth-shaped microfluidic channel. The confluent streams of silver colloids and trace analytes are effectively mixed in the channel through the triangular structures, which are located on upper and lower surfaces of the channel in a zigzag way. The flow rate was 5 mL/min ([22], Reproduced with permission of the Royal Society of Chemistry). (**c**) Schematic diagram of the integrated microfluidic chip and the biomolecular Raman imaging system (Reprinted with permission from [23]. Copyright 2005, American Institute of Physics)

Furthermore, the feasibility of using the multi-component detection ability of Raman spectroscopy in microfluidics was demonstrated by several groups through detection of a mixture of dye-labeled oligonucleotides through multiplexed SERRS detection in a PDMS microfluidic chip [24, 25]. These enabled highly sensitive SERS detection on microfluidic platform. The microfluidic architecture has also seen improvements as several groups used PDMS chips with alligator teeth-like structures for the efficient mixing of colloids with samples for SERS detection, as shown in Fig. 2b [22, 25]. Other than colloid-based SERS detection, there have been attempts to develop efficient SERS substrates in PDMS which could be used to obtain reproducible SERS spectra of biomolecules, as shown in Fig. 2c [23].

Even though SERS-based detection offers high sensitivity and proves efficient for qualitative chemical analysis, the quantitative analysis of chemicals using SERS is not easy to achieve as it is difficult to control various experimental parameters such as degree of aggregation, particle sizes of colloidal nanoparticles, and distribution of molecules on a metal surface. The sample manipulation ability offered by microfluidics, however, makes it possible to achieve quantitative studies in SERS-based MRS. With specially fabricated three-dimensional micromixers for efficient sample mixing with colloids, several groups demonstrated quantitative SERS detection of samples [26, 27]. Unlike previous microfluidic SERS embodiments, where Raman measurements were taken in a static condition [24], it was observed that the reproducibility of SERS would be better in a flow mode [26]. The success in the implementation of SERS-based LoC devices urged researchers to use this as a technique to standardize detection achieved through other methods. In one study, confocal SERS detection was used to complement the fluorescence resonance energy transfer (FRET) data of DNA hybridization in a PDMS-based microfluidic system [28]. An exhaustive discussion on the implementation of SERS in microfluidics may be found in the review by Chen and Choo [29].

2.4 Raman Spectroscopic Probing of Microdroplets

Microfluidic devices that can generate sub-nanoliter microdroplets, dispersed within an immiscible continuous phase of oil in a rapid, efficient, and controllable manner, are gaining attention of the analytical community for a wide range of applications [30]. Microdroplet-based microfluidic systems are preferred for bio-chemical reactions and analysis as the compartmentalization provides the advantage of keeping the reactants or the sample isolated. Microdroplets are of interest for biologists as it is possible to mimic a cell-like system within a microdroplet for genomics, proteomics, or system biology studies [30]. There have been a number of reported works where Raman spectroscopy was used to probe the samples in microdroplets generated in a microfluidic system.

In one of the first reported studies of combining a microdroplet-based microfluidic system with Raman spectroscopy, a microdroplet-based micro-reactor was implemented in a PDMS chip and confocal Raman spectroscopy was used to probe

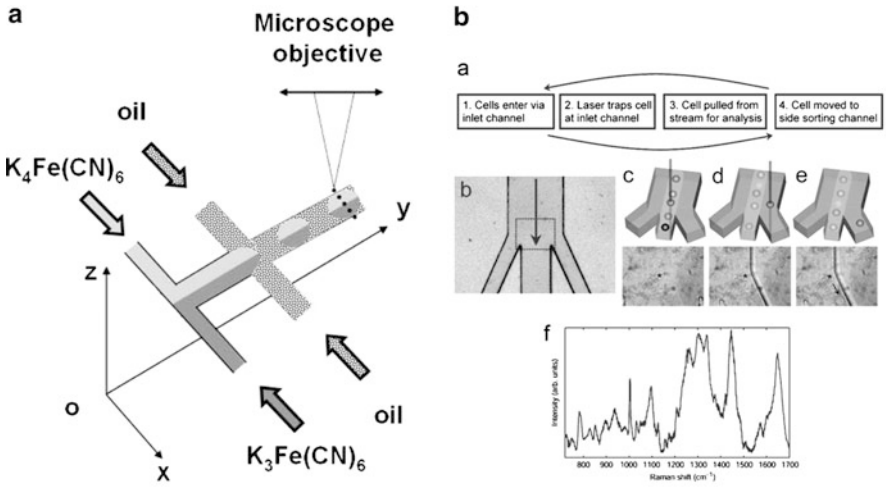

Fig. 3 (**a**) Two fluids co-flow over a short length before they meet two transversal oil streams at the "flow focusing" junction. Droplets presenting two unmixed moieties are dropped off the junction ([31], Reproduced with permission of the Royal Society of Chemistry). (**b**) Illustration of the operating principles of the optofluidic Raman-activated cell sorting (RACS) platform ([32], Reproduced with permission of the Royal Society of Chemistry)

the microdroplets [31]. It was observed that the droplet-based micro-reactors are ideal as they can host a rapid exothermal chemical reaction in a controlled condition. In situ probing of the composition of the droplets was achieved using Raman spectroscopy, and the mixing dynamics within the droplets were studied—a schematic of which is shown in Fig. 3a. However, acquisition time had to be kept high to achieve sufficient sensitivity for probing the sample; hence, multiple droplets would pass through the interrogation region during an acquisition, giving only the signal averaged to several droplets. There would also be interference in the spectra from the oil phase which had to be subtracted when post-processing the spectra. Another embodiment of microdroplet-based MRS studied on-chip photopolymerization of benzyl methacrylate in a borosilicate glass-based microfluidic device using a low-resolution Raman system. In this study, a fiber probe was used instead of an objective to excite and collect the Raman signal [33]. However, comparatively long acquisition time (3 min) made this system unsuitable for online monitoring of the process.

In order to avoid issues of sensitivity and background from the oil, SERS detection was combined with a microdroplet-based glass microfluidic system [34]. Samples mixed with gold colloids were sequestered in microdroplets and SERS signals were acquired from the sample with an acquisition time of 1 s. Such a detection scheme has the potential for use in process diagnostics in which online detection of drugs, water pollutants, or food additives is required. The dynamics of microdroplets was studied using confocal Raman spectroscopy through monitoring the isotopic exchange reaction between D_2O and H_2O [35]. Even though the comparatively long acquisition time created issues with obtaining average signals

from multiple droplets, this system could be used to study interdiffusion mixing and droplet mixing within a microfluidic channel through spatially resolved concentration maps of the sample.

2.5 *Microfluidic Raman spectroscopy in Cell Science*

The use of microfluidic systems for cell biology research is a rapidly growing area of research [36]. The main use of microfluidic systems in cell biology is to obtain the chemical information of cells and tissues at a molecular level. The ability of Raman spectroscopy to probe the molecular fingerprint of a sample makes it desirable to be combined with microfluidics to answer fundamental questions in cell biology. The relatively long acquisition time of Raman spectroscopy (a few seconds to several minutes) makes it necessary to have a tool which can noninvasively hold the cell within the microfluidic channel, away from the fluidic channel walls, while Raman spectra are acquired. A solution to this is to use optical tweezers which has its proven track record for its ability in single cell manipulation [37]. Interestingly, the combination of optical tweezers with micro-Raman spectroscopy has developed as a field of its own, finding a variety of applications in the area of biophotonics [38]. The combination of micro-Raman tweezers technology with microfluidics turns out to be a powerful technology where microfluidics adds the advantage of providing more controlled environment for single cell studies.

One of the first attempts toward this was by combining micro-Raman tweezers with microfluidics to study the oxygenation cycle of red blood cells (RBC) [39]. A single RBC was trapped in a PDMS-based microfluidic chip, and the oxygenation cycle of hemoglobin with respect to the surrounding environment was studied through confocal resonance Raman spectroscopy. The same group used this system for further studies on protein denaturization in RBC [40] and for studies of several globin-containing cells, where in vivo conditions were mimicked in a microfluidic channel [41]. In another study, instead of micro-Raman tweezers, combined with microfluidics, a PDMS-based microfluidic system was used along with a dual beam fiber optical trap to trap HL60 human Promyelocytic leukemia cells, and a confocal Raman system was used to record Raman spectra of the cells [42]. In another study, in situ chemical characterization of Chinese Hamster Ovary cells (CHO-K1) with spatial and temporal resolution was achieved by recording SERS of immobilized cells mixed with gold nanoparticle in a microfluidic channel using a confocal Raman microscope [43].

The prospect of obtaining Raman spectra of single cell in a flow-based microfluidic system, in combination with micro-Raman tweezers, offers the opportunity to develop Raman-activated microfluidic cell-sorting devices. Such a system was realized in which sorting of leukemia cells was demonstrated as a proof of principle. In this study, optical tweezers trapped the cells, the Raman signals of which were acquired by using a confocal Raman microscope,

as shown in Fig. 3b [32]. After analyzing the Raman spectra, the optical tweezers moved the cell toward the corresponding sorted channel. This technique, however, had very low throughput due to relatively long Raman acquisition time.

2.6 *Recent Developments*

The ultimate goal of LoC technology is to create analytical devices that are portable so that they can be used for point-of-care testing and field analysis. This makes miniaturization of MRS devices important. In a recently reported study, a microfluidic system for confocal SERS detection of dipicolinic acid and malachite green was realized [44]. Specially fabricated micropillars on the PDMS chip was used to achieve efficient mixing of colloidal nanoparticles with the sample. The notable achievement of this work is the implementation of the detection on a benchtop Raman microscope, as shown in Fig. 4. This is a step forward toward developing MRS devices for real field test applications.

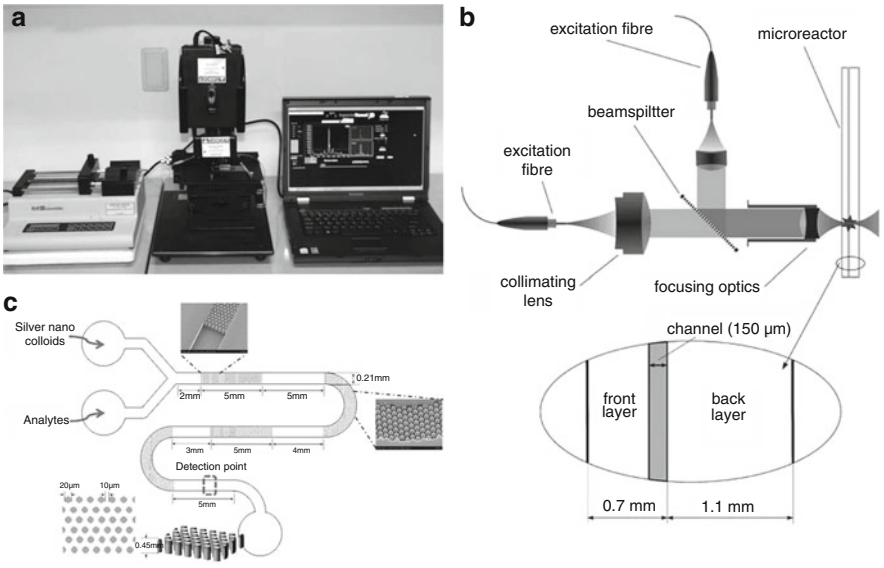

Fig. 4 (**a**) Schematic illustration of a portable Raman system combined with a pillar array PDMS microfluidic channel. (**b**) Schematic illustration of a pillar array PDMS microfluidic channel for the SERS detection of hazardous materials. Dimensions of the PDMS device are 20 mm (width), 24 mm (length), and 8 mm (height). SEM images at the insets show the structure of the micro-pillars ([44], Reproduced with permission of the Royal Society of Chemistry). (**c**) Raman optical setup and micro-reactor cross-section schematic ([45], Reproduced with permission of the Royal Society of Chemistry)

In all previously mentioned studies, conventional Raman microscopes were used to record Raman spectra from the microfluidic channels using high numerical aperture objectives. A recently reported study looks into the aspects of optimizing Raman signal collection from microfluidic channels [45]. In this work, a glass-based micro-reactor was used to probe the acid catalyzed esterification of butanol with acetic anhydride to produce butyl acetate and acetic acid. It was shown that for a non-confocal setup, a miniature aspheric lens would be better than high numerical aperture microscope objective to collect Raman spectra from the sample in the microfluidic channels. This paper contains a detailed discussion regarding the issues that can arise when detecting Raman signals from a microfluidic chip. The relatively high power of excitation (100 s of mW) needed to overcome the low Raman cross-section issue can create localized heating which can affect the reaction dynamics. This issue would be serious when high numerical aperture objectives are used to collect Raman signal in which Raman excitation beam is tightly focused to a very small volume, resulting in relatively high power density at the focal spot. The refractive index change induced by photo-thermal effects can affect the collection efficiency. There may also be the creation of bubbles inside the microfluidic channels due to cavitations, which would disrupt the flow inside the microfluidic channel. Another issue is the localized imperfections on the substrate that might affect the quality of the acquired data. The impurities that might be presented in the substrate would introduce unwanted fluorescence background which is difficult to remove through processing.

3 Microfluidic Raman Spectroscopy: State of the Art

Sect. 2 gives a detailed overview of various works where Raman spectroscopy was used as a potential optical detection method to probe samples in microfluidic chips. These works proved that MRS is a powerful analytical approach that can have various applications in bio-chemical analytics. However, there are various issues associated with this approach that makes it less favorable compared with other spectroscopic detection schemes [1]. This section gives a summary of the state of the art of MRS. Also, we present a discussion on the advantages and disadvantages of the conventional MRS approaches.

The advancement of MRS has been mainly application driven. The technology found applications in sensing and bio-chemical process monitoring. There has been several microfluidic architectures with which MRS was implemented. Microfluidic chips, fabricated in various substrates like glass [15], PDMS [21], and polymer films [43] were used for different applications of MRS. Specialized SERS substrates [21, 23] and micromixers [22, 25] were fabricated in microfluidic chips to obtain efficient SERS detection. Raman spectroscopy was also used to probe droplets in microdroplet-based microfluidic systems [31]. Raman detection schemes were another aspect on which different novel approaches have been attempted so as to enhance the sensitivity. SERS, SERRS, and confocal Raman

spectroscopy were some of the approaches used to improve the detection sensitivity. There have been various approaches on the Raman detection setup such as commercially available confocal Raman setups [21, 46], portable Raman microscopes [44], low-resolution Raman systems using fiber probes [33], and specially designed Raman probes.

Even though the previously mentioned studies differ in applications, microfluidic architecture, or the Raman detection scheme, they all probed the microfluidic chips from outside, using a lens [45], fiber probes [33], or high numerical aperture objectives [3]. On this basis, these works can commonly be categorized as free-space microfluidic Raman detection. One of the advantages of the free-space Raman approach is the fact that a conventional Raman microscope could be used for implementing MRS. The microfluidic chip could be used to analyze a sample on a commercially available Raman microscope [39]. This detection scheme also offers the opportunity to achieve spatial mapping of microfluidic channels to study the reaction or fluidic dynamics within a microfluidic channel [15, 20].

Even though MRS proves to be a powerful analytical tool, some inherent limitations make it less favorable to many applications. One of the major concerns associated with MRS is the inherent low cross-section of Raman scattering process when compared to fluorescence. SERS-based approaches [21] were implemented mostly to overcome this issue and to enhance the detection sensitivity. Another concern is the background signal from the substrate when Raman spectra are collected from a microfluidic chip [1, 45]. In free-space geometries, the Raman excitation beam and the Raman signal must pass through the substrate from which the microfluidic chip is fabricated. In order to obtain a good SNR for the obtained Raman spectra, it is essential to reduce the fluorescence background from both the sample and the substrate. It is, therefore, essential to make careful choice on the material and thickness of the substrate on which the microfluidic chip is fabricated. Even though polymer substrates like PDMS and PMMA are relatively cheap, they are less favorable for MRS as these polymer materials are highly Raman active and their Raman peaks may interfere with those of the analyte in the fingerprint region [29]. A solution for this would be to use confocal Raman systems [15, 17]; however, this results in an increase in the acquisition time. Because of this, many researchers continue to use a glass substrate as it remains relatively transparent in the visible and near-IR region when implementing MRS using free-space systems.

A fiber-based on-chip Raman detection scheme provides a possible solution to the issues of background from the substrate and also improves the portability of the system. Recently, our group implemented fiber-based Raman spectroscopic detection schemes in microfluidics (discussed in detail in Sects. 4 and 5).

4 Fiber Probe-Based Microfluidic Raman Spectroscopy

Embedding optical waveguides such as optical fibers is a route to the manufacture of microfluidic chips which incorporate optical detection schemes while retaining portability and eliminating the need for optical alignment. This also helps to

minimize the number of required optical components [6]. This approach has been successfully implemented for various optical detection methods. However, implementation of fiber-based Raman spectroscopic detection schemes in microfluidics was not exploited until recently due to practical difficulties.

In order to explain this issue, it is worthwhile exploring how fiber-based detection schemes were implemented for other spectroscopic methods. In one of the first studies where a fiber-based on-chip fluorescent excitation was used in microfluidics, a fiber insertion channel was etched into the microfluidic chip in such a way that the tip of the fiber, when fiber was inserted in the fiber insertion channel, would remain 190 μm away from the fluidic channel [47]. In a recently reported study, on-chip absorption spectroscopy was implemented using optical fiber-based excitation and collection for high-throughput cell screening [48]. As before, the fiber insertion channel is separated from the fluidic channel by a wall.

Due to the inherent characteristics of Raman spectroscopy, a slightly different approach is necessary when implementing fiber-based Raman systems. Due to the low Raman cross-section, it is essential to enhance the collection efficiency and reduce the fluorescence background in order to achieve satisfactory detection sensitivity. There can be significant fluorescence contribution from the optical fiber itself when Raman excitation beam gets guided through it. To reduce this background, low hydroxyl (OH) optical fibers are used for near-IR applications. Also unlike other spectroscopic probes, specialized filters must be introduced at the probe head so as to filter out the fluorescent background from the excitation fiber and prevent Rayleigh-scattered photons getting into the collection fiber [49].

When embedded fiber probes were used for optical detection in microfluidic chips, a wall separated the fiber tip within its insertion channel from the fluidic channel through which the analyte flows. This approach is not desirable for a fiber-based Raman detection scheme in microfluidics as there will be interfering signal from the substrate. A modified microfluidic design is required to implement fiber-based Raman detection in microfluidics such that the fiber probe is embedded in a chip without walls that physically separate the tip of the probe from the fluidic channel.

Our group demonstrated the first implementation of on-chip fiber-based Raman spectroscopic detection on a PDMS-based microfluidic platform [50]. In our work, a PDMS microfluidic chip with a predefined fiber probe insertion channel was fabricated and a specially designed split fiber probe was embedded into the fluidic chip, thus enabling fiber-based on-chip Raman excitation and collection. This work achieved the desired characteristics for a fiber-based Raman detection system in microfluidics and demonstrated that the key ideas which enabled the implementation of this system were the design of the microfluidic chip, the design of Raman probe, and the Raman detection geometry.

The PDMS chip was fabricated using conventional soft lithography [51]. A specialized protocol was used to define the fiber probe insertion channel by fixing a sleeve with the same dimension as that of the probe head on the mould [50]. As a result, it will be possible to define a pre-aligned fiber insertion channel within the fluidic chip, in which the fiber probe can be inserted and embedded in a leak-

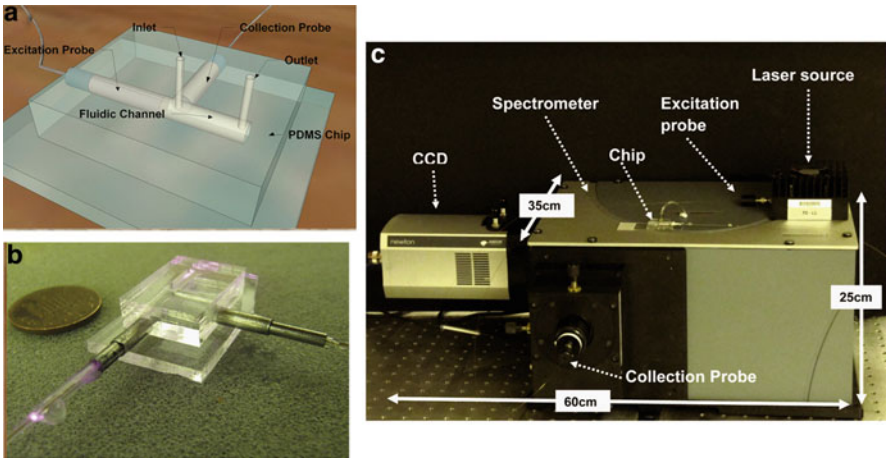

Fig. 5 (**a**) Design of the microfluidic chip. The head of the fiber probe is inserted into the chip, and the analyte to be detected is injected into the chip through inlet and goes out through outlet. (**b**) Photograph of the PDMS-based chip where collection and excitation probes are inserted. (**c**) Photograph of the probe-based microfluidic Raman detection system ([50], Reproduced with permission of the Optical Society of America)

proof manner. The design of the chip is shown in Fig. 5a. As mentioned previously, fiber-based Raman probes require specialized filters at the probe head in order to avoid fluorescent background from the fibers. Conventional Raman probes that are used for tissue imaging [49, 52, 53] are designed with a backscattering geometry, and the excitation and collection part of the probes can be combined in a single housing. This demands complex optics with micro-optic elements at the probe head, and since the beam is not collimated in passing through the filters, the filtering efficiency in some designs will be compromised [53]. In our system, since the microfluidic design determines the collection geometry, we decouple the excitation and collection parts of the probes into two different housings, making it a split Raman probe, simplifying the design of the probe heads. As shown in Fig. 5, the excitation and collection probe head includes a filter sandwiched between a pair of collimating and focusing achromatic doublet lenses of diameter 2.5 mm. The excitation probe head contained a bandpass filter to remove the fluorescent background while passing the excitation wavelength from the 785-nm excitation laser. A long-pass filter with cut-off wavelength at 795.2 nm was used for the collection probe head to prevent the Rayleigh-scattered photonics in the excitation wavelength getting into the collection fiber. Due to the collimating and refocusing geometry, it was possible to make the filters work at their maximum efficiency, while the split configuration avoided the requirement of specialized dichroic mirror or filters at the probe head. Though the diameter of the fiber used for the probe was 250 μm, the diameter of the probe head was 3 mm, mainly due to the difficulty in obtaining smaller size filters.

Another advantage of the split probe was the ability to choose the most efficient detection geometry, simply by modifying the microfluidic chip design. We compared collinear and orthogonal collection geometry, and it was observed that the orthogonal collection geometry is the desired geometry with minimal fluorescence background; this geometry helps to eliminate most of the forward scattering photons at excitation wavelength [50].

In order to prove the ability of this device to detect bio-analyte, concentration analysis of urea solution was performed. At 200 mW excitation and 5 s acquisition time, the minimum detection limit of this device was estimated to be 140 mM. This value is relevant when human physiological limit of urea in human urine is considered. Consequently, this system has the potential to be used for analyte detection and monitoring with relatively low acquisition times. This system is the first stepping stone toward implementing fiber-based Raman detection scheme in a microfluidic platform. With a simple fluidic system and embedded fiber probes, a completely alignment-free microfluidic system for Raman spectroscopic analyte detection was achieved. This fluidic chip can be incorporated into a chemical reactor for online process monitoring, or when combined with a portable Raman spectrometer, this could be used for field testing of analytes.

Even though the fiber probe-based microfluidic Raman system proved to be rugged and portable, there are certain limitations which make it less favorable for wider applications. Since the diameter of the filter is one order larger than that of the fiber used to collect the signal, there is a throughput (Etendue) mismatch at the probe head which would reduce the collection efficiency of the probe. Another concern is further miniaturization. The size of the fluidic channel depends on the size of the probe head, and the size of the probe head mainly depends on the size of the filters used. Obtaining filters of smaller sizes is difficult and expensive. This makes it difficult to achieve fluidic devices in true microfluidic dimensions with this approach. This motivated the development of the second generation of a fiber-based microfluidic Raman spectroscopic system, explained in the following section.

5 Waveguide Confined Raman Spectroscopy

As mentioned in Sect. 4, the successful implementation of fiber-based Raman detection system in microfluidics should ensure maximum collection efficiency and minimum fluorescent background from the substrate as well as the sample. The significant Etendue mismatch at the probe head and the issue of scalability limit the applicability of probe-based MRS. Our group recently demonstrated an alternative approach called waveguide confined Raman spectroscopy (WCRS) which solves the issues of collection efficiency and scalability [54].

The basic concept of WCRS is the confinement of the Raman signal excitation and collection region through embedded waveguides along with confinement of the analyte through the microfluidic channel. In WCRS, two embedded waveguides, one for excitation and one for collection of the Raman signal, meet at the signal

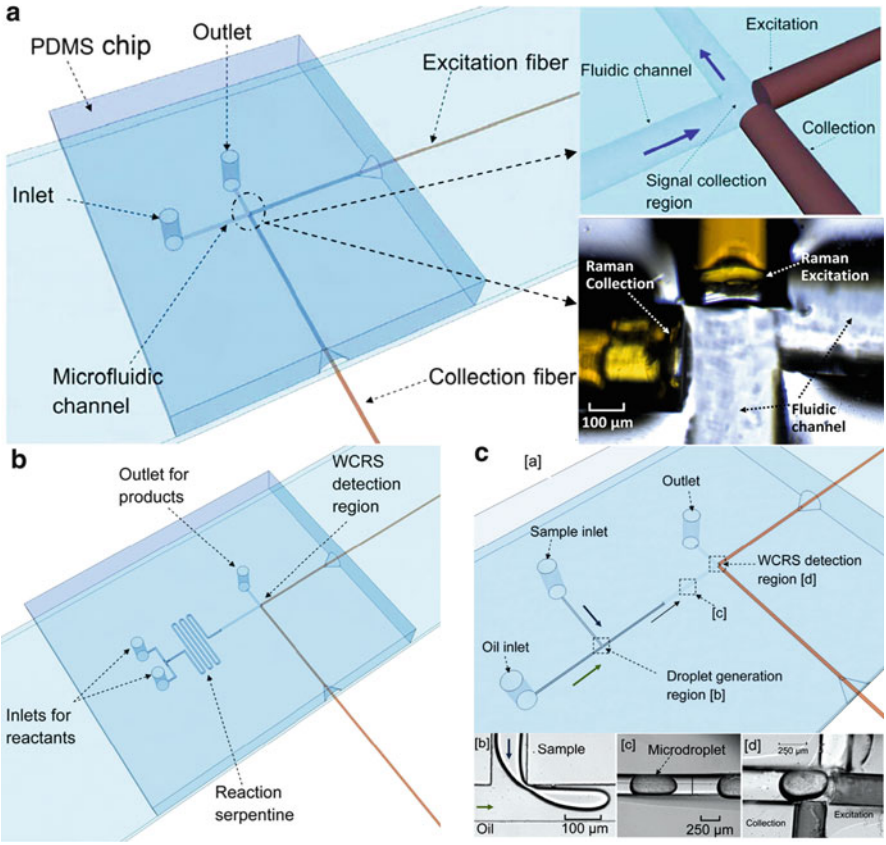

Fig. 6 (**A**) Schematic of the PDMS microfluidic chip where WCRS was implemented. (**B**) Design of the WCRS incorporated micro-reactor chip (only a representative drawing of the serpentine region is shown; in the actual microfluidic chip, the serpentine region is longer). (**C**) (a) Design of the microfluidic chip for microdroplet generation combined with WCRS. (b) Microdroplet generation region. (c) Microdroplet flowing through the microfluidic channel. (d) WCRS detection of microdroplets ([54], Reproduced with permission of the Royal Society of Chemistry)

collection region; neither waveguide has any optical elements at the tip to modify the beam profile. This system has been implemented with a pair of embedded low OH multimode fibers for excitation and collection, as shown in Fig. 6a. The distance between the ends of excitation and collection fibers should be of the order as the size of the fiber core. Since the Raman signal collection is confined to the close vicinity of the ends of the fibers, the diameter of the incident beam is comparable to the size of the core within the collection region despite the divergence of the incidence beam on emergence from the fiber. The same applies to the acceptance angle of the collection fiber, maximizing the collection efficiency of the system. The orthogonal collection geometry eliminated collection of the unscattered incident beam, ensuring that the Raman signal is not masked by the

high-intensity incident radiation or background fluorescence from the probe fiber. When compared to its probe-based counterpart, there is no Etendue mismatch at the collection side of WCRS. This improved collection efficiency results in better sensitivity of detection for WCRS when compared to its probe-based counterpart, even though the fluorescent background might be higher due to the lack of filters at the collection region of the waveguides.

The microfluidic channel also allows confinement of the required sample volume. Since a diverging beam is used for sampling, the whole cross-section of the microfluidic channel is probed unlike the fiber probe-based MRS system or confocal MRS systems.

The sensitivity of the WCRS system was compared to that of its probe-based counterpart by detecting urea under similar experimental conditions. The minimum detectable limit was found to be 80 mM, an improvement over the probe-based system, while the required sample volume was five orders lower in the WCRS-based system. Since bare fiber or embedded waveguide can be used for WCRS, without any other optical elements, this technique is scalable solely depending on the size of the waveguide used for excitation and collection. Low OH multimode fibers are commercially available in a range of sizes ranging from 100 μm – 300 μm, enabling implementation of WCRS in true microfluidic dimensions (channel size in the order of 100 μm).

In practice, these features make WCRS an ideal candidate for developing microfluidic devices where rapid and alignment-free Raman spectroscopic detection is possible with minimal background from the substrate. Due to the highly sensitive detectors used for Raman detection, it is necessary to darken the whole microscope when bulk microscope-based MRS systems are used to take Raman measurements in broad daylight. As waveguides are used for exciting and collecting Raman signal, it is only necessary to darken the fluidic chip in the case of WCRS, making MRS more amenable for field applications.

Fundamentally, WCRS is an architecture that allows Raman spectroscopic sensing in microfluidics. The applicability of this technology is not limited to analyte sensing. An attractive feature of this architecture is its compatibility to be combined into other microfluidic platforms with multiple functionalities, where WCRS would act as the detection scheme of the device. We recently reported implementation of two proof-of-principle experiments to demonstrate the extended functionality of WCRS to be used as a generic sensing technique that can be implemented in a wide variety of applications [54]. The first of these was the use of WCRS for reaction monitoring in a micro-reactor, the design of which is shown in Fig. 6b. The progress of a binary reaction could be monitored in real time (with relatively low acquisition times) for different flow rates of the reactants. Another implementation of WCRS demonstrated its use for probing microdroplets in a microdroplet-based microfluidic chip, as shown in Fig. 6c. It was shown that it is possible to probe single microdroplet using WCRS-based detection, which could lead to Raman-activated microdroplet sorting devices in the future.

Our recently reported work discusses the implementation of WCRS for acquiring standard Raman spectra [54]. However, techniques like surface enhancement or

fluorescent suppression could help to improve the sensitivity of the acquired Raman signal [29, 55–57]. Such techniques can be easily incorporated in WCRS to further enhance the sensitivity of the device. To demonstrate the feasibility of such modifications [58], we implemented a recently developed fluorescent suppression technique using continuous modulation of excitation wavelength [55, 59] in WCRS. In this form, the same WCRS architecture can be used in which the only modification was the use of frequency-modulated Raman excitation source. With the modulated Raman spectra, a sevenfold enhancement in the sensitivity could be achieved for urea detection [58].

WCRS has proved to be a generic technology, providing a solution to the fundamental limitations of MRS detection systems. The relevant ease with which this technology can be combined with other techniques increases the relevance of this approach. Portable, alignment-free MRS devices realized using WCRS have the potential to affect several fields such as point-of-care diagnosis, environmental sensing, process monitoring, drug development, cell biology, and proteomics.

5.1 Future Outlook

Moving to embedded or integrated waveguide-based architecture from a bulk optics approach will help MRS to be realized in a form which is both portable and free of alignment. This will instigate the future translation of techniques currently only possible with bulk optics to the fiber-based platform with the result that the technology is more amenable for field applications. The fiber-based detection scheme would not, however, completely replace the benchtop implementation of MRS; despite the capability for WCRS to achieve temporal mapping of an evolving process within a microfluidic channel, it is unable to achieve spatial mapping of a process as its detection region is fixed.

Further investigations are necessary on WCRS to extend its applicability to all types of samples. For example, detection of turbid analyte is yet to be demonstrated using WCRS where necessary normalization algorithms need to be incorporated to take into account the scattering and absorption properties of the sample [60]. Another aspect is the demonstration of the ability of WCRS to be used for cell biology applications. There is also opportunity to improve the architecture of WCRS by designing an integrated waveguide-based WCRS chip, where the microfluidic channel size can be further reduced and the collection geometry at the Raman collection region can be optimized.

6 Conclusion

The field of Raman spectroscopy has seen significant advancement both in technology and in application over the last two decades, which has made it a powerful tool for bio-chemical analysis. Combining Raman spectroscopy with microfluidics has

resulted in the development of devices that can achieve rapid bio-chemical analysis of samples using Raman spectroscopy with a significantly reduced sample volume. However, there are several limitations such as weak Raman signal, background from the substrate, requirement for alignment, and lack of portability, which limited the wider applicability of MRS. Moving from a bulk optics-based architecture toward a fiber-based architecture has helped to overcome majority of the aforementioned issues [50, 54]. The fiber-based implementation of MRS will help the field of microfluidics to exploit the advantages of Raman spectroscopy, resulting in the development of efficient, alignment-free, portable Raman spectroscopy-based microfluidic devices for bio-chemical sensing and analysis.

Acknowledgments We thank the UK Engineering and Physical Sciences Research Council for funding. KD is a Royal Society-Wolfson Merit Award holder. The authors are grateful to Dr Andrew McKinley for critical reading of the manuscript and useful discussions.

References

1. Viskari PJ, Landers JP (2006) Unconventional detection methods for microfluidic devices. Electrophoresis 27(9):1797–1810. doi:10.1002/elps.200500565
2. Mogensen KB, Klank H, Kutter JP (2004) Recent developments in detection for microfluidic systems. Electrophoresis 25(21–22):3498–3512. doi:10.1002/elps.200406108
3. Hunt HC, Wilkinson JS (2008) Optofluidic integration for microanalysis. Microfluid Nanofluid 4(1–2):53–79. doi:10.1007/s10404-007-0223-y
4. Raman CV, Krishnan KS (1928) A new type of secondary radiation. Nature 121:501–502. doi:10.1038/121501c0
5. Lombardi JR, Birke RL (2008) A unified approach to surface-enhanced Raman spectroscopy. J Phys Chem C 112(14):5605–5617. doi:10.1021/Jp800167v
6. Gotz S, Karst U (2007) Recent developments in optical detection methods for microchip separations. Anal Bioanal Chem 387(1):183–192. doi:10.1007/s00216-006-0820-8
7. Chen CY, Morris MD (1988) Raman-spectroscopic detection system for capillary zone electrophoresis. Appl Spectrosc 42(3):515–518
8. Chen C-Y, Morris MD (1991) On-line multichannel Raman spectroscopic detection system for capillary zone electrophoresis. J Chromatogr A 540:355–363
9. Walker PA, Kowalchyk WK, Morris MD (1995) Online Raman spectroscopy of ribonucleotides preconcentrated by capillary isotachophoresis. Anal Chem 67(23):4255–4260. doi:10.1021/ac00119a009
10. Walker PA, Morris MD, Burns MA, Johnson BN (1998) Isotachophoretic separations on a microchip. Normal Raman spectroscopy detection. Anal Chem 70(18):3766–3769
11. Pan DH, Mathies RA (2001) Chromophore structure in lumirhodopsin and metarhodopsin I by time-resolved resonance Raman microchip spectroscopy. Biochemistry 40(26):7929–7936. doi:10.1021/Bi010670x
12. Pan DH, Ganim Z, Kim JE, Verhoeven MA, Lugtenburg J, Mathies RA (2002) Time-resolved resonance Raman analysis of chromophore structural changes in the formation and decay of rhodopsin's BSI intermediate. J Am Chem Soc 124(17):4857–4864. doi:10.1021/Ja012666e
13. Keir R, Igata E, Arundell M, Smith WE, Graham D, McHugh C, Cooper JM (2002) SERRS. In situ substrate formation and improved detection using microfluidics. Anal Chem 74 (7):1503–1508. doi:10.1021/Ac015625+

14. Fortt R, Wootton RCR, de Mello AJ (2003) Continuous-flow generation of anhydrous diazonium species: monolithic microfluidic reactors for the chemistry of unstable intermediates. Org Process Res Dev 7(5):762–768. doi:10.1021/Op025586j
15. Fletcher PDI, Haswell SJ, Zhang XL (2003) Monitoring of chemical reactions within microreactors using an inverted Raman microscopic spectrometer. Electrophoresis 24 (18):3239–3245. doi:10.1002/elps.200305532
16. Lee M, Lee JP, Rhee H, Choo J, Chai YG, Lee EK (2003) Applicability of laser-induced Raman microscopy for in situ monitoring of imine formation in a glass microfluidic chip. J Raman Spectrosc 34(10):737–742. doi:10.1002/Jrs.1038
17. Park T, Lee M, Choo J, Kim YS, Lee EK, Kim DJ, Lee SH (2004) Analysis of passive mixing behavior in a poly(dimethylsiloxane) microfluidic channel using confocal fluorescence and Raman microscopy. Appl Spectrosc 58(10):1172–1179
18. Leung SA, Winkle RF, Wootton RCR, deMello AJ (2005) A method for rapid reaction optimisation in continuous-flow microfluidic reactors using online Raman spectroscopic detection. Analyst 130(1):46–51. doi:10.1039/B412069h
19. Urakawa A, Trachsel F, von Rohr PR, Baiker A (2008) On-chip Raman analysis of heterogeneous catalytic reaction in supercritical co_2: phase behaviour monitoring and activity profiling. Analyst 133(10):1352–1354. doi:10.1039/B808984c
20. Salmon JB, Ajdari A, Tabeling P, Servant L, Talaga D, Joanicot M (2005) In situ Raman imaging of interdiffusion in a microchannel. Appl Phys Lett 86(9):094106. doi:10.1063/1.1873050; Artn 094106
21. Connatser RM, Riddle LA, Sepaniak MJ (2004) Metal-polymer nanocomposites for integrated microfluidic separations and surface enhanced Raman spectroscopic detection. J Sep Sci 27 (17–18):1545–1550. doi:10.1002/jssc.200401886
22. Yea K, Lee S, Kyong JB, Choo J, Lee EK, Joo SW, Lee S (2005) Ultra-sensitive trace analysis of cyanide water pollutant in a PDMS microfluidic channel using surface-enhanced Raman spectroscopy. Analyst 130(7):1009–1011. doi:10.1039/B501980j
23. Liu GL, Lee LP (2005) Nanowell surface enhanced Raman scattering arrays fabricated by soft-lithography for label-free biomolecular detections in integrated microfluidics. Appl Phy Lett 87(7):074101. doi:10.1063/1.2031935
24. Docherty FT, Monaghan PB, Keir R, Graham D, Smith WE, Cooper JM (2004) The first SERRS multiplexing from labelled oligonucleotides in a microfluidics lab-on-a-chip. Chem Commun 1:118–119
25. Park T, Lee S, Seong GH, Choo J, Lee EK, Kim YS, Ji WH, Hwang SY, Gweon D-G, Lee S (2005) Highly sensitive signal detection of duplex dye-labelled DNA oligonucleotides in a pdms microfluidic chip: confocal surface-enhanced Raman spectroscopic study. Lab Chip 5 (4):437–442
26. Lee D, Lee S, Seong GH, Choo J, Lee EK, Gweon DG, Lee S (2006) Quantitative analysis of methyl parathion pesticides in a polydimethylsiloxane microfluidic channel using confocal surface-enhanced Raman spectroscopy. Appl Spectrosc 60(4):373–377
27. Jung JH, Choo J, Kim DJ, Lee S (2006) Quantitative determination of nicotine in a PDMS microfluidic channel using surface enhanced Raman spectroscopy. Bull Kor Chem Soc 27 (2):277–280
28. Jung J, Chen LX, Lee S, Kim S, Seong GH, Choo J, Lee EK, Oh CH, Lee S (2007) Fast and sensitive DNA analysis using changes in the fret signals of molecular beacons in a PDMS microfluidic channel. Anal Bioanal Chem 387(8):2609–2615. doi:10.1007/s00216-007-1158-6
29. Chen L, Choo J (2008) Recent advances in surface-enhanced Raman scattering detection technology for microfluidic chips. Electrophoresis 29(9):1815–1828. doi:10.1002/elps.200700554
30. Huebner A, Sharma S, Srisa-Art M, Hollfelder F, Edel JB, Demello AJ (2008) Microdroplets: a sea of applications? Lab Chip 8(8):1244–1254. doi:10.1039/B806405a
31. Cristobal G, Arbouet L, Sarrazin F, Talaga D, Bruneel JL, Joanicot M, Servant L (2006) On-line laser Raman spectroscopic probing of droplets engineered in microfluidic devices. Lab Chip 6(9):1140–1146. doi:10.1039/B602702d

32. Lau AY, Lee LP, Chan JW (2008) An integrated optofluidic platform for Raman-activated cell sorting. Lab Chip 8(7):1116–1120. doi:10.1039/b803598a
33. Barnes SE, Cygan ZT, Yates JK, Beers KL, Amis EJ (2006) Raman spectroscopic monitoring of droplet polymerization in a microfluidic device. Analyst 131(9):1027–1033. doi:10.1039/B603693g
34. Strehle KR, Cialla D, Rosch P, Henkel T, Kohler M, Popp J (2007) A reproducible surface-enhanced Raman spectroscopy approach. Online SERS measurements in a segmented microfluidic system. Anal Chem 79(4):1542–1547. doi:10.1021/Ac0615246
35. Sarrazin F, Salmon JB, Talaga D, Servant L (2008) Chemical reaction imaging within microfluidic devices using confocal Raman spectroscopy: the case of water and deuterium oxide as a model system. Anal Chem 80(5):1689–1695. doi:10.1021/Ac7020147
36. Salieb-Beugelaar GB, Simone G, Arora A, Philippi A, Manz A (2010) Latest developments in microfluidic cell biology and analysis systems. Anal Chem 82(12):4848–4864. doi:10.1021/ac1009707
37. Stevenson DJ, Gunn-Moore F, Dholakia K (2010) Light forces the pace: optical manipulation for biophotonics. J Biomed Opt 15(4):041503
38. Petrov DV (2007) Raman spectroscopy of optically trapped particles. J Opt A Pure Appl Opt 9 (8):S139–S156. doi:10.1088/1464-4258/9/8/S06
39. Ramser K, Enger J, Goksor M, Hanstorp D, Logg K, Kall M (2005) A microfluidic system enabling Raman measurements of the oxygenation cycle in single optically trapped red blood cells. Lab Chip 5(4):431–436. doi:10.1039/b416749j
40. Eriksson E, Scrimgeour J, Graneli A, Ramser K, Wellander R, Enger J, Hanstrop D, Goksor M (2007) Optical manipulation and microfluidics for studies of single cell dynamics. J Opt A Pure Appl Opt 9(8):S113–S121. doi:10.1088/1464-4258/9/8/S02
41. Ramser K, Wenseleers W, Dewilde S, Van Doorslaer S, Moens L (2008) The combination of resonance Raman spectroscopy, optical tweezers and microfluidic systems applied to the study of various heme-containing single cells. Spectrosc-Int J 22(4):287–295. doi:10.3233/Spe-2008-0353
42. Jess P, Garces-Chavez V, Smith D, Mazilu M, Riches A, Herrington CS, Sibbett W, Dholakia K (2006) A dual beam fibre trap for Raman micro-spectroscopy of single cells. J Pathol 210:28
43. Zhang XL, Yin HB, Cooper JM, Haswell SJ (2008) Characterization of cellular chemical dynamics using combined microfluidic and Raman techniques. Anal Bioanal Chem 390 (3):833–840. doi:10.1007/s00216-007-1564-9
44. Quang LX, Lim C, Seong GH, Choo J, Do KJ, Yoo SK (2008) A portable surface-enhanced Raman scattering sensor integrated with a lab-on-a-chip for field analysis. Lab Chip 8 (12):2214–2219. doi:10.1039/B808835g
45. Mozharov S, Nordon A, Girkin JM, Littlejohn D (2010) Non-invasive analysis in micro-reactors using Raman spectrometry with a specially designed probe. Lab Chip 10 (16):2101–2107. doi:10.1039/C004248j
46. Connatser RM, Cochran M, Harrison RJ, Sepaniak MJ (2008) Analytical optimization of nanocomposite surface-enhanced Raman spectroscopy/scattering detection in microfluidic separation devices. Electrophoresis 29(7):1441–1450. doi:10.1002/elps.200700585
47. Li HF, Lin JM, Su RG, Uchiyama K, Hobo T (2004) A compactly integrated laser-induced fluorescence detector for microchip electrophoresis. Electrophoresis 25(12):1907–1915. doi:10.1002/elps.200305867
48. Ibarlucea B, Fernandez-Rosas E, Vila-Planas J, Demming S, Nogues C, Plaza JA, Büttgenbach S, Llobera A (2010) Cell screening using disposable photonic lab on a chip systems. Anal Chem 82(10):4246–4251. doi:10.1021/ac100590z
49. Mahadevan-Jansen A, Mitchell MF, Ramanujam N, Utzinger U, Richards-Kortum R (1998) Development of a fiber optic probe to measure NIR Raman spectra of cervical tissue in vivo. Photochem Photobiol 68(3):427–431
50. Ashok PC, Singh GP, Tan KM, Dholakia K (2010) Fiber probe based microfluidic Raman spectroscopy. Opt Express 18(8):7642–7649

51. McDonald JC, Duffy DC, Anderson JR, Chiu DT, Wu H, Schueller OJA, Whitesides GM (2000) Fabrication of microfluidic systems in poly(dimethylsiloxane). Electrophoresis 21 (1):27–40
52. Utzinger U, Richards-Kortum RR (2003) Fiber optic probes for biomedical optical spectroscopy. J Biomed Opt 8(1):121–147
53. Motz JT, Hunter M, Galindo LH, Gardecki JA, Kramer JR, Dasari RR, Feld MS (2004) Optical fiber probe for biomedical Raman spectroscopy. App Optics 43(3):542–554
54. Ashok PC, Singh GP, Rendall HA, Krauss TF, Dholakia K (2011) Waveguide confined Raman spectroscopy for microfluidic interrogation. Lab Chip. doi:10.1039/c0lc00462f
55. De Luca AC, Mazilu M, Riches A, Herrington CS, Dholakia K (2010) Online fluorescence suppression in modulated Raman spectroscopy. Anal Chem 82(2):738–745. doi:10.1021/Ac9026737
56. Shreve AP, Cherepy NJ, Mathies RA (1992) Effective rejection of fluorescence interference in Raman spectroscopy using a shifted excitation difference technique. Appl Spectrosc 46 (4):707–711
57. Campani E et al (1981) A pulsed dye laser Raman spectrometer employing a new type of gated analogue detection. J Phys D Appl Phys 14(12):2189
58. Ashok PC, Luca ACD, Mazilu M, Dholakia K (2011) Enhanced bioanalyte detection in waveguide confined Raman spectroscopy using modulation techniques. J Biophot. doi:10.1002/jbio.201000107
59. Mazilu M, De Luca AC, Riches A, Herrington CS, Dholakia K (2010) Optimal algorithm for fluorescence suppression of modulated Raman spectroscopy. Opt Express 18(11):11382–11395
60. Barman I, Singh GP, Dasari RR, Feld MS (2009) Turbidity-corrected Raman spectroscopy for blood analyte detection. Anal Chem 81(11):4233–4240. doi:10.1021/Ac8025509

Part V
Optical Characterization and Manipulation in Bioreactors

Polymeric Microfluidic Devices for High Performance Optical Imaging and Detection Methods in Bioanalytics

Holger Becker and Claudia Gärtner

Abstract The commercialization of miniaturized systems for bioanalytical applications demands fabrication methods which allow the generation of disposable devices which on the one hand fulfill requirements with respect to high geometrical precision and compatibility with the chemistries involved and, on the other hand, offer manufacturing cost which allows these devices to become low-cost disposables. We present a technology chain for the realization of such devices using polymer replication methods and subsequent back-end processing steps. Due to the usual complex set of requirements faced during the development of a bioanalytical system utilizing microfluidic functionality, development strategies for their implementation will be discussed. Practical examples of devices for the use in biotechnological applications will be presented.

Keywords Injection molding • Integrated device • Polymer microfabrication

Contents

H. Becker (✉) • C. Gärtner
microfluidic ChipShop GmbH, Stockholmer Str. 20, 07747 Jena, Germany
e-mail: hb@microfluidic-chipshop.com

W. Fritzsche and J. Popp (eds.), *Optical Nano- and Microsystems for Bioanalytics*,
Springer Series on Chemical Sensors and Biosensors (2012) 10: 271–288,
DOI 10.1007/978-3-642-25498-7_10,

1 Introduction

Just like the microelectronic revolution changed the way how electronic components and circuits were manufactured 50 years ago, which led to an explosive growth in the applications of integrated circuits and a birth of new industries, a similar development can be seen with the introduction of miniaturization in the Life Sciences with the initial concept of the so-called miniaturized total analysis system (μ-TAS), also often called "Lab-on-a-Chip" technology, which deals with the handling and manipulation of miniature amounts of liquid in the Life Sciences and was introduced about 20 years ago [1]. The functional key elements for this technology are microstructures which have typical dimensions in the range of some 10 to some 100 μm [2]. The large and economically successful areas like microfluidics for inkjet printing, automotive applications like fuel injection, and microelectronic applications like chip cooling will not be discussed here. Recent years have seen an explosive growth of scientific activities in the Lab-on-a-Chip technology which now finally also make their way into an increasing number of commercial devices and instruments [3]. There are many drivers behind this development: first, the fundamental method of mass transport by diffusion which governs many processes in chemistry and biology scales with length^{-2}. This scaling allows to develop systems, e.g., for clinical diagnostics or analytical chemistry, where the overall time from the input of a sample to the analytical result can be decreased to the time frame of minutes rather than current hours or even days. Similar scaling advantages can be found for other physical parameters, e.g., heat transport which is important for processes like polymerase chain reaction (PCR). Second, the cost and the overall available volume of reagents in the Life Sciences is often a critical factor, e.g., in protein crystallization or drug discovery. By reducing these volumes, not only a cost reduction can be achieved but often this represents the only way of handling and processing scarce material. Third, many functional elements of biology, e.g., cells, blood vessels, bacteria, etc. have a size which lies exactly in the range of microtechnological methods, i.e., from 0.5 μm to about 100 μm, making it an ideal fit between available manufacturing technologies and applications. Fourth, the very high geometrical accuracies of miniaturized systems together with the high surface-to-volume ratio (which also scales favorably with length^{-1}) makes the environment in which the fluids are contained extremely well controlled, allowing, e.g., chemical reactions to be performed on a microfluidic device with a substantially higher yield than in conventional systems. Due to the small lateral dimensions, flows in such microstructures are practically always laminar (low Reynolds number) which makes the flow extremely well controllable. Last but not least, miniaturization offers the potential to automate many laborious laboratory processes which often include many manual steps like pipetting, sample transfer, etc., again reducing the cost and time of the complete analytical process and reducing the risk of procedural error. These advantages have proven to be very attractive, first spurning a very large scientific activity in the field and increasingly also in form of commercial products.

The next section explains the typical process steps in the analytical or diagnostic process performed on a microfluidic device and describes strategies for functional

integration of these steps, followed by a section on the use of optical technologies. In Sect. 4, the fabrication chain for the manufacturing of polymer-based microfluidic devices will be discussed. The subsequent section contains an example for the development and realization process of an integrated microfluidic device.

2 Development and Integration Strategies

One of the crucial success factors for microfluidics on the way to a broadly used enabling technology is the ability to integrate the complete (bio-)analytical process with its numerous process steps which are shown schematically in Fig. 1 onto a single device, keeping issues like manufacturability and fabrication cost in mind.

In the first step, the sample has to be brought onto the device through some interface. As the type of sample can be very different (e.g., biopsy, swab, sputum, and blood), this interface has to be adapted to the type of sample to, on the one hand, safeguard a most efficient sample transfer to the device and, on the other hand, ensure the absence of any contamination of the sample or infection risk of the operator. These "world-to-chip" interfaces still are often an overlooked but important item during the development of microfluidic systems; more and more use of existing standards from the targeted application area (e.g., Luer-Lok compatible interfaces in clinical diagnostics) is established, however, with disadvantages mainly in terms of size. For this reason, we have developed a similar press-fit interface with a reduced footprint (called "Mini-Luer"), allowing up to 32 fluidic ports on a device the size of a microscopy slide. Figure 2 shows in comparison microfluidic chips with (from left to right) tube connectors, Mini-Luer, and full-size Luer connectors.

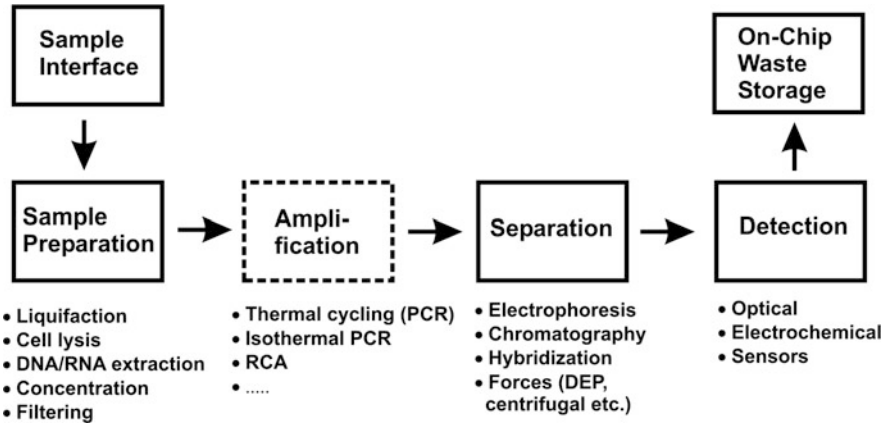

Fig. 1 Schematic diagram of the typical process steps involved in a bioanalytical or diagnostic process flow in a microfluidic device

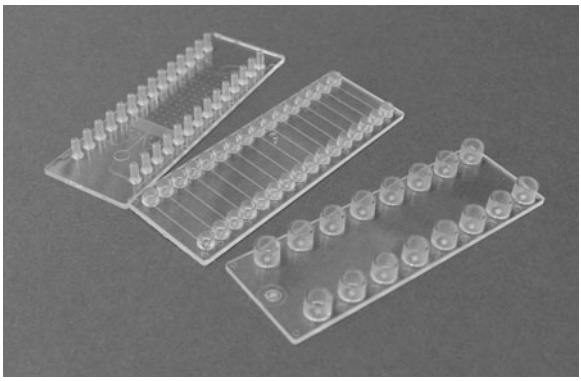

Fig. 2 Microfluidic chips with a standard format (microscopy slide) and different fluidic interfaces. From *left* to *right*: tube connectors, Mini-Luer, and full-size Luer connectors

The next step, the various sample preparation processes like liquefaction of the sample, the lysis of cells, extraction of DNA/RNA, the sample concentration, etc., have so far been typically carried out off-chip due to their complexity and the different nature of the various samples. Moving these steps onto the device represents the biggest challenge mainly due to the fact that usually several media (wash buffer, carrier buffer, beads, lysing agents, etc.) have to be handled sequentially as well as in parallel, all of which require interfaces and plumbing in very restricted device areas. Furthermore, many of these steps have to be carried out with a high precision in terms of volume, times, or sequence, which in specialized (and often costly) laboratory equipment is much less difficult to achieve. It is therefore a specific requirement in the development of miniaturized assays that the assay should be as robust as possible in terms of, e.g., process steps, volumetry, and timing in order to be carried out on-chip. As an example, a volumetric precision of $\pm 5\%$ of e.g., a 1-µl volume requires a manufacturing precision of a microchannel with a dimension of 100×100 µm of $\pm 2\%$ in each dimension, a factor which is directly related to the manufacturing cost of the device. Thus a more robust assay with reduced process precision requirements also helps keeping the fabrication cost of the devices in bay. In recent years, several groups have demonstrated the integration of such sample preparation steps on-chip, see e.g., [4, 5]. For the development of such an integrated device, a two-prong approach has proven to be advisable. On the one hand, a holistic top–down approach from the system level is necessary in order to ensure the inclusion of all necessary functions as well as the definition of all interfaces (fluidic, mechanic, optic, etc.). A flow diagram of all process steps performed on the device can then be translated into individual functional modules. The second line of approach is then a development (e.g., by simulation and subsequent prototyping) of the individual module (e.g., a DNA extraction chamber, a mixing structure for the lysis buffer, etc.) where the individual functions can be validated before integration. One significant difference to other engineering disciplines, especially mechanical or electrical engineering, however, exists in the realm of microfluidics. In these fields, the development of individual modules tends to be simpler due to the fact that the mutual interactions of the individual modules are more limited and often calculable with simple restraints, allowing the assembly of module libraries which can simply be transferred from

one development case to another. In microelectronics, an operation amplifier or a storage capacitor will behave (almost) identical regardless of the overall system layout. In microfluidics, however, the performance of a single module is often to a large extent dependent on the overall system layout. A typical example would be the parameter of flow speed in a microfluidic module, e.g., a simple T-shaped microchannel. This flow speed can be easily calculated given the dimension of the various arms of the channel. However, as the flow speed depends (amongst others) on the back pressure the different arms of the T are experiencing, the flow distribution changes depending on the back pressure generated by preceding or succeeding modules. If this happens in a time series, already the functional description of such a simple module can become quite difficult. It is therefore emerging as best practice in the development to combine the theoretical (or modeling) approach (see e.g., Fig. 3 as example) with some experimental data from module prototypes.

The next process step usually in devices using molecular biology methods involves an amplification of target molecules, using methods like conventional or isothermal PCR and rolling circle amplification (RCA) in order to increase the number of target molecules to achieve better detection selectivity and sensitivity. This amplification step is then frequently followed by a separation step like

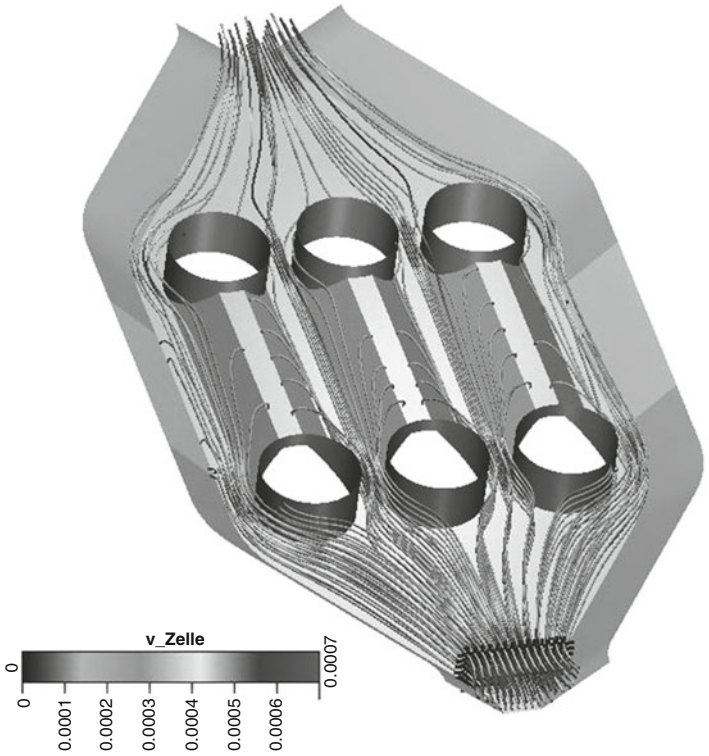

Fig. 3 Multiphysics simulation of cell trajectories in a cell-assembly chip (Image courtesy of BioMEMS and Sensors group, NMI, Tübingen, Germany)

electrophoresis, chromatography (up to now not well developed on-chip), the use of capture probes (e.g., DNA arrays), or other filtration mechanisms in order to isolate the desired component spatiotemporally or remove unwanted components from the mixture.

The final analytical step comprises the detection of the analyte of interest. While for many larger, lab-based systems, optical detection methods like laser-induced fluorescence (LIF) still act as a benchmark with respect to sensitivity, for portable systems, electrochemical analysis methods, or various other sensor methods (e.g., surface acoustic waves (SAW), quartz crystal microbalance (QCM), thermal measurements) are becoming increasingly of interest. It should be noted that all the preceding process steps have to be matched to the selected detection method in order to generate the best results.

A minor but nevertheless important design step of an integrated device in diagnostics is the layout of a waste container system in order to retain all liquids used in the process on-chip. This is often necessary to avoid the contamination risk of the instrument and to prevent carryover from one measurement to the next. Critical can be the required volume of such waste reservoirs, frequently stressing the limited real estate on the chip.

As a method to develop microfluidic systems which contain the above listed analytical steps, a stepwise approach has proven to be advisable. Functional modules for specific functions are defined (e.g., DNA extraction) and realized in order to validate their performance.

Once these functions have been verified, a stepwise integration into a single device then can take place. This stepwise approach also simplifies the search for and correction of possible errors observed in the performance of the device.

3 The Importance of Optical Technologies in Microfluidics

Optical technologies have always played an important role in conjunction with microfluidic systems in the Life Sciences, primarily for detection means [6, 7]. For many applications, the most sensitive and selective method for detection and/or imaging is fluorescence detection, usually induced by one or several lasers, where the respective target is labeled with a fluorescent dye. LIF has been the primary method for the detection of biomolecules in miniaturized CE systems, for PCR products (see example in Sect. 5) as well as for practically all cell-based methods. Optical components can also be directly integrated in microfluidic chips. Optical waveguides for the coupling of the excitation light into a microchannel as well as the collection of the fluorescent light have been generated on microfluidic chips using femtosecond laser machining [8]. Photonics has furthermore been used in many other microfluidic applications such as the actuation and manipulation of droplets using intense light fields [9, 10] or even complex “optofluidic” circuits [11], where the variability of physical parameters of liquid media in a microfluidic device is utilized. Even microfluidic dye lasers have been realized [12].

4 Manufacturing Technologies

The progress made in polymer microfabrication technologies [13] has greatly contributed to the onset of the commercial applicability of microfluidic devices. The possibility to generate devices at a cost which makes them usable as disposable is one of the important breakthroughs for this technology. The necessary technology chain for the manufacturing of such devices is shown in Fig. 4. It starts with the design of the device. At this point, it is important to notice that in the device design beyond the application-driven aspects, input from the complete manufacturing chain is necessary to achieve what is called design-to-manufacture, i.e., a device design which allows the manufacturing at a given cost. As for polymer disposables, replication methods like injection molding and hot embossing are the preferred manufacturing methods, the device design has to be translated into a replication master (often also with some verbal unspecificity referred to as "replication tool," "mold," or "mold insert"). Although the requirements for such a master structure differ with respect to the physical parameters of the chosen replication method (e.g., force, temperature), four basic statements can be made: (a) the geometrical replication result can only be as good (or as bad) as the geometrical accuracy of the master, (b) for the ability to separate mold and molded part (demolding step), no undercuts in the structure itself can be allowed, (c) the surface roughness of the master should be as low as possible (ideally peak-valley values of below 100 nm), and (d) a suitable interface chemistry between master and substrate has to be chosen. In order to generate the master structure, principally all microfabrication methods are suited. The proper selection of the master fabrication technology is one of the crucial steps in the product development of commercial microfluidic devices, especially as there is no generic recipe for this selection. Table 1 lists the most common master fabrication methods with their properties. For commercial applications, the most suitable methods are precision-machined masters made out of steel for structural

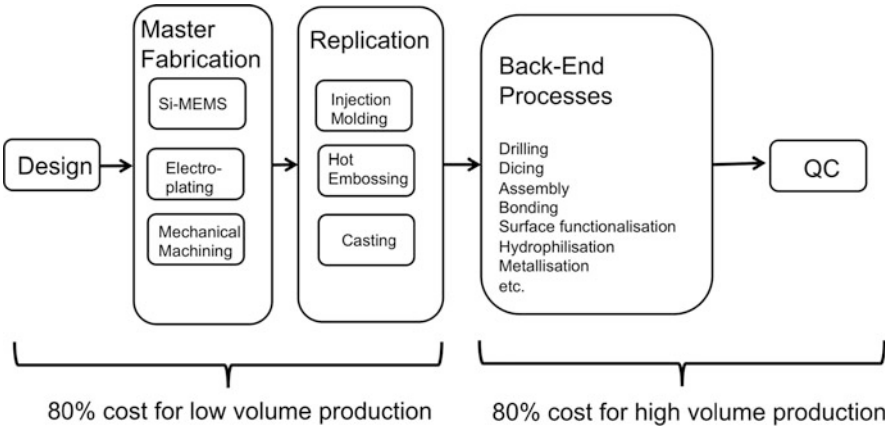

Fig. 4 Technology chain for the manufacturing of polymer-based microfluidic devices

Table 1 Overview on main master fabrication methods

Microfabrication technology	Choice of geometry	Minimum feature size	Structural height	Total surface area	Aspect ratio	Lifetime	Cost	Commercial availability
Wet silicon etching	− −	+	0	+	−	0	+	+
Dry silicon etching	+	++	+	+	++	− −	0	++
Lithography and electroplating	0	++	+	++	+	+	0	0
Laser ablation and electroplating	+	+	+	++	0	+	−	−
Femtosecond laser machining	+	+	0	− −	0	+	−	−
Mechanical (ultra) precision micromachining	++	0	++	++	+	++	−	0
LIGA	+	++	+	−	++	+	− −	− −
Thermoset structuring	0	++	+	++	+	−	0	−
μ-EDM	−	0	+	++	+	++	−	−

dimensions down to about 30–50 μm or, for smaller structures, nickel masters which are generated by electroplating of photoresist or silicon. For larger structures, micro electrode discharge machining (μ-EDM), which is among the most common methods for stainless steel tooling in the macroworld, becomes possible. Both methods combine long master lifetimes with good geometrical definition at reasonable cost and availability. The LIGA process generates the masters with the highest precision and best surface roughness available; however, the manufacturing process is complex, expensive, and time-consuming. On the opposite side, masters consisting of silicon can be made quickly at low cost; due to the brittleness of the material, they can mainly be used for casting and hot embossing. A recent development is the use of polymers (e.g., fully cured SU-8 photoresist) as a material for replication masters. The master lifetime in this case is limited typically to a few 10–100 replications at moderately complex designs and low aspect ratios. For more complex geometries, namely when comparatively large structural dimensions (mm-sized features) have to be combined with small features, hybrid tooling such as the combination of precision machining for the larger features and lithography or laser ablation for the finer features can offer a solution. Figure 5 shows as an example a precision-machined stainless steel master structure.

For the high-volume manufacturing of disposable microfluidic devices, high-precision injection molding has established itself as the method of choice. As it is by far the most widespread fabrication process for polymers in the macroworld, it is not surprising that the first application of this production technology for microfluidic components was already published more than 10 years ago [14]. Due to the comparatively high demands in equipment and process, it is seldom used in academics compared to industrial use. For the commercial success of microfluidics, it will nevertheless play a crucial role.

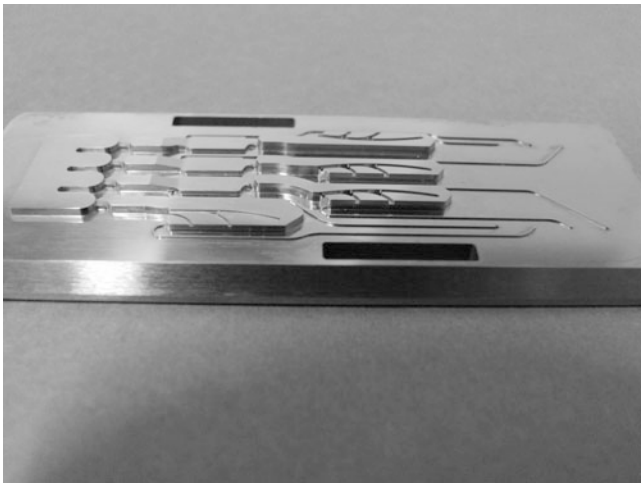

Fig. 5 Mold insert for a standardized injection molding tool (microscopy slide size) made with precision mechanical machining

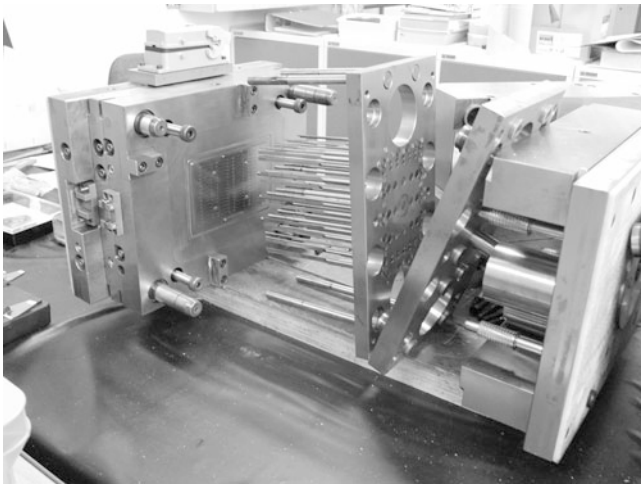

Fig. 6 Injection molding tool for microfluidic devices with the size of a microtiter plate. Note the mechanical complexity

One of the constraining factors for the use of injection molding is the high requirements for the so-called injection molding tool. It has to perform very precise mechanical motions under high temperature variations and forces. In Fig. 6, an example of such an injection molding tool for microtiter plate-sized devices is shown. The mechanical complexity of such an injection molding tool becomes apparent. One of the strategies to reduce the development cost of microfluidic devices is the use of so-called family tools, which use exchangeable mold inserts and can thus be used for molding different device designs. The molding process itself consists of the following steps: The polymer material is fed as pre-dried granules into the hopper. In the heated barrel, a screw transports the material toward the injection port of the molding tool. During this transport, the polymer melts and reaches the tool in liquid form with a melt temperature of the order of 200–350°C depending on the polymer. It is now injected under high pressure (typically between 600 and 1,000 bars) into the mold which contains the microstructured mold insert. For microstructure replication, it has to be evacuated to achieve a good filling of the mold and to prevent the formation of air pockets. Depending on the surface-to-volume ratio of the structure, the mold can be kept at temperatures below the solidification temperature of the polymer (typically between 60 and 120°C, so-called cold cavity process) or, in case of small injection volumes and high aspect ratio structures, has to be kept at temperatures above the so-called glass-transition temperature T_g and cooled together with the melt. The need for this so-called variotherm process drastically increases the cycle time; therefore in commercial applications the development of the microstructure has as a goal the moldability with a cold cavity process. Typical cycle times for a cold-cavity process are of the order of 30 s–2 min, a variotherm process can take up to 5 min. After opening of the mold, the molded part will be ejected from the mold. Normally, remains of the

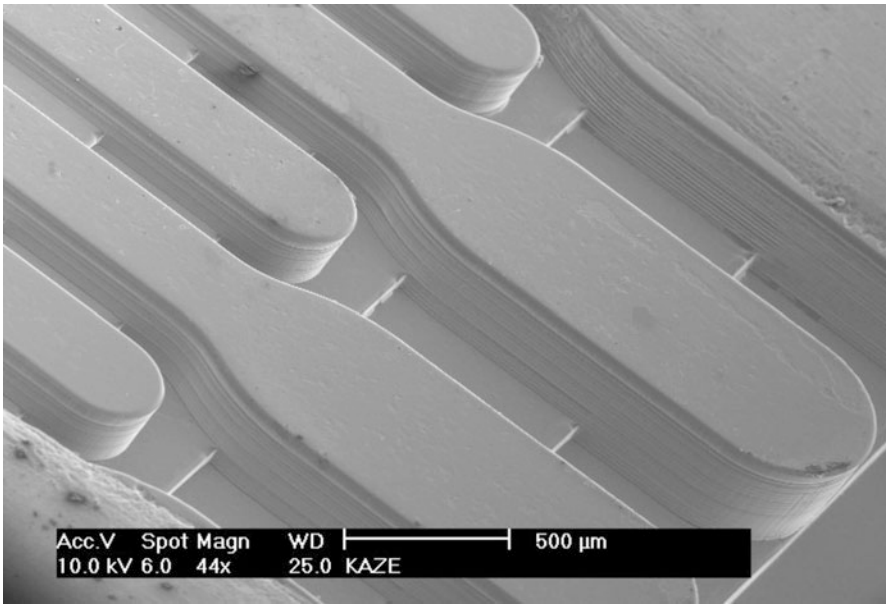

Fig. 7 Multilevel microfluidic structure injection molded from a mechanically machined mold insert

material from the injection port (so-called sprue) will still be connected to the part which has to be removed, either mechanically by cutting, sawing, and breaking off or using a laser.

Figure 7 shows an example of a multilevel structure injection molded from a mechanically machined mold insert. The big advantages of injection molding are the ability to form three-dimensional objects, which, in case of microfluidic devices, means e.g., the integration of fluidic interconnects [15] (see Fig. 3) or through-holes. Furthermore, the ejected part does not normally need additional mechanical process steps, thus reducing the need for mechanical back-end processes (see below).

At this point in manufacturing, one has a microstructured polymer part. While for prototyping or low-volume manufacturing, most of the cost is concentrated in this part [16], for higher volumes, the majority of production cost lies in the subsequent back-end processing steps. These can be roughly divided into two groups:

1. Physical processes: In this category, steps like bonding of a cover lid, e.g., with adhesives, laser or ultrasonic welding, thermal or solvent-assisted bonding (for a recent review see, e.g. [17]) in order to close the channels, the assembly of the device in case of the integration of sensors, gaskets, membranes, septa, or other components and mechanical processes like dicing or drilling are used. A special process is the integration of electrodes onto the polymer device. This can be realized using thin-film processes like thermal evaporation or sputtering or thick-film processes like screen-printing. Recently, inkjet printing of conductive

inks has received increasing attention due to its cost structure and ease of integration of this process in the overall production line [18].

2. Chemical processes: These processes are related to the surface chemistry of the device. Frequently, this surface chemistry, especially the hydrophilicity/hydrophobicity of the device, has to be tuned for a specific device [19–21]. As most thermoplastic polymers have a fairly hydrophobic surface (contact angle typically 80–90°), the contact angle has to be decreased in order to get devices which fill by capillary action. This can be realized using a plasma treatment [22], UV light [23], or by flush-coating the enclosed microchannel [20]. Other surface-modification steps include the local binding of (bio-) molecules to the surface (e.g., for array-based assays) or a local deposition of reagents, e.g., lyophilized or in biostabilized form. This form of chemical patterning usually is realized using a spotting tool or inkjet-like printing.

In an industrial setting, the manufacturing chain is finished by a quality control process, usually a combination of optical inspection with a functional test of a subsample which is selected by statistical process control (SPC) methods and the subsequent packaging of the device in a suitable form, e.g., pouches or sealed foil packs.

It is important to notice at this point that by a clever device design the biggest potential for cost-saving lies in reducing or simplifying the back-end processing steps [16].

5 Application Example

In order to elucidate the development and manufacturing processes described above, the stepwise realization of an integrated device for the simultaneous detection of eight different pathogens is described. It starts with the selection and development of individual functional modules and culminates in the complete device integration.

5.1 Functional Modules

The first example of such a functional module is a chip which contains magnetic beads for DNA extraction. The chip (with the size of a microscopy slide) contains two rhombic chambers with a volume of 120 µl each. These chambers are either preloaded with coated magnetic beads or can be loaded after assembly, as shown in Fig. 8. The sample is introduced into the chamber together with lysis buffer and incubated for 5 min. This is followed by three subsequent washing steps with wash buffer; after each washing step, the magnetic beads are held at one end of the chamber using a magnet to concentrate the beads at the desired location. After the final wash step, the buffer is replaced by an elution buffer in which the DNA bound on the magnetic beads is released. After collecting the eluate DNA, it can be then

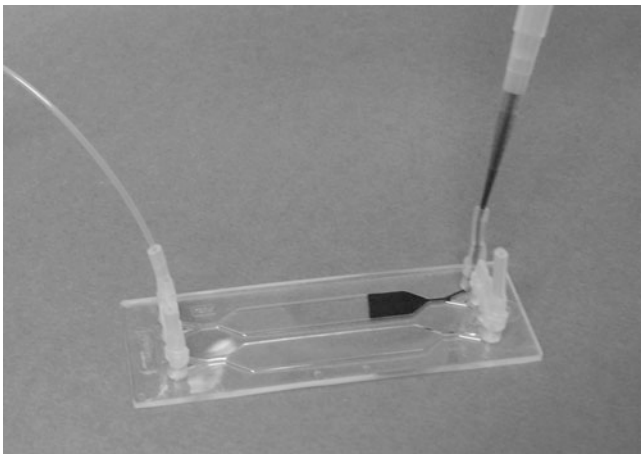

Fig. 8 Chip for DNA extraction using magnetic beads. The beads together with lysis buffer are pipetted into the chip

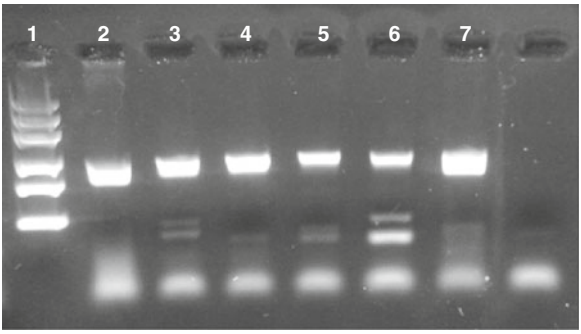

Fig. 9 PCR results of a dilution series of *Salmonella* from 200,000 to 200 bacteria from DNA extracted with the chip shown in Fig. 8

transferred to an amplification module. Figure 9 shows the amplification results in a 36-cycle PCR chip (see next paragraph) of a dilution series of *Salmonella* as a model organism for the pathogens. The lanes contain from left to right: Lane 1: Mass ruler. Lane 2: 200,000 bacteria. Lane 3: 20,000 bacteria. Lane 4: 2,000 bacteria. Lane 5: 200 bacteria. Lane 6: positive control for 200 bacteria in a conventional PCR cycler. Lane 7: negative control. The specific fragment size of the PCR product was 263 bp.

The next module is an amplification module utilizing the principle of continuous-flow PCR [24, 25]. This principle is especially suited for long-term, decentralized monitoring purposes as it operates with stationary temperature zones instead of conventional thermocycling, thus greatly reducing the energy requirements for an instrument. At the same time, the analysis speed is improved while at the same time very low sample volumes are required. Furthermore, this principle lends itself for continuous monitoring, e.g., in the case of air-borne pathogen monitoring with the

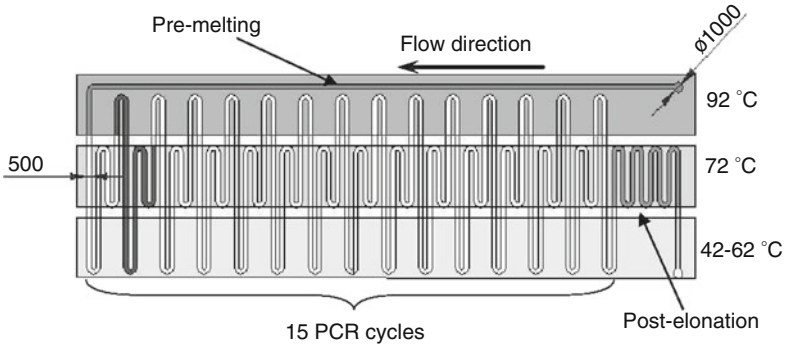

Fig. 10 Principle of chip-based continuous-flow PCR. The sample is pumped over three stationary temperature zones, thus eliminating the need for thermocycling

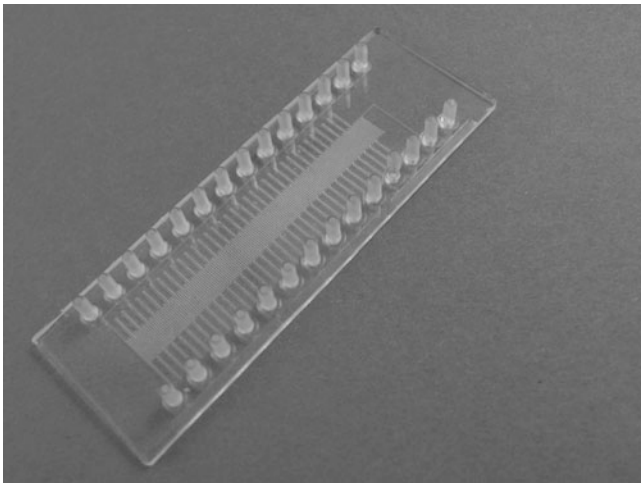

Fig. 11 Picture of the 36-cycle injection-molded PCR chip

sample being continuously taken from an air sampler. Figure 10 shows the principle layout of such a continuous-flow PCR chip with the three temperature zones required to perform the PCR process; Fig. 11 shows the actual chip with 36 PCR cycles as used above, injection molded in polycarbonate (PC) [26].

The final step in the analytical process is the detection of the relevant sample. Up to now in most cases, optical detection methods, namely fluorescence, are used due to their high sensitivity as well as due to the large number of protocols and dyes available.

An example of a chip module made for the fluorescence end-point detection of a qPCR process is shown in Fig. 12a, a subsequent fluorescence image of the detection area in Fig. 12b, and the measurement of qPCR products in Fig. 12c.

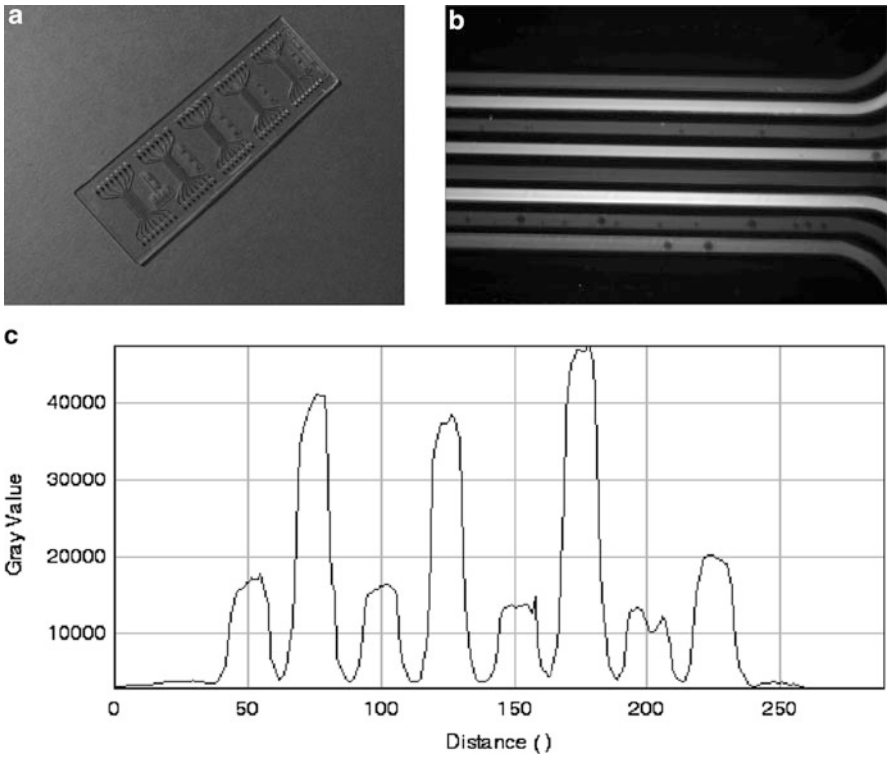

Fig. 12 (**a**) Channel array chip for the optimization of the detection zone geometry. (**b**) Fluorescence image of PCR products in the detection zone. (**c**) Fluorescence data of PCR products in detection zone

The channels contain from top to bottom (equivalent to the peaks from left to right in Fig. 12c): negative control *Coxiella burnetii* from conventional thermocycler; positive control *C. burnetii* from conventional thermocycler; negative control *C. burnetii* from chip PCR; positive control *C. burnetii* from chip PCR; negative control *Brucella melitensis* from conventional thermocycler; positive control *B. melitensis* from conventional thermocycler; negative control *B. melitensis* from chip PCR; positive control *B. melitensis* from chip PCR. As in the final device, an 8-plex detection was targeted, the spacing of the microchannels after qPCR had to be very narrow in order to have all channels within the field of vision of the detection system in order to avoid the need for optical scanning. This led to 200-µm wide, 300-µm deep microchannels with a spacing of only 150 µm which poses a significant challenge in the leak-tight bonding of the device with a thin cover foil. As can be seen from the fluorescence image, no cross-talk due to incomplete bonding is visible.

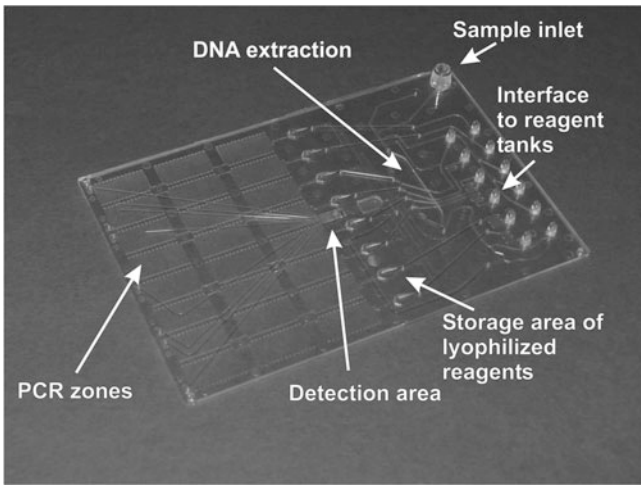

Fig. 13 Integrated microfluidic device for 8-plex pathogen identification

5.2 Integrated Device

After validating the modules above, an integrated device for the detection of eight different pathogens from a single sample was developed. The chip with the footprint of an SBS titerplate is shown in Fig. 13 which is made by injection molding and which contains microfluidic structures on the top as well as on the bottom side. The sample is introduced in the upper right hand corner through a Luer connector. Then, a bead-based DNA extraction and concentration takes place. The sample is subsequently divided into eight aliquots which flow through the storage area where the lyophilized PCR master mixes are stored. After liquefaction of the PCR mixes through the sample, the continuous-flow PCR takes place. The sample is then transported through microchannels on the top side of the chip to the detection area, where the fluorescence detection takes place before the samples are carried off to waste.

With this device, experiments for the simultaneous detection of *B. melitensis, Burkholderia mallei, B. pseudomallei, C. burnetii, Francisella tularensis, Yersinia pestis,* and orthopox virus are currently under way to determine the performance of the device. An overall analysis time including all sample preparation steps as well as PCR of 40–45 min is targeted, which is comparable to the fastest commercially available but significantly more complex and expensive systems like the Genexpert from Cepheid [27].

6 Conclusions

By now microfluidics has reached a stage where it has gained widespread attention in many scientific disciplines. A significant development in the field of microfluidics can be noted in recent years, leading to a maturing of the technology and the

subsequent growth in applications and products. The example described above gives a good indication of the ability to develop and manufacture complex microfluidic devices. Although no single "killer application" so far has captured the headlines, it is the long list of widely accepted advantages which nowadays makes microfluidics an essential tool in product development in almost any field of the Life Sciences. The availability of suitable fabrication methods for high-volume manufacturing of disposable microfluidic devices plays an important role to bring this technology to commercial success which will have a significant impact on the whole Life Science industry [28].

Acknowledgments Parts of this work were funded by the German Federal Ministry of Education and Research (BMBF) (grant no. 13N9556) and managed by the Projektträger VDI-Technologiezentrum Physikalische Technologien. We would like to acknowledge the kind support by all partners of the joint project

References

1. Manz A, Graber N, Widmer M (1990) Miniaturized total chemical analysis systems: a novel concept for chemical sensing. Sens Actuators B1:244–248
2. Whitesides GM (2006) The origins and the future of microfluidics. Nature 442:368–373
3. Becker H (2009) Hype, hope and hubris: the quest for the killer application in microfluidics. Lab Chip 9:2119–2122
4. Legendre LA, Morris CJ, Bienvenue JM, Barron A, McClure R, Landers JP (2008) Toward a simplified microfluidic device for ultra-fast genetic analysis with sample-in/answer-out capability: application to T-cell lymphoma diagnosis. JALA 13(6):351–360
5. Yager P, Edwards T, Fu E, Helton K, Nelson K, Tam M, Weigl B (2006) Microfluidic diagnostic technologies for global public health. Nature 442(7101):412–418
6. Götz S, Karst U (2007) Recent developments in optical detection methods for microchip separations. Anal Bioanal Chem 387:183–192
7. Baker CA, Duong CT, Grimley A, Roper MG (2009) Recent advances in microfluidic detection systems. Bioanalysis 1(5):967–975
8. Martinez Vazquez R, Osellame R, Nolli D et al (2009) Waveguide integration in a lab-on-a-chip for fluorescence detection. Lab Chip 9:91–96
9. Delville JP, de Saint Vincent MR, Schroll RD et al (2009) Laser microfluidics: fluid actuation by light. J Opt A Pure Appl Opt 11:034015, 15 pp
10. Kotz KT, Noble KA, Faris GW (2004) Optical microfluidics. Appl Phys Lett 85:2658–2661
11. Psaltis D, Quake SR, Yang SD (2006) Developing optofluidic technology through the fusion of microfluidics and optics. Nature 442:381–386
12. Cheng Y, Sugioka K, Midorikawa K (2004) Microfluidic laser embedded in glass by three-dimensional femtosecond laser microprocessing. Opt Lett 29(17):2007–2009
13. Becker H, Gärtner C (2008) Polymer microfabrication technologies for microfluidic systems. Anal Bioanal Chem 390:89–111
14. McCormick RM, Nelson RJ, Alonso-Amigo MG, Benvegnu DJ, Hooper HH (1997) Microchannel electrophoretic separations of DNA in injection-molded plastic substrates. Anal Chem 69:2626–2630
15. Gärtner C, Becker H, Anton B, Rötting O (2003) Microfluidic toolbox: tools and standardization solutions for microfluidic devices for life sciences applications. In: Proceedings of SPIE microfluidics, BioMEMS, and medical microsystems II, San Jose, vol 5345, pp 159–162
16. Becker H (2009) It's the economy. Lab Chip 9:2759–2762

17. Tsao CW, DeVoe DL (2009) Bonding of thermoplastic polymer microfluidics. Microfluid Nanofluid 6:1–16
18. Pabst O, Perelaer J, Beckert E, et al. (2010) Inkjet printing and argon plasma sintering of an electrode pattern on polymer substrates using silver nanoparticle ink. In: Proceedings of NIP26: international conference on digital printing technologies and digital fabrication, Austin, pp 146–149
19. Soper SA, Henry AC, Vaidya B, Galloway M, Wabuyele M, McCarley RL (2002) Surface modification of polymer-based microfluidic devices. Anal Chim Acta 470:87–99
20. Locascio LE, Henry AC, Johnson TJ, Ross D (2003) Surface chemistry in polymer microfluidic systems. In: Oosterbroeck RE, van den Berg A (eds) Lab-on-a-chip. Elsevier, Amsterdam, pp 65–82
21. Belder D, Ludwig M (2003) Surface modification in microchip electrophoresis. Electrophoresis 24:3595–3606
22. Nitschk M (2008) Plasma modification of polymer surfaces and plasma polymerization. In: Stamm M (ed) Polymer surfaces and interfaces: characterization, modification and applications. Springer, Berlin, pp 203–214
23. Lin R, Burns MA (2005) Surface-modified polyolefin microfluidic devices for liquid handling. J Micromech Microeng 15:2156–2162
24. Köhler JM, Dillner U, Mokansky A, Poser S, Schulz T (1998) Micro channel reactors for fast thermocycling. In: Proceedings of 2nd international conference on microreaction technology, New Orleans, 241–247. German Patent DE000004435107, 30 Sept 1994
25. Kopp MU, De Mello AJ, Manz A (1998) Chemical amplification: continuous-flow PCR on a chip. Science 280:1046–1048
26. Gärtner C, Klemm R, Becker H (2007) Methods and instruments for continuous-flow PCR on a chip. In: Proceedings of SPIE microfluidics, BioMEMS and medical microsystems V, San Jose, vol 6465, pp 6465502–1 – 6465502–8
27. Ulrich MP, Christensen DR, Coyne SR et al (2006) Evaluation of the cepheid GeneXpert system for detecting *Bacillus anthracis*. J Appl Microbiol 100:1011–1016
28. Becker H (2008) Microfluidics: a technology coming of age. Med Device Technol 19(3):21–24

Chip Systems for Analysis of Nucleic Acids with Integrated Amplification and Detection

Wolfgang Fritzsche, Mark Kielpinski, Matthias Urban, Thomas Henkel, Sabine Werres, Robert Möller, Stefan Wagner, Marko Riedel, and Sandra Julich

Please note the Erratum at the end of this book.

Abstract Analytical methods for the detection of nucleic acids are suitable for a variety of applications as, for example, the analytical applications in that field are diagnosis of infectious or hereditary diseases, analysis of microbial contaminations, determination of family relations, or identification of genetically modified organisms. In many cases, the available number of DNA or RNA molecules is not sufficient for common detection methods based on hybridization processes. The standard procedure for nucleic acid amplification is polymerase chain reaction (PCR). This thermally controlled, enzymatically catalyzed, and cyclically performed process enables the synthesis of small amounts of nucleic acids.

In this chapter, a microchip thermocycler with integrated heaters and temperature sensors for droplet-based on-chip PCR is described. The chip is coupled with a

W. Fritzsche (✉) • M. Kielpinski • M. Urban • T. Henkel • S. Werres
Nanobiophotonics Department, Institute of Photonic Technology (IPHT), PO Box 100 239, 07702 Jena, Germany
e-mail: fritzsche@ipht-jena.de

R. Möller
Nanobiophotonics Department, Institute of Photonic Technology (IPHT), PO Box 100 239, 07702 Jena, Germany
Present address: Analytik Jena AG, Konrad-Zuse-Str. 1, 07745 Jena, Germany

S. Wagner
Julius-Kühn-Institute (JKI), Messeweg 11/12, 38104 Braunschweig, Germany

M. Riedel
Julius-Kühn-Institute (JKI), Messeweg 11/12, 38104 Braunschweig, Germany
Present address: Landesamt für ländliche Entwicklung, Landwirtschaft und Flurneuordnung, Steinplatz 1, 15806 Zossen, Germany

S. Julich
Nanobiophotonics Department, Institute of Photonic Technology (IPHT), PO Box 100 239, 07702 Jena, Germany
Present address: microfluidic ChipShop GmbH, Stockholmer Str. 20, 07747 Jena, Germany
e-mail: Sandra.Julich@microfluidic-chipshop.com

W. Fritzsche and J. Popp (eds.), *Optical Nano- and Microsystems for Bioanalytics*, Springer Series on Chemical Sensors and Biosensors (2012) 10: 289–304
DOI 10.1007/978-3-642-25498-7_11,

temperature controlling unit and a device for measuring the fluorescence intensity. Different amounts of initial DNA down to 2 molecules/µl could be successfully detected. The applied template DNA was obtained from different *Phytophthora* species, a group of phytopathogenic organisms with worldwide significance. Small numbers of cells could also be applied and added directly to the PCR mixture. This was studied successfully with human brain microvascular endothelial (HBME) cells and with spores from *Phytophthora*.

Furthermore, another lab-on-a-chip system is presented that combines on-chip PCR and microarray technology within one chip. The chip consists of a DNA chip with integrated electrode structures and a silicone-based chip with incorporated microchannels and reaction chambers. For temperature management, there are heating elements and temperature sensors connected to the chip. Fluidic transportation is implemented by small peristaltic pumps that are installed to the system. Detection is based on enzymatically catalyzed silver deposition. In case of successful hybridization, the microarray spots turn gray or black, and the electric resistance at the electrode gap will decrease. So the hybridization can be analyzed either by optical-based measurement of the gray scale value or by electrical readout of the electrodes.

Advantages of lab-on-a-chip systems are low necessary amounts of reagents and power supply, short reaction times, and small dimensions of the systems. These make the lab-on-a-chip system transportable and, therefore, well suited for point-of-care applications.

Keywords Lab-on-a-chip system • Microarray • Real-time PCR • Diagnosis • *Phytophthora* • Human brain microvascular endothelial cells

Contents

1 Introduction

Bioanalytical methods for the analysis of nucleic acids, such as polymerase chain reaction (PCR), hybridization techniques, or electrophoresis, are important in diagnostics and research. Due to the identification of specific sequences or sequence variations, there is an enormous potential of applications for nucleic acid-based analysis. Identification of organisms or species, determination of infectious or hereditary diseases, cancer diagnostics, identification of genetic modification, determination of family relations, and even pharmacogenomics for individualized

therapy are examples for bioanalytical applications based on analysis of nucleic acids. Within the technical progress today, a lot of research is done to translate these methods into miniaturized scale [2]. In this context, the concept of lab-on-a-chip technologies is often mentioned [1, 5, 9, 11, 14]. The implementation of bioanalytical processes into microchip scale provides advantages toward conventional applications, like less requirements of material, reagents, energy, and space [18]. Especially, faster performance of temperature-dependent reactions is possible because of less thermal mass. Although there is a great economic interest in saving time and costs, another aim of lab-on-a-chip development is the integration of all necessary laboratory processes for a diagnostic analysis into one system. Ideally these systems are suitable for point-of-care analysis, whereby long transportation distances to specialized laboratories become no longer necessary.

The number of scientific articles about lab-on-a-chip developments and applications is still increasing. Aspects of microfabrication and microfluidics must be considered in developing miniaturized biochips. Biocompatibility of materials plays an important role as well. There are a lot of developments transferring single analytical steps into chip-scale, like amplification of nucleic acids or electrophoresis. For nucleic acid amplification, different types of PCR chips have been constructed [6, 12, 30]. The PCR consists of three steps that are implemented at different temperatures. At first, DNA is denatured at 94°C, and then short single-stranded oligonucleotides that are complementary to the borders of the DNA sequence that has to be amplified anneal to the appropriate areas. Thereby the annealing temperature depends on the length of these primers and their guanine and cytosine content. Normally, the annealing temperature ranges between 50°C and 60°C. In the third step, double-stranded DNA is synthesized by Taq polymerase connecting the nucleoside triphosphates. The three steps are cyclically repeated 25–45 times, whereby ideally during each cycle the number of DNA fragments is doubled.

The reaction mixture is either filled into a chamber device [7, 20, 22] or put as droplet onto the chip surface [8, 23] and heated stationary by adjusting temperatures necessary for DNA amplification. Or, the solution is led through microchannels that are integrated into a chip and guided over different temperature zones [19, 25, 29]. Different chips have also been developed for electrophoresis to analyze nucleic acid fragments according to their length. Thereby often the principle of capillary electrophoresis is applied [4]. To analyze nucleic acids according to their sequence, microarray chips are preferably used [3, 10, 27]. On a microarray, a high amount of different samples represented by capture oligonucleotides with specific nucleic acid sequences is arranged on a small area. By precise positioning, the obtained results can be assigned exactly. Often the amount of nucleic acids that can be extracted from a sample is too low for reliable analysis. For this reason, usually the DNA or selected fragments are amplified by PCR before analysis is performed by hybridization or electrophoresis. Furthermore, the PCR products can be modified simultaneously during the PCR process by application of primers with appropriate labels. The labels can represent, e.g., fluorescent dyes [21] that allow an optical readout of the microarray after hybridization. Because the combination of nucleic acid amplification and analysis is very useful, combined chip systems integrating

both parts have also been developed. Besides a combined PCR and microarray or PCR and electrophoresis, also a fluorescent-based detection of the PCR product during the amplification is possible. The technology of commonly used real-time PCR thermocyclers has also been transferred into chip scale so far.

Another much discussed aspect in molecular biological analysis and especially lab-on-a-chip development is the sample preparation. Although a preceding reverse transcription process can be used if RNA has to be analyzed and also thermally lysed cells were directly added to the PCR mixture, nucleic acid extraction cannot be omitted in all cases. While cellular material like blood is easy to disrupt, others have thick cell membranes or cell walls that necessitate chemical disruption. In that case, a purification of the extracted nucleic acids is essential because the chemicals that are applied for this purpose inhibit polymerase activity during PCR process. Additionally, to lyse cells, nucleic acid extraction and purification have also been implemented on chip systems. While there are a few solutions only for sample preparation [16], combined versions with integrated analysis were also described [13, 15, 24]. In 1990, Manz defined the concept of a Micro Total Analysis System (μTAS) [17], which describes lab-on-a-chip systems that integrate entire processes that are necessary for the analysis of chemical samples in an automated implementation. This concept is absolutely transferrable on biological analysis. Still today the μTAS is the aim of many researching activities, because only in that case the complete laboratory is transferred onto a chip system.

2 Presentation of Two Developed Chip Systems for Analysis of Nucleic Acids

As examples for lab-on-a-chip systems applicable for analysis of nucleic acids, two systems are described in the following. Thereby application fields are demonstrated and appropriate results are shown. As template, different material was applied such as purified DNA or even cells. Also, the technical realization is illustrated including the laboratory setup and the applied chips. In both systems, PCR for amplification of small amounts of nucleic acids or their labeling is implemented. To verify successful amplification and confirm the results of the real-time detection, agarose gel electrophoresis was always carried out. PCR products according to the emerged bands were visualized by ethidiumbromide staining.

2.1 Droplet-Based on-Chip Real-Time PCR

Real-Time PCR offers fluorescence-based detection of PCR products already during the amplification process, thereby saving time as long-lasting analysis procedures of the amplified products subsequent to the PCR process, e.g., by gel electrophoresis, are unnecessary. In the experiments, SYBR green [28] was applied that intercalates into double-stranded DNA and thereby offers especially

quantitative analysis by increasing fluorescence intensity according to the amount of amplified DNA. But the application of SYBR green also offers semi-qualitative analysis of PCR products by implementation of a melting curve analysis [26]. For this purpose, the solution is heated up constantly from 50 to 95°C. Thereby a sudden decrease in the fluorescence intensity can be observed that indicates the specific melting temperature of the DNA fragment. The melting temperature depends on the length of the fragments and their guanine and cytosine content.

2.1.1 Presentation of a Chip System for Real-Time PCR

Laboratory Setup

The laboratory setup for the application of the droplet-based on-chip real-time PCR consists of a box impervious to light including equipment to fasten the chip as well as optical fibers, photomultiplier, and light source (Fig. 1b). For temperature management and data processing, a microcontroller is attached. For parameter setting as well as data analysis, a computer with appropriate software is also connected (Fig. 1a).

Chips

The PCR chip includes microstructured heaters and temperature sensors. These are represented on the chip surface. These thin-film platinum structures are fabricated by photolithographic technologies inside a clean room. In the middle of each structure, there is an optical transparent window that enables fluorescence detection using the combined optical fiber installed underneath the chip for excitation and detection. Each chip contains four of these PCR structures. The chips are attached to circuit boards with arranged electrical connections (Fig. 2a). Via ultrasonic bonding they are connected to the circuit board and at least the temperature control unit.

Because fabrication of the PCR chips is quite expensive and each position can only be used once to avoid cross-contamination, a disposable sample carrier for application on the PCR chip was developed. This sample carrier is a Teflon-coated glass chip with ring structures of untreated glass (Fig. 2b). By these hydrophobic and hydrophilic ring structures, round-shaped droplet consisting of 10 µl mineral oil and 3 µl PCR mixture can be applied on the chip surface (Fig. 2c). Mineral oil is used for prevention against evaporation especially during the denaturation steps.

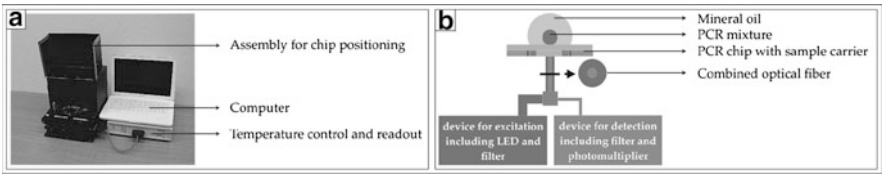

Fig. 1 Laboratory setup (**a**) and detailed scheme of the construction for fluorescence detection during the amplification process occurring inside a droplet arranged on the chip surface (**b**)

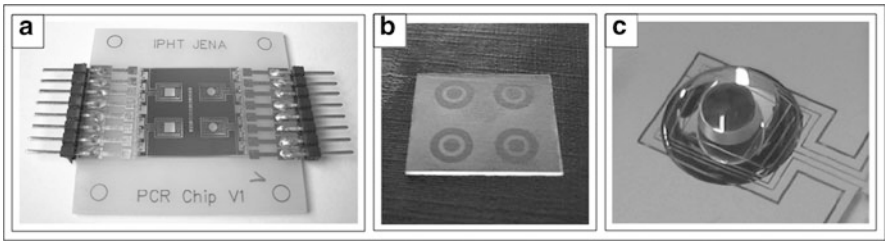

Fig. 2 Entire PCR chip (**a**), Teflon-coated sample carrier with hydrophilic ring structures (**b**), and droplet consisting of clear mineral oil and colored PCR mixture arranged on a heating structure of the PCR chip

2.1.2 Application of Purified Nucleic Acids

Normally DNA serves as template for PCR applications. But RNA or even cells can also be applied, although modification of the protocol is necessary—an additional lysis or reverse transcription step. In the following, results of on-chip real-time PCR are shown whereby extracted and purified DNA was added as initial sample.

Dilution Series

For demonstration of the operability of the PCR chip, a dilution series was applied using initial concentrations between 200,000 and 2 molecules/µl in a total volume of 3 µl of PCR mixture per experiment. All reactions were performed both on the chip and in a conventional thermocycler keeping all parameters identical. The results of the agarose gel electrophoresis (Fig. 3) as well as real-time detection (Fig. 4) demonstrate that PCR on the chip works well and similar to conventional technology. The detection limit with a total number of only six molecules could be achieved in both cases.

Also real-time detection succeeds like expected. With lower initial DNA concentrations, the curve raised up later and the distances between the particular curves were almost consistent. For generation of the standard curves, a threshold value of the fluorescence intensity was defined for measuring the c_t values (crossing points of the curves with a threshold value of the fluorescence intensity). The calculated efficiency for the amplification of the selected DNA fragment from *Phytophthora* using the applied protocol on the PCR chip is 99% and for the conventional cycler 77%.

Analysis of RNA

In case of the detection of a fragment of the coding sequence for the ribosomal protein L13A from HBME cells, either extracted DNA or RNA was applied (Fig. 5a). In case of RNA immediately before PCR, a reverse transcription step

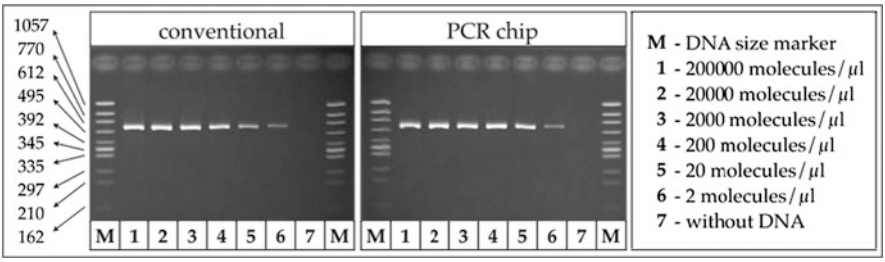

Fig. 3 Results of an agarose gel electrophoresis following PCR on chip and with a conventional thermocycler applying different initial DNA concentrations in a total volume of 3 µl reaction solution

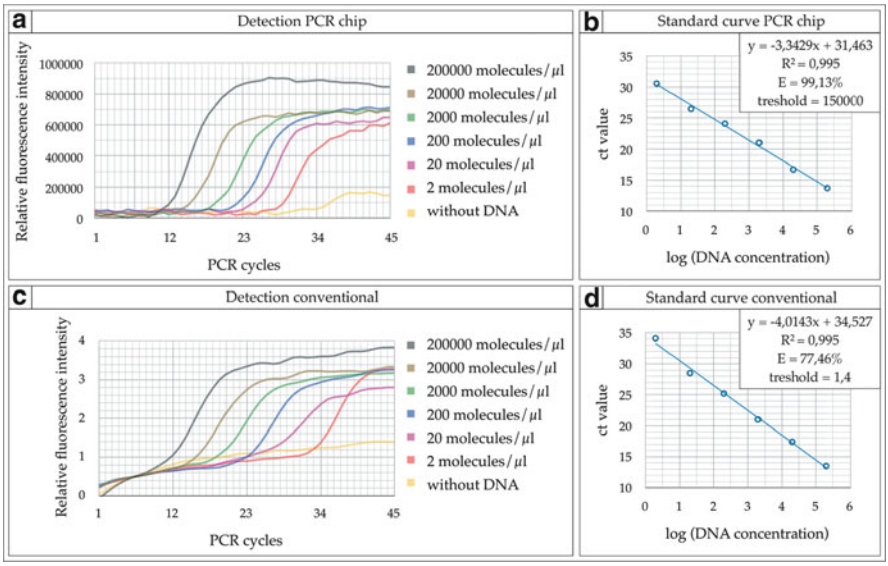

Fig. 4 Results of real-time detection (**a**, **c**) as well as melting curve analysis (**b**, **d**) during amplification of different initial DNA concentrations on the PCR chip (**a**, **b**) and with a conventional thermocycler (**c**, **d**)

was carried out. Therefore in the reaction mixture, not only polymerase but also reverse transcriptase was added.

Multiplex PCR

Multiplex PCR is a beneficial tool for the analysis of several nucleic acid sequences within one tube or droplet. Thereby saving time and material, especially cost-intensive enzymes like polymerase, is possible. Nevertheless, amplification of several DNA fragments simultaneously in one single droplet is a special challenge

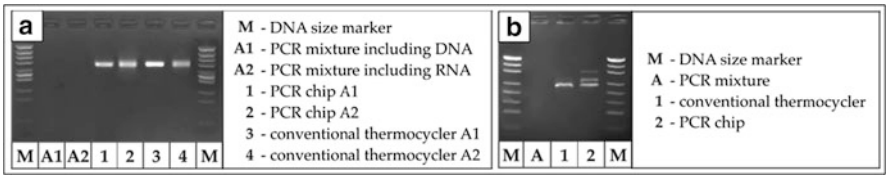

Fig. 5 Results of an agarose gel electrophoresis following PCR on chip and with a conventional thermocycler, on the one hand, applying DNA and RNA from HBME cells amplifying a gene fragment encoding for RPL13A (**a**) and, on the other hand, performing a triplex PCR of gene fragments encoding for RPL13A, gremlin, and vimentin (**b**)

because annealing temperatures of the different primer pairs may only differ marginally. Also inhibition or interference of the PCR products among each other can occur. In some cases, necessary reaction times for multiplex PCR are longer compared to that for amplification of the single products. High variations in the content of guanine and cytosine of the several PCR products can also induce failure of the amplification via multiplex PCR. The agarose gel shown in Fig. 5b demonstrates results of multiplex experiments for amplification of three DNA fragments from purified genomic DNA from HBME cells. An exemplary example for both conventional thermocycler and PCR chip is shown. The selected fragments include gene sections from the coding sequences of the ribosomal protein L13A, as well as the proteins gremlin and vimentin. The experimental results show that in case of the PCR chip, bands for all three products are visible after ethidium bromide staining, although not with homogenous intensity. Using a conventional thermocycler, only the shorter fragments like RPL13A and with a weak band like the gremlin fragment are visible. Therefore, it could be shown that for such particular application, on-Chip PCR is more suitable.

2.1.3 Application of Cells

In modern diagnostics, analysis of cells or even single cells is often required. Therefore the use of cellular material for PCR avoiding time-consuming extraction of nucleic acids is also of great interest today. The identification and discrimination of several *Phytophthora* species are of great interest because some of those parasitic fungus-like species cause plant losses worldwide. Sudden oak death induced by *Phytophthora ramorum* and potato blight induced by *Phytophthora infestans* are famous plant diseases caused by this phytopathogen. Amplification of DNA fragments directly from spores has been successful only by thermal lysis. Therefore, the spores were transferred to the chip surface or into a reaction tube, allowed to dry, frozen at −80°C, and heated at 75°C and 95°C immediately before adding PCR mixture. PCR was performed using the established protocol applied also with DNA as the source material. The success of the experiment was surprising because spores are reproductive structures that are adapted for dispersal and survival for extended periods of time in unfavorable conditions. Therefore, the spores are equipped with thick cell

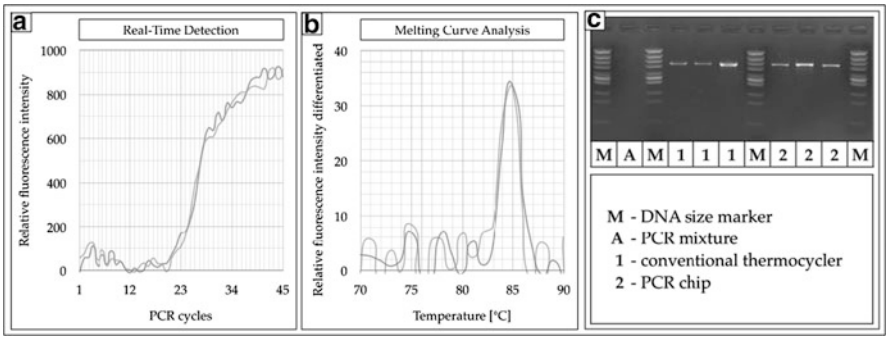

Fig. 6 Results of the on-chip real-time detection (**a**), on-chip melting curve analysis (**b**), and agarose gel electrophoresis of spores direclty added to the PCR mixture

walls. By the visible product bands on the gel shown in Fig. 6c and the detection and melting curves in Fig. 6a, b, it is proven that the spores could be damaged obviously by exposure to cold and heat to make a sufficient amount of DNA accessible for the amplification process. In this case, a number of about 85 spores per experiment were used. For practical application, this number is realistic because spores are produced in high number and thereby could be smeared from the bottom of the leaves for sampling.

In some diagnostic applications, only a few or single cells are available for sampling and analysis. For verification of single cell analysis on the developed lab-on-a-chip system for real-time PCR, single HBME cells were immobilized and thermally lysed appropriate to the *Phytophthora* spores, because in that case, RNA for translation of the L13A protein should be detected by a reverse transcription step to the PCR after adding the reaction mixture to the cells located on the chip or in the tube. Reverse transcription and PCR were performed subsequently, for which reason both enzymes (reverse transcriptase and polymerase) were contained in the mixture. Lysis of animal or human cells is more easy than that of spores because they possess only thin cell membranes that are easy to perforate for extraction of nucleic acids. The results of the single-cell PCR experiments are shown by the agarose gel in Fig. 7c. In both cases, PCR chip and conventional thermocycler-amplified PCR products of the selected fragment with a size of 229 bp are visible, whereas the intensity of the bands according to the on-chip PCR is higher. Also real-time detection and melting curve analysis could be implemented successfully by applying the PCR chip.

2.2 Lab-on-a-Chip System with Integrated PCR and Microarray

Real-time PCR for analysis of nucleic acids is preferably applied for quantitative measurements because the c_t values provide information of the initial content of

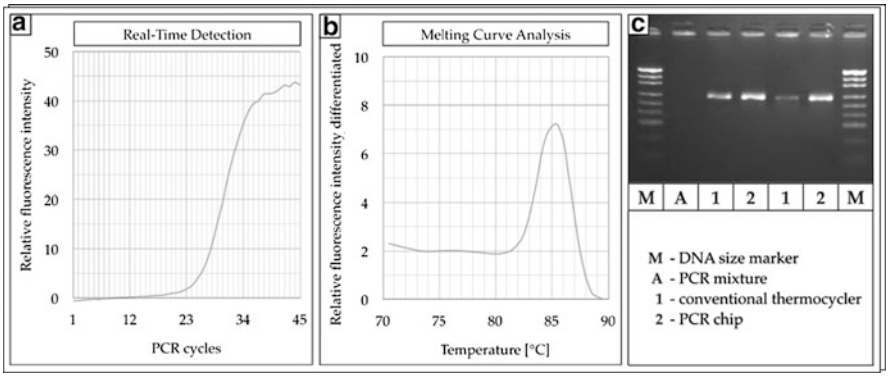

Fig. 7 Results of the on-chip real-time detection (**a**), on-chip melting curve analysis (**b**), and agarose gel electrophoresis of single HBME cells directly added to the PCR mixture

nucleic acids in the PCR mixture. Also a combination with qualitative analysis using fluorescent-labeled probes is possible, but the number of probes that can be analyzed at the same time is restricted. The technical implementation of modern thermocyclers provides a maximum of six different colors for detection in parallel. Also from a biochemical point of view, a high number of different probes and DNA fragments in one sample are not favorable because probability of unrequested hybridization among each other increases. If a sample including nucleic acids has to be analyzed for a high number of sequences or genetic variations, the application of a DNA microarray is preferred. On a microarray, a high number of probes can be immobilized on defined positions within a small area. Therefore hundreds of probes can be placed on about a centimeter. Microarrays are often arranged on small planar chips where special surface modifications for immobilization of the capture probes are required. Under specific conditions and according to the temperature or buffer composition, single mismatches between the sequences of target DNA and capture probe can be determined. The application of a microarray is very useful, e.g., for screening of biological samples of a high number of species according to specific sequence regions. The example that was selected for demonstrating the functionality of that new lab-on-a-chip system with integrated PCR and DNA microarray comprises the differentiation of five different *Phytophthora* species. The presented lab-on-a-chip system includes reaction chambers for amplification and simultaneous labeling of target DNA as well as for hybridization on an applied microarray area. Although the results of that microarray detection can be readout, resistance measurement allows readout already during the hybridization step. For realization of an electrical readout, target DNA is biotin-labeled during the amplification step via appropriate primers, and elementary silver can be deposited after linking of streptavidin-coupled horseradish peroxidase. In case of successful hybridization, the electrode gaps can be closed by deposited silver and an increasing conductivity can be measured.

2.2.1 Presentation of a Chip System for Nucleic Acid Amplification and Detection Via Microarray

A chip system was developed including several technical components for control and measurement. Microarrays offer the analysis of a variety of samples or especially sequence variations within one experiment. For realization of an analytical process using a lab-on-a-chip system, not only the development of the chips itself but also the technical environment including devices for temperature or fluidic management as well as measurement and detection of the obtained results has to be implemented. By developing lab-on-a-chip systems, one's aim should be to construct these technical parts as small and as compact as possible to make the system portable and enable application for point-of-care analysis.

Laboratory Setup

For realization of the identification of several species of a genus using a lab-on-a-chip system with integrated microfluidic structures for amplification and microarray-based detection, a lab-on-a-chip system has been developed and is shown in Fig. 8a. Several technical components are included, such as pumps for fluidic transportation, a device for temperature control, and another one for electrical readout.

The central part of the system is an assembly for chip positioning including Peltier elements for heating and cooling, such as Pt1000 sensors for measurement of the current temperature. The inner construction of this assembly in detail is shown in Fig. 8b. The two heating zones are separated from each other by a gap, whereby thermal crosstalk is minimized. The chip components are placed on the heating plates. Since the microarray is arranged to one side of the chip, this analysis part is connected to one heating zone. The amplification part on the other side of the chip is connected to a second heating zone. The assembly also has a lid that enables to put some pressure on the chip after insertion, whereby tightness of the included microchannels and reaction chambers is assured.

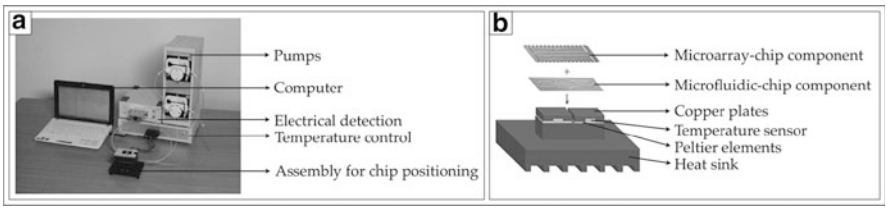

Fig. 8 Laboratory setup (**a**) and detailed scheme of the assembly for chip positioning with integrated components for temperature management (**b**)

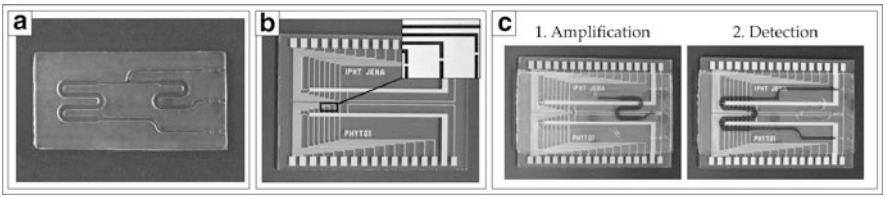

Fig. 9 Microfluidic chip component (**a**), microarray chip component with electrode structures (**b**), and both components after joining with filled reaction chambers for amplification and detection (**c**)

Chips

There are two chip components that are combined to sandwich-like entity. One of these components is a microfluidic chip with integrated reaction chambers and channels for fluid transportation (Fig. 9a). This component is made of polydimethylsiloxane (PDMS), a silicone that is flexible even after the curing process. For fabrication of these chip components, silicone monomers are mixed with a cross-linking agent and the viscous mixture is cast into a molding and hardened overnight. The second component is a microarray chip based on a glass substrate with gold electrode structures on its surface (Fig. 9b). These structures can be fabricated either by microstructuring and photolithography or by application of screen printing which is more inexpensive, especially in large scale.

Because both chip components get in contact with the reaction mixture and the sample, their application as disposables is absolutely necessary whereby cross-contamination is inhibited. Therefore, an inexpensive production of the disposable chip components and appropriate hoses is advisable. After combination of both chip components, the first reaction chamber (S-shaped) will be filled with PCR mixture, and in the second step, the amplified and labeled PCR products will be transferred to the precooled M-shaped microarray zone with simultaneous addition of hybridization buffer (Fig. 9c).

2.2.2 Detection and Differentiations of Several Species of the Genus *Phytophthora*

With the help of the described chip system that is one example for miniaturized nucleic acid analysis, it could be demonstrated that the combination of on-chip PCR and DNA microarray technology is well suitable for detection and discrimination of several species from a biological sample. As one example the differentiation of several *Phytophthora* species could be successfully implemented on that system. Figure 10 shows successful results of the chip-based PCR performed inside the S-shaped reaction chamber of the chip device. It could be demonstrated that the amplification process works similarly and reproducible to those applied in conventional thermocyclers. The selected primer pair not only works well in case of all selected *Phytophthora* species with high phytopathological relevance, but is also

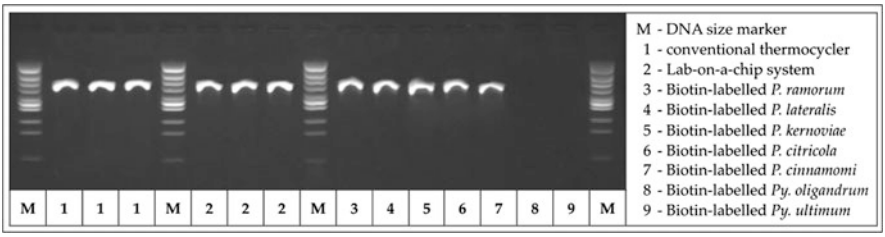

Fig. 10 Results of an agarose gel electrophoresis following PCR on chip and with a conventional thermocycler including verification of reproducibility and specificity of the genus *Phytophthora*

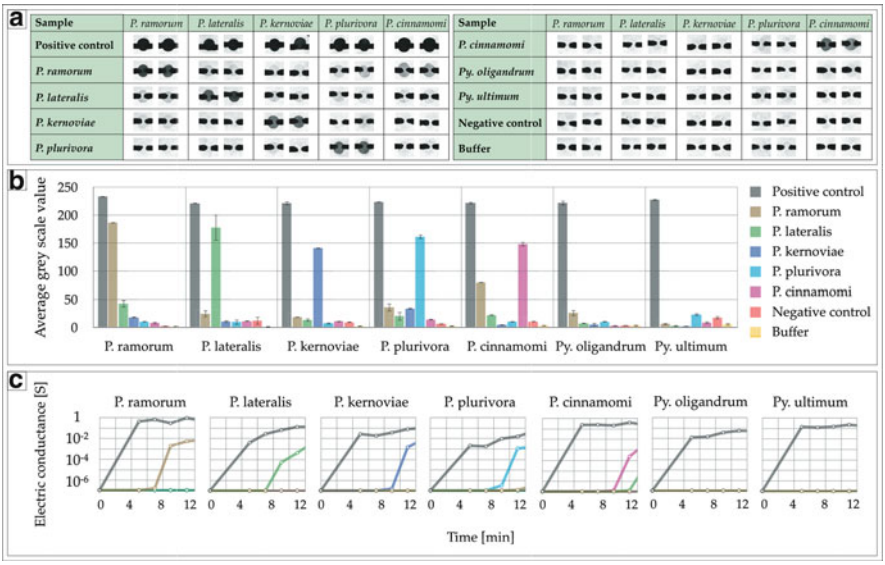

Fig. 11 Optical micrographs from the electrode gaps (**a**), results of corresponding gray scale analysis (**b**), and electrical conductance measurement as a function of time (**c**) after analysis of the DNA from different selected *Phytophthora* and *Pythium* species

selective in case of closely related phytopathogens from the genus *Phytium*. The primer sequences are located on the 5.8 S and 28 S rDNA section of the genomic DNA of *Phytophthora*. These rDNA regions are highly conserved in case of the several *Phytophthora* species, but there are differences between several genera.

The amplified DNA fragment includes a highly variable internal transcribed spacer region that should be applied for discrimination of the several *Phytophthora* species. By means of the light optical micrographs shown in Fig. 11a and the associated results of the gray scale analysis shown in Fig. 11b, it could be demonstrated that all selected *Phytophthora* species are identifiable by optical

detection after the analytical reaction is applied on the chip system. The electrical readout is already permitted during the silver enhancement process performed inside the chip. Therefore, the electrical conductance is measured as a function of time. The results of that electrical detection are shown in Fig. 11c and demonstrate that only in case of the positive control or consistence of template and capture DNA, an increasing conductivity can be measured. The reason for the staggered increase in conductivity from positive control compared to hybridized samples is a higher amount of biotin-labeled probes on the appropriate spots according to the positive control, because the capture molecule consists of direct labeled oligonucleotides. The lower amount of biotin-labeled PCR products is caused by a renaturation effect of the DNA during hybridization, whereby not all capture molecules are coupled with the target DNA. In conclusion, electrical detection is more sensitive and selective because there is almost no background signal detectable because conductivity can only be measured if there is a continuous silver layer on the spot.

3 Summary

According to the obtained results that were achieved by applying the represented lab-on-a-chip systems for analysis of nucleic acids, it could be demonstrated that a combination of nucleic acid amplification and detection is well feasible in miniaturized scale. Both fluorescence-based real-time detection and analysis on electrically readable microarrays can be implemented on chip. For that reason two different lab-on-a-chip systems have been constructed. On-chip real-time PCR is particularly well suited for quantitative analysis because fluorescence intensity is always directly related to the amount of DNA contained in the PCR mixture. Qualitative measurements are also possible, but the number of sequences that can be analyzed in parallel is restricted. For the purpose of analyzing a template according to a high number of sequences, the combination of amplification and simultaneous labeling with a microarray is preferable. Detection of hybridized nucleic acids by enzymatically catalyzed silver deposition is a promising alternative to fluorescence-labeled target DNA because electrical readout can be carried out quite fast and has no need for complicate detection equipment. Also direct application of cellular material such as HBME cells or spores obtained from plants infected by *Phytophthora* was successful, and thereby time-consuming extraction of nucleic acids could be omitted. Presented systems offer fast analysis with low requirements of material, power, and especially initial sample. Complete analysis within a few hours is enabled by using the applied protocol, but there is also potential for time-dependent optimization. If point-of-care application is possible, time-consuming transportation could be minimized.

4 Conclusion and Outlook

On the basis of the developed chip systems, it could be demonstrated that nucleic acid analysis is well convertible in miniaturized scale. Although the development of lab-on-a-chip systems is still advanced and first systems are already commercially available, they did not really find their way in routine diagnostics yet. Further development regarding robustness and automation as well as smaller and faster implementation are required.

Nevertheless, it is not always possible to do nucleic acid analysis of complex biological samples without DNA extraction; processes of cell lysis or nucleic acid purification also have to be adapted in miniaturized scale for implementation of the complete analytical procedure in one single chip system. Because different methods are necessary, according to different analytic or diagnostic questions, there will not be one universal lab-on-a-chip for nucleic acid analysis at all because the technical equipment around the chip would be too extensive to achieve a compact system that is portable and adequate for point-of-care application. Rather several systems for special applications or different analytical questions should be developed.

Acknowledgments The research projects where the presented results could be obtained were funded by grants of the Federal Agency for Agriculture and Food (BLE) belonging to the German Federal Ministry of Food, Agriculture and Consumer Protection (BMELV) in the context of the program for advancement of innovations (FKZ: 28-1-42.028-06). This work was also supported by the German Academic Exchange Service (FKZ: 50152979). The authors would also like to specially thank Anne Haverlah for excellent technical assistance. Our thanks also go to Paul Beales (UK) and Everett Hansen (USA) who kindly supplied the *P. kernoviae* and the *P. lateralis* isolates, respectively.

References

1. Abgrall P, Gue AM (2007) Lab-on-chip technologies: making a microfluidic network and coupling it into a complete microsystem—a review. J Micromech Microeng 17(5):R15–R49
2. Auroux PA, Koc Y, deMello A, Manz A, Day PJR (2004) Miniaturised nucleic acid analysis. Lab Chip 4(6):534–546
3. DeRisi J (2001) Overview of nucleic acid arrays, Chapter 4. Curr Protoc Neurosci
4. Dolnik V, Liu SR, Jovanovich S (2000) Capillary electrophoresis on microchip. Electrophoresis 21(1):41–54
5. Figeys D, Pinto D (2000) Lab-on-a-chip: a revolution in biological and medical sciences. Anal Chem 72(9):330A–335A
6. Giordano BC, Ferrance J, Swedberg S, Huhmer AFR, Landers JP (2001) Polymerase chain reaction in polymeric microchips: DNA amplification in less than 240 seconds. Anal Biochem 291(1):124–132
7. Gong HQ, Ramalingam N, Chen LQ, Che J, Wang QH, Wang YM, Yang XH, Yap PHE, Neo CH (2006) Microfluidic handling of PCR solution and DNA amplification on a reaction chamber array biochip. Biomed Microdevices 8(2):167–176

8. Guttenberg Z, Muller H, Habermuller H, Geisbauer A, Pipper J, Felbel J, Kielpinski M, Scriba J, Wixforth A (2005) Planar chip device for PCR and hybridization with surface acoustic wave pump. Lab Chip 5(3):308–317
9. Haeberle S, Zengerle R (2007) Microfluidic platforms for lab-on-a-chip applications. Lab Chip 7(9):1094–1110
10. Heller MJ (2002) DNA microarray technology: devices, systems, and applications. Annu Rev Biomed Eng 4:129–153
11. Kopf-Sill AR (2002) Successes and challenges of lab-on-a-chip. Lab Chip 2(3):42N–47N
12. Kricka LJ, Wilding P (2003) Microchip PCR. Anal Bioanal Chem 377(5):820–825
13. Lee JG, Cheong KH, Huh N, Kim S, Choi JW, Ko C (2006) Microchip-based one step DNA extraction and real-time PCR in one chamber for rapid pathogen identification. Lab Chip 6(7):886–895
14. Legge CH (2002) Chemistry under the microscope – Lab-on-a-chip technologies. J Chem Educ 79(2):173–178
15. Liu RH, Yang JN, Lenigk R, Bonanno J, Grodzinski P (2004) Self-contained, fully integrated biochip for sample preparation, polymerase chain reaction amplification, and DNA microarray detection. Anal Chem 76(7):1824–1831
16. Mahalanabis M, Do J, Almuayad H, Zhang JY, Klapperich CM (2010) An integrated disposable device for DNA extraction and helicase dependent amplification. Biomed Microdevices 12(2):353–359
17. Manz A, Graber N, Widmer HM (1990) Miniaturized total chemical-analysis systems – a novel concept for chemical sensing. Sens Actuator B-Chem 1(1–6):244–248
18. Mark D, Haeberle S, Roth G, von Stetten F, Zengerle R (2010) Microfluidic lab-on-a-chip platforms: requirements, characteristics and applications. Chem Soc Rev 39(3):1153–1182
19. Markey AL, Mohr S, Day PJR (2010) High-throughput droplet PCR. Methods 50(4):277–281
20. Nagai H, Murakami Y, Morita Y, Yokoyama K, Tamiya E (2001) Development of a microchamber array for picoliter PCR. Anal Chem 73(5):1043–1047
21. Nagl S, Schaeferling M, Wolfbeis OS (2005) Fluorescence analysis in microarray technology. Microchim Acta 151(1–2):1–21
22. Northrup MA, Benett B, Hadley D, Landre P, Lehew S, Richards J, Stratton P (1998) A miniature analytical instrument for nucleic acids based on micromachined silicon reaction chambers. Anal Chem 70(5):918–922
23. Pipper J, Inoue M, Ng LFP, Neuzil P, Zhang Y, Novak L (2007) Catching bird flu in a droplet. Nat Med 13(10):1259–1263
24. Pipper J, Zhang Y, Neuzil P, Hsieh TM (2008) Clockwork PCR including sample preparation. Angew Chem Int Edn 47(21):3900–3904
25. Reichert A, Felbel J, Kielpinski M, Urban M, Steinbrecht B, Henkel T (2008) Micro flow-through thermocycler with simple meandering channel with symmetric temperature zones for disposable PCR-devices in microscope slide format. J Bionic Eng 5(4):291–298
26. Ririe KM, Rasmussen RP, Wittwer CT (1997) Product differentiation by analysis of DNA melting curves during the polymerase chain reaction. Anal Biochem 245(2):154–160
27. Schena M, Heller RA, Theriault TP, Konrad K, Lachenmeier E, Davis RW (1998) Microarrays: biotechnology's discovery platform for functional genomics. Trends Biotechnol 16(7):301–306
28. Schneeberger C, Speiser P, Kury F, Zeillinger R (1995) Quantitative detection of reverse transcriptase-PCR products by means of a novel and sensitive DNA stain. PCR Methods Appl 4(4):234–238
29. Schneegaß I, Brautigam R, Kohler JM (2001) Miniaturized flow-through PCR with different template types in a silicon chip thermocycler. Lab Chip 1(1):42–49
30. Zhang YH, Ozdemir P (2009) Microfluidic DNA amplification-a review. Anal Chim Acta 638 (2):115–125

Optofluidic Microsystems for Application in Biotechnology and Life Sciences

S. Sinzinger, B.P. Cahill, J. Metze, and M. Hoffmann

Abstract Microfluidic systems have been shown to have a large potential for applications in biotechnology and life sciences. This includes traditional fluid actuators alongside alternative techniques such as nanofluidic and multiphase systems. While the fluidic systems are often highly miniaturized and integrated, the systems for optical testing, probing, and manipulation lack this degree of integration. The goal of our research focuses on the integration of fluidic, optical, and mechanical functionalities in complex optical microsystems. We report on fundamental investigations carried out in close cooperation between the Institute of Micro- and Nanotechnologies (IMN-MacroNano®) at Ilmenau University of Technology, and the Institute for Bioprocessing and Analytical Measurement Techniques (IBA), Heiligenstadt, Germany.

Keywords Microfluidics • MOEMs • Optofluidics • Optical tweezers • Optical Microsystems

S. Sinzinger (✉)
Technische Universität Ilmenau, IMN-MacroNano, Technische Optik, P.O. Box 100565 Ilmenau, Germany
e-mail: stefan.sinzinger@tu-ilmenau.de

B.P. Cahill • J. Metze
Fachbereich Bioprozesstechnik, Institut für Bioprozess- und Analysenmesstechnik e.V. (iba), Rosenhof, 37308 Heilbad Heiligenstadt, Germany

M. Hoffmann
Technische Universität Ilmenau, IMN-MacroNano, Mikromechanische Systeme, P.O. Box 100565 Ilmenau, Germany

W. Fritzsche and J. Popp (eds.), *Optical Nano- and Microsystems for Bioanalytics*, Springer Series on Chemical Sensors and Biosensors (2012) 10: 305–324
DOI 10.1007/978-3-642-25498-7_12,

Contents

1 Introduction

Intensive efforts to use microsystems for performing biotechnological tasks have been undertaken since the 1990s. The keystone of the necessary technical foundations for such systems is microfluidics, the technological basis of which requires the integration of mechanics, optics, electronics, and also nanotechnology. The great potential for exploitation of this approach in the field of biotechnology and life sciences is shown by the explosion of the number of publications in this field by many different working groups worldwide.

In the field of biotechnology and life sciences, cells or biological specimen are cultivated as well as manipulated and analyzed. Optical procedures for micromanipulation (so-called optical tweezers) and analytics play a leading role in cell culture and biotechnology. In this respect, the possibilities for reproducible contactless manipulation of cells or droplets that contain cells of comparable orders of magnitude could be of use. In particular, for cells in contact with interfaces, for example, micromechanical manipulators or phase boundaries can lead to undesired interactions or even completely changed cell characteristics.

While substantial research and development activity has already been expended on developing dispensing technology to its present state, additional opportunities for development still exist in pipetting and transportation processes for biogenic media and miniaturized biotechnology. This includes traditional fluid actuators alongside alternative techniques such as nanofluidic and multiphase systems. While such fluidic systems are often highly miniaturized and integrated, the systems for optical testing, probing, and manipulation lack this degree of integration. The goal of our research focuses on the integration of fluidic, optical, and mechanical functionalities in complex optical microsystems. We report on fundamental investigations carried out in close cooperation between the Institute of Micro- and Nanotechnologies (IMN-MacroNano®) at Ilmenau University of Technology, and the Institute for Bioprocessing and Analytical Measurement Techniques (IBA), Heiligenstadt, Germany.

2 Microsystems for Biotechnology and Life Sciences

The micromanipulation of cells is a research field that requires a great deal of innovation; in particular, it is necessary to deal with the current awareness in cell biology that making mechanical contact with a cell is likely to affect its further development. The capture and directed transport of cells by means of "light" or "electric fields" could be a way to address this challenge. Therefore, it is the more important to open new research directions in optofluidic microsystems. The hitherto accepted methods for removing cells have been by taking a full sample and/or by using a bypass with an integrated three-way valve that facilitates sample removal. By working with integrated optofluidic microsystems, cultivation in bioreactor volume sizes from milliliter (mL) down to microliter (μL) range is permitted. Coupled with the optical techniques for micromanipulation presented here, this represents an important cost reduction. At the same time, the possibility of parallel processing is strongly improved by the considerably smaller space requirement.

The authors have carried out comprehensive investigations for screening of applications with regard to the sensory and handling potential of the system. The influence of the surface properties and various coating materials on the performance of microfluidic channels was fundamentally examined. In particular, the control of the adhesion of proteins and microorganisms to channel walls is of great practical significance.

Optical tweezers have become an established handling tool in cell technology in recent years. Although hitherto developed systems have been characterized by their macroscopic experimental setups, completely new applications are opened up by microengineered and integrated systems.

From a biotechnological point of view, possible applications in microsystems are the following:

1. Holding and/or directing cells.
2. Controlling the distance between cells through start–stop laser sequencing.
3. Diversion of cells from a channel can be achieved by bringing the cell to the intersection point of two fluidic streams and switching the flow direction.
4. Defined positioning of cells on a sensor.
5. Measurement of adhesion forces through investigation of the interaction of the cell and other object.
6. Cell fusion through application of two laser tweezers or one laser tweezers and an electric field cage.

One could imagine handling transparent fluid compartments in the same way. These aqueous compartments embedded in a nonpolar medium, for example, could serve as a reactor for microorganisms.

To this end, the Department of Bioprocess Technology of the IBA has developed a technology platform that in the meantime led to the phrase "pipe-based bioreactors" being registered as a trademark (Fig. 1).

Fig. 1 "Pipe-based bioreactors" is a registered trademark of iba

The principles of flow injection analysis systems were published a few decades ago [1, 2]. This enabled the automation of assays in a fluidic phase in combination with low consumption of reagents and sample liquid. In recent years, a strong positive trend in the development and application of microfluidics is ascertainably reflected in an enormous increase of patents in this field and a remarkable number of companies which produce and commercialize miniaturized analytical devices [3]. Custom-made microfluidic chips and entire measuring systems are provided by several companies, and microfluidic systems have been adapted to most of the common analytical techniques [4]. For many applications, the theoretical fundamentals even on the nanoliter scale have been studied and implemented [5]. Widely used fabrication materials are silicon, glass, and a variety of polymers [6]. By minimizing the dimensions of fluidic structures, the surface-to-volume ratio increases in a way that surface interactions become almost dominant. Therefore, the surface properties of microfluidic channels are crucial to the behavior of the liquids, especially in a two-fluid system. Today, the microtiter plate consisting of a flat plate with multiple open wells at a microliter scale is still standard in analytical research and clinical diagnostic testing. Further miniaturization of assay systems requires the use of closed fluidic systems to prevent vaporization, a serious problem during handling of very small sample volumes. Downscaling intensifies this effect, and the evaporation of such droplets occurs very quickly and rapidly. To prevent this phenomenon, it is evident that test formats have to be established in closed microfluidic systems. One of the main features will be the use of many separate fluidic segments to enable self-contained experimental conditions in each droplet. The utilization of flow channels with small diameters requires a precise control of the flow conditions regarding fluid transport and mixing conditions caused by dispersion and diffusion. Working with segmented flow in closed microchannels, which is characterized by fluid volumes separated by air or immiscible carrier liquids, leads to distinct compartments in the system. Such droplet-based microfluidic platforms allow microfluidic unit operations, whereby lateral diffusion (Taylor diffusion) is prevented [7]. In addition to properly designed geometries of the flow channels, surfaces which hinder wetting by the droplet fluids are required. Otherwise, droplets will partially stick to the walls and may lose their integrity. The droplets can be generated at high reproducibility and high frequency at nanoliter volumes by the use of specially designed microfluidic chips [8–10]. The channel walls composed of glass [8] or polydimethylsiloxane (PDMS) [9] are coated with octadecyltrichlorosilane (ODTS), resulting in a hydrophobic surface. Silane molecules form a covalent binding to hydroxyl surface groups and can also covalently link via condensation to neighboring silane molecules, resulting in an ordered monomolecular film coating [11]. The alkyl chains are oriented toward the liquid

phase and determine the hydrophobicity due to their molecular structure. Alkylsilane bindings are found to be very stable against chemical and thermal factors [12]. Therefore, wetting of the walls by aqueous droplets was minimized, and the droplets embedded in an oily carrier liquid take a round convex shape. Due to these characteristics, the droplets maintain their regular distances and can be transported serially through the system like pearls on a string. Recently, microorganisms from soil samples have been cultivated in media droplets by incubation in polytetrafluoroethylene (PTFE) capillaries [13]. Growth rates similar to that of shake flask cultures could be observed even in the case of strictly aerobic bacteria [14].

A material of great current interest for manufacturing bio-micro-electro-mechanical systems (MEMS) is the epoxy-based UV-sensitive polymer SU-8. Examples of microchannels fabricated using this polymer have recently been published [15–17]. It provides biocompatibility [18] and chemical inertness against most biological substances [19] and, due to its transparency, allows optical inspection during system operation. The low surface roughness and vertical sidewalls enable the use of different optical analytical techniques (e.g., fluorescence-based or spectrometric assays). Furthermore, it facilitates low-cost batch processing and is suitable to form deep and smooth fluidic channels in the necessary geometrical dimensions for segmented flow operation [20]. The possibility of easily integrating functional components (electrodes, waveguides) in intermediate layers and the low temperature bonding capability make it a suitable material for the manufacturing of hybrid biofluidic MEMS.

3 Scientific Results

The stability of the silane monolayer coated on the surfaces of the channel of the microfluidic chip built completely from glass to infrared light exposure has been investigated. Experiments with an optical tweezers laser setup showed that yeast cells could be held in the middle of the microchannel. These experiments were also confirmed for aqueous compartments in a nonpolar carrier medium. Yeast cells could be captured and held in the focus of the laser tweezers while a compartment moved through the channel. A change of direction in throughflow could not be observed. Corresponding experiments with structured illumination showed that cells were pushed out of focus and moved further in the direction of flow. Furthermore, fluidic characterization and various experiments to optimize the fluidic properties of prototype microfluidic chips as well as chips with SU-8 channels and others with integrated electric field cages were carried out. The current results show great promise (Fig. 2).

The application of segmented flow technology requires a hydrophobic surface, and in many cases, this requires a robust permanent hydrophobization method for channel walls (Fig. 2).

A special chip holder was built for the electric field cage experiments (Fig. 3) so that the chip could be connected electrically and fluidically.

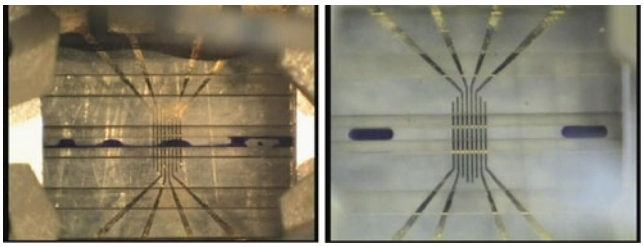

Fig. 2 Fluidic characterization of the SU-8-chip channel (aqueous phase (*blue*), nonpolar carrier fluid (*colorless*)): *left*: the aqueous phase adheres to the walls in segmented flow on untreated SU-8 channel walls; *right*: after chemical modification: flawless passage of compartments through the channel

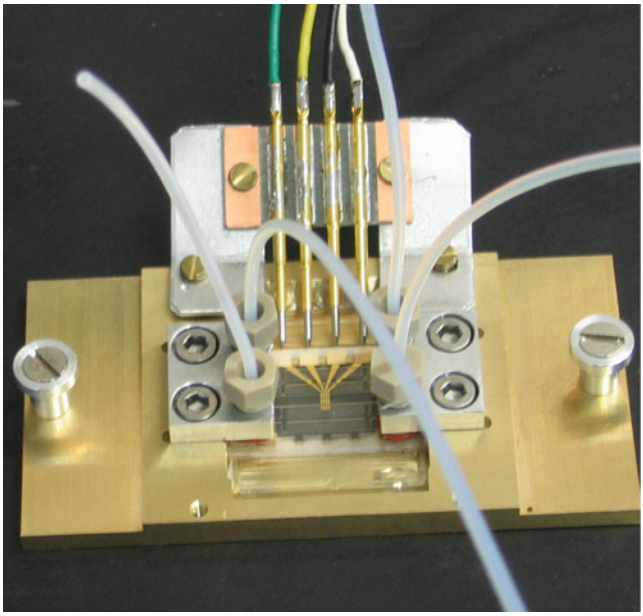

Fig. 3 Spring loaded electrical contacts connecting the optofluidic microsystem with SU-8 channels

Experiments were carried out to investigate the influence of dielectropohoresis on yeast cells, the results of which were extremely positive. Yeast cells could be transported in the channel and gathered at electrodes under the influence of high-frequency alternating current fields (Fig. 4).

One of the interesting results of the experiments was the improvement of the effectiveness of planar optical systems through integration of (discrete) refractive elements. It was shown that sustainable progress can be achieved through the combination of mechanics, optics, electronics, and nanotechnology in the field of micro-opto-electro-mechanical systems (MOEMS) [21]. The simultaneous

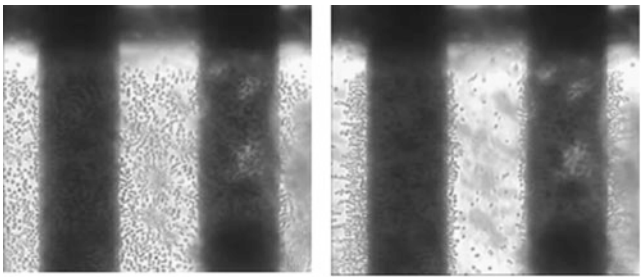

Fig. 4 Dielectrophoresis of yeast cell suspensions in a microfluidic channel (gold electrodes appear black). *Left*: no electric field applied, *right*: high-frequency alternating current fields applied

integration of fluidic systems allowed the suitability of such systems for cell cultures to be tested. In connection with this point, it is important to note that microtechnology enables the consumption of culture medium, which can be highly expensive in biotechnology, to be minimized.

4 Technologies for Optofluidic MOEMS

Special care has to be taken to design optofluidic chips that fulfill various different requirements: a fluidic part that guarantees the smooth transport of fluid segments, and an optical layout that is suitable for optical functionalities and full biocompatibility of the system. The additional integration of electrodes requires an additional process that allows one to include fully coated electrodes beneath a thin isolation. So the required properties of the optofluidic chip are as follows:

Optical requirements

- High transparency/very low absorption, under intensive laser radiation at a wavelength of $\lambda = 1{,}064$ nm
- High surface quality (flatness, roughness)
- Refractive index close to that of the fluid, no major index steps

Fluidic requirements

- Lateral resolution of 5 μm or better at a channel height larger than 200 μm
- Reliable coating with hydrophobic layers
- Very low surface roughness (stick/slip of fluidic segments)

Biological and chemical needs

- Compatibility with the carrier fluids of segmented flows (chemically inert against, e.g., alcohols, DMSO, and tetradecane)
- Biocompatibility of all parts and materials
- Temperature resistant to at least 40°C

– Transparent in the wavelength range $450 < \lambda < 600$ nm (fluorescence, optical inspection)

General issues

– Low-cost processing of devices, favorably in a batch process
– Easy change of layouts by changing only masks (requires design rules)

A careful analysis of these requirements led to the selection of SU-8-based microchannels. SU-8 is highly transparent in the required wavelength regions, and it can be fabricated in thicknesses from some microns up to some hundred microns. The device layout is achieved by simple UV lithography and thus changes in the chip design only require a new lithographic mask. This is an important advantage for a rapid prototyping against, e.g., injection molded devices that require much more complex processes for mold preparation. Nevertheless, a fabrication of larger quantities of these devices by injection molding is a suitable option. Optofluidic devices made from wet-etched or milled glass require a careful surface treatment after etching to achieve optically flat surfaces that are suitable for the optical part.

Silicon-based devices suffer from the lack of transparency in the required wavelength range. Even at 1,064 nm wavelength, silicon has a significant absorption resulting in a localized heating of the walls and the fluid close to the laser beam.

Additionally, the layer-by-layer approach of stacked SU-8 layers allows the integration of electrodes with or without contact to the liquid in the flow channels. SU-8-based chips are a perfect solution for fast sample preparation and tests.

5 Layout of Microfluidic Channels for Segmented Flow Applications

The microfluidic channels for this application should have a height of 200 μm, which is rather high for typical MEMS processes. On the contrary, "smooth" shapes are required to prevent the droplets from sticking to curved areas or at the inlet and outlet port. Also, a reliable closure of the channels is needed, which in itself does not cause sticking areas for the fluid. For all these reasons, an SU-8-based bonding process was chosen as the most suitable process. Both halves of the fluidic chip can be prepared in a very similar way; the key issue is the bonding process.

As the additional investigation of dielectrophoresis also requires capacitive electrodes reliably isolated from the fluid, a process was investigated that allows a full protection of the electrodes.

6 How to Fabricate Closed Channels Made From SU-8?

SU-8 is a UV-curing polymer suitable for spin coating. It can be applied in various thicknesses depending on the viscosity of the liquid polymer. In a final curing step after UV exposure and development, it can be fully cross-linked. After this, the polymer is extremely stable; even oxygen-based plasma etching does not remove the material significantly. The adhesion of SU-8 to typical substrate materials is usually good, although the stress within the polymer has to be taken into account to avoid stress-induced damage. Therefore, a proper curing regime is very important (Fig. 5).

As a substrate for both parts of the fluidic device (upper and lower half of the channel), commercially available borosilicate glass wafers were chosen. It was found that a prime coating of the glass surface with a thin SU-8 layer improves the adhesion of the SU-8-based parts against samples without closed film. The advantage of thin SU-8 films is that all the surfaces of the channel that the fluid contacts are from SU-8. For film preparation, low-viscosity SU-8 resulting in a 4–5-µm-thick film during spin coating was selected.

This thickness is also high enough, to bury electrodes (about 100-nm thick) completely that are favorably fabricated on the glass. The electrodes themselves are made from chromium (adhesion promoter on glass) and gold, and are structured by lift-off.

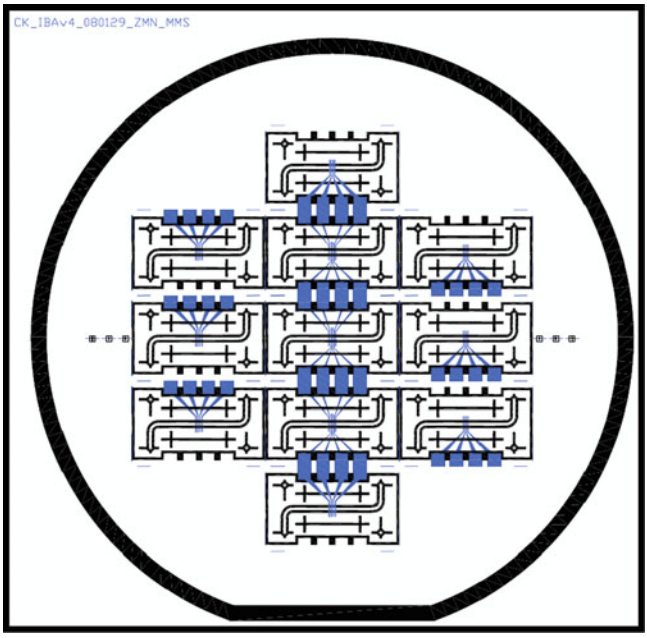

Fig. 5 Layout of test chips with a 2-mask process; wide *black lines* show the remaining SU-8 walls; electrodes with contact pads are also shown (*gray areas*)

During process development, it was found that large areas of thick SU-8 films that remain on the substrate tend to show cracks after cross-linking. Intrinsic stress on these large areas leads to a significant damage. Also, an insufficient drying after spin coating caused problems due to bubbles that appeared in the cross-linked polymer. As a result of these findings, a channel geometry was defined that prepares walls along the channels, only, to reduce the area of closed thick SU-8 layers. As a rough estimation, the wall thickness was chosen in the range of the channel width, and all structures exhibit nearly the same width, including supporting posts and walls that stabilize the sandwich structure.

One of the most important properties of SU-8 that is used here is the stepwise lithography: It is possible to expose areas of SU-8 to UV followed by a bake to support a soft cross-linking. In a next step, another layer of SU-8 can be applied and again an exposure can take place. In this case, the already performed bake makes the bottom layer insensitive to further UV radiation. After a second bake, the unexposed SU-8 of both layers can be washed out with a suitable developer; only the structures exposed to UV directly after spin coating remain. If the baking procedures are performed with great care, the structures are now stable enough to dice and handle the chips, but the cross-linking is not yet finished.

After careful cleaning and inspection of the separated chips, the upper and lower parts are aligned against each other and then the full stack is baked again, now at elevated temperature. During this procedure, a tight connection between the two SU-8 surfaces appears. No further layers of SU-8 or other glues are required. This is a big advantage for the use in biological systems because it avoids any type of glue or monomers that could come into contact with the inner walls of the channel. The only critical step is the bonding because it is responsible for the smoothness of the fluidic walls.

The use of otherwise functional materials used in MOEMS also for bonding is in general a very suitable technology. As most of these materials are already tested to be biocompatible, it avoids the addition of any other glue that may cause problems due to residual monomers. In this case, the most critical requirement is a transparent cover plate on an Si-based microfluidic chip. In principle, this technology is also suitable for glass–glass bonds.

For tight interfaces between polymers and silicon, a glueless technology is highly suitable: Stubenrauch et al. [22] used deep reactive ion etching (DRIE) to produce needle-like structures around through-holes in microfluidic devices in silicon. The needles are etched in a way making them very robust. A lithographic step for each needle is not required. Leopold et al. [23] investigated the process in detail and showed that carbon-based chains are the origin of a self-masking within the first cycles of etching. But how to join a polymer-based part to the silicon needles?—At least all thermoplastic polymers can be easily assembled. At first, the chip is heated above T_G of the polymer. If the polymer is now brought into contact with the device, the needles melt the polymer and enter the device. After cooling down, the polymer has a very tight contact with the needles. Again, no glue is required. This process is currently limited to silicon–polymer interfaces due to the material properties of silicon (Fig. 6).

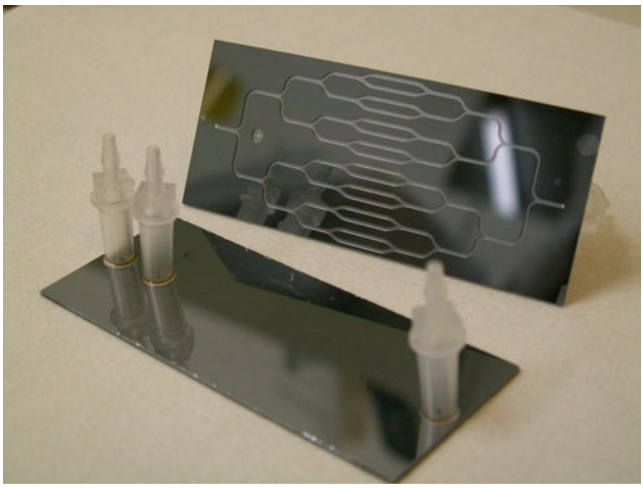

Fig. 6 Si-based fluidic chip with glueless assembly of connectors based on Si-glass

7 Coating of the Fluidic Channels

After chip preparation, the surface of SU-8 has to be prepared with hydrophobic coating [20]. It has to prevent sticking of fluid segments to hydrophilic surface elements, especially at inhomogeneities of the channel walls.

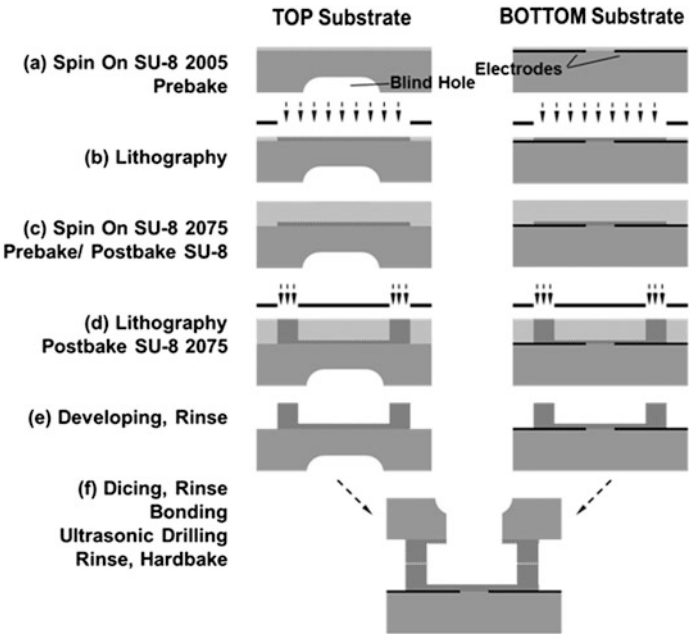

Fig. 7 Process flow for the fabrication of SU-8-based microfluidic devices with buried electrodes

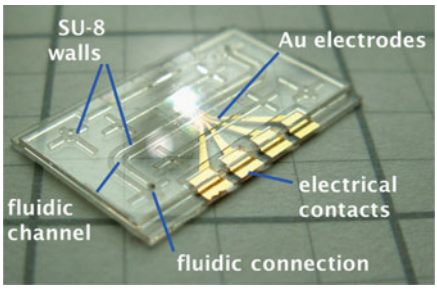

Fig. 8 Micro-opto-electro-fluidic chip based on SU-8

For sufficient adhesion of the silane layer, an activation of the surface is required. Here, the extremely high stability of SU-8 against oxidizing agents is helpful. The channels are flushed with hot piranha solution (a mixture of sulfuric acid and hydrogen peroxide) for some minutes. Surprisingly, this very aggressive solution does not attack the organic SU-8 resin; it only changes the surface in a way that the following coating has very high adhesion.

Careful purging between the steps and after silanization is required because of the risk of cross-contaminations. Here, the absence of capillary voids due to misalignments or design-induced errors during lithography is essential (Figs. 7 and 8).

8 Optical Microsystems for Micromanipulation and Sensing

A variety of approaches to microoptical systems integration have been suggested and demonstrated for applications such as optical interconnects or optical sensing [24]. Among these, the planar optical integration of free-space optical systems enables the most compact and stable integration of optical systems. To this end, the optical axis of the system is folded in such a way that all optical components can be arranged in a planar configuration [25]. Planar fabrication processes, in this case, can be exploited not only for the fabrication of the individual components. The whole system can rather be fabricated with one single fabrication procedure (lithographic or non-lithographic), where all components are, e.g., integrated in the surfaces of a single transparent substrate [26, 27]. Due to the folded optical axis, very specific design knowledge and fabrication technologies are necessary to avoid aberrations and achieve systems with optimum performance [28, 29]. These fundamental concepts for layout, design, and fabrication of planar optical systems can be exploited for the realization of complex optofluidic systems for micromanipulation and sensing in microfluidic environments [30–32]. Specifically, innovative fabrication technologies such as ultraprecision micromilling combined with diffractive microstructures offer new potential for the integration of complex optofluidic functionality [33, 34].

The fundamental concept of optical tweezing is based on the forces resulting from the interaction of light with microscopic particles. As first noted by Ashkin in the 1970s and 1980s [35], in addition to the repulsive scattering forces, the refraction and scattering of photons at microscopic particles may also result in gradient forces, allowing a 3D trapping of small particles such as cells or bacteria [36]. One of the most prominent challenges for optical tweezing in microfluidic environments stems from the limited working distance (i.e., distance between the objective lens and the optical trap) of conventional optical tweezing systems. In order to achieve reasonable trapping forces (i.e., reasonably stiff traps), it is necessary to use highly focused (high NA) beams for trapping. In the generally applied inverted microscopes, this automatically results in extremely small working distances in the range of 100 μm in immersion liquids. This contradicts the application in microfluidic channel systems with channel walls in the range of several 100 μm. Such an environment imposes specific challenges to the integration of the optical functionality.

In order to achieve optical manipulation within the segmented flow systems, we applied two different strategies. On the one hand, the concept of counter-propagating traps [37–39] has been demonstrated to work within the microfluidic systems made of transparent substrates such as fused silica or SU-8. For a second approach, we demonstrated the integration of microoptical elements into the microfluidic system in order to enhance and adapt the optical performance to the optical microsystem [40].

For counter-propagating optical tweezers, the fluidic channel is illuminated from opposite directions by moderately focused laser beams. Due to the two beams propagating in opposite directions, the scattering forces on the microparticles are compensated in such a way that 3D trapping is possible even at relatively large distances of several millimeters through the channel walls with low NA beams. Figure 9a schematically shows the layout of the system. Two microscope objective lenses optimized for large working distances are used to focus the laser beam from

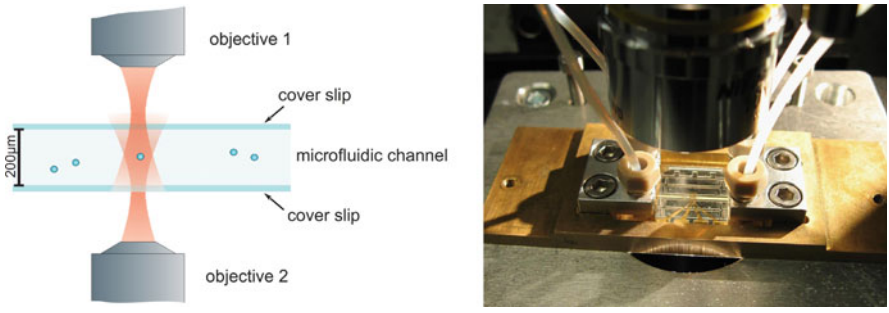

Fig. 9 (**a**) Schematic configuration of counter-propagating optical tweezers; (**b**) close-up of the experimental setup showing the upper objective lens and the microfluidic system including connectors

opposite directions into the fluidic channel. The radiation pressure and thus the positioning in axial direction can be compensated by controlling the focusing as well as the laser power in the two counter-propagating beams. At the same time, the lateral forces can be used to trap and manipulate the particles perpendicular to the optical axis. Figure 9b shows that this approach allows one to combine the optical trapping setup with the microfluidic system requiring significant space for, e.g., the fluidic connectors. We successfully demonstrated the trapping and manipulation of yeast cells within segmented flow systems with this configuration.

Microsystems integration allows one to integrate optical functionality directly into the microfluidic system. This enables the integration of additional optical functionality such as diffractive optical beam splitters. Furthermore, it is possible to define precisely the interface between the optical environment and the fluidic system. Figure 10 shows the integration of a beam-splitting diffractive optical element (DOE) into a microfluidic channel system replicated in PDMS. By integrating the DOE into a converging wave front (Fig. 10a), it is possible to achieve a compact configuration which is easy to integrate in an optofluidic setup, as shown in Fig. 10b. The DOE in such a configuration may serve a variety of purposes. The most widespread application is the generation of multiple optical traps. In this case, the multiple diffraction orders generated by the DOE may be used as individual traps. In the case of the use of immersion lenses, specific care has to be taken in order to guarantee the necessary depth of the phase profile of the DOE. In the example shown in Fig. 10, this has been achieved by additionally covering the DOE with a cover slip in order to avoid index matching of the immersion oil and the DOE profile. Figure 11 shows a sequence of photographs illustrating the performance of the system with an array of diffraction orders generated inside the fluidic channel. Each of the large NA diffraction orders may be used for the trapping of individual particles in the fluidic flow. Alternatively, the diffractive optical elements may be applied for the optimization of the optical performance of the trapping system. This way it is possible to correct for aberrations in the focus distribution that occur due to the fluidic environment. By integrating an additional focusing functionality, the DOE may also be used to extend the working distance between the external optical elements and the integrated optofluidic system.

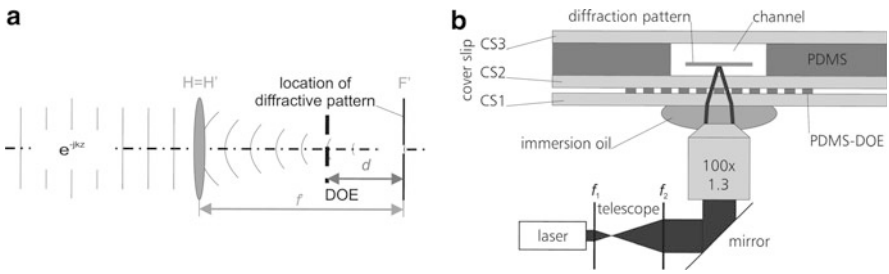

Fig. 10 Optofluidic integration of diffractive beam splitting in a compact microfluidic system: (**a**) schematic of the optical setup for a compact and flexible integration of the DOE into the optical trapping system; (**b**) schematic of the integrated system

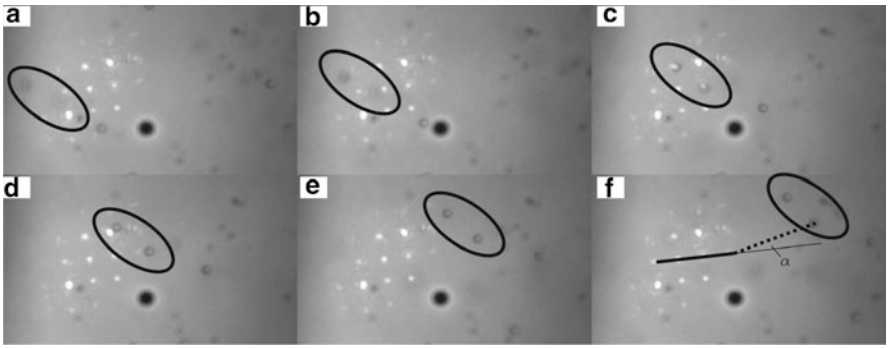

Fig. 11 Sequence of photographs showing 3D optical trapping inside an optofluidic system containing an integrated diffractive optical beam splitter

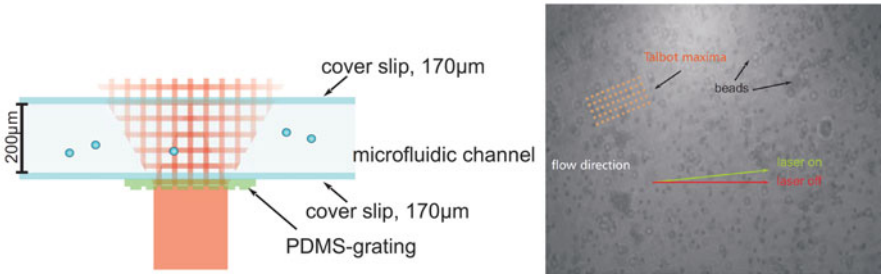

Fig. 12 Demonstration of an integrated multiple trapping system based on the Talbot effect: (**a**) schematic of the integrated system; (**b**) photograph of the particle flow inside the microfluidic channel showing the particle deflection due Talbot carpets

A third and intriguingly simple optical configuration for the implementation and integration of compact optical trapping systems is based on the so-called Talbot self-imaging of periodic diffraction gratings [41, 42]. Due to diffraction and interference of the light in the area behind a diffraction grating, a three-dimensional periodic pattern of light intensity is formed. This light distribution is sometimes called a Talbot carpet. Due to the fact that the formation of such Talbot carpets occurs without any focusing elements such as lenses or objectives, they provide the conceptually simplest approach for the formation of multiple optical traps. For the integration, it is sufficient to integrate a periodic diffraction grating into the fluidic system (Fig. 12). Upon illumination by a plane wavefront, the periodic Talbot carpets are formed. These provide a large array of multiple optical traps. Figure 12b shows the deflection of particles in a fluidic flow through such a periodic array of Talbot traps. The Talbot carpet cannot be observed here since the IR wavelength of the traping laser is filtered in order to be able to observe the flowing particles.

Since the deflection of the particles, in this case, depends on the size and further characteristics of the particles, such a highly compact system can be applied, e.g., for particle sorting inside the fluidic system.

These examples demonstrate the potential of microoptical technology to improve the applicability of optical tweezing in microfluidic systems. The combination and integration of microoptical components help to define and improve the control of the interface between the inverted microscope used to provide the highly focused trapping beam and the microfluidic system. Further improvements can be achieved if the whole optical system is designed according to the very specific needs of optical trapping. In this case, the efficiency and the working distance can be improved significantly [43].

9 Conclusions and Future Perspective

The application of a laser tweezers to hold yeast cells in the middle of a channel showed that the cells could be retained in both segmented and continuous flow. Yeast cells could be trapped and held in the laser focus during the passage of the compartments through the channel.

In order to achieve this for both the chip with SU-8 channels and the chip with integrated electric field cages, it was necessary to carry out various fluidic characterizations to improve the fluidic properties of the prototype microfluidic chips (see Fig. 13).

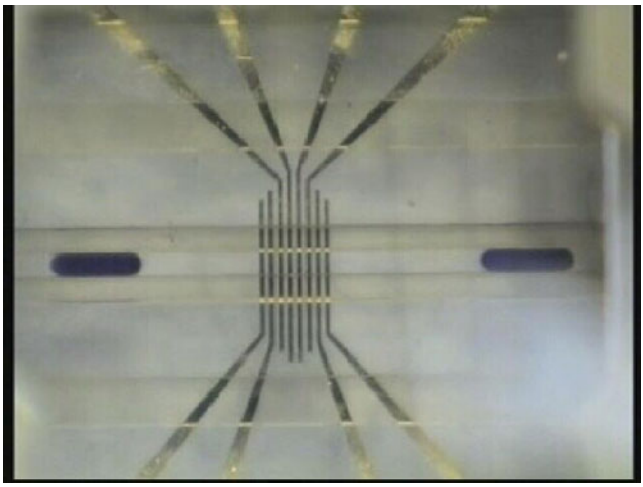

Fig. 13 Passage of compartments through the SU-8 Chip channel with integrated electric field cage electrodes

It can be expected that new concepts that make use of the complexity of integrated microsystems will lead to new applications in biotechnology and cell technology.

These concepts contain a large economic potential, as the possible functionality of the analysis platforms is substantially increased and the handling is decisively simplified. At the same time, microtechnological integration allows the consumption of very expensive culture media common in biotechnology to be minimized.

The development of completely integrated microsystems with complex optical functionality on the basis of planar optical integrated systems offers a very wide spectrum of applications across cell technology and biotechnology. Solely on the basis of the efficient handling of these systems in comparison with classic modular setups, many opportunities are opened in the already existing markets of, for instance, sensors, communications, and safety technology. On the contrary, complex microsystems open new areas of application in fields that were previously excluded by the instability and bulkiness of classically built systems. For these reasons, an economic breakthrough is predicted for integrated optical microsystems in the next years.

Acknowledgments The authors would like to acknowledge the support by all the members of their research groups. Specific contributions to the success of this project have been made by M. Amberg, A. Grodrian, Chr. Kremin, and A. Oeder.
The project has been partially funded by the "Bundesministerium für Bildung und Forschung (BMBF)," e.g., within the program "Spitzenforschung und Innovation in den neuen Ländern (PROSIN)" in the project "Kompetenzdreieck Optische Mikrosysteme—KD OptiMi" (FKZ: 16SV3700) and "Thüringer Ministerium für Bildung, Wissenschaft und Kultur (TMBWK)" with the project "Integrierte optisch-fluidische Mikrosysteme für die Mikromanipulation und Sensorik in der Biotechnologie (integrierte mikrooptische Pinzette)" (FZK: B 514—06006).

References

1. Ruzicka J, Hansen EH (1981) Flow injection analysis, chemical analysis. vol 62. Wiley, New York
2. Valcarcel M, Luque de Castro MD (1987) Flow-injection analysis. Ellis Horwood, Chichester
3. Haber C (2006) Microfluidics in commercial applications; an industry perspective. Lab Chip 6:1118–21
4. Dittrich PS, Manz A (2006) Lab-on-a-chip: microfluidics in drug discovery. Nat Rev Drug Discov 5:210–8
5. Squires TM, Quake SR (2005) Microfluidics: fluid physics at the nanoliter scale. Rev Mod Phys 77:977–1026
6. Niemeyer CM, Mirkin CA (2004) Nanobiotechnology. Wiley-VCH, Weinheim
7. Haeberle S, Zengerle R (2007) Microfluidic platforms for lab-on-a-chip applications. Lab Chip 7:1094–110
8. Henkel T, Bermig T, Kielpinski M, Grodrian A, Metze J, Köhler JM (2004) Chip modules for generation and manipulation of fluid segments for micro serial flow processes. Chem Eng J 101:439–45
9. Adzima BJ, Velankar SS (2006) Pressure drops for droplet flows in microfluidic channels. J Micromech Microeng 16:1504–10

10. Song H, Tice HD, Ismagilov RF (2003) A microfluidic system for controlling reaction networks in time. Angew Chem 42:767–72
11. Allara DL, Parikh AN, Rondelez F (1995) Evidence for a unique chain organization in long chain silane monolayers deposited on two widely different solid substrates. Langmuir 11:2357–60
12. Geerken MJ, van Zanten TS, Lammertink RGH, Bornemann Z, Nijdam W, van Rijn CJM, Wessling M (2004) Chemical and thermal stability of alkylsilane based coatings for membrane emulsification. Adv Eng Mater 6:749–54
13. Grodrian A, Metze J, Henkel T, Martin K, Roth M, Köhler JM (2004) Segmented flow generation by chip reactors for highly parallelized cell cultivation. Biosens Bioelectron 19:1421–8
14. Martin K, Henkel T, Baier V, Grodrian A, Schön T, Roth M, Köhler JM, Metze J (2003) Generation of larger numbers of separated microbial populations by cultivation in segmented-flow microdevices. Lab Chip 3:202–7
15. Carlier J, Chuda K, Arscott S, Thomy V, Verbeke B, Coqueret X, Camart JC, Druon C, Tabourier P (2006) High pressure- resistant SU-8 microchannels for monolithic porous structure integration. J Micromech Microeng 16:2211–9
16. Sato H, Matsumura H, Keino S, Shoji S (2006) An all SU-8 microfluidic chip with built-in 3D fine microstructures. J Micromech Microeng 16:2318–22
17. Jenke MG, Schreiter C, Kim GM, Vogel H, Brugger J (2007) Micropositioning and microscopic observation of individual picoliter-sized containers within SU-8 microchannels. Microfluid Nanofluid 3:189–94
18. Voskerician G, Shive MS, Shawgo RS, von Recum H, Anderson JM, Cima MJ, Langer R (2003) Biocompatibility and biofouling of MEMS drug delivery devices. Biomaterials 24:1959–67
19. Christensen TB, Pedersen CM, Gröndahl KG, Jensen TG, Sekulovic A, Bang DD, Wolff A (2007) PCR biocompatibility of lab-on-a-chip and MEMS materials. J Micromech Microeng 17:1527–32
20. Schumacher JT, Grodrian A, Kremin C, Hoffmann M, Metze J (2008) Hydrophobic coating of microfluidic chips structured by SU-8 polymer for segmented flow operation. J Micromech Microeng 18:055019
21. Motamedi ME (2005) Micro-opto-electro-mechanical-systems. ISBN 0-8194-5021-9 1
22. Stubenrauch M, Fischer M, Kremin C, Hoffmann M, Müller J (2007) Bonding of silicon with filled and unfilled polymers based on black silicon. Micro Nano Lett 2(1):S6–8
23. Leopold S, Kremin C, Ulbrich A, Krischok S, Hoffmann M (2011) Formation of silicon grass: nanomasking by carbon clusters in cyclic deep reactive ion etching. J Vac Sci Technol B 29 (1):10.1116/1.3521490
24. Sinzinger S, Jahns J (2003) Microoptics. Wiley, Weinheim. ISBN 978-3-527-40355-4
25. Jahns J, Huang A (1989) Planar integration of free—space optical components. Appl Opt 28:1602–1605
26. Sinzinger S, Jahns J (1997) Integrated micro-optical imaging system with a high interconnection capacity fabricated in planar optics. Appl Opt 36:4729–4735
27. Barbieri R, Benabes P, Bierhoff Th, Caswell JJ, Gauthier A, Jahns J, Jarczyski M, Lukowicz P, Oksman J, Russell GA, Schrage J, Snowdon JF, Stübbe O, Troster G, Wirz M (2008) Design and construction of the high-speed optoelectronic memory system demonstrator. Appl Opt 47:3500–3512
28. Testorf M, Jahns J (1999) Imaging properties of planar-integrated micro-optics. J Opt Soc Am A 16:1175–1183
29. Stoebenau S, Sinzinger S (2009) Ultraprecision machining techniques for the fabrication of freeform surfaces in highly integrated optical microsystems. SPIE-conference "Optical Manufacturing and Testing VIII", San Diego. Proc SPIE 7426:742608
30. Jahns J, Sinzinger S (2000) Microoptics for biomedical applications. American Biotechnol Lab 11, Oktober 52–54

31. Amberg M, Stoebenau S, Sinzinger S (2010) Integrated free-space optical fluorescence detector for microfluidic applications. SPIE Proc. 7716–27
32. Amberg M, Stoebenau S, Sinzinger S (2010) Single-step replication of a highly integrated PDMS optofluidic analysis system. Appl Opt 49:4326–4330
33. Stoebenau S, Kleindienst R, Kampmann R, Sinzinger S (2011) Enhanced optical functionalities by integrated ultraprecision machining techniques (keynote paper). In: 11th international conference of the European Society of Precision Engineering and Nanotechnology (EUSPEN), Lake Como, Italy. 23.5.-27.5.2011
34. Kleindienst R, Stoebenau S, Kampmann R, Sinzinger S (2011) Hybrid optical (Freeform) components – functionalization of non-planar optical surfaces by direct ps-laser ablation. Appl Opt 50:3221–3228
35. Ashkin A, Dziedzic JM, Bjorkholm JE, Chu S (1986) Observation of a single-beam gradient force optical trap for dielectric particles. Opt Lett 11(5):288–290
36. Grier DG (2003) A revolution in optical manipulation. Nature 424(6950):810–816
37. Ashkin A (1970) Acceleration and trapping of particles by radiation pressure. Phys Rev Lett 24 (4):156–159
38. Rodrigo PJ, Kelemen L, Palima D, Alonzo CA, Ormos P, Glückstad J (2009) Optical microassembly platform for constructing reconfigurable microenvironments for biomedical studies. Opt Express 17(8):6578–6583
39. Thalhammer SBG, Steiger R, Ritsch-Marte M (2011) Optical macro-tweezers: trapping of highly motile micro-organisms. J Opt 13(4):044024
40. Sinzinger S, Amberg M, Oeder A, Hein D (2007) Integrated micro-opto-fluidic systems for optical manipulation of cell cultures. OSA Annual Meeting, Frontiers in Optics, San Jose, CA. USA, 16.9.-20.9.2007
41. Talbot HF (1836) Facts relating to optical science. Phil Mag 9
42. Fournier J-M, Rohner J, Jacquot P, Johann R, Mias S, Salathé R-P (2005) Assembling mesoscopic particles by various optical schemes. Proc of SPIE, 59300Y-1
43. Oeder A, Stoebenau S, Sinzinger S (2011) Free-form optical trapping systems. In Optical Trapping Applications, OSA Technical Digest (CD) (Optical Society of America, 2011), paper OTTuC2p (Postdeadline paper) http://www.opticsinfobase.org/abstract.cfm?URI=OTA-2011-OTTuC2p

Erratum to:

Chip Systems for Analysis of Nucleic Acids with Integrated Amplification and Detection

Wolfgang Fritzsche, Mark Kielpinski, Matthias Urban, Thomas Henkel, Sabine Werres, Robert Möller, Stefan Wagner, Marko Riedel, and Sandra Julich

Erratum to:
Chip Systems for Analysis of Nucleic Acids with Integrated Amplification and Detection. In: W. Fritzsche and J. Popp (eds.), Optical Nano- and Microsystems for Bioanalytics, *Springer Series on Chemical Sensors and Biosensors* (2012) 10: 289–304
DOI 10.1007/978-3-642-25498-7_11,

In this chapter, the names of the authors ***Wolfgang Fritzsche*** *and* ***Sandra Julich*** *have erroneously been exchanged, and the indicated affiliation of the author* ***Sabine Werres*** *is wrong.*

The correct order of authors is:

Sandra Julich, Mark Kielpinski, Matthias Urban, Thomas Henkel, Sabine Werres, Robert Möller, Stefan Wagner, Marko Riedel, and Wolfgang Fritzsche

The correct affiliation of Sabine Werres is:

Julius-Kühn-Institute (JKI), Messeweg 11/12, 38104 Braunschweig, Germany

---

The online version of the original chapter can be found under
DOI 10.1007/978-3-642-25498-7_11

DOI 10.1007/978-3-642-25498-7_13,

Index

W. Fritzsche and J. Popp (eds.), *Optical Nano- and Microsystems for Bioanalytics*, Springer Series on Chemical Sensors and Biosensors (2012) 10: 325–330, DOI 10.1007/978-3-642-25498-7,